Advances in Geophysical and Environmental Mechanics and Mathematics

AGEM²

Ioana Luca
Yih-Chin Tai
Chih-Yu Kuo

Shallow Geophysical Mass Flows down Arbitrary Topography

Model Equations in Topography-fitted Coordinates, Numerical Simulation and Back-calculations of Disastrous Events

Springer

Advances in Geophysical and Environmental Mechanics and Mathematics

More information about this series at http://www.springer.com/series/7540

Ioana Luca · Yih-Chin Tai · Chih-Yu Kuo

Shallow Geophysical Mass Flows down Arbitrary Topography

Model Equations in Topography-fitted Coordinates, Numerical Simulation and Back-calculations of Disastrous Events

Springer

Ioana Luca
Department of Mathematical Methods and Models
University Politehnica of Bucharest
Bucharest
Romania

Chih-Yu Kuo
Research Center for Applied Sciences
Academia Sinica
Taipei
Taiwan

Yih-Chin Tai
Department of Hydraulic and Ocean Engineering
National Cheng Kung University
Tainan
Taiwan

ISSN 1866-8348 ISSN 1866-8356 (electronic)
Advances in Geophysical and Environmental Mechanics and Mathematics
ISBN 978-3-319-02626-8 ISBN 978-3-319-02627-5 (eBook)
DOI 10.1007/978-3-319-02627-5

Library of Congress Control Number: 2015958915

Printed on acid-free paper

This Springer imprint is published by SpringerNature
The registered company is Springer International Publishing AG Switzerland

To Professor Kolumban Hutter

Preface

The topic in the book was initiated by the long-term collaboration with Prof. Kolumban Hutter. He was consecutively invited to visit Academia Sinica, National Chi Nan University and National Cheng Kung University, Taiwan, between 2006 and 2009. During his stay and his frequent guiding communications, the research direction was planned and the ingredients were set up. The work was about the mathematical description of shallow geophysical mass flows on realistic topographies. Significant progress towards this topic has previously been made by K. Hutter and collaborators, who investigated granular flows in arbitrarily curved and twisted channels. The book, *Avalanche Dynamics* by S.P. Pudasaini and K. Hutter, is a comprehensive collection of their results. The paper by Bouchut and Westdickenberg [1] treated the basal topography as an arbitrary surface, and stimulated the interest in the modelling of flows on complex topographies. The paper deals with an ideal fluid as a model for the flowing mass and a rigid bed surface. It was the aim of our group to account for more elaborated rheologies in the description of shallow gravity-driven flows on arbitrarily curved surfaces, with the erosion/deposition process included. We concentrated the efforts in two directions—derivation of modelling equations for various geophysical flows and numerical implementation of some modelling equations, corroborated with experimental and field observations.

The objective of this monograph is twofold. First, to present, in as detailed and accessible form as possible, a way to formulate depth-averaged models for gravity-driven shallow mass flows on arbitrary topographies. Second, to show how these models can be numerically treated, experimentally tested and ultimately used for back calculations of realistic events. The presentation is based on earlier papers by the authors; however, much of the text and the derived thin-layer model equations are new.

The book is intended for civil engineers, geophysicists, geologists, physical scientists, applied mathematicians, engineers responsible for hazard management and for classroom use by students interested in geophysical flows. There are modest

demands on the student's mathematical background in linear algebra, calculus, geometry of a surface, and most of them are covered in various chapters.

To deduce modelling equations for shallow flows on arbitrary topographies, curvilinear coordinates, suitable for numerical purposes and ordering approximations even in steep topographies, are introduced. These coordinates have been used by several authors, but the depth-integration along the normal to the bed surface and the matrix form of the modelling equations are due to Buchut and Westdickenberg [1]. We have adopted the approach from [1]; however, unlike [1], we use vectors and tensors to derive the main results, making the derivations more transparent, and formulate the model equations in a more general context. To keep the presentation sufficiently accessible, we confined ourselves to the derivation of depth-averaged model equations for a shallow one-layer, one-phase fluid-like material. For shallow two-layer fluids or solid–fluid mixtures, references are given.

Two routes, called conventional and non-conventional, are followed. In the conventional route, the intrinsic modelling equations are expressed in the topography-fitted coordinates, as it is customary in continuum mechanics, and the tangential linear momentum balance equation is depth-integrated. In the non-conventional route, a hybrid form (i.e. using both Cartesian and contravariant components of vectors and tensors as functions of the terrain-fitted coordinates) of the horizontal–vertical linear momentum balance equation is depth-integrated. The depth-averaged modelling equations emerging from these two routes are not equivalent. Those in the non-conventional method seem to be more appealing, since several terms stemming from the Christoffel symbols do not arise here as they do in the modelling equations derived in the conventional route. In this monograph, the numerical implementation, experimental validation and back calculations of realistic events are performed for cases where the modelling equations as derived with the two methods coincide. Therefore, the question of the depth-averaged equations (derived by the two methods here and in fact by any other method), best suited to describe a realistic flow on arbitrary topography, is an open problem. The non-conventional route combines the approach by Bouchut and Westdickenberg [1] and Hui's unified coordinates method [2]. The unified coordinates method is a mesh velocity approach in computational fluid dynamics, based on a hybrid form (i.e. using both Cartesian and contravariant components of vectors and tensors as functions of curvilinear coordinates) of the mass and linear momentum balance equations. For the case where erosion/deposition takes place, it inspired a certain choice for the time-dependent terrain-fitted coordinates, which simplifies the modelling equations (in both routes) and avoids complicated calculations in numerical simulations.

We have endeavoured to use the same notation, style and spirit throughout. To maintain clarity in exposure, we have relegated sophisticated proofs to appendices and proposed a few exercises at the end of Chap. 2. We have also refrained from giving a list of symbols. Instead, we have collected definitions of some quantities and important rules which they satisfy at the end of a few sections.

Acknowledgements

All the authors are deeply indebted to Prof. Kolumban Hutter for bringing them together, for his motivating enthusiasm and involvement along the research progress of the group and for the invitation to prepare this book within the Springer series, *Advances in Geophysical and Environmental Mechanics and Mathematics*. We dedicate our most sincere acknowledgement to him. I. Luca takes the opportunity to express her great intellectual debts to F. Bouchut and M. Westdickenberg, whose paper [1] in *Comm. Math. Sci.* inspired her work in modelling gravity-driven shallow mass flows. Sincere gratitude goes also to all of those who made her research stay so enjoyable in Puli (National Chi Nan University), Taipei (Academia Sinica) and Tainan (National Cheng Kung University), ending as a fascinating life experience. Y.C. Tai and C.Y. Kuo express their sincere gratitude to Prof. Wai-How Hui for lecturing on the unified coordinate method during his stay in Academia Sinica, Taipei, in 2005, which inspired them to the concept of the non-conventional route. During the preparation of the manuscript, we received tremendous help from our colleagues, research assistants and students: Profs. Jia-Jyun Dong, Chien-Chih Chen, Chyi-Tyi Lee, Rou-Fei Chen, Kuo-Jen Chang, Yu-Chang Chan, Toshihiko Shimamoto, Mr. Yang-Chen Lin and Mr. Che-Ming Yang, for their efforts in rock/soil laboratory experiments and field studies; Mr. Ying-Tsao Li, Shen-En Lin, Ms. Ruo-Ying Wu, for their help in numerical simulations and results presentation; Profs. Ruey-Der Hwang, Pi-Wen Tsai and Mr. Shao-Kuan Wei, for seismic motion analysis; and Ms. Chia-Chi Shen, for typing drafts of iterated versions of different chapters. We thank all those who have supported us in this endeavour; the former and present students and scientific researchers for the fruitful collaboration that made this book possible. The grants received from the various Taiwanese research organizations and agents: Academia Sinica, Ministry of Science and Technology (former National Science Council), National Chi Nan University and National Cheng Kung University are greatly appreciated. Without their support the research would not have been possible.

Last but not least, our special thanks go to the staff, especially to Ms. Abirami Purushothaman of Springer-Verlag, for all their support in preparing the manuscript for publication.

Romania — Ioana Luca
Taiwan — Yih-Chin Tai
Taiwan — Chih-Yu Kuo
November 2015

References

[1] F. Bouchut, M. Westdickenberg, Gravity driven shallow water models for arbitrary topography. Comm. Math. Sci., **2**(3), 359–389 (2004)
[2] W.H. Hui, K. Xu, *Computational Fluid Dynamics Based on the Unified Coordinates*. (Springer-Verlag, Berlin Heidelberg New York, 2012)

Contents

Part I
Introduction

Chapter 1
Introduction

This chapter gives a brief introduction into the subject of the book, outlines the content and gathers notations and some mathematical rules that we will often use.

1.1 The Subject

Geophysical mass flows are frequent large mass movement processes, usually arising in mountain area. Examples are debris and mud flows, landslides, snow and rock avalanches, glacier flows, pyroclastic flows, lahars, clouds of ash or dust flows. They often claim many lives, produce huge damages on the surrounding areas, and are hard to be predicted. Measures intended to mitigate the impact of these natural hazards are needed, where assessing the levels of risk is one of the key tasks of the mitigation process. This requires good knowledge of the mass movement dynamics, and models predicting the flow behavior are highly desired. The rheologic complexity of the fluidized geomaterial, a lack of full understanding of how the motion is initiated and bed entrainment develops, coupled with the mathematical problem of modelling and computing, are just a few things which issue a real challenge for the scientific community in describing the dynamics of geophysical mass flows.

Many such mass flows are *shallow*, that is, their downslope or horizontal dimension is much larger than the extent in the perpendicular direction to the topographic bed. With such a geometric property the model formulation can be simplified with the aid of a shallowness parameter and depth-integration, reducing the spatial dimension from three to two. There is a large literature on shallow flows, a history of it being presented by Pudasaini and Hutter [1]. Efforts have been devoted to modelling the inception mechanism of avalanche flows, e.g. Pastor et al. [2], Cascini et al. [3, 4], Fernandez Merodo et al. [5] and the cited papers therein. Equally great interest was shown in modelling shallow geophysical mass flows in complex topographies, from their initiation to run-out. This book shares this interest, and for this reason next we refer to previous work related to this topic.

I. Luca et al., *Shallow Geophysical Mass Flows down Arbitrary Topography*,
Advances in Geophysical and Environmental Mechanics and Mathematics,
DOI 10.1007/978-3-319-02627-5_1

The Saint-Venant equations, or the so-called shallow water equations, are the first system of depth-integrated equations intended to describe free surface thin mass flows. They refer to an inviscid fluid, are based on the assumptions of hydrostatic pressure and uniform horizontal velocity component over a vertical cross section, and are commonly used for rivers and lakes with mild bed curvature. For flows on largely curved topographies these assumptions are violated. A convincing figure to support this statement is given by Dressler [6] (Fig. 2). Consequently, the applicability of the shallow water equations in many practical situations, such as spillway simulations and debris flows or snow avalanches in highly curved valleys, is limited.

Another reason of concern when dealing with arbitrarily curved terrain is that, defining the flowing mass depth vertically and applying the shallowness approximation referred to a horizontal-vertical aspect ratio, one introduces non-controllable ordering approximations in steep topographies.

The issue is how to derive modelling equations

(i) similar to the shallow water equations,
(ii) based on plausible ordering approximations,
(iii) accounting for complex rheologies, and
(iv) which incorporate effects of the bed curvature.

Coupled with the model formulation is the numerical implementation of the corresponding boundary value problem, followed by experimental tests and application to prediction or back calculation of real events.

Addressing these challenges, Savage and Hutter [7] developed a depth-averaged model for a granular material with Mohr-Coulomb rheology flowing on an inclined plane. The key ideas of the derivation of depth-averaged models for shallow mass flows of complex materials, as stated in items (i) to (iii) above, are laid down in this paper. The good prediction capabilities of the model encouraged further efforts in this direction. Depth-averaged models obeying material constitutive laws similar to those used by Savage and Hutter [7] were also derived by Denlinger and Iverson [8, 9], Iverson and Denlinger [10], Iverson et al. [11], Pitman and collaborators [12–16], Bouchut et al. [17], and Mangeney-Castelnau et al. [18, 19]. Rickenmann et al. [20], Ionescu [21] implemented viscoplastic fluids, and Gray and Edwards [22] the $\mu(I)$ rheology, in depth-averaged models.

Aiming at including curvature effects into the modelling equations (item (iv) above) quite numerous authors used coordinates that follow as far as possible the topography over which the avalanche mass is moving. Koch et al. [23–25] have done this for chute flows, Hutter et al. [26–28] for flows down a ruled surface, adequate for laboratory avalanches, and Hutter et al. [29–33] for channel flows of a granular fluid based on a curved and twisted master curve mimicking the thalweg of a valley. Dressler [6] and Sivakumaran and Dressler [34] used topography-fitted coordinates consisting of two parameters on the basal surface, and a coordinate measured along the normal to this surface. Their pressure distribution incorporates, apart from a hydrostatic contribution, a so-called centrifugal component, clearly showing that the curvature effects are accounted for by the model. These coordinates have been

further used by several authors, like Berger and Carey [35], Dewals et al. [36], De Toni and Scotton [37], Bouchut and Westdickenberg [38], Issler [39], Ionescu [40], to deduce depth-averaged modelling equations. What differentiate these models are mainly the assumptions on the velocity profile, constitutive law, the direction of depth-averaging (vertical or perpendicular to the bed surface), and the equations which are depth-integrated.

Our work follows the approach initiated by Bouchut and Westdickenberg [38], by which

- the depth-average of a quantity is defined along the flow depth, conceived as perpendicular to the bed surface,
- the averaging of the (mass and tangential momentum) balance equations is performed along the flow depth, and
- the results are expressed in matrix form.

This definition of the flow depth allows ordering approximations (in terms of a shallowness parameter) suitable even in steep topographies. Then, averaging the balance equations along the flow depth so defined turns these equations into equations for the flow depth and mean tangential velocity. Finally, the matrix form makes the results more readable and computationally appealing, benefiting from efficient numerical algorithms in matrix algebra.

To make the computations more transparent and geometrically intuitive we use the vector and tensor formalism. We follow two routes to derive general depth-averaged equations valid for arbitrarily curved topographic surfaces, be they erodible or not, and able to include any rheology consistent with the underlying ordering approximations. In the first route, which we called conventional, the mass balance and the tangential momentum balance equation are depth-averaged. In the second route, which we called non-conventional, the mass balance equation and a combination of the horizontal and vertical components of the momentum balance equation are depth-integrated. This second route was suggested by the unified coordinates approach by Hui et al. [41–43], and was motivated by the search for a moving mesh-velocity based numerical method. It revealed a computationally efficient parameterization for a moving basal surface, which can be applied for the equations derived in both routes. A numerical scheme including this parameterization is provided in the book. Laboratory experimental results and field data of realistic events are compared with the corresponding values predicted by numerical models deduced from the general depth-averaged modelling equations, showing the capabilities of these models to account for arbitrarily curved terrains.

1.2 Outline

Here is a listing of the book topics.

Part I contains this introductory chapter, in which the remaining Sect. 1.3 provides notations and some basic manipulations of matrices, vectors and tensors, needed throughout the book.

Part II addresses the main ingredients for obtaining depth-averaged modelling equations for thin flows down arbitrary topographies, be they active (i.e., deformable, moving or associated with erosion/deposition processes) or not, and is divided in two chapters.

- **Chapter** 2 Here the topography-fitted coordinates in the neighborhood of a surface are introduced.
  The chapter begins with a survey on the mathematical concept of surface, Sect. 2.1. This is intended as background material to embark the reader on the mathematical description of a topographic surface in Sect. 2.2. For an easier understanding the terrain surface is separately presented for stationary and active beds, and so are the topography-fitted coordinates introduced in Sect. 2.3. Section 2.4 identifies these coordinates as a special case of the so-called unified coordinates (UC) used by Hui and Xu [43], and shows how, in the case of an active topographic bed, the mesh movement induced by the normal velocity of the topographic surface serves to determine the parameterization of this surface.
- **Chapter** 3 It covers the need to express, in terms of the topography-fitted coordinates, some quantities (e.g., strain-rate and surface strain-rate) and the mass and linear momentum balance equations.
  First, space and time differential operators are transformed with respect to these coordinates in Sect. 3.1. Saying that operators "are expressed in curvilinear coordinates" generally means that the operators, when applied to vectors/tensors, are expressed in terms of the contravariant components of these vectors/tensors. This conception is also employed here, and we referred to the procedure based on it to deduce the modelling equations as the *conventional route*. Additionally, the divergence of a tensor field (which will play the role of the stress tensor) is written in terms of some mixed (i.e., Cartesian-contravariant) components, and the procedure based on this hybrid representation was called the *non-conventional route*. The conventional route was followed in papers by Luca et al. [44–46] and the non-conventional one (with mild basal curvature) in papers by Tai et al. [47, 48]. In this book we have unified the notations from the cited papers, followed both routes (with arbitrary basal curvature and accounting for erosion/deposition processes) for the same physical problem, and disclosed (for the first time in a public script) the relationship between the corresponding thin-layer modelling equations.
  In Sect. 3.2 the expressions of the strain-rate and surface strain-rate tensors in the topography-fitted coordinates are deduced. They will be later used when formulating constitutive equations for the flowing mass.
  Section 3.3 aims at deducing the mass and linear momentum balance laws in the topography-fitted coordinates, using both conventional and non-conventional routes. In the conventional method, which uses contravariant components of vectors and tensors, the linear momentum balance equation is split into a component normal to the topographic surface and a component tangent to this surface (a glance at these components will immediately clarify the significance of "normal" and "tangent" attributes). The non-conventional method uses both Cartesian

and contravariant components of vectors and tensors, and the linear momentum balance equation is split into a vertical component and a horizontal component.

Part III is devoted to the derivation of depth-averaged modelling equations for a gravity-driven thin mass flow down a stagnant or active (due to erosion/deposition) arbitrary topography. For simplicity the avalanching mass is conceived as a one-layer, one-constituent (or single-phase) continuum body. For two-layer or/and two-component mass flows the reader is referred to the papers Luca et al. [44, 45, 49, 50]. The material in this part is organized in three chapters.

- **Chapter** 4 Here the purpose is to deduce depth-averaged modelling equations for a thin mass flow for which the material properties are left unspecified. The equations, intended to be used to describe geophysical flows, can thus be equally applied e.g. in the lubrication theory.
  Section 4.1 states the physical problem and formulates the corresponding intrinsic 3D modelling equations. They consist of the mass and linear momentum balance equations, complemented by boundary conditions at the basal surface and at the free surface. These equations and boundary conditions are used in the subsequent sections as expressed in the topography-fitted coordinates, in both conventional and non-conventional routes.
  In Sect. 4.2 the boundary conditions are formulated in these curvilinear coordinates.
  The asymptotic analysis exploiting the shallowness of the avalanching mass requires non-dimensional variables, and these are introduced in Sect. 4.3. In the non-dimensionalization process we use a single length, L. The variables will be later scaled (Sect. 4.5.2) in terms of the aspect ratio ε of a typical thickness to the typical length L, with $\varepsilon \ll 1$.
  Section 4.4 roughly presents the depth-averaging method, in both conventional and non-conventional routes, to deduce modelling equations for the thin flow. The main point to be mentioned here is that the depth of the flowing mass is measured along the normal direction to the bed surface.
  In Sect. 4.5 the conventional route in the depth-averaging process is followed. Section 4.5.1 is devoted to the derivation of the depth-integrated mass and tangential linear momentum balance equations. The thin-layer approximations, expressed in terms of the aspect ratio ε, are stated in Sect. 4.5.2. They specify orders of magnitude of the stress components, erosion/deposition rate, and take into account the non-uniformity of the tangential velocity along the thickness of the flowing mass by approximations of Boussinesq type. The depth-averaged modelling equations for the thin mass flow are deduced in Sect. 4.5.3 by corroborating the depth-integrated mass and tangential linear momentum balance equations with the thin-layer approximations. The constitutive nature of the flowing material is not specified, and the curvature of the topographic surface is arbitrary. Section 4.5.4 hierarchically structures these models in terms of the relative weights in the stress contribution, and Sect. 4.5.5 simplifies the equations under the assumption of small curvature of the topographic surface.

In Sect. 4.6, based on the same thin-layer approximations as in Sect. 4.5.2, the non-conventional route is followed and depth-averaged modelling equations for the thin flow are derived. A motivation for following this second route is given, and the relation between the corresponding modelling equations and those from Sect. 4.5.3 is identified.

- **Chapter 5** It is devoted to the formulation of closure relations for the bed friction force, extra-stress components, and erosion/deposition rate, such that the ordering approximations are satisfied, and to indicate possible ways of choosing the parameterization of the basal surface.
  In Sect. 5.1 a sliding law, linearly combining viscous friction with bed Coulomb friction, is suggested, as in the paper by Luca et al. [51].
  Section 5.2 formulates constitutive relations for the depth-averaged stress components arising in the modelling equations. First, in Sect. 5.2.1 it is shown how the Newtonian/non-Newtonian rheology fits the ordering approximations on the stress components, and hence can stand as a candidate for constitutively describing the thin flowing mass within the modelling approach of this book. Then, in Sect. 5.2.2 Mohr-Coulomb type closure relations are presented. They are topography-adapted versions of the models by Iverson and Denlinger [10] and Savage and Hutter [7, 52, 53].
  In Sect. 5.3 a threshold criterion predicting the onset of the erosion/deposition mechanism and a law for the erosion/deposition rate are proposed, as in the paper by Tai et al. [48].
  In Sect. 5.4 we write the 2D depth-averaged modelling equations for a special case of the topographic surface (implying the reduction to a 1D version of the modelling equations) and for a Mohr-Coulomb type flowing material. Two different parameterizations of the basal surface are proposed. One of them uses arc lengths on planar cuts in the downward direction and perpendicular to it, as in the paper by Bouchut et al. [54]. The other parameterization, suitable for beds associated with erosion/deposition processess and suggested by Tai and Kuo [47], is determined by the assumption that the mesh velocity evaluated on the topographic surface equals the normal velocity of the bed surface. It is shown that, for the special surface considered here, the two parameterizations are, practically, the same. However, generally it is expected that the velocity-based moving mesh is numerically more convenient than the grid based on arc lengths.
- **Chapter 6** We discuss the findings in Chaps. 4, 5 and draw the conclusions.

Part IV elaborates the numerical implementation for the solution of the model equations. We demonstrate the applicability of the proposed model equations by numerical examples and experimental validation. Applications address back-calculation of realistic events.

- **Chapter 7** We give a brief introduction of the applied NOC schemes [55, 56] for one- and two-dimensional conservation laws. The emerging numerical schemes are explicit in time. In Sect. 7.2 we detail the implementation of the NOC schemes for the model equations over slightly curved topographic surfaces.

- **Chapter** 8 We simulate the motion of a granular material sliding down an inclined plane and merging onto a horizontal plane. The chapter is divided into three parts. In the first two parts we discuss and illustrate the key features of the model regarding two, one-dimensional and two-dimensional, numerical benchmark problems. In the third part an experimental validation is demonstrated.
  Section 8.1 is about a one-dimensional benchmark problem. Simulations are performed with and without considering the deposition process. It is shown that the numerical simulation is able to mimic the development of the deposition heap. The impact of the deposition heap on the flow behavior is documented. The effect of the earth pressure coefficient is also reported.
  In Sect. 8.2 we consider the flow of a finite granular mass sliding down an inclined chute and depositing on the horizontal plane—the two-dimensional benchmark problem. Since the development process, shapes and geometries of the deposition heap can be well described by the numerical simulation, we investigate the impacts of (a) the velocity ratio $\tilde{\chi}_b$ between the tangential velocity at the bed surface and the tangential velocity at the free surface, and of (b) the velocity profile in the flow thickness direction, on the flow behavior and final deposition heap.
  In Sect. 8.3 we consider experiments, of which the measurements are compared with the theoretical predictions. Sound agreements are obtained.
- **Chapter** 9 To conclude the continuum, shallow-water type of landslide models, the developed numerical scheme mentioned in Sect. 7.2 is applied to two important landslides in Taiwan. These landslides are first the Tsaoling landslide, triggered by the Chi-Chi earthquake, 1999, and second, the Hsiaolin landslide, triggered by the excessive rainfall brought by Typhoon Morakot in 2009. They both are deep-seated, fast and long, avalanche types of landslides. The former was situated in a geological fragile area and has long been an important site for landslide related studies. On the other hand, the latter caused more than 450 fatalities, made a strong social impact and invoked a new generation of hazard mitigation policies. With the simulation tools, the landslide motion is back-analyzed and related research validating the simulation is reviewed.

1.3 Miscellanea

The purpose of this section is to fix notations, terminology and some rules of linear algebra which we use throughout the book. It is assumed that the reader is familiar with the basic matrix operations, the concepts of vector space, inner vector space and second order tensors. In the book only real vector spaces are considered, and matrices are used as representations of vectors and tensors with respect to various bases.

Some notations

- Greek indices have the values 1 and 2, while Latin indices range from 1 to 3 or from 1 to an arbitrary positive integer n. We use the Einstein summation convention over repeated indices.
- The symbol "$\equiv$" is used to define a quantity. For instance, $v \equiv a + b$ means that v denotes the sum $a + b$. This is different from $v = a + b$, which is the assertion that a, b and v satisfy this relation.
- The Kronecker symbol is

$$\delta_{ij} \equiv \begin{cases} 1\,, & \text{if } i = j\,, \\ 0\,, & \text{if } i \neq j\,, \end{cases}$$

  where $i, j = 1, \ldots, n$. If $n = 2$, notation $\delta^{\alpha}_{\ \beta}$, where α, β are known to run from 1 to 2, will be also used for the Kronecker symbol.
- Sometimes the same symbol is used for different quantities. For instance, $\boldsymbol{I}$ denotes both the 3×3 unit matrix and the identity second order tensor on the vector space $\mathcal{V}_3$ as defined below. The context in which these symbols appear makes clear their significance.
- $\mathbb{R}$ denotes the set of real numbers.

On vectors and tensors

- To recall rules on vectors and tensors we use an arbitrary (real) vector space $\mathcal{V}$. The translation vector space of the three-dimensional Euclidean point space $\mathcal{E}$ will be denoted by $\mathcal{V}_3$. For vectors in $\mathcal{V}$ or $\mathcal{V}_3$ we use *boldface small italic* letters, e.g. $\boldsymbol{v}$. For the inner product of two vectors $\boldsymbol{u}$, $\boldsymbol{v}$, the dot product notation, $\boldsymbol{u}\cdot\boldsymbol{v}$, will be used. The second order tensors (i.e., linear transformations of a finite dimensional, real inner product space) are denoted by *boldface capital italic* letters, e.g. $\boldsymbol{D}$, or *boldface Greek* letters, e.g. $\boldsymbol{\sigma}$, or *Euler script* letters, e.g. $\mathcal{H}$.
- Let $\{\boldsymbol{e}_1, \ldots, \boldsymbol{e}_n\}$ and $\{\boldsymbol{f}_1, \ldots, \boldsymbol{f}_n\}$ be bases of a finite dimensional vector space $\mathcal{V}$, and let $\boldsymbol{f}_1, \ldots, \boldsymbol{f}_n$ be represented in terms of the basis vectors $\boldsymbol{e}_1, \ldots, \boldsymbol{e}_n$ as

$$\boldsymbol{f}_j = C_{ij}\boldsymbol{e}_i\,, \quad j = 1, \ldots, n\,.$$

  The matrix $\mathbf{C} \equiv (C_{ij})$ is called the *change of basis matrix* from $\{\boldsymbol{e}_1, \ldots, \boldsymbol{e}_n\}$ to $\{\boldsymbol{f}_1, \ldots, \boldsymbol{f}_n\}$. For a vector $\boldsymbol{v} \in \mathcal{V}$,

$$\boldsymbol{v} = v_i\boldsymbol{e}_i = v'_j\boldsymbol{f}_j\,,$$

  the components $v_1, \ldots, v_n$ and $v'_1, \ldots, v'_n$ are related by the formula

$$\begin{pmatrix} v_1 \\ \vdots \\ v_n \end{pmatrix} = \mathbf{C} \begin{pmatrix} v'_1 \\ \vdots \\ v'_n \end{pmatrix}\,. \tag{1.1}$$

- If $\boldsymbol{a}$ and $\boldsymbol{b}$ are vectors in a finite dimensional inner product space $\mathcal{V}$, $\boldsymbol{a} \otimes \boldsymbol{b}$ denotes the tensor product of $\boldsymbol{a}$ and $\boldsymbol{b}$, that is, the second order tensor on $\mathcal{V}$ defined by

$$(\boldsymbol{a} \otimes \boldsymbol{b})\boldsymbol{v} \equiv (\boldsymbol{b} \cdot \boldsymbol{v})\, \boldsymbol{a} \,.$$

- If $\{\boldsymbol{e}_1, \ldots, \boldsymbol{e}_n\}$ and $\{\boldsymbol{f}_1, \ldots, \boldsymbol{f}_n\}$ are bases of an inner product space $\mathcal{V}$, the sets

$$\left\{\boldsymbol{e}_i \otimes \boldsymbol{e}_j\right\}_{i,j=1,\ldots,n} \,, \quad \left\{\boldsymbol{e}_i \otimes \boldsymbol{f}_j\right\}_{i,j=1,\ldots,n}$$

  are bases of the vector space of second order tensors on $\mathcal{V}$.
- Let $\{\boldsymbol{e}_1, \ldots, \boldsymbol{e}_n\}$ be a basis of an inner product space $\mathcal{V}$. There exist unique vectors $\boldsymbol{e}^1, \ldots, \boldsymbol{e}^n \in \mathcal{V}$ satisfying the conditions

$$\boldsymbol{e}^i \cdot \boldsymbol{e}_j = \delta^i{}_j \,, \quad \text{for} \quad i, j = 1, \ldots, n \,. \tag{1.2}$$

  The set $\{\boldsymbol{e}^1, \ldots, \boldsymbol{e}^n\}$ is also a basis for $\mathcal{V}$. It is called the *reciprocal basis* associated to $\{\boldsymbol{e}_1, \ldots, \boldsymbol{e}_n\}$. A vector $\boldsymbol{v} \in \mathcal{V}$ and a second order tensor $\boldsymbol{\sigma}$ on $\mathcal{V}$ can then be represented as

$$\boldsymbol{v} = v^i \boldsymbol{e}_i = v_j \boldsymbol{e}^j \,, \quad \boldsymbol{\sigma} = T^{ij} \boldsymbol{e}_i \otimes \boldsymbol{e}_j = T_{ij} \boldsymbol{e}^i \otimes \boldsymbol{e}^j \,.$$

  The components v^i and T^{ij}, $i, j = 1, \ldots, n$, are called *contravariant*, while v_i and T_{ij}, $i, j = 1, \ldots, n$, are the *covariant* components of $\boldsymbol{v}$ and $\boldsymbol{\sigma}$, respectively. In the representations

$$\boldsymbol{\sigma} = T^i{}_j \boldsymbol{e}^i \otimes \boldsymbol{e}_j = \Sigma^{ij} \boldsymbol{e}_i \otimes \boldsymbol{f}_j \,,$$

  where $\{\boldsymbol{f}_1, \ldots, \boldsymbol{f}_n\}$ is another basis than $\{\boldsymbol{e}_1, \ldots, \boldsymbol{e}_n\}$ and $\{\boldsymbol{e}^1, \ldots, \boldsymbol{e}^n\}$, the components $T^i{}_j$, Σ^{ij} are called *mixed*.
  With g^{ij} and g_{ij} defined by

$$g_{ij} \equiv \boldsymbol{e}_i \cdot \boldsymbol{e}_j \,, \quad g^{ij} \equiv \boldsymbol{e}^i \cdot \boldsymbol{e}^j \,,$$

  one can check the relations

$$\boldsymbol{e}_j = g_{ij} \boldsymbol{e}^i \,, \quad \boldsymbol{e}^j = g^{ij} \boldsymbol{e}_i \,, \quad (g^{ij}) = (g_{ij})^{-1} \,. \tag{1.3}$$

  A basis $\{\boldsymbol{e}_1, \ldots, \boldsymbol{e}_n\}$ of $\mathcal{V}$ satisfying $\boldsymbol{e}_i \cdot \boldsymbol{e}_j = \delta_{ij}$ is called *orthonormal*. Clearly, the reciprocal basis associated to an orthonormal basis $\{\boldsymbol{e}_1, \ldots, \boldsymbol{e}_n\}$ coincides with $\{\boldsymbol{e}_1, \ldots, \boldsymbol{e}_n\}$: $\boldsymbol{e}^i = \boldsymbol{e}_i$, with $i = 1, \ldots, n$. For this case, the covariant components of vectors and tensors are identical with the corresponding contravariant components.
- We let $\{\boldsymbol{e}_1, \boldsymbol{e}_2, \boldsymbol{e}_3\}$ be the basis of $\mathcal{V}_3$ associated to an orthogonal Cartesian coordinate system $Ox_1x_2x_3$. We refer to $\{\boldsymbol{e}_1, \boldsymbol{e}_2, \boldsymbol{e}_3\}$ as a *Cartesian basis*. The vector space $\mathcal{V}_3$ is endowed with the inner product

$$\boldsymbol{u}\cdot\boldsymbol{v}\equiv\begin{cases}|\boldsymbol{u}||\boldsymbol{v}|\cos\theta\,, & \text{if } \boldsymbol{u},\boldsymbol{v}\neq\boldsymbol{0}\,,\\ 0\,, & \text{if } \boldsymbol{u} \text{ or } \boldsymbol{v}=\boldsymbol{0}\,,\end{cases}$$

where $|\boldsymbol{v}|$ denotes the length of $\boldsymbol{v}$ (i.e., the Euclidean distance between two points in $\mathcal{E}$ defining $\boldsymbol{v}$) and $\theta\in[0,\pi]$ is the angle between $\boldsymbol{u}$ and $\boldsymbol{v}$. With respect to this inner product the basis $\{\boldsymbol{e}_1,\boldsymbol{e}_2,\boldsymbol{e}_3\}$ is orthonormal.
The components of vectors in $\mathcal{V}_3$ and of tensors on $\mathcal{V}_3$ when using the basis $\{\boldsymbol{e}_1,\boldsymbol{e}_2,\boldsymbol{e}_3\}$ will be called Cartesian. For them the lower index notation is employed, e.g.,

$$\boldsymbol{v}=v_i\boldsymbol{e}_i\,,\quad \boldsymbol{\sigma}=\sigma_{ij}\boldsymbol{e}_i\otimes\boldsymbol{e}_j\,.$$

The inner product of $\boldsymbol{u}=u_i\boldsymbol{e}_i$ and $\boldsymbol{v}=v_i\boldsymbol{e}_i$ can be computed as $\boldsymbol{u}\cdot\boldsymbol{v}=u_iv_i$.

- The nabla symbol, ∇, designates the gradient operator of a scalar or vector field on an open subset of the three-dimensional Euclidean point space $\mathcal{E}$, that is,

$$\nabla F\equiv\frac{\partial F}{\partial x_i}\boldsymbol{e}_i\,,\quad \nabla\boldsymbol{v}\equiv\frac{\partial v_i}{\partial x_j}\boldsymbol{e}_i\otimes\boldsymbol{e}_j\,, \tag{1.4}$$

where $\{\boldsymbol{e}_1,\boldsymbol{e}_2,\boldsymbol{e}_3\}$ is the basis of $\mathcal{V}_3$ associated to the orthogonal Cartesian coordinate system $Ox_1x_2x_3$, and $\boldsymbol{v}=v_i\boldsymbol{e}_i$. The divergence operator div acting on a vector or tensor field on an open subset of $\mathcal{E}$ is defined by

$$\operatorname{div}\boldsymbol{v}\equiv\frac{\partial v_i}{\partial x_i}\,,\quad \operatorname{div}\boldsymbol{\sigma}\equiv\frac{\partial\sigma_{ij}}{\partial x_j}\,\boldsymbol{e}_i\,, \tag{1.5}$$

with $\boldsymbol{v}=v_i\boldsymbol{e}_i$ and $\boldsymbol{\sigma}=\sigma_{ij}\boldsymbol{e}_i\otimes\boldsymbol{e}_j$.

On matrices

- For an arbitrary positive integer n we denote the n-column matrices by boldface small roman letters and the $n\times n$ matrices by boldface capital roman letters. For instance,

$$\mathbf{a}\equiv(a_1,\ldots,a_n)^T\,,\quad\text{and}\quad \mathbf{A}\equiv(A_{ij})\quad\text{for}\quad i,j\in\{1,\ldots,n\}\,, \tag{1.6}$$

where the superscript T stands for the transpose of a matrix. In this book the entries of a matrix are real numbers or real functions, and we are mostly dealing with $n=2$ and $n=3$. In order to make a distinction between the cases $n=2$ and $n=3$, we resort to *boldface roman* letters and *blackboard bold* characters for 2-columns and 2×2 matrices, while *boldface italic* letters are reserved for 3-columns and 3×3 matrices. Here is a list of these notations:

$\mathbf{a}\,,\ \mathbf{b}\,,\ \ldots$	$\rightsquigarrow$	n-columns, 2-columns
$\mathbb{s}\,,\ \mathbb{t}\,,\ \ldots$	$\rightsquigarrow$	2-columns
$\boldsymbol{a}\,,\ \boldsymbol{b}\,,\ \ldots$	$\rightsquigarrow$	3-columns
$\mathbf{A}\,,\ \mathbf{B}\,,\ \ldots$	$\rightsquigarrow$	$n \times n$-matrices,2×2-matrices
$\mathbb{S}\,,\ \mathbb{T}\,,\ \ldots$	$\rightsquigarrow$	2×2-matrices
$\boldsymbol{A}\,,\ \boldsymbol{B}\,,\ \ldots$	$\rightsquigarrow$	3×3-matrices
$\mathbf{I}$	$\rightsquigarrow$	the 2×2 unit matrix
$\boldsymbol{I}$	$\rightsquigarrow$	the 3×3 unit matrix

- If $\mathbf{a}$ and $\mathbf{b}$ are both n-column matrices, $\mathbf{a} \otimes \mathbf{b}$ stands for the dyadic product of $\mathbf{a}$ and $\mathbf{b}$, that is

$$\mathbf{a} \otimes \mathbf{b} \equiv \mathbf{a}\mathbf{b}^T = (a_i b_j) \quad \text{for} \quad i, j \in \{1, \ldots, n\}\,.$$

- The set of all n-column matrices and the set of $n \times n$ matrices with real entries are vector spaces under the usual operations of matrix addition and multiplication by scalars (real numbers). Moreover, they are inner vector spaces with the inner products

$$\mathbf{a}\cdot\mathbf{b} \equiv a_i b_i \quad \text{and} \quad \mathbf{A}\cdot\mathbf{B} \equiv \mathrm{tr}\,(\mathbf{A}\mathbf{B}^T) = \mathrm{tr}\,(\mathbf{A}^T\mathbf{B})\,, \tag{1.7}$$

  where tr denotes the trace of a matrix.
- We let $\mathbf{e}_i$ denote the n-column matrix given by

$$\mathbf{e}_i \equiv (0, \ldots, \underset{i}{0}, 1, 0, \ldots 0)^T\,, \tag{1.8}$$

  with $i = 1, \ldots, n$. The set $\{\mathbf{e}_1, \ldots, \mathbf{e}_n\}$ is a basis of the vector space of n-column matrices, and $\{\mathbf{e}_i \otimes \mathbf{e}_j\}_{i,j=1,\ldots,n}$ is a basis of the vector space of $n \times n$ matrices. For a column matrix $\mathbf{a}$ and a square matrix $\mathbf{A}$, see (1.6), we have the representations

$$\mathbf{a} = a_i \mathbf{e}_i\,, \quad \mathbf{A} = A_{ij}\, \mathbf{e}_i \otimes \mathbf{e}_j\,.$$

  For $n = 2$ and $n = 3$ the vectors (1.8) are

$$\mathbf{e}_1 \equiv \begin{pmatrix} 1 \\ 0 \end{pmatrix}\,, \quad \mathbf{e}_2 \equiv \begin{pmatrix} 0 \\ 1 \end{pmatrix}\,, \tag{1.9}$$

$$\boldsymbol{e}_1 \equiv \begin{pmatrix} 1 \\ 0 \\ 0 \end{pmatrix}\,, \quad \boldsymbol{e}_2 \equiv \begin{pmatrix} 0 \\ 1 \\ 0 \end{pmatrix}\,, \quad \boldsymbol{e}_3 \equiv \begin{pmatrix} 0 \\ 0 \\ 1 \end{pmatrix}\,. \tag{1.10}$$

  Note that $\boldsymbol{e}_1, \boldsymbol{e}_2, \boldsymbol{e}_3$ are also used to denote the vectors of a Cartesian basis in $\mathcal{V}_3$.
- Let $\mathbf{A}$, $\mathbf{B}$, $\mathbf{C}$ be square matrices of order n, and let $\mathbf{a}$, $\mathbf{b}$, $\mathbf{c}$, $\mathbf{d}$, $\mathbf{v}$ be n-column matrices. The following rules of linear algebra hold true:
  (R1) $\mathbf{A}(\mathbf{a} \otimes \mathbf{b}) = \mathbf{A}\mathbf{a} \otimes \mathbf{b}$, $\quad (\mathbf{a} \otimes \mathbf{b})\mathbf{A} = \mathbf{a} \otimes \mathbf{A}^T\mathbf{b}$, $\quad (\mathbf{a} \otimes \mathbf{b})^T = \mathbf{b} \otimes \mathbf{a}$;

(R2) $(\mathbf{a}\otimes\mathbf{b})\mathbf{c}=(\mathbf{b}\cdot\mathbf{c})\mathbf{a}$, $(\mathbf{a}\otimes\mathbf{b})(\mathbf{c}\otimes\mathbf{d})=(\mathbf{b}\cdot\mathbf{c})(\mathbf{a}\otimes\mathbf{d})$;
(R3) $\mathbf{A}\mathbf{a}\cdot\mathbf{b}=\mathbf{a}\cdot\mathbf{A}^T\mathbf{b}$, $\mathbf{a}\cdot\mathbf{e}_i=a_i$, $\mathbf{A}\mathbf{e}_j\cdot\mathbf{B}\mathbf{e}_j=\mathbf{A}\cdot\mathbf{B}$;
(R4) $\mathbf{A}\cdot\mathbf{B}=\mathbf{A}^T\cdot\mathbf{B}^T$, $\mathbf{A}\cdot\mathbf{B}\mathbf{C}=\mathbf{A}\mathbf{C}^T\cdot\mathbf{B}=\mathbf{B}^T\mathbf{A}\cdot\mathbf{C}$, $\mathbf{A}\cdot(\mathbf{a}\otimes\mathbf{b})=\mathbf{A}\mathbf{b}\cdot\mathbf{a}$;
(R5) if $\mathbf{a}_1,\ldots,\mathbf{a}_n$ are the columns of $\mathbf{A}$, then $\mathbf{a}_j=\mathbf{A}\mathbf{e}_j$.

- For $n=3$ we record the following rules of multiplication of two block matrices,

(R6)

$$\begin{pmatrix}\mathbf{A} & \mathbf{a}\\ \mathbf{b}^T & \mathrm{a}\end{pmatrix}\begin{pmatrix}\mathbf{v}\\ \mathrm{v}\end{pmatrix}=\begin{pmatrix}\mathbf{A}\mathbf{v}+\mathrm{v}\mathbf{a}\\ \mathbf{b}\cdot\mathbf{v}+\mathrm{a}\mathrm{v}\end{pmatrix},$$

(R7)

$$\begin{pmatrix}\mathbf{A} & \mathbf{u}\\ \mathbf{a}^T & \mathrm{u}\end{pmatrix}\begin{pmatrix}\mathbf{B} & \mathbf{v}\\ \mathbf{b}^T & \mathrm{v}\end{pmatrix}=\begin{pmatrix}\mathbf{A}\mathbf{B}+\mathbf{u}\otimes\mathbf{b} & \mathbf{A}\mathbf{v}+\mathrm{v}\mathbf{u}\\ (\mathbf{B}^T\mathbf{a}+\mathrm{u}\mathbf{b})^T & \mathbf{a}\cdot\mathbf{v}+\mathrm{u}\mathrm{v}\end{pmatrix},$$

where $\mathbf{A}$, $\mathbf{B}$ are square matrices of order 2, $\mathbf{a}$, $\mathbf{b}$, $\mathbf{u}$, $\mathbf{v}$ are 2-column matrices, and a, u, v are real numbers. The rules *R1–R7* will generally be used without explicitly mentioning them.

- For differentiable scalar functions f, v_1, v_2 depending on x, y, and with $\mathbf{v}\equiv(v_1,v_2)^T$, we use grad f and grad $\mathbf{v}$ to denote the gradients

$$\operatorname{grad} f\equiv\begin{pmatrix}\dfrac{\partial f}{\partial x}\\ \dfrac{\partial f}{\partial y}\end{pmatrix},\quad \operatorname{grad}\mathbf{v}\equiv\begin{pmatrix}\dfrac{\partial v_1}{\partial x} & \dfrac{\partial v_1}{\partial y}\\ \dfrac{\partial v_2}{\partial x} & \dfrac{\partial v_2}{\partial y}\end{pmatrix}. \tag{1.11}$$

If f and $\mathbf{v}\equiv(v^1,v^2)$ depend on ξ^1, ξ^2, we use Grad instead of grad, i.e.,

$$\operatorname{Grad} f\equiv\begin{pmatrix}\dfrac{\partial f}{\partial\xi^1}\\ \dfrac{\partial f}{\partial\xi^2}\end{pmatrix},\quad \operatorname{Grad}\mathbf{v}\equiv\begin{pmatrix}\dfrac{\partial v^1}{\partial\xi^1} & \dfrac{\partial v^1}{\partial\xi^2}\\ \dfrac{\partial v^2}{\partial\xi^1} & \dfrac{\partial v^2}{\partial\xi^2}\end{pmatrix}. \tag{1.12}$$

Notation Div stands for the divergence operator referring to ξ^1, ξ^2,

$$\operatorname{Div}\mathbf{v}\equiv\frac{\partial v^\alpha}{\partial\xi^\alpha},\quad \operatorname{Div}\mathbf{T}\equiv\frac{\partial T^{\alpha\beta}}{\partial\xi^\beta}\,\mathbf{e}_\alpha, \tag{1.13}$$

where $\mathbf{v}=(v^1,v^2)$ and $\mathbf{T}$ is a 2×2 -matrix function with $T^{\alpha\beta}$ as entries.

- Here we record some differential rules, the quantities entering them being defined as previously explained:

$$\operatorname{Grad}(\mathbf{A}\mathbf{v})=\mathbf{A}\operatorname{Grad}\mathbf{v}+\frac{\partial\mathbf{A}}{\partial\xi^\alpha}\mathbf{v}\otimes\mathbf{e}_\alpha, \tag{1.14}$$

$$\mathbf{A}\mathrm{Grad}\,(\mathbf{Bv}) = \mathrm{Grad}\,(\mathbf{ABv}) - \frac{\partial \mathbf{A}}{\partial \xi^\alpha}\mathbf{Bv}\otimes\mathbf{e}_\alpha\,, \tag{1.15}$$

$$\mathrm{Grad}\,(f\mathbf{v}) = f\,\mathrm{Grad}\,\mathbf{v} + \mathbf{v}\otimes\mathrm{Grad}\,f\,, \tag{1.16}$$

$$\mathrm{Div}\,\mathbf{AB} = \mathbf{A}\,\mathrm{Div}\,\mathbf{B} + \frac{\partial \mathbf{A}}{\partial \xi^\alpha}\mathbf{Be}_\alpha\,. \tag{1.17}$$

- Here we prove that, if a second order matrix $\mathbf{A} = A_{\alpha\beta}\mathbf{e}_\alpha\otimes\mathbf{e}_\beta$ with real entries depending on $(\xi^1,\xi^2)\in\mathbb{R}^2$ has the property

$$\frac{\partial A_{\alpha\beta}}{\partial \xi^\gamma} = \frac{\partial A_{\alpha\gamma}}{\partial \xi^\beta}\,, \tag{1.18}$$

for $\alpha,\beta,\gamma = 1,2$, then, for any 2-column matrices $\mathbf{u} = u_\alpha\mathbf{e}_\alpha$ and $\mathbf{v} = v_\alpha\mathbf{e}_\alpha$, relation

$$\frac{\partial \mathbf{A}}{\partial \xi^\alpha}(\mathbf{u}\otimes\mathbf{v} - \mathbf{v}\otimes\mathbf{u})\mathbf{e}_\alpha = \mathbf{0} \tag{1.19}$$

holds. Indeed, we have

$$\begin{aligned} v_\alpha\frac{\partial \mathbf{A}}{\partial \xi^\alpha} &= v_\alpha\frac{\partial A_{\beta\gamma}}{\partial \xi^\alpha}\mathbf{e}_\beta\otimes\mathbf{e}_\gamma = v_\alpha\frac{\partial A_{\beta\alpha}}{\partial \xi^\gamma}\mathbf{e}_\beta\otimes\mathbf{e}_\gamma \\ &= \frac{\partial A_{\beta\alpha}}{\partial \xi^\gamma}(\mathbf{e}_\beta\otimes\mathbf{e}_\alpha)(\mathbf{v}\otimes\mathbf{e}_\gamma) = \frac{\partial \mathbf{A}}{\partial \xi^\gamma}(\mathbf{v}\otimes\mathbf{e}_\gamma)\,, \end{aligned}$$

and therefore

$$\begin{aligned} \frac{\partial \mathbf{A}}{\partial \xi^\alpha}(\mathbf{u}\otimes\mathbf{v} - \mathbf{v}\otimes\mathbf{u})\mathbf{e}_\alpha &= v_\alpha\frac{\partial \mathbf{A}}{\partial \xi^\alpha}\mathbf{u} - u_\alpha\frac{\partial \mathbf{A}}{\partial \xi^\alpha}\mathbf{v} \\ &= \frac{\partial \mathbf{A}}{\partial \xi^\alpha}(\mathbf{v}\otimes\mathbf{e}_\alpha)\mathbf{u} - u_\alpha\frac{\partial \mathbf{A}}{\partial \xi^\alpha}\mathbf{v} = \mathbf{0}\,, \end{aligned}$$

which proves (1.19).

References

1. S.P. Pudasaini, K. Hutter, *Avalanche Dynamics: Dynamics of Rapid Flows of Dense Granular Avalanches*. (Springer, 2007)
2. M. Pastor, M. Quecedo, J.A. Fernandez, Meroo, M.I. Herreros, E. Gonzales, P. Mira, Flows of materials with yield. J. Rheol. **31**, 385–404 (1987)
3. L. Cascini, S. Cuomo, M. Pastor, G. Sorbino, Modelling of rainfall-induced shallow landslides of the flow-type catastrophic landslides. J. Geotech. Geoenviron. Eng. **136**(1), 85–98 (2010)
4. L. Cascini, S. Cuomo, M. Pastor, Inception of debris avalanches: remarks on geomechanical modelling. Landslides **10**(6), 701–711 (2013)

5. J.A. Fernandez Merodo, M. Pastor, P. Mira, L. Tonni, M. Quecedo, M.I. Herreros, E. Gonzales, R. Tamagnini, Modelling of diffuse failure mechanisms of catastrophic landslides. Comput. Methods Appl. Mech. Eng. **193**(27), 2911–2939 (2004)
6. R.F. Dressler, New nonlinear shallow flow equations with curvature. J. Hydraul. Res. **16**, 205–222 (1978)
7. S.B. Savage, K. Hutter, The motion of a finite mass of granular material down a rough incline. J. Fluid. Mech. **199**, 177–215 (1989)
8. R.P. Denlinger, R.M. Iverson, Flow of variably fluidised granular masses across three-dimensional terrain. II. J. Geophys. Res. **106**, 552–566 (2001)
9. R.P. Denlinger, R.M. Iverson, Granular avalanches across irregular three-dimensional terrain. I: theory and computation. J. Geophys. Res. **109**(F1), (2004)
10. R.M. Iverson, R.P. Denlinger, Flow of variably fluidised granular masses across three-dimensional terrain. I. Coulomb mixture theory. J. Geophys. Res. **106**, 537–552 (2001)
11. R.M. Iverson, M. Logan, R.P. Denlinger, Granular avalanches across irregular three-dimensional terrain. II: experimental tests. J. Geophys. Res., **109**(No. F1):F01015 (2004). doi:10.1029/2003JF000084
12. A.K. Patra, A.C. Bauer, C.C. Nichita, E.B. Pitman, M.F. Sheridan, M. Bursik, B. Rupp, A. Weber, A. Stinto, L. Namikawa, C. Renschler, Parallel adaptive numerical simulation of dry avalanches over natural terrain. J. Volcanol. Geoth. Res. **139**(1–2), 1–21 (2005)
13. E.B. Pitman, The mechanics of particle-fluid flow at high solids volume fraction, in *Proceedings of IUTAM Symposium on Segregation in Granular Materials*, ed. by A. Rosato, D. Blackmore (Boston: Kluver, 2000), pp. 241–254
14. E.B. Pitman, A.K. Patra, A.C. Bauer, C.C. Nichita, M.F. Sheridan, M. Bursik, Computing granular avalanches and landslides. Phys. Fluids **15**, 3638–3646 (2003)
15. M.F. Sheridan, J.L. Macias, Estimation of risk probability for gravity driven pyroclastic flows at Volcano Colima. Mexico. J. Volcanol. Geoth. Res. **66**, 251–256 (1995)
16. M.F. Sheridan, A.J. Stinton, A.K. Patra, E.B. Pitman, A.C. Bauer, C.C. Nichita, Evaluating TITAN2D mass flow using the 1963 Little Tahoma Peak Avalanches. J. Volcanol. Geoth. Res. **139**(1–2), 89–102 (2005)
17. F. Bouchut, A. Mangeney-Castelnau, B. Perthame, J.P. Vilotte, A new model of Saint-Venant and Savage-Hutter type for gravity driven shallow water flows. C. R. Acad. Sci. Paris **I336**, 531–536 (2003)
18. A. Mangeney-Castelnau, J.P. Vilotte, M.O. Bristeau, B. Perthame, F. Bouchut, C. Simeoni, S. Yerneni, Numerical modelling of avalanches based on Saint Venant equations using a kinetic scheme. J. Geophys. Res. **108**:(B11)2527 (2003)
19. A. Mangeney, F. Bouchut, N. Thomas, J.P. Vilotte, M.O. Bristeau, Numerical modeling of self channeling granular flows and of their levee/channel deposits. J. Geophys. Res. **112**, F02017 (2007)
20. D. Rickenmann, D. Laigle, B.W. McArdell, J. Hübl, Comparison of 2D debris-flow simulation models with field events. Comput. Geosci. **10**, 241–264 (2006)
21. I.R. Ionescu, Onset and dynamic shallow flow of a viscoplastic fluid on a plane slope. J. Non-Newton. Fluid Mech. **165**, 1328–1341 (2010)
22. J.M.N.T. Gray, A.N. Edwards, A depth-averaged $\mu(I)$ rheology for shallow granular free surface flows. J. Fluid Mech. **755**, 503–534 (2014)
23. K. Hutter, T. Koch, Motion of a granular avalanche in an exponentially curved chute: experiments and theoretical predictions. Phil. Trans. R. Soc. A **334**, 93–138 (1991)
24. R. Greve, K. Hutter, Motion of a granular avalanche in a convex and concave curved chute: experiments and theoretical predictions. Phil. Trans. R. Soc. A **342**, 573–600 (1993)
25. R. Greve, T. Koch, K. Hutter, Unconfined flow of granular avalanches along a partly curved surface. I: theory. Proc. R. Soc. A. **445**, 399–413 (1994)
26. J.M.N.T. Gray, M. Wieland, K. Hutter, Gravity-driven free surface flow of granular avalanches over complex basal topography. Proc. R. Soc. A. **455**, 1841–1874 (1999)
27. T. Koch, R. Greve, K. Hutter, Unconfined flow of granular avalanches along a partly curved chute, II. Experiments and numerical computations. Proc. R. Soc. A. **445**, 415–435 (1994)

28. M. Wieland, J.M.N.T. Gray, K. Hutter, Channelized free surface flow of cohessionless granular avalanches in a chute with shallow lateral curvature. J. Fluid Mech. **392**, 73–100 (1999)
29. S.P. Pudasaini, W. Eckart, K. Hutter, Gravity-driven rapid shear flows of dry granular masses in helically curved and twisted channels. Math. Mod. Meth. Appl. Sci. **13**(7), 1019–1052 (2003)
30. S.P. Pudasaini, K. Hutter, Rapid shear flows of dry granular masses down curved and twisted channels. J. Fluid Mech. **495**, 193–208 (2003)
31. S.P. Pudasaini, Y. Wang, K. Hutter, Rapid motions of free-surface avalanches down curved and twisted channels and their numerical simulations. Phil. Trans. R. Soc. A. **363**, 1551–1571 (2005)
32. S.P. Pudasaini, Y. Wang, K. Hutter, Dynamics of avalanches along general mountain slopes. Ann. Glacol. **38**, 357–362 (2005)
33. S.P. Pudasaini, Y. Wang, L.T. Sheng, Y.C. Tai, S.H. Chou, S.S. Hsiau, K. Hutter, Avalanching granular flow down curved and twisted channels: theory and particle tracking velocimetry (PTV) experiments, Department of Mechanics, Darmstadt University of Technology, Preprint, 2005
34. N.S. Sivakumaran, R.F. Dressler, Unsteady density-current equations for highly curved terrain. J. Atmos. Sci. **46**(20), 3192–3201 (1989)
35. R.C. Berger, G.F. Carey, A perturbation anlysis and finite element approximate model for free surafce flows over curved beds. Int. J. Num. Meth. Eng. **31**, 493–507 (1991)
36. B.J. Dewals, S. Erpicum, P. Archambau, S. Detrembleur, M. Pirotton, Depth-integrated flow modeling taking into account bottom curvature. J. Hydraul. Res. **44**, 785–795 (2006)
37. S. De Toni, P. Scotton, Two-dimensional mathematical and numerical model for the dynamics of granular avalanches. Cold Reg. Sci. Technol. **43**, 36–48 (2005)
38. F. Bouchut, M. Westdickenberg, Gravity driven shallow water models for arbitrary topography. Comm. Math. Sci. **2**(3), 359–389 (2004)
39. D. Issler, Depth-averaged flow models on arbitrarily curved topography, pp.1–39 (2007). http://snf.ngi.no/reports/issler_Curvature.pdf
40. I.R. Ionescu, Viscoplastic shallow flow equations with topography. J. Non-Newton. Fluid Mech. **193**, 116–128 (2013)
41. W.H. Hui, S. Koudriakov, Computation of the shallow water equations using the unified coordinates. SIAM J. Sci. Comput. **23**, 1615 (2002)
42. W.H. Hui, The unified coordinate system in computational fluid dynamics. Commun. Comput. Phys. **2**(4), 577–610 (2007)
43. W.H. Hui, K. Xu, *Computational Fluid Dynamics Based on the Unified Coordinates* (Springer, Berlin, 2012)
44. K. Hutter, I. Luca, Two-layer debris mixture flows on arbitrary terrain with mass exchange at the base and the interface. Continuum Mech. Thermodyn. **24**(4–6), 525–558 (2012)
45. I. Luca, K. Hutter, C.Y. Kuo, Y.C. Tai, Two-layer models for shallow avalanche flows over arbitrary variable topography. Int. J. Adv. Eng. Sci. Appl. Math. **1**, 99–121 (2009)
46. I. Luca, Y.C. Tai, C.Y. Kuo, Non-Cartesian topography-based avalanche equations and approximations of gravity driven flows of ideal and viscous fluids. Math. Mod. Meth. Appl. Sci. **19**, 127–171 (2009)
47. Y.C. Tai, C.Y. Kuo, A new model of granular flows over general topography with erosion and deposition. Acta Mech. **199**, 71–96 (2008)
48. Y.C. Tai, C.Y. Kuo, W.H. Hui, An alternative depth-integrated formulation for granular avalanches over temporally varying topography with small curvature. Geophys. Astrophys. Fluid Dyn. **106**(6), 596–629 (2012)
49. I. Luca, Y.C. Tai, C.Y. Kuo, Modelling shallow gravity-driven solid-fluid mixtures over arbitrary topography. Comm. Math. Sci. **7**(1), 1–36 (2009)
50. I. Luca, C.Y. Kuo, K. Hutter, Y.C. Tai, Modeling shallow over-saturated mixtures on arbitrary rigid topography. J. Mech. **28**(3), 523–541 (2012)
51. I. Luca, K. Hutter, Y.C. Tai, C.Y. Kuo, A hierarchy of avalanche models on arbitrary topography. Acta Mech. **205**, 121–149 (2009)

52. K. Hutter, S. B. Savage. Avalanche dynamics: the motion of a finite mass of gravel down a mountain side, in Proceedings of the 5th International Symposium on Landslides (Lausanne, 1988), pp. 691–697
53. S.B. Savage, K. Hutter, The dynamics of avalanches of granular materials from initiation to runout. Part I: analysis. Acta Mech. **86**, 201–223 (1991)
54. F. Bouchut, E.D. Fernández-Nieto, A. Mangeney, P.-Y. Lagrée, On new erosion models of Savage-Hutter type for avalanches. Acta Mech. **199**, 181–208 (2008)
55. H. Nessyahu, E. Tadmor, Non-oscillatory central differencing for hyperbolic conservation laws. J. Comput. Phys. **87**(2), 408–463 (1990)
56. G.S. Jiang, E. Tadmor, Non-oscillatory central schemes for multidimensional hyperbolic conservation laws. SIAM J. Sci. Comput. **19**(6), 1892–1917 (1998)

Part II
A Topography-Fitted Coordinate System and Related Issues

Chapter 2
A Topography-Fitted Coordinate System

This chapter is devoted to the presentation of the curvilinear coordinates that we use for the description of a shallow mass flow down arbitrary topography. In the first section basic concepts on the geometry and kinematics of a surface are provided. They will be smoothly applied in the next section, which deals with the parameterization of the topographic surface. With these prerequisites topography-fitted coordinates are then introduced. These coordinates have been used to describe thin flows by Dressler [1], De Toni and Scotton [2], Bouchut and Westdickenberg [3], Ionescu [4], to name only a few. We follow the approach initiated by Bouchut and Westdickenberg [3], by which the results are expressed in matrix form. However, unlike [3], we use vectors and tensors and their contravariant components to derive the main results, which makes the computations geometrically more intuitive, and allows an easy extension of the flow modelling from ideal fluids to arbitrary materials, from slightly curved topographic surfaces to those with arbitrary curvature, and from rigid to moving material and erodible topographies.

2.1 Basics of the Geometry and Kinematics of a Surface

We present some elementary concepts and rules from the geometry and kinematics of a surface. These concepts/rules are probably already familiar to the reader, but providing them here we offer careful definitions, notations and a collection of properties which will enable us to model the basal topography. Besides, the material serves to keep the book self-determined as much as possible.

2.1.1 Basics of the Geometry of a Surface

Consider a regular surface $\mathcal{S}$ in the three-dimensional Euclidean space $\mathcal{E}$, given by the parametrization

I. Luca et al., *Shallow Geophysical Mass Flows down Arbitrary Topography*,
Advances in Geophysical and Environmental Mechanics and Mathematics,
DOI 10.1007/978-3-319-02627-5_2

$$x_1 = x_1(\Delta^1, \Delta^2)\,, \quad x_2 = x_2(\Delta^1, \Delta^2)\,, \quad x_3 = x_3(\Delta^1, \Delta^2) \tag{2.1}$$

with respect to an orthogonal Cartesian coordinate system $Ox_1x_2x_3$. Here, (Δ^1, Δ^2) belongs to some open set $\mathcal{D} \subset \mathbb{R}^2$, the functions x_1, x_2, x_3 are in $C^2(\mathcal{D})$ (i.e., x_1, x_2, x_3 are twice continuously differentiable on $\mathcal{D}$), and

$$\operatorname{rank}\left(\frac{\partial x_i}{\partial \Delta^\alpha}\right) = 2\,. \tag{2.2}$$

A point $Q \in \mathcal{S}$ has the Cartesian coordinates determined by (2.1) for some $(\Delta^1, \Delta^2) \in \mathcal{D}$, and the position vector $\boldsymbol{r}$ given by

$$\boldsymbol{r}(\Delta^1, \Delta^2) = x_1(\Delta^1, \Delta^2)\,\boldsymbol{e}_1 + x_2(\Delta^1, \Delta^2)\,\boldsymbol{e}_2 + x_3(\Delta^1, \Delta^2)\,\boldsymbol{e}_3\,,$$

where $\{\boldsymbol{e}_1, \boldsymbol{e}_2, \boldsymbol{e}_3\}$ is the standard basis of the translation vector space $\mathcal{V}_3$ of $\mathcal{E}$ and associated to the Cartesian system $Ox_1x_2x_3$, see Fig. 2.1a. Condition (2.2) guarantees the linear independence of the vectors

$$\boldsymbol{\tau}_\alpha \equiv \frac{\partial \boldsymbol{r}}{\partial \Delta^\alpha}\,, \quad \alpha \in \{1, 2\}\,, \tag{2.3}$$

at Q, and so $\boldsymbol{\tau}_1$ and $\boldsymbol{\tau}_2$ build a basis, called the *natural basis*, for the vector space which they generate (called, the *tangent space* to $\mathcal{S}$ at Q). Let $\{\boldsymbol{\tau}^1, \boldsymbol{\tau}^2\}$ be the reciprocal basis corresponding to the natural basis $\{\boldsymbol{\tau}_1, \boldsymbol{\tau}_2\}$ (see (1.2) for the concept of reciprocal basis). With the following definitions of the scalars $\phi_{\alpha\beta}, \phi^{\alpha\beta}, \alpha, \beta \in \{1, 2\}$,

$$\phi_{\alpha\beta} \equiv \boldsymbol{\tau}_\alpha \cdot \boldsymbol{\tau}_\beta\,, \quad \phi^{\alpha\beta} \equiv \boldsymbol{\tau}^\alpha \cdot \boldsymbol{\tau}^\beta\,, \tag{2.4}$$

we immediately obtain the relations

$$\boldsymbol{\tau}_\beta = \phi_{\alpha\beta}\boldsymbol{\tau}^\alpha, \quad \boldsymbol{\tau}^\beta = \phi^{\alpha\beta}\boldsymbol{\tau}_\alpha\,, \quad \left(\phi^{\alpha\beta}\right) = \left(\phi_{\alpha\beta}\right)^{-1}\,, \tag{2.5}$$

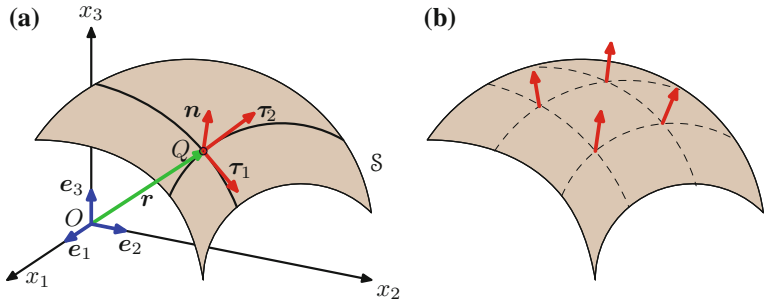

Fig. 2.1 **a** The Cartesian coordinate system $Ox_1x_2x_3$, the position vector $\boldsymbol{r}$ of a point Q on the surface $\mathcal{S}$, and the bases $\{\boldsymbol{e}_1, \boldsymbol{e}_2, \boldsymbol{e}_3\}$, $\{\boldsymbol{\tau}_1, \boldsymbol{\tau}_2, \boldsymbol{n}\}$ of $\mathcal{V}_3$; **b** a unit normal vector field on $\mathcal{S}$

see also (1.3). According to (2.4), it is clear that the matrices $\left(\phi_{\alpha\beta}\right)$ and $\left(\phi^{\alpha\beta}\right)$ are symmetric and positive definite; the scalars $\phi_{\alpha\beta}$ are called the *coefficients of the first fundamental form* of $\mathcal{S}$ at Q (corresponding to the parametrization (2.1) of the surface $\mathcal{S}$).

In the next considerations we assume that we are given a unit normal vector field $\boldsymbol{n}$ to $\mathcal{S}$, varying continuously on $\mathcal{S}$,[1] see Fig. 2.1b. We take such a vector field as

$$\boldsymbol{n} = \frac{\boldsymbol{\tau}_1 \times \boldsymbol{\tau}_2}{\|\boldsymbol{\tau}_1 \times \boldsymbol{\tau}_2\|}\,; \tag{2.6}$$

this $\boldsymbol{n}$ is shown in Fig. 2.1a. For further use we note that $\boldsymbol{\tau}_1, \boldsymbol{\tau}_2, \boldsymbol{n}$, evaluated at $Q \in \mathcal{S}$, form a basis of the vector space $\mathcal{V}_3$.

Now, since $\boldsymbol{n} \cdot \boldsymbol{n} = 1$, the derivatives of $\boldsymbol{n}$ with respect to Δ^1 and Δ^2 are vectors in the tangent space to $\mathcal{S}$ at Q,[2] so that we have the representation

$$\frac{\partial \boldsymbol{n}}{\partial \Delta^\beta} = -b_{\alpha\beta}\,\boldsymbol{\tau}^\alpha\,, \tag{2.7}$$

which defines the *coefficients $b_{\alpha\beta}$ of the second fundamental form* of $\mathcal{S}$ (corresponding to the parametrization (2.1) and to the normal vector field $\boldsymbol{n}$). With the relation $\boldsymbol{\tau}_\alpha \cdot \boldsymbol{n} = 0$ it can be shown that $(b_{\alpha\beta})$ is a symmetric matrix. Indeed,

$$\begin{aligned} b_{\alpha\beta} &\overset{(2.7)}{=} -\boldsymbol{\tau}_\alpha \cdot \frac{\partial \boldsymbol{n}}{\partial \Delta^\beta} = \frac{\partial \boldsymbol{\tau}_\alpha}{\partial \Delta^\beta} \cdot \boldsymbol{n} \overset{(2.3)}{=} \frac{\partial}{\partial \Delta^\beta}\left(\frac{\partial \boldsymbol{r}}{\partial \Delta^\alpha}\right) \cdot \boldsymbol{n} \\ &= \frac{\partial}{\partial \Delta^\alpha}\left(\frac{\partial \boldsymbol{r}}{\partial \Delta^\beta}\right) \cdot \boldsymbol{n} \overset{(2.3)}{=} \frac{\partial \boldsymbol{\tau}_\beta}{\partial \Delta^\alpha} \cdot \boldsymbol{n} = -\boldsymbol{\tau}_\beta \cdot \frac{\partial \boldsymbol{n}}{\partial \Delta^\alpha} \overset{(2.7)}{=} b_{\beta\alpha}\,. \end{aligned} \tag{2.8}$$

The *curvature tensor* of the surface $\mathcal{S}$ (to which the unit vector field $\boldsymbol{n}$ has been associated) is defined by

$$\mathcal{H} \equiv b_{\alpha\beta}\,\boldsymbol{\tau}^\alpha \otimes \boldsymbol{\tau}^\beta\,. \tag{2.9}$$

Relation $(2.5)_2$ can be used to represent $\mathcal{H}$ as

$$\mathcal{H} = b_{\gamma\beta}\,\boldsymbol{\tau}^\gamma \otimes \boldsymbol{\tau}^\beta = \phi^{\alpha\gamma} b_{\gamma\beta}\,\boldsymbol{\tau}_\alpha \otimes \boldsymbol{\tau}^\beta = W^\alpha{}_\beta\,\boldsymbol{\tau}_\alpha \otimes \boldsymbol{\tau}^\beta\,, \tag{2.10}$$

where

$$W^\alpha{}_\beta \equiv \phi^{\alpha\gamma} b_{\gamma\beta}\,.$$

The matrix $\mathbf{W} \equiv (W^\alpha{}_\beta)$ is called the *Weingarten curvature matrix*, and the scalar

$$\Omega \equiv \tfrac{1}{2}\mathrm{tr}\,\mathcal{H} = \tfrac{1}{2}\mathrm{tr}\,\mathbf{W} \tag{2.11}$$

---

[1] The pair $(\mathcal{S}, \boldsymbol{n})$ is called an *oriented surface*. Of course, $(\mathcal{S}, -\boldsymbol{n})$ is another oriented surface.

[2] $\boldsymbol{n} \cdot \boldsymbol{n} = 1 \implies \dfrac{\partial}{\partial \Delta^\alpha}(\boldsymbol{n} \cdot \boldsymbol{n}) = 0 \implies \dfrac{\partial \boldsymbol{n}}{\partial \Delta^\alpha} \cdot \boldsymbol{n} = 0\,.$

defines the *mean curvature* of $\mathcal{S}$. Note that the following matrix relation

$$\mathbf{W} = (\phi^{\alpha\gamma})(b_{\gamma\beta}) \tag{2.12}$$

holds. We also mention that relation (2.7) can be further written as

$$\frac{\partial \boldsymbol{n}}{\partial \Delta^\beta} = -b_{\gamma\beta}\,\boldsymbol{\tau}^\gamma = -\phi^{\alpha\gamma} b_{\gamma\beta}\,\boldsymbol{\tau}_\alpha = -W^\alpha{}_\beta\,\boldsymbol{\tau}_\alpha\,. \tag{2.13}$$

Let us now change the parametric representation of $\mathcal{S}$, i.e., consider the change of variables

$$\Delta^\alpha = \Delta^\alpha(\xi^1, \xi^2)\,, \quad (\xi^1, \xi^2) \in \mathcal{D}_0\,, \quad \alpha \in \{1, 2\}\,, \tag{2.14}$$

with $\mathcal{D}_0$ an open subset of $\mathbb{R}^2$. Thus, according to (2.1), another parameterization of $\mathcal{S}$ is expressible as

$$x_k = x_k(\Delta^1(\xi^1, \xi^2),\ \Delta^2(\xi^1, \xi^2)) \equiv \tilde{x}_k(\xi^1, \xi^2)\,, \quad k \in \{1, 2, 3\}\,, \tag{2.15}$$

and the position vector $\boldsymbol{r}$ can be written as

$$\boldsymbol{r} = \tilde{\boldsymbol{r}}(\xi^1, \xi^2) = \tilde{x}_1(\xi^1, \xi^2)\boldsymbol{e}_1 + \tilde{x}_2(\xi^1, \xi^2)\boldsymbol{e}_2 + \tilde{x}_3(\xi^1, \xi^2)\boldsymbol{e}_3\,.$$

On $\mathcal{S}$ we consider the normal vector field $\boldsymbol{n}$ defined in (2.6). We denote by $\mathbf{F}$ the Jacobian matrix of the transformation (2.14),

$$\mathbf{F} \equiv \left(\frac{\partial \Delta^\alpha}{\partial \xi^\beta}\right)\,, \quad \det \mathbf{F} \neq 0\,, \tag{2.16}$$

and by $\tilde{\phi}_{\alpha\beta}, \tilde{b}_{\alpha\beta}, \widetilde{\mathbf{W}}$ the quantities corresponding to the parametrization (2.15), similar to $\phi_{\alpha\beta}$, $b_{\alpha\beta}$ and $\mathbf{W}$. It can be checked that the following relations,

$$(\tilde{\phi}_{\alpha\beta}) = \mathbf{F}^T(\phi_{\alpha\beta})\mathbf{F}\,, \quad (\tilde{b}_{\alpha\beta}) = \mathbf{F}^T(b_{\alpha\beta})\mathbf{F}\,, \quad \widetilde{\mathbf{W}} = \mathbf{F}^{-1}\mathbf{W}\mathbf{F}\,, \tag{2.17}$$

hold (see Exercise 2.1). Notice that, if $\boldsymbol{n}$ is given by (2.6), as we have agreed, $\boldsymbol{n}$ can be computed by a similar formula when dealing with the parameterization (2.15), that is,

$$\boldsymbol{n} = \frac{\tilde{\boldsymbol{\tau}}_1 \times \tilde{\boldsymbol{\tau}}_2}{\|\tilde{\boldsymbol{\tau}}_1 \times \tilde{\boldsymbol{\tau}}_2\|}\,, \quad \text{with} \quad \tilde{\boldsymbol{\tau}}_\alpha \equiv \frac{\partial \tilde{\boldsymbol{r}}}{\partial \xi^\alpha}\,, \quad \alpha \in \{1, 2\}, \tag{2.18}$$

if and only if $\det \mathbf{F} > 0$ (see Exercise 2.2).

2.1.2 Basics of a Moving Surface

Just to be not so abstract and to motivate the introduction of the concept of a moving surface, we mention that the topographic surface corresponding to a topographic bed which is erodible, or on which sediment may be deposited, is described as a moving surface; its speed of propagation (see the definition below) is the erosion/deposition rate (see the forthcoming Sect. 2.2.2).

We consider a moving surface (with respect to the reference system $Ox_1x_2x_3$), that is, a one-parameter family $\mathcal{S} \equiv \{\mathcal{S}_t\}_{t\in I}$ ($I \subset \mathbb{R}$—open interval) of regular surfaces $\mathcal{S}_t$ given as

$$x_1 = x_1(\Delta^1, \Delta^2, t), \quad x_2 = x_2(\Delta^1, \Delta^2, t), \quad x_3 = x_3(\Delta^1, \Delta^2, t)\,, \tag{2.19}$$

where $(\Delta^1, \Delta^2) \in \mathcal{D} \subset \mathbb{R}^2$, $\mathcal{D}$ is an open subset, and the functions $x_1,\ x_2,\ x_3$ are of class C^2 on $\mathcal{D} \times I$.

Clearly, for each instant t we are given a parameterized surface $\mathcal{S}_t$ as in Sect. 2.1.1. By choosing a continuous unit normal vector field to $\mathcal{S}_t$ according to (2.6), everything that has been shown in Sect. 2.1.1 is valid for $\mathcal{S}_t$. Of course, the geometric quantities, e.g. the coefficients of the fundamental forms, $\phi_{\alpha\beta}, b_{\alpha\beta}$, are generally time dependent. Now we are interested in the time dependence of $x_1,\ x_2,\ x_3$. With the aid of the position vector of the surface point (Δ^1, Δ^2) at time t,

$$\boldsymbol{r} = \boldsymbol{r}(\Delta^1, \Delta^2, t) = x_1(\Delta^1, \Delta^2, t)\,\boldsymbol{e}_1 + x_2(\Delta^1, \Delta^2, t)\,\boldsymbol{e}_2 + x_3(\Delta^1, \Delta^2, t)\,\boldsymbol{e}_3,$$

we define the *velocity* $\boldsymbol{u}_{\mathcal{S}}$ of (Δ^1, Δ^2) at the instant t by

$$\boldsymbol{u}_{\mathcal{S}} \equiv \frac{\partial \boldsymbol{r}}{\partial t}\,. \tag{2.20}$$

With respect to the basis $\{\boldsymbol{\tau}_1, \boldsymbol{\tau}_2, \boldsymbol{n}\}$ of $\mathcal{V}_3$, $\boldsymbol{u}_{\mathcal{S}}$ has the representation

$$\boldsymbol{u}_{\mathcal{S}} = \mathcal{U}^\beta\,\boldsymbol{\tau}_\beta + \mathcal{U}\,\boldsymbol{n}\,. \tag{2.21}$$

The normal component $\mathcal{U}$ of $\boldsymbol{u}_{\mathcal{S}}$ satisfies the relation

$$\mathcal{U} = \boldsymbol{u}_{\mathcal{S}} \cdot \boldsymbol{n}\,, \tag{2.22}$$

and is a quantity intrinsic to $\mathcal{S}$, that is, independent of the parameterization of $\mathcal{S}$ (see the forthcoming $(2.26)_2$). It is called the *speed of displacement* (*propagation*) of the surface $\mathcal{S}$.

If the moving surface (2.19) is implicitly described by

$$F(x_1, x_2, x_3, t) = 0\,, \tag{2.23}$$

a unit normal vector $\boldsymbol{n}$ to $\mathcal{S}_t$ can be determined as

$$\boldsymbol{n} = \nabla F / \|\nabla F\| \quad \text{with} \quad \nabla F \equiv \frac{\partial F}{\partial x_k}\, \boldsymbol{e}_k \,. \tag{2.24}$$

We suppose that F is chosen in such a way that $\boldsymbol{n}$ computed via (2.24) is the same as the prescribed unit normal vector (2.6). Inserting (2.19) into (2.23) and differentiating the emerging relation with respect to t, we obtain

$$\frac{\partial F}{\partial t} + \nabla F \cdot \boldsymbol{u}_{\mathcal{S}} = 0 \,, \tag{2.25}$$

which is called the *evolution equation* for $\mathcal{S}$ or the *kinematic equation* of $\mathcal{S}$. Substituting $\nabla F = \|\nabla F\| \boldsymbol{n}$ into (2.25) and using (2.22), we deduce

$$\frac{\partial F}{\partial t} + \|\nabla F\| \mathcal{U} = 0 \quad \Longleftrightarrow \quad \mathcal{U} = -\frac{\partial F}{\partial t} / \|\nabla F\| \,. \tag{2.26}$$

If the speed of displacement $\mathcal{U}$ is known, however F in (2.23) is unknown, relation $(2.26)_1$ stands for the determination of F as a function of space and time. This is the case in this book when modelling an erosion/deposition process: the erosion/deposition rate $\mathcal{U}$ is postulated, and the evolution of the topographic profile is determined via the kinematic equation. Relation $(2.26)_2$ indicates the independence of $\mathcal{U}$ of the parameterization of $\mathcal{S}$.

2.2 Mathematical Description of the Topographic Surface

Nowadays, remote sensing technology, such as Light Detection and Ranging (LIDAR) or Interferometric Synthetic Aperture Radar (InSAR), are widely applied in the modern Geographic Information Systems (GIS), where the topographic surface is generally represented by a set of altitudes of terrain locations over a regular horizontal grid, i.e., the DTM. These profile data can be interpolated for an explicit representation in Cartesian coordinates, which explains the mathematical description which we give below for the topographic surface.

If the topographic bed is deformable[3] or moving or is associated with erosion/deposition processes, it will be called *active*. If not active, the topographic bed will be designated as *stationary* or *rigid* or *stagnant*. In Sect. 2.2.1 we consider a rigid bed, so that the corresponding topographic surface is modelled as a stationary surface. In Sect. 2.2.2 we switch to an active topographic bed, and model its topographic surface as a moving surface.

[3]For slow motion of a large (ice) mass on a deforming lithosphere, this case is important.

2.2.1 Topographic Surface as a Stationary Surface

In this section we assume a rigid topographic bed, and describe the topographic surface as a surface $\mathcal{S}_b$ given explicitly by

$$x_3 = b(x_1, x_2)\,, \quad (x_1, x_2) \in \mathcal{D} \subset \mathbb{R}^2\,,$$

where $\mathcal{D}$ is an open set, and $b \in C^2(\mathcal{D})$. Physically, x_1 and x_2 lie on the horizontal plane, whilst x_3 points upwards against the direction of gravity; b gives the bed elevation. Our derivations use the implicit representation of $\mathcal{S}_b$,

$$F_b(x_1, x_2, x_3) = 0\,, \quad \text{with} \quad F_b(x_1, x_2, x_3) \equiv x_3 - b(x_1, x_2)\,, \tag{2.27}$$

and the parametric representation

$$x_1 = x\,, \quad x_2 = y\,, \quad x_3 = b(x, y) \quad \text{for} \quad (x,\ y) \in \mathcal{D}\,, \tag{2.28}$$

which gives the position vector $\boldsymbol{r}_b$ of a point Q on $\mathcal{S}_b$ as

$$\boldsymbol{r}_b = \boldsymbol{r}_b(x, y) = x\boldsymbol{e}_1 + y\boldsymbol{e}_2 + b(x, y)\boldsymbol{e}_3\,. \tag{2.29}$$

We may think of the representation (2.28) as corresponding to the choice $\Delta^1 \equiv x$, $\Delta^2 \equiv y$ in the general presentation from Sect. 2.1.1. We take the continuous unit normal vector field $\boldsymbol{n}_b$ on $\mathcal{S}_b$ to point *into* the flowing material. Figure 2.1, in which the surface $\mathcal{S}$ was designed to represent the topographic surface $\mathcal{S}_b$, can be used to have a geometric/physical representation on $\mathcal{S}_b$.

Considering parameterization (2.28) of $\mathcal{S}_b$ and the above mentioned unit vector $\boldsymbol{n}_b$, we determine the matrices $(\phi_{\alpha\beta})$, $(\phi^{\alpha\beta})$ and the Weingarten matrix $\mathbf{W}$, which have been introduced in Sect. 2.1.1.

First, the two vectors of the natural basis of the tangent space to $\mathcal{S}_b$ are given by

$$\boldsymbol{\tau}_1 \equiv \frac{\partial \boldsymbol{r}_b}{\partial x} = \boldsymbol{e}_1 + \frac{\partial b}{\partial x}\,\boldsymbol{e}_3\,, \quad \boldsymbol{\tau}_2 \equiv \frac{\partial \boldsymbol{r}_b}{\partial y} = \boldsymbol{e}_2 + \frac{\partial b}{\partial y}\,\boldsymbol{e}_3\,, \tag{2.30}$$

implying the following expressions for the coefficients of the first fundamental form,

$$\phi_{11} \equiv \boldsymbol{\tau}_1 \cdot \boldsymbol{\tau}_1 = 1 + \left(\frac{\partial b}{\partial x}\right)^2\,, \quad \phi_{22} \equiv \boldsymbol{\tau}_2 \cdot \boldsymbol{\tau}_2 = 1 + \left(\frac{\partial b}{\partial y}\right)^2\,,$$
$$\phi_{12} \equiv \boldsymbol{\tau}_1 \cdot \boldsymbol{\tau}_2 = \frac{\partial b}{\partial x}\,\frac{\partial b}{\partial y}\,.$$

With these expressions it can be easily checked that the matrix $(\phi_{\alpha\beta})$ emerges as

$$(\phi_{\alpha\beta}) = \mathbf{I} + \operatorname{grad} b \otimes \operatorname{grad} b\,, \tag{2.31}$$

which yields, see Exercise 2.4,

$$(\phi^{\alpha\beta}) = (\phi_{\alpha\beta})^{-1} = \mathbf{I} - \frac{1}{1 + \operatorname{grad} b \cdot \operatorname{grad} b} \operatorname{grad} b \otimes \operatorname{grad} b \,. \tag{2.32}$$

With the notations

$$c \equiv (1 + \operatorname{grad} b \cdot \operatorname{grad} b)^{-1/2} \,, \quad \mathbf{s} \equiv c \operatorname{grad} b \,, \tag{2.33}$$

the matrices $(\phi_{\alpha\beta})$, $(\phi^{\alpha\beta})$ can be written in a more compact form as

$$(\phi_{\alpha\beta}) = \mathbf{I} + \frac{1}{c^2} \mathbf{s} \otimes \mathbf{s} \,, \quad (\phi^{\alpha\beta}) = \mathbf{I} - \mathbf{s} \otimes \mathbf{s} \,. \tag{2.34}$$

We explicitly record the relation

$$\left(\mathbf{I} + \frac{1}{c^2} \mathbf{s} \otimes \mathbf{s} \right)^{-1} = \mathbf{I} - \mathbf{s} \otimes \mathbf{s} \,, \tag{2.35}$$

to which we will refer in some derivations.

The unit normal vector $\boldsymbol{n}_b$ can be determined by using representation (2.27) of $\mathcal{S}_b$. One obtains

$$\boldsymbol{n}_b = \frac{\nabla F_b}{\|\nabla F_b\|} = -s_1 \boldsymbol{e}_1 - s_2 \boldsymbol{e}_2 + c \boldsymbol{e}_3 \,, \tag{2.36}$$

where s_1, s_2 are the components of $\mathbf{s}$, $(s_1, s_2)^T \equiv \mathbf{s}$. Now we are able to compute the coefficients of the second fundamental form,

$$\begin{aligned}
b_{11} = -\boldsymbol{\tau}_1 \cdot \frac{\partial \boldsymbol{n}_b}{\partial x} &= -\left(\boldsymbol{e}_1 + \frac{\partial b}{\partial x} \boldsymbol{e}_3 \right) \cdot \left(-\frac{\partial s_1}{\partial x} \boldsymbol{e}_1 - \frac{\partial s_2}{\partial x} \boldsymbol{e}_2 + \frac{\partial c}{\partial x} \boldsymbol{e}_3 \right) \\
&= \frac{\partial s_1}{\partial x} - \frac{\partial b}{\partial x} \frac{\partial c}{\partial x} = c \, \frac{\partial^2 b}{\partial x^2} \,, \\
b_{12} = -\boldsymbol{\tau}_1 \cdot \frac{\partial \boldsymbol{n}_b}{\partial y} &= -\left(\boldsymbol{e}_1 + \frac{\partial b}{\partial x} \boldsymbol{e}_3 \right) \cdot \left(-\frac{\partial s_1}{\partial y} \boldsymbol{e}_1 - \frac{\partial s_2}{\partial y} \boldsymbol{e}_2 + \frac{\partial c}{\partial y} \boldsymbol{e}_3 \right) \\
&= \frac{\partial s_1}{\partial y} - \frac{\partial b}{\partial x} \frac{\partial c}{\partial y} = c \, \frac{\partial^2 b}{\partial x \partial y} = b_{21} \,, \\
b_{22} = -\boldsymbol{\tau}_2 \cdot \frac{\partial \boldsymbol{n}_b}{\partial y} &= -\left(\boldsymbol{e}_2 + \frac{\partial b}{\partial y} \boldsymbol{e}_3 \right) \cdot \left(-\frac{\partial s_1}{\partial y} \boldsymbol{e}_1 - \frac{\partial s_2}{\partial y} \boldsymbol{e}_2 + \frac{\partial c}{\partial y} \boldsymbol{e}_3 \right) \\
&= \frac{\partial s_2}{\partial y} - \frac{\partial b}{\partial y} \frac{\partial c}{\partial y} = c \, \frac{\partial^2 b}{\partial y^2} \,,
\end{aligned} \tag{2.37}$$

which implies

$$(b_{\alpha\beta}) = c\,\mathbf{H}\,, \quad \text{with} \quad \mathbf{H} \equiv \operatorname{grad}(\operatorname{grad} b) = \begin{pmatrix} \dfrac{\partial^2 b}{\partial x^2} & \dfrac{\partial^2 b}{\partial x \partial y} \\ \dfrac{\partial^2 b}{\partial x \partial y} & \dfrac{\partial^2 b}{\partial y^2} \end{pmatrix}. \tag{2.38}$$

With (2.12), $(2.34)_2$ and (2.38) we immediately deduce that the Weingarten matrix $\mathbf{W}$ is given by

$$\mathbf{W} = (\phi^{\alpha\beta})(b_{\beta\gamma}) = c\,(\mathbf{I} - \mathbf{s} \otimes \mathbf{s})\,\mathbf{H}\,. \tag{2.39}$$

We note the following relations,

$$\mathbf{s}\cdot\mathbf{s} + c^2 = 1\,, \tag{2.40}$$

$$\operatorname{grad} c = -\frac{1}{c}\,(\operatorname{grad}\mathbf{s})^T\mathbf{s} = -c^2\,\mathbf{H}\mathbf{s}\,, \quad \operatorname{grad}\mathbf{s} = \mathbf{W}\,, \tag{2.41}$$

which we will need in some computations. Relation (2.40) expresses the fact that $\|\boldsymbol{n}\| = 1$, and for the proof of (2.41) we refer the interested reader to Exercise 2.3.

For numerical computations it is sometimes more convenient to use surface parameters on $\mathcal{S}_b$ different from the Cartesian parameters x, y as in (2.28). We denote these parameters by ξ^1, ξ^2. Thus, the change of variables

$$x = x(\xi^1, \xi^2)\,, \quad y = y(\xi^1, \xi^2)\,, \quad (\xi^1, \xi^2) \in \mathcal{D}_0\,, \tag{2.42}$$

with functions x, y of class C^2 on the computational domain $\mathcal{D}_0$, yields the parameterization

$$x_1 = x(\xi^1, \xi^2), \quad x_2 = y(\xi^1, \xi^2), \quad x_3 = b\big(x(\xi^1, \xi^2), y(\xi^1, \xi^2)\big) \equiv \tilde{b}(\xi^1, \xi^2)\,, \tag{2.43}$$

and the position vector $\boldsymbol{r}_b$ of a point on $\mathcal{S}_b$, see (2.29), as

$$\boldsymbol{r}_b(x, y) = x(\xi^1, \xi^2)\boldsymbol{e}_1 + y(\xi^1, \xi^2)\boldsymbol{e}_2 + \tilde{b}(\xi^1, \xi^2)\boldsymbol{e}_3 \equiv \tilde{\boldsymbol{r}}_b(\xi^1, \xi^2)\,. \tag{2.44}$$

We denote by $\mathbf{F}$ the Jacobian matrix of the transformation (2.42),

$$\mathbf{F} \equiv \begin{pmatrix} \dfrac{\partial x}{\partial \xi^1} & \dfrac{\partial x}{\partial \xi^2} \\ \dfrac{\partial y}{\partial \xi^1} & \dfrac{\partial y}{\partial \xi^2} \end{pmatrix}, \quad \det\mathbf{F} \neq 0\,. \tag{2.45}$$

If we assume

$$\det\mathbf{F} > 0\,, \tag{2.46}$$

the prescribed normal vector field on $\mathcal{S}_b$ can be determined by formula (2.18), where now $\tilde{\boldsymbol{\tau}}_1, \tilde{\boldsymbol{\tau}}_2$ correspond to (2.43), see Exercise 2.1. However, in the derivations employed in this book we will never express $\boldsymbol{n}_b$ by this formula, so that assumption (2.46) is not important, only $\det \mathbf{F} \neq 0$ counts.

From now on, we will no longer use the natural basis $\{\boldsymbol{\tau}_1, \boldsymbol{\tau}_2\}$ corresponding to the Cartesian parameterization, see (2.30). That is why the vectors $\tilde{\boldsymbol{\tau}}_1, \tilde{\boldsymbol{\tau}}_2$ will be simply denoted by $\boldsymbol{\tau}_1, \boldsymbol{\tau}_2$, and they should not be confused with $\boldsymbol{\tau}_1, \boldsymbol{\tau}_2$ from (2.30). In short, $\boldsymbol{\tau}_1, \boldsymbol{\tau}_2$ refer to the parameterization (2.43), and, therefore, with (2.44) we have

$$\boldsymbol{\tau}_1 = \frac{\partial x}{\partial \xi^1}\boldsymbol{e}_1 + \frac{\partial y}{\partial \xi^1}\boldsymbol{e}_2 + \frac{\partial \tilde{b}}{\partial \xi^1}\boldsymbol{e}_3\,, \quad \boldsymbol{\tau}_2 = \frac{\partial x}{\partial \xi^2}\boldsymbol{e}_1 + \frac{\partial y}{\partial \xi^2}\boldsymbol{e}_2 + \frac{\partial \tilde{b}}{\partial \xi^2}\boldsymbol{e}_3\,. \tag{2.47}$$

However, we indicate by the tilde symbol the coefficients of the first and second fundamental forms referring to the parameterization (2.43). We further introduce the notations

$$\mathbf{M}_0 \equiv (\tilde{\phi}^{\alpha\beta})\,, \quad \widetilde{\mathbf{H}} \equiv (\tilde{b}_{\alpha\beta})\,, \tag{2.48}$$

and use them, together with (2.34), (2.38), (2.39) and $(2.41)_1$, to rewrite formulae (2.17), now relating quantities corresponding to the parameterizations (2.28) and (2.43). That is,

$$\begin{aligned} (\tilde{\phi}_{\alpha\beta}) = \mathbf{F}^T(\phi_{\alpha\beta})\mathbf{F} \quad &\Longleftrightarrow \quad \mathbf{M}_0^{-1} = \mathbf{F}^T\left(\mathbf{I} + \frac{1}{c^2}\mathbf{s}\otimes\mathbf{s}\right)\mathbf{F}\,, \\ (\tilde{b}_{\alpha\beta}) = \mathbf{F}^T(b_{\alpha\beta})\mathbf{F} \quad &\Longleftrightarrow \quad \widetilde{\mathbf{H}} = c\,\mathbf{F}^T\mathbf{H}\mathbf{F}\,, \\ \widetilde{\mathbf{W}} = \mathbf{F}^{-1}\mathbf{W}\mathbf{F} \quad &\Longleftrightarrow \quad \widetilde{\mathbf{W}} = \mathbf{M}_0\widetilde{\mathbf{H}}\,. \end{aligned} \tag{2.49}$$

In $(2.49)_3$ we have used the relation

$$\mathbf{M}_0 = \mathbf{F}^{-1}(\mathbf{I} - \mathbf{s}\otimes\mathbf{s})\mathbf{F}^{-T}\,, \tag{2.50}$$

as deduced from $(2.49)_1$ and (2.35).

We close this section by the following two remarks. First, recalling definition (1.12) for Grad f, Grad $\mathbf{v}$, where f is a scalar field and $\mathbf{v}$ is a 2-column matrix field depending on ξ^1 and ξ^2, we have

$$\operatorname{Grad} c = \mathbf{F}^T \operatorname{grad} c\,, \quad \operatorname{Grad}\mathbf{s} = (\operatorname{grad}\mathbf{s})\mathbf{F}\,.$$

When combined with (2.41), $(2.49)_2$ and $\mathbf{W}\mathbf{F} = \mathbf{F}\widetilde{\mathbf{W}}$, this yields the formulae

$$\operatorname{Grad} c = -c\,\widetilde{\mathbf{H}}\mathbf{F}^{-1}\mathbf{s}\,, \quad \operatorname{Grad}\mathbf{s} = \mathbf{F}\widetilde{\mathbf{W}}\,. \tag{2.51}$$

Secondly, we will need the change of basis matrix $\boldsymbol{P}$ from the basis $\{\boldsymbol{e}_1, \boldsymbol{e}_2, \boldsymbol{e}_3\}$ to the basis $\{\boldsymbol{\tau}_1, \boldsymbol{\tau}_2, \boldsymbol{n}_b\}$ of $\mathcal{V}_3$, as well as the inverse matrix $\boldsymbol{P}^{-1}$. Inspection of (2.36) and (2.47) shows that

$$\boldsymbol{P} = \begin{pmatrix} \dfrac{\partial x}{\partial \xi^1} & \dfrac{\partial x}{\partial \xi^2} & -s_1 \\ \dfrac{\partial y}{\partial \xi^1} & \dfrac{\partial y}{\partial \xi^2} & -s_2 \\ \dfrac{\partial b}{\partial x}\dfrac{\partial x}{\partial \xi^1} + \dfrac{\partial b}{\partial y}\dfrac{\partial y}{\partial \xi^1} & \dfrac{\partial b}{\partial x}\dfrac{\partial x}{\partial \xi^2} + \dfrac{\partial b}{\partial y}\dfrac{\partial y}{\partial \xi^2} & c \end{pmatrix} \tag{2.52}$$

$$= \begin{pmatrix} \mathbf{F} & -\mathbf{s} \\ (\mathbf{F}^T \operatorname{grad} b)^T & c \end{pmatrix} = \begin{pmatrix} \mathbf{F} & -\mathbf{s} \\ \frac{1}{c}(\mathbf{F}^T\mathbf{s})^T & c \end{pmatrix}.$$

To deduce $\boldsymbol{P}^{-1}$ we decompose $\boldsymbol{P}$ as[4]

$$\boldsymbol{P} = \begin{pmatrix} \mathbf{I} & -\mathbf{s} \\ \frac{1}{c}\mathbf{s}^T & c \end{pmatrix} \begin{pmatrix} \mathbf{F} & \mathbf{0} \\ \mathbf{0} & 1 \end{pmatrix}, \tag{2.53}$$

which immediately allows the derivation in block-form of $\boldsymbol{P}^{-1}$,

$$\begin{aligned} \boldsymbol{P}^{-1} = \begin{pmatrix} \mathbf{F} & \mathbf{0} \\ \mathbf{0} & 1 \end{pmatrix}^{-1} \begin{pmatrix} \mathbf{I} & -\mathbf{s} \\ \frac{1}{c}\mathbf{s}^T & c \end{pmatrix}^{-1} &= \begin{pmatrix} \mathbf{F}^{-1} & \mathbf{0} \\ \mathbf{0} & 1 \end{pmatrix} \begin{pmatrix} \mathbf{I} - \mathbf{s}\otimes\mathbf{s} & c\,\mathbf{s} \\ -\mathbf{s}^T & c \end{pmatrix} \\ &= \begin{pmatrix} \mathbf{F}^{-1}(\mathbf{I} - \mathbf{s}\otimes\mathbf{s}) & c\,\mathbf{F}^{-1}\mathbf{s} \\ -\mathbf{s}^T & c \end{pmatrix}. \end{aligned} \tag{2.54}$$

SUMMARY of notations and relations

$$\begin{aligned} &\mathcal{S}_b : \boldsymbol{r}_b(x, y) = x\boldsymbol{e}_1 + y\boldsymbol{e}_2 + b(x, y)\boldsymbol{e}_3 \\ &\qquad\quad || \\ &\qquad \tilde{\boldsymbol{r}}_b(\xi^1, \xi^2) = x(\xi^1, \xi^2)\boldsymbol{e}_1 + y(\xi^1, \xi^2)\boldsymbol{e}_2 + \tilde{b}(\xi^1, \xi^2)\boldsymbol{e}_3 \\ &\tilde{b}(\xi^1, \xi^2) \equiv b(x(\xi^1, \xi^2), y(\xi^1, \xi^2)) \\ &\mathbf{F} \equiv \begin{pmatrix} \dfrac{\partial x}{\partial \xi^1} & \dfrac{\partial x}{\partial \xi^2} \\ \dfrac{\partial y}{\partial \xi^1} & \dfrac{\partial y}{\partial \xi^2} \end{pmatrix} \\ &\boldsymbol{\tau}_\alpha \equiv \frac{\partial \tilde{\boldsymbol{r}}_b}{\partial \xi^\alpha} = \frac{\partial x}{\partial \xi^\alpha}\boldsymbol{e}_1 + \frac{\partial y}{\partial \xi^\alpha}\boldsymbol{e}_2 + \frac{\partial \tilde{b}}{\partial \xi^\alpha}\boldsymbol{e}_3\,, \quad \alpha \in \{1, 2\} \end{aligned}$$

[4] Bouchut and Westdickenberg [3] noticed this useful decomposition.

$$c \equiv (1 + \operatorname{grad} b \cdot \operatorname{grad} b)^{-1/2}\,, \quad \mathbf{s} \equiv c\, \operatorname{grad} b\,, \quad \mathbf{s}\cdot\mathbf{s} + c^2 = 1$$

$$\boldsymbol{n}_b = \frac{\boldsymbol{\tau}_1 \times \boldsymbol{\tau}_2}{\|\boldsymbol{\tau}_1 \times \boldsymbol{\tau}_2\|} = -s_1\boldsymbol{e}_1 - s_2\boldsymbol{e}_2 + c\boldsymbol{e}_3\,, \quad (s_1, s_2)^T \equiv \mathbf{s}$$

$$\left(\mathbf{I} + \frac{1}{c^2}\,\mathbf{s}\otimes\mathbf{s}\right)^{-1} = \mathbf{I} - \mathbf{s}\otimes\mathbf{s} \qquad \tilde{\phi}_{\alpha\beta} \equiv \tau_\alpha \cdot \tau_\beta\,, \quad \tilde{\phi}^{\alpha\beta} \equiv \tau^\alpha \cdot \tau^\beta$$

$$\mathbf{M}_0 \equiv (\tilde{\phi}^{\alpha\beta}) = \mathbf{F}^{-1}(\mathbf{I} - \mathbf{s}\otimes\mathbf{s})\mathbf{F}^{-T}$$

$$\mathbf{M}_0^{-1} = (\tilde{\phi}_{\alpha\beta}) = \mathbf{F}^T\left(\mathbf{I} + \frac{1}{c^2}\,\mathbf{s}\otimes\mathbf{s}\right)\mathbf{F}$$

$$\frac{\partial \boldsymbol{n}_b}{\partial \xi^\beta} = -\tilde{b}_{\alpha\beta}\,\boldsymbol{\tau}^\alpha$$

$$\mathbf{H} \equiv \operatorname{grad}(\operatorname{grad} b)\,, \quad \widetilde{\mathbf{H}} \equiv (\tilde{b}_{\alpha\beta}) = c\,\mathbf{F}^T\mathbf{H}\mathbf{F}$$

$$\mathbf{W} = c\,(\mathbf{I} - \mathbf{s}\otimes\mathbf{s})\,\mathbf{H}\,, \quad \widetilde{\mathbf{W}} = \mathbf{F}^{-1}\mathbf{W}\mathbf{F} = \mathbf{M}_0\widetilde{\mathbf{H}}$$

$$\Omega = \tfrac{1}{2}\operatorname{tr}\mathbf{W} = \tfrac{1}{2}\operatorname{tr}\widetilde{\mathbf{W}}\,,$$

$$\operatorname{Grad} c = -c\,\widetilde{\mathbf{H}}\mathbf{F}^{-1}\mathbf{s}\,, \quad \operatorname{Grad}\mathbf{s} = \mathbf{F}\widetilde{\mathbf{W}}\,.$$

2.2.2 *Topographic Surface as a Moving Surface*

Now we assume an active topographic bed. The topographic surface varies in time, and its mathematical model is a moving surface $\mathcal{S}_b \equiv \{\mathcal{S}_t\}_{t\in I}$, see Sect. 2.1.2, given explicitly by

$$x_3 = b(x_1, x_2, t)\,, \quad (x_1, x_2) \in \mathcal{D} \subset \mathbb{R}^2\,, \quad t \in I \subset \mathbb{R}\,,$$

where $\mathcal{D}$ is open and $b \in C^2(\mathcal{D}\times I)$. Analogously to the case of a rigid topography, we use the implicit representation of $\mathcal{S}_b$,

$$F_b(x_1, x_2, x_3, t) = 0\,, \quad \text{with} \quad F_b(x_1, x_2, x_3, t) \equiv x_3 - b(x_1, x_2, t)\,, \tag{2.55}$$

and the parametric representation

$$x_1 = x\,, \quad x_2 = y\,, \quad x_3 = b(x, y, t)\,, \tag{2.56}$$

which gives the position vector $\boldsymbol{r}_b$ of a point on $\mathcal{S}_t$ as

$$\boldsymbol{r}_b = \boldsymbol{r}_b(x, y, t) = x\boldsymbol{e}_1 + y\boldsymbol{e}_2 + b(x, y, t)\boldsymbol{e}_3\,. \tag{2.57}$$

Furthermore, we consider the transformation

$$x = x(\xi^1, \xi^2, t)\,, \quad y = y(\xi^1, \xi^2, t)\,, \tag{2.58}$$

where the functions x, y are of class C^2 on $\mathcal{D}_0 \times I$ and such that $\det \mathbf{F} \neq 0$, with $\mathbf{F}$ defined as in (2.45). This implies another parameterization of $\mathcal{S}_b$,

$$x_1 = x(\xi^1, \xi^2, t)\,, \quad x_2 = y(\xi^1, \xi^2, t)\,, \quad x_3 = \tilde{b}(\xi^1, \xi^2, t)\,, \tag{2.59}$$

where

$$\tilde{b}(\xi^1, \xi^2, t) \equiv b(x(\xi^1, \xi^2, t),\ y(\xi^1, \xi^2, t),\ t)\,. \tag{2.60}$$

The position vector $\boldsymbol{r}_b$ of a point on $\mathcal{S}_t$, see (2.57), emerges as

$$\boldsymbol{r}_b(x, y, t) = x(\xi^1, \xi^2, t)\boldsymbol{e}_1 + y(\xi^1, \xi^2, t)\boldsymbol{e}_2 + \tilde{b}(\xi^1, \xi^2, t)\boldsymbol{e}_3 \equiv \tilde{\boldsymbol{r}}_b(\xi^1, \xi^2, t)\,. \tag{2.61}$$

Clearly, the description of a topographic bed which is eroded or on which sediments are deposited is similar to that of a rigid topographic bed. What is different is the time dependence of the surface elevation b and of the change of parameters (2.58). Consequently, the geometric properties deduced for a rigid topography in Sect. 2.2.1 hold also for an active topography, and next we only refer to properties implied by the above mentioned time dependence.

Let $\boldsymbol{u}_{\mathcal{S}}$ denote the *velocity* of some surface point $(\xi^1,\ \xi^2)$ at the instant t, that is,

$$\boldsymbol{u}_{\mathcal{S}} \equiv \frac{\partial \tilde{\boldsymbol{r}}_b}{\partial t} = \frac{\partial x}{\partial t}\boldsymbol{e}_1 + \frac{\partial y}{\partial t}\boldsymbol{e}_2 + \frac{\partial \tilde{b}}{\partial t}\boldsymbol{e}_3\,. \tag{2.62}$$

As pointed out in Sect. 2.1.2, its normal component $\mathcal{U} = \boldsymbol{u}_{\mathcal{S}} \cdot \boldsymbol{n}_b$ is the speed of propagation of $\mathcal{S}_b$, and can be deduced by formula $(2.26)_2$ with $F = F_b$, where F_b is given by (2.55). We obtain

$$\mathcal{U} = c\,\frac{\partial b}{\partial t} \quad \text{with} \quad c \equiv \left[1 + \left(\frac{\partial b}{\partial x}\right)^2 + \left(\frac{\partial b}{\partial y}\right)^2\right]^{-1/2}\,, \tag{2.63}$$

where definition $(2.33)_1$ of c is repeated for convenience. In sediment transport context, the speed of propagation $\mathcal{U}$ is called *erosion/deposition rate*, see Sect. 4.1. If $\mathcal{U} > 0$, sediments are deposited, and erosion occurs for $\mathcal{U} < 0$.

For later use we are interested in the determination of the tangential components $\mathcal{U}^1$ and $\mathcal{U}^2$ of the velocity $\boldsymbol{u}_{\mathcal{S}}$ in the representation

$$\boldsymbol{u}_{\mathcal{S}} = \mathcal{U}^\alpha\,\boldsymbol{\tau}_\alpha + \mathcal{U}\,\boldsymbol{n}_b\,, \tag{2.64}$$

in terms of the components of $\boldsymbol{u}_{\mathcal{S}}$ with respect to the Cartesian basis. In (2.64) the vectors $\boldsymbol{\tau}_1$ and $\boldsymbol{\tau}_2$ tangent to $\mathcal{S}_t$ refer to parameterization (2.59), that is,

$$\boldsymbol{\tau}_1 = \frac{\partial x}{\partial \xi^1}\boldsymbol{e}_1 + \frac{\partial y}{\partial \xi^1}\boldsymbol{e}_2 + \frac{\partial \tilde{b}}{\partial \xi^1}\boldsymbol{e}_3\,, \quad \boldsymbol{\tau}_2 = \frac{\partial x}{\partial \xi^2}\boldsymbol{e}_1 + \frac{\partial y}{\partial \xi^2}\boldsymbol{e}_2 + \frac{\partial \tilde{b}}{\partial \xi^2}\boldsymbol{e}_3\,, \tag{2.65}$$

see also (2.47) for the case of a rigid topography. With the notations

$$\mathbf{v}_{\mathcal{S}} \equiv \begin{pmatrix} \dfrac{\partial x}{\partial t} \\ \dfrac{\partial y}{\partial t} \end{pmatrix}\,, \quad \mathbf{u}_{\mathcal{S}} \equiv \begin{pmatrix} \mathcal{U}^1 \\ \mathcal{U}^2 \end{pmatrix}\,, \tag{2.66}$$

formula (1.1) and representations (2.62) and (2.64) of $\boldsymbol{u}_{\mathcal{S}}$ yield

$$\begin{pmatrix} \mathbf{u}_{\mathcal{S}} \\ \mathcal{U} \end{pmatrix} = \boldsymbol{P}^{-1} \begin{pmatrix} \mathbf{v}_{\mathcal{S}} \\ \dfrac{\partial \tilde{b}}{\partial t} \end{pmatrix}\,. \tag{2.67}$$

In (2.67), $\boldsymbol{P}$ is the change of basis matrix from $\{\boldsymbol{e}_1, \boldsymbol{e}_2, \boldsymbol{e}_3\}$ to $\{\boldsymbol{\tau}_1, \boldsymbol{\tau}_2, \boldsymbol{n}_b\}$, see (2.52), and its inverse $\boldsymbol{P}^{-1}$ is shown in (2.54). Insertion of $\boldsymbol{P}^{-1}$ and of $\partial\tilde{b}/\partial t$ as given by

$$\frac{\partial \tilde{b}}{\partial t} = \frac{\partial b}{\partial t} + \operatorname{grad} b \cdot \mathbf{v}_{\mathcal{S}} = \frac{\partial b}{\partial t} + \frac{1}{c}\mathbf{s} \cdot \mathbf{v}_{\mathcal{S}} = \frac{1}{c}\left(\mathcal{U} + \mathbf{s} \cdot \mathbf{v}_{\mathcal{S}}\right)\,, \tag{2.68}$$

into (2.67), yields

$$\begin{pmatrix} \mathbf{u}_{\mathcal{S}} \\ \mathcal{U} \end{pmatrix} = \begin{pmatrix} \mathbf{F}^{-1}(\mathbf{v}_{\mathcal{S}} + \mathcal{U}\mathbf{s}) \\ \mathcal{U} \end{pmatrix} \iff \mathbf{u}_{\mathcal{S}} = \mathbf{F}^{-1}(\mathbf{v}_{\mathcal{S}} + \mathcal{U}\mathbf{s})\,, \tag{2.69}$$

which we wanted to show.

Remark Assuming that the erosion/deposition rate $\mathcal{U}$ is known, relation (2.63), written in the form

$$\frac{\partial b}{\partial t} = \frac{1}{c}\mathcal{U}\,, \tag{2.70}$$

stands as an evolution equation for the bed elevation b. If the (ξ^1, ξ^2) coordinates are used, the equation for the bed elevation reads

$$\frac{\partial \tilde{b}}{\partial t} = \frac{1}{c}\left(\mathcal{U} + \mathbf{s} \cdot \mathbf{v}_{\mathcal{S}}\right)\,, \tag{2.71}$$

see (2.68). A law for the erosion/deposition rate $\mathcal{U}$ will be given in Sect. 5.3.

SUMMARY of notations and relations

$$\mathcal{S}_b : \boldsymbol{r}_b(x, y, t) = x\boldsymbol{e}_1 + y\boldsymbol{e}_2 + b(x, y, t)\boldsymbol{e}_3$$
$$||$$
$$\tilde{\boldsymbol{r}}_b(\xi^1, \xi^2, t) = x(\xi^1, \xi^2, t)\boldsymbol{e}_1 + y(\xi^1, \xi^2, t)\boldsymbol{e}_2 + \tilde{b}(\xi^1, \xi^2, t)\boldsymbol{e}_3$$

$$\tilde{b}(\xi^1, \xi^2, t) \equiv b(x(\xi^1, \xi^2, t), y(\xi^1, \xi^2, t), t)$$

$$\boldsymbol{u}_{\mathcal{S}} \equiv \frac{\partial \tilde{\boldsymbol{r}}_b}{\partial t} = \frac{\partial x}{\partial t}\boldsymbol{e}_1 + \frac{\partial y}{\partial t}\boldsymbol{e}_2 + \frac{\partial \tilde{b}}{\partial t}\boldsymbol{e}_3 = \mathcal{U}^\alpha \boldsymbol{\tau}_\alpha + \mathcal{U}\boldsymbol{n}_b$$

$$\mathcal{U} = c\,\frac{\partial b}{\partial t}\,, \quad \mathbf{v}_{\mathcal{S}} \equiv \left(\frac{\partial x}{\partial t}, \frac{\partial y}{\partial t}\right)^T, \quad \mathbf{u}_{\mathcal{S}} \equiv \left(\mathcal{U}^{\mathbf{1}}, \mathcal{U}^{\mathbf{2}}\right)^{\mathbf{T}} = \mathbf{F}^{-\mathbf{1}}(\mathbf{v}_{\mathcal{S}} + \mathcal{U}\mathbf{s})\,.$$

2.3 Topography-Fitted Coordinates

In this section we introduce curvilinear coordinates for the points lying in the vicinity of the basal surface $\mathcal{S}_b$. Two of such coordinates are ξ^1, ξ^2 from the parametric representation of the ground surface $\mathcal{S}_b$. The third coordinate, ζ, measures the distance from a point near $\mathcal{S}_b$ to $\mathcal{S}_b$, and adequately serves to apply the shallowness approximations, even in steep topographies. We divide the content of this section into two parts, depending on whether the erosion/deposition process is taken into account or not.

2.3.1 Coordinates Fitted to a Stationary Topographic Surface

In this section the topographic bed is assumed rigid, and so the bed surface is described as the stationary topographic surface given by (2.43), to which the assigned unit normal vector field $\boldsymbol{n}_b$ points *into* the flowing mass. We denote the Cartesian coordinates of a point $P \in \mathcal{E}$ near the surface $\mathcal{S}_b$ by (x_1, x_2, x_3), and use $(\xi^1, \xi^2, \xi^3 \equiv \zeta)$ for the topography-fitted curvilinear coordinates of P, introduced as follows.

Let $\boldsymbol{r}$ be the position vector of P,

$$\boldsymbol{r}(x_1, x_2, x_3) = x_1\boldsymbol{e}_1 + x_2\boldsymbol{e}_2 + x_3\boldsymbol{e}_3\,,$$

and let $\boldsymbol{r}_b$ be the position vector of the point $Q \in \mathcal{S}_b$ representing the orthogonal projection of P onto $\mathcal{S}_b$,

$$\boldsymbol{r}_b = \tilde{\boldsymbol{r}}_b(\xi^1, \xi^2) = x(\xi^1, \xi^2)\boldsymbol{e}_1 + y(\xi^1, \xi^2)\boldsymbol{e}_2 + \tilde{b}(\xi^1, \xi^2)\boldsymbol{e}_3\,, \tag{2.72}$$

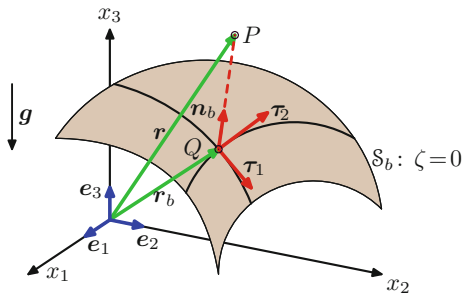

Fig. 2.2 The vector relation $\boldsymbol{r}(x_1, x_2, x_3) = \boldsymbol{r}_b(x, y) + \zeta \boldsymbol{n}_b(x, y) = \tilde{\boldsymbol{r}}_b(\xi^1, \xi^2) + \zeta \tilde{\boldsymbol{n}}_b(\xi^1, \xi^2) \equiv \tilde{\boldsymbol{r}}(\xi^1, \xi^2, \zeta)$ defines the change of coordinates $(x_1, x_2, x_3) \longleftrightarrow (\xi^1, \xi^2, \zeta)$ near the basal surface $\mathcal{S}_b$

see (2.44). The relation, see Fig. 2.2,

$$\boldsymbol{r} = \boldsymbol{r}_b + \zeta \boldsymbol{n}_b \,,$$

more specifically,

$$\boldsymbol{r}(x_1, x_2, x_3) = \tilde{\boldsymbol{r}}_b(\xi^1, \xi^2) + \zeta\, \tilde{\boldsymbol{n}}_b(\xi^1, \xi^2) \equiv \tilde{\boldsymbol{r}}(\xi^1, \xi^2, \zeta) \,, \tag{2.73}$$

defines the change of coordinates

$$(x_1, x_2, x_3) \longleftrightarrow (\xi^1, \xi^2, \zeta) \,, \tag{2.74}$$

on the condition that the Jacobian J of the transformation (2.74) is not zero,[5]

$$J \equiv \det \boldsymbol{A}^{-1} \neq 0 \,, \quad \text{with} \quad \boldsymbol{A}^{-1} \equiv \left(\frac{\partial x_i}{\partial \xi^j} \right)_{i,j \in \{1,2,3\}} . \tag{2.75}$$

The geometric interpretation of the curvilinear coordinates (ξ^1, ξ^2, ζ) of P is clear, namely, ξ^1, ξ^2 are the surface coordinates of the orthogonal projection Q of P onto $\mathcal{S}_b$, and $|\zeta|$ is the distance from P to $\mathcal{S}_b$.

To use this change of coordinates in analytical derivations we need to know the matrices $\boldsymbol{A}^{-1}$ and $\boldsymbol{A}$. This will also allow an explicit expression of restriction $(2.75)_1$, which we henceforth assume to be fulfilled. In order to obtain $\boldsymbol{A}^{-1}$ we introduce the vectors

$$\boldsymbol{g}_k \equiv \frac{\partial \tilde{\boldsymbol{r}}}{\partial \xi^k} = A^{-1}_{jk} \boldsymbol{e}_j \,, \quad k \in \{1, 2, 3\}, \tag{2.76}$$

which build the *natural basis of* $\mathcal{V}_3$ *at the point* P, *associated to the coordinates* (ξ^1, ξ^2, ζ). Relation (2.76) shows that the Jacobian matrix $\boldsymbol{A}^{-1}$ defined in (2.75) represents the change of basis matrix from $\{\boldsymbol{e}_1, \boldsymbol{e}_2, \boldsymbol{e}_3\}$ to $\{\boldsymbol{g}_1, \boldsymbol{g}_2, \boldsymbol{g}_3\}$. With definitions (2.47) and (2.76), the position vectors (2.72), (2.73), and relation (2.13), we have

[5] Denoting the Jacobian matrix of (2.74) by the inverse of a matrix $\boldsymbol{A}$ we preserve the notation used by Bouchut and Westdickenberg [3] for the same quantity.

$$\begin{aligned}
\boldsymbol{g}_1 &= \frac{\partial \tilde{\boldsymbol{r}}_b}{\partial \xi^1} + \zeta \frac{\partial \tilde{\boldsymbol{n}}_b}{\partial \xi^1} = (1 - \zeta\, \widetilde{W}^1{}_1)\boldsymbol{\tau}_1 - \zeta\, \widetilde{W}^2{}_1 \boldsymbol{\tau}_2\,, \\
\boldsymbol{g}_2 &= \frac{\partial \tilde{\boldsymbol{r}}_b}{\partial \xi^2} + \zeta \frac{\partial \tilde{\boldsymbol{n}}_b}{\partial \xi^2} = -\zeta\, \widetilde{W}^1{}_2 \boldsymbol{\tau}_1 + (1 - \zeta\, \widetilde{W}^2{}_2)\boldsymbol{\tau}_2\,, \\
\boldsymbol{g}_3 &= \boldsymbol{n}_b\,,
\end{aligned} \tag{2.77}$$

or, with a shorter notation,

$$\boldsymbol{g}_\alpha = (\delta^\beta{}_\alpha - \zeta\, \widetilde{W}^\beta{}_\alpha)\, \boldsymbol{\tau}_\beta\,, \quad \boldsymbol{g}_3 = \boldsymbol{n}_b\,. \tag{2.78}$$

This indicates that $\boldsymbol{A}^{-1}$ is the outcome of two successive transformations,

$$\boldsymbol{A}^{-1} = \boldsymbol{P}_1 \boldsymbol{P}\,,$$

where $\boldsymbol{P}$, $\boldsymbol{P}_1$ are the following change of basis matrices,

$$\begin{aligned}
\boldsymbol{P} &\;- \text{from } \{\boldsymbol{e}_1, \boldsymbol{e}_2, \boldsymbol{e}_3\} \text{ to } \{\boldsymbol{\tau}_1, \boldsymbol{\tau}_2, \boldsymbol{n}_b\}\,, \\
\boldsymbol{P}_1 &- \text{from } \{\boldsymbol{\tau}_1, \boldsymbol{\tau}_2, \boldsymbol{n}_b\} \text{ to } \{\boldsymbol{g}_1, \boldsymbol{g}_2, \boldsymbol{g}_3\}\,.
\end{aligned}$$

The matrix $\boldsymbol{P}$ is given by (2.52), and $\boldsymbol{P}_1$ can immediately be deduced from (2.77),

$$\boldsymbol{P}_1 = \begin{pmatrix} 1 - \zeta \widetilde{W}^1{}_1 & -\zeta \widetilde{W}^1{}_2 & 0 \\ -\zeta \widetilde{W}^2{}_1 & 1 - \zeta \widetilde{W}^2{}_2 & 0 \\ 0 & 0 & 1 \end{pmatrix} = \begin{pmatrix} \mathbf{I} - \zeta \widetilde{\mathbf{W}} & \mathbf{0} \\ \mathbf{0} & 1 \end{pmatrix},$$

so that

$$\boldsymbol{A}^{-1} = \boldsymbol{P}_1 \boldsymbol{P} = \begin{pmatrix} \mathbf{F}(\mathbf{I} - \zeta \widetilde{\mathbf{W}}) & -\mathbf{s} \\ \frac{1}{c}\left((\mathbf{I} - \zeta \widetilde{\mathbf{W}})^T \mathbf{F}^T \mathbf{s}\right)^T & c \end{pmatrix}.$$

Introducing the notation

$$\mathbf{B} \equiv \mathbf{F}(\mathbf{I} - \zeta \widetilde{\mathbf{W}}) = \big(\mathbf{I} - \zeta \mathbf{W}\big)\mathbf{F}\,, \tag{2.79}$$

where $\mathbf{F}\widetilde{\mathbf{W}} = \mathbf{W}\mathbf{F}$ has been used, $\boldsymbol{A}^{-1}$ is expressible as

$$\boldsymbol{A}^{-1} \equiv \left(\frac{\partial x_i}{\partial \xi^j}\right) = \begin{pmatrix} \mathbf{B} & -\mathbf{s} \\ \frac{1}{c}\,(\mathbf{B}^T \mathbf{s})^T & c \end{pmatrix}. \tag{2.80}$$

Now, similarly to (2.53), we decompose $\boldsymbol{A}^{-1}$ as

$$\boldsymbol{A}^{-1} = \begin{pmatrix} \mathbf{I} & -\mathbf{s} \\ \frac{1}{c}\,\mathbf{s}^T & c \end{pmatrix} \begin{pmatrix} \mathbf{B} & \mathbf{0} \\ \mathbf{0} & 1 \end{pmatrix},$$

which immediately allows the derivation in block form of the matrix $\boldsymbol{A}$,

$$\boldsymbol{A} = \begin{pmatrix} \mathbf{B} & \mathbf{0} \\ \mathbf{0} & 1 \end{pmatrix}^{-1} \begin{pmatrix} \mathbf{I} & -\mathbf{s} \\ \frac{1}{c}\mathbf{s}^T & c \end{pmatrix}^{-1} = \begin{pmatrix} \mathbf{B}^{-1} & \mathbf{0} \\ \mathbf{0} & 1 \end{pmatrix} \begin{pmatrix} \mathbf{I} - \mathbf{s} \otimes \mathbf{s} & c\mathbf{s} \\ -\mathbf{s}^T & c \end{pmatrix},$$

and therefore

$$\boldsymbol{A} = \left(\frac{\partial \xi^i}{\partial x_j} \right) = \begin{pmatrix} \mathbf{B}^{-1}(\mathbf{I} - \mathbf{s} \otimes \mathbf{s}) & c\,\mathbf{B}^{-1}\mathbf{s} \\ -\mathbf{s}^T & c \end{pmatrix}. \tag{2.81}$$

With $\boldsymbol{A}^{-1}$ given in (2.80), we can compute the Jacobian determinant J,

$$J \equiv \det \boldsymbol{A}^{-1} = \frac{1}{c} \det \mathbf{B} = \frac{1}{c} \det \mathbf{F} \det(\mathbf{I} - \zeta \widetilde{\mathbf{W}}), \tag{2.82}$$

and explicit condition $(2.75)_1$. Since $\det \mathbf{F} \neq 0$, $(2.75)_1$ reads

$$\det(\mathbf{I} - \zeta \widetilde{\mathbf{W}}) = \det(\mathbf{I} - \zeta \mathbf{W}) \neq 0, \tag{2.83}$$

where $(2.17)_3$ has been used. This restricts the use of the change of coordinates (2.74) to realistic situations: (2.74) can be applied if and only if the basal topography plus the domain occupied by the flowing mass satisfy (2.83). We record expression (2.82) for the Jacobian J in the form

$$J = J_0 \det(\mathbf{I} - \zeta \widetilde{\mathbf{W}}), \quad J_0 \equiv \frac{1}{c} \det \mathbf{F}. \tag{2.84}$$

We return to the basis $\{\boldsymbol{g}_1, \boldsymbol{g}_2, \boldsymbol{g}_3\}$ in (2.76) and introduce its reciprocal basis $\{\boldsymbol{g}^1, \boldsymbol{g}^2, \boldsymbol{g}^3\}$. The combination of (2.76) and (2.81) implies the following formulae for the contravariant coefficients $g^{ij} \equiv \boldsymbol{g}^i \cdot \boldsymbol{g}^j$ and the covariant coefficients $g_{ij} \equiv \boldsymbol{g}_i \cdot \boldsymbol{g}_j$ of the metric tensor,

$$(g^{ij}) = \boldsymbol{A}\boldsymbol{A}^T = \begin{pmatrix} \mathbf{M} & \mathbf{0} \\ \mathbf{0} & 1 \end{pmatrix}, \quad (g_{ij}) = (\boldsymbol{A}\boldsymbol{A}^T)^{-1} = \begin{pmatrix} \mathbf{M}^{-1} & \mathbf{0} \\ \mathbf{0} & 1 \end{pmatrix}, \tag{2.85}$$

where

$$\mathbf{M} \equiv \mathbf{B}^{-1}(\mathbf{I} - \mathbf{s} \otimes \mathbf{s})\mathbf{B}^{-T}. \tag{2.86}$$

Since $\{\boldsymbol{g}^1, \boldsymbol{g}^2, \boldsymbol{g}^3 = \boldsymbol{n}_b\}$ is a basis of $\mathcal{V}_3$, the matrix (g^{ij}) is positive definite, therefore $\mathbf{M}$ is equally a positive definite matrix. We notice that

$$\mathbf{M}|_{\zeta=0} = \mathbf{M}_0, \tag{2.87}$$

which yields (2.86) as

$$\mathbf{M} = (\mathbf{I} - \zeta\widetilde{\mathbf{W}})^{-1}\mathbf{M}_0(\mathbf{I} - \zeta\widetilde{\mathbf{W}})^{-T}\,, \tag{2.88}$$

see expressions (2.50) and (2.79) of $\mathbf{M}_0$ and $\mathbf{B}$, respectively.

SUMMARY of notations and relations

$$\boldsymbol{r} = \boldsymbol{r}_b + \zeta\boldsymbol{n}_b \iff \boldsymbol{r}(x_1, x_2, x_3) = \tilde{\boldsymbol{r}}_b(\xi^1, \xi^2) + \zeta\,\tilde{\boldsymbol{n}}_b(\xi^1, \xi^2)$$

$$\equiv \tilde{\boldsymbol{r}}(\xi^1, \xi^2, \zeta)\,, \quad \text{with} \quad \xi^3 \equiv \zeta$$

$$\boldsymbol{g}_k \equiv \frac{\partial\tilde{\boldsymbol{r}}}{\partial\xi^k}\,, \quad k \in \{1, 2, 3\}$$

$$\boldsymbol{g}_\alpha = (\delta^\beta_{\ \alpha} - \zeta\,\widetilde{W}^\beta_{\ \alpha})\,\boldsymbol{\tau}_\beta\,, \quad \alpha \in \{1, 2\}, \quad \boldsymbol{g}_3 = \boldsymbol{n}_b$$

$$\mathbf{B} \equiv \mathbf{F}(\mathbf{I} - \zeta\widetilde{\mathbf{W}}) = \big(\mathbf{I} - \zeta\mathbf{W}\big)\mathbf{F}$$

$$\mathbf{M} \equiv \mathbf{B}^{-1}(\mathbf{I} - \mathbf{s}\otimes\mathbf{s})\mathbf{B}^{-T} = (\mathbf{I} - \zeta\widetilde{\mathbf{W}})^{-1}\mathbf{M}_0(\mathbf{I} - \zeta\widetilde{\mathbf{W}})^{-T}$$

$$\mathbf{M}|_{\zeta=0} = \mathbf{M}_0$$

$$\boldsymbol{A}^{-1} \equiv \left(\frac{\partial x_i}{\partial\xi^j}\right) = \begin{pmatrix} \mathbf{B} & -\mathbf{s} \\ \frac{1}{c}\,(\mathbf{B}^T\mathbf{s})^T & c \end{pmatrix}$$

$$\boldsymbol{g}_k \equiv \frac{\partial\tilde{\boldsymbol{r}}}{\partial\xi^k} = A^{-1}_{jk}\boldsymbol{e}_j\,, \quad k \in \{1, 2, 3\}$$

$$\boldsymbol{A} = \left(\frac{\partial\xi^i}{\partial x_j}\right) = \begin{pmatrix} \mathbf{B}^{-1}(\mathbf{I} - \mathbf{s}\otimes\mathbf{s}) & c\,\mathbf{B}^{-1}\mathbf{s} \\ -\mathbf{s}^T & c \end{pmatrix}$$

$$J_0 \equiv \frac{1}{c}\,\det\mathbf{F}\,, \quad J \equiv \det\boldsymbol{A}^{-1} = J_0\det(\mathbf{I} - \zeta\widetilde{\mathbf{W}})$$

$$g^{ij} \equiv \boldsymbol{g}^i\cdot\boldsymbol{g}^j\,, \quad g_{ij} \equiv \boldsymbol{g}_i\cdot\boldsymbol{g}_j$$

$$(g^{ij}) = \boldsymbol{A}\boldsymbol{A}^T = \begin{pmatrix} \mathbf{M} & \mathbf{0} \\ \mathbf{0} & 1 \end{pmatrix}, \quad (g_{ij}) = (\boldsymbol{A}\boldsymbol{A}^T)^{-1} = \begin{pmatrix} \mathbf{M}^{-1} & \mathbf{0} \\ \mathbf{0} & 1 \end{pmatrix},$$

2.3.2 On the Components of Vectors and Tensors

We use the basis vectors $\boldsymbol{g}_1, \boldsymbol{g}_2, \boldsymbol{g}_3$ to represent vectors in $\mathcal{V}_3$ and second order tensors on $\mathcal{V}_3$,

$$\boldsymbol{v} = v^i \boldsymbol{g}_i \,, \quad \boldsymbol{\sigma} = T^{ij} \boldsymbol{g}_i \otimes \boldsymbol{g}_j \,. \tag{2.89}$$

Expressions (2.77) of $\boldsymbol{g}_1, \boldsymbol{g}_2, \boldsymbol{g}_3$ show that $\boldsymbol{g}_1, \boldsymbol{g}_2$ are parallel to the surface $\mathcal{S}_b$, and $\boldsymbol{g}_3$ is perpendicular to $\mathcal{S}_b$. Due to these geometric properties it is convenient to decompose a vector $\boldsymbol{v} \in \mathcal{V}_3$ into a *tangential component* $\boldsymbol{v}_\tau$ and a *normal component* $\boldsymbol{v}_n$,

$$\boldsymbol{v} = \underbrace{v^1 \boldsymbol{g}_1 + v^2 \boldsymbol{g}_2}_{\boldsymbol{v}_\tau} + \underbrace{v^3 \boldsymbol{g}_3}_{\boldsymbol{v}_n} \quad \text{with} \quad \boldsymbol{v}_\tau \equiv v^1 \boldsymbol{g}_1 + v^2 \boldsymbol{g}_2 \,, \quad \boldsymbol{v}_n \equiv v^3 \boldsymbol{g}_3 \,. \tag{2.90}$$

This decomposition is independent of the choice of the surface coordinates ξ^1, ξ^2, a fact which can also be seen from the relations

$$\boldsymbol{v}_n = (\boldsymbol{v} \cdot \boldsymbol{n}_b) \boldsymbol{n}_b \,, \quad \boldsymbol{v}_\tau = \boldsymbol{v} - (\boldsymbol{v} \cdot \boldsymbol{n}_b) \boldsymbol{n}_b \,,$$

which are satisfied by $\boldsymbol{v}_\tau$ and $\boldsymbol{v}_n$. We collect the components of $\boldsymbol{v}_\tau$ with respect to $\boldsymbol{g}_1, \boldsymbol{g}_2$ in a 2-column matrix, and use the notation v for the normal component $v^3 = \boldsymbol{v} \cdot \boldsymbol{n}_b$ of $\boldsymbol{v}$, i.e.,

$$\mathbf{v} \equiv \begin{pmatrix} v^1 \\ v^2 \end{pmatrix} \,, \quad \mathrm{v} \equiv v^3 \,.$$

Similarly, we collect the components T^{ij} of a symmetric second order tensor $\boldsymbol{\sigma}$, see (2.89), as follows,

$$\mathbf{T} \equiv \begin{pmatrix} T^{11} & T^{12} \\ T^{12} & T^{22} \end{pmatrix} = \mathbf{T}^T, \quad \mathbf{t} \equiv \begin{pmatrix} T^{13} \\ T^{23} \end{pmatrix} = \begin{pmatrix} T^{31} \\ T^{32} \end{pmatrix} .$$

We, therefore, use the following block matrices for the contravariant components of vectors and symmetric second order tensors,

$$\begin{pmatrix} v^1 \\ v^2 \\ v^3 \end{pmatrix} = \begin{pmatrix} \mathbf{v} \\ \mathrm{v} \end{pmatrix} \,, \quad (T^{ij}) = \begin{pmatrix} \mathbf{T} & \mathbf{t} \\ \mathbf{t}^T & T^{33} \end{pmatrix} . \tag{2.91}$$

Note that, using $(2.78)_1$ in $(2.90)_2$, $\boldsymbol{v}_\tau$ can be written as

$$\boldsymbol{v}_\tau = (\delta^\alpha_{\ \beta} - \zeta \, \widetilde{W}^\alpha_{\ \beta}) \, v^\beta \boldsymbol{\tau}_\alpha \,, \tag{2.92}$$

which is the representation of $\boldsymbol{v}_\tau$ with respect to $\boldsymbol{\tau}_1$, $\boldsymbol{\tau}_2$. Moreover, with $(2.85)_2$ we have

$$\|\boldsymbol{v}_\tau\|^2 = (v^\alpha \boldsymbol{g}_\alpha)\cdot(v^\beta \boldsymbol{g}_\beta) = (\boldsymbol{g}_\alpha \cdot \boldsymbol{g}_\beta) v^\alpha v^\beta = \mathbf{M}^{-1}\mathbf{v}\cdot\mathbf{v}\,. \tag{2.93}$$

We will also use the Cartesian components of vectors and the mixed components of a symmetric second order tensor, that is

$$\boldsymbol{v} = v_i \boldsymbol{e}_i\,, \quad \boldsymbol{\sigma} = \Sigma^{ij}\boldsymbol{e}_i \otimes \boldsymbol{g}_j\,. \tag{2.94}$$

For them we introduce the notations

$$\mathbb{v} \equiv \begin{pmatrix} v_1 \\ v_2 \end{pmatrix}, \quad v \equiv v_3\,,$$

and

$$\mathbb{S} \equiv \begin{pmatrix} \Sigma^{11} & \Sigma^{12} \\ \Sigma^{21} & \Sigma^{22} \end{pmatrix}, \quad \mathbb{s} \equiv \begin{pmatrix} \Sigma^{13} \\ \Sigma^{23} \end{pmatrix}, \quad \mathbb{t} \equiv \begin{pmatrix} \Sigma^{31} \\ \Sigma^{32} \end{pmatrix}, \quad \sigma \equiv \Sigma^{33}\,,$$

so that

$$\begin{pmatrix} v_1 \\ v_2 \\ v_3 \end{pmatrix} = \begin{pmatrix} \mathbb{v} \\ v \end{pmatrix}, \quad (\Sigma^{ij}) = \begin{pmatrix} \mathbb{S} & \mathbb{s} \\ \mathbb{t}^T & \sigma \end{pmatrix}. \tag{2.95}$$

Note that $\mathbb{S}$ is not a symmetric matrix as $\mathbf{T}$ in $(2.91)_2$. Recalling that the change of basis matrix from $\{\boldsymbol{e}_1, \boldsymbol{e}_2, \boldsymbol{e}_3\}$ to $\{\boldsymbol{g}_1, \boldsymbol{g}_2, \boldsymbol{g}_3\}$ is $\boldsymbol{A}^{-1}$, see (2.75), formula (1.1) yields the relation between the contravariant components v^i and the Cartesian components v_i of $\boldsymbol{v}$, see $(2.89)_1$ and $(2.94)_1$,

$$\begin{pmatrix} \mathbb{v} \\ v \end{pmatrix} = \boldsymbol{A}^{-1}\begin{pmatrix} \mathbf{v} \\ \mathrm{v} \end{pmatrix},$$

which gives, owing to (2.80),

$$\mathbb{v} = \mathbf{B}\mathbf{v} - \mathrm{v}\mathbf{s}\,, \qquad v = \frac{1}{c}\,\mathbf{s}\cdot\mathbf{B}\mathbf{v} + c\mathrm{v} \tag{2.96}$$

In particular, the relation between the Cartesian coordinates, $\mathbb{v}_\tau$, v_τ, and the curvilinear coordinates, $\mathbf{v}$, 0, of the tangential component $\boldsymbol{v}_\tau$ of the vector $\boldsymbol{v}$, see (2.90), is

$$\begin{pmatrix} \mathbb{v}_\tau \\ v_\tau \end{pmatrix} = \boldsymbol{A}^{-1}\begin{pmatrix} \mathbf{v} \\ 0 \end{pmatrix},$$

that is,

$$\mathbb{v}_\tau = \mathbf{B}\mathbf{v}\,, \qquad v_\tau = \frac{1}{c}\,\mathbf{s}\cdot\mathbf{B}\mathbf{v} \tag{2.97}$$

Then, inserting $\boldsymbol{g}_i = A_{ki}^{-1}\boldsymbol{e}_k$ into $(2.89)_2$ and comparing the emerging representation of the symmetric tensor $\boldsymbol{\sigma}$ with $(2.94)_2$, we obtain the relation between the contravariant components T^{ij} and the mixed components Σ^{ij} of $\boldsymbol{\sigma}$,

$$\left(\Sigma^{ij}\right) = \boldsymbol{A}^{-1}\left(T^{kl}\right)\,.$$

This is equivalent to

$$\begin{aligned} \mathbb{S} &= \mathbf{B}\mathbf{T} - \mathbf{s}\otimes\mathbf{t}\,, \qquad \mathbb{s} = \mathbf{B}\mathbf{t} - T^{33}\mathbf{s}\,, \\ \mathbb{t} &= \frac{1}{c}\,\mathbf{T}\mathbf{B}^T\mathbf{s} + c\,\mathbf{t}\,, \qquad \sigma = \frac{1}{c}\,\mathbf{s}\cdot\mathbf{B}\mathbf{t} + c\,T^{33}\,. \end{aligned} \tag{2.98}$$

2.3.3 *Coordinates Fitted to a Moving Topographic Surface*

Now we consider a moving topographic surface $\mathcal{S}_b$, described by (2.59), so that the position vector of a point on $\mathcal{S}_b$ is given by (2.61), which we rewrite here for convenience,

$$\boldsymbol{r}_b = \tilde{\boldsymbol{r}}_b(\xi^1,\xi^2,t) = x(\xi^1,\xi^2,t)\boldsymbol{e}_1 + y(\xi^1,\xi^2,t)\boldsymbol{e}_2 + \tilde{b}(\xi^1,\xi^2,t)\boldsymbol{e}_3\,. \tag{2.99}$$

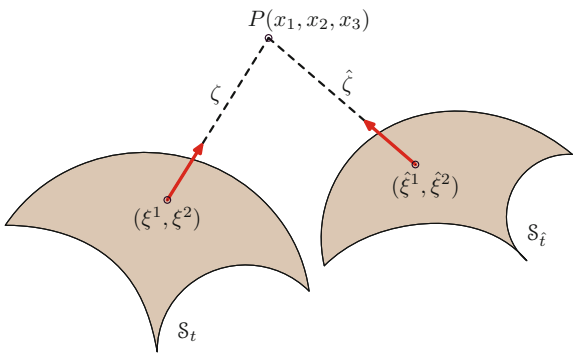

Fig. 2.3 The coordinates (ξ^1,ξ^2,ζ) and $(\hat{\xi}^1,\hat{\xi}^2,\hat{\zeta})$ of the point P at times t and $\hat{t}$, respectively

The change of coordinates which we introduce for points in a neighbourhood of the surface $\mathcal{S}_b$ emerges from the same vector relation as that from Sect. 2.3.1, i.e., $\boldsymbol{r} = \boldsymbol{r}_b + \zeta \boldsymbol{n}_b$. Explicitly,

$$\boldsymbol{r}(x_1, x_2, x_3) = \tilde{\boldsymbol{r}}_b(\xi^1, \xi^2, t) + \zeta\, \tilde{\boldsymbol{n}}_b(\xi^1, \xi^2, t) \equiv \tilde{\boldsymbol{r}}(\xi^1, \xi^2, \zeta, t)\,. \tag{2.100}$$

However, the coordinates ξ^1, ξ^2, ζ of $P \in \mathcal{E}$ are now time-dependent,

$$\xi^1(x_1, x_2, x_3, t)\,, \quad \xi^2(x_1, x_2, x_3, t)\,, \quad \zeta(x_1, x_2, x_3, t)\,, \tag{2.101}$$

which is geometrically obvious: since the surface is moving, the orthogonal projection of P onto $\mathcal{S}_b$ and the distance of P to the surface $\mathcal{S}_b$ are changing in time, see Fig. 2.3, where the coordinates $(\hat{\xi}^1, \hat{\xi}^2, \hat{\zeta})$ of the point P at the instant $\hat{t}$ are

$$\hat{\xi}^1 \equiv \xi^1(x_1, x_2, x_3, \hat{t})\,, \quad \hat{\xi}^2 \equiv \xi^2(x_1, x_2, x_3, \hat{t})\,, \quad \hat{\zeta} \equiv \zeta(x_1, x_2, x_3, \hat{t})\,.$$

As a consequence, as soon as the dependence of ξ^1, ξ^2, ζ on x_1, x_2, x_3 is envisaged, we simply take over the results from Sect. 2.3.1, e.g. formula (2.81) for the matrix $\boldsymbol{A}$, which gives the partial derivatives of (2.101) with respect to the Cartesian coordinates. Additionally, we are interested in obtaining the partial derivatives with respect to t of the coordinates (2.101),

$$\dot{\xi}^1 \equiv \frac{\partial \xi^1}{\partial t}\,, \quad \dot{\xi}^2 \equiv \frac{\partial \xi^2}{\partial t}\,, \quad \dot{\zeta} \equiv \frac{\partial \zeta}{\partial t}\,.$$

They are needed for the derivation of some rules of differentiation when the change of coordinates (2.100) is used, see Sect. 3.1.3. We deduce the *coordinate velocities* $\dot{\xi}^1, \dot{\xi}^2, \dot{\zeta}$ by using the identity, see (2.100) and (2.101),

$$\boldsymbol{r}(x_1, x_2, x_3) = \tilde{\boldsymbol{r}}(\xi^1(x_1, x_2, x_3, t),\ \xi^2(x_1, x_2, x_3, t),\ \xi^3(x_1, x_2, x_3, t),\ t)\,,$$

which we differentiate with respect to t to obtain

$$\boldsymbol{0} = \frac{\partial \tilde{\boldsymbol{r}}}{\partial t} + \dot{\xi}^k \frac{\partial \tilde{\boldsymbol{r}}}{\partial \xi^k} \iff \boldsymbol{w} = -\dot{\xi}^k \boldsymbol{g}_k\,, \tag{2.102}$$

with

$$\boldsymbol{w} \equiv \frac{\partial \tilde{\boldsymbol{r}}}{\partial t}\,, \tag{2.103}$$

and where definition (2.76) of $\boldsymbol{g}_k$ has been used. In the context of computational methods, $\boldsymbol{w}$ is called the *mesh velocity*. Relation $(2.102)_2$ indicates that the coordinate velocities $\dot{\xi}^1, \dot{\xi}^2, \dot{\zeta}$ are the contravariant components of the vector $-\boldsymbol{w}$ with respect to $\boldsymbol{g}_1, \boldsymbol{g}_2, \boldsymbol{g}_3 = \boldsymbol{n}_b$. That is, with

$$\boldsymbol{w} = w^{\alpha}\boldsymbol{g}_{\alpha} + \mathrm{w}\boldsymbol{n}_b\,, \quad \mathbf{w} \equiv \begin{pmatrix} w^1 \\ w^2 \end{pmatrix}, \tag{2.104}$$

we have

$$\begin{pmatrix} \dot{\xi}^1 \\ \dot{\xi}^2 \end{pmatrix} = -\mathbf{w}, \quad \dot{\zeta} = -\mathrm{w}\,. \tag{2.105}$$

It is therefore necessary to determine $\mathbf{w}$ and w. To this end we use definitions (2.100) and (2.64) of $\tilde{\boldsymbol{r}}$ and $\boldsymbol{u}_{\mathcal{S}}$, respectively, which yields

$$\boldsymbol{w} = \frac{\partial \tilde{\boldsymbol{r}}_b}{\partial t} + \zeta \frac{\partial \tilde{\boldsymbol{n}}_b}{\partial t} = \boldsymbol{u}_{\mathcal{S}} + \zeta \frac{\partial \tilde{\boldsymbol{n}}_b}{\partial t}\,. \tag{2.106}$$

First, let us obtain the representation of $\boldsymbol{u}_{\mathcal{S}}$ with respect to $\boldsymbol{g}_1, \boldsymbol{g}_2, \boldsymbol{n}_b$. From (2.78) we deduce that $\boldsymbol{\tau}_1, \boldsymbol{\tau}_2$ are written in terms of $\boldsymbol{g}_1, \boldsymbol{g}_2$ as

$$\boldsymbol{\tau}_{\beta} = \underset{\sim}{W}{}^{\alpha}_{\beta}\boldsymbol{g}_{\alpha}, \quad \underset{\sim}{\mathbf{W}} \equiv (\mathbf{I} - \zeta\widetilde{\mathbf{W}})^{-1},$$

and hence representation (2.64) emerges as

$$\boldsymbol{u}_{\mathcal{S}} = \mathcal{U}^{\beta}\boldsymbol{\tau}_{\beta} + \mathcal{U}\,\boldsymbol{n}_b = \underset{\sim}{W}{}^{\alpha}_{\beta}\mathcal{U}^{\beta}\boldsymbol{g}_{\alpha} + \mathcal{U}\,\boldsymbol{n}_b\,. \tag{2.107}$$

Here $\mathbf{u}_{\mathcal{S}} \equiv (\mathcal{U}^1, \mathcal{U}^2)^T$ and $\mathcal{U}$ are given by (2.69) and (2.63), respectively.

Next consider $\partial\tilde{\boldsymbol{n}}_b/\partial t$. The relation $\boldsymbol{n}_b \cdot \boldsymbol{n}_b = 1$ implies $\boldsymbol{n}_b \cdot \partial\tilde{\boldsymbol{n}}_b/\partial t = 0$, so that $\partial\tilde{\boldsymbol{n}}_b/\partial t$ is a tangent vector to $\mathcal{S}_t$, i.e.,

$$\frac{\partial \tilde{\boldsymbol{n}}_b}{\partial t} = a^{\alpha}\boldsymbol{g}_{\alpha}\,, \tag{2.108}$$

with

$$a^{\alpha} = \frac{\partial \tilde{\boldsymbol{n}}_b}{\partial t} \cdot \boldsymbol{g}^{\alpha} = g^{\beta\alpha}\frac{\partial \tilde{\boldsymbol{n}}_b}{\partial t} \cdot \boldsymbol{g}_{\beta} \overset{(2.78)}{=} g^{\beta\alpha}(\delta^{\gamma}_{\beta} - \zeta\widetilde{W}^{\gamma}_{\beta})\frac{\partial \tilde{\boldsymbol{n}}_b}{\partial t} \cdot \boldsymbol{\tau}_{\gamma}\,.$$

Moreover, we compute

$$\begin{aligned}
\frac{\partial \tilde{\boldsymbol{n}}_b}{\partial t} \cdot \boldsymbol{\tau}_{\gamma} &= -\boldsymbol{n}_b \cdot \frac{\partial \boldsymbol{\tau}_{\gamma}}{\partial t} = -\boldsymbol{n}_b \cdot \frac{\partial}{\partial t}\left(\frac{\partial \tilde{\boldsymbol{r}}_b}{\partial \xi^{\gamma}}\right) = -\boldsymbol{n}_b \cdot \frac{\partial}{\partial \xi^{\gamma}}\left(\frac{\partial \tilde{\boldsymbol{r}}_b}{\partial t}\right) \\
&= -\boldsymbol{n}_b \cdot \frac{\partial \boldsymbol{u}_{\mathcal{S}}}{\partial \xi^{\gamma}} \overset{(2.107)}{=} -\boldsymbol{n}_b \cdot \frac{\partial}{\partial \xi^{\gamma}}\left(\mathcal{U}^{\beta}\boldsymbol{\tau}_{\beta} + \mathcal{U}\,\boldsymbol{n}_b\right) \\
&= -\mathcal{U}^{\beta}\boldsymbol{n}_b \cdot \frac{\partial \boldsymbol{\tau}_{\beta}}{\partial \xi^{\gamma}} - \frac{\partial \mathcal{U}}{\partial \xi^{\gamma}} = \mathcal{U}^{\beta}\frac{\partial \tilde{\boldsymbol{n}}_b}{\partial \xi^{\gamma}} \cdot \boldsymbol{\tau}_{\beta} - \frac{\partial \mathcal{U}}{\partial \xi^{\gamma}} \overset{(2.7)}{=} -\tilde{b}_{\omega\gamma}\mathcal{U}^{\omega} - \frac{\partial \mathcal{U}}{\partial \xi^{\gamma}}\,.
\end{aligned}$$

Therefore, we obtain

$$\frac{\partial \tilde{\boldsymbol{n}}_b}{\partial t} = -g^{\beta\alpha}(\delta^{\gamma}_{\beta} - \zeta\widetilde{W}^{\gamma}_{\beta})\left(\tilde{b}_{\omega\gamma}\mathcal{U}^{\omega} + \frac{\partial \mathcal{U}}{\partial \xi^{\gamma}}\right)\boldsymbol{g}_{\alpha}\,. \tag{2.109}$$

Finally, substituting (2.107) and (2.109) into (2.106), we deduce

$$\boldsymbol{w} = \left\{ \underset{\sim}{W}{}^{\alpha}_{\beta}\mathcal{U}^{\beta} - \zeta\, g^{\beta\alpha}(\delta^{\gamma}_{\beta} - \zeta\, \widetilde{W}^{\gamma}_{\beta}) \left(\tilde{b}_{\omega\gamma}\mathcal{U}^{\omega} + \frac{\partial \mathcal{U}}{\partial \xi^{\gamma}} \right) \right\} \boldsymbol{g}_{\alpha} + \mathcal{U}\boldsymbol{n}_{b}\,,$$

which, after a routine calculus using (2.48), $(2.49)_3$, $(2.85)_1$ and (2.88), yields the components $\mathbf{w}$, w (see (2.104)) of $\boldsymbol{w}$ as

$$\mathbf{w} = \mathbf{u}_{\mathcal{S}} - \zeta(\mathbf{I} - \zeta\widetilde{\mathbf{W}})^{-1}\mathbf{M}_0 \mathrm{Grad}\,\mathcal{U}\,, \quad \mathrm{w} = \mathcal{U}\,. \tag{2.110}$$

Relation $(2.110)_1$ is essential when selecting the parameterization of the moving topographic surface as described in the next section.

SUMMARY of notations and relations

$$\boldsymbol{r} = \boldsymbol{r}_b + \zeta\boldsymbol{n} \iff \boldsymbol{r}(x_1, x_2, x_3) = \tilde{\boldsymbol{r}}_b(\xi^1, \xi^2, t) + \zeta\, \tilde{\boldsymbol{n}}_b(\xi^1, \xi^2, t)$$
$$\equiv \tilde{\boldsymbol{r}}(\xi^1, \xi^2, \zeta, t)$$

$$\boldsymbol{w} \equiv \frac{\partial \tilde{\boldsymbol{r}}}{\partial t} = -\dot{\xi}^k \boldsymbol{g}_k$$

$$\boldsymbol{w} = w^{\alpha}\boldsymbol{g}_{\alpha} + \mathrm{w}\boldsymbol{n}_b\,, \quad \mathbf{w} \equiv \begin{pmatrix} w^1 \\ w^2 \end{pmatrix}$$

$$\mathbf{w} = \mathbf{u}_{\mathcal{S}} - \zeta(\mathbf{I} - \zeta\widetilde{\mathbf{W}})^{-1}\mathbf{M}_0 \mathrm{Grad}\,\mathcal{U}\,, \quad \mathrm{w} = \mathcal{U}\,.$$

To conclude, by (2.73)/(2.100) in this section we have introduced the curvilinear coordinates ξ^1, ξ^2, ζ replacing the Cartesian coordinates x_1, x_2, x_3 of points lying in that vicinity of the topographic surface defined by condition (2.83). Using these curvilinear coordinates when deducing the modelling equations for shallow flows in the following chapter, the computational mesh results in a body-fitted grid that follows the geometry of the topography. For active topographic beds, at all times the topographic surface corresponds to $\zeta = 0$ in the computational (ξ^1, ξ^2, ζ)—domain. Note that the change of parameters on the topographic surface, see (2.42) or (2.58), is left arbitrary. It can be freely chosen to the benefit of the numerical method. Most authors use the arc lengths on the coordinate lines $y = \text{constant}$, $x = \text{constant}$ on $\mathcal{S}_b$ as parameters ξ^1 and ξ^2, respectively. Another choice for the time-dependent transformation (2.58) is discussed in the next section. Both these parameterizations of the basal surface are used in the example given in Sect. 5.4.

2.4 The Topography-Fitted Coordinates in the Context of the Unified Coordinates (UC) Approach

It is generally non-trivial to determine the change of parameters (2.58) for a complex terrain surface when erosion/deposition processes occur. An idea of how to face this problem was proposed by Tai and Kuo [5], and was suggested by the unified coordinates (UC) approach (see e.g. Hui [6, 7], Hui and Xu [8]). In this section we shortly describe this method and show how it inspired the choice for the change of parameters (2.58) in [5].

The UC method is essentially an approach to search for an optimum coordinate system (ξ^1, ξ^2, ξ^3) in Computational Fluid Dynamics, in the sense that, (a) the system of partial differential equations, when expressed in terms of (ξ^1, ξ^2, ξ^3), is in conservative form, (b) contact discontinuities are sharply resolved, and (c) a body-fitted mesh, commonly adopted in computing flows of complex geometries, can be automatically generated. With x_1, x_2, x_3—the Cartesian coordinates, the new coordinate system is searched for as defined by a space-time change of coordinates

$$(x_1, x_2, x_3, t) \quad \Longleftrightarrow \quad (\xi^1, \xi^2, \xi^3, \lambda) \tag{2.111}$$

of the form

$$\begin{aligned} dx_1 &= A\, d\xi^1 + L\, d\xi^2 + P\, d\xi^3 + U\, d\lambda\,, \\ dx_2 &= B\, d\xi^1 + M\, d\xi^2 + Q\, d\xi^3 + V\, d\lambda\,, \\ dx_3 &= C\, d\xi^1 + N\, d\xi^2 + R\, d\xi^3 + W\, d\lambda\,, \\ dt &= d\lambda\,, \end{aligned} \tag{2.112}$$

or, equivalently,

$$\begin{pmatrix} \dfrac{\partial x_1}{\partial \xi^1} & \dfrac{\partial x_1}{\partial \xi^2} & \dfrac{\partial x_1}{\partial \xi^3} & \dfrac{\partial x_1}{\partial \lambda} \\ \dfrac{\partial x_2}{\partial \xi^1} & \dfrac{\partial x_2}{\partial \xi^2} & \dfrac{\partial x_2}{\partial \xi^3} & \dfrac{\partial x_2}{\partial \lambda} \\ \dfrac{\partial x_3}{\partial \xi^1} & \dfrac{\partial x_3}{\partial \xi^2} & \dfrac{\partial x_3}{\partial \xi^3} & \dfrac{\partial x_3}{\partial \lambda} \\ \dfrac{\partial t}{\partial \xi^1} & \dfrac{\partial t}{\partial \xi^2} & \dfrac{\partial t}{\partial \xi^3} & \dfrac{\partial t}{\partial \lambda} \end{pmatrix} = \begin{pmatrix} A & L & P & U \\ B & M & Q & V \\ C & N & R & W \\ 0 & 0 & 0 & 1 \end{pmatrix}. \tag{2.113}$$

The mesh velocity components U, V, W are assigned to fulfill the above mentioned requirements (b), (c), and the unknown functions $A, B, \ldots, R$ in (2.112) are determined by the rules of differentiations which they satisfy.[6] These rules emerge as additional equations which are solved in conjunction with the physical equations.

[6] For instance, $A = \partial x_1/\partial \xi^1$, $U = \partial x_1/\partial \lambda$, so that, $\partial A/\partial \lambda = \partial U/\partial x_1$, and once U is known, this represents an evolution equation for A.

Thus, the curvilinear coordinates (ξ^1, ξ^2, ξ^3) are generated while advancing in time the numerical procedure. For several prescriptions of the grid velocity (U, V, W) and for more details on the UC approach see Hui and Xu [8].

When erosion/deposition processes are taken into account, the time-dependent change of coordinates (2.101) can be conceived as a space-time change of coordinates (2.111), where

$$\begin{pmatrix} \frac{\partial \xi^1}{\partial x_1} & \frac{\partial \xi^1}{\partial x_2} & \frac{\partial \xi^1}{\partial x_3} & \frac{\partial \xi^1}{\partial t} \\ \frac{\partial \xi^2}{\partial x_1} & \frac{\partial \xi^2}{\partial x_2} & \frac{\partial \xi^2}{\partial x_3} & \frac{\partial \xi^2}{\partial t} \\ \frac{\partial \xi^3}{\partial x_1} & \frac{\partial \xi^3}{\partial x_2} & \frac{\partial \xi^3}{\partial x_3} & \frac{\partial \xi^3}{\partial t} \\ \frac{\partial \lambda}{\partial x_1} & \frac{\partial \lambda}{\partial x_2} & \frac{\partial \lambda}{\partial x_3} & \frac{\partial \lambda}{\partial t} \end{pmatrix} = \left(\begin{array}{c|c} \boldsymbol{A} & \begin{matrix} -\mathbf{w} \\ -\mathrm{w} \end{matrix} \\ \hline \mathbf{0} & 1 \end{array}\right), \tag{2.114}$$

see (2.81) and (2.105). This gives,

$$\begin{pmatrix} \frac{\partial x_1}{\partial \xi^1} & \frac{\partial x_1}{\partial \xi^2} & \frac{\partial x_1}{\partial \xi^3} & \frac{\partial x_1}{\partial \lambda} \\ \frac{\partial x_2}{\partial \xi^1} & \frac{\partial x_2}{\partial \xi^2} & \frac{\partial x_2}{\partial \xi^3} & \frac{\partial x_2}{\partial \lambda} \\ \frac{\partial x_3}{\partial \xi^1} & \frac{\partial x_3}{\partial \xi^2} & \frac{\partial x_3}{\partial \xi^3} & \frac{\partial x_3}{\partial \lambda} \\ \frac{\partial t}{\partial \xi^1} & \frac{\partial t}{\partial \xi^2} & \frac{\partial t}{\partial \xi^3} & \frac{\partial t}{\partial \lambda} \end{pmatrix} = \left(\begin{array}{c|c} \boldsymbol{A}^{-1} & \boldsymbol{A}^{-1}\begin{pmatrix} \mathbf{w} \\ \mathrm{w} \end{pmatrix} \\ \hline \mathbf{0} & 1 \end{array}\right), \tag{2.115}$$

see Exercise 2.5, which indicates that the transformation (2.111) corresponding to the topography-fitted coordinates has the form (2.113), with

$$\begin{pmatrix} A & L & P \\ B & M & Q \\ C & N & R \end{pmatrix} = \boldsymbol{A}^{-1}, \quad \begin{pmatrix} U \\ V \\ W \end{pmatrix} = \boldsymbol{A}^{-1}\begin{pmatrix} \mathbf{w} \\ \mathrm{w} \end{pmatrix}. \tag{2.116}$$

Based on this remark we show how the change of parameters (2.58) can be chosen. Note that in expression $(2.110)_1$ of $\mathbf{w}$, $\mathbf{u}_S$ is a term which refers solely to the transformation (2.58) that has not yet been prescribed. One effect is that the mesh velocity $(2.116)_2$ bears some degree of freedom, which resembles the UC and other moving mesh approaches. Thus, for simplicity, the mesh velocity $(2.116)_2$ can be taken such that

$$\mathbf{u}_S = \mathbf{0}\,. \tag{2.117}$$

According to (2.66), this choice for $\mathbf{u}_S$ reads as

$$\mathbf{v}_{\mathcal{S}} = -\mathcal{U}\mathbf{s}\,, \tag{2.118}$$

or, componentwise,

$$\frac{\partial x}{\partial t} = -c\,\mathcal{U}\frac{\partial b}{\partial x}\,, \quad \frac{\partial y}{\partial t} = -c\,\mathcal{U}\frac{\partial b}{\partial y}\,, \tag{2.119}$$

see (2.69). Therefore, assumption (2.117) prescribes the time derivatives of $x(\xi^1, \xi^2, t)$ and $y(\xi^1, \xi^2, t)$, and it only remains to define the initial values $x(\xi^1, \xi^2, 0)$, $y(\xi^1, \xi^2, 0)$ to obtain the functions x, y by forward integration. These initial values can be determined e.g., by considering the parameters ξ^1, ξ^2 as being the arc lengths on the coordinate lines $y =$ constant and $x =$ constant on the topographic surface at time $t = 0$, see also the forthcoming Sect. 5.4. With this choice, $\det \mathbf{F}(\xi^1, \xi^2, 0) > 0$, and so, for sufficiently smooth right-hand sides in (2.119), $\det \mathbf{F} > 0$ for at least a short time interval $[0, T)$. That is, conditions (2.119) do indeed define a (time-dependent) change of coordinates $(x, y) \longleftrightarrow (\xi^1, \xi^2)$ on $[0, T)$. As a matter of fact, the case $\det \mathbf{F} = 0$ can be avoided in a numerical algorithm. In the numerical computations by Y.C. Tai, C.Y. Kuo and collaborators [5, 9–11], $\det \mathbf{F}$ emerging from (2.119) never happened to vanish.

In view of (2.110), assumption (2.117) is equivalent to the requirement

$$\boldsymbol{w}|_{\zeta=0} = \mathcal{U}\boldsymbol{n}_b\,, \tag{2.120}$$

which has been used by Tai and Kuo [5]. Thus, (2.117) states that, at the basal topography the computational mesh moves along the normal direction to the topographic surface with the velocity $\mathcal{U}$.

The requirements (a) and (b) of the UC method are also taken into account in [5], resulting in a distinct approach, in this book called non-conventional method (see the forthcoming Sect. 4.6), to formulate depth-averaged models for thin flows.

Exercises to Chap. 2

Ex 2.1 Prove (2.17).

Ex 2.2 Show that $\tilde{\boldsymbol{\tau}}_1 \times \tilde{\boldsymbol{\tau}}_2 = (\det \mathbf{F})\,\boldsymbol{\tau}_1 \times \boldsymbol{\tau}_2$, with $\boldsymbol{\tau}_1, \boldsymbol{\tau}_2$ as defined by (2.3), $\mathbf{F}$ given by (2.16), and for $\tilde{\boldsymbol{\tau}}_1, \tilde{\boldsymbol{\tau}}_2$ see (2.18). With the aid of this relation justify the remark following (2.17).

Ex 2.3 Prove (2.41).

Ex 2.4 Show that, if $\mathbf{a} \equiv (a_1, a_2)^T$ is a 2-column matrix, then $\mathbf{I} + \mathbf{a} \otimes \mathbf{a}$ is invertible and

$$(\mathbf{I} + \mathbf{a} \otimes \mathbf{a})^{-1} = \mathbf{I} - \frac{1}{\mathbf{a} \cdot \mathbf{a}} \mathbf{a} \otimes \mathbf{a} .$$

Ex 2.5 Let $\mathbf{A}$ be an invertible 3×3 matrix and let $\mathbf{b}$ be a 3-column matrix. Check that

$$\begin{pmatrix} \mathbf{A} & \mathbf{b} \\ \mathbf{0} & 1 \end{pmatrix}^{-1} = \begin{pmatrix} \mathbf{A}^{-1} & -\mathbf{A}^{-1}\mathbf{b} \\ \mathbf{0} & 1 \end{pmatrix} .$$

Ex 2.6 Prove formula (3.11).

Ex 2.7 Prove formula (3.70).

Ex 2.8 Use relations (2.36) and (2.109) to show that

$$\frac{\partial c}{\partial t} = -c\mathbf{F}^{-1}\mathbf{s} \cdot (\widetilde{\mathbf{H}}\mathbf{u}_{\mathcal{S}} + \mathrm{Grad}\,\mathcal{U}) , \quad \frac{\partial \mathbf{s}}{\partial t} = \mathbf{F}\widetilde{\mathbf{W}}\mathbf{u}_{\mathcal{S}} + \mathbf{F}\mathbf{M}_0\mathrm{Grad}\,\mathcal{U} ,$$

where c and $\mathbf{s}$ are defined in (2.33) (considered with $b = b(x, y, t)$), and are understood as functions of (ξ^1, ξ^2, t) via the transformation (2.58).

References

1. R.F. Dressler, New nonlinear shallow flow equations with curvature. J. Hydraul. Res. **16**, 205–222 (1978)
2. S. De Toni, P. Scotton, Two-dimensional mathematical and numerical model for the dynamics of granular avalanches. Cold Reg. Sci. Technol. **43**, 36–48 (2005)
3. F. Bouchut, M. Westdickenberg, Gravity driven shallow water models for arbitrary topography. Comm. Math. Sci. **2**(3), 359–389 (2004)
4. I.R. Ionescu, Viscoplastic shallow flow equations with topography. J. Nonnewton. Fluid Mech. **193**, 116–128 (2013)
5. Y.C. Tai, C.Y. Kuo, A new model of granular flows over general topography with erosion and deposition. Acta Mech. **199**, 71–96 (2008)
6. W.H. Hui, A unified coordinates approach to computational fluid dynamics. J. Comp. Appl. Math. **163**, 15 (2004)
7. W.H. Hui, The unified coordinate system in computational fluid dynamics. Commun. Comput. Phys. **2**(4), 577–610 (2007)
8. W.H. Hui, K. Xu, *Computational Fluid Dynamics Based on the Unified Coordinates* (Springer, Heidelberg, 2012)
9. Y.C. Tai, Y.C. Lin, A focused view of the behavior of granular flows down a confined inclined chute into horizontal run-out zone. Phys. Fluids **20**, 123302 (2008)
10. Y.C. Tai, C.Y. Kuo, W.H. Hui, An alternative depth-integrated formulation for granular avalanches over temporally varying topography with small curvature. Geophys. Astrophys. Fluid Dyn. **106**(6), 596–629 (2012)
11. Y.C. Tai, C.Y. Kuo, Modelling shallow debris flows of the Coulomb-mixture type over temporally varying topography. Nat. Hazards Earth Syst. Sci. **12**(2), 269–280 (2012)

Chapter 3
Differential Operators and Balance Laws in the Topography-Fitted Coordinates

The ultimate goal of this chapter is to deduce the mass and linear momentum balance laws in the topography-fitted coordinates introduced in Chap. 2, and to be prepared with some mathematical prerequisites when we formulate constitutive equations for the flowing material down arbitrary topography. Thus, some differential operators in Sect. 3.1, and the strain-rate and surface strain-rate in Sect. 3.2, are expressed in the topography-fitted coordinates. In Sect. 3.3 we obtain the mass and linear momentum balance laws in the same coordinates.

3.1 Differential Operators in the Topography-Fitted Coordinates

In this section we express the gradient of a scalar and a vector field, the divergence of a vector and a tensor field in the topography-fitted coordinates introduced in Sect. 2.3. First, in Sect. 3.1.1 we recall the expressions of these operators in general curvilinear coordinates. Then, in Sect. 3.1.2 we particularize these expressions to the case of the topography-fitted coordinates. The time derivative in the time dependent terrain-fitted coordinates is also of interest and will be discussed in Sect. 3.1.3.

3.1.1 Differential Operators in Curvilinear Coordinates

Consider an arbitrary C^2-change of coordinates $(x_1, x_2, x_3) \leftrightarrow (\xi^1, \xi^2, \xi^3)$, where x_1, x_2, x_3 are the Cartesian coordinates, and let $\{\boldsymbol{g}_1, \boldsymbol{g}_2, \boldsymbol{g}_3\}$ be the corresponding natural basis,

$$\boldsymbol{g}_j \equiv \frac{\partial \tilde{\boldsymbol{r}}}{\partial \xi^j}\,, \quad \text{with} \quad \tilde{\boldsymbol{r}}(\xi^1, \xi^2, \xi^3) \equiv x_i(\xi^1, \xi^2, \xi^3)\boldsymbol{e}_i\,, \tag{3.1}$$

I. Luca et al., *Shallow Geophysical Mass Flows down Arbitrary Topography*,
Advances in Geophysical and Environmental Mechanics and Mathematics,
DOI 10.1007/978-3-319-02627-5_3

where $\{\boldsymbol{e}_1, \boldsymbol{e}_2, \boldsymbol{e}_3\}$ is the Cartesian basis. Let f be a scalar field, $\boldsymbol{v}$—a vector field, and $\boldsymbol{\sigma}$—a tensor field,

$$\boldsymbol{v} = v_i \boldsymbol{e}_i = v^j \boldsymbol{g}_j\,, \quad \boldsymbol{\sigma} = \sigma_{ij} \boldsymbol{e}_i \otimes \boldsymbol{e}_j = T^{ij} \boldsymbol{g}_i \otimes \boldsymbol{g}_j\,,$$

which are supposed to be continuously differentiable functions of x_1, x_2, x_3. The following formulae for the gradient of f, $\boldsymbol{v}$, and the divergence of $\boldsymbol{v}$, $\boldsymbol{\sigma}$, can be found in many standard books on continuum mechanics, e.g. Eringen [1] or Bowen and Wang [2],

$$\nabla f \equiv \frac{\partial f}{\partial x_i}\, \boldsymbol{e}_i = \frac{\partial f}{\partial \xi^k} \boldsymbol{g}^k\,, \tag{3.2}$$

$$\nabla \boldsymbol{v} \equiv \frac{\partial v_i}{\partial x_j} \boldsymbol{e}_i \otimes \boldsymbol{e}_j = \left(\frac{\partial v^i}{\partial \xi^j} + \Gamma^i_{jk} v^k \right) \boldsymbol{g}_i \otimes \mathbf{g}^j\,, \tag{3.3}$$

$$\operatorname{div} \boldsymbol{v} \equiv \frac{\partial v_i}{\partial x_i} = \frac{\partial v^i}{\partial \xi^i} + \Gamma^i_{ik} v^k\,, \tag{3.4}$$

$$\operatorname{div} \boldsymbol{\sigma} \equiv \frac{\partial \sigma_{ij}}{\partial x_j} \boldsymbol{e}_i = \left(\frac{\partial T^{ij}}{\partial \xi^j} + \Gamma^i_{jk} T^{kj} + \Gamma^j_{jk} T^{ik} \right) \boldsymbol{g}_i\,. \tag{3.5}$$

Here, $\{\boldsymbol{g}^1, \boldsymbol{g}^2, \boldsymbol{g}^3\}$ is the reciprocal basis associated to $\{\boldsymbol{g}_1, \boldsymbol{g}_2, \boldsymbol{g}_3\}$, and the *Christoffel symbols of the second kind*, Γ^i_{jk}, are defined by

$$\Gamma^i_{jk} \equiv \frac{\partial^2 x_l}{\partial \xi^j \partial \xi^k} \frac{\partial \xi^i}{\partial x_l} = A_{il} \frac{\partial A^{-1}_{lk}}{\partial \xi^j} = \left(\boldsymbol{A} \frac{\partial \boldsymbol{A}^{-1}}{\partial \xi^j} \right)_{ik} = \Gamma^i_{kj}\,, \tag{3.6}$$

where $\boldsymbol{A}^{-1}$ denotes the matrix of components $\partial x_i / \partial \xi^j$. In (3.6) the equality $\Gamma^i_{jk} = \Gamma^i_{kj}$ holds due to the assumption that x_1, x_2, x_3 are twice continuously differentiable functions on ξ^1, ξ^2, ξ^3.

Both formulae (3.4) and (3.5) for div $\boldsymbol{v}$ and div $\boldsymbol{\sigma}$ can be further written as follows. With $J \equiv \det \boldsymbol{A}^{-1}$, we have

$$\frac{\partial J}{\partial \xi^k} = \frac{\partial J}{\partial A^{-1}_{ij}} \frac{\partial A^{-1}_{ij}}{\partial \xi^k} = J A_{ji} \frac{\partial A^{-1}_{ij}}{\partial \xi^k} = J \operatorname{tr}\left(\boldsymbol{A} \frac{\partial \boldsymbol{A}^{-1}}{\partial \xi^k} \right) = J \Gamma^i_{ik}\,, \tag{3.7}$$

so that Γ^i_{ik} can be replaced in (3.4) and (3.5) by $(1/J)\partial J / \partial \xi^k$. As a consequence, with $\boldsymbol{T} \equiv (T^{ij})$, formulae (3.4) and (3.5) turn into

$$\operatorname{div} \boldsymbol{v} = \frac{1}{J} \frac{\partial}{\partial \xi^i} \left(J v^i \right)\,, \tag{3.8}$$

$$\operatorname{div}\boldsymbol{\sigma} = \frac{1}{J}\left(\frac{\partial}{\partial\xi^j}(JT^{ij}) - J\Gamma^i(\boldsymbol{T})\right)\boldsymbol{g}_i\,, \quad \Gamma^i(\boldsymbol{T}) \equiv -\Gamma^i_{jk}T^{kj}\,, \tag{3.9}$$

respectively. From relation (3.7) we extract the formula

$$\frac{\partial J}{\partial\xi^k} = J\,\mathrm{tr}\left(\boldsymbol{A}\frac{\partial\boldsymbol{A}^{-1}}{\partial\xi^k}\right), \quad k \in \{1,2,3\}\,. \tag{3.10}$$

Furthermore, $\operatorname{div}\boldsymbol{\sigma}$ can be expressed in terms of the components Σ^{ik} in the mixed representation

$$\boldsymbol{\sigma} = \Sigma^{ik}\boldsymbol{e}_i \otimes \boldsymbol{g}_k\,,$$

as

$$\operatorname{div}\boldsymbol{\sigma} = \frac{1}{J}\frac{\partial}{\partial\xi^k}\left(J\Sigma^{ik}\right)\boldsymbol{e}_i\,, \tag{3.11}$$

see Exercise 2.6. Formulae (3.8) and (3.11) are called *conservation forms* of $\operatorname{div}\boldsymbol{v}$ and $\operatorname{div}\boldsymbol{\sigma}$.

Let us comment on the various forms of the divergence of a vector and a tensor. Both (3.8) and (3.9) are needed to write the mass and linear momentum balance laws in curvilinear coordinates, as it is commonly encountered in continuum mechanics, see for example Eringen [1] or Bowen and Wang [2]. Another way to write these balance laws in curvilinear coordinates, less known in the continuum mechanics community, is based on (3.8) and (3.11), and dates back to Viviand [3] and Vinokur [4]. When developing models for shallow flows down arbitrary topographies, we will use the mass and momentum balance equations in the topography-fitted coordinates as deduced by these two ways, and refer to these routes as

- *the conventional route*—based on (3.8) and (3.9),
- *the non-conventional route*—based on (3.8) and (3.11).

Therefore, we need explicit expressions of (3.8), (3.9) and (3.11) for the particular case of topography-fitted coordinates. These expressions are derived in the next section.

3.1.2 Gradient and Divergence in the Topography-Fitted Coordinates

In this section we consider the curvilinear coordinates introduced in Sect. 2.2.1 and express the right-hand sides of (3.2), (3.3), (3.8), (3.9) and (3.11) for this particular choice. More precisely,

- when referring to (3.2), (3.3) and (3.9) we are interested in obtaining the contravariant components $(\nabla f)^i$, $(\nabla\boldsymbol{v})^{ij}$ and $(\operatorname{div}\boldsymbol{\sigma})^i$ in the representations

$$\nabla f = (\nabla f)^i \boldsymbol{g}_i\,, \quad \nabla \boldsymbol{v} = (\nabla \boldsymbol{v})^{ij} \boldsymbol{g}_i \otimes \boldsymbol{g}_j\,, \quad \operatorname{div} \boldsymbol{\sigma} = (\operatorname{div} \boldsymbol{\sigma})^i \boldsymbol{g}_i\,, \tag{3.12}$$

collected in block-matrices as in (2.91);

- formula (3.8) for div $\boldsymbol{v}$ will be written by using notation $(2.91)_1$ for the components v^i;
- the Cartesian components $(\operatorname{div} \boldsymbol{\sigma})_i$ of div $\boldsymbol{\sigma}$ as given in (3.11) will be expressed in the block-matrix form $(2.95)_1$.

To simplify a bit the derivations we assume that $\boldsymbol{\sigma}$ is a symmetric tensor, since this is the only case which we will use in the ensuing chapters. We proceed sequentially.

(i) We begin with (3.2), in which we insert $\boldsymbol{g}^k = g^{ik} \boldsymbol{g}_i$ to deduce

$$\nabla f = g^{ik} \frac{\partial f}{\partial \xi^k} \boldsymbol{g}_i \quad \Longleftrightarrow \quad (\nabla f)^i = g^{ik} \frac{\partial f}{\partial \xi^k}\,.$$

Using (1.12) and (2.85) yields

The contravariant components $(\nabla f)^i$ of ∇f *in the topography-fitted coordinates,*

$$\nabla f = (\nabla f)^i \boldsymbol{g}_i\,,$$

are given by

$$\begin{pmatrix} (\nabla f)^1 \\ (\nabla f)^2 \\ (\nabla f)^3 \end{pmatrix} = \begin{pmatrix} \mathbf{M} & \mathbf{0} \\ \mathbf{0} & 1 \end{pmatrix} \begin{pmatrix} \operatorname{Grad} f \\ \dfrac{\partial f}{\partial \zeta} \end{pmatrix} = \begin{pmatrix} \mathbf{M} \operatorname{Grad} f \\ \dfrac{\partial f}{\partial \zeta} \end{pmatrix}. \tag{3.13}$$

(ii) Formula (3.3) for $\nabla \boldsymbol{v}$ is more involved, since we need to compute the Christoffel symbols. According to definition (3.6), these symbols are the entries of the matrices

$$\overset{(j)}{\boldsymbol{\Gamma}} \equiv \boldsymbol{A} \frac{\partial \boldsymbol{A}^{-1}}{\partial \xi^j}\,, \quad j = 1, 2, 3\,, \tag{3.14}$$

which we next determine. First, using the expressions (2.80) and (2.81) of $\boldsymbol{A}^{-1}$ and $\boldsymbol{A}$, respectively, and the relation $\mathbf{s} \cdot \mathbf{s} + c^2 = 1$, see (2.40), we obtain

$$\overset{(j)}{\boldsymbol{\Gamma}} = \begin{pmatrix} \mathbf{B}^{-1} \left\{ \dfrac{\partial \mathbf{B}}{\partial \xi^j} + \mathbf{s} \otimes \mathbf{B}^T \left(\dfrac{\partial \mathbf{s}}{\partial \xi^j} - \dfrac{1}{c} \dfrac{\partial c}{\partial \xi^j} \mathbf{s} \right) \right\} & -\mathbf{B}^{-1} \dfrac{\partial \mathbf{s}}{\partial \xi^j} \\ \left\{ \mathbf{B}^T \left(\dfrac{\partial \mathbf{s}}{\partial \xi^j} - \dfrac{1}{c} \dfrac{\partial c}{\partial \xi^j} \mathbf{s} \right) \right\}^T & 0 \end{pmatrix}. \tag{3.15}$$

By the formulae

$$\frac{\partial c}{\partial \xi^\alpha} = \mathrm{Grad}\, c \cdot \mathbf{e}_\alpha\,, \quad \frac{\partial \mathbf{s}}{\partial \xi^\alpha} = (\mathrm{Grad}\, \mathbf{s})\mathbf{e}_\alpha\,, \quad \alpha \in \{1,2\},$$

and (2.51), $(2.49)_3$, relation (3.15) for $j = 1, 2$ turns into

$$\overset{(\alpha)}{\boldsymbol{\Gamma}} = \begin{pmatrix} \mathbf{B}^{-1}\left\{\dfrac{\partial \mathbf{B}}{\partial \xi^\alpha} + \mathbf{s} \otimes \left(\mathbf{B}^T \mathbf{F}^{-T} \widetilde{\mathbf{H}} \mathbf{e}_\alpha\right)\right\} & -\mathbf{B}^{-1}\mathbf{F}\widetilde{\mathbf{W}}\mathbf{e}_\alpha \\ \left(\mathbf{B}^T \mathbf{F}^{-T} \widetilde{\mathbf{H}} \mathbf{e}_\alpha\right)^T & 0 \end{pmatrix}, \tag{3.16}$$

with $\alpha = 1, 2$. Then, $\overset{(3)}{\boldsymbol{\Gamma}}$ follows at once from definition (2.79) of $\mathbf{B}$ and since c and $\mathbf{s}$ are independent of $\xi^3 \equiv \zeta$,

$$\overset{(3)}{\boldsymbol{\Gamma}} = \begin{pmatrix} -\mathbf{B}^{-1}\mathbf{F}\widetilde{\mathbf{W}} & \mathbf{0} \\ \mathbf{0} & 0 \end{pmatrix}. \tag{3.17}$$

The Christoffel symbols (3.6) are therefore determined and shown in formulae (3.16) and (3.17), with definition (3.14) of $\overset{(j)}{\boldsymbol{\Gamma}}$, $j = 1, 2, 3$. For further use we mention the relation

$$\frac{\partial J}{\partial \zeta} = -J\,\mathrm{tr}\left\{(\mathbf{I} - \zeta\widetilde{\mathbf{W}})^{-1}\widetilde{\mathbf{W}}\right\}, \tag{3.18}$$

as a consequence of (3.10), (3.17) and (2.79).

We can now go further to obtain the components of $(\nabla \boldsymbol{v})^{ij}$ in the representation $(3.12)_2$. From (3.3) we have

$$(\nabla \boldsymbol{v})^{ij} = v^i{}_{;k}\, g^{kj}\,, \quad \text{where} \quad v^i{}_{;k} \equiv \frac{\partial v^i}{\partial \xi^k} + \Gamma^i_{kl} v^l\,,$$

implying the matrix equivalent

$$\left((\nabla \boldsymbol{v})^{ij}\right) = (v^i{}_{;k})(g^{kj})\,, \quad \text{with} \quad (v^i{}_{;j}) = \left(\frac{\partial v^i}{\partial \xi^j}\right) + \left(\Gamma^i_{jk} v^k\right). \tag{3.19}$$

The challenging matrix in $(3.19)_2$ is $\left(\Gamma^i_{jk} v^k\right)$, which we deduce as follows. Recalling notations (1.10) for the 3-columns $\boldsymbol{e}_1, \boldsymbol{e}_2, \boldsymbol{e}_3$, we obtain

$$\begin{aligned} \left(\Gamma^i_{jk} v^k\right) = \Gamma^i_{jk} v^k \boldsymbol{e}_i \otimes \boldsymbol{e}_j = (\Gamma^i_{jk} v^k \boldsymbol{e}_i) \otimes \boldsymbol{e}_j = \overset{(j)}{\boldsymbol{\Gamma}} \begin{pmatrix} \mathbf{v} \\ \mathrm{v} \end{pmatrix} \otimes \boldsymbol{e}_j \\ = \overset{(\alpha)}{\boldsymbol{\Gamma}} \begin{pmatrix} \mathbf{v} \\ \mathrm{v} \end{pmatrix} \otimes \begin{pmatrix} \mathbf{e}_\alpha \\ 0 \end{pmatrix} + \overset{(3)}{\boldsymbol{\Gamma}} \begin{pmatrix} \mathbf{v} \\ \mathrm{v} \end{pmatrix} \otimes \begin{pmatrix} \mathbf{0} \\ 1 \end{pmatrix}. \end{aligned} \tag{3.20}$$

In (3.20) we have used the summation convention for Greek indices running from 1 to 2, as we have agreed in Sect. 1.3. Now we substitute $\overset{(\alpha)}{\boldsymbol{\Gamma}}$, $\overset{(3)}{\boldsymbol{\Gamma}}$ given by (3.16) and (3.17) into (3.20), recall the rules *R2*, *R3* in Sect. 1.3, and perform straightforward calculations using

$$
\begin{aligned}
(\mathbf{B}^T\mathbf{F}^{-T}\widetilde{\mathbf{H}}\mathbf{e}_\alpha\cdot\mathbf{v})\mathbf{e}_\alpha &\overset{(R3)_1}{=} (\mathbf{e}_\alpha\cdot\widetilde{\mathbf{H}}\mathbf{F}^{-1}\mathbf{B}\mathbf{v})\,\mathbf{e}_\alpha \overset{(R3)_3}{=} \widetilde{\mathbf{H}}\mathbf{F}^{-1}\mathbf{B}\mathbf{v}\,,\\
(\mathbf{B}^T\mathbf{F}^{-T}\widetilde{\mathbf{H}}\mathbf{e}_\alpha\cdot\mathbf{v})\,\mathbf{s}\otimes\mathbf{e}_\alpha &\overset{(R3)_1}{=} (\mathbf{e}_\alpha\cdot\widetilde{\mathbf{H}}\mathbf{F}^{-1}\mathbf{B}\mathbf{v})\,\mathbf{s}\otimes\mathbf{e}_\alpha\\
&\overset{(R2)_2}{=} (\mathbf{s}\otimes\widetilde{\mathbf{H}}\mathbf{F}^{-1}\mathbf{B}\mathbf{v})\,\mathbf{e}_\alpha\otimes\mathbf{e}_\alpha = \mathbf{s}\otimes\widetilde{\mathbf{H}}\mathbf{F}^{-1}\mathbf{B}\mathbf{v}
\end{aligned}
$$

to obtain

$$
\left(\Gamma^i_{jk}v^k\right) = \left(\begin{array}{c|c} \mathbf{B}^{-1}\left\{\dfrac{\partial\mathbf{B}}{\partial\xi^\alpha}\,\mathbf{v}\otimes\mathbf{e}_\alpha + \mathbf{s}\otimes\widetilde{\mathbf{H}}\mathbf{F}^{-1}\mathbf{B}\mathbf{v} - \mathrm{v}\mathbf{F}\widetilde{\mathbf{W}}\right\} & -\mathbf{B}^{-1}\mathbf{F}\widetilde{\mathbf{W}}\mathbf{v} \\ \hline (\widetilde{\mathbf{H}}\mathbf{F}^{-1}\mathbf{B}\mathbf{v})^T & 0 \end{array}\right).
$$

Finally, recalling (3.19), we add this matrix to

$$
\left(\frac{\partial v^i}{\partial\xi^j}\right) = \left(\begin{array}{c|c} \mathrm{Grad}\,\mathbf{v} & \dfrac{\partial\mathbf{v}}{\partial\zeta} \\ \hline (\mathrm{Grad}\,\mathrm{v})^T & \dfrac{\partial\mathrm{v}}{\partial\zeta} \end{array}\right),
$$

and multiply the result with the matrix (g^{ij}) given in $(2.85)_1$. In this way we deduce that

The contravariant components $(\nabla\boldsymbol{v})^{ij}$ of $\nabla\boldsymbol{v}$ in the topography-fitted coordinates,

$$
\nabla\boldsymbol{v} = (\nabla\boldsymbol{v})^{ij}\boldsymbol{g}_i\otimes\boldsymbol{g}_j\,,
$$

are given by

$$\left((\nabla \boldsymbol{v})^{ij}\right) = \left(\begin{array}{c|c} \left[\text{Grad}\,\mathrm{v} + \mathbf{B}^{-1}\left\{\dfrac{\partial \mathbf{B}}{\partial \xi^{\alpha}}\,\mathrm{v}\otimes \mathbf{e}_{\alpha} + \mathrm{s}\otimes \widetilde{\mathbf{H}}\mathbf{F}^{-1}\mathbf{B}\mathrm{v} - \mathrm{v}\mathbf{F}\widetilde{\mathbf{W}}\right\}\right]\mathbf{M} & \dfrac{\partial \mathrm{v}}{\partial \zeta} - \mathbf{B}^{-1}\mathbf{F}\widetilde{\mathbf{W}}\mathrm{v} \\ \hline (\text{Grad}\,\mathrm{v} + \widetilde{\mathbf{H}}\mathbf{F}^{-1}\mathbf{B}\mathrm{v})^{T} & \dfrac{\partial \mathrm{v}}{\partial \zeta} \end{array}\right). \tag{3.21}$$

(**iii**) In expression (3.8) for $\text{div}\,\boldsymbol{v}$ we only use notation $(2.91)_1$ and definition (1.13) of $\text{Div}\,\mathbf{v}$. Thus, we can state that

The divergence of a vector $\boldsymbol{v}$ in the topography-fitted coordinates can be written as

$$J\,\text{div}\,\boldsymbol{v} = \text{Div}\,(J\mathbf{v}) + \frac{\partial J\mathrm{v}}{\partial \zeta}\,. \tag{3.22}$$

(**iv**) Now we refer to formula (3.9) for $\text{div}\,\boldsymbol{\sigma}$, where $\boldsymbol{\sigma}$ is a symmetric tensor. The Christoffel symbols are given by (3.16) and (3.17), and we have to compute $\Gamma^{i}(\boldsymbol{T})$, $i = 1, 2, 3$, defined in $(3.9)_2$. Letting $\boldsymbol{t}_1, \boldsymbol{t}_2$ and $\boldsymbol{t}_3$ be the columns of $\boldsymbol{T}$, with definition $(3.9)_2$ of $\overset{(j)}{\boldsymbol{\Gamma}}(\boldsymbol{T})$, we have

$$\begin{pmatrix} \Gamma^{1}(\boldsymbol{T}) \\ \Gamma^{2}(\boldsymbol{T}) \\ \Gamma^{3}(\boldsymbol{T}) \end{pmatrix} = -\left(\overset{(1)}{\boldsymbol{\Gamma}}\boldsymbol{t}_1 + \overset{(2)}{\boldsymbol{\Gamma}}\boldsymbol{t}_2 + \overset{(3)}{\boldsymbol{\Gamma}}\boldsymbol{t}_3\right). \tag{3.23}$$

The aim is to deduce the right-hand side of (3.23) in block form as in $(2.91)_1$. We work separately on $\overset{(1)}{\boldsymbol{\Gamma}}\boldsymbol{t}_1 + \overset{(2)}{\boldsymbol{\Gamma}}\boldsymbol{t}_2$ and $\overset{(3)}{\boldsymbol{\Gamma}}\boldsymbol{t}_3$, using the schematic notation

$$\overset{(j)}{\boldsymbol{\Gamma}} = \begin{pmatrix} \mathbf{Y}_j & \mathbf{a}_j \\ \mathbf{b}_j^{T} & 0 \end{pmatrix}, \quad j \in \{1, 2, 3\}. \tag{3.24}$$

Recalling the block form $(2.91)_2$ of the 3×3 symmetric matrix $\boldsymbol{T}$,

$$\boldsymbol{T} = \begin{pmatrix} \mathbf{T} & \mathbf{t} \\ \mathbf{t}^{T} & T^{33} \end{pmatrix},$$

and denoting by $\mathbf{p}_1$, $\mathbf{p}_2$ the columns of $\mathbf{T}$, it is clear that

$$\overset{(1)}{\boldsymbol{\Gamma}}\boldsymbol{t}_1+\overset{(2)}{\boldsymbol{\Gamma}}\boldsymbol{t}_2=\begin{pmatrix}\mathbf{Y}_1\mathbf{p}_1+\mathbf{Y}_2\mathbf{p}_2+T^{31}\mathbf{a}_1+T^{32}\mathbf{a}_2\\ \mathbf{b}_1\cdot\mathbf{p}_1+\mathbf{b}_2\cdot\mathbf{p}_2\end{pmatrix}\equiv\begin{pmatrix}\mathbf{Y}_\alpha\,\mathbf{p}_\alpha+T^{3\alpha}\mathbf{a}_\alpha\\ \mathbf{b}_\alpha\cdot\mathbf{p}_\alpha\end{pmatrix}, \tag{3.25}$$

$$\overset{(3)}{\boldsymbol{\Gamma}}\boldsymbol{t}_3=\overset{(3)}{\boldsymbol{\Gamma}}\begin{pmatrix}\mathbf{t}\\ T^{33}\end{pmatrix}=\begin{pmatrix}-\mathbf{B}^{-1}\mathbf{F}\widetilde{\mathbf{W}}\mathbf{t}\\ 0\end{pmatrix}. \tag{3.26}$$

By rules *R3* and *R5*, see Sect. 1.3, for the third entry of the 3-column matrix (3.25) we obtain

$$\mathbf{b}_\alpha\cdot\mathbf{p}_\alpha=\mathbf{B}^T\mathbf{F}^{-T}\widetilde{\mathbf{H}}\mathbf{e}_\alpha\cdot\mathbf{T}\mathbf{e}_\alpha=\mathbf{B}^T\mathbf{F}^{-T}\widetilde{\mathbf{H}}\cdot\mathbf{T}\,. \tag{3.27}$$

Using the last equality arising in (3.27), the expression of $\mathbf{Y}_\alpha$, $\alpha=1,2$, and

$$T^{3\alpha}\mathbf{a}_\alpha=-T^{3\alpha}\mathbf{B}^{-1}\mathbf{F}\widetilde{\mathbf{W}}\mathbf{e}_\alpha=-\mathbf{B}^{-1}\mathbf{F}\widetilde{\mathbf{W}}\mathbf{t}\,,$$

the first two entries of the 3-column matrix (3.25) turn into

$$\mathbf{Y}_\alpha\,\mathbf{p}_\alpha+T^{3\alpha}\mathbf{a}_\alpha=\mathbf{B}^{-1}\left\{\frac{\partial\mathbf{B}}{\partial\xi^\alpha}\,\mathbf{T}\mathbf{e}_\alpha+(\mathbf{B}^T\mathbf{F}^{-T}\widetilde{\mathbf{H}}\cdot\mathbf{T})\,\mathbf{s}\right\}-\mathbf{B}^{-1}\mathbf{F}\widetilde{\mathbf{W}}\mathbf{t}\,. \tag{3.28}$$

Therefore, substituting (3.28) and (3.27) into (3.25), then adding the emerging matrix to (3.26), by relation (3.23) we arrive at

$$\begin{pmatrix}\Gamma^1(\boldsymbol{T})\\ \Gamma^2(\boldsymbol{T})\end{pmatrix}=\boldsymbol{\Gamma}(\mathbf{T},\mathbf{t})\,,\quad \Gamma^3(\boldsymbol{T})=\Gamma(\mathbf{T})\,,$$

with

$$\Gamma(\mathbf{T})\equiv-\mathbf{B}^T\mathbf{F}^{-T}\widetilde{\mathbf{H}}\cdot\mathbf{T}\,, \tag{3.29}$$

$$\boldsymbol{\Gamma}(\mathbf{T},\mathbf{t})\equiv-\mathbf{B}^{-1}\frac{\partial\mathbf{B}}{\partial\xi^\alpha}\mathbf{T}\mathbf{e}_\alpha+2\mathbf{B}^{-1}\mathbf{F}\widetilde{\mathbf{W}}\mathbf{t}+\Gamma(\mathbf{T})\mathbf{B}^{-1}\mathbf{s}\,. \tag{3.30}$$

Thus, noting that

$$\begin{pmatrix} \dfrac{\partial T^{1j}}{\partial \xi^j} \\ \dfrac{\partial T^{2j}}{\partial \xi^j} \\ \dfrac{\partial T^{3j}}{\partial \xi^j} \end{pmatrix} = \begin{pmatrix} \dfrac{\partial T^{1\alpha}}{\partial \xi^\alpha} + \dfrac{\partial T^{13}}{\partial \zeta} \\ \dfrac{\partial T^{2\alpha}}{\partial \xi^\alpha} + \dfrac{\partial T^{23}}{\partial \zeta} \\ \dfrac{\partial T^{3\alpha}}{\partial \xi^\alpha} + \dfrac{\partial T^{33}}{\partial \zeta} \end{pmatrix} = \begin{pmatrix} \mathrm{Div}\,\mathbf{T} + \dfrac{\partial \mathbf{t}}{\partial \zeta} \\ \mathrm{Div}\,\mathbf{t} + \dfrac{\partial T^{33}}{\partial \zeta} \end{pmatrix}, \tag{3.31}$$

we can state the following rule:

Consider a symmetric second order tensor $\boldsymbol{\sigma}$. *The contravariant components* $(\mathrm{div}\,\boldsymbol{\sigma})^i$ *of* $\mathrm{div}\,\boldsymbol{\sigma}$ *in the topography-fitted coordinates,*

$$\mathrm{div}\,\boldsymbol{\sigma} = (\mathrm{div}\,\boldsymbol{\sigma})^i \boldsymbol{g}_i\,,$$

emerge as

$$J \begin{pmatrix} (\mathrm{div}\,\boldsymbol{\sigma})^1 \\ (\mathrm{div}\,\boldsymbol{\sigma})^2 \\ (\mathrm{div}\,\boldsymbol{\sigma})^3 \end{pmatrix} = \begin{pmatrix} \mathrm{Div}\,(J\mathbf{T}) + \dfrac{\partial J\mathbf{t}}{\partial \zeta} - J\boldsymbol{\Gamma}(\mathbf{T},\mathbf{t}) \\ \mathrm{Div}\,(J\mathbf{t}) + \dfrac{\partial JT^{33}}{\partial \zeta} - J\Gamma(\mathbf{T}) \end{pmatrix}, \tag{3.32}$$

where the quantities $\Gamma(\mathbf{T})$ *and* $\boldsymbol{\Gamma}(\mathbf{T},\mathbf{t})$ *are due to the Christoffel symbols and are given by* (3.29) *and* (3.30), *respectively.*

(**v**) With notation $(2.95)_2$ for the hybrid components Σ^{ij} of a second order tensor $\boldsymbol{\sigma}$, similarly to (3.31) we can deduce the following result:

Consider the symmetric second order tensor $\boldsymbol{\sigma} = \Sigma^{ij}\boldsymbol{e}_i \otimes \boldsymbol{g}_j$. *The Cartesian components* $(\mathrm{div}\,\boldsymbol{\sigma})_i$ *of* $\mathrm{div}\,\boldsymbol{\sigma}$,

$$\mathrm{div}\,\boldsymbol{\sigma} = (\mathrm{div}\,\boldsymbol{\sigma})_i \boldsymbol{e}_i\,,$$

as emerging from the conservation form (3.11) *of* $\mathrm{div}\,\boldsymbol{\sigma}$ *when using the topography-fitted coordinates, are given by*

$$J \begin{pmatrix} (\mathrm{div}\,\boldsymbol{\sigma})_1 \\ (\mathrm{div}\,\boldsymbol{\sigma})_2 \\ (\mathrm{div}\,\boldsymbol{\sigma})_3 \end{pmatrix} = \begin{pmatrix} \mathrm{Div}\,(J\mathbb{S}) + \dfrac{\partial J\mathbb{s}}{\partial \zeta} \\ \mathrm{Div}\,(J\mathbf{t}) + \dfrac{\partial J\sigma}{\partial \zeta} \end{pmatrix}. \tag{3.33}$$

3.1.3 Time Derivative in the Topography-Fitted Coordinates

Here we deduce the rule for computing the time derivative of a function $f(x_1, x_2, x_3, t)$ in terms of the time derivative of $f(\xi^1, \xi^2, \xi^3, t)$, where x_1, x_2, x_3 are Cartesian coordinates related to curvilinear coordinates ξ^1, ξ^2, ξ^3 by a time dependent transformation,

$$x_i = x_i(\xi^1, \xi^2, \xi^3, t) \quad \longleftrightarrow \quad \xi^k = \xi^k(x_1, x_2, x_3, t)\,, \tag{3.34}$$

and

$$\begin{aligned} f(x_1, x_2, x_3, t) &= f(x_1(\xi^1, \xi^2, \xi^3, t), x_2(\xi^1, \xi^2, \xi^3, t), x_3(\xi^1, \xi^2, \xi^3, t), t) \\ &\equiv f(\xi^1, \xi^2, \xi^3, t)\,. \end{aligned} \tag{3.35}$$

Of course, we are interested in the time-dependent topography-fitted coordinates explained in Sect. 2.3.3. However, the reasonings to get the rule for this case are the same as those from the general case, and do not use the special relation (2.100) between (x_1, x_2, x_3, t) and (ξ^1, ξ^2, ξ^3, t). Thus, we perform the analysis for an arbitrary transformation (3.34). We will use the definitions

$$\boldsymbol{g}_k \equiv \frac{\partial \tilde{\boldsymbol{r}}}{\partial \xi^k} \quad \text{with} \quad \tilde{\boldsymbol{r}}(\xi^1, \xi^2, \xi^3, t) \equiv x_i(\xi^1, \xi^2, \xi^3, t)\boldsymbol{e}_i\,, \tag{3.36}$$

$$\boldsymbol{w} \equiv \frac{\partial \tilde{\boldsymbol{r}}}{\partial t} = w_i \boldsymbol{e}_i = w^k \boldsymbol{g}_k\,, \tag{3.37}$$

and the notations $\zeta \equiv \xi^3$, $\mathbf{w} \equiv (w^1, w^2)^T$, $\mathrm{w} \equiv w^3$. The components w_i and w^k enjoy the properties

$$w_i = \frac{\partial x_i}{\partial t}\,, \quad w^k = -\dot{\xi}^k\,, \quad \dot{\xi}^k \equiv \frac{\partial \xi^k}{\partial t}\,. \tag{3.38}$$

For the case of the topography-fitted coordinates both $\mathbf{w}$ and w have been computed and can be found in (2.110).

Note that we have used the same letter, f, for both functions in relation (3.35).[1] To distinguish between their time derivatives we use

$$\frac{\partial f}{\partial t} \quad \text{for} \quad f(x_1, x_2, x_3, t)\,, \quad \text{and} \quad \frac{\tilde{\partial} f}{\partial t} \quad \text{for} \quad f(\xi^1, \xi^2, \xi^3, t)\,.$$

[1] This is the rule when dealing with physical quantities, e.g. density ρ, velocity $\boldsymbol{v}$, otherwise we would have used the "tilde" notation for f, i.e., $\tilde{f}(\xi^1, \xi^2, \xi^3, t)$.

In the next chapters, when we apply the time differentiation rule, see e.g. (3.62)–(3.64) below, we will switch from $\tilde{\partial} f/\partial t$ to $\partial f/\partial t$, since the context makes clear which time differentiation is understood. The same argument justifies the use of $\partial x_i/\partial t$ and $\partial \tilde{\boldsymbol{r}}/\partial t$ instead of $\tilde{\partial} x_i/\partial t$ and $\tilde{\partial} \tilde{\boldsymbol{r}}/\partial t$, respectively, see (3.37), (3.38).

Now, by differentiation of (3.35) with respect to t, we have

$$\frac{\partial f}{\partial t} = \frac{\tilde{\partial} f}{\partial t} + \frac{\partial f}{\partial \xi^k}\dot{\xi}^k ,$$

which can be further written as

$$\frac{\partial f}{\partial t} = \frac{\tilde{\partial} f}{\partial t} - \frac{\partial f}{\partial \xi^k} w^k = \frac{\tilde{\partial} f}{\partial t} - \mathrm{Grad}\, f \cdot \mathbf{w} - \frac{\partial f}{\partial \zeta}\mathrm{w} . \tag{3.39}$$

Clearly, if the change of coordinates is time independent, formula (3.39) turns into

$$\frac{\partial f}{\partial t} = \frac{\tilde{\partial} f}{\partial t} . \tag{3.40}$$

We will also need the following relation,

$$J\frac{\partial f}{\partial t} = \frac{\tilde{\partial} Jf}{\partial t} - \mathrm{Div}\,(Jf\mathbf{w}) - \frac{\partial Jf\mathrm{w}}{\partial \zeta} , \tag{3.41}$$

which can be immediately derived from (3.39) by using

$$\frac{\tilde{\partial} J}{\partial t} = \frac{\partial J w^k}{\partial \xi^k} . \tag{3.42}$$

Indeed, assuming (3.42), by (3.39) we have

$$\begin{aligned} J\frac{\partial f}{\partial t} &= J\frac{\tilde{\partial} f}{\partial t} - J\frac{\partial f}{\partial \xi^k} w^k = \frac{\tilde{\partial} Jf}{\partial t} - f\frac{\tilde{\partial} J}{\partial t} - \frac{\partial f}{\partial \xi^k} J w^k \\ &= \frac{\tilde{\partial} Jf}{\partial t} - f\frac{\partial J w^k}{\partial \xi^k} - \frac{\partial f}{\partial \xi^k} J w^k = \frac{\tilde{\partial} Jf}{\partial t} - \frac{\partial Jf w^k}{\partial \xi^k} , \end{aligned}$$

which corroborates (3.41). Now we prove (3.42), by recalling that

$$\frac{\partial J}{\partial A^{-1}_{jk}} = J A_{kj}\,, \quad \frac{\partial A^{-1}_{jl}}{\partial \xi^k} = \frac{\partial A^{-1}_{jk}}{\partial \xi^l}\,, \quad J\mathrm{tr}\left(\boldsymbol{A}\frac{\partial \boldsymbol{A}^{-1}}{\partial \xi^l}\right) = \frac{\partial J}{\partial \xi^l}\,.$$

We have

$$\begin{aligned}
\frac{\tilde{\partial} J}{\partial t} &= \frac{\partial J}{\partial A^{-1}_{jk}}\frac{\tilde{\partial} A^{-1}_{jk}}{\partial t} = J A_{kj}\frac{\tilde{\partial}}{\partial t}\left(\frac{\partial x_j}{\partial \xi^k}\right) = J A_{kj}\frac{\partial}{\partial \xi^k}\left(\frac{\partial x_j}{\partial t}\right)\\
&= J A_{kj}\frac{\partial w_j}{\partial \xi^k} = J A_{kj}\frac{\partial A^{-1}_{jl} w^l}{\partial \xi^k} = J A_{kj}\left(\frac{\partial A^{-1}_{jl}}{\partial \xi^k} w^l + A^{-1}_{jl}\frac{\partial w^l}{\partial \xi^k}\right)\\
&= J A_{kj}\frac{\partial A^{-1}_{jl}}{\partial \xi^k} w^l + J\frac{\partial w^k}{\partial \xi^k} = J A_{kj}\frac{\partial A^{-1}_{jk}}{\partial \xi^l} w^l + J\frac{\partial w^l}{\partial \xi^l}\\
&= J\mathrm{tr}\left(\boldsymbol{A}\frac{\partial \boldsymbol{A}^{-1}}{\partial \xi^l}\right) w^l + J\frac{\partial w^l}{\partial \xi^l} = \frac{\partial J}{\partial \xi^l} w^l + J\frac{\partial w^l}{\partial \xi^l} = \frac{\partial J w^l}{\partial \xi^l}\,,
\end{aligned}$$

which yields (3.42).

3.2 Strain-Rate and Surface Strain-Rate in the Topography-Fitted Coordinates

In this section we search for the contravariant components of the strain-rate tensor in the topography-based coordinates, and determine the expression of the surface strain-rate when the parameterization (2.43) of the basal topography is used.

(**i**) The *strain-rate* tensor $\boldsymbol{D}$ is defined by

$$\boldsymbol{D} \equiv \tfrac{1}{2}\left(\nabla \boldsymbol{v} + (\nabla \boldsymbol{v})^T\right)\,, \tag{3.43}$$

where $\boldsymbol{v}$ denotes the velocity vector. Having obtained the components of the gradient of a vector, see (3.21), we can readily deduce the components D^{ij} of $\boldsymbol{D}$ in the representation $\boldsymbol{D} = D^{ij}\boldsymbol{g}_i \otimes \boldsymbol{g}_j$. We write the matrix of these components in block form,

$$(D^{ij}) = \begin{pmatrix} \mathbf{D} & \mathbf{d} \\ \mathbf{d}^T & D^{33} \end{pmatrix}. \tag{3.44}$$

Using definition (3.43) of $\boldsymbol{D}$, relation (3.21) for the matrix $((\nabla \boldsymbol{v})^{ij})$ and noticing that $\mathbf{M}\widetilde{\mathbf{H}}\mathbf{F}^{-1}\mathbf{B} = \mathbf{B}^{-1}\mathbf{F}\widetilde{\mathbf{W}}$, we conclude that,

The contravariant components D^{ij} of the strain-rate tensor $\boldsymbol{D}$ in the topography-fitted coordinates,

$$\boldsymbol{D} = D^{ij}\boldsymbol{g}_i \otimes \boldsymbol{g}_j\,,$$

collected as indicated in (3.44), are given by

$$\begin{aligned}
\mathbf{D} &= \frac{1}{2}\left\{\left[\operatorname{Grad}\mathbf{v} + \mathbf{B}^{-1}\left(\frac{\partial \mathbf{B}}{\partial \xi^\alpha}\,\mathbf{v}\otimes\mathbf{e}_\alpha + \mathbf{s}\otimes\widetilde{\mathbf{H}}\mathbf{F}^{-1}\mathbf{B}\mathbf{v} - \mathrm{v}\mathbf{F}\widetilde{\mathbf{W}}\right)\right]\mathbf{M}\right.\\
&\qquad \left. + \mathbf{M}\left[\operatorname{Grad}\mathbf{v} + \mathbf{B}^{-1}\left(\frac{\partial \mathbf{B}}{\partial \xi^\alpha}\,\mathbf{v}\otimes\mathbf{e}_\alpha + \mathbf{s}\otimes\widetilde{\mathbf{H}}\mathbf{F}^{-1}\mathbf{B}\mathbf{v} - \mathrm{v}\mathbf{F}\widetilde{\mathbf{W}}\right)\right]^T\right\},\\
\mathbf{d} &= \frac{1}{2}\left\{\frac{\partial \mathbf{v}}{\partial \zeta} + \mathbf{M}\operatorname{Grad}\mathrm{v}\right\}, \qquad D^{33} = \frac{\partial \mathrm{v}}{\partial \zeta}\,.
\end{aligned} \tag{3.45}$$

We are also interested in expressing the second invariant of $\boldsymbol{D}$ in terms of the components D^{ij}. With $g_{ij} \equiv \boldsymbol{g}_i \cdot \boldsymbol{g}_j$, we have

$$\boldsymbol{D}^2 = (D^{ij}\boldsymbol{g}_i \otimes \boldsymbol{g}_j)(D^{kl}\boldsymbol{g}_k \otimes \boldsymbol{g}_l) = D^{ij}g_{jk}D^{kl}\boldsymbol{g}_i \otimes \boldsymbol{g}_l\,,$$

so that

$$\operatorname{tr}\boldsymbol{D}^2 = D^{ij}g_{jk}D^{kl}g_{li} = \operatorname{tr}\left((D^{ij})(g_{jk})\right)^2\,.$$

Recalling (2.85) and (3.44), it follows that

The second invariant $II_{\boldsymbol{D}}$ of the strain-rate tensor $\boldsymbol{D}$ is obtained as

$$II_{\boldsymbol{D}} \equiv \tfrac{1}{2}\operatorname{tr}\boldsymbol{D}^2 = \frac{1}{2}\left\{\operatorname{tr}(\mathbf{D}\mathbf{M}^{-1})^2 + 2\mathbf{M}^{-1}\mathbf{d}\cdot\mathbf{d} + (D^{33})^2\right\}, \tag{3.46}$$

with $\mathbf{D}$, $\mathbf{d}$ *and* D^{33} *given by* (3.45).

(**ii**) Let $\mathcal{S}$ be a surface given by the parametrization $x_k = x_k(\xi^1, \xi^2)$, $k = 1, 2, 3$. Consider a vector field $\boldsymbol{u}$ tangent to $\mathcal{S}$ and represented with respect to the basis vectors $\boldsymbol{\tau}_1, \boldsymbol{\tau}_2$ as

$$\boldsymbol{u} = u^1\boldsymbol{\tau}_1 + u^2\boldsymbol{\tau}_2\,.$$

The *surface gradient* of $\boldsymbol{u}$ is the second order tensor on the tangent space to $\mathcal{S}$ defined by

$$\nabla_{\mathcal{S}}\boldsymbol{u} \equiv u^\alpha{}_{;\beta}\boldsymbol{\tau}_\alpha \otimes \boldsymbol{\tau}^\beta,$$

where the covariant derivative $u^{\alpha}_{;\beta}$ is given by

$$u^{\alpha}_{;\beta} \equiv \frac{\partial u^{\alpha}}{\partial \xi^{\beta}} + \Gamma^{\alpha}_{\gamma\beta}\, u^{\gamma}, \quad \Gamma^{\alpha}_{\gamma\beta} \equiv \phi^{\alpha\sigma} \frac{\partial^2 x_i}{\partial \xi^{\beta} \partial \xi^{\gamma}} \frac{\partial x_i}{\partial \xi^{\sigma}}, \quad \phi^{\alpha\sigma} \equiv \boldsymbol{\tau}^{\alpha} \cdot \boldsymbol{\tau}^{\sigma}, \tag{3.47}$$

with $\{\boldsymbol{\tau}^1, \boldsymbol{\tau}^2\}$ the reciprocal basis of $\{\boldsymbol{\tau}_1, \boldsymbol{\tau}_2\}$. If $\boldsymbol{u}$ is a velocity field, the symmetric part of its surface gradient,

$$\boldsymbol{D}_{\mathcal{S}} \equiv \tfrac{1}{2} \left(\nabla_{\mathcal{S}} \boldsymbol{u} + (\nabla_{\mathcal{S}} \boldsymbol{u})^T \right), \tag{3.48}$$

is called the *surface strain-rate* tensor.

We want to determine the components of the surface strain-rate $\boldsymbol{D}_{\mathcal{S}}$ in the representation

$$\boldsymbol{D}_{\mathcal{S}} = \mathcal{D}^{\alpha}_{\ \beta} \boldsymbol{\tau}_{\alpha} \otimes \boldsymbol{\tau}^{\beta}, \tag{3.49}$$

when the surface $\mathcal{S}$ is the basal topography $\mathcal{S}_b$, parameterized as in (2.43). To this end we note that

$$\mathcal{D}^{\alpha}_{\ \beta} = \tfrac{1}{2} \left\{ u^{\alpha}_{;\beta} + \phi^{\alpha\sigma} u^{\gamma}_{\ ;\sigma} \phi_{\gamma\beta} \right\},$$

implying the matrix equality

$$(\mathcal{D}^{\alpha}_{\ \beta}) = \tfrac{1}{2} \left\{ (u^{\alpha}_{\ ;\beta}) + \mathbf{M}_0 (u^{\alpha}_{\ ;\beta})^T \mathbf{M}_0^{-1} \right\}, \tag{3.50}$$

see (2.50). We therefore need to obtain $(u^{\alpha}_{\ ;\beta})$. Thus, definition $(3.47)_1$ gives the matrix equality

$$(u^{\alpha}_{\ ;\beta}) = \left(\frac{\partial u^{\alpha}}{\partial \xi^{\beta}} \right) + \left(\Gamma^{\alpha}_{\gamma\beta}\, u^{\gamma} \right) = \mathrm{Grad}\, \mathbf{u} + u^{\gamma} \overset{(\gamma)}{\boldsymbol{\Gamma}}, \tag{3.51}$$

where the 2-column $\mathbf{u}$ and the 2×2 matrix $\overset{(\gamma)}{\boldsymbol{\Gamma}}$ are given by

$$\mathbf{u} \equiv (u^1, u^2)^T, \quad \overset{(\gamma)}{\boldsymbol{\Gamma}} \equiv \left(\Gamma^{\alpha}_{\gamma\beta} \right)_{\alpha,\beta \in \{1,2\}}.$$

By (2.45) and $(3.47)_2$, the entries $\Gamma^{\alpha}_{\gamma\beta}$ of $\overset{(\gamma)}{\boldsymbol{\Gamma}}$ read

$$\Gamma^{\alpha}_{\gamma\beta} = \tilde{\phi}^{\alpha\sigma} \sum_{i=1}^{2} \frac{\partial F_{i\beta}}{\partial \xi^{\gamma}} F_{i\sigma} + \tilde{\phi}^{\alpha\sigma} \frac{\partial}{\partial \xi^{\gamma}} \left(\frac{\partial \tilde{b}}{\partial \xi^{\beta}} \right) \frac{\partial \tilde{b}}{\partial \xi^{\sigma}},$$

which yields, see $(2.48)_1$,

$$\overset{(\gamma)}{\mathbf{\Gamma}} = \mathbf{M}_0\mathbf{F}^T\frac{\partial \mathbf{F}}{\partial \xi^\gamma} + \mathbf{M}_0\mathrm{Grad}\,\tilde{b}\otimes\frac{\partial}{\partial \xi^\gamma}(\mathrm{Grad}\,\tilde{b})\,.$$

Furthermore, using $(2.33)_2$, $(2.51)_1$, we get

$$\mathrm{Grad}\,\tilde{b} = \mathbf{F}^T\mathrm{grad}\,b = \frac{1}{c}\mathbf{F}^T\mathbf{s}\,,\quad \frac{\partial c}{\partial \xi^\gamma} = -c\widetilde{\mathbf{H}}\mathbf{F}^{-1}\mathbf{s}\cdot\mathbf{e}_\gamma = -c\mathbf{F}^{-1}\mathbf{s}\cdot\widetilde{\mathbf{H}}\mathbf{e}_\gamma\,,$$

and by expression (2.50) of $\mathbf{M}_0$ and a routine calculation we obtain

$$\mathbf{M}_0\mathrm{Grad}\,\tilde{b} = c\mathbf{F}^{-1}\mathbf{s}\,,\quad \frac{\partial}{\partial \xi^\gamma}(\mathrm{Grad}\,\tilde{b}) = \frac{1}{c}\widetilde{\mathbf{H}}\mathbf{e}_\gamma + \frac{1}{c}\frac{\partial \mathbf{F}^T}{\partial \xi^\gamma}\mathbf{s}\,.$$

Thus, $\overset{(\gamma)}{\mathbf{\Gamma}}$ becomes

$$\overset{(\gamma)}{\mathbf{\Gamma}} = \mathbf{F}^{-1}\left[\frac{\partial \mathbf{F}}{\partial \xi^\gamma} + (\mathbf{s}\otimes\mathbf{e}_\gamma)\widetilde{\mathbf{H}}\right].$$

To deduce $u^\gamma\overset{(\gamma)}{\mathbf{\Gamma}}$ in (3.51) it is necessary to compute $u^\gamma\partial\mathbf{F}/\partial\xi^\gamma$. This calculation reveals that

$$\begin{aligned} u^\gamma\frac{\partial \mathbf{F}}{\partial \xi^\gamma} &= u^\gamma\frac{\partial F_{\alpha\beta}}{\partial \xi^\gamma}\,\mathbf{e}_\alpha\otimes\mathbf{e}_\beta = u^\gamma\frac{\partial F_{\alpha\gamma}}{\partial \xi^\beta}\,\mathbf{e}_\alpha\otimes\mathbf{e}_\beta \\ &= \left(\frac{\partial F_{\alpha\gamma}}{\partial \xi^\beta}u^\gamma\mathbf{e}_\alpha\right)\otimes\mathbf{e}_\beta = \left(\frac{\partial \mathbf{F}}{\partial \xi^\beta}\mathbf{u}\right)\otimes\mathbf{e}_\beta = \frac{\partial \mathbf{F}}{\partial \xi^\beta}\,\mathbf{u}\otimes\mathbf{e}_\beta\,, \end{aligned}$$

where the identity $\partial F_{\alpha\beta}/\partial\xi^\gamma = \partial F_{\alpha\gamma}/\partial\xi^\beta$ has been used. Thus, (3.51) turns into

$$(u^\alpha{}_{;\beta}) = \mathrm{Grad}\,\mathbf{u} + \mathbf{F}^{-1}\left[\frac{\partial \mathbf{F}}{\partial \xi^\gamma}\,(\mathbf{u}\otimes\mathbf{e}_\gamma) + (\mathbf{s}\otimes\mathbf{u})\widetilde{\mathbf{H}}\right]. \tag{3.52}$$

From (3.50) and (3.52) we now summarize the result:

Consider the surface strain-rate $\boldsymbol{D}_\mathcal{S}$ corresponding to the velocity field $\boldsymbol{u}$ tangent to the topographic surface $\mathcal{S}_b$. When using parameterization (2.43) of $\mathcal{S}_b$, the components $\mathcal{D}^\alpha{}_\beta$ of $\boldsymbol{D}_\mathcal{S}$ in the representation

$$\boldsymbol{D}_\mathcal{S} = \mathcal{D}^\alpha{}_\beta\boldsymbol{\tau}_\alpha\otimes\boldsymbol{\tau}^\beta$$

are given by

$$(\mathcal{D}^{\alpha}{}_{\beta}) = \frac{1}{2}\left\{\text{Grad}\,\mathbf{u} + \mathbf{F}^{-1}\left(\frac{\partial \mathbf{F}}{\partial \xi^{\gamma}}\,\mathbf{u}\otimes\mathbf{e}_{\gamma} + \mathbf{s}\otimes\widetilde{\mathbf{H}}\mathbf{u}\right)\right.$$
$$\left. + \mathbf{M}_0\left[\text{Grad}\,\mathbf{u} + \mathbf{F}^{-1}\left(\frac{\partial \mathbf{F}}{\partial \xi^{\gamma}}\,\mathbf{u}\otimes\mathbf{e}_{\gamma} + \mathbf{s}\otimes\widetilde{\mathbf{H}}\mathbf{u}\right)\right]^{T}\mathbf{M}_0^{-1}\right\}, \tag{3.53}$$

where $\mathbf{u} \equiv (u^1, u^2)^T$, *with* u^1, u^2 *the coordinates of* $\boldsymbol{u}$ *with respect to the basis vectors* $\boldsymbol{\tau}_1, \boldsymbol{\tau}_2$.

3.3 Balance Laws in the Topography-Fitted Coordinates

In the description of a thin fluid flow on an arbitrary topographic surface we ignore the temperature effects. Thus, we restrict attention to the mass and linear momentum balance laws,

$$\frac{\partial \rho}{\partial t} + \text{div}\,(\rho \boldsymbol{v}) = 0\,, \quad \frac{\partial \rho \boldsymbol{v}}{\partial t} + \text{div}\,(\rho \boldsymbol{v}\otimes\boldsymbol{v} - \boldsymbol{\sigma}) = \rho \boldsymbol{b}\,. \tag{3.54}$$

Here ρ is the mass density, $\boldsymbol{v}$ is the velocity, $\boldsymbol{\sigma}$ is the Cauchy stress tensor, $\boldsymbol{\sigma}^T = \boldsymbol{\sigma}$, and $\boldsymbol{b}$ is the specific body force, $\boldsymbol{b} = -g\boldsymbol{e}_3$, where g is the gravitational acceleration. In our applications the closure relations for the stress tensor assume the decomposition

$$\boldsymbol{\sigma} = -p\boldsymbol{I} + \boldsymbol{\sigma}_E\,, \tag{3.55}$$

with the scalar p interpreted as *pressure*, and $\boldsymbol{\sigma}_E$ called the *extra-stress tensor*. From now on $\boldsymbol{\sigma}$ will be considered to have the form (3.55). Next we want to express the balance laws (3.54) in the topography-fitted coordinates. As already mentioned at the end of Sect. 3.1.1, we follow two ways (conventional and non-conventional routes, as defined in Sect. 3.1.1) to accomplish this task. We recall that the two approaches depend on whether the form (3.32) or (3.33) of div $\boldsymbol{\sigma}$ is used. We therefore differentiate two cases, which we treat in separate sections.

3.3.1 Conventional Route (i.e., based on (3.32))

The representations

$$\boldsymbol{v} = v^i \boldsymbol{g}_i\,, \quad \boldsymbol{b} = b^i \boldsymbol{g}_i\,, \quad \boldsymbol{\sigma} = T^{ij}\boldsymbol{g}_i\otimes\boldsymbol{g}_j\,, \quad \boldsymbol{\sigma}_E = P^{ij}\boldsymbol{g}_i\otimes\boldsymbol{g}_j \tag{3.56}$$

introduce the notations for the contravariant components of $\boldsymbol{v}$, $\boldsymbol{b}$, $\boldsymbol{\sigma}$ and $\boldsymbol{\sigma}_E$. In block matrix form these components are written as

$$\begin{gathered}\begin{pmatrix} v^1 \\ v^2 \\ v^3 \end{pmatrix} = \begin{pmatrix} \mathbf{v} \\ \mathrm{v} \end{pmatrix}, \quad \begin{pmatrix} b^1 \\ b^2 \\ b^3 \end{pmatrix} = \begin{pmatrix} \mathbf{b} \\ \mathrm{b} \end{pmatrix}, \\ (T^{ij}) = \begin{pmatrix} \mathbf{T} & \mathbf{t} \\ \mathbf{t}^T & T^{33} \end{pmatrix}, \quad (P^{ij}) = \begin{pmatrix} \mathbf{P} & \mathbf{p} \\ \mathbf{p}^T & P^{33} \end{pmatrix}. \end{gathered} \tag{3.57}$$

The components $\mathbf{b}$ and b of the gravity vector $\boldsymbol{b} = -g\boldsymbol{e}_3$ can be determined by using relation (2.96),

$$\begin{pmatrix} \mathbf{b} \\ \mathrm{b} \end{pmatrix} = \boldsymbol{A} \begin{pmatrix} \mathbf{0} \\ -g \end{pmatrix},$$

which yields, see (2.81),

$$\mathbf{b} = -cg\mathbf{B}^{-1}\mathbf{s}, \quad \mathrm{b} = -cg. \tag{3.58}$$

Since $\boldsymbol{I} = g^{ij}\boldsymbol{g}_i \otimes \boldsymbol{g}_j$, implying $T^{ij} = -pg^{ij} + P^{ij}$, by $(2.85)_1$ we have

$$\mathbf{T} = -p\mathbf{M} + \mathbf{P}, \quad \mathbf{t} = \mathbf{p}, \quad T^{33} = -p + P^{33}. \tag{3.59}$$

Note also that the block-matrix form of the components $v^i v^j$ in the expansion $\boldsymbol{v} \otimes \boldsymbol{v} = v^i v^j \boldsymbol{g}_i \otimes \boldsymbol{g}_j$ are given by

$$(v^i v^j) = \begin{pmatrix} \mathbf{v} \otimes \mathbf{v} & \mathrm{v}\mathbf{v} \\ \mathrm{v}\mathbf{v}^T & \mathrm{v}^2 \end{pmatrix}. \tag{3.60}$$

Although the coordinates adapted to a stationary topographic surface can be viewed as a particular case of those related to a moving surface, for an easier understanding of how to express the conservation laws (3.54) in the topography-fitted coordinates we successively consider stationary and moving basal surfaces.

3.3.1.1 Stationary Topographic Bed

For the case of a stationary topographic surface, it is a simple matter to apply the results of Sect. 3.1 to (3.54) in which $\boldsymbol{\sigma}$ has the decomposition (3.55). Indeed, $\partial f/\partial t = \tilde{\partial} f/\partial t$, see (3.40), and since the Jacobian J and the vectors $\boldsymbol{g}_i$ are time independent, the balance equations (3.54) can be written as

$$\frac{\tilde{\partial} J\rho}{\partial t} + J\,\mathrm{div}\,(\rho\boldsymbol{v}) = 0, \quad \frac{\tilde{\partial}\rho v^i}{\partial t}\boldsymbol{g}_i + (\mathrm{div}\,(\rho\boldsymbol{v} \otimes \boldsymbol{v} + p\boldsymbol{I} - \boldsymbol{\sigma}^E))^i \boldsymbol{g}_i = \rho b^i \boldsymbol{g}_i.$$

The first equation above will be transformed by appealing to formula (3.22) in order to alternatively express $J\,\mathrm{div}\,(\rho\boldsymbol{v})$. Then, the second equation is equivalent to

$$\frac{\tilde{\partial}\rho v^i}{\partial t} + (\mathrm{div}\,(\rho\boldsymbol{v}\otimes\boldsymbol{v} + p\boldsymbol{I} - \boldsymbol{\sigma}^E))^i = \rho b^i\,, \tag{3.61}$$

$i = 1, 2, 3$. Here we use (3.32). For example, recalling (3.60) we get

$$J\begin{pmatrix}(\mathrm{div}\,(\rho\boldsymbol{v}\otimes\boldsymbol{v}))^1\\(\mathrm{div}\,(\rho\boldsymbol{v}\otimes\boldsymbol{v}))^2\\(\mathrm{div}\,(\rho\boldsymbol{v}\otimes\boldsymbol{v}))^3\end{pmatrix} = \begin{pmatrix}\mathrm{Div}\,(J\rho\mathbf{v}\otimes\mathbf{v}) + \dfrac{\partial}{\partial\zeta}(J\rho\mathrm{v}\mathbf{v}) - J\boldsymbol{\Gamma}(\rho\mathbf{v}\otimes\mathbf{v},\rho\mathrm{v}\mathbf{v})\\ \mathrm{Div}\,(J\rho\mathrm{v}\mathbf{v}) + \dfrac{\partial}{\partial\zeta}(J\rho\mathrm{v}^2) - J\Gamma(\rho\mathbf{v}\otimes\mathbf{v})\end{pmatrix},$$

where the functions Γ and $\boldsymbol{\Gamma}$ are defined in (3.29) and (3.30), and when evaluated as above, they give[2]

$$\begin{aligned}\Gamma(\rho\mathbf{v}\otimes\mathbf{v}) &= -\mathbf{B}^T\mathbf{F}^{-T}\widetilde{\mathbf{H}}\cdot(\rho\mathbf{v}\otimes\mathbf{v}) = -\rho\mathbf{B}^T\mathbf{F}^{-T}\widetilde{\mathbf{H}}\cdot(\mathbf{v}\otimes\mathbf{v})\\ &\equiv \rho\Gamma(\mathbf{v})\,,\\ \boldsymbol{\Gamma}(\rho\mathbf{v}\otimes\mathbf{v},\rho\mathrm{v}\mathbf{v}) &= -\mathbf{B}^{-1}\frac{\partial\mathbf{B}}{\partial\xi^\alpha}(\rho\mathbf{v}\otimes\mathbf{v})\mathbf{e}_\alpha + 2\mathbf{B}^{-1}\mathbf{F}\widetilde{\mathbf{W}}(\rho\mathrm{v}\mathbf{v}) + \rho\Gamma(\mathbf{v})\mathbf{B}^{-1}\mathbf{s}\\ &\equiv \rho\boldsymbol{\Gamma}(\mathbf{v},\mathrm{v})\,.\end{aligned}$$

Similarly one computes the components $(\mathrm{div}\,(p\boldsymbol{I}))^i$ and $(\mathrm{div}\,(\boldsymbol{\sigma}_E))^i$ which occur in (3.61). This way and changing the notation $\tilde{\partial}/\partial t$ into $\partial/\partial t$ we deduce the following result.

Balance laws in the conventional route

Considering a ***stationary topographic bed****, the mass and linear momentum balance equations* (3.54) *in the time independent topography-fitted coordinates are given by*

$$\frac{\partial J\rho}{\partial t} + \mathrm{Div}\{J\rho\mathbf{v}\} + \frac{\partial}{\partial\zeta}\{J\rho\mathrm{v}\} = 0\,, \tag{3.62}$$

$$\begin{aligned}\frac{\partial}{\partial t}\{J\rho\mathbf{v}\} + \mathrm{Div}\{J\,(\rho\mathbf{v}\otimes\mathbf{v} + p\,\mathbf{M} - \mathbf{P})\} + \frac{\partial}{\partial\zeta}\{J(\rho\mathrm{v}\mathbf{v} - \mathbf{p})\}\\ + J\boldsymbol{\Gamma}(-p\,\mathbf{M},\mathbf{0}) + J\boldsymbol{\Gamma}(\mathbf{P},\mathbf{p}) = J\rho\mathbf{b} + J\rho\boldsymbol{\Gamma}(\mathbf{v},\mathrm{v})\,,\end{aligned} \tag{3.63}$$

[2]Clearly, in these relations there is an abuse of notations consisting in the way Γ and $\boldsymbol{\Gamma}$ have been used.

$$\frac{\partial}{\partial t}\{J\rho \mathrm{v}\} + \mathrm{Div}\{J(\rho \mathrm{v}\mathbf{v} - \mathbf{p})\} + \frac{\partial}{\partial \zeta}\{J\,(\rho \mathrm{v}^2 - P^{33})\} + J\,\frac{\partial p}{\partial \zeta} + J\Gamma(\mathbf{P}) = J\rho \mathrm{b} + J\rho\Gamma(\mathbf{v})\,. \tag{3.64}$$

Here the γ-terms are due to the Christoffel symbols and are given by

$$\mathbf{\Gamma}(-p\,\mathbf{M}, \mathbf{0}) \equiv p\left\{\mathbf{B}^{-1}\frac{\partial \mathbf{B}}{\partial \xi^\alpha}\,\mathbf{M}\mathbf{e}_\alpha + \mathrm{tr}\,(\widetilde{\mathbf{W}}(\mathbf{I} - \zeta\widetilde{\mathbf{W}})^{-1})\,\mathbf{B}^{-1}\mathbf{s}\right\}, \tag{3.65}$$

$$\mathbf{\Gamma}(\mathbf{P}, \mathbf{p}) \equiv -\mathbf{B}^{-1}\frac{\partial \mathbf{B}}{\partial \xi^\alpha}\,\mathbf{P}\mathbf{e}_\alpha + 2\mathbf{B}^{-1}\mathbf{F}\widetilde{\mathbf{W}}\mathbf{p} + \Gamma(\mathbf{P})\mathbf{B}^{-1}\mathbf{s}\,, \tag{3.66}$$

$$\mathbf{\Gamma}(\mathbf{v}, \mathrm{v}) \equiv -\mathbf{B}^{-1}\frac{\partial \mathbf{B}}{\partial \xi^\alpha}\,(\mathbf{v}\otimes\mathbf{v})\mathbf{e}_\alpha + 2\mathrm{v}\mathbf{B}^{-1}\mathbf{F}\widetilde{\mathbf{W}}\mathbf{v} + \Gamma(\mathbf{v})\mathbf{B}^{-1}\mathbf{s}\,, \tag{3.67}$$

$$\Gamma(\mathbf{P}) \equiv -\mathbf{B}^T\mathbf{F}^{-T}\widetilde{\mathbf{H}}\cdot\mathbf{P}\,, \qquad \Gamma(\mathbf{v}) \equiv -\mathbf{B}^T\mathbf{F}^{-T}\widetilde{\mathbf{H}}\cdot(\mathbf{v}\otimes\mathbf{v})\,. \tag{3.68}$$

Equations (3.63) and (3.64) will be often referred to as the *tangential* and *normal* components, respectively, of the linear momentum balance equation.

3.3.1.2 Active Topographic Bed

Now consider writing (3.54) when the curvilinear coordinates fitted to a moving topographic surface are used. The mass balance equation $(3.54)_1$ is treated as for the case of a rigid topographic bed: multiply (3.54) by J, use (3.41) and $\mathrm{w} = \mathcal{U}$ to compute

$$J\frac{\partial \rho}{\partial t} = \frac{\tilde{\partial} J\rho}{\partial t} - \mathrm{Div}\,(J\rho\mathbf{w}) - \frac{\partial J\rho\mathcal{U}}{\partial \zeta}\,,$$

and appeal to (3.22) for the term $J\mathrm{div}\,\rho\boldsymbol{v}$. In the linear momentum balance equation $(3.54)_2$ only the first term requires a different treatment from that followed to deduce (3.63) and (3.64). Thus, with the Cartesian representation $\boldsymbol{v} = v_j\boldsymbol{e}_j$, we have

$$\begin{aligned}\frac{\partial \rho\boldsymbol{v}}{\partial t} &= \frac{\partial \rho v_j}{\partial t}\,\boldsymbol{e}_j = \frac{\partial}{\partial t}\left(\rho A^{-1}_{jk}v^k\right)A_{ij}\boldsymbol{g}_i \\ &= \left\{\frac{\partial \rho v^k}{\partial t}A^{-1}_{jk} + \rho v^k\frac{A^{-1}_{jk}}{\partial t}\right\}A_{ij}\boldsymbol{g}_i = \left\{\frac{\partial \rho v^i}{\partial t} + \rho A_{ij}v^k\frac{A^{-1}_{jk}}{\partial t}\right\}\boldsymbol{g}_i\,,\end{aligned}$$

so that $(3.54)_2$ is equivalent to

$$\frac{\partial \rho v^i}{\partial t} + \rho A_{ij}v^k\frac{A^{-1}_{jk}}{\partial t} + (\mathrm{div}\,(\rho\boldsymbol{v}\otimes\boldsymbol{v} + p\boldsymbol{I} - \boldsymbol{\sigma}^E))^i = \rho b^i\,,$$

$i = 1, 2, 3$. Now, multiply the above equation by J to obtain

$$J\frac{\partial \rho v^i}{\partial t} + J\rho A_{ij} v^k \frac{A^{-1}_{jk}}{\partial t} + J(\mathrm{div}\,(\rho \boldsymbol{v} \otimes \boldsymbol{v} + p\boldsymbol{I} - \boldsymbol{\sigma}^E))^i = J\rho b^i\,. \tag{3.69}$$

Here we appeal to (3.41), and set $\mathrm{w} = \mathcal{U}$ to get

$$J\frac{\partial \rho v^i}{\partial t} = \frac{\tilde{\partial} J\rho v^i}{\partial t} - \mathrm{Div}\,(J\rho v^i \mathbf{w}) - \frac{\partial}{\partial \zeta}(J\rho v^i \mathcal{U})\,.$$

Moreover, we make use of

$$\frac{\partial A^{-1}_{jk}}{\partial t} = A^{-1}_{jl}\frac{\partial w^l}{\partial \xi^k}\,, \tag{3.70}$$

see Exercise 2.7, and treat the divergence term in (3.69) just as in case (a). Proceeding this way and changing the notation $\tilde{\partial}/\partial t$ into $\partial/\partial t$, we obtain the following result.

Balance laws in the conventional route

Considering an ***active topographic bed****, the mass and linear momentum balance equations* (3.54) *in the time dependent topography-fitted coordinates are given by*

$$\frac{\partial}{\partial t}\{J\rho\} + \mathrm{Div}\,\{J\rho\,(\mathbf{v} - \mathbf{w})\} + \frac{\partial}{\partial \zeta}\{J\rho\,(\mathrm{v} - \mathcal{U})\} = 0\,, \tag{3.71}$$

$$\begin{aligned}\frac{\partial}{\partial t}\{J\rho\mathbf{v}\} + &\mathrm{Div}\,\{J\,[\rho\,\mathbf{v}\otimes(\mathbf{v}-\mathbf{w}) + p\mathbf{M} - \mathbf{P}\,]\}\\ &+ \frac{\partial}{\partial \zeta}\left\{J\left[\rho\,(\mathrm{v}-\mathcal{U})\mathbf{v} - \mathbf{p}\right]\right\} + J\Gamma(-p\,\mathbf{M}, \mathbf{0}) + J\boldsymbol{\Gamma}(\mathbf{P}, \mathbf{p})\\ &= J\rho\mathbf{b} + J\rho\boldsymbol{\Gamma}(\mathbf{v}, \mathrm{v}) - J\rho\left\{(\mathrm{Grad}\,\mathbf{w})\mathbf{v} + \mathrm{v}\frac{\partial \mathbf{w}}{\partial \zeta}\right\},\end{aligned} \tag{3.72}$$

$$\begin{aligned}\frac{\partial}{\partial t}\{J\rho\mathrm{v}\} + \mathrm{Div}\{J\left[\rho\,\mathrm{v}(\mathbf{v}-\mathbf{w}) - \mathbf{p}\right]\} + \frac{\partial}{\partial \zeta}\left\{J\left[\rho\,\mathrm{v}(\mathrm{v}-\mathcal{U}) - P^{33}\right]\right\}\\ + J\frac{\partial p}{\partial \zeta} + J\Gamma(\mathbf{P}) = J\rho\mathrm{b} + J\rho\Gamma(\mathbf{v}) - J\rho\,\mathrm{Grad}\,\mathcal{U}\cdot\mathbf{v}\,.\end{aligned} \tag{3.73}$$

The γ-terms are defined in (3.65)–(3.68).

Clearly, for a stationary topographic bed equations (3.62)–(3.64) can be deduced from (3.71)–(3.73) by setting $\mathbf{w} = \mathbf{0}$ and $\mathcal{U} = 0$. We further notice that,

If the material is incompressible with uniform density, the mass balance equation in the topography-fitted coordinates has the same form for both stationary and active beds, namely,

$$\mathrm{Div}\{J\mathbf{v}\} + \frac{\partial}{\partial\zeta}\{J\mathrm{v}\} = 0\,. \tag{3.74}$$

Indeed, with $\rho = \rho_0 =$ constant, Eq. (3.62) turns into (3.74), since the Jacobian J is time independent. On the other hand, dividing (3.71) by the constant ρ, we obtain

$$\frac{\partial J}{\partial t} + \mathrm{Div}\,\{J\,(\mathbf{v} - \mathbf{w})\} + \frac{\partial}{\partial\zeta}\{J\,(\mathrm{v} - \mathcal{U})\} = 0\,.$$

Here we only have to substitute $\partial J/\partial t$ from formula (3.42) to obtain (3.74).

3.3.2 *Non-conventional route (i.e., based on (3.33))*

In this second approach the mass balance law $(3.54)_1$ is used in the form (3.62)/(3.65), but the linear momentum balance law $(3.54)_2$ expressed in the topography-fitted coordinates stems from the conservation form (3.33) for div $\boldsymbol{\sigma}$. Thus, next we refer to $(3.54)_2$. We note that, as in the conventional route, the field equations in curvilinear coordinates and corresponding to an active topographic bed comprise, as a particular case, the analogous equations in the case that no erosion/deposition occurs. Thus, with the experience gained in deducing (3.63), (3.64), (3.72) and (3.73), we may directly consider the coordinates fitted to a moving topographic surface.

Now, the linear momentum balance equation $(3.54)_2$ is taken to be equivalent to its Cartesian representation,

$$\frac{\partial\rho v_i}{\partial t} + (\mathrm{div}\,(\rho\boldsymbol{v}\otimes\boldsymbol{v} - \boldsymbol{\sigma}))_i = \rho b_i\,,$$

$i = 1, 2, 3$, where v_i and b_i are the Cartesian components of the velocity $\boldsymbol{v}$ and the body force per unit mass $\boldsymbol{b}$, respectively,

$$\boldsymbol{v} = v_i\boldsymbol{e}_i\,, \quad \boldsymbol{b} = b_i\boldsymbol{e}_i\,.$$

We multiply the above equation by J,

$$J\frac{\partial \rho v_i}{\partial t} + J(\mathrm{div}\,(\rho \boldsymbol{v}\otimes \boldsymbol{v} - \boldsymbol{\sigma}))_i = J\rho b_i\,,$$

use (3.41) and $\mathrm{w} = \mathcal{U}$ to deduce that

$$J\frac{\partial \rho v_i}{\partial t} = \frac{\tilde{\partial} J\rho v_i}{\partial t} - \mathrm{Div}\,(J\rho v_i \mathbf{w}) - \frac{\partial}{\partial \zeta}(J\rho v_i \mathcal{U})\,,$$

and treat the divergence term with the aid of formula (3.33). Doing so the tensor product $\boldsymbol{v}\otimes\boldsymbol{v}$ and the stress tensor $\boldsymbol{\sigma}$ must be written in the mixed representations

$$\boldsymbol{v}\otimes\boldsymbol{v} = v_i v^j \boldsymbol{e}_i\otimes\boldsymbol{g}_j\,,\quad \boldsymbol{\sigma} = \Sigma^{ij}\boldsymbol{e}_i\otimes\boldsymbol{g}_j\,.$$

In order to express the result of these computations, the Cartesian components of $\boldsymbol{v}$, $\boldsymbol{b} = \boldsymbol{g}$ (with $\boldsymbol{g}$—gravitational acceleration), and the components in the above representations are collected in block-matrix form,

$$\begin{gathered}\begin{pmatrix} v_1\\ v_2\\ v_3\end{pmatrix} = \begin{pmatrix}\mathbb{v}\\ v\end{pmatrix},\quad \begin{pmatrix} b_1\\ b_2\\ b_3\end{pmatrix} = \begin{pmatrix}\mathbb{0}\\ -g\end{pmatrix},\\ (v_i v^j) = \begin{pmatrix}\mathbb{v}\otimes\mathbf{v} & \mathbb{v}\mathbb{v}\\ (v\mathbf{v})^T & v\mathbb{v}\end{pmatrix},\quad (\Sigma^{ij}) = \begin{pmatrix}\mathbb{S} & \mathbb{s}\\ \mathbb{t}^T & \sigma\end{pmatrix}.\end{gathered} \tag{3.75}$$

The connection between the Cartesian components $\mathbb{v}$, v, $\mathbb{S}$, $\mathbb{s}$, $\mathbb{t}$, σ and the contravariant components $\mathbf{v}$, v, $\mathbf{T}$, $\mathbf{t}$, T^{33} of $\boldsymbol{v}$ and $\boldsymbol{\sigma}$ can be found in (2.96) and (2.98). Therefore, the field equations in the non-conventional route are as follows.

Balance laws in the non-conventional route

Corresponding to an ***active topographic bed*** *and expressed in the time dependent topography-fitted coordinates, the mass balance equation is* (3.71)*, and the linear momentum balance equation* $(3.54)_2$ *emerges as*

$$\frac{\partial J\rho\mathbb{v}}{\partial t} + \mathrm{Div}\left\{J\left(\rho\mathbb{v}\otimes(\mathbf{v}-\mathbf{w}) - \mathbb{S}\right)\right\} + \frac{\partial}{\partial\zeta}\left\{J\left(\rho(\mathrm{v}-\mathcal{U})\mathbb{v} - \mathbb{s}\right)\right\} = \mathbb{0}\,, \tag{3.76}$$

$$\frac{\partial J\rho v}{\partial t} + \mathrm{Div}\left\{J\left(\rho v(\mathbf{v}-\mathbf{w}) - \mathbb{t}\right)\right\} + \frac{\partial}{\partial\zeta}\left\{J\left(\rho v(\mathrm{v}-\mathcal{U}) - \sigma\right)\right\} = -J\rho g\,. \tag{3.77}$$

Table 3.1 Mass balance and linear momentum balance equations in the topography-fitted coordinates and applicable in the conventional and non-conventional routes

	Conventional route		Non-conventional route
	Rigid topographic bed	Active topographic bed	Active topographic bed
Mass balace equation	(3.62)	(3.71)	(3.71)
Linear momentum balace equations	(3.63)	(3.72)	(3.76)
	(3.64)	(3.73)	(3.77)

Equations (3.76) and (3.77), in which the Christoffel symbols are avoided, are said to express the linear momentum balance law in *conservation* or *conservative* or *hybrid form*, see Vinokur [4]. To (3.76) we will refer as the *horizontal* linear momentum balance equation, and to (3.77) as the *vertical* linear momentum balance equation, in hybrid form. When describing the mass flow in the next chapter both the conventional and non-conventional route are followed and a motivation for doing so will be given. Table 3.1 concisely summarizes the field equations deduced in this section and used in each of these routes. We note that, setting $\mathbf{w} = \mathbf{0}$ and $\mathcal{U} = 0$ in (3.76) and (3.77), one obtains the hybrid form of the linear momentum balance equation in the curvilinear coordinates fitted to a rigid topography.

References

1. C.A. Eringen, *Mechanics of Continua*. Krieger Pub. Co., 2nd edn. (1980)
2. R.M. Bowen, C.C. Wang, *Introduction to Vectors and Tensors* (Plenum Press, New York, 1976)
3. H. Viviand, Formes conservatives des équations de la dynamique des gaz. Rech. Aosp. **1**, 65–66 (1974)
4. M. Vinokur, Conservation equations of gasdynamics in curvilinear coordinate systems. J. Comp. Phys. **14**, 105–125 (1974)

Part III
Model Equations for Shallow Geophysical Mass Flows down Arbitrary Topographies

Chapter 4
Depth-Averaged Modelling Equations for Single-Phase Material Flows

In this chapter we deduce depth-averaged model equations for thin mass flows down arbitrary topographies, be they stationary or active, when the flowing material is assumed a single-phase (or one-component) continuum body. We use the mass and momentum balance equations expressed in the topography-fitted coordinates in both conventional and non-conventional approaches. Based on thin-layer approximations for various geometric, kinematic and dynamic fields entering these balance equations, depth-averaged model equations for the flow of a shallow single-phase material are derived. The model equations are sufficiently general, in the sense that they are suitable to account for any constitutive behavior matching the thin-layer approximations. The chapter is organized as follows:

- In Sect. 4.1 we describe the physical problem and state the corresponding intrinsic (i.e., independent of any coordinate system) 3D modelling equations. These equations are the mass and linear momentum balance equations, complemented by boundary conditions at the basal surface and at the free surface. They are used in the subsequent sections as written in the topography-fitted coordinates, in both conventional and non-conventional routes.
- The mass and linear momentum balance equations are already expressed in the topography-fitted coordinates, see Table 3.1 in Sect. 3.3, so that only the boundary conditions remain to be formulated in the curvilinear coordinates. Section 4.2 is entirely devoted to this task.
- Sect. 4.3 introduces non-dimensional quantities, and presents the 3D modelling equations expressed in non-dimensional form and in the topography-based coordinates.
- The depth-averaging method is described in Sect. 4.4.
- In Sect. 4.5, following the *conventional route* and based on thin-layer approximations, depth-averaged modelling equations for a thin flow down arbitrary topography are deduced. The constitutive nature of the flowing material is not yet specified. A hierarchy of these models in terms of the relative weights in the stress contribution is then addressed.

I. Luca et al., *Shallow Geophysical Mass Flows down Arbitrary Topography*,
Advances in Geophysical and Environmental Mechanics and Mathematics,
DOI 10.1007/978-3-319-02627-5_4

- In Sect. 4.6, based on the same thin-layer approximations as in Sect. 4.5, the *non-conventional route* is followed and depth-averaged modelling equations for the thin flow are derived. The relation between these equations and those from Sect. 4.5 is then identified.

To ensure a fast and easy reading the technical proofs are relegated to appendices.

4.1 Physical Background and Intrinsic 3D Modelling Equations

As a first simplification in modelling e.g. the soil motion down mountains, debris flows or mud flows, we consider the material flowing down a topographic surface under the action of gravity as a *single-phase continuum body*. In the ensuing sections of this chapter we base our derivations on the following assumptions.

- The domain Ω occupied by the avalanching mass is bounded from below by the topographic surface $\mathcal{S}_b$, with the unit normal vector $\boldsymbol{n}_b$ pointing into the avalanching body, and from above by the free surface $\mathcal{S}$, for which the unit normal vector pointing into the atmosphere is denoted by $\boldsymbol{n}$. Beneath $\mathcal{S}_b$ the topographic bed, Ω_b, has its own rheology and is assumed at rest.[1] The depth of the flowing mass is measured along the normal direction to $\mathcal{S}_b$ and is denoted by h. A Cartesian coordinate system is chosen with the x_3-axis vertical against the gravity $\boldsymbol{b}$. Figure 4.1 sketches the flow and shows these notations.
- If the topographic bed Ω_b is erodible or if material is deposited on it,[2] the basal surface $\mathcal{S}_b$ is a moving surface, with an evolution which must be determined from the final system of modelling equations. We assume that the topographic surface $\mathcal{S}_b$ is given by

$$\begin{array}{ll} x_3 = b(x_1, x_2) & \text{for a stationary topographic bed, and} \\ x_3 = b(x_1, x_2, t) & \text{for an active topographic bed.} \end{array} \tag{4.1}$$

The free surface $\mathcal{S}$ of the flowing material is not known and is assumed to be given by

$$F(x_1, x_2, x_3, t) = 0\,. \tag{4.2}$$

The determination of the bed elevation b in $(4.1)_2$ and of the free surface profile function F in (4.2) is part of the initial boundary value problem which ultimately must be solved.

[1] This assumption is only made to simplify the jump across $\mathcal{S}_b$ of the mass balance equation, see the forthcoming (4.9).

[2] To such a topographic bed we will henceforth refer as being active, according to the convention made at the beginning of Sect. 2.2.

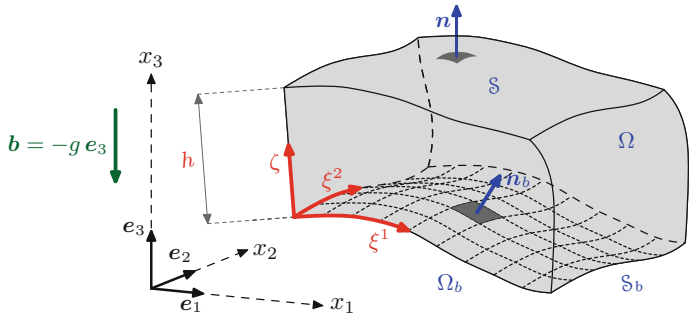

Fig. 4.1 The gravity-driven flowing mass as a single-phase continuum body in the domain Ω, the topographic surface $\mathcal{S}_b$ with its normal vector field $\boldsymbol{n}_b$, the free surface $\mathcal{S}$ with its normal vector field $\boldsymbol{n}$, the topographic bed Ω_b, the depth h of the flowing body, the Cartesian coordinates $x_1,\ x_2,\ x_3$, the topography-fitted coordinates ξ^1, ξ^2, ζ, and the gravity $\boldsymbol{b}$. (Adapted from [1].)

- The sliding mass is long and shallow, in the sense that its depth h is much smaller than one of its dimensions "parallel" to the topography. This assumption allows ordering approximations in terms of the aspect ratio ϵ of a typical thickness H to a typical length L parallel to the topography, characteristic to the flowing mass,

$$\epsilon \equiv \frac{H}{L} \ll 0\,. \tag{4.3}$$

  Realistically, the shallowness parameter ϵ is 10^{-3} to 10^{-2}. The dimensionless orders of magnitude of quantities arising in the subsequent modelling equations are expressed as certain powers of ϵ, e.g.,

$$\epsilon^{\gamma}, \quad 0 < \gamma < 1\,.$$

- The sliding continuum body is density preserving with uniform density ρ_0,

$$\rho(\boldsymbol{x}, t) = \rho_0 = \text{constant}, \quad (\boldsymbol{x}, t) \in \Omega \times (0, \infty)\,. \tag{4.4}$$

This assumption is legitimate if the flowing mass is clear water. For other masses, rapidly sliding down mountains, it may be an acceptable assumption, as laboratory experiments have proved.

- Temperature effects on the flowing mass do not exist or are negligibly small. Thus, the governing equations describing the gravity-driven motion of the continuum body are the mass and linear momentum balance equations, see (3.54), which now take the form

$$\operatorname{div} \boldsymbol{v} = 0\,, \tag{4.5}$$

$$\frac{\partial \boldsymbol{v}}{\partial t} + \operatorname{div}\left\{\boldsymbol{v} \otimes \boldsymbol{v} - \frac{1}{\rho_0}\boldsymbol{\sigma}\right\} = \boldsymbol{b}\,. \tag{4.6}$$

We recall that $\boldsymbol{v}$ is the velocity field and $\boldsymbol{\sigma}$ is the symmetric Cauchy stress tensor characterizing the moving mass. Due to the incompressibility condition (4.4) we consider the decomposition (3.55), that is,

$$\boldsymbol{\sigma} = -p\boldsymbol{I} + \boldsymbol{\sigma}_E\,. \tag{4.7}$$

The *pressure* p is taken as a basic unknown field in the final modelling equations, and the *extra-stress* tensor $\boldsymbol{\sigma}_E$ is thought to be given by a constitutive law. The rheological properties of the avalanching mass will be expressed as ordering approximations on the stress components. Explicit constitutive assumptions are postponed to Sect. 5.2. Doing so we will obtain a set of general modelling equations, able to account for (in principle) any constitutive law compatible with the above mentioned assumptions.

- For a stationary topographic bed the velocity $\boldsymbol{v}$ is supposed to satisfy the non-penetration condition,

$$\boldsymbol{v} \cdot \boldsymbol{n}_b = 0 \quad \text{on} \quad \mathcal{S}_b\,. \tag{4.8}$$

For an active topographic bed the mass balance equation

$$[\![\rho(\boldsymbol{v} - \mathcal{U}\boldsymbol{n}_b)]\!] \cdot \boldsymbol{n}_b = 0 \quad \text{on} \quad \mathcal{S}_b \tag{4.9}$$

holds.[3] The speed of propagation $\mathcal{U}$ of the surface $\mathcal{S}_b$ is called *erosion/deposition rate*. Clearly, since $\boldsymbol{n}_b$ points into the avalanching body, if $\mathcal{U} > 0$ material from Ω is deposited, and $\mathcal{U} < 0$ means that the bed Ω_b is eroded.[4] The erosion/deposition rate $\mathcal{U}$ is not a basic unknown in the final modelling equations. Instead, it is given by an erosion/deposition law, see the forthcoming Sect. 5.3. With ρ_b—the mass density of the topographic bed at rest, condition (4.9) reads

$$\rho_0(\boldsymbol{v} \cdot \boldsymbol{n}_b - \mathcal{U}) = -\rho_b \mathcal{U}\,,$$

[3] Notation $[\![f]\!]$ stands for the jump of f at the moment t across a given surface. That is, for the case that the surface is $\mathcal{S}_b$, separating Ω from Ω_b, at each time t the function f is assumed continuous on $\Omega \cup \mathcal{S}_b$ and $\Omega_b \cup \mathcal{S}_b$, but may be discontinuous on $\mathcal{S}_b$; the difference between the limits of f on $\mathcal{S}_b$ taken from both parts Ω, Ω_b,

$$[\![f]\!]_Q \equiv \lim_{\substack{P \to Q \\ P \in \Omega}} f - \lim_{\substack{P \to Q \\ P \in \Omega_b}} f\,, \qquad Q \in \mathcal{S}_b\,,$$

is the *jump of* f *across* $\mathcal{S}_b$ at the point Q.

[4] If the topographic bed is deformable and no erosion/deposition processes occur, we simply set $\mathcal{U} = 0$ in (4.9), i.e., $[\![\rho\boldsymbol{v}]\!] \cdot \boldsymbol{n}_b = 0$.

which gives

$$\boldsymbol{v} \cdot \boldsymbol{n}_b = \left(1 - \frac{\rho_b}{\rho_0}\right) \mathcal{U} \quad \text{on} \quad \mathcal{S}_b \,. \tag{4.10}$$

Note that (4.8) is a special case of (4.10), obtained by setting $\mathcal{U} = 0$ in (4.10). Either (4.8) or (4.10) is referred to as a *kinematic boundary condition* for the field equations (4.5) and (4.6).

- If the roughness scale of the basal surface is smaller than the typical diameter of the material particles, it is expected that the avalanche mass slips on the surface. For this situation we consider the *dynamic boundary condition*

$$\boldsymbol{\sigma} \boldsymbol{n}_b - (\boldsymbol{\sigma} \boldsymbol{n}_b \cdot \boldsymbol{n}_b) \boldsymbol{n}_b = -\boldsymbol{f}_b \quad \text{on} \quad \mathcal{S}_b \,. \tag{4.11}$$

  It states that, on the basal surface the tangential traction equilibrates the *bed friction force* $\boldsymbol{f}_b$, which must be given by a so-called *sliding law*, expressing the interaction of the flowing mass with the basal surface. As with the stress tensor and the erosion/deposition rate, for the time being the phenomenological law for $\boldsymbol{f}_b$ is left unspecified. A law for $\boldsymbol{f}_b$ will be given later in Sect. 5.1.
  If the avalanching mass exhibits no slip on the ground surface, which means that the tangential velocity at the base vanishes,

$$\boldsymbol{v} - (\boldsymbol{v} \cdot \boldsymbol{n}_b) \boldsymbol{n}_b = 0 \qquad \text{on} \quad \mathcal{S}_b \,, \tag{4.12}$$

  condition (4.12) is used instead of (4.11). The ensuing analysis assumes sliding motion of the avalanching mass, and so the dynamic boundary condition will be (4.11). We consider the no-slip condition (4.12) solely in Sect. 5.2.1.
- At the free surface $\mathcal{S}$ we do not consider any mass exchange due e.g. to precipitations, so that $\mathcal{S}$ is a material surface. This implies that the function F introduced in (4.2) satisfies the kinematic equation

$$\frac{\partial F}{\partial t} + \nabla F \cdot \boldsymbol{v} = 0 \quad \text{at} \quad F = 0 \,. \tag{4.13}$$

Moreover, the free surface is assumed traction-free, that is,

$$\boldsymbol{\sigma} \boldsymbol{n} = \boldsymbol{0} \quad \text{at} \quad F = 0 \,. \tag{4.14}$$

Thus, wind blowing and surface pressure effects are not accounted for; the free surface separates the material from the atmosphere, where the pressure is set equal to zero.

4.2 3D Modelling Equations in the Topography-Fitted Coordinates

The topography-fitted coordinates provide the mean to properly make ordering approximations for vector and tensor components when the flowing material is shallow. This section aims at presenting the preceding system of field equations and boundary conditions in the topography-fitted coordinates, following both the conventional and non-conventional routes. For the reader's convenience, in the conventional route we treat separately the rigid topographic beds and the active beds, although the equations corresponding to a rigid bed are a particular case of those which correspond to an active bed. In the non-conventional route we spare the length of the exposure and treat directly the case with erosion/deposition processes. Table 3.1 in Sect. 3.3 shows the field equations which are used in each of these routes.

For the special case of an incompressible material, as considered in this chapter, the expressions of the mass and linear momentum balance equations (4.5), (4.6) in the topography-fitted coordinates can be obtained by setting $\rho = \rho_0$ in (3.62)–(3.64)/(3.71)–(3.73) and (3.71), (3.76), (3.77). To shorten the text, we do not display here the emerging equations. They will be given in the next section in non-dimensional form. We are rather interested in writing the boundary conditions in these curvilinear coordinates. The boundary conditions are given on the basal surface $\mathcal{S}_b$ and on the free surface $\mathcal{S}$. In the topography-fitted coordinates the equation of the topographic surface $\mathcal{S}_b$ is

$$\mathcal{S}_b : \quad \zeta = 0 \,,$$

irrespective of the fact that erosion/deposition processes are present or not. Then, we assume that the equation $F(x_1, x_2, x_3, t) = 0$ of the free surface $\mathcal{S}$ can be written in the form

$$\mathcal{S} : \quad \zeta = h(\xi^1, \xi^2, t) \,.$$

Therefore, the *avalanche depth* h gives the free surface shape; h will be a basic unknown field in the final system of modelling equations.

4.2.1 Boundary Conditions in the Conventional Route

Here we express the boundary conditions (4.8)/(4.10) and (4.11) at the basal surface, and conditions (4.13) and (4.14) at the free surface, in the topography-fitted coordinates. We use the contravariant components of the velocity $\boldsymbol{v}$, of the stress tensor $\boldsymbol{\sigma}$ and of the bed friction force $\boldsymbol{f}_b$, that is, v^i, T^{ij}, f^α in the representations

$$\boldsymbol{v} = v^i \boldsymbol{g}_i \,, \quad \boldsymbol{\sigma} = T^{ij} \boldsymbol{g}_i \otimes \boldsymbol{g}_j \,, \quad \boldsymbol{f}_b = f^\alpha \boldsymbol{g}_\alpha \Big|_{\zeta=0} = f^\alpha \boldsymbol{\tau}_\alpha \,. \tag{4.15}$$

Writing $(4.15)_3$ we have used the fact that the bed friction force $\boldsymbol{f}_b$ is a tangent vector to $\mathcal{S}_b$. We recall that the contravariant components v^i and T^{ij} are collected in block matrices, see (3.57), and we do the same for the components of $\boldsymbol{f}_b$,

$$\mathbf{f}_b \equiv (f^1, f^2)^T . \tag{4.16}$$

First we state the results and then we prove them.

(i) Stationary Topographic Bed

At the basal surface $\mathcal{S}_b \Longleftrightarrow$ at $\zeta = 0$:
The non-penetration condition (4.8) *takes the form*

$$\mathrm{v} = 0 , \tag{4.17}$$

and the dynamic boundary condition (4.11) *emerges as*

$$\mathbf{p} = -\mathbf{f}_b , \tag{4.18}$$

with $\mathbf{f}_b$ defined in (4.16).
At the free surface $\mathcal{S} \Longleftrightarrow$ at $\zeta = h(\boldsymbol{\xi}, t)$, where $\boldsymbol{\xi} \equiv (\xi^1, \xi^2)$:
The kinematic boundary condition (4.13) *turns into*

$$\frac{\partial h}{\partial t} + \mathrm{Grad}\, h \cdot \mathbf{v} = \mathrm{v} , \tag{4.19}$$

and the dynamic boundary condition (4.14) *splits into*

$$\mathbf{T}\mathrm{Grad}\, h - \mathbf{t} = \mathbf{0} , \quad \mathbf{t} \cdot \mathrm{Grad}\, h - T^{33} = 0 . \tag{4.20}$$

(ii) Active Topographic Bed

At the basal surface $\mathcal{S}_b \Longleftrightarrow$ at $\zeta = 0$:
Condition (4.10) *is expressed as*

$$\mathrm{v} = \left(1 - \frac{\rho_b}{\rho_0}\right) \mathcal{U} , \tag{4.21}$$

and the dynamic boundary condition (4.11) *takes the same form, i.e.* (4.18), *as for the case of a rigid bed.*

At the free surface $\mathcal{S} \Longleftrightarrow$ at $\zeta = h(\boldsymbol{\xi}, t)$:
The kinematic boundary condition (4.13) *turns into*

$$\frac{\partial h}{\partial t} + \operatorname{Grad} h \cdot (\mathbf{v} - \mathbf{w}) = \mathrm{v} - \mathcal{U}\,, \tag{4.22}$$

and the traction-free surface condition (4.14) *appears as for the case of stationary beds, see* (4.20).

Let us now prove the preceding statements. Condition (4.17) is clear, since $\boldsymbol{g}_3 = \boldsymbol{n}_b$ and $\boldsymbol{g}_1, \boldsymbol{g}_2$ are orthogonal to $\boldsymbol{n}_b$, so that

$$\boldsymbol{v} \cdot \boldsymbol{n}_b = (v^\alpha \boldsymbol{g}_\alpha + \mathrm{v}\boldsymbol{g}_3) \cdot \boldsymbol{n}_b = \mathrm{v}\,.$$

To justify (4.18) we note that, with $\boldsymbol{g}^3 = \boldsymbol{n}_b$, we have

$$\boldsymbol{\sigma}\boldsymbol{n}_b = \left(T^{ij}\boldsymbol{g}_i \otimes \boldsymbol{g}_j\right)\boldsymbol{g}^3 = T^{i3}\boldsymbol{g}_i = T^{\alpha 3}\boldsymbol{g}_\alpha + T^{33}\boldsymbol{n}_b\,, \quad \boldsymbol{\sigma}\boldsymbol{n}_b \cdot \boldsymbol{n}_b = T^{33}\,,$$

which implies

$$\boldsymbol{\sigma}\boldsymbol{n}_b - (\boldsymbol{\sigma}\boldsymbol{n}_b \cdot \boldsymbol{n}_b)\boldsymbol{n}_b = T^{\alpha 3}\boldsymbol{g}_\alpha\,.$$

Recalling (3.57), $(3.59)_2$ and (4.16) one can then see that (4.11) is equivalent to (4.18).

Next we refer to the boundary conditions at the free surface $\mathcal{S}$, which is given as $F(x_1, x_2, x_3, t) = 0$. With $F(x_1, x_2, x_3, t) = \tilde{F}(\xi^1, \xi^2, \xi^3, t)$ via the change of coordinates, we have assumed a special form of $\tilde{F}$,

$$\tilde{F}(\xi^1, \xi^2, \zeta, t) = \zeta - h(\xi^1, \xi^2, t)\,.$$

Since the coordinates $\xi^1, \xi^2, \zeta \equiv \xi^3$ are time independent, we have

$$\frac{\partial F}{\partial t} = \frac{\partial \tilde{F}}{\partial t} = -\frac{\partial h}{\partial t}\,,$$

and

$$\begin{aligned} \nabla F \cdot \boldsymbol{v} &= \left(\frac{\partial \tilde{F}}{\partial \xi^i}\boldsymbol{g}^i\right) \cdot \left(v^j \boldsymbol{g}_j\right) = \frac{\partial \tilde{F}}{\partial \xi^i} v^i = \frac{\partial \tilde{F}}{\partial \xi^\alpha} v^\alpha + \frac{\partial \tilde{F}}{\partial \zeta}\mathrm{v} \\ &= \mathrm{v} - \operatorname{Grad} h \cdot \mathbf{v}\,, \end{aligned} \tag{4.23}$$

so that (4.13) yields (4.19). Then, referring to (4.14), we have

$$\boldsymbol{\sigma n} = \boldsymbol{0} \iff \boldsymbol{\sigma}\nabla F = \boldsymbol{0} \iff \left(T^{ik}\boldsymbol{g}_i \otimes \boldsymbol{g}_k\right)\left(\frac{\partial \tilde{F}}{\partial \xi^j}\boldsymbol{g}^j\right) = \boldsymbol{0} \iff$$

$$T^{ij}\frac{\partial \tilde{F}}{\partial \xi^j}\boldsymbol{g}_i = \boldsymbol{0} \iff T^{ij}\frac{\partial \tilde{F}}{\partial \xi^j} = 0\,, \quad i = 1,2,3 \iff$$

$$\begin{pmatrix} \mathbf{T} & \mathbf{t} \\ \mathbf{t}^T & T^{33} \end{pmatrix}\begin{pmatrix} -\mathrm{Grad}\, h \\ 1 \end{pmatrix} = \begin{pmatrix} \mathbf{0} \\ 0 \end{pmatrix},$$

which is equivalent to (4.20).

Next we switch to the case of an active topographic bed. The same argument as for (4.17) applies to easily obtain condition (4.21). Then, from the remaining boundary conditions, i.e., (4.11), (4.13), (4.14), only the kinematic boundary condition (4.13) turns into another form than (4.19). The reason is that the rules for spatial differentiation are the same for rigid and active beds, but the time differentiation rule changes, according to whether there is erosion/deposition or not. Thus, with the rule of time differentiation, (3.39), we have

$$\frac{\partial F}{\partial t} = \frac{\partial \tilde{F}}{\partial t} - \mathrm{Grad}\,\tilde{F}\cdot\mathbf{w} - \frac{\partial \tilde{F}}{\partial \zeta}\mathrm{w} = -\frac{\partial h}{\partial t} + \mathrm{Grad}\, h\cdot\mathbf{w} - \mathcal{U}\,,$$

and using $\nabla F\cdot\boldsymbol{v} = \mathrm{v} - \mathrm{Grad}\, h\cdot\mathbf{v}$, see (4.23), we obtain (4.22).

It is clear that both kinematic conditions (4.17) and (4.19) are particular cases of (4.21) and (4.22), respectively, and are obtained for $\mathbf{w} = \mathbf{0}$ and $\mathcal{U} = 0$.

4.2.2 *Boundary Conditions in the Non-conventional Route*

As already mentioned, in the non-conventional route we directly treat active beds. The only boundary conditions which are taken differently expressed in the topography-fitted coordinates in comparison to those in the conventional route are the dynamic boundary conditions (4.11) and (4.14). Now, (4.11) and (4.14) must be expressed in terms of the mixed components Σ^{ij} of the stress tensor $\boldsymbol{\sigma} = \Sigma^{ij}\boldsymbol{e}_i \otimes \boldsymbol{g}_j$. We state the results and then we prove them.

Active Topographic Bed

At the basal surface $\mathcal{S}_b \iff$ at $\zeta = 0$:
Condition (4.10) *is expressed as* (4.21), *and the dynamic boundary condition* (4.11) *is written as*

$$\mathbf{s} = -\mathbf{F}\mathbf{f}_b - T^{33}\mathbf{s}\,. \tag{4.24}$$

At the free surface $\mathcal{S} \iff$ at $\zeta = h(\boldsymbol{\xi}, t)$:
The kinematic boundary condition (4.13) *is expressed as* (4.22), *while*

$$\mathbb{S}\mathrm{Grad}\, h - \mathbb{s} = \mathbb{0}\,, \quad \mathbb{t}\cdot\mathrm{Grad}\, h - \sigma = 0 \tag{4.25}$$

are found to represent the traction-free surface condition (4.14).

Relation (4.24), expressing the boundary condition (4.11), follows immediately if we recall that (see $(2.98)_2$, $(3.59)_2$), 2.79),

$$\mathbb{s} = \mathbf{B}\mathbb{t} - T^{33}\mathbf{s}\,, \quad \mathbf{t} = \mathbf{p}\,, \quad \mathbf{B}\big|_{\zeta=0} = \mathbf{F}\,,$$

and invoke (4.18). The proof of (4.25) is similar to (4.20):

$$\begin{aligned}
&\boldsymbol{\sigma}\boldsymbol{n} = \boldsymbol{0} \iff \boldsymbol{\sigma}\nabla F = \boldsymbol{0} \iff \left(\Sigma^{ik}\boldsymbol{e}_i\otimes\boldsymbol{g}_k\right)\left(\frac{\partial\tilde{F}}{\partial\xi^j}\boldsymbol{g}^j\right) = \boldsymbol{0} \iff\\
&\Sigma^{ij}\frac{\partial\tilde{F}}{\partial\xi^j}\boldsymbol{e}_i = \boldsymbol{0} \iff \Sigma^{ij}\frac{\partial\tilde{F}}{\partial\xi^j} = 0\,, \quad i = 1,2,3 \iff\\
&\begin{pmatrix}\mathbb{S} & \mathbb{s}\\ \mathbb{t}^T & \sigma\end{pmatrix}\begin{pmatrix}-\mathrm{Grad}\, h\\ 1\end{pmatrix} = \begin{pmatrix}\mathbb{0}\\ 0\end{pmatrix}\,,
\end{aligned}$$

which gives (4.25).

4.3 Dimensionless 3D Modelling Equations in the Topography-Fitted Coordinates

In the ensuing analysis the thin layer assumption on the flow geometry is accounted for by ordering approximations in terms of the aspect ratio ϵ, see (4.3). The ordering approximations are applied to dimensionless variables which we obtain by using

the typical length L "tangent" to the topography and entering (4.3),
the constant gravitational acceleration g, and
the density ρ_0 of the flowing mass.

We scale all distances with L, time with $\sqrt{L/g}$, velocities with $\sqrt{Lg}$, stresses with $\rho_0 Lg$ and gravitational acceleration with g, by writing

$$\begin{aligned}
&(x_1, x_2, x_3, b, h) = L\,(x_1, x_2, x_3, b, h)_{\text{dimless}}\,, \quad t = \sqrt{L/g}\,t_{\text{dimless}}\,,\\
&\boldsymbol{v} = \sqrt{Lg}\,\boldsymbol{v}_{\text{dimless}}\,, \quad (\boldsymbol{\sigma}, \boldsymbol{f}_b) = \rho_0 Lg\,(\boldsymbol{\sigma}, \boldsymbol{f}_b)_{\text{dimless}}\,, \quad \boldsymbol{b} = g\,\boldsymbol{b}_{\text{dimless}}\,.
\end{aligned} \tag{4.26}$$

Moreover, assuming that the curvilinear coordinates ξ^1, ξ^2 have dimension of length, we introduce the dimensionless coordinates $(\xi^1, \xi^2, \zeta)_{\text{dimless}}$, surface velocity $\boldsymbol{u}_{\mathcal{S}\text{dimless}}$ (see 2.62) and mesh velocity $\boldsymbol{w}_{\text{dimless}}$ (see 2.102) by

$$(\xi^1, \xi^2, \zeta) = L\,(\xi^1, \xi^2, \zeta)_{\text{dimless}}\,, \quad (\boldsymbol{u}_{\mathcal{S}},\ \boldsymbol{w}) = \sqrt{Lg}\,(\boldsymbol{u}_{\mathcal{S}},\ \boldsymbol{w})_{\text{dimless}}\,. \tag{4.27}$$

Note that, by using only one length, L, in (4.26) and (4.27), we have not estimated the physical variables according to their magnitude in the flow process. The estimations will be given later as ordering approximations on the physical variables. This allows more flexibility when assuming the relative contributions of these variables to the flow process.[5]

As a consequence of $(4.26)_1$ and (4.27), the vectors $\boldsymbol{g}_1, \boldsymbol{g}_2, \boldsymbol{g}_3$ are dimensionless, see their definition (2.76), and hence the contravariant components with respect to $\boldsymbol{g}_1, \boldsymbol{g}_2, \boldsymbol{g}_3$ of the velocities $\boldsymbol{v}_{\text{dimless}}$, $\boldsymbol{w}_{\text{dimless}}$, gravity force density $\boldsymbol{b}_{\text{dimless}}$ and stress tensor $\boldsymbol{\sigma}_{\text{dimless}}$ emerge as dimensionless scalars.

The non-dimensional modelling equations for the shallow flow described in Sect. 4.1 can be straightforwardly deduced in the topography-fitted coordinates by noticing that

$$\begin{aligned} (c,\ \mathbf{s},\ J,\ \mathbf{F},\ \mathbf{B},\ \mathbf{M}) &= (c,\ \mathbf{s},\ J,\ \mathbf{F},\ \mathbf{B},\ \mathbf{M})_{\text{dimless}}\,, \\ (\widetilde{\mathbf{H}},\ \widetilde{\mathbf{W}}) &= (1/L)(\widetilde{\mathbf{H}},\ \widetilde{\mathbf{W}})_{\text{dimless}}\,, \end{aligned} \tag{4.28}$$

and using the balance laws and boundary conditions as deduced in Sects. 3.3 and 4.2, respectively. The results are summarized below by omitting the 'dimless' specification.

4.3.1 *Dimensionless 3D Model Equations in the Conventional Route*

The non-dimensional model equations corresponding to rigid topographic beds are obtained from the conservation laws (3.62)–(3.64), with the γ-terms shown in (3.65)–(3.68), and the boundary conditions (4.17)–(4.20). If the topographic bed is active, the conservation laws (3.71)–(3.73) (see also 3.74) and the boundary conditions (4.18), (4.20)–(4.22) are used. Here are the results.

4.3.1.1 Stationary Topographic Bed

Balance Equations

(i) the mass balance equation

$$\text{Div}\{J\mathbf{v}\} + \frac{\partial}{\partial \zeta}\{J\mathrm{v}\} = 0\,, \tag{4.29}$$

[5] Suppose that other scales than those which we have adopted here are used for the physical quantities entering the 3D modelling equations. That is, assume the physical quantity Q_{dim} to be non-dimensionalized as $Q_{\text{dim}} = \beta\tilde{Q}$, while in this book $Q_{\text{dim}} = \alpha Q_{\text{dimless}}$, $\alpha \neq \beta$. Then, our final modelling equations, expressed in terms of quantities like Q_{dimless}, can be immediately written in terms of quantities like $\tilde{Q}$ by the identification $Q_{\text{dimless}} = \frac{\beta}{\alpha}\tilde{Q}$.

(ii) the tangential linear momentum balance equation

$$\frac{\partial}{\partial t}\{J\mathbf{v}\} + \mathrm{Div}\{J\,(\mathbf{v}\otimes\mathbf{v} + p\,\mathbf{M} - \mathbf{P})\} + \frac{\partial}{\partial\zeta}\{J(\mathrm{v}\mathbf{v} - \mathbf{p})\} + J\Gamma(-p\,\mathbf{M}, \mathbf{0}) + J\Gamma(\mathbf{P}, \mathbf{p}) = J\mathbf{b} + J\Gamma(\mathbf{v}, \mathrm{v})\,, \tag{4.30}$$

(iii) the normal linear momentum balance equation

$$\frac{\partial}{\partial t}\{J\mathrm{v}\} + \mathrm{Div}\{J(\mathrm{v}\mathbf{v} - \mathbf{p})\} + \frac{\partial}{\partial\zeta}\{J\,(\mathrm{v}^2 - P^{33})\} + J\,\frac{\partial p}{\partial\zeta} + J\Gamma(\mathbf{P}) = J\mathrm{b} + J\Gamma(\mathbf{v})\,, \tag{4.31}$$

where the dimensionless γ-terms are formally the same as those in (3.65)–(3.68), that is,

$$\Gamma(-p\,\mathbf{M}, \mathbf{0}) \equiv p\left\{\mathbf{B}^{-1}\frac{\partial\mathbf{B}}{\partial\xi^\alpha}\,\mathbf{M}\mathbf{e}_\alpha + \mathrm{tr}\,(\widetilde{\mathbf{W}}(\mathbf{I} - \zeta\widetilde{\mathbf{W}})^{-1})\,\mathbf{B}^{-1}\mathbf{s}\right\}, \tag{4.32}$$

$$\Gamma(\mathbf{P}, \mathbf{p}) \equiv -\mathbf{B}^{-1}\frac{\partial\mathbf{B}}{\partial\xi^\alpha}\,\mathbf{P}\mathbf{e}_\alpha + 2\mathbf{B}^{-1}\mathbf{F}\widetilde{\mathbf{W}}\mathbf{p} + \Gamma(\mathbf{P})\mathbf{B}^{-1}\mathbf{s}\,, \tag{4.33}$$

$$\Gamma(\mathbf{v}, \mathrm{v}) \equiv -\mathbf{B}^{-1}\frac{\partial\mathbf{B}}{\partial\xi^\alpha}\,(\mathbf{v}\otimes\mathbf{v})\mathbf{e}_\alpha + 2\mathrm{v}\mathbf{B}^{-1}\mathbf{F}\widetilde{\mathbf{W}}\mathbf{v} + \Gamma(\mathbf{v})\mathbf{B}^{-1}\mathbf{s}\,, \tag{4.34}$$

$$\Gamma(\mathbf{P}) \equiv -\mathbf{B}^T\mathbf{F}^{-T}\widetilde{\mathbf{H}}\cdot\mathbf{P}\,, \qquad \Gamma(\mathbf{v}) \equiv -\mathbf{B}^T\mathbf{F}^{-T}\widetilde{\mathbf{H}}\cdot(\mathbf{v}\otimes\mathbf{v})\,, \tag{4.35}$$

and the non-dimensional gravity components are given, see (3.58), by

$$\mathbf{b} = -c\mathbf{B}^{-1}\mathbf{s}\,, \quad \mathrm{b} = -c\,. \tag{4.36}$$

Boundary Conditions

At the basal surface $\mathcal{S}_b \Longleftrightarrow$ at $\zeta = 0$:

(i) the kinematic boundary condition

$$\mathrm{v} = 0\,, \tag{4.37}$$

(ii) the dynamic boundary condition

$$\mathbf{p} = -\mathbf{f}_b\,. \tag{4.38}$$

At the free surface $\mathcal{S} \Longleftrightarrow$ at $\zeta = h(\boldsymbol{\xi}, t)$:

(i) the kinematic boundary condition

$$\frac{\partial h}{\partial t} + \mathrm{Grad}\,h\cdot\mathbf{v} = \mathrm{v}\,, \tag{4.39}$$

(ii) the dynamic boundary conditions

$$\mathbf{T}\mathrm{Grad}\, h - \mathbf{t} = \mathbf{0}\,, \qquad \mathbf{t}\cdot \mathrm{Grad}\, h - T^{33} = 0\,, \tag{4.40}$$

or, in terms of the pressure p and the components $\mathbf{P}$, $\mathbf{p}$, P^{33} of the extra-stress tensor $\boldsymbol{\sigma}_E$, see (3.59),

$$(-p\mathbf{M} + \mathbf{P})\mathrm{Grad}\, h - \mathbf{p} = \mathbf{0}\,, \qquad \mathbf{p}\cdot \mathrm{Grad}\, h - (-p + P^{33}) = 0\,. \tag{4.41}$$

4.3.1.2 Active Topographic Bed

Balance Equations

(i) the mass balance equation

$$\frac{\partial J}{\partial t} + \mathrm{Div}\,\{J\,(\mathbf{v} - \mathbf{w})\} + \frac{\partial}{\partial \zeta}\{J\,(\mathrm{v} - \mathcal{U})\} = 0\,, \tag{4.42}$$

or, equivalently,

$$\mathrm{Div}\{J\mathbf{v}\} + \frac{\partial}{\partial \zeta}\,\{J\mathrm{v}\} = 0\,, \tag{4.43}$$

(ii) the tangential linear momentum balance equation

$$\begin{aligned} &\frac{\partial}{\partial t}\{J\mathbf{v}\} + \mathrm{Div}\,\{J\,[\,\mathbf{v}\otimes(\mathbf{v}-\mathbf{w}) + p\mathbf{M} - \mathbf{P}\,]\} \\ &+ \frac{\partial}{\partial \zeta}\left\{J\,\left[(\mathrm{v} - \mathcal{U})\mathbf{v} - \mathbf{p}\,\right]\right\} + J\Gamma(-p\,\mathbf{M}, \mathbf{0}) + J\Gamma(\mathbf{P}, \mathbf{p}) \\ &= J\mathbf{b} + J\Gamma(\mathbf{v}, \mathrm{v}) - J\left\{(\mathrm{Grad}\,\mathbf{w})\mathbf{v} + \mathrm{v}\frac{\partial \mathbf{w}}{\partial \zeta}\right\}\,, \end{aligned} \tag{4.44}$$

(iii) the normal linear momentum balance equation

$$\begin{aligned} &\frac{\partial}{\partial t}\{J\mathrm{v}\} + \mathrm{Div}\left\{J\left[\mathrm{v}(\mathbf{v} - \mathbf{w}) - \mathbf{p}\,\right]\right\} + \frac{\partial}{\partial \zeta}\left\{J\left[\mathrm{v}(\mathrm{v} - \mathcal{U}) - P^{33}\right]\right\} \\ &+ J\,\frac{\partial p}{\partial \zeta} + J\Gamma(\mathbf{P}) = J\mathrm{b} + J\Gamma(\mathbf{v}) - J\,\mathrm{Grad}\,\mathcal{U}\cdot\mathbf{v}\,. \end{aligned} \tag{4.45}$$

Boundary Conditions

At the basal surface $\mathcal{S}_b \Longleftrightarrow$ at $\zeta = 0$:

(i) the kinematic boundary condition

$$\mathrm{v} = \left(1 - \frac{\rho_b}{\rho_0}\right)\mathcal{U}\,, \tag{4.46}$$

(ii) the dynamic boundary condition (4.38).

At the free surface $\mathcal{S} \Longleftrightarrow$ at $\zeta = h(\boldsymbol{\xi}, t)$:

(i) the kinematic boundary condition

$$\frac{\partial h}{\partial t} + \text{Grad}\, h \cdot (\mathbf{v} - \mathbf{w}) = \mathrm{v} - \mathcal{U}\,, \tag{4.47}$$

(ii) the dynamic boundary conditions (4.40) or, equivalently, (4.41).

4.3.2 Dimensionless 3D Model Equations in the Non-conventional Route

In the non-conventional route the dimensionless model equations follow from the conservation laws (3.71), (3.76), (3.77) (see also (3.74)), and the boundary conditions (4.21), (4.22), (4.24), (4.25).

4.3.2.1 Active Topographic Bed

Balance Equations

(i) the mass balance equation

$$\frac{\partial J}{\partial t} + \text{Div}\,\{J(\mathbf{v} - \mathbf{w})\} + \frac{\partial}{\partial \zeta}\{J(\mathrm{v} - \mathcal{U})\} = 0\,, \tag{4.48}$$

or, equivalently,

$$\text{Div}\{J\mathbf{v}\} + \frac{\partial}{\partial \zeta}\{J\mathrm{v}\} = 0\,, \tag{4.49}$$

(ii) the hybrid form of the horizontal linear momentum balance equation

$$\frac{\partial J\mathbb{v}}{\partial t} + \text{Div}\,\{J[\mathbb{v} \otimes (\mathbf{v} - \mathbf{w}) - \mathbb{S}]\} + \frac{\partial}{\partial \zeta}\{J[(\mathrm{v} - \mathcal{U})\mathbb{v} - \mathbb{s}]\} = \mathbb{0}\,, \tag{4.50}$$

(iii) the hybrid form of the vertical linear momentum balance equation

$$\frac{\partial J v}{\partial t} + \text{Div}\,\{J[v(\mathbf{v} - \mathbf{w}) - \mathbb{t}]\} + \frac{\partial}{\partial \zeta}\{J[v(\mathrm{v} - \mathcal{U}) - \sigma]\} = -J\,. \tag{4.51}$$

Boundary Conditions

At the basal surface $\mathcal{S}_b \Longleftrightarrow$ at $\zeta = 0$:

(i) the kinematic boundary condition

$$\mathrm{v} = \left(1 - \frac{\rho_b}{\rho_0}\right)\mathcal{U}\,, \tag{4.52}$$

(ii) the dynamic boundary condition

$$\mathbb{s} = -\mathbf{F}\mathbf{f}_b - T^{33}\mathbf{s}\,. \tag{4.53}$$

At the free surface $\mathcal{S} \Longleftrightarrow$ at $\zeta = h(\boldsymbol{\xi}, t)$:

(i) the kinematic boundary condition

$$\frac{\partial h}{\partial t} + \mathrm{Grad}\, h \cdot (\mathbf{v} - \mathbf{w}) = \mathrm{v} - \mathcal{U}\,, \tag{4.54}$$

(ii) the dynamic boundary conditions

$$\mathbb{S}\mathrm{Grad}\, h - \mathbb{s} = \mathbb{0}\,, \quad \mathbb{t} \cdot \mathrm{Grad}\, h - \sigma = 0\,. \tag{4.55}$$

4.4 Depth-Averaging Approach

The system of modelling equations, either for rigid topographic beds (4.29–4.41) or active beds (2.71, 4.41–4.47), must be complemented by a constitutive law for the extra-stress tensor $\boldsymbol{\sigma}_E$ and a sliding law for the bed friction $\boldsymbol{f}_b$. Moreover, if there are erosion/deposition processes, the erosion/deposition rate $\mathcal{U}$ must be prescribed. As such, the system of modelling equations stands for the determination of the basic fields

$\mathbf{v}$—tangential velocity,
v—normal velocity,
p—pressure,
h—flow depth,
b—elevation of the bed surface if there is erosion or deposition.

However, this system is by far too complicated in order to be solved. One way to handle this complexity is to follow the *depth-averaging* (or *depth-integration*) *approach*, as in the seminal work by Savage and Hutter [2]. In this approach, based on the observation that in a realistic rapid geophysical flow the normal velocity is negligibly small in comparison with the magnitude of the tangential velocity, the depth-averaged tangential velocity components, $\overline{\mathbf{v}}$, are sought for, rather than the velocity $\mathbf{v}$. Here, by the *depth-average*, $\overline{f}$, of a quantity f we mean the ratio

$$\overline{f}\,(\boldsymbol{\xi}, t) \equiv \frac{1}{h(\boldsymbol{\xi}, t)} \int_0^{h(\boldsymbol{\xi},t)} f\,(\boldsymbol{\xi}, \zeta, t)\, d\zeta\,.$$

Knowing $\overline{\mathbf{v}}$ and neglecting the small terms in (2.96), one can then estimate the depth-averaged velocity vector as

$$\overline{\mathbb{v}} \approx \mathbf{F}\overline{\mathbf{v}}\,, \quad \overline{v} \approx \frac{1}{c}\,\mathbf{s}\cdot\mathbf{F}\overline{\mathbf{v}}\,,$$

see the forthcoming (4.85). The depth-averaging technique uses ordering approximations justified by the shallowness of the flowing mass, and ultimately leads to a system of equations for

$\overline{\mathbf{v}}$—depth-averaged tangential velocity,
h—flow depth,
b—elevation of the bed surface if there is erosion or deposition.

The major benefit of the method is that it yields a system of 2D equations (the mean value $\overline{\mathbf{v}}$ and the elevations h, b are independent of ζ), which clearly reduces the costs in the numerical computations. We will refer to these 2D equations as the *depth-averaged* or *thin-layer modelling equations*. Loosely speaking, the idea of the depth-averaging technique is

- to use thin-layer approximations in one of the three scalar equations representing the linear momentum balance to obtain the pressure p;
- to integrate along the avalanche depth the mass balance equation and the other two scalar equations representing the linear momentum balance;
- to use thin-layer assumptions in the depth-integrated mass and linear momentum balance equations to deduce equations for $\overline{\mathbf{v}}$, h.

Yet the selection of the scalar momentum balance equations to be depth-integrated is important, since different equations (even if equivalent), may lead to different final modelling equations. In this book we have followed the conventional and non-conventional routes and obtained two different sets of scalar linear momentum balance equations expressed in the topography-fitted coordinates. We use both these sets of equations within the depth-averaging technique. Doing so we indeed obtain different final modelling equations. In Sect. 4.3 we deal with the system of equations from the conventional route, and the system of equations in the non-conventional route is exploited in Sect. 4.6. In each of these sections we use the Leibniz formulae

$$
\begin{aligned}
\int_{f(\boldsymbol{\xi},t)}^{g(\boldsymbol{\xi},t)} \frac{\partial \phi}{\partial t}\, d\zeta &= \frac{\partial}{\partial t} \int_{f(\boldsymbol{\xi},t)}^{g(\boldsymbol{\xi},t)} \phi\, d\zeta + \phi\Big|_{\zeta=f(\boldsymbol{\xi},t)} \frac{\partial f}{\partial t} - \phi\Big|_{\zeta=g(\boldsymbol{\xi},t)} \frac{\partial g}{\partial t}\,, \\
\int_{f(\boldsymbol{\xi},t)}^{g(\boldsymbol{\xi},t)} \mathrm{Div}\, \mathbf{v}\, d\zeta &= \mathrm{Div} \int_{f(\boldsymbol{\xi},t)}^{g(\boldsymbol{\xi},t)} \mathbf{v}\, d\zeta \\
&\quad + \mathbf{v}\Big|_{\zeta=f(\boldsymbol{\xi},t)} \cdot \mathrm{Grad}\, f - \mathbf{v}\Big|_{\zeta=g(\boldsymbol{\xi},t)} \cdot \mathrm{Grad}\, g\,, \qquad (4.56) \\
\int_{f(\boldsymbol{\xi},t)}^{g(\boldsymbol{\xi},t)} \mathrm{Div}\, \mathbf{P}\, d\zeta &= \mathrm{Div} \int_{f(\boldsymbol{\xi},t)}^{g(\boldsymbol{\xi},t)} \mathbf{P}\, d\zeta \\
&\quad + \mathbf{P}\Big|_{\zeta=f(\boldsymbol{\xi},t)} \mathrm{Grad}\, f - \mathbf{P}\Big|_{\zeta=g(\boldsymbol{\xi},t)} \mathrm{Grad}\, g\,,
\end{aligned}
$$

which hold for a scalar function $\phi(\boldsymbol{\xi}, \zeta, t)$, a 2-column matrix function $\mathbf{v}(\boldsymbol{\xi}, \zeta, t)$, and a 2×2 matrix function $\mathbf{P}(\boldsymbol{\xi}, \zeta, t)$, all of them sufficiently smooth.

4.5 Depth-Averaged Model Equations in the Conventional Route

In this section the depth-integration method, schematically shown in Sect. 4.4, is pursued for the non-dimensional equations derived within the conventional route. First, the depth-integrated mass and tangential momentum balance equations are deduced in Sect. 4.5.1. Then, thin-layer assumptions are formulated in Sect. 4.5.2. These are used in Sect. 4.5.3 to obtain asymptotic approximations which allow to solve the normal momentum balance equation for the pressure p, and to simplify the depth-integrated mass and tangential momentum balance equations. The emerging depth-averaged equations constitute the modelling equations which describe the shallow mass flow. They are sufficiently general, in the sense that the constitutive properties of the material are not yet accounted for. A hierarchy of these models in terms of the relative weights in the stress contribution is provided in Sect. 4.5.4, and Sect. 4.5.5 shows the model equations corresponding to small curvature of the basal surface.

4.5.1 Depth-Averaging in the Conventional Route

We start to apply the depth-averaging technique in the conventional route. More precisely, in this section we deduce the depth-integrated mass balance equation and the depth-integrated tangential momentum balance equation. We do this separately for rigid beds and active beds.

4.5.1.1 Stationary Topographic Bed

(i) From the mass balance equation (4.29) and the boundary condition (4.37) we obtain that,

The normal velocity v *is given by*

$$\mathrm{v} = -\frac{1}{J}\int_0^{\zeta} \mathrm{Div}\{J\mathbf{v}\}\, d\zeta' \,. \tag{4.57}$$

(ii) We evaluate the normal velocity (4.57) at $\zeta = h$ by using Leibniz formula $(4.56)_2$ and deduce

$$\begin{aligned} \mathrm{v}\Big|_{\zeta=h} &= -\frac{1}{J\Big|_{\zeta=h}}\int_0^{h} \mathrm{Div}\{J\mathbf{v}\}\, d\zeta \\ &= -\frac{1}{J\Big|_{\zeta=h}}\,\mathrm{Div}\int_0^{h} J\mathbf{v}\, d\zeta + \mathbf{v}\Big|_{\zeta=h}\cdot \mathrm{Grad}\, h \,. \end{aligned} \tag{4.58}$$

With $\mathrm{v}\Big|_{\zeta=h}$ as given by the preceding formula, the kinematic boundary condition (4.39) turns into

$$J\Big|_{\zeta=h}\frac{\partial h}{\partial t} + \mathrm{Div}\int_0^{h} J\mathbf{v}\, d\zeta = 0 \,,$$

which can be further written by accounting for Leibniz formula $(4.56)_1$ and the time-independence of the Jacobian J. We therefore obtain,

The kinematic boundary condition (4.39) *emerges as*

$$\frac{\partial}{\partial t}\int_0^{h} J\, d\zeta + \mathrm{Div}\int_0^{h} J\mathbf{v}\, d\zeta = 0 \,. \tag{4.59}$$

The preceding relation can also be deduced by integrating from 0 to h the mass balance equation (4.29) and using the boundary conditions (4.37) and (4.39). This is the reason that (4.59) is called *the depth-integrated mass balance equation*. However, the way followed here to deduce (4.59) clearly shows that (4.57) and (4.59) are independent relations, a fact which will on some occasions be used.

(iii) We integrate the tangential linear momentum balance equation (4.30) from 0 to h by using Leibniz formulae $(4.56)_{1,3}$ and the kinematic boundary conditions (4.37) and (4.39). A straightforward calculation yields

$$\begin{aligned}
&\frac{\partial}{\partial t}\int_0^h J\,\mathbf{v}\,d\zeta + \mathrm{Div}\int_0^h J\,(\mathbf{v}\otimes\mathbf{v} + p\mathbf{M} - \mathbf{P})\,d\zeta \\
&\quad + \left\{J\left[(-p\mathbf{M}+\mathbf{P})\mathrm{Grad}\,h - \mathbf{p}\right]\right\}_{\zeta=h} + \int_0^h J\,\Gamma(-p\,\mathbf{M},\mathbf{0})\,d\zeta \\
&+ \int_0^h J\,\Gamma(\mathbf{P},\mathbf{p})\,d\zeta = -J_0\,\mathbf{p}\Big|_{\zeta=0} + \int_0^h J\,\mathbf{b}\,d\zeta + \int_0^h J\,\Gamma(\mathbf{v},\mathrm{v})\,d\zeta\,,
\end{aligned} \tag{4.60}$$

where

$$J_0 \equiv J\Big|_{\zeta=0} = \frac{1}{c}\det\mathbf{F}\,, \tag{4.61}$$

see (2.82). Insertion of the dynamic boundary conditions (4.38) and $(4.41)_1$ into (4.60) gives the following result:

Corresponding to a rigid topographic bed, in the conventional route the depth-integrated tangential linear momentum balance equation is

$$\begin{aligned}
&\frac{\partial}{\partial t}\int_0^h J\,\mathbf{v}\,d\zeta + \mathrm{Div}\int_0^h J\,(\mathbf{v}\otimes\mathbf{v} + p\mathbf{M} - \mathbf{P})\,d\zeta \\
&\quad + \int_0^h J\,\Gamma(-p\,\mathbf{M},\mathbf{0})\,d\zeta + \int_0^h J\,\Gamma(\mathbf{P},\mathbf{p})\,d\zeta \\
&= -J_0\mathbf{p}\big|_{\zeta=0} + \int_0^h J\,\mathbf{b}\,d\zeta + \int_0^h J\,\Gamma(\mathbf{v},\mathrm{v})\,d\zeta\,.
\end{aligned} \tag{4.62}$$

(iv) Relation (4.62) can be also obtained by replacing the expression of $\left\{J\left[(-p\mathbf{M}+\mathbf{P})\mathrm{Grad}\,h - \mathbf{p}\right]\right\}_{\zeta=h}$, as deduced from (4.60), into the dynamic boundary condition $(4.41)_1$. That is, (4.62) can be conceived as replacing the dynamic boundary condition $(4.41)_1$ within the system of modelling equations. This way one can better see that the *local* tangential linear momentum balance equation (4.30) and the *depth-integrated* tangential linear momentum balance equation (4.62) are independent equations, similarly to the *local* mass balance equation (4.29) and the *depth-integrated* mass balance equation (4.59). Thus, looking for solutions $\mathbf{v}$, v, p, h of the system of equations

the mass balance equation, (4.29),
the tangential linear momentum balance equation, (4.30),
the normal linear momentum balance equation, (4.31),
the kinematic boundary condition at the basal surface, (4.37),
the dynamic boundary condition at the basal surface, (4.38),
the kinematic boundary condition at the free surface, (4.39),
the dynamic boundary conditions at the free surface, $(4.40)_{1,2}$,

is the same as looking for solutions of

the tangential linear momentum balance equation, (4.30),
the normal linear momentum balance equation, (4.31),
the depth-integrated mass balance equation, (4.59),
the depth-integrated tangential momentum balance equation, (4.62),
the dynamic boundary condition at the basal surface, (4.38),
the dynamic boundary condition at the free surface, $(4.41)_2$,

where the normal velocity v is given by (4.57). Both the preceding equivalent systems of equations are sufficiently complicated. In the depth-averaging approach this complexity is reduced by handling the second above system as follows: the local tangential linear momentum balance equation (4.30) is ignored, and replaced with ordering approximations, suggested by the shallowness of the avalanching mass, on the fields entering the equations of the system. Doing so, the aim is

- to solve the local normal linear momentum balance equation, (4.31), for the pressure p, with account of the dynamic boundary condition at the free surface, $(4.41)_2$, and
- to transform the depth-integrated mass and tangential linear momentum balance equations, (4.59) and (4.62), into equations for the depth-averaged velocity $\overline{\mathbf{v}}$ and the avalanche depth h.

Next we refer to the case of a topographic bed associated with erosion/deposition processes. We treat the corresponding system of equations, see Sect. 4.3, in the same manner as we did for a rigid bed.

4.5.1.2 Active Topographic Bed

(i) The mass balance equations (4.42), (4.43) and the boundary condition (4.46) yield:

The normal velocity v *is computed as*

$$\mathrm{v} = \mathcal{U} - \frac{1}{J}\left\{\int_0^\zeta \frac{\partial J}{\partial t}\,d\zeta' + \int_0^\zeta \mathrm{Div}\,\{J(\mathbf{v}-\mathbf{w})\}\,d\zeta' + J_0\frac{\rho_b}{\rho_0}\mathcal{U}\right\}, \tag{4.63}$$

or, equivalently,

$$\mathrm{v} = \frac{J_0}{J}\left(1-\frac{\rho_b}{\rho_0}\right)\mathcal{U} - \frac{1}{J}\int_0^\zeta \mathrm{Div}\,\{J\mathbf{v}\}\,d\zeta'. \tag{4.64}$$

(ii) Using the form (4.63) for the normal velocity and Leibniz formulae $(4.56)_{1,2}$ we deduce

$$\begin{aligned}\mathrm{v}\Big|_{\zeta=h} &= \mathcal{U} - \frac{1}{J\Big|_{\zeta=h}}\left\{\int_0^h \frac{\partial J}{\partial t}\,d\zeta + \int_0^h \mathrm{Div}\,\{J(\mathbf{v}-\mathbf{w})\}\,d\zeta + J_0\frac{\rho_b}{\rho_0}\mathcal{U}\right\}\\ &= \mathcal{U} - \frac{1}{J\Big|_{\zeta=h}}\left\{\frac{\partial}{\partial t}\int_0^h J\,d\zeta + \mathrm{Div}\int_0^h J(\mathbf{v}-\mathbf{w})\,d\zeta + J_0\frac{\rho_b}{\rho_0}\mathcal{U}\right\}\\ &\quad + \frac{\partial h}{\partial t} + (\mathbf{v}-\mathbf{w})|_{\zeta=h}\cdot\mathrm{Grad}\,h\,.\end{aligned}$$

When inserting $\mathrm{v}\Big|_{\zeta=h}$ from the preceding formula into the kinematic boundary condition (4.47) we obtain:

The kinematic boundary condition (4.47) *emerges as*

$$\frac{\partial}{\partial t}\int_0^h J\,d\zeta + \mathrm{Div}\int_0^h J(\mathbf{v}-\mathbf{w})\,d\zeta = -J_0\frac{\rho_b}{\rho_0}\mathcal{U}\,. \tag{4.65}$$

With a similar argument to that used for a rigid bed, relation (4.65) can be interpreted as the depth-integrated mass balance equation. Of course, we could have substituted $\mathrm{v}\Big|_{\zeta=h}$ as deduced from (4.64) into the kinematic boundary condition (4.47). However, the form (4.65) of the kinematic boundary condition (4.47) is more suitable for the ensuing analysis.

(iii) We integrate the tangential linear momentum balance equation (4.44) from 0 to h by using the Leibniz formulae $(4.56)_{1,3}$, the kinematic boundary conditions (4.46) and (4.47), and the dynamic boundary conditions (4.38), $(4.41)_1$. This yields:

Corresponding to an active topographic bed, the depth-integrated tangential linear momentum balance equation in the conventional route appears as

$$\begin{aligned}
&\frac{\partial}{\partial t}\int_0^h J\,\mathbf{v}\,d\zeta + \mathrm{Div}\int_0^h J\,\{\mathbf{v}\otimes(\mathbf{v}-\mathbf{w}) + p\mathbf{M}-\mathbf{P}\}\,d\zeta \\
&\qquad + \int_0^h J\,\Gamma(-p\,\mathbf{M},\mathbf{0})\,d\zeta + \int_0^h J\,\Gamma(\mathbf{P},\mathbf{p})\,d\zeta \\
&= -J_0\,\frac{\rho_b}{\rho_0}\,\mathcal{U}\,\mathbf{v}\big|_{\zeta=0} - J_0\mathbf{p}\big|_{\zeta=0} + \int_0^h J\,\mathbf{b}\,d\zeta + \int_0^h J\,\Gamma(\mathbf{v},\mathrm{v})\,d\zeta \\
&\qquad - \int_0^h J\left\{(\mathrm{Grad}\,\mathbf{w})\mathbf{v} + \mathrm{v}\frac{\partial \mathbf{w}}{\partial \zeta}\right\}d\zeta\,.
\end{aligned} \tag{4.66}$$

(iv) The depth-integration approach deals with

the normal linear momentum balance equation, (4.45),

the depth-integrated mass balance equation, (4.65),

the depth-integrated tangential linear momentum balance equation, (4.66),

the dynamic boundary condition at the basal surface, (4.38),

the dynamic boundary condition at the free surface, $(4.41)_2$,

the equation for the bed elevation, (2.71),

in the same way as for a rigid topography. Of course, this time the normal velocity v is given by (4.63).

Inspection of the equations which we use in the depth-averaging approach for both stationary and active beds reveals the following

Remark In the depth-averaging approach, the modelling equations for the case of rigid topographic beds emerge from the modelling equations which correspond to active topographic beds, by setting the mesh velocity equal to zero, that is, $\mathbf{w} = \mathbf{0}$ and $\mathcal{U} = 0$.

This remark allows to further refer solely to the case when there is erosion/deposition. The final modelling equations for flows on rigid beds can be obtained from the final modelling equations corresponding to flows on active beds by taking $\mathcal{U} = 0$ and $\mathbf{w} = \mathbf{0}$.

4.5.2 Thin-Layer Approximations

In this section we introduce the *thin-layer approximations* which we need to exploit the modelling equations as stated in the previous section. We still keep the discussion general, that is, we do not specify closure relations for the extra-stress tensor $\boldsymbol{\sigma}_E$, bed friction $\boldsymbol{f}_b$ and erosion/deposition rate $\mathcal{U}$; such relations that fit our approximations will be presented in Sects. 5.1–5.3. To express the thin-layer approximations we use the aspect ratio $\epsilon \equiv H/L$, see (4.3), and a constant $\gamma \in (0, 1)$.

(a) Geometric approximation: the depth h of the flowing mass is of the order of the aspect ratio ϵ,

$$h = O(\epsilon)\,. \tag{4.67}$$

Motivation Assumption **(a)** states that the avalanching body is shallow. It implies $\zeta = O(\epsilon)$, for $\zeta \in [0, h]$. Moreover, with $\boldsymbol{\tau}_\alpha = O(1)$, $\alpha = 1, 2$, and $\zeta = O(\epsilon)$, we have

$$\boldsymbol{g}_\alpha = \boldsymbol{\tau}_\alpha + O(\epsilon) = O(1)\,, \quad \alpha = 1, 2\,,$$

which legitimates ordering approximations on the contravariant components of vectors and tensors, as in items **(b)** and **(c)** below.

(b) Flow rule approximations:

- If there is erosion/deposition, its rate $\mathcal{U}$ is supposed sufficiently small,

$$\mathcal{U} = O(\epsilon)\,. \tag{4.68}$$

- The components of the tangential velocity are significant,

$$\mathbf{v} = O(1)\,. \tag{4.69}$$

- We assume the following approximations of Boussinesq type,

$$\int_0^h \zeta \mathbf{v}\, d\zeta = \tfrac{1}{2} m_1 h^2\, \overline{\mathbf{v}} + O(\epsilon^{2+\gamma}), \quad \int_0^h \mathbf{v} \otimes \mathbf{v}\, d\zeta = m_2 h\, \overline{\mathbf{v}} \otimes \overline{\mathbf{v}} + O(\epsilon^{2+\gamma}),$$
$$\int_0^h \zeta \mathbf{v} \otimes \mathbf{v}\, d\zeta = \tfrac{1}{2} m_3 h^2\, \overline{\mathbf{v}} \otimes \overline{\mathbf{v}} + O(\epsilon^{2+\gamma})\,. \tag{4.70}$$

Moreover, if the topographic bed is rigid, we suppose

$$\int_0^h \mathrm{v}\mathbf{v}\, d\zeta = \tfrac{1}{2} \beta h^2\, \overline{\mathbf{v}} + O(\epsilon^{2+\gamma})\,, \tag{4.71}$$

and for an active bed we take

$$\int_0^h \mathrm{v}\mathbf{v}\, d\zeta = h \left(1 - \frac{\rho_b}{\rho_0}\right) \mathcal{U}\, \overline{\mathbf{v}} + \tfrac{1}{2} \beta h^2\, \overline{\mathbf{v}} + O(\epsilon^{2+\gamma}) \tag{4.72}$$

as granted. In (4.70)–(4.72) the coefficients m_1 to m_3 and β are supposed to be scalar functions of $\boldsymbol{\xi}, t$ of order $O(1)$. We refer to m_1, m_2, m_3 and β as *momentum correction factors* or *Boussinesq coefficients*. Since the velocity profile is influenced by the material properties, these coefficients indirectly reflect the rheology of the flowing mass.

Motivation Since the depth of the flowing mass is $h = O(\epsilon)$, $\mathcal{U} = O(\epsilon)$ or even smaller is a reasonable assumption.

Then, assuming $\mathbf{v} = O(1)$ means that the tangential velocity $\boldsymbol{v}_\tau$ of the flowing material is dominant,

$$\boldsymbol{v}_\tau = v^\alpha \boldsymbol{g}_\alpha = v^\alpha \boldsymbol{\tau}_\alpha + O(\epsilon) = O(1)\,,$$

in comparison to the normal velocity $\boldsymbol{v}_n \equiv \mathrm{v}\boldsymbol{n}_b$, which emerges as

$$\boldsymbol{v}_n = \mathrm{v}\boldsymbol{n}_b = O(\epsilon)\,,$$

since $\mathrm{v} = O(\epsilon)$. Indeed, recalling definition (4.61) of J_0, relation (2.82) and $\zeta = O(\epsilon)$ yield

$$J = J_0 \det(\mathbf{I} - \zeta\widetilde{\mathbf{W}}) = J_0(1 - 2\Omega\zeta) + O(\epsilon^2) = J_0 + O(\epsilon)\,. \tag{4.73}$$

Thus, with (4.73), for the case of a rigid topographic bed formula (4.57) for v gives

$$\mathrm{v} = -\frac{1}{J_0}\int_0^{\zeta} \mathrm{Div}\,\{J_0\mathbf{v}\}\,d\zeta' + O(\epsilon^2) = O(\epsilon)\,, \tag{4.74}$$

while for an active bed, using $\mathcal{U} = O(\epsilon)$, expression (4.64) of v reads as

$$\mathrm{v} = \left(1 - \frac{\rho_b}{\rho_0}\right)\mathcal{U} - \frac{1}{J_0}\int_0^{\zeta} \mathrm{Div}\,\{J_0\mathbf{v}\}\,d\zeta' + O(\epsilon^2) = O(\epsilon)\,. \tag{4.75}$$

In short, assumption $\mathbf{v} = O(1)$ expresses the fact that the motion is predominant in planes parallel to the topography,

$$\boldsymbol{v} = \boldsymbol{v}_\tau + \mathrm{v}\boldsymbol{n}_b = v^\alpha \boldsymbol{\tau}_\alpha + O(\epsilon) \approx v^\alpha \boldsymbol{\tau}_\alpha\,, \quad v^\alpha = v^\alpha(\boldsymbol{\xi}, \zeta, t)\,, \tag{4.76}$$

which is realistic in many rapid geophysical mass flows.

The estimates of the integrals on the left-hand sides of (4.70)–(4.72) are needed when performing approximations in the depth-integrated balance equations. Relations (4.70)–(4.72) are suggested by the consideration of the plug flow and power law velocity profiles as approximations for realistic flow velocities. Both these velocity profiles satisfy the Boussinesq approximations (4.70)–(4.72) for some coefficients m_1 to m_3 and β. We show this below.

(i) The **plug flow** is defined by the condition $\mathbf{v} = \mathbf{v}(\boldsymbol{\xi}, t)$. Owing to (4.76), this expresses the fact that along the normal to the basal surface $\mathcal{S}_b$ the velocity $\boldsymbol{v}$ is almost uniform and parallel to $\mathcal{S}_b$:

$$\boldsymbol{v} \approx v^\alpha \boldsymbol{\tau}_\alpha\,, \quad v^\alpha = v^\alpha(\boldsymbol{\xi}, t)\,.$$

The plug flow velocity profile may not be a realistic assumption in a soil motion, however, it is a first rough approximation for the physical reality. Condition $\mathbf{v} = \mathbf{v}(\boldsymbol{\xi}, t)$ yields $\mathbf{v} = \overline{\mathbf{v}}$ and the values

$$m_1 = m_2 = m_3 = 1$$

in the flow rule relations (4.70). Then, from (4.74) we deduce

$$\mathrm{v} = -\frac{1}{J_0}\,\zeta\,\mathrm{Div}\,\{J_0\overline{\mathbf{v}}\} + O(\epsilon^2)\,,$$

and therefore, due to assumption $\mathbf{v} = \mathbf{v}(\boldsymbol{\xi}, t)$,

$$\int_0^h \mathrm{v}\mathbf{v}\,d\zeta = -\frac{h^2}{2J_0}\,(\mathrm{Div}\,\{J_0\overline{\mathbf{v}}\})\,\overline{\mathbf{v}} + O(\epsilon^3)\,, \tag{4.77}$$

showing that (4.71) is satisfied with

$$\beta = -\frac{1}{J_0}\,\mathrm{Div}\,\{J_0\overline{\mathbf{v}}\}\,. \tag{4.78}$$

For an active bed, (4.75) yields

$$\int_0^h \mathrm{v}\mathbf{v}\,d\zeta = h\left(1-\frac{\rho_b}{\rho_0}\right)\mathcal{U}\,\overline{\mathbf{v}} - \frac{h^2}{2J_0}\,(\mathrm{Div}\,\{J_0\overline{\mathbf{v}}\})\,\overline{\mathbf{v}} + O(\epsilon^3)\,, \tag{4.79}$$

and hence (4.72) is satisfied with (4.78).
(ii) The **power law velocity profile** is defined as, see Pudasaini and Hutter [3],

$$\mathbf{v} = \mathbf{v}_h - \left(1-\frac{\zeta}{h}\right)^{n+1}(\mathbf{v}_h - \mathbf{v}_0)\,, \quad \mathbf{v}_0 = \tilde{\chi}_b\mathbf{v}_h\,, \quad n > 0\,, \quad \tilde{\chi}_b \in [0,1]\,, \tag{4.80}$$

where $\mathbf{v}_0 \equiv \mathbf{v}|_{\zeta=0}$, $\mathbf{v}_h \equiv \mathbf{v}|_{\zeta=h}$, n is a constant, and the velocity ratio $\tilde{\chi}_b$ is a function of $\boldsymbol{\xi}, t$. For $\tilde{\chi}_b = 1$ the power law flow (4.80) degenerates into plug flow, and $\tilde{\chi}_b = 0$ implies $\mathbf{v}_0 = \mathbf{0}$.

By the power law profile (4.80), in which $n \geq 3$ is expected, one postulates tangential velocity components (and thereby, apart from $O(\epsilon)$ terms, velocity profiles $\boldsymbol{v}$) that are almost uniform through the depth, except near the ground surface. Power law velocity profiles have been obtained as exact solutions of the equations describing the stationary motion on an inclined plane of a power law fluid, see e.g. Berezin and Spodareva [4], Perazzo and Gratton [5].

We show that the profile (4.80) satisfies (4.70)–(4.72) with suitable correction coefficients. To this end it is advantageous to represent $\mathbf{v}$ as given by (4.80) in terms of its depth-average $\overline{\mathbf{v}}$ and $\mathbf{v}_0$. The depth-average $\overline{\mathbf{v}}$ is obtained as

$$\overline{\mathbf{v}} = \frac{n+2}{n+1}\,\mathbf{v}_h + \frac{1}{n+1}\,\mathbf{v}_0\,.$$

This yields

$$\mathbf{v}_h = \overline{\mathbf{v}} + \frac{1}{n+1}\,(\overline{\mathbf{v}} - \mathbf{v}_0)\,,$$

which is now substituted into (4.80). Thus, we have

$$\begin{aligned} \mathbf{v} &= \overline{\mathbf{v}} + \frac{1}{n+1}\left\{1-(n+2)\left(1-\frac{\zeta}{h}\right)^{n+1}\right\}(\overline{\mathbf{v}}-\mathbf{v}_0)\,, \\ \mathbf{v}_0 &= \chi_b\overline{\mathbf{v}}\,, \quad \chi_b \equiv \frac{(n+2)\tilde{\chi}_b}{n+1+\tilde{\chi}_b} \in [0,1]\,. \end{aligned} \tag{4.81}$$

Now it can be checked that assumptions (4.70) are satisfied with

$$\begin{aligned} m_1 &= 1+\frac{1-\chi_b}{n+3}\,, \quad m_2 = 1+\frac{(1-\chi_b)^2}{2n+3}\,, \\ m_3 &= 1+\frac{2(1-\chi_b)}{n+3}+\frac{3(1-\chi_b)^2}{(n+3)(2n+3)}\,, \end{aligned} \tag{4.82}$$

and (4.71), (4.72) hold with

$$\beta = -\frac{2}{J_0h^2}\int_0^h (1+\alpha m_4)\,\mathrm{Div}\{J_0(\zeta+\alpha\, m_5 h)\overline{\mathbf{v}}\}\,d\zeta\,, \tag{4.83}$$

where

$$\begin{aligned} \alpha &\equiv 1-\chi_b\,, \quad m_4 \equiv \frac{1}{n+1}\left\{1-(n+2)\left(1-\frac{\zeta}{h}\right)^{n+1}\right\}, \\ m_5 &\equiv \frac{1}{n+1}\left\{\left(1-\frac{\zeta}{h}\right)^{n+2}-\left(1-\frac{\zeta}{h}\right)\right\}. \end{aligned}$$

From (4.82) we can see that $1 \le m_1,\ m_2,\ m_3 < 2$. When sliding of the avalanching mass is significant (implying a sliding coefficient χ_b close to 1), the Boussinesq coefficients (4.82) and (4.83) simplify considerably:

- If we can estimate that $\mathbf{v}_0 = \overline{\mathbf{v}} + O(\epsilon^\gamma)$ holds, that is, $1-\chi_b = O(\epsilon^\gamma)$, we have

$$m_1 = m_3 = 1 + O(\epsilon^\gamma)\,,$$

  implying that the parameters m_1, m_3 can be replaced by 1 in $(4.70)_{1,3}$. Moreover, $\alpha \equiv 1-\chi_b = O(\epsilon^\gamma)$ turns expression (4.83) of β into

$$\beta = -\frac{1}{J_0}\,\mathrm{Div}\,\{J_0\overline{\mathbf{v}}\} + O(\epsilon^\gamma)\,,$$

  and hence β can be replaced by (4.78) in approximations (4.71) and (4.72).

- If $\mathbf{v}_0 = \overline{\mathbf{v}} + O(\epsilon)$, that is, $1 - \chi_b = O(\epsilon)$, we obtain

$$m_2 = 1 + O(\epsilon^2)\,,$$

and therefore m_2 too can be replaced by 1 in (4.70). It is clear, then, that condition $1 - \chi_b = O(\epsilon)$ gives the same Boussinesq coefficients m_1, m_2, m_3, β as for the plug flow velocity profile.

(c) Dynamic approximations: corresponding to the motion of the avalanching mass, the stress tensor $\boldsymbol{\sigma}$ is such that

$$p = O(\epsilon)\,, \quad \mathbf{P} = O(\epsilon)\,, \quad \mathbf{p} = O(\epsilon^{\gamma})\,, \quad P^{33} = O(\epsilon^{1+\gamma})\,. \tag{4.84}$$

Motivation Assumptions (4.84) show that the pressure p and the shear and normal stresses parallel to the base, $\mathbf{P}$, are of the order of the hydrostatic pressure. The shear stresses on planes perpendicular to the base and pointing upwards, $\mathbf{p}$, are assumed the strongest, for the deformation in a typical rapid gravity driven flow is mainly in the downhill direction. The extra-stress P^{33}, orthogonal to the base and responsible for the normal stress effects, is of the smallest order, $O(\epsilon^{1+\gamma})$. All these assumptions, depicted in Fig. 4.2, express the relative importance of the components of the stress tensor in a rapid thin flow driven by gravity; they are suggested by closure relations for the stress tensor already used in avalanche modelling. In Sect. 5.2 we will give closure relations for $\boldsymbol{\sigma}$ fitting these scalings.

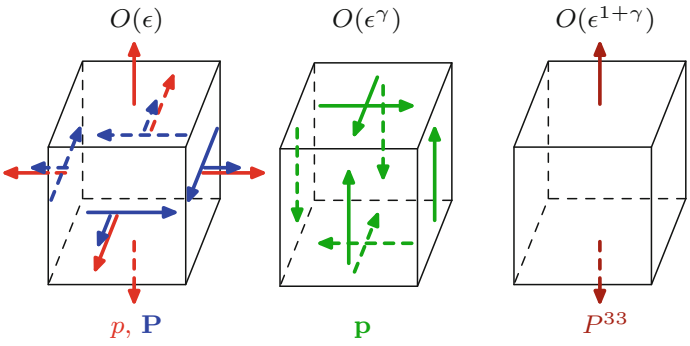

Fig. 4.2 The stress components, dashed on invisible faces, acting on a material differential element with surfaces "parallel" to ξ^1, ξ^2 and ζ. (Adapted from [1].)

Remark Relation (4.76) shows that, once we know $\overline{\mathbf{v}}$ by solving the final system of modelling equations, apart from $O(\epsilon)$ terms we know the depth-averaged velocity vector:

$$\overline{\boldsymbol{v}} = \overline{v^{\alpha}}\,\boldsymbol{\tau}_{\alpha} + O(\epsilon)\,.$$

The approximate Cartesian components $(\overline{\mathbb{v}}, \overline{v})$ of $\overline{\boldsymbol{v}}$ can be deduced from (2.96) owing the estimations $\mathbf{v} = O(1)$, $\mathrm{v} = O(\epsilon)$, $\zeta = O(\epsilon)$ and definition (2.79) of the matrix $\mathbf{B}$:

$$\overline{\mathbb{v}} = \mathbf{F}\overline{\mathbf{v}} + O(\epsilon)\,, \quad \overline{v} = \frac{1}{c}\,\mathbf{s}\cdot\mathbf{F}\overline{\mathbf{v}} + O(\epsilon)\,. \tag{4.85}$$

These relations are used when plotting the depth-averaged velocity field emerging from the numerical computations.

4.5.3 *Depth-Averaged Modelling Equations*

In this section we derive the thin-layer modelling equations corresponding to active beds in the conventional depth-averaging approach. According to the remark stated at the end of Sect. 4.5.1, the thin-layer modelling equations for rigid beds emerge from these as a special case.

We need the following asymptotic expansions which are based on the thin-layer assumptions presented in Sect. 4.5.2. Their derivation is relegated to Appendix A.1.

$$J = J_0(1 - 2\Omega\zeta) + O(\epsilon^2)\,, \tag{4.86a}$$

$$J\mathbf{v} = J_0\Big\{\mathbf{v} - 2\Omega(\zeta\mathbf{v})\Big\} + O(\epsilon^2)\,, \tag{4.86b}$$

$$J\mathbf{v}\otimes\mathbf{v} = J_0\Big\{(\mathbf{v}\otimes\mathbf{v}) - 2\Omega\ (\zeta\mathbf{v}\otimes\mathbf{v})\Big\} + O(\epsilon^2)\,, \tag{4.86c}$$

$$J(p\,\mathbf{M} - \mathbf{P}) = J_0(p\,\mathbf{M}_0 - \mathbf{P}) + O(\epsilon^2)\,, \tag{4.86d}$$

$$J\Gamma(-p\,\mathbf{M}, \mathbf{0}) = J_0 p\left\{\mathbf{F}^{-1}\frac{\partial\mathbf{F}}{\partial\xi^{\alpha}}\,\mathbf{M}_0\mathbf{e}_{\alpha} + 2\Omega\mathbf{F}^{-1}\mathbf{s}\right\} + O(\epsilon^2)\,, \tag{4.86e}$$

$$J\Gamma(\mathbf{P}, \mathbf{p}) = -J_0\left\{\mathbf{F}^{-1}\frac{\partial\mathbf{F}}{\partial\xi^{\alpha}}\,\mathbf{P}\,\mathbf{e}_{\alpha} - 2\widetilde{\mathbf{W}}\mathbf{p} + (\widetilde{\mathbf{H}}\cdot\mathbf{P})\mathbf{F}^{-1}\mathbf{s}\right\} + O(\epsilon^{1+\gamma})\,, \tag{4.86f}$$

$$\Gamma(\mathbf{v}) = -\widetilde{\mathbf{H}}\cdot(\mathbf{v}\otimes\mathbf{v}) + O(\epsilon)\,, \tag{4.86g}$$

$$J\Gamma(\mathbf{v}) = -J_0(1 - 2\Omega\zeta)\,\widetilde{\mathbf{H}}\cdot(\mathbf{v}\otimes\mathbf{v}) + J_0\zeta\widetilde{\mathbf{W}}^{T}\widetilde{\mathbf{H}}\cdot(\mathbf{v}\otimes\mathbf{v}) + O(\epsilon^2) \tag{4.86h}$$

$$
\begin{aligned}
J\Gamma(\mathbf{v},\mathrm{v}) = & -J_0\mathbf{F}^{-1}\frac{\partial \mathbf{F}}{\partial \xi^\alpha}\Big\{(\mathbf{v}\otimes\mathbf{v}) - 2\Omega(\zeta\mathbf{v}\otimes\mathbf{v})\Big\}\mathbf{e}_\alpha \\
& + J_0\mathbf{F}^{-1}\frac{\partial}{\partial \xi^\alpha}(\mathbf{F}\widetilde{\mathbf{W}}\mathbf{F}^{-1})\mathbf{F}(\zeta\mathbf{v}\otimes\mathbf{v})\mathbf{e}_\alpha + 2J_0\widetilde{\mathbf{W}}(\mathrm{v}\mathbf{v}) \\
& - J_0\Big\{\widetilde{\mathbf{H}}\cdot(\mathbf{v}\otimes\mathbf{v}) - 2\Omega\,\widetilde{\mathbf{H}}\cdot(\zeta\mathbf{v}\otimes\mathbf{v}) - \widetilde{\mathbf{W}}^T\widetilde{\mathbf{H}}\cdot(\zeta\mathbf{v}\otimes\mathbf{v})\Big\}\mathbf{F}^{-1}\mathbf{s} \\
& - J_0\Big(\widetilde{\mathbf{H}}\cdot(\zeta\mathbf{v}\otimes\mathbf{v})\Big)\widetilde{\mathbf{W}}\mathbf{F}^{-1}\mathbf{s} + O(\epsilon^2)\,,
\end{aligned}
\tag{4.86i}
$$

$$
J\mathbf{b} = -J_0c\,(1-2\Omega\zeta)\,\mathbf{F}^{-1}\mathbf{s} - J_0c\,\zeta\,\widetilde{\mathbf{W}}\mathbf{F}^{-1}\mathbf{s} + O(\epsilon^2)\,, \tag{4.86j}
$$

$$
J\mathbf{w} = J_0\Big\{\mathbf{u}_{\mathcal{S}} - 2\Omega\zeta\mathbf{F}^{-1}\mathbf{v}_{\mathcal{S}}\Big\} + O(\epsilon^2)\,, \tag{4.86k}
$$

$$
J\mathbf{v}\otimes\mathbf{w} = J_0\Big\{\mathbf{v}\otimes\mathbf{u}_{\mathcal{S}} - 2\Omega(\zeta\mathbf{v})\otimes\mathbf{F}^{-1}\mathbf{v}_{\mathcal{S}}\Big\} + O(\epsilon^2)\,, \tag{4.86l}
$$

$$
\begin{aligned}
J\left\{(\mathrm{Grad}\,\mathbf{w})\mathbf{v} + \mathrm{v}\frac{\partial \mathbf{w}}{\partial \zeta}\right\} = & J_0\Big\{(\mathrm{Grad}\,\mathbf{u}_{\mathcal{S}})\mathbf{v} \\
& - 2\Omega\Big(\mathrm{Grad}\,(\mathbf{F}^{-1}\mathbf{v}_{\mathcal{S}})\Big)(\zeta\mathbf{v})\Big\} + O(\epsilon^2)\,.
\end{aligned}
\tag{4.86m}
$$

First we refer to the normal linear momentum balance equation (4.45) which, combined with the boundary condition $(4.41)_2$, will give the pressure p up to $O(\epsilon^{1+\gamma})$ terms. The contribution of each term in (4.45) is indicated below,

$$
\begin{aligned}
& \underbrace{\frac{\partial}{\partial t}\{J\mathrm{v}\}}_{O(\epsilon)} + \underbrace{\mathrm{Div}\big\{J\left[\mathrm{v}(\mathbf{v}-\mathbf{w})-\mathbf{p}\right]\big\}}_{O(\epsilon^\gamma)} + \underbrace{\frac{\partial}{\partial \zeta}\left\{J\left[\mathrm{v}(\mathrm{v}-\mathcal{U})-P^{33}\right]\right\}}_{O(\epsilon^\gamma)} \\
& \qquad + \underbrace{J\frac{\partial p}{\partial \zeta}}_{O(1)} + \underbrace{J\Gamma(\mathbf{P})}_{O(\epsilon)} = \underbrace{J\mathrm{b}}_{O(1)} + \underbrace{J\Gamma(\mathbf{v})}_{O(1)} - \underbrace{J\,\mathrm{Grad}\,\mathcal{U}\cdot\mathbf{v}}_{O(\epsilon)}\,.
\end{aligned}
$$

This shows that the normal linear momentum balance equation (4.45) turns into

$$
\frac{\partial p}{\partial \zeta} = b + \Gamma(\mathbf{v}) + O(\epsilon^\gamma)\,.
$$

With $b=-c$, see $(4.36)_2$, and $\Gamma(\mathbf{v})$ as given by (4.86g), this implies

$$
\frac{\partial p}{\partial \zeta} = -c - \widetilde{\mathbf{H}}\cdot(\mathbf{v}\otimes\mathbf{v}) + O(\epsilon^\gamma)\,. \tag{4.87}
$$

The boundary condition $(4.41)_2$ appears as

$$
p = -\mathbf{p}\cdot\mathrm{Grad}\,h + P^{33} = O(\epsilon^{1+\gamma}) \quad \text{at} \quad \zeta = h\,,
$$

so that, integration of (4.87) from ζ to h yields

$$p = c(h-\zeta) + \widetilde{\mathbf{H}} \cdot \int_{\zeta}^{h} \mathbf{v} \otimes \mathbf{v}\, \mathrm{d}\zeta' + O(\epsilon^{1+\gamma})\,. \tag{4.88}$$

Formula (4.88) shows that the pressure p consists of the hydrostatic pressure, $c(h-\zeta)$, and a kinematic/curvature contribution, indicating the influence of the topographic surface on the flow pressure.

We will need the pressure p evaluated on the basal surface and the depth-averaged pressure $\overline{p}$. Using the Boussinesq approximation $(4.70)_2$, we deduce

$$\begin{aligned} p\big|_{\zeta=0} &= ch + \widetilde{\mathbf{H}} \cdot \int_{0}^{h} \mathbf{v} \otimes \mathbf{v}\, \mathrm{d}\zeta + O(\epsilon^{1+\gamma}) \\ &= ch + \widetilde{\mathbf{H}} \cdot (m_2 h\, \overline{\mathbf{v}} \otimes \overline{\mathbf{v}}) + O(\epsilon^{1+\gamma})\,, \end{aligned}$$

so that, with the notation

$$a \equiv \widetilde{\mathbf{H}} \cdot (\overline{\mathbf{v}} \otimes \overline{\mathbf{v}}) = \widetilde{\mathbf{H}}\overline{\mathbf{v}} \cdot \overline{\mathbf{v}}\,, \tag{4.89}$$

the pressure at the basal surface reads as

$$p\Big|_{\zeta=0} = h(c + m_2 a) + O(\epsilon^{1+\gamma})\,. \tag{4.90}$$

Then, to obtain the depth-averaged pressure $\overline{p}$ we compute the integral of p given in (4.88) from 0 to h by interchanging the order of integration and using the Boussinesq approximation $(4.70)_3$:

$$\begin{aligned} \int_0^h p\, d\zeta &= \tfrac{1}{2}ch^2 + \widetilde{\mathbf{H}} \cdot \int_0^h \left(\int_{\zeta}^{h} \mathbf{v} \otimes \mathbf{v}\, d\zeta' \right) d\zeta + O(\epsilon^{2+\gamma}) \\ &= \tfrac{1}{2}ch^2 + \widetilde{\mathbf{H}} \cdot \int_0^h \left(\int_0^{\zeta'} \mathbf{v} \otimes \mathbf{v}\, d\zeta \right) d\zeta' + O(\epsilon^{2+\gamma}) \\ &= \tfrac{1}{2}ch^2 + \widetilde{\mathbf{H}} \cdot \int_0^h \zeta' \mathbf{v} \otimes \mathbf{v}\, d\zeta' + O(\epsilon^{2+\gamma}) \\ &= \tfrac{1}{2}ch^2 + \widetilde{\mathbf{H}} \cdot (\tfrac{1}{2}m_3 h^2\, \overline{\mathbf{v}} \otimes \overline{\mathbf{v}}) + O(\epsilon^{2+\gamma})\,. \end{aligned}$$

With a defined in (4.89) this implies

$$\overline{p} = \tfrac{1}{2}h(c + m_3 a) + O(\epsilon^{1+\gamma})\,. \tag{4.91}$$

Now, the asymptotic expansions (4.86) are inserted into the depth-integrated mass and tangential momentum balance equations (4.65), (4.66). Straightforward computations using the Boussinesq approximations (4.70) (see Appendix A.2) give the thin-layer or depth-averaged modelling equations which we were looking for.

Depth-averaged modelling equations of a thin flow down arbitrary topography (conventional route)
Under the thin-layer approximations the depth-integrated mass balance equation (4.65) *emerges as*

$$\begin{aligned}&\frac{\partial}{\partial t}\Big\{J_0 h(1-\Omega h)\Big\}\\ &+\mathrm{Div}\Big\{J_0 h\Big[(1-m_1\Omega h)\,\overline{\mathbf{v}} - \mathbf{u}_{\mathcal{S}} + \Omega h \mathbf{F}^{-1}\mathbf{v}_{\mathcal{S}}\Big]\Big\}\\ &\qquad = -J_0\frac{\rho_b}{\rho_0}\mathcal{U} + O(\epsilon^{2+\gamma})\,,\end{aligned} \tag{4.92}$$

and the depth-integrated tangential linear momentum balance equation (4.66) *becomes*

$$\begin{aligned}&\frac{\partial}{\partial t}\Big\{J_0 h(1-m_1\Omega h)\mathbf{F}\,\overline{\mathbf{v}}\Big\}\\ &\qquad+\mathrm{Div}\Big\{J_0 h\mathbf{F}\Big[(m_2 - m_3\Omega h)\,\overline{\mathbf{v}}\otimes\overline{\mathbf{v}} + \overline{p}\,\mathbf{M}_0 - \overline{\mathbf{P}}\\ &\qquad\qquad -\overline{\mathbf{v}}\otimes\mathbf{u}_{\mathcal{S}} + m_1\Omega h\,\overline{\mathbf{v}}\otimes\mathbf{F}^{-1}\mathbf{v}_{\mathcal{S}}\Big]\Big\}\\ &= -J_0 h\left(c + a m_2 - \tfrac{1}{2}m_3\tilde{a}h - \widetilde{\mathbf{H}}\cdot\overline{\mathbf{P}} + \mathrm{Grad}\,\mathcal{U}\cdot\overline{\mathbf{v}}\right)\mathbf{s}\\ &\quad+2J_0 h\,\mathbf{F}\widetilde{\mathbf{W}}\left(\tfrac{1}{2}\beta h\overline{\mathbf{v}} - \overline{\mathbf{p}}\right) + J_0 h\left(1 - 2\frac{\rho_b}{\rho_0}\right)\mathcal{U}\,\mathbf{F}\widetilde{\mathbf{W}}\overline{\mathbf{v}}\\ &-J_0 h\,\overline{p}\,\mathbf{F}\widetilde{\mathbf{W}}\mathbf{F}^{-1}\mathbf{s} + \tfrac{1}{2}J_0 m_3 h^2\frac{\partial}{\partial\xi^\alpha}(\mathbf{F}\widetilde{\mathbf{W}}\mathbf{F}^{-1})\mathbf{F}(\overline{\mathbf{v}}\otimes\overline{\mathbf{v}})\mathbf{e}_\alpha\\ &\qquad-J_0\frac{\rho_b}{\rho_0}\mathcal{U}\mathbf{F}\,\mathbf{v}\big|_{\zeta=0} - J_0\mathbf{F}\mathbf{p}\big|_{\zeta=0} + O(\epsilon^{2+\gamma})\,,\end{aligned} \tag{4.93}$$

where the mean pressure $\overline{p}$ *is given by* (4.91), *and*

$$a \equiv \widetilde{\mathbf{H}}\,\overline{\mathbf{v}}\cdot\overline{\mathbf{v}}\,,\quad \tilde{a} \equiv \widetilde{\mathbf{H}}\,\overline{\mathbf{v}}\cdot\widetilde{\mathbf{W}}\,\overline{\mathbf{v}} = \widetilde{\mathbf{H}}\,\overline{\mathbf{v}}\cdot\mathbf{M}_0\widetilde{\mathbf{H}}\,\overline{\mathbf{v}} \geq 0\,.$$

The highlighted term in (4.93) will be referred to in Sect. 4.6, when comparing (4.93) with its counterpart (4.111) in the non-conventional route. It is worth mentioning that equation (4.93) is equivalent with (A.3), so that (A.3) can be equally used instead of (4.93). The form (4.93) of the depth-averaged tangential linear momentum balance equation is more compact than (A.3), and serves to compare the depth-averaged modelling equations in the conventional route with those which will be obtained in the non-conventional route.

The aim is to have (2.71), (4.92) and (4.93) as a set of equations which stand for the determination of the fluid depth, h, depth-averaged velocity, $\overline{\mathbf{v}}$, and bed elevation, b. To this end, in Sects. 5.1–5.3 the bed friction $\mathbf{f}_b$, the mean stresses $\overline{\mathbf{P}}$, $\overline{\mathbf{p}}$, and the erosion/deposition rate $\mathcal{U}$ will be given in terms of the basic unknown fields h, $\overline{\mathbf{v}}$ and b. The velocity $\mathbf{v}$ evaluated at $\zeta = 0$ must be also related to these fields. We suppose

$$\mathbf{v}\big|_{\zeta=0} = \chi_b\,\overline{\mathbf{v}} + O(\epsilon^{1+\gamma})\,, \quad \chi_b \in (0,1]\,. \tag{4.94}$$

The sliding coefficient χ_b may depend e.g. on the curvature of the surface, but it is difficult to guess such a dependence, so that χ_b can be viewed as a constant. For a power law velocity profile χ_b has been determined in (4.81).

In the special case of rigid topographies, equations (4.92) and (4.93) have been deduced by Luca et al. [6], and classified in terms of the degrees of scaling of the extra-stress components. This classification will be now presented for the general case of active beds, captured in equations (4.92) and (4.93) derived in this book. The exposure follows closely that from [6].

4.5.4 A Hierarchy of Depth-Averaged Modelling Equations

Gravity driven shallow flows occur in various forms, and the magnitude of the stresses which develop inside the flowing masses generally differ from one event to another. Depending on the relative weights of the stress components, some of these components may be neglected in a thin-layer model. This may yield a model of such a simplified rheological complexity, that the constitutive properties present in the original 3D model are partly or completely lost. The question then arises whether thin-layer models can be classified according to the order of magnitude of the stress components in the moving material.

We answer below this question, by choosing several dynamic assumptions replacing (4.84). These are given in Table 4.1, together with the non-negligible extra-stress components, present in the corresponding final modelling equation (4.93). We distinguish four main classes of thin-layer models:

Class (i) A first class corresponds to the case for which

all the extra-stress components in the avalanche equations are negligible,

Table 4.1 Classification of depth-averaged models in terms of the scalings of the extra-stress components

	Extra-stresses $\mathbf{P}$	Shear stresses $\mathbf{p}$	Normal extra-stress P^{33}	Non-negligible stress components in (4.93)
c)	$O(\epsilon)$	$O(\epsilon^{\gamma})$	$O(\epsilon^{1+\gamma})$	$\overline{\mathbf{P}}, \overline{\mathbf{p}}, \mathbf{p}\big\vert_{\zeta=0}$
c^{i})	$O(\epsilon^{1+\gamma})$	$O(\epsilon^{\gamma})$	$O(\epsilon^{1+\gamma})$	$\overline{\mathbf{p}}, \mathbf{p}\big\vert_{\zeta=0}$
c^{ii})	$O(\epsilon^{1+\gamma})$	$O(\epsilon)$	$O(\epsilon^{1+\gamma})$	$\overline{\mathbf{p}}, \mathbf{p}\big\vert_{\zeta=0}$
c^{iii})	$O(\epsilon^{1+\gamma})$	$O(\epsilon^{1+\gamma})$	$O(\epsilon^{1+\gamma})$	$\mathbf{p}\big\vert_{\zeta=0}$
c^{iv})	$O(\epsilon^{1+\gamma})$	$O(\epsilon^{2+\gamma})$	$O(\epsilon^{1+\gamma})$	–
c^{v})	$O(\epsilon)$	$O(\epsilon^{1+\gamma})$	$O(\epsilon^{1+\gamma})$	$\overline{\mathbf{P}}, \mathbf{p}\big\vert_{\zeta=0}$

see c^{iv}). That is, resistance to shearing and sliding may occur, but are so small that only the pressure due to incompressibility survives. Irrespective of the original constitutive model, the material behaves as if it were an incompressible inviscid fluid. There is no basal shear stress, and material properties different from those of an incompressible ideal fluid can be indirectly captured only in the Boussinesq coefficients, which reflect the non-uniformity of the velocity components along the depth. Pudasaini and Hutter [3] pointed out that this model is physically reasonable in chute flows far from the deposition zone.

Class (ii) A second class is that in which

$$\textit{only the basal shear stress } \mathbf{p}\big\vert_{\zeta=0} \textit{ enters the governing equations,}$$

see c^{iii}). That is, slightly larger resistance to shearing manifests in the thin-layer model only as basal shear stresses. When there is basal sliding, the frictional properties at the contact surface are important. In this case the rheological properties of the avalanching mass enter the model via the Boussinesq coefficients and the bed friction law. This complexity of depth-averaged models has been very popular in the past. The snow avalanche models by Voellmy [7], Perla et al. [8], Salm [9], early Russian scientists (see Eglit [10], Harbitz [11], Pudasaini and Hutter [3]) are of this type. Models which belong to this class have been used in the computational avalanche literature by Gray et al. [12] and Bouchut and collaborators [13, 14].

Class (iii) The third class is that in which

$$\mathbf{p}\big\vert_{\zeta=0} \textit{ and } \overline{\mathbf{p}} \textit{ are significant, however } \overline{\mathbf{P}} \textit{ can be neglected,}$$

see c^{i}), c^{ii}). Here, the rheological properties of the fluid play a more significant role. They manifest through the basal shear stresses and the depth-averaged values of the shear stresses on planes parallel to the basal surface. This may be the case for a dense slurry with particle diameters smaller than the roughness scales at the basal surface. Dense clay suspensions in water and creeping flow of a non-linearly viscous fluid are other examples of flows which belong to this class.

Class (iv) The fourth class is that in which

$$\overline{\mathbf{P}} \textit{ is non-negligible,}$$

see *c*) and c^{v}). It comprises the most complex thin-layer models. Here, the depth-integrated normal and shear stresses acting on planes perpendicular to the basal surface are large, and generally the interaction with the basal surface via the sliding law is also important. Such cases prevail when stress anisotropies or normal stress differences are important, or when the base-parallel distortions are large. The former arise e.g. in all earth pressure models in which the normal stresses parallel to the basal surface are expressed in terms of the normal stress perpendicular to it, with an earth pressure coefficient that is either invariant against rotations perpendicular to the basal surface (Iverson [15], McDougall and Hungr [16, 17]), or direction dependent according to the sign of the stretching (Savage-Hutter, see Luca et al. [6, 18] or the forthcoming Sect. 5.2).

The hierarchical classification of the thin-layer model equations (4.92) and (4.93) shows that differences due to rheological properties are largely eliminated by scalings of the stresses versus the aspect ratio of the shallowness approximation. The form of these equations depends also on the order of magnitude of the basal surface curvature. This will be made clear in the next section.

4.5.5 *Depth-Averaged Modelling Equations for Flows On Slightly Curved Topographies*

The depth-averaged modelling equations (4.92) and (4.93) simplify significantly when the topographic surface is only slightly bent.

Depth-averaged modelling equations of a thin flow down a slightly curved surface (conventional route)
Under the assumption of small curvature of the topographic surface,

$$\mathcal{H} = O(\epsilon^{\gamma'}), \quad \gamma' \in (0,1), \tag{4.95}$$

the mean pressure (4.91) *turns into*

$$\overline{p} = \tfrac{1}{2} c\, h + O(\epsilon^{1+\hat{\gamma}}), \quad \hat{\gamma} \equiv min\{\gamma, \hat{\gamma}\}. \tag{4.96}$$

The depth-averaged mass balance equation (4.92) *simplifies to*

$$\frac{\partial}{\partial t}\Big\{J_0 h\Big\} + \mathrm{Div}\Big\{J_0 h(\overline{\mathbf{v}} - \mathbf{u}_{\mathcal{S}})\Big\} = -J_0 \frac{\rho_b}{\rho_0}\mathcal{U} + O(\epsilon^{2+\hat{\gamma}}), \tag{4.97}$$

and the depth-averaged tangential linear momentum balance equation (4.93) *takes the simpler form*

$$\begin{aligned}\frac{\partial}{\partial t}\Big\{J_0 h\mathbf{F}\,\overline{\mathbf{v}}\Big\} + \mathrm{Div}\Big\{J_0 h\mathbf{F}\Big[m_2\,\overline{\mathbf{v}}\otimes\overline{\mathbf{v}} + \overline{p}\,\mathbf{M}_0 - \overline{\mathbf{P}} - \overline{\mathbf{v}}\otimes\mathbf{u}_{\mathcal{S}}\Big]\Big\} \\ = -\,2J_0 h\,\mathbf{F}\widetilde{\mathbf{W}}\,\overline{\mathbf{p}} - J_0 h\,(c + am_2 + \mathrm{Grad}\,\mathcal{U}\cdot\overline{\mathbf{v}})\,\mathbf{s} \\ - J_0\frac{\rho_b}{\rho_0}\,\mathcal{U}\mathbf{F}\mathbf{v}\big|_{\zeta=0} - J_0\mathbf{F}\mathbf{p}\big|_{\zeta=0} + O(\epsilon^{2+\hat{\gamma}})\,.\end{aligned} \tag{4.98}$$

The red term in (4.98) stems from the red one in Eq. (4.93) and will be referred to in Sect. 4.6. The only equation in which the curvature of the topography manifests is (4.98). The presence of the scalar a and of the Weingarten matrix $\widetilde{\mathbf{W}}$ in (4.98) shows this. Equations (4.97) and (4.98) have been noticed by Luca et al. [19].

Remark Assume that the parameterization of the basal surface satisfies the condition $\mathbf{u}_{\mathcal{S}} = \mathbf{0}$, see Sect. 2.4, and that the constitutive behavior of the flowing material satisfies the scalings stated in item c^{v}) of Table 4.1. Thereby Eqs. (4.97) and (4.98) reduce to those obtained by Tai et al. [20], which we reproduce below as stated in terms of the dimensionless quantities from this chapter.

Model by Tai et al. [20]
For a parameterization of the basal surface satisfying the condition

$$\mathbf{u}_{\mathcal{S}} = \mathbf{0}\,,$$

and for depth-averaged shear stresses $\overline{\mathbf{p}}$ negligibly small,

$$\overline{\mathbf{p}} = O(\epsilon^{1+\gamma})\,,$$

the equations describing the material flow over a slightly curved topographic surface read as

$$\frac{\partial}{\partial t}\Big\{J_0 h\Big\} + \mathrm{Div}\Big\{J_0 h\,\overline{\mathbf{v}}\Big\} = -J_0\frac{\rho_b}{\rho_0}\,\mathcal{U}\,, \tag{4.99}$$

$$\begin{aligned}\frac{\partial}{\partial t}\Big\{J_0 h\mathbf{F}\,\overline{\mathbf{v}}\Big\} + \mathrm{Div}\Big\{J_0 h\mathbf{F}\Big[m_2\,\overline{\mathbf{v}}\otimes\overline{\mathbf{v}} + \overline{p}\,\mathbf{M}_0 - \overline{\mathbf{P}}\Big]\Big\} \\ = -\,J_0 h\,(c + am_2 + \mathrm{Grad}\,\mathcal{U}\cdot\overline{\mathbf{v}})\,\mathbf{s} - J_0\frac{\rho_b}{\rho_0}\,\mathcal{U}\mathbf{F}\mathbf{v}\big|_{\zeta=0} - J_0\mathbf{F}\mathbf{p}\big|_{\zeta=0}\,,\end{aligned} \tag{4.100}$$

with the negligible terms omitted and $\overline{p}$ given by (4.96).

The modelling equations (4.99) and (4.100) have been obtained by Tai et al. [20] by starting from the mass and linear momentum balance balance equations as expressed in the topography-fitted coordinates *following the non-conventional route* (see the next section for the reason of doing so). As such their modelling equations are expressed in terms of both $\overline{\mathbf{v}}$ and $\overline{\mathbb{v}}_\tau$, where $\mathbb{v}_\tau$ collects the x_1, x_2 Cartesian components of the tangential velocity vector $\boldsymbol{v}_\tau$, see (2.97). Nevertheless, for small curvature assumption $\mathcal{H} = O(\epsilon^{\gamma'})$ (as is the case in [20]), from (2.97) we deduce

$$\mathbb{v}_\tau = \mathbf{B}\mathbf{v} = \mathbf{F}(\mathbf{I} - \zeta\widetilde{\mathbf{W}})\mathbf{v} = \mathbf{F}\mathbf{v} + O(\epsilon^{1+\gamma'}),$$

which implies

$$\overline{\mathbb{v}}_\tau = \mathbf{F}\overline{\mathbf{v}} + O(\epsilon^{1+\gamma'}), \quad \mathbf{F}\mathbf{v}\big|_{\zeta=0} = \mathbb{v}_\tau\big|_{\zeta=0}. \tag{4.101}$$

Therefore, (4.100) can be written as

$$\begin{aligned} &\frac{\partial}{\partial t}\Big\{J_0 h\overline{\mathbb{v}}_\tau\Big\} + \mathrm{Div}\Big\{J_0 h\Big[m_2\,\overline{\mathbb{v}}_\tau \otimes \overline{\mathbf{v}} + \mathbf{F}\left(\overline{p}\,\mathbf{M}_0 - \overline{\mathbf{P}}\right)\Big]\Big\} \\ &\quad = -J_0 h\big(c + am_2 + \mathrm{grad}\,\mathcal{U}\cdot\overline{\mathbb{v}}_\tau\big)\mathbf{s} - J_0\frac{\rho_b}{\rho_0}\mathcal{U}\mathbb{v}_\tau\big|_{\zeta=0} - J_0\mathbf{F}\mathbf{p}\big|_{\zeta=0}. \end{aligned} \tag{4.102}$$

Expression (4.102) of (4.100) is handled by Tai et al. [20] in the numerical computations.

In the next section we reconsider the idea developed in [20], yet in the most general case, that is, without restricting the curvature of the basal surface to satisfy (4.95), without specifying constitutive relations, other than the dynamic thin-layer approximations (4.84), and with arbitrary parameterization of the basal surface. We will see that, for the general case, the non-conventional route followed in [20] yields a system of modelling equations which is not the same as the system consisting of (4.92) and (4.93), even if the curvature of the topographic surface is small.

4.6 Depth-Averaged Modelling Equations in the Non-conventional Route

In a series of papers by Tai et al. e.g. [21] (1D case), [20] (3D case), a depth-averaged model for a shallow debris flow down a topographic bed with erosion/deposition has been derived by

- assuming small curvature of the basal surface,
- depth-averaging the *horizontal* linear momentum equation in the hybrid form (4.50),
- considering Coulomb type constitutive laws for the averaged stress tensor and basal shear friction, matching the thin-layer approximations of item c^{v}) in Table 4.1,

- taking a mesh velocity $\boldsymbol{w}$ having the property $\boldsymbol{w}|_{\zeta=0} = \mathcal{U}\boldsymbol{n}_b$ (equivalently, $\mathbf{u}_{\mathcal{S}} = \mathbf{0}$), see (2.120).

The idea, inspired by the UC approach (see Sect. 2.4), was

- to obtain a conservative system of modelling equations (avoiding the Christoffel symbols being a useful step toward this aim), and
- to use a body-fitted mesh.

Tai et al. [20] indeed obtained a conservative system of equations. Nevertheless, it is nothing else than the system (4.96), (4.99) and (4.100), with

- $\overline{\mathbf{P}}$, $\overline{\mathbf{p}}$ and $\mathbf{f}_b$ given by Coulomb type laws, see Sects. 5.1 and 5.2, and
- the erosion/deposition rate $\mathcal{U}$ as assumed in the forthcoming Sect. 5.3.

That is, the approach in Sect. 4.3, followed as in papers by Luca et al. e.g. [1], and the non-conventional approach followed by Tai et al. [20], give the same result for the special case investigated in [20]. Of course, the question then arises—what happens if another case than the special case considered in [20] is treated by using the non-conventional approach? More exactly,

- **Q1** Which are the depth-averaged model equations, analogous to (4.92), (4.93), and obtained following the non-conventional route?
- **Q2** Is there any difference between the model equations (4.92) and (4.93) obtained in the conventional route and their analogous model equations obtained in the non-conventional route?

In this section we answer questions **Q1** and **Q2**. To this aim we consider the 3D dimensionless modelling equations in the non-conventional route, see (4.48)–(4.55), and derive depth-averaged model equations for thin flows satisfying the thin-layer approximations from Sect. 4.5.2.

Depth-averaging the mass balance equation (4.48) The mass balance equation (4.48) is treated in exactly the same way as in the conventional route. Thus, the normal velocity v is obtained as (4.63) or (4.64), and the depth-integrated mass balance equation is (4.65).

Obtaining the pressure p Now, similarly to the conventional route, we may try to use the vertical linear momentum balance equation (4.51), in conjunction with the thin-layer approximations, to obtain the pressure p. However, recalling that the thin-layer assumptions are expressed in terms of the contravariant components of the velocity and stress tensor, and that

$$v = \frac{1}{c}(\mathbb{v}\cdot\mathbf{s}+\mathrm{v})\,,\quad \mathbb{t} = \frac{1}{c}\left(\mathbb{S}^T\mathbf{s}+\mathbf{t}\right)\,,\qquad \sigma = \frac{1}{c}\left(\mathbb{s}\cdot\mathbf{s}+T^{33}\right)\,, \tag{4.103}$$

see (2.96) and (2.98), it is merely the combination

$$c\,(4.51) - (4.50)\cdot\mathbf{s}\,, \tag{4.104}$$

and not (4.51), which is used when applying the thin-layer approximations. This is so, because in (4.104) the time derivative of the integral containing the horizontal velocity $\mathbb{v}$ cancels out. Performing the operations indicated in (4.104) by using (2.51) and

$$\frac{\partial c}{\partial t} = -c\mathbf{F}^{-1}\mathbf{s}\cdot(\widetilde{\mathbf{H}}\mathbf{u}_{\mathcal{S}} + \mathrm{Grad}\,\mathcal{U})\,, \quad \frac{\partial \mathbf{s}}{\partial t} = \mathbf{F}\widetilde{\mathbf{W}}\mathbf{u}_{\mathcal{S}} + \mathbf{F}\mathbf{M}_0\mathrm{Grad}\,\mathcal{U}\,, \tag{4.105}$$

see Exercise 2.8, one obtains nothing else than the normal linear momentum balance equation (4.45). We therefore take over the result from the conventional route, that is, the pressure p given by (4.88), the pressure on the basal surface, see (4.90), and the mean pressure $\overline{p}$, see (4.91).

Depth-averaging the hybrid form of the horizontal linear momentum balance equation (4.50) We integrate equation (4.50) from 0 to h by using the Leibniz rules (4.56) and the boundary conditions (4.52), (4.54) and $(4.55)_1$. We easily obtain

$$\begin{aligned}\frac{\partial}{\partial t}\int_0^h J\mathbb{v}\,d\zeta + \mathrm{Div}\int_0^h J\,\{\mathbb{v}\otimes(\mathbf{v}-\mathbf{w}) - \mathbb{S}\}\,d\zeta \\ = -J_0\frac{\rho_b}{\rho_0}\mathcal{U}\mathbb{v}\big|_{\zeta=0} - J_0\,\mathbb{s}\big|_{\zeta=0}\,,\end{aligned} \tag{4.106}$$

where $\mathbb{s}\big|_{\zeta=0}$ is given by the dynamic boundary condition (4.53). Clearly, the depth-integrated horizontal linear momentum balance equation (4.106) is more appealing than the depth-integrated tangential linear momentum balance (4.66) from the conventional approach. However, the occurrence of the normal component v of the velocity in the expression of $\mathbb{v}$,

$$\mathbb{v} = \mathbf{B}\mathbf{v} - \mathrm{v}\mathbf{s}\,,$$

see $(2.96)_1$, requires (4.106) to be transformed so that $\partial J\mathrm{v}/\partial t$ is eliminated. To this end we first integrate along the depth the vertical linear momentum balance equation (4.51). By using the Leibniz rules (4.56) and the boundary conditions (4.52), (4.54) and $(4.55)_2$, we get

$$\begin{aligned}\frac{\partial}{\partial t}\int_0^h J\,v\,d\zeta + \mathrm{Div}\int_0^h J\,\{v(\mathbf{v}-\mathbf{w}) - \mathbb{t}\}\,d\zeta \\ = -J_0\frac{\rho_b}{\rho_0}\mathcal{U}v\,\big|_{\zeta=0} - J_0\,\sigma\big|_{\zeta=0} - \int_0^h J\,d\zeta\,.\end{aligned} \tag{4.107}$$

Then, we consider the combination

$$c\,(4.106) + (4.107)\,\mathbf{s}\,, \tag{4.108}$$

by which the time derivative of the integral containing the normal velocity v cancels out (have a look at (A.8) and (A.9) in order to see how this is obtained). After a long routine calculus exposed in Appendix (A.3) we deduce that,

Combination (4.108) involving the depth-integrated hybrid forms of the horizontal and vertical linear momentum balance equations emerges as

$$\begin{aligned}
&\frac{\partial}{\partial t}\int_0^h J\mathbf{B}\mathbf{v}\,d\zeta + \mathrm{Div}\int_0^h J\mathbf{B}\left(\mathbf{v}\otimes(\mathbf{v}-\mathbf{w}) + p\mathbf{M}-\mathbf{P}\right)d\zeta \\
&\qquad = -\left\{\left(\int_0^h J\mathbf{B}\left(\mathbf{v}\otimes\mathbf{v} + p\mathbf{M}-\mathbf{P}\right)d\zeta\right)\cdot\mathbf{F}^{-T}\widetilde{\mathbf{H}}\right\}\mathbf{s} \\
&\qquad + \mathbf{F}\widetilde{\mathbf{W}}\int_0^h J\,(\mathrm{v}\mathbf{v}-\mathbf{p})\,d\zeta - \left\{\left(\int_0^h J\mathbf{v}\,d\zeta\right)\cdot\mathrm{Grad}\,\mathcal{U}\right\}\mathbf{s} \\
&\qquad - c\left(\int_0^h J\,d\zeta\right)\mathbf{s} + \mathbf{F}\left\{\int_0^h J\mathrm{v}(\mathbf{I}-\zeta\widetilde{\mathbf{W}})^{-1}\,d\zeta\right\}\mathbf{M}_0\mathrm{Grad}\,\mathcal{U} \\
&\qquad\qquad - J_0\frac{\rho_b}{\rho_0}\mathcal{U}\mathbf{F}\mathbf{v}\big|_{\zeta=0} - J_0\mathbf{F}\mathbf{p}\big|_{\zeta=0}\,. \qquad (4.109)
\end{aligned}$$

We refer to (4.109) as the depth-integrated hybrid linear momentum balance equation.

Equation (4.109) plays the same role as that of the depth-integrated tangential linear momentum balance equation (4.66) from the conventional route. That is, it functions, using the thin-layer approximations, as an equation for the depth-averaged velocity $\overline{\mathbf{v}}$. In passing, note that the "conserved" quantity in (4.109) contains the horizontal Cartesian components, $\mathbb{v}_\tau$, of the tangential velocity. Indeed, $\mathbf{B}\mathbf{v} = \mathbb{v}_\tau$ (see $(2.97)_1$), so that

$$\int_0^h J\mathbf{B}\mathbf{v}\,d\zeta = \int_0^h J\mathbb{v}_\tau\,d\zeta\,.$$

Remark One can prove relation (4.109) in another way, see Appendix A.4: one multiplies the tangential linear momentum balance equation (4.44) by $\mathbf{B}$, and then one depth-averages the emerging equation. Since $\mathbf{B}\equiv\mathbf{F}(\mathbf{I}-\zeta\widetilde{\mathbf{W}})$ depends on ζ, this clearly shows that (4.109) is not equivalent to the depth-integrated tangential linear momentum balance equation (4.66).

Final modelling equations in the non-conventional route Next, the depth-integrated hybrid linear momentum balance equation (4.109) is exploited under the thin-layer assumptions from Sect. 4.5.2. This is done in Appendix A.5. The results are shown below, and with this we have answered question **Q1**.

Answering Q1
Depth-averaged modelling equations of a thin flow down arbitrary topography (non-conventional route)
Under the thin-layer approximations the depth-integrated mass balance equation (4.65) *emerges as*

$$\begin{aligned}&\frac{\partial}{\partial t}\Big\{J_0 h(1-\Omega h)\Big\}\\&+\mathrm{Div}\Big\{J_0 h\Big[(1-m_1\Omega h)\,\overline{\mathbf{v}}-\mathbf{u}_{\mathcal{S}}+\Omega h\mathbf{F}^{-1}\mathbf{v}_{\mathcal{S}}\Big]\Big\}\\&\qquad=-J_0\frac{\rho_b}{\rho_0}\mathcal{U}+O(\epsilon^{2+\gamma})\,,\end{aligned}\tag{4.110}$$

and the depth-integrated hybrid linear momentum balance equation (4.109) *turns into*

$$\begin{aligned}&\frac{\partial}{\partial t}\left\{J_0 h\mathbf{F}\left[(1-m_1\Omega h)\overline{\mathbf{v}}-\tfrac{1}{2}m_1 h\widetilde{\mathbf{W}}\,\overline{\mathbf{v}}\right]\right\}\\&+\mathrm{Div}\left\{J_0 h\mathbf{F}\Big[(m_2-m_3\Omega h)\overline{\mathbf{v}}\otimes\overline{\mathbf{v}}+\overline{p}\mathbf{M}_0-\overline{\mathbf{P}}\right.\\&\left.-(1-m_1\Omega h)\overline{\mathbf{v}}\otimes\mathbf{u}_{\mathcal{S}}-\tfrac{1}{2}h\widetilde{\mathbf{W}}\,\overline{\mathbf{v}}\otimes(m_3\overline{\mathbf{v}}-m_1\mathbf{u}_{\mathcal{S}})\Big]\right\}\\&=-J_0 h\left\{c+m_2 a-\tfrac{1}{2}m_3\tilde{a}h-\widetilde{\mathbf{H}}\cdot\overline{\mathbf{P}}+\mathrm{Grad}\,\mathcal{U}\cdot\overline{\mathbf{v}}\right\}\mathbf{s}\\&+J_0 h\mathbf{F}\widetilde{\mathbf{W}}\left(\tfrac{1}{2}\beta h\overline{\mathbf{v}}-\overline{\mathbf{p}}\right)-J_0\frac{\rho_b}{\rho_0}\mathcal{U}\mathbf{F}\mathbf{v}\big|_{\zeta=0}-J_0\mathbf{F}\mathbf{p}\big|_{\zeta=0}+O(\epsilon^{2+\gamma})\,,\end{aligned}\tag{4.111}$$

where the mean pressure $\overline{p}$ *and the functions* a *and* $\tilde{a}$ *are given, respectively, by*

$$\overline{p}=\tfrac{1}{2}h(c+m_3 a)+O(\epsilon^{1+\gamma})\,,\quad a\equiv\widetilde{\mathbf{H}}\,\overline{\mathbf{v}}\cdot\overline{\mathbf{v}}\,,\quad \tilde{a}\equiv\widetilde{\mathbf{H}}\,\overline{\mathbf{v}}\cdot\widetilde{\mathbf{W}}\,\overline{\mathbf{v}}\,.$$

From the above relations it is not difficult to see that,

Under the assumption of small curvature,

$$\mathcal{H}=O(\epsilon^{\gamma'})\,,\quad \gamma'\in(0,1)\,,\tag{4.112}$$

the mean pressure becomes

$$\overline{p}=\tfrac{1}{2}\,c\,h+O(\epsilon^{1+\hat{\gamma}})\,,\quad \hat{\gamma}\equiv min\{\gamma,\hat{\gamma}\}\,,$$

the depth-averaged mass balance equation (4.110) *simplifies to*

$$\frac{\partial}{\partial t}\Big\{J_0 h\Big\} + \mathrm{Div}\Big\{J_0 h(\overline{\mathbf{v}} - \mathbf{u}_S)\Big\} = -J_0 \frac{\rho_b}{\rho_0}\mathcal{U} + O(\epsilon^{2+\hat{\gamma}})\,, \tag{4.113}$$

and the depth-averaged hybrid linear momentum balance equation (4.111) *takes the simpler form*

$$\begin{aligned}\frac{\partial}{\partial t}\Big\{J_0 h\mathbf{F}\,\overline{\mathbf{v}}\Big\} + \mathrm{Div}\Big\{J_0 h\mathbf{F}\Big[m_2\,\overline{\mathbf{v}}\otimes\overline{\mathbf{v}} + \overline{p}\,\mathbf{M}_0 - \overline{\mathbf{P}} - \overline{\mathbf{v}}\otimes\mathbf{u}_S\Big]\Big\} \\ = -J_0 h\,\mathbf{F}\widetilde{\mathbf{W}}\,\overline{\mathbf{p}} - J_0 h\,(c + am_2 + \mathrm{Grad}\,\mathcal{U}\cdot\overline{\mathbf{v}})\,\mathbf{s} \\ - J_0\frac{\rho_b}{\rho_0}\mathcal{U}\mathbf{F}\mathbf{v}\big|_{\zeta=0} - J_0\mathbf{F}\mathbf{p}\big|_{\zeta=0} + O(\epsilon^{2+\hat{\gamma}})\,.\end{aligned} \tag{4.114}$$

Now we can answer question **Q2**: *Eq.* (4.111) *is not equivalent to its analogous counterpart* (4.93) *from the conventional approach*, a fact which was expected in view of the remark above. This can be clearly seen by comparing the highlighted terms in (4.111) and (4.93). The term

$$J_0 h\mathbf{F}\widetilde{\mathbf{W}}\big(\tfrac{1}{2}\beta\, h\,\overline{\mathbf{v}} - \overline{\mathbf{p}}\big)$$

arises in (4.111) as multiplied by 1, while in (4.93) it arises as multiplied by 2. Besides, no other terms in (4.111) and (4.93) contain the functions β and $\overline{\mathbf{p}}$, so that one could hope to show the equivalence of (4.111) and (4.93). Even if the basal surface is only slightly curved, the two approaches deliver different modelling equations, as it can be seen by comparing the highlighted terms in Eqs. (4.98) and (4.114). We can therefore draw the conclusion.

Answering Q2
The two depth-averaging approaches yield different modelling equations for both large and small curvature of the basal surface.

Yet for this latter case the equations in the conventional and non-conventional route are the same if

$$J_0 h\,\mathbf{F}\widetilde{\mathbf{W}}\,\overline{\mathbf{p}} = O(\epsilon^{2+\hat{\gamma}})\,.$$

This happens, for example, if the depth-averaged shear stresses $\overline{\mathbf{p}}$ are of order $O(\epsilon^{1+\gamma})$. This is exactly the case in the papers by Tai et al. [20, 21], see (4.99) and (4.100).

Note that, generally, neither (4.92) and (4.93) nor (4.110) and (4.111) represent a conservative system of equations, as desired when choosing the non-conventional route to derive modelling equations.

The modelling system of equations, either (4.92) and (4.93), or (4.110) and (4.111), must be complemented by closure relations, fitting the flow rule approximations and the dynamical assumptions stated in Sect. 4.5.2, for

- the depth-averaged extra-stress components $\overline{\mathbf{P}}$, $\overline{\mathbf{p}}$,
- the basal shear stress $\mathbf{p}\big|_{\zeta=0}$,
- the erosion/deposition rate $\mathcal{U}$,
- the parameters m_1 to m_3 and β arising in the flow rule approximations, see Sect. 4.5.2,
- the sliding coefficient χ_b relating linearly the tangential velocity at the basal surface, $\mathbf{v}\big|_{\zeta=0}$, to the depth-averaged tangential velocity, $\overline{\mathbf{v}}$, see (4.94).

We refer to such closure relations in the next chapter.

References

1. I. Luca, C.Y. Kuo, K. Hutter, Y.C. Tai, Modeling shallow over-saturated mixtures on arbitrary rigid topography. J. Mech. **28**(3), 523–541 (2012)
2. S.B. Savage, K. Hutter, The motion of a finite mass of granular material down a rough incline. J. Fluid. Mech. **199**, 177–215 (1989)
3. S.P. Pudasaini, K. Hutter, *Avalanche Dynamics: Dynamics of Rapid Flows of Dense Granular Avalanches* (Springer, 2007)
4. Y.A. Berezin, L.A. Spodareva, Slow motion of a granular layer on an inclined plane. J. Appl. Mech. Tech. Phys. **39**(2), 261–264 (1998)
5. C.A. Perazzo, J. Gratton, Thin film of non-Newtonian fluid on an incline. Phys. Rev. **67**, 016307 (2003)
6. I. Luca, K. Hutter, Y.C. Tai, C.Y. Kuo, A hierarchy of avalanche models on arbitrary topography. Acta Mech. **205**, 121–149 (2009)
7. A. Voellmy. über die Zerstörungskraft von Lawinen. Schweiz. Bauzeitung, Jahrg. 73, s. 159–165, 212–217, 246–249, 280–285. English as: On the destructive force of avalanches. 63p. Alta Avalanche Study Center, Transl, 2:1964, 1955
8. I.P. Perla, T.T. Cheng, D.M. McClung, A two-parameter model of snow avalanche motion. J. Glaciol. **26**(94), 197–207 (1980)
9. B. Salm, Contribution to avalanche dynamics. IAHS AISH Publ. **69**, 199–214 (1966)
10. M.E. Eglit, Some mathematical models of snow avalanches, volume II of Advances in the Mechanics and the Flow of Granular Materials. Trans. Tech. Publications, Clausthal-Zellerfeld, Germany, 1st edition, 1983. 577–588
11. C.B. Harbitz, Snow avalanche modelling, Mapping and Warning in Europe (SAME). Report of the Fourth European Framework Programme: Environment and Climate. NGI, Norway, C. B. Harbitz, ed. edition, 1998
12. J.M.N.T. Gray, Rapid granular avalanches, in *Dynamic Response of Granular and Porous Materials under Large and Catastrophic Deformations* (Springer, 2003), pp. 3–42
13. F. Bouchut, M. Westdickenberg, Gravity driven shallow water models for arbitrary topography. Comm. Math. Sci. **2**(3), 359–389 (2004)
14. F. Bouchut, E.D. Fernández-Nieto, A. Mangeney, P.-Y. Lagrée, On new erosion models of Savage-Hutter type for avalanches. Acta Mech. **199**, 181–208 (2008)

15. R.M. Iverson, The physics of debris flows. Rev. Geophys. **35**, 245–296 (1997)
16. S. McDougall, O. Hungr, A model for the analysis of the rapid landslide motion across three dimensional terrain. Canad. Geotech. J. **41**(6), 1084–1097 (2004)
17. S. McDougall, O. Hungr, Dynamic modeling of entrainment in rapid landslides. Canad. Geotech. J. **42**(5), 1437–1448 (2005)
18. I. Luca, Y.C. Tai, C.Y. Kuo, Modelling shallow gravity-driven solid-fluid mixtures over arbitrary topography. Comm. Math. Sci. **7**(1), 1–36 (2009)
19. I. Luca, K. Hutter, C.Y. Kuo, Y.C. Tai, Two-layer models for shallow avalanche flows over arbitrary variable topography. Int. J. Adv. Engng. Sci. Appl. Math. **1**, 99–121 (2009)
20. Y.C. Tai, C.Y. Kuo, W.H. Hui, An alternative depth-integrated formulation for granular avalanches over temporally varying topography with small curvature. Geophys. Astrophys. Fluid Dyn. **106**(6), 596–629 (2012)
21. Y.C. Tai, C.Y. Kuo, A new model of granular flows over general topography with erosion and deposition. Acta Mech. **199**, 71–96 (2008)

Chapter 5
Closure Relations for the Depth-Averaged Modelling Equations

The depth-averaged modelling equations in Sects. 4.5, 4.6 apply to flowing materials for which the constitutive properties are only required to satisfy ordering approximations on the components of the stress tensor and on the erosion/deposition rate. This chapter is focused on the formulation of closure relations matching the ordering approximations. Thus, Sect. 5.1 addresses the formulation of a bed friction law, constitutive models for the thin material layer are given in Sect. 5.2, and an erosion/deposition law is shown in Sect. 5.3. In Sect. 5.4 we explicitly write the modelling equations for a special case of the topographic surface and for a Mohr-Coulomb type flowing material. Special attention is given to the parameterization of the basal surface, a subject which is only slightly touched in the preceding sections of the book.

5.1 Bed Friction Law

When the flowing material experiences sliding on the basal surface, we have assumed the dynamic boundary condition (4.11), equivalently, $\mathbf{p}|_{\zeta=0} = -\mathbf{f}_b$. The bed friction force $\boldsymbol{f}_b$ must be prescribed as a phenomenological relation, expressing the local kinematic and/or dynamic state. The aim of this section is to formulate a law for $\boldsymbol{f}_b$. We follow closely the presentation given by Luca et al. [1].

Bed Coulomb friction versus viscous friction In dense granular avalanches the basal friction force $\boldsymbol{f}_b$ is due (i) to the *rubbing* of the particles on the surface, corresponding to e.g. Coulomb friction, $-\boldsymbol{\tau}_{Coulomb}$, and (ii) to particle *collisions*, corresponding e.g. to viscous friction, $-\boldsymbol{\tau}_{viscous}$, with

$$\boldsymbol{\tau}_{Coulomb} = (\tan\delta)\,(-\boldsymbol{\sigma}\boldsymbol{n}_b\cdot\boldsymbol{n}_b)_+\,\operatorname{sgn}\boldsymbol{v}_\tau\,,\quad \boldsymbol{\tau}_{viscous} = \rho_0 C(\|\boldsymbol{v}_\tau\|)\,\boldsymbol{v}_\tau\,. \tag{5.1}$$

I. Luca et al., *Shallow Geophysical Mass Flows down Arbitrary Topography*,
Advances in Geophysical and Environmental Mechanics and Mathematics,
DOI 10.1007/978-3-319-02627-5_5

In (5.1) the stress tensor $\boldsymbol{\sigma}$ and the tangential component $\boldsymbol{v}_\tau$ of the velocity $\boldsymbol{v}$ are evaluated on the basal surface $\mathcal{S}_b$, then

$$\operatorname{sgn} \boldsymbol{v}_\tau \equiv \begin{cases} \dfrac{1}{\|\boldsymbol{v}_\tau\|}\, \boldsymbol{v}_\tau\,, & \text{if } \ \boldsymbol{v}_\tau \neq 0\,, \\ \text{any tangent vector } \boldsymbol{m} \text{ to } \mathcal{S}_b\,, \ \|\boldsymbol{m}\| \leq 1\,, & \text{if } \ \boldsymbol{v}_\tau = 0\,, \end{cases} \tag{5.2}$$

δ is the *angle of basal friction* or *bed friction angle*, $\tan\delta > 0$, and the index $+$ stands for the positive part of a quantity, i.e. $f_+ \equiv \max\{0,\, f\}$. Moreover, $C > 0$ is the *drag coefficient*, which is constant in the linear case, however, often taken to be linear in $\|\boldsymbol{v}_\tau\|$. In this latter case,

$$C(\|\boldsymbol{v}_\tau\|) = \tilde{c}\, \|\boldsymbol{v}_\tau\|\,, \quad \text{with dimensionless} \quad \tilde{c} \lessapprox 2.5 \times 10^{-3}\,,$$

implying $\tilde{c} = O(\epsilon^{1+\gamma})$ if $\epsilon \approx 10^{-2}$, $\gamma \approx \frac{1}{2}$.

The contribution of the dry friction and viscous friction to the shear traction depends on the mean free path between the particles: in a slurry $\|\boldsymbol{\tau}_{Coulomb}\| \ll \|\boldsymbol{\tau}_{viscous}\|$, whilst in a very dense debris flow $\|\boldsymbol{\tau}_{Coulomb}\| \gg \|\boldsymbol{\tau}_{viscous}\|$. Both these cases are conveniently captured by assuming

$$\boldsymbol{f}_b = -\phi\, \boldsymbol{\tau}_{Coulomb} - (1-\phi)\boldsymbol{\tau}_{viscous}\,, \quad \text{with} \quad \phi \in [0,1]\,, \tag{5.3}$$

see e.g. Voellmy [2], Gray and Tai [3], Pudasaini and Hutter, [4] p. 145. With such a law for $\boldsymbol{f}_b$, δ can be determined from a static heap test, and C from a flow test at dilute concentration. We stress the fact that any closure relation for the friction force, other than (5.3), can be assumed.

We need the law (5.3) in non-dimensional form and expressed in the topography-fitted coordinates.

Non-dimensional bed friction law For $\boldsymbol{\tau}_{Coulomb}$ and $\boldsymbol{\tau}_{viscous}$ we use the same scaling as for $\boldsymbol{f}_b$, see (4.26), that is,

$$\boldsymbol{\tau}_{Coulomb} = \rho_0 g L\, \hat{\boldsymbol{\tau}}_{Coulomb}\,, \quad \boldsymbol{\tau}_{viscous} = \rho_0 g L\, \hat{\boldsymbol{\tau}}_{viscous}\,, \tag{5.4}$$

where the superposed hat indicates a dimensionless quantity. This implies that the non-dimensional version of (5.3) is

$$\hat{\boldsymbol{f}}_b = -\phi\, \hat{\boldsymbol{\tau}}_{Coulomb} - (1-\phi)\hat{\boldsymbol{\tau}}_{viscous}\,, \quad \text{with} \quad \phi \in [0,1]\,. \tag{5.5}$$

Using $\boldsymbol{v}_\tau = \sqrt{Lg}\, \hat{\boldsymbol{v}}_\tau$ and $\boldsymbol{\sigma} = \rho_0 g L \hat{\boldsymbol{\sigma}}$, see (4.26), from (5.4) and (5.1) we obtain

$$\hat{\boldsymbol{\tau}}_{Coulomb} = (\tan\delta)\, (-\hat{\boldsymbol{\sigma}}\boldsymbol{n}_b \cdot \boldsymbol{n}_b)_+ \operatorname{sgn} \hat{\boldsymbol{v}}_\tau\,, \quad \hat{\boldsymbol{\tau}}_{viscous} = \hat{C}(\|\hat{\boldsymbol{v}}_\tau\|)\, \hat{\boldsymbol{v}}_\tau\,, \tag{5.6}$$

where

$$\hat{C}(\|\hat{\boldsymbol{v}}_\tau\|) \equiv C(\sqrt{Lg}\, \|\hat{\boldsymbol{v}}_\tau\|)/\sqrt{Lg}\,.$$

Inserting (5.6) into (5.5) and dropping the hat, we deduce the dimensionless bed friction law

$$\boldsymbol{f}_b = -\phi(\tan\delta)\,(-\boldsymbol{\sigma}\boldsymbol{n}_b\cdot\boldsymbol{n}_b)_+\,\mathrm{sgn}\,\boldsymbol{v}_\tau - (1-\phi)C(\|\boldsymbol{v}_\tau\|)\,\boldsymbol{v}_\tau\,. \tag{5.7}$$

Bed friction law in the topography-fitted coordinates When the topography-fitted coordinates are used, the non-dimensional Coulomb/viscous bed friction law (5.7) takes the form

$$\mathbf{f}_b = -\phi(\tan\delta)\left\{(-T^{33})\big|_{\zeta=0}\right\}_+\,\mathrm{sgn}\,\mathbf{v}_0 - (1-\phi)C\left(\sqrt{\mathbf{M}_0^{-1}\mathbf{v}_0\cdot\mathbf{v}_0}\right)\mathbf{v}_0\,, \tag{5.8}$$

where $\mathbf{v}_0 \equiv \mathbf{v}|_{\zeta=0}$, and for a 2-column $\mathbf{x}$ the multivalued function $\mathrm{sgn}\,\mathbf{x}$ is defined as

$$\mathrm{sgn}\,\mathbf{x} \equiv \begin{cases} \dfrac{1}{\sqrt{\mathbf{M}_0^{-1}\mathbf{x}\cdot\mathbf{x}}}\,\mathbf{x}\,, & \text{if } \mathbf{x}\neq\mathbf{0}\,,\\ \text{any 2-column } \mathbf{m}\,,\ \mathbf{M}_0^{-1}\mathbf{m}\cdot\mathbf{m}\le 1\,, & \text{if } \mathbf{x}=\mathbf{0}\,. \end{cases} \tag{5.9}$$

To justify (5.8) we recall that $\boldsymbol{g}^3 = \boldsymbol{n}_b$, which implies $\boldsymbol{\sigma}\boldsymbol{n}_b\cdot\boldsymbol{n}_b = T^{33}$. Moreover, with (2.93) and (2.87) we deduce

$$\|\boldsymbol{v}_\tau\|^2\big|_{\zeta=0} = \mathbf{M}_0^{-1}\mathbf{v}_0\cdot\mathbf{v}_0\,. \tag{5.10}$$

A further calculation gives (5.8).

Bed friction law matching the thin-layer approximations We recall the dynamic assumption $(4.84)_3$ and the boundary condition (4.38), that is,

$$\mathbf{p} = O(\epsilon^\gamma)\,,\quad \mathbf{p}\big|_{\zeta=0} = -\mathbf{f}_b\,.$$

As a consequence, the friction angle δ, the (non-dimensional) drag coefficient C and the parameter ϕ in (5.8) must be so chosen that condition

$$\mathbf{f}_b = O(\epsilon^\gamma) \tag{5.11}$$

is fulfilled. First, we refer to the Coulomb friction contribution in $\mathbf{f}_b$, and recall that

(i) $T^{33} = -p + P^{33} = -p + O(\epsilon^{1+\gamma}) = O(\epsilon)$, see the dynamic assumptions (4.84),
(ii) the negligible terms in the pressure p are $O(\epsilon^{1+\gamma})$, see (4.88),
(iii) the negligible terms in the depth-averaged tangential linear momentum balance equation (4.93) are $O(\epsilon^{2+\gamma})$.

We assume

$$\phi\,(\tan\delta) = O(\epsilon)\,, \tag{5.12}$$

which makes sure that the negligible $O(\epsilon^{1+\gamma})$ terms in $T^{33}\big|_{\zeta=0}$ do not play any role in the combination

$$\phi\,(\tan\delta)\left\{T^{33}\big|_{\zeta=0}\right\}\,.$$

Then, we refer to the viscous friction contribution in (5.8). We recall the kinematic assumptions $\mathbf{v} = O(1)$ and $\mathbf{v}_0 = \chi_b\overline{\mathbf{v}}$, see (4.69) and (4.94). Therefore, to match assumption (5.11) we must have

$$(1-\phi)\chi_b C\left(\chi_b\sqrt{\mathbf{M}_0^{-1}\overline{\mathbf{v}}\cdot\overline{\mathbf{v}}}\right) = O(\epsilon^{\gamma})\,. \tag{5.13}$$

We summarize the results:

Coulomb/viscous bed friction law

Under the thin-layer approximations, in particular

$$p = O(\epsilon)\,,\quad \mathbf{P} = O(\epsilon)\,,\quad \mathbf{p} = O(\epsilon^{\gamma})\,,\quad P^{33} = O(\epsilon^{1+\gamma})\,,$$

and apart from $O(\epsilon^{2+\gamma})$ terms, the non-dimensional Coulomb/viscous bed friction law (5.8) appears as

$$\mathbf{f}_b = -\underbrace{\phi\,(\tan\delta)}_{O(\epsilon)}\left\{p\big|_{\zeta=0}\right\}_+\operatorname{sgn}\overline{\mathbf{v}} - \underbrace{(1-\phi)\chi_b C\left(\chi_b\sqrt{\mathbf{M}_0^{-1}\overline{\mathbf{v}}\cdot\overline{\mathbf{v}}}\right)}_{O(\epsilon^{\gamma})}\overline{\mathbf{v}} = O(\epsilon^{\gamma})\,, \tag{5.14}$$

where $p\big|_{\zeta=0}$ is given by (4.90), the bed friction angle δ, the drag coefficient C and the parameters $\phi \in [0,1]$, $\chi_b \in (0,1]$ satisfy conditions (5.12) and (5.13).

Remark We note that, if the dynamic assumptions $\mathbf{p} = O(\epsilon^{\gamma})$ and $P^{33} = O(\epsilon^{1+\gamma})$ in (4.84) are replaced by

$$\mathbf{p} = O(\epsilon)\quad \text{or less}\,,\qquad P^{33} = O(\epsilon^2)\quad \text{or less}\,,$$

the negligible terms in the pressure $p = O(\epsilon)$ are $O(\epsilon^2)$, see the derivation of formula (4.88). Thus, (4.90) appears as

$$p\Big|_{\zeta=0} = h(c + m_2 a) + O(\epsilon^2)\,. \tag{5.15}$$

Consequently, recalling that the negligible terms in $\mathbf{f}_b$ are $O(\epsilon^{2+\gamma})$, instead of (5.12) one may assume the less restrictive condition

$$\phi(\tan\delta) = O(\epsilon^{\gamma}),$$

while handling the viscous term in $\mathbf{f}_b$ so as to ensure the same order of magnitude for $\mathbf{f}_b$ and the shear stresses $\mathbf{p}$. For instance,

If

$$\mathbf{p} = O(\epsilon^{1+\gamma}), \qquad P^{33} = O(\epsilon^{2+\gamma}), \tag{5.16}$$

we can assume

$$\begin{aligned}\mathbf{f}_b &= -\underbrace{\phi\,(\tan\delta)}_{O(\epsilon^{\gamma})}\left\{p\big|_{\zeta=0}\right\}_{+}\operatorname{sgn}\overline{\mathbf{v}} - \underbrace{(1-\phi)\chi_b C\left(\chi_b\sqrt{\mathbf{M}_0^{-1}\overline{\mathbf{v}}\cdot\overline{\mathbf{v}}}\right)}_{O(\epsilon^{1+\gamma})}\overline{\mathbf{v}} \\ &= O(\epsilon^{1+\gamma}).\end{aligned} \tag{5.17}$$

We shall refer to (5.17) in the next section.

5.2 Constitutive Models for the Thin Material Layer

In this section we formulate closure relations for the depth-averaged extra-stress components $\overline{\mathbf{P}}$ and $\overline{\mathbf{p}}$ matching the thin-layer approximations (4.84). We couple these relations with appropriate basal viscous friction laws and parameters m_1, m_2, m_3 and β, to obtain particular models for geophysical flows down arbitrary topography. However, the erosion/deposition rate is left unspecified. It will be discussed in Sect. 5.3.

We propose two classes of closure relations for the depth-averaged equations, be these derived in the conventional route or in the non-conventional route. The first class issues from the assumption that the avalanching mass is a Newtonian/non-Newtonian viscous fluid, and the second class is developed in the spirit of the Savage-Hutter avalanche modelling approach. Both these classes have been considered by Luca et al. [1, 5].

5.2.1 Avalanching Mass as a Newtonian/Non-Newtonian Viscous Fluid

Many thin film flows assume (viscous/viscoplastic) non-Newtonian behavior of the flowing mass, see e.g. Perazzo and Gratton [6], Ng and Mei [7], Huang and Garcia

[8], Ionescu [9, 10], Bovet et al. [11], Gray and Edwards [12]. Here we show that, when applied to snow and debris avalanches, the viscous Newtonian/non-Newtonian constitutive law fits the thin-layer approximations stated in Sect. 4.5.2. It will appear that the extra stresses parallel to the basal surface, **P**, are negligibly small in the depth-averaged modelling equations. The stresses in the normal direction, **p**, may survive, and are computed by assuming a power law tangential velocity field. The presentation in this subsection follows closely Luca et al. [1], but here we consider the general case of active topographic beds.

Newtonian/non-Newtonian viscous fluid An incompressible **Newtonian fluid** is defined by the (dimensional) constitutive law

$$\boldsymbol{\sigma} = -p\boldsymbol{I} + 2\eta\boldsymbol{D}\,, \quad \eta = \text{constant}\,, \quad \text{tr}\,\boldsymbol{D} = 0\,, \tag{5.18}$$

where p is the pressure, and $\boldsymbol{D}$ is the strain-rate tensor, see (3.43), satisfying condition $(5.18)_3$ due to the incompressibility assumption. The scalar η is called the *dynamic* (or *effective*, or *apparent*) *viscosity*. An incompressible **viscous non-Newtonian fluid** is specified by a similar constitutive law, with the viscosity η depending on the *shear rate* (or *stretching*) $\dot{\gamma}$, that is,

$$\boldsymbol{\sigma} = -p\boldsymbol{I} + 2\eta(\dot{\gamma})\boldsymbol{D}\,, \quad \dot{\gamma} \equiv 2\sqrt{II_{\boldsymbol{D}}}\,, \quad \text{tr}\,\boldsymbol{D} = 0\,. \tag{5.19}$$

For the definition of the second invariant $II_{\boldsymbol{D}}$ of $\boldsymbol{D}$ and its expression in the topography-fitted curvilinear coordinates see (3.46). In terms of the extra-stress tensor, see (4.7), the Newtonian/non-Newtonian laws (5.18) and (5.19) read as

$$\boldsymbol{\sigma}_E = 2\eta\boldsymbol{D}\,, \quad \text{tr}\,\boldsymbol{D} = 0\,, \tag{5.20}$$

with $\eta = \text{constant}$ or $\eta = \eta(\dot{\gamma}) \neq \text{constant}$.

Dimensionless Newtonian/non-Newtonian constitutive law We introduce the dimensionless strain-rate tensor by the relation

$$\boldsymbol{D} = \frac{1}{\sqrt{L/g}}\boldsymbol{D}_{\text{dimless}}\,. \tag{5.21}$$

From $(5.19)_2$ and (5.21) we immediately derive the non-dimensional shear rate,

$$\dot{\gamma} = \frac{1}{\sqrt{L/g}}\,\dot{\gamma}_{\text{dimless}}\,.$$

Then, with the scalings $(4.26)_4$ for $\boldsymbol{\sigma}$ and (5.21) for $\boldsymbol{D}$, in non-dimensional form the law (5.20) emerges as

$$\boldsymbol{\sigma}_{E\,dimless} = 2\eta_{dimless}\boldsymbol{D}_{dimless}\,, \qquad \eta_{dimless} \equiv \frac{\eta}{\rho_0 L\sqrt{Lg}}\,. \tag{5.22}$$

Omitting the "dimless" index in $(5.22)_1$ we obtain the dimensionless form of (5.20),

$$\boldsymbol{\sigma}_E = 2\eta \boldsymbol{D}\,, \quad \text{tr}\,\boldsymbol{D} = 0\,. \tag{5.23}$$

Note that, the non-dimensional dynamic viscosity $\eta_{dimless}$ appears as the inverse of a Reynolds number Re, that is,

$$\eta_{dimless} = \frac{1}{Re}\,, \quad Re \equiv \frac{\rho_0 L\sqrt{Lg}}{\eta}\,. \tag{5.24}$$

The Newtonian/non-Newtonian law (5.23) in the topography-fitted coordinates As a consequence of the scalings (5.21), (4.26) and (4.27), the contravariant components of the dimensionless strain-rate tensor $\boldsymbol{D}$ with respect to the basis $\{\boldsymbol{g}_1, \boldsymbol{g}_2, \boldsymbol{g}_3\}$ are formally the same as those from (3.45). Therefore, recalling notations (3.44) and (3.57) for the contravariant components of the strain-rate tensor $\boldsymbol{D}$ and the extra-stress tensor $\boldsymbol{\sigma}_E$, that is,

$$\boldsymbol{D} \rightsquigarrow \begin{pmatrix} \mathbf{D} & \mathbf{d} \\ \mathbf{d}^T & D^{33} \end{pmatrix}\,, \qquad \boldsymbol{\sigma}_E \rightsquigarrow \begin{pmatrix} \mathbf{P} & \mathbf{p} \\ \mathbf{p}^T & P^{33} \end{pmatrix}\,,$$

it is clear that the dimensionless Newtonian/non-Newtonian law (5.23) is equivalent to

$$\mathbf{P} = 2\eta\,\mathbf{D}\,, \quad \mathbf{p} = 2\eta\,\mathbf{d}\,, \quad P^{33} = 2\eta D^{33}\,. \tag{5.25}$$

Consequences of the thin-layer approximations With $\zeta = O(\epsilon)$, $\mathbf{v} = O(1)$ and $\mathrm{v} = O(\epsilon)$, see (4.67), (4.69), (4.74) and (4.75), in view of (3.45) we have

$$\mathbf{D} = O(1)\,, \quad \mathbf{d} = O(\epsilon^{-1})\,, \quad D^{33} = O(1)\,. \tag{5.26}$$

From (5.25) and (5.26) we deduce

$$\mathbf{P} = O(\eta)\,, \quad \mathbf{p} = O(\eta/\epsilon)\,, \quad P^{33} = O(\eta)\,. \tag{5.27}$$

For snow and debris avalanches we have $\epsilon \approx 10^{-2}$, $\gamma \approx \frac{1}{2}$ (see Pudasaini and Hutter [4], p. 188), and typical Reynolds numbers range from 10^3 to 10^7. This yields, see (5.24), typical (non-dimensional) viscosities

$$\eta = O(\epsilon^{1+\gamma}) \quad \text{or less}\,. \tag{5.28}$$

For $\eta = O(\epsilon^{1+\gamma})$, the estimations from (5.27) appear as

$$\mathbf{P} = O(\epsilon^{1+\gamma})\,, \quad \mathbf{p} = O(\epsilon^{\gamma})\,, \quad P^{33} = O(\epsilon^{1+\gamma})\,,$$

Table 5.1 Non-negligible stress components of Newtonian/non-Newtonian avalanche models in terms of the scaling of viscosity

Non-dimensional viscosity η	Non-negligible stress components in (4.93) and (4.111)
$O(\epsilon^{3+\gamma})$	–
$O(\epsilon^{2+\gamma})$, $O(\epsilon^3)$	$\mathbf{p}\big\vert_{\zeta=0}$
$O(\epsilon^{1+\gamma})$, $O(\epsilon^2)$	$\overline{\mathbf{p}}$, $\mathbf{p}\big\vert_{\zeta=0}$

which clearly shows that the dynamic thin-layer approximations (4.84) are satisfied. Moreover, with (5.28) we have situations in which various dynamic assumptions are fulfilled, and thus various simplified versions of equation (4.93) (or (4.111)) are available. Table 5.1 concisely expresses the non-negligible stress components in (4.93) (or (4.111)) in terms of the order of magnitude of the (non-dimensional) viscosity η.

We can see from Table 5.1 that the normal stresses and shear stresses parallel to the base, $\mathbf{P}$, do not arise in the modelling equations (4.93) and (4.111), which is a major simplification of these equations. However, the shear stresses in the normal direction, $\mathbf{p}$, survive as $\mathbf{p}\big\vert_{\zeta=0}$ and $\overline{\mathbf{p}}$. One therefore needs to express $\mathbf{p}\big\vert_{\zeta=0}$ and $\overline{\mathbf{p}}$ in terms of the basic unknown fields h, $\overline{\mathbf{v}}$ and b.

Closure relations for $\mathbf{p}\vert_{\zeta=0}$ and $\overline{\mathbf{p}}$ We discuss separately two cases, depending on the O-order of the viscosity, see Table 5.1.

Case 1 *Viscous fluids with viscosity* $\eta = O(\epsilon^{1+\gamma})$ *or* $\eta = O(\epsilon^2)$

In this case we need to prescribe both $\mathbf{p}\vert_{\zeta=0}$ and $\overline{\mathbf{p}}$. For concreteness we refer to $\eta = O(\epsilon^{1+\gamma})$. As in many models of thin film flows of non-Newtonian fluids (e.g. Ng and Mei [7], Berezin and Spodareva [13], Perazzo and Gratton [6], Huang and Garcia [8]), we assume the no-slip condition (4.12), equivalently,

$$\mathbf{v} = \mathbf{0} \qquad \text{at} \quad \zeta = 0\,.$$

Moreover, we suppose that the tangential velocity $\mathbf{v}$ has a power law profile,

$$\mathbf{v} = \frac{n+2}{n+1}\left\{1-\left(1-\frac{\zeta}{h}\right)^{n+1}\right\}\overline{\mathbf{v}}\,, \tag{5.29}$$

see (4.81) in which $\mathbf{v}_0 = \mathbf{0}$. The assumption on $\mathbf{v}$ allows the derivation of $\mathbf{p}\big\vert_{\zeta=0}$ and $\overline{\mathbf{p}}$ from the constitutive law $(5.25)_2$. Thus, using $(5.25)_2$ and $(3.45)_2$, we have

$$\mathbf{p} = \eta\left\{\frac{\partial \mathbf{v}}{\partial \zeta} + \mathbf{M}\,\mathrm{Grad}\,\mathrm{v}\right\} = \eta\,\frac{n+2}{h}\left(1-\frac{\zeta}{h}\right)^{n}\overline{\mathbf{v}} + \eta\,\mathbf{M}\mathrm{Grad}\,\mathrm{v}\,.$$

With $\eta = O(\epsilon^{1+\gamma})$ and $\mathrm{v} = O(\epsilon)$, this relation emerges as

$$\mathbf{p} = \eta \frac{n+2}{h} \left(1 - \frac{\zeta}{h}\right)^n \overline{\mathbf{v}} + O(\epsilon^{2+\gamma}) ,$$

which implies

$$\mathbf{p}\big|_{\zeta=0} = \eta\big|_{\zeta=0} \frac{n+2}{h} \overline{\mathbf{v}} + O(\epsilon^{2+\gamma}) , \tag{5.30}$$

and

$$\overline{\mathbf{p}} = \frac{n+2}{h} \overline{\eta(\dot{\gamma}) \left(1 - \frac{\zeta}{h}\right)^n} \overline{\mathbf{v}} + O(\epsilon^{2+\gamma}) . \tag{5.31}$$

For a *Newtonian fluid* the averaged shear stresses $\overline{\mathbf{p}}$ can be immediately computed. For this case we show below the complete set of modelling equations.

Newtonian model with $\eta = O(\epsilon^{1+\gamma})$ or $\eta = O(\epsilon^2)$

Assume Newtonian behavior of the avalanching mass with the viscosity $\eta = O(\epsilon^{1+\gamma})$ or $\eta = O(\epsilon^2)$. The equations which describe the shallow flow fit Class (iii), see Sect. 4.5.4. *Considering the no-slip condition and a power law velocity profile, apart from $O(\epsilon^{2+\gamma})$ terms, these equations are*

(i) *the depth-averaged mass balance equation* (4.92), *and*
(ii) *the depth-averaged tangential linear momentum balance equation* (4.93), *or the depth-averaged hybrid linear momentum balance equation* (4.111), *with*

$$\mathbf{v}\big|_{\zeta=0} = \mathbf{0} , \quad \mathbf{p}\big|_{\zeta=0} = \eta \frac{n+2}{h} \overline{\mathbf{v}} , \qquad \overline{\mathbf{p}} = \frac{n+2}{n+1} \frac{\eta}{h} \overline{\mathbf{v}} , \quad \overline{\mathbf{P}} = \mathbf{0} , \tag{5.32}$$

and the Boussinesq coefficients m_1, m_2, m_3, β as given by (4.82) *and* (4.83) *with $\chi_b = 0$.*

Now, for a *non-Newtonian fluid*, in (5.30) and (5.31) the quantities

$$\eta\big|_{\zeta=0} = \eta(\dot{\gamma}_0) , \qquad \dot{\gamma}_0 \equiv \dot{\gamma}\big|_{\zeta=0} \qquad \text{and} \qquad \overline{\eta(\dot{\gamma}) \left(1 - \frac{\zeta}{h}\right)^n}$$

must be computed up to $O(\epsilon^{2+\gamma})$ terms as soon as the viscosity function η is known. We do not enter into details of such computations. They can be done by using the velocity profile (5.29) in expression (3.46) of $II_{\boldsymbol{D}}$ to obtain the shear rate $\dot{\gamma}$, and then by deriving the asymptotic expansion of the viscosity $\eta(\dot{\gamma})$. To get an idea on these computations we show how $\dot{\gamma}_0$ is determined. Thus, condition $\mathbf{v} = \mathbf{0}$ at $\zeta = 0$ and expression $(3.45)_1$ for $\mathbf{D}$ give

$$\mathbf{D}\Big|_{\zeta=0} = -\frac{1}{2}\mathrm{v}|_{\zeta=0}\left(\widetilde{\mathbf{W}}\mathbf{M}_0 + \mathbf{M}_0\widetilde{\mathbf{W}}^T\right) .$$

Using the relation $\widetilde{\mathbf{W}} = \mathbf{M}_0\widetilde{\mathbf{H}}$, see (2.49), and the symmetry of the matrices $\widetilde{\mathbf{H}}$ and $\mathbf{M}_0$, we obtain

$$\mathbf{D}\mathbf{M}^{-1}\Big|_{\zeta=0} = -\mathrm{v}|_{\zeta=0}\widetilde{\mathbf{W}} . \tag{5.33}$$

Next, $(3.45)_2$ and the velocity profile (5.29) imply

$$\mathbf{d}\Big|_{\zeta=0} = \frac{1}{2}\left\{\frac{n+2}{h}\,\overline{\mathbf{v}} + \mathbf{M}_0\mathrm{Grad}\,\left(\mathrm{v}|_{\zeta=0}\right)\right\} ,$$

and hence

$$\begin{aligned}\mathbf{M}^{-1}\mathbf{d}\cdot\mathbf{d}\,\Big|_{\zeta=0} = \frac{1}{4}\Big\{&\frac{(n+2)^2}{h^2}\,\mathbf{M}_0^{-1}\overline{\mathbf{v}}\cdot\overline{\mathbf{v}} + 2\frac{n+2}{h}\,\overline{\mathbf{v}}\cdot\mathrm{Grad}\,\left(\mathrm{v}|_{\zeta=0}\right)\\ &+\mathbf{M}_0\mathrm{Grad}\,\left(\mathrm{v}|_{\zeta=0}\right)\cdot\mathrm{Grad}\,\left(\mathrm{v}|_{\zeta=0}\right)\Big\} .\end{aligned} \tag{5.34}$$

Then, using the mass balance equation (4.43) to compute $\partial\mathrm{v}/\partial\zeta$,

$$\frac{\partial\mathrm{v}}{\partial\zeta} = -\frac{1}{J}\left\{\mathrm{v}\frac{\partial J}{\partial\zeta} + \mathrm{Div}\,(J\mathbf{v})\right\} ,$$

and again $\mathbf{v} = \mathbf{0}$ at $\zeta = 0$, from $(3.45)_3$ and (3.18) we infer

$$D^{33}\Big|_{\zeta=0} = \frac{\partial\mathrm{v}}{\partial\zeta}\Big|_{\zeta=0} = -\frac{1}{J_0}\left(\mathrm{v}\,\frac{\partial J}{\partial\zeta}\right)_{\zeta=0} = 2\Omega\,\mathrm{v}|_{\zeta=0} . \tag{5.35}$$

In (5.33)–(5.35) the velocity $\mathrm{v}|_{\zeta=0}$ is given by (4.46). Now, use of (5.33)–(5.35) in (3.46) leads to

$$\begin{aligned}II_{\boldsymbol{D}}\Big|_{\zeta=0} = &\frac{(n+2)^2}{4h^2}\,\mathbf{M}_0^{-1}\overline{\mathbf{v}}\cdot\overline{\mathbf{v}} + \left(\tfrac{1}{2}\,\mathrm{tr}\,\widetilde{\mathbf{W}}^2 + 2\Omega^2\right)\left(\mathrm{v}|_{\zeta=0}\right)^2\\ &+\frac{n+2}{2h}\,\overline{\mathbf{v}}\cdot\mathrm{Grad}\,\left(\mathrm{v}|_{\zeta=0}\right) + \frac{1}{4}\mathbf{M}_0\mathrm{Grad}\,\left(\mathrm{v}|_{\zeta=0}\right)\cdot\mathrm{Grad}\,\left(\mathrm{v}|_{\zeta=0}\right) .\end{aligned}$$

For rigid topographic beds we have $\mathrm{v}|_{\zeta=0} = 0$, implying the simpler relation

$$II_{\boldsymbol{D}}\Big|_{\zeta=0} = \frac{(n+2)^2}{4h^2}\,\mathbf{M}_0^{-1}\overline{\mathbf{v}}\cdot\overline{\mathbf{v}} .$$

Now, $\dot{\gamma}_0$ can be computed using $(5.19)_2$.

Case 2 *Viscous fluids with viscosity* $\eta = O(\epsilon^{2+\gamma})$

Here we have only to give the basal shear stresses $\mathbf{p}\big|_{\zeta=0}$, see Table 5.1. We assume sliding motion and the Coulomb/viscous bed friction law (5.8), with the Coulomb and viscous terms adjusted according to the thin-layer assumptions. Thus, with $\eta = O(\epsilon^{2+\gamma})$, conditions (5.16) are fulfilled, and so we can assume the Coulomb/viscous friction with the parameters ϕ, δ, χ_b and C as shown in (5.17).

In the modelling equations the correction coefficients m_1 to m_3, β and χ_b in (5.17) are not yet specified. We indicate a possible way to choose them. The idea is to assume the power law velocity profile (4.80). This will give the correction Boussinesq coefficients m_1–m_3 and β, see (4.82) and (4.83), in terms of the sliding coefficient χ_b which is still not specified. The coefficient χ_b will be determined as follows. Knowing the velocity profile we can determine the shear stresses $\mathbf{p}$ according to the Newtonian/non-Newtonian constitutive law. Then, invoking the continuity of $\mathbf{p}$ we can compute $\mathbf{p}\big|_{\zeta=0}$. However, for the basal shear stresses we have assumed the friction law (5.17). The two expressions of $\mathbf{p}\big|_{\zeta=0}$ must therefore be equal. This equality stands for the determination of χ_b, assuming that a solution $\chi_b \in (0, 1]$ does exist.

We show that, for

(i) a Newtonian fluid with $\eta = O(\epsilon^{2+\gamma})$,
(ii) the viscous bed friction law

$$\boldsymbol{f}_b = -C(\|\boldsymbol{v}_\tau\|)\,\boldsymbol{v}_\tau = O(\epsilon^{1+\gamma})\,, \tag{5.36}$$

see (5.7) with $\phi = 0$,
(iii) and the drag coefficient C given by

$$C(\|\boldsymbol{v}_\tau\|) = \tilde{c}\,\|\boldsymbol{v}_\tau\|\,, \quad \tilde{c} = \text{constant} = O(\epsilon^{1+\gamma})\,, \tag{5.37}$$

these reasonings yield $\chi_b \in (0, 1]$, and hence the parameters m_1 to m_3 and β. Thus, combining (5.36), (5.37) and recalling (5.10), (5.17), apart from $O(\epsilon^{2+\gamma})$ terms we have

$$\mathbf{f}_b = -\chi_b^2 \tilde{c} \sqrt{\mathbf{M}_0^{-1}\overline{\mathbf{v}}\cdot\overline{\mathbf{v}}}\,\overline{\mathbf{v}}\,. \tag{5.38}$$

On the other hand, we use the power law velocity profile (4.81) in which $\mathbf{v}_0 = \chi_b\,\overline{\mathbf{v}}$ to compute the stresses $\mathbf{p} = 2\eta\mathbf{d}$, with $\mathbf{d}$ given by $(3.45)_2$:

$$\begin{aligned}\mathbf{p} = 2\eta\mathbf{d} &= \eta\left\{\frac{\partial \mathbf{v}}{\partial \zeta} + \mathbf{M}\mathrm{Grad}\,\mathrm{v}\right\} = \eta\,\frac{\partial \mathbf{v}}{\partial \zeta} + O(\epsilon^{3+\gamma}) \\ &= (1-\chi_b)\eta\,\frac{n+2}{h}\left(1-\frac{\zeta}{h}\right)^n \overline{\mathbf{v}} + O(\epsilon^{3+\gamma})\,.\end{aligned}$$

From here we infer that, apart from $O(\epsilon^{3+\gamma})$ terms,

$$\mathbf{p}\big|_{\zeta=0} = (1-\chi_b)\eta\,\frac{n+2}{h}\,\overline{\mathbf{v}}\,. \tag{5.39}$$

Now, with (5.38) and (5.39), the sliding condition $\mathbf{p}|_{\zeta=0} = -\mathbf{f}_b$ turns into a second order algebraic equation for the determination of the sliding coefficient χ_b, that is,

$$(1-\chi_b)\eta\,\frac{n+2}{h} = \chi_b^2\tilde{c}\,\sqrt{\mathbf{M}_0^{-1}\overline{\mathbf{v}}\cdot\overline{\mathbf{v}}}\,. \tag{5.40}$$

Provided $\overline{\mathbf{v}} \neq \mathbf{0}$, Eq. (5.40) has two real distinct roots, from which only one,

$$\chi_b = \frac{-b+\sqrt{b^2+4ab}}{2a}\,, \quad a \equiv \tilde{c}\sqrt{\mathbf{M}_0^{-1}\overline{\mathbf{v}}\cdot\overline{\mathbf{v}}}\,, \quad b \equiv \eta\,\frac{n+2}{h}\,, \tag{5.41}$$

is positive. Moreover, one can easily see that the positive solution χ_b belongs to $(0, 1]$, which we wanted to show. We therefore have obtained a model for a shallow avalanching mass with small viscosity down arbitrary topography:

Newtonian model with $\eta = O(\epsilon^{2+\gamma})$

The equations which describe the shallow flow of a Newtonian fluid with viscosity $\eta = O(\epsilon^{2+\gamma})$ and viscous sliding (5.37), (5.38) fit Class (ii), see Sect. 4.5.4. *With a power law velocity profile, these equations are*

(i) *the depth-averaged mass balance equation* (4.92), *and*
(ii) *the depth-averaged tangential linear momentum balance equation* (4.93), *or the depth-averaged hybrid linear momentum balance equation* (4.111), *with*

- *negligible* $\overline{\mathbf{P}}$, $\overline{\mathbf{p}}$,
- *the sliding coefficient* χ_b *given by* (5.41),
- *the basal shear stresses* $\mathbf{p}|_{\zeta=0}$ *given by* (5.39) *or, equivalently,*

$$\mathbf{p}|_{\zeta=0} = \chi_b^2\tilde{c}\sqrt{\mathbf{M}_0^{-1}\overline{\mathbf{v}}\cdot\overline{\mathbf{v}}}\,\overline{\mathbf{v}}\,, \quad \tilde{c} = \text{constant} = O(\epsilon^{1+\gamma})\,,$$

- *the Boussinesq coefficients* m_1, m_2, m_3 *and* β *given by* (4.82) *and* (4.83), *with* χ_b *as shown in* (5.41).

Note that, assuming a *plug flow* velocity profile, that is $\mathbf{v} = \mathbf{v}(\boldsymbol{\xi}, t)$, according to $(3.45)_2$ and $\mathrm{v} = O(\epsilon)$, we have $\mathbf{d} = O(\epsilon)$, and so the shear stresses $\mathbf{p}$ are estimated as

$$\mathbf{p} = O(\eta\epsilon)\,.$$

With $\eta = O(\epsilon^{1+\gamma})$, this implies that $\overline{\mathbf{p}}$ and $\mathbf{p}|_{\zeta=0}$ are negligibly small in the modelling equations. The ensuing thin flow model is, however, too simple to describe a realistic debris flow. The dependence of $\mathbf{v}$ on ζ is therefore mandatory for viscosities of order $O(\epsilon^{1+\gamma})$ or less in a Newtonian/non-Newtonian model for a shallow flow.

5.2.2 Avalanching Mass as a Mohr-Coulomb Type Material

Now the aim is to present topography-adapted closure relations of Mohr-Coulomb type for the depth-averaged stress components arising in the thin-layer modelling equations. Coupled with this is the formulation of the bed friction law. The emerging models represent generalizations to arbitrary topographies of the models by Iverson and Denlinger [14] and Savage and Hutter [15] for flowing granular materials, and have been formulated by Luca et al. [1, 5].

We consider

$$\mathbf{P} = O(\epsilon)\,, \quad \mathbf{p} = O(\epsilon^{1+\gamma})\,, \quad P^{33} = 0\,, \tag{5.42}$$

so that the pressure p is interpreted as the normal stress in the direction perpendicular to the basal surface,

$$p \equiv -T^{33}\,,$$

and the significant stresses in the depth-averaged tangential momentum balance equation (4.93) are

$$\mathbf{p}|_{\zeta=0} \quad \text{and} \quad \overline{\mathbf{P}}\,.$$

Closure relation for $\mathbf{p}|_{\zeta=0}$ We assume that the interaction of the flowing material with the basal surface is described by the Coulomb friction law, that is, (5.14) with $\phi = 1$. Since conditions (5.16) are fulfilled, the friction law takes the form (5.17) with $\phi = 1$, implying

$$\mathbf{p}\big|_{\zeta=0} = (\tan\delta)\left\{p\big|_{\zeta=0}\right\}_+ \operatorname{sgn}\mathbf{v}_0\,, \quad \mathbf{v}_0 \equiv \mathbf{v}\big|_{\zeta=0}\,, \quad \tan\delta = O(\epsilon^{\gamma})\,. \tag{5.43}$$

With the pressure $p\big|_{\zeta=0}$ given by (4.90) and assumption

$$\mathbf{v}_0 = \chi_b\overline{\mathbf{v}}\,, \quad \chi_b \in (0,1]\,,$$

apart from negligible terms, the Coulomb friction condition (5.43) turns into

$$\mathbf{p}\big|_{\zeta=0} = h(\tan\delta)\{c + m_2 a\}_+ \operatorname{sgn}\overline{\mathbf{v}}\,, \quad \tan\delta = O(\epsilon^{\gamma})\,. \tag{5.44}$$

Note that the sliding coefficient χ_b does not arise in the friction law (5.44).

Closure relation for $\overline{\mathbf{P}}$ First, we show that a closure relation for $\overline{\mathbf{P}}$ can be obtained by specifying the mean stress tensor $\overline{\boldsymbol{\sigma}}$ up to $O(\epsilon^{1+\gamma})$ terms. Thus, using relation (3.59), assumptions (5.42) and approximation $\boldsymbol{g}_\alpha = \boldsymbol{\tau}_\alpha + O(\epsilon)$, we have

$$\begin{aligned}\boldsymbol{\sigma} = T^{ij}\boldsymbol{g}_i \otimes \boldsymbol{g}_j &= T^{\alpha\beta}\boldsymbol{g}_\alpha \otimes \boldsymbol{g}_\beta + T^{\alpha 3}(\boldsymbol{g}_\alpha \otimes \boldsymbol{n}_b + \boldsymbol{n}_b \otimes \boldsymbol{g}_\alpha) + T^{33}\boldsymbol{n}_b \otimes \boldsymbol{n}_b \\ &= T^{\alpha\beta}\boldsymbol{g}_\alpha \otimes \boldsymbol{g}_\beta + T^{\alpha 3}(\boldsymbol{g}_\alpha \otimes \boldsymbol{n}_b + \boldsymbol{n}_b \otimes \boldsymbol{g}_\alpha) - p\,\boldsymbol{n}_b \otimes \boldsymbol{n}_b \\ &= \underbrace{T^{\star\alpha\beta}\boldsymbol{\tau}_\alpha \otimes \boldsymbol{\tau}_\beta - p\,\boldsymbol{n}_b \otimes \boldsymbol{n}_b}_{\boldsymbol{\sigma}^\star} + O(\epsilon^{1+\gamma}) = O(\epsilon)\,,\end{aligned}$$

with

$$\left(T^{\star\alpha\beta}\right) \equiv -p\mathbf{M}_0 + \mathbf{P}\,.$$

This yields

$$\overline{\boldsymbol{\sigma}} = \overline{\boldsymbol{\sigma}}^\star + O(\epsilon^{1+\gamma})\,,$$

where

$$\overline{\boldsymbol{\sigma}}^\star = \overline{T}^{\star\alpha\beta}\boldsymbol{\tau}_\alpha \otimes \boldsymbol{\tau}_\beta - \overline{p}\,\boldsymbol{n}_b \otimes \boldsymbol{n}_b\,, \quad (\overline{T}^{\star\alpha\beta}) = -\overline{p}\mathbf{M}_0 + \overline{\mathbf{P}}\,. \tag{5.45}$$

Therefore, it is clear that any assumption on $\overline{\boldsymbol{\sigma}}$ as evaluated up to $O(\epsilon^{1+\gamma})$ terms, that is on $\overline{\boldsymbol{\sigma}}^\star$, yields $\overline{\mathbf{P}}$.

Next we focus on $\overline{\boldsymbol{\sigma}}^\star$. From $(5.45)_1$ we deduce

$$\overline{\boldsymbol{\sigma}}^\star \boldsymbol{n}_b = -\overline{p}\,\boldsymbol{n}_b\,,$$

which shows that $-\overline{p}$ is an eigenvalue of $\overline{\boldsymbol{\sigma}}^\star$, and $\boldsymbol{n}_b$ is an eigenvector corresponding to this eigenvalue. As a symmetric tensor, $\overline{\boldsymbol{\sigma}}^\star$ is then completely determined if the other two eigenvalues and principal directions (mutually orthogonal and perpendicular to $\boldsymbol{n}_b$) are specified. We shall give them in terms of the eigenvalues and eigenvectors of the surface strain-rate (see Sect. 3.2) corresponding to the depth-averaged tangential velocity $\overline{\boldsymbol{v}_\tau}$ (as evaluated up to terms $O(\epsilon^{1+\gamma})$), that is

$$\boldsymbol{D}_{\mathcal{S}} \equiv \tfrac{1}{2}\left(\nabla_{\mathcal{S}}\overline{\boldsymbol{v}_\tau} + (\nabla_{\mathcal{S}}\overline{\boldsymbol{v}_\tau})^T\right)\,, \quad \boldsymbol{v}_\tau \equiv v^\alpha \boldsymbol{g}_\alpha\,.$$

We refer to $\boldsymbol{D}_{\mathcal{S}}$ as the *mean surface stretching* and suppose $\boldsymbol{D}_{\mathcal{S}} \neq 0$. A motivation for relating $\overline{\boldsymbol{\sigma}}^\star$ to the mean the surface stretching $\boldsymbol{D}_{\mathcal{S}}$ will be given in the remark following the presentation of the models.

So, let λ_1, λ_2 be the eigenvalues of the mean surface stretching $\boldsymbol{D}_{\mathcal{S}}$, and let $\boldsymbol{f}_1$, $\boldsymbol{f}_2$ be corresponding (for the moment arbitrary) orthonormal eigenvectors.[1] We shall propose three models for $\overline{\boldsymbol{\sigma}}^\star$. Common to these models is the assumption that, if $\lambda_1 \neq \lambda_2$ (in which case, there are two principal directions of $\boldsymbol{D}_{\mathcal{S}}$ uniquely defined), $\overline{\boldsymbol{\sigma}}^\star$ has exactly two principal directions parallel to the topography; moreover, these directions coincide with the principal directions of the mean surface stretching. Three different assumptions on the corresponding eigenvalues will differentiate three constitutive models for the flowing material. The case $\lambda_1 = \lambda_2$ will be discussed separately for each model.

[1] The matrix $(\mathcal{D}^\alpha{}_\beta)$ in the representation $\boldsymbol{D}_{\mathcal{S}} = \mathcal{D}^\alpha{}_\beta \boldsymbol{\tau}_\alpha \otimes \boldsymbol{\tau}^\beta$ is needed to obtain the eigenvalues and eigenvectors of $\boldsymbol{D}_{\mathcal{S}}$, and it has been derived in Sect. 3.2, formula (3.53).

Before proceeding to state the closure relations for the mean stress tensor $\overline{\boldsymbol{\sigma}}^{\star}$ we show how $\overline{\mathbf{P}}$ can be deduced from our assumptions. We denote by $\mathbf{C} \equiv (C^{\alpha}{}_{\beta})$ the change of basis matrix from $\{\boldsymbol{\tau}_1, \boldsymbol{\tau}_2\}$ to the basis $\{\boldsymbol{f}_1, \boldsymbol{f}_2\}$ of the tangent space to $\mathcal{S}_b$, i.e.,

$$\boldsymbol{f}_{\beta} = C^{\alpha}{}_{\beta}\boldsymbol{\tau}_{\alpha}\,, \quad \beta \in \{1, 2\}\,, \tag{5.46}$$

and mention that

$$\mathbf{C}\mathbf{C}^{T} = \mathbf{M}_0\,, \tag{5.47}$$

which holds since the basis $\{\boldsymbol{f}_1, \boldsymbol{f}_2\}$ is orthonormal and $\boldsymbol{\tau}_{\alpha} \cdot \boldsymbol{\tau}_{\beta}$ are the entries of the matrix $\mathbf{M}_0^{-1}$, see (2.48).[2] Now, recalling expression $(5.45)_1$ of $\overline{\boldsymbol{\sigma}}^{\star}$, the representation of $\overline{\boldsymbol{\sigma}}^{\star}$ in terms of $\{\boldsymbol{f}_1, \boldsymbol{f}_2, \boldsymbol{n}_b\}$ is

$$\overline{\boldsymbol{\sigma}}^{\star} = \tilde{T}^{\alpha\beta}\boldsymbol{f}_{\alpha} \otimes \boldsymbol{f}_{\beta} - \overline{p}\,\boldsymbol{n}_b \otimes \boldsymbol{n}_b\,, \tag{5.48}$$

and we have

$$(\overline{T}^{\star\alpha\beta}) = \mathbf{C}\,(\tilde{T}^{\alpha\beta})\mathbf{C}^{T}\,.$$

When combined with $(5.45)_2$ this last relation gives

$$\overline{\mathbf{P}} = \overline{p}\,\mathbf{M}_0 + \mathbf{C}\,(\tilde{T}^{\alpha\beta})\mathbf{C}^{T}\,. \tag{5.49}$$

Our assumptions on $\overline{\boldsymbol{\sigma}}^{\star}$ will immediately give $(\tilde{T}^{\alpha\beta})$, and hence $\overline{\mathbf{P}}$ can be deduced from relation (5.49). Finally, note that (5.49) holds, in fact, for any orthonormal vectors $\boldsymbol{f}_1$, $\boldsymbol{f}_2$ in the tangent space to $\mathcal{S}_b$, and not necessarily just for eigenvectors of $\boldsymbol{D}_{\mathcal{S}}$.

Model 1

If the eigenvalues of $\boldsymbol{D}_{\mathcal{S}}$ are not equal, $\lambda_1 \neq \lambda_2$, we suppose that the orthonormal eigenvectors $\boldsymbol{f}_1$, $\boldsymbol{f}_2$ of $\boldsymbol{D}_{\mathcal{S}}$ are eigenvectors of $\overline{\boldsymbol{\sigma}}^{\star}$ corresponding to the eigenvalue $-\overline{p}$, that is,[3]

$$\overline{\boldsymbol{\sigma}}^{\star} = -\overline{p}\,\boldsymbol{f}_{\alpha} \otimes \boldsymbol{f}_{\alpha} - \overline{p}\,\boldsymbol{n}_b \otimes \boldsymbol{n}_b = -\overline{p}\,\boldsymbol{I}\,.$$

We also assume that $\overline{\boldsymbol{\sigma}}^{\star} = -\overline{p}\,\boldsymbol{I}$ holds if $\lambda_1 = \lambda_2$, and thus, up to terms of order $O(\epsilon^{1+\gamma})$, the granular material is modelled as an inviscid fluid. The stresses $\tilde{T}^{\alpha\beta}$

---

[2] $\delta_{\beta\gamma} = \boldsymbol{f}_{\beta} \cdot \boldsymbol{f}_{\gamma} = (C^{\alpha}{}_{\beta}\boldsymbol{\tau}_{\alpha}) \cdot (C^{\lambda}{}_{\gamma}\boldsymbol{\tau}_{\lambda}) = C^{\alpha}{}_{\beta}C^{\lambda}{}_{\gamma}M^{-1}_{0\alpha\lambda} \iff \mathbf{I} = \mathbf{C}^{T}\mathbf{M}_0^{-1}\mathbf{C}$
$\iff \mathbf{C}^{-T}\mathbf{C}^{-1} = \mathbf{M}_0^{-1} \iff \mathbf{C}\mathbf{C}^{T} = \mathbf{M}_0$.

[3] A symmetric second order tensor $\boldsymbol{\sigma}$ on a three-dimensional Euclidean real vector space $\mathcal{V}$ has the spectral decomposition

$$\boldsymbol{\sigma} = \lambda_1 \boldsymbol{f}_1 \otimes \boldsymbol{f}_1 + \lambda_2 \boldsymbol{f}_2 \otimes \boldsymbol{f}_2 + \lambda_3 \boldsymbol{f}_3 \otimes \boldsymbol{f}_3\,,$$

where $\lambda_1, \lambda_2, \lambda_3$ are the (real) eigenvalues of $\boldsymbol{\sigma}$, and $\{\boldsymbol{f}_1, \boldsymbol{f}_2, \boldsymbol{f}_3\}$ is an orthonormal basis of eigenvectors for $\mathcal{V}$.

introduced in (5.48) are then given by the diagonal matrix $(\tilde{T}^{\alpha\beta}) = -\overline{p}\,\mathbf{I}$, and from (5.47) and (5.49) we deduce $\overline{\mathbf{P}} = \mathbf{0}$. With this we have the first constitutive model for the avalanching mass.

Model 1 *Apart from negligible terms the stress components in the depth-averaged modelling equations are as follows:*

$$\overline{\mathbf{P}} = \mathbf{0}\,, \quad \overline{\mathbf{p}} = \mathbf{0}\,, \quad \text{for } \mathbf{p}\big|_{\zeta=0} \text{ see (5.44)}\,.$$

Therefore, the extra stresses are present in the depth-averaged tangential linear momentum balance equation (4.93) (or the depth-averaged hybrid linear momentum balance equation (4.111)) only as basal shear stresses, modelled by a Coulomb bed friction law, see (5.44). The rheology of the flowing material manifests itself indirectly through the Boussinesq coefficients and the bed friction angle δ. Such a model, with plug flow velocity profile, has been studied by Bouchut and Westdickenberg [16].

Model 2

Now, again with $\lambda_1 \neq \lambda_2$, we suppose that $\boldsymbol{f}_1$, $\boldsymbol{f}_2$ are eigenvectors of $\overline{\boldsymbol{\sigma}}^{\star}$ corresponding to the eigenvalue $-k\,\overline{p}$, that is,

$$\overline{\boldsymbol{\sigma}}^{\star} = -k\,\overline{p}\,\boldsymbol{f}_\alpha \otimes \boldsymbol{f}_\alpha - \overline{p}\,\boldsymbol{n}_b \otimes \boldsymbol{n}_b\,, \tag{5.50}$$

where the *earth pressure coefficient* k is defined by

$$k \equiv \begin{cases} k^1_{act}\,, & \text{if} \quad \lambda_1 + \lambda_2 \geq 0 \\ k^1_{pass}\,, & \text{if} \quad \lambda_1 + \lambda_2 < 0 \end{cases},$$

with

$$k^1_{act/pass} \equiv \frac{2}{\cos^2\varphi}\left\{1 \mp \sqrt{1 - \sec^2\delta\,\cos^2\varphi}\right\} - 1\,. \tag{5.51}$$

In (5.51) the constant φ is the *angle of internal friction*, $\varphi > \delta$, and the minus sign corresponds to k^1_{act}, while the plus refers to k^1_{pass}. Moreover, recalling that $\overline{p} = O(\epsilon)$ and that the idea of introducing $\overline{\boldsymbol{\sigma}}^{\star}$ in (5.45) was to collect the $O(\epsilon)$ terms of $\overline{\boldsymbol{\sigma}}$, we can approximate the earth pressure coefficients $k^1_{act/pass}$ arising in (5.50) as follows: with $\tan\delta = O(\epsilon^\gamma)$ and values of the angle of internal friction $\varphi \in (30°, 40°)$, see e.g. Pudasaini and Hutter [4], we have

$$\sqrt{1 - \sec^2\delta\,\cos^2\varphi} = \sin\varphi + O(\epsilon^{2\gamma})\,,$$

and hence from (5.51) we deduce

$$\begin{aligned} k^1_{act/pass} &= \tilde{k}^1_{act/pass} + O(\epsilon^{2\gamma})\,, \\ \tilde{k}^1_{act/pass} &\equiv 2\sec^2\varphi - 1 \mp 2\sec\varphi\,\tan\varphi\,. \end{aligned} \tag{5.52}$$

Note, in passing, that

$$\tilde{k}^1_{act} < 1 \qquad \text{and} \qquad \tilde{k}^1_{pass} > 1\,.$$

Therefore, apart from the negligible terms, (5.50) emerges as

$$\overline{\boldsymbol{\sigma}}^{\star} = -\tilde{k}\,\overline{p}\,\boldsymbol{f}_{\alpha}\otimes\boldsymbol{f}_{\alpha} - \overline{p}\,\boldsymbol{n}_b\otimes\boldsymbol{n}_b\,, \tag{5.53}$$

where

$$\tilde{k} \equiv \begin{cases} \tilde{k}^1_{act}\,, & \text{if} \quad \lambda_1+\lambda_2 \geq 0 \\ \tilde{k}^1_{pass}\,, & \text{if} \quad \lambda_1+\lambda_2 < 0 \end{cases}\,. \tag{5.54}$$

Now, since

$$\boldsymbol{f}_{\alpha}\otimes\boldsymbol{f}_{\alpha} = \boldsymbol{I} - \boldsymbol{n}_b\otimes\boldsymbol{n}_b\,,$$

Equation (5.53) can be written as

$$\overline{\boldsymbol{\sigma}}^{\star} = -\tilde{k}\,\overline{p}\,(\boldsymbol{I} - \boldsymbol{n}_b\otimes\boldsymbol{n}_b) - \overline{p}\,\boldsymbol{n}_b\otimes\boldsymbol{n}_b\,.$$

This clearly shows that (5.53) makes also sense for the case $\lambda_1 = \lambda_2$, and that in (5.53) we can actually take any two orthonormal vectors $\boldsymbol{f}_1$, $\boldsymbol{f}_2$ in the tangent space to $\mathcal{S}_b$.

Thus, in Model 2 of the avalanching material we assume (5.53), in which $\boldsymbol{f}_1$, $\boldsymbol{f}_2$ are arbitrary orthonormal vectors tangent to $\mathcal{S}_b$. From (5.48) and (5.53) we deduce $(\tilde{T}^{\alpha\beta}) = -\tilde{k}\,\overline{p}\,\mathbf{I}$, so that relations (5.47) and (5.49) immediately yield

Model 2 *Apart from negligible terms the stress components in the depth-averaged modelling equations are*

$$\overline{\mathbf{P}} = (1-\tilde{k})\,\overline{p}\,\mathbf{M}_0\,, \quad \overline{\mathbf{p}} = \mathbf{0}\,, \quad \text{for } \mathbf{p}\big|_{\zeta=0} \text{ see (5.44)}\,,$$

where $\tilde{k}$ is given by (5.54), with $\tilde{k}^1_{act/pass}$ as shown in $(5.52)_2$.

Model 2 is an adapted version to the case of an arbitrary bed surface of the model due to Iverson and Denlinger [14].

Model 3

Suppose $\lambda_1 \neq \lambda_2$. Now, the ordering of the eigenvectors in the basis $\{\boldsymbol{f}_1, \boldsymbol{f}_2\}$ becomes important. We choose $\{\boldsymbol{f}_1, \boldsymbol{f}_2\}$ to be so ordered that

$$|\,\tilde{v}_\tau^1| \geq |\,\tilde{v}_\tau^2|\,, \tag{5.55}$$

where $\tilde{v}_\tau^1$, $\tilde{v}_\tau^2$ are the components of the depth-averaged tangential velocity $\overline{\boldsymbol{v}_\tau}$ with respect to this basis, i.e.,

$$\overline{\boldsymbol{v}_\tau} = \tilde{v}_\tau^1 \boldsymbol{f}_1 + \tilde{v}_\tau^2 \boldsymbol{f}_2\,.$$

Next, we assume that $\boldsymbol{f}_1, \boldsymbol{f}_2$ are eigenvectors of $\overline{\boldsymbol{\sigma}}^\star$ corresponding to the eigenvalues $-k_1\overline{p}$ and $-k_2\overline{p}$, respectively, that is,

$$\overline{\boldsymbol{\sigma}}^\star = -k_1\overline{p}\,\boldsymbol{f}_1 \otimes \boldsymbol{f}_1 - k_2\overline{p}\,\boldsymbol{f}_2 \otimes \boldsymbol{f}_2 - \overline{p}\,\boldsymbol{n}_b \otimes \boldsymbol{n}_b\,. \tag{5.56}$$

Here the *earth pressure coefficients* k_1, k_2 are given by

$$k_1 = \begin{cases} k_{act}^1\,, & \text{if} \quad \lambda_1 \geq 0 \\ k_{pass}^1\,, & \text{if} \quad \lambda_1 < 0 \end{cases}, \qquad k_2 = \begin{cases} k_{act}^2\,, & \text{if} \quad \lambda_2 \geq 0 \\ k_{pass}^2\,, & \text{if} \quad \lambda_2 < 0 \end{cases},$$

where $k_{act/pass}^1$ is defined in (5.51), and

$$k_{act/pass}^2 \equiv \frac{1}{2}\left\{k_{act/pass}^1 + 1 \mp \sqrt{\left(k_{act/pass}^1 - 1\right)^2 + 4\tan^2\delta}\right\},$$

with the same sign rule as in (5.51) and the choice of k_{act}^1 and k_{pass}^1 as depending on whether $\lambda_1 \geq 0$ or $\lambda_1 < 0$, respectively. As in the case of Model 2, the earth pressure coefficients k_1, k_2 become

$$k_1 = \tilde{k}_1 + O(\epsilon^{2\gamma})\,, \quad k_2 = \tilde{k}_2 + O(\epsilon^{2\gamma})\,,$$

where

$$\begin{aligned} \tilde{k}_1 &\equiv \begin{cases} \tilde{k}_{act}^1\,, & \text{if} \quad \lambda_1 \geq 0\,, \\ \tilde{k}_{pass}^1\,, & \text{if} \quad \lambda_1 < 0\,, \end{cases} \\ \tilde{k}_2 &\equiv \begin{cases} \tilde{k}_{act}^1\,, & \text{if} \quad \lambda_1 \geq 0\,, \quad \lambda_2 \geq 0\,, \\ \tilde{k}_{pass}^1\,, & \text{if} \quad \lambda_1 < 0\,, \quad \lambda_2 < 0\,, \\ 1\,, & \text{if} \quad \lambda_1 \geq 0\,, \quad \lambda_2 < 0\,, \quad \text{or} \quad \lambda_1 < 0\,, \quad \lambda_2 \geq 0\,, \end{cases} \end{aligned} \tag{5.57}$$

with $\tilde{k}_{act/pass}^1$ introduced in (5.52). Therefore, apart from negligible terms, assumption (5.56), stated for the case $\lambda_1 \neq \lambda_2$, emerges as

$$\overline{\boldsymbol{\sigma}}^{\star} = -\tilde{k}_1 \overline{p}\, \boldsymbol{f}_1 \otimes \boldsymbol{f}_1 - \tilde{k}_2 \overline{p}\, \boldsymbol{f}_2 \otimes \boldsymbol{f}_2 - \overline{p}\, \boldsymbol{n}_b \otimes \boldsymbol{n}_b \,,$$

or, explicitly,

$$\overline{\boldsymbol{\sigma}}^{\star} = \begin{cases} -\tilde{k}^1_{act}\, \overline{p}\, \boldsymbol{f}_\alpha \otimes \boldsymbol{f}_\alpha - \overline{p}\, \boldsymbol{n}_b \otimes \boldsymbol{n}_b \,, & \text{if} \quad \lambda_1 \geq 0\,, \quad \lambda_2 \geq 0\,, \\ -\tilde{k}^1_{pass}\, \overline{p}\, \boldsymbol{f}_\alpha \otimes \boldsymbol{f}_\alpha - \overline{p}\, \boldsymbol{n}_b \otimes \boldsymbol{n}_b \,, & \text{if} \quad \lambda_1 < 0\,, \quad \lambda_2 < 0\,, \\ -\tilde{k}^1_{act}\, \overline{p}\, \boldsymbol{f}_1 \otimes \boldsymbol{f}_1 - \overline{p}\, \boldsymbol{f}_2 \otimes \boldsymbol{f}_2 - \overline{p}\, \boldsymbol{n}_b \otimes \boldsymbol{n}_b \,, & \text{if} \quad \lambda_1 \geq 0\,, \quad \lambda_2 < 0\,, \\ -\tilde{k}^1_{pass}\, \overline{p}\, \boldsymbol{f}_1 \otimes \boldsymbol{f}_1 - \overline{p}\, \boldsymbol{f}_2 \otimes \boldsymbol{f}_2 - \overline{p}\, \boldsymbol{n}_b \otimes \boldsymbol{n}_b \,, & \text{if} \quad \lambda_1 < 0\,, \quad \lambda_2 \geq 0\,. \end{cases} \tag{5.58}$$

Now, we have only to remark that the orthonormal eigenvectors $\boldsymbol{f}_1$, $\boldsymbol{f}_2$ in $(5.58)_{1,2}$ can be replaced by any two orthonormal vectors in the tangent space to $\mathcal{S}_b$, and so $(5.58)_{1,2}$ can be also assumed for the case $\lambda_1 = \lambda_2$. Clearly, in $(5.58)_{3,4}$ we have $\lambda_1 \neq \lambda_2$, and hence we have not to refer to $(5.58)_{3,4}$ when $\lambda_1 = \lambda_2$.

To conclude, in Model 3 of the flowing material we take (5.58), where $\boldsymbol{f}_1$, $\boldsymbol{f}_2$ arising in $(5.58)_{1,2}$ are orthonormal vectors tangent to $\mathcal{S}_b$ (be they eigenvectors of $\boldsymbol{D}_{\mathcal{S}}$ or not), and $\boldsymbol{f}_1$, $\boldsymbol{f}_2$ in $(5.58)_{3,4}$ are eigenvectors of $\boldsymbol{D}_{\mathcal{S}}$, ordered as indicated in (5.55). Comparison of (5.48) and (5.58) implies

$$(\tilde{T}^{\alpha\beta}) = -\overline{p} \begin{pmatrix} \tilde{k}_1 & 0 \\ 0 & \tilde{k}_2 \end{pmatrix},$$

and from (5.49) we deduce

Model 3 *Apart from negligible terms the stress components in the depth-averaged modelling equations are*

$$\overline{\mathbf{P}} = \overline{p}\, \mathbf{M}_0 - \overline{p}\, \mathbf{C} \begin{pmatrix} \tilde{k}_1 & 0 \\ 0 & \tilde{k}_2 \end{pmatrix} \mathbf{C}^T \,, \quad \overline{\mathbf{p}} = \mathbf{0}\,, \quad \text{for } \mathbf{p}\big|_{\zeta=0} \text{ see (5.44)}\,,$$

where $\tilde{k}_1, \tilde{k}_2$ are defined in (5.57), with $\tilde{k}^1_{act/pass}$ as shown in $(5.52)_2$.

Model 3 is a version adapted to arbitrary topography of the Savage-Hutter model [17, 18]. Clearly, the bulk stresses in Models 2 and 3 of the flowing material depend on the angle of internal friction, but are independent of the basal friction angle. The Boussinesq coefficients in Models 1–3 may be assumed at will.

Remark For a plug flow velocity profile, $\mathbf{v} = \mathbf{v}(\boldsymbol{\xi}, t)$, and up to $O(\epsilon)$ terms, we will show below that the depth-average of the strain-rate tensor $\boldsymbol{D}$ is related to the mean surface stretching $\boldsymbol{D}_{\mathcal{S}}$ according to

$$\overline{\boldsymbol{D}} = \mathcal{D}^{\alpha}{}_{\beta} \boldsymbol{\tau}_\alpha \otimes \boldsymbol{\tau}^\beta + \overline{D^{33}}\, \boldsymbol{n}_b \otimes \boldsymbol{n}_b \,, \quad \boldsymbol{D}_{\mathcal{S}} = \mathcal{D}^{\alpha}{}_{\beta} \boldsymbol{\tau}_\alpha \otimes \boldsymbol{\tau}^\beta \,. \tag{5.59}$$

Here, it is understood that the $O(\epsilon)$ terms in the mean surface stretching $\boldsymbol{D}_{\mathcal{S}}$ and $\overline{D^{33}}$ have been neglected. Thus, relating $\overline{\boldsymbol{\sigma}}^{\star}$ in Models 1, 2, 3 to the mean surface stretching $\boldsymbol{D}_{\mathcal{S}}$ is equivalent to relating $\overline{\boldsymbol{\sigma}}^{\star}$ to the depth-averaged strain-rate tensor, $\overline{\boldsymbol{D}}$. Moreover, comparison of expression (5.45) for $\overline{\boldsymbol{\sigma}}^{\star}$ with expression (5.59) of $\overline{\boldsymbol{D}}$ reveals that, in Models 1–3 applied to a plug flow, $\overline{\boldsymbol{\sigma}}^{\star}$ and $\overline{\boldsymbol{D}}$ ($\overline{\boldsymbol{D}}$, as given up to $O(\epsilon)$ terms) share the same principal directions. This remark makes plausible the conjecture in Models 1–3 (not necessarily connected to a plug flow) on the common principal directions of $\overline{\boldsymbol{\sigma}}^{\star}$ and $\boldsymbol{D}_{\mathcal{S}}$. The proof of $(5.59)_1$ is almost immediate: with $\mathbf{v} = \mathbf{v}(\boldsymbol{\xi}, t)$ we obtain

$$\overline{\boldsymbol{v}_{\tau}} = \overline{v^{\alpha}\boldsymbol{g}_{\alpha}} = \overline{v^{\alpha}\boldsymbol{\tau}_{\alpha}} + O(\epsilon) = \overline{v^{\alpha}}\boldsymbol{\tau}_{\alpha} + O(\epsilon) = v^{\alpha}\boldsymbol{\tau}_{\alpha} + O(\epsilon)\,,$$

and hence formula (3.53) for the components $\mathcal{D}^{\alpha}{}_{\beta}$ of the mean surface stretching emerges as

$$\begin{aligned}(\mathcal{D}^{\alpha}{}_{\beta}) = \frac{1}{2}\Bigg\{&\operatorname{Grad}\mathbf{v} + \mathbf{F}^{-1}\left(\frac{\partial \mathbf{F}}{\partial \xi^{\gamma}}\,\mathbf{v}\otimes\mathbf{e}_{\gamma} + \mathbf{s}\otimes\widetilde{\mathbf{H}}\mathbf{v}\right)\\ &+ \mathbf{M}_0\left[\operatorname{Grad}\mathbf{v} + \mathbf{F}^{-1}\left(\frac{\partial \mathbf{F}}{\partial \xi^{\gamma}}\,\mathbf{v}\otimes\mathbf{e}_{\gamma} + \mathbf{s}\otimes\widetilde{\mathbf{H}}\mathbf{v}\right)\right]^{T}\mathbf{M}_0^{-1}\Bigg\} + O(\epsilon)\,.\end{aligned}$$

On the other hand, see $(3.45)_1$,

$$\begin{aligned}\mathbf{D} = \frac{1}{2}\Bigg\{&\left[\operatorname{Grad}\mathbf{v} + \mathbf{F}^{-1}\left(\frac{\partial \mathbf{F}}{\partial \xi^{\alpha}}\,\mathbf{v}\otimes\mathbf{e}_{\alpha} + \mathbf{s}\otimes\widetilde{\mathbf{H}}\mathbf{v}\right)\right]\mathbf{M}_0\\ &+ \mathbf{M}_0\left[\operatorname{Grad}\mathbf{v} + \mathbf{F}^{-1}\left(\frac{\partial \mathbf{F}}{\partial \xi^{\alpha}}\,\mathbf{v}\otimes\mathbf{e}_{\alpha} + \mathbf{s}\otimes\widetilde{\mathbf{H}}\mathbf{v}\right)\right]^{T}\Bigg\} + O(\epsilon)\,,\end{aligned}$$

showing that

$$\overline{\mathbf{D}} = (\mathcal{D}^{\alpha}{}_{\beta})\mathbf{M}_0 + O(\epsilon)\,, \tag{5.60}$$

where the $O(\epsilon)$ terms in $(\mathcal{D}^{\alpha}{}_{\beta})$ are assumed to be neglected. Now, using the assumption $\mathbf{v} = \mathbf{v}(\boldsymbol{\xi}, t)$ and expression $(3.45)_2$ of the components $\mathbf{d}$ of the strain-rate tensor $\boldsymbol{D}$, we infer

$$\begin{aligned}\boldsymbol{D} &= D^{ij}\boldsymbol{g}_i\otimes\boldsymbol{g}_j\\ &= D^{\alpha\beta}\boldsymbol{g}_{\alpha}\otimes\boldsymbol{g}_{\beta} + D^{\alpha 3}(\boldsymbol{g}_{\alpha}\otimes\boldsymbol{n}_b + \boldsymbol{n}_b\otimes\boldsymbol{g}_{\alpha}) + D^{33}\boldsymbol{n}_b\otimes\boldsymbol{n}_b\\ &= D^{\alpha\beta}\boldsymbol{\tau}_{\alpha}\otimes\boldsymbol{\tau}_{\beta} + D^{33}\boldsymbol{n}_b\otimes\boldsymbol{n}_b + O(\epsilon)\,.\end{aligned}$$

Therefore, with (2.50) and (5.60) we deduce

$$\begin{aligned}\overline{\boldsymbol{D}} &= \overline{D^{\alpha\beta}}\boldsymbol{\tau}_{\alpha}\otimes\boldsymbol{\tau}_{\beta} + \overline{D^{33}}\boldsymbol{n}_b\otimes\boldsymbol{n}_b + O(\epsilon)\\ &= \overline{D^{\alpha\beta}}\tilde{\phi}_{\beta\gamma}\boldsymbol{\tau}_{\alpha}\otimes\boldsymbol{\tau}^{\gamma} + \overline{D^{33}}\boldsymbol{n}_b\otimes\boldsymbol{n}_b + O(\epsilon)\\ &= \mathcal{D}^{\alpha}{}_{\gamma}\boldsymbol{\tau}_{\alpha}\otimes\boldsymbol{\tau}^{\gamma} + \overline{D^{33}}\boldsymbol{n}_b\otimes\boldsymbol{n}_b + O(\epsilon)\,,\end{aligned}$$

which proves $(5.59)_1$.

5.3 Erosion/Deposition Rate Law

To close the system of depth-averaged equations in the case of an active topographic bed associated with erosion/deposition processes, we are left with the prescription of the erosion/deposition rate $\mathcal{U}$. A closure relation for $\mathcal{U}$ will be called *erosion/deposition law*. There are many proposals for such laws, e.g. Pitman et al. [19], Naaim et al. [20], Eglit and Demidov [21] or Sovilla et al. [22]. Here we present the erosion/deposition rate suggested by Tai and Kuo [23]; it will be later used in numerical simulations. A single formula for $\mathcal{U}$ catches the effects of both erosion and deposition, and is based on a criterion which identifies the three processes of the topographic bed—erosion, deposition and no erosion/deposition (stagnancy).

Motivated by experimental observation it is assumed that the mechanism of erosion/deposition in a granular flow is controlled by

- two parameters,
  - the *threshold velocity*, v_{th},
  - the *neutral angle*, θ_n, that is, the maximum stable slope angle, often called the *angle of repose*,
- the magnitude of the *tangential velocity at the basal surface*, $\|\boldsymbol{v}_\tau\|\big|_{\zeta=0}$, and
- the *local inclination angle*, θ, defined as

$$\theta = \arcsin\left(\frac{-v_\tau}{\|\boldsymbol{v}_\tau\|}\Big|_{\zeta=0}\right), \tag{5.61}$$

where v_τ is the component of the tangential velocity $\boldsymbol{v}_\tau$ in the vertical direction, see (2.97). Specifically,

*The **threshold criterion** predicting the onset of erosion/deposition mechanism states that stagnancy of the topographic surface, erosion and deposition arise according to the rules*

$$\begin{aligned}
&\text{stagnancy } (\mathcal{U}=0): \quad \text{for } \theta < \theta_n \text{ and } \|\boldsymbol{v}_\tau\|\big|_{\zeta=0} > v_{\text{th}}\,,\\
&\text{deposition } (\mathcal{U}>0): \quad \text{for } \theta < \theta_n \text{ and } \|\boldsymbol{v}_\tau\|\big|_{\zeta=0} < v_{\text{th}}\,,\\
&\text{erosion } \quad (\mathcal{U}<0): \quad \text{for } \theta > \theta_n\,.
\end{aligned} \tag{5.62}$$

In the simplistic approach (5.62), entrainment occurs when the inclination angle is larger than the angle of repose. However, small inclination angle does not guarantee the occurrence of deposition. The kinetic energy $\rho\|\boldsymbol{v}_\tau\|^2/2$ at the basal surface has a significant impact: deposition takes place only when both the inclination angle is

less than the angle of repose, and the kinetic energy $\rho\|\boldsymbol{v}_\tau\|^2/2$ is less than a threshold value. This threshold value is given in terms of a threshold flow speed, v_{th}, so that

$$\|\boldsymbol{v}_\tau\|\big|_{\zeta=0} < v_{\text{th}} \quad \text{or} \quad \|\boldsymbol{v}_\tau\|\big|_{\zeta=0} > v_{\text{th}}$$

expresses the relation between the kinetic energy $\rho\|\boldsymbol{v}_\tau\|^2\big|_{\zeta=0}/2$ and the threshold kinetic energy $\rho {v_{\text{th}}}^2/2$. For the threshold velocity v_{th} the following ad hoc relation,

$$v_{\text{th}} = \alpha_v(\theta - \theta_n)^2\,, \tag{5.63}$$

is assumed. Here α_v is an empirical coefficient, and the angles are measured in radians. By (5.63) it is meant that

- small positive inclination angle θ, or negative θ (upslope movement), implies a large value of v_{th}, indicating that deposition begins to take place at a higher flow speed (kinetic energy);
- when the granular medium flows on a slope around the neutral angle, deposition only takes place when the flow speed is almost zero.

Figure 5.1 illustrates the three states—stagnancy, erosion, deposition—with respect to the inclination angle and the corresponding threshold speed.

Now, the erosion/deposition rate $\mathcal{U}$ is assumed to be proportional to the product of the difference $\theta_n - \theta$ and a function $\tilde{h}$ depending on the local thickness h of the flowing layer. That is, we have the following proposal for $\mathcal{U}$.

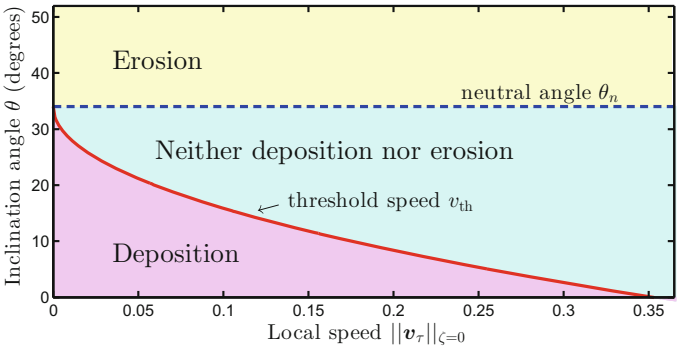

Fig. 5.1 The three states of the topographic bed with respect to the local speed $\|\boldsymbol{v}_\tau\|_{\zeta=0}$ and the inclination angle θ. The neutral angle is $\theta_n = 34°$ and the threshold speed v_{th} (as assumed in (5.63)) is computed with $\alpha_v = 1.0$. (Reproduced from [24] with permission.)

The erosion/deposition rate (Tai and Kuo [23])
The erosion/deposition rate $\mathcal{U}$ is taken to be

$$\mathcal{U} = \mathcal{F}_e\,(\theta_n - \theta)\,\tilde{h}\,, \tag{5.64}$$

with the proportionality coefficient $\mathcal{F}_e$ and the function $\tilde{h}$ given by

$$\begin{aligned} \mathcal{F}_e &= \alpha_e\Big\{\mathcal{F}_{\text{reg}}\,\mathcal{H}(\theta_n - \theta) + \mathcal{H}(\theta - \theta_n)\Big\}\,, \\ \tilde{h} &= h + \alpha_h\sqrt{h}\,, \end{aligned} \tag{5.65}$$

where

- *α_e is an empirical constant rate factor;*
- *$\mathcal{H}$ stands for the Heaviside step function,*

$$\mathcal{H}(x) \equiv \begin{cases} 0, & x < 0 \\ 1, & x \geq 0\,; \end{cases}$$

- *$\mathcal{F}_{\text{reg}}$ is defined by*

$$\mathcal{F}_{\text{reg}} = \tfrac{1}{2}\left\{1 - \tanh\left(e_\alpha\Big(\|\boldsymbol{v}_\tau\|\big|_{\zeta=0} - v_{\text{th}}\Big)\right)\right\}\,, \tag{5.66}$$

  with a constant transition steepness factor e_α;
- *the term $\alpha_h\sqrt{h}$ in (5.65)$_2$, with a constant adjustment factor α_h, is intended to better account for the influence of the layer depth h on the erosion/deposition rate when the flow is very thin.*

It is clear that the first $\mathcal{H}$ in (5.65) is not zero for deposition/stagnancy, and the second one is not zero for erosion. The function $\mathcal{F}_e$ incorporates the velocities v_{th}, $\|\boldsymbol{v}_\tau\|\big|_{\zeta=0}$ into the erosion/deposition rate $\mathcal{U}$ and, at the same time, distinguishes the deposition from stagnancy. Explicitly, (5.65) reads

$$\begin{aligned} &\text{stagnancy and deposition } (\theta < \theta_n): && \mathcal{F}_e = \alpha_e\mathcal{F}_{\text{reg}}\,(\theta_n - \theta)\tilde{h}\,, \\ &\text{erosion } (\theta > \theta_n): && \mathcal{F}_e = \alpha_e\,(\theta_n - \theta)\tilde{h}\,. \end{aligned}$$

The dependence of the regularization function $\mathcal{F}_{\text{reg}}$ on $\|\boldsymbol{v}_\tau\|\big|_{\zeta=0}$ for given v_{th} and α_e is shown in Fig. 5.2.

Remark Definition (5.61) of the inclination angle θ uses the tangential velocity vector $\boldsymbol{v}_\tau$ evaluated on the topographic surface. It is useful to express θ in terms

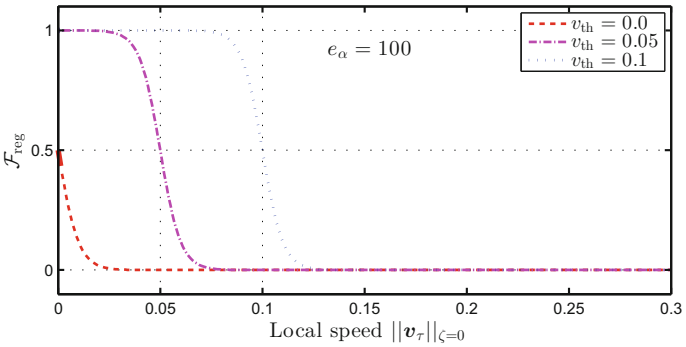

Fig. 5.2 The regularization function $\mathcal{F}_{\rm reg}$ for $v_{\rm th} = 0.0,\ 0.05$ and 0.1, where $e_\alpha = 100$ is applied

of the mean tangential velocity $\overline{\mathbf{v}}$, which is one of the unknowns in the system of modelling equations. Thus, it is not difficult to see that

$$\theta = \arcsin\left(\frac{-\mathrm{Grad}\,\tilde{b}\cdot\overline{\mathbf{v}}}{\sqrt{\mathbf{M}_0^{-1}\overline{\mathbf{v}}\cdot\overline{\mathbf{v}}}}\right). \tag{5.67}$$

Indeed, recalling the assumption

$$\mathbf{v}\big|_{\zeta=0} = \chi_b\overline{\mathbf{v}}\,,\quad \chi_b > 0\,,$$

from (2.97) we have

$$v_\tau\big|_{\zeta=0} = \frac{1}{c}\mathbf{s}\cdot\mathbf{B}\mathbf{v}\Big|_{\zeta=0} = \mathrm{grad}\,b\cdot\mathbf{F}\mathbf{v}\big|_{\zeta=0} = \chi_b\,\mathrm{grad}\,b\cdot\mathbf{F}\overline{\mathbf{v}} = \chi_b\mathrm{Grad}\,\tilde{b}\cdot\overline{\mathbf{v}}\,.$$

Then, formula (2.93) gives

$$\|\boldsymbol{v}_\tau\|\big|_{\zeta=0} = \chi_b\sqrt{\mathbf{M}_0^{-1}\overline{\mathbf{v}}\cdot\overline{\mathbf{v}}}\,.$$

It only remains to insert the above expressions of $v_\tau\big|_{\zeta=0}$ and $\|\boldsymbol{v}_\tau\|\big|_{\zeta=0}$ into (5.61) to deduce (5.67). We note that, in the paper by Tai et al. [25], expression $\mathrm{Grad}\,\tilde{b}\cdot\overline{\mathbf{v}}$ in (5.67) is used in the form $\mathrm{grad}\,b\cdot\mathbf{F}\overline{\mathbf{v}}$, and $\mathbf{F}\overline{\mathbf{v}}$ is interpreted as the depth-averaged horizontal components of the tangential velocity vector $\boldsymbol{v}_\tau$. That is, $\overline{\mathbb{v}}_\tau$, see (4.101). Relation $\mathbf{F}\overline{\mathbf{v}} = \overline{\mathbb{v}}_\tau$ holds apart of negligible terms, since [25] treats the case of slightly curved basal surface.

5.4 Example—One-Dimensional Thin Flow on a Slightly Curved Surface

In this section we write the modelling equations (4.97) and (4.98) for a special type of topographic surface and for special kinematic/constitutive assumptions on the flowing material. Moreover, we will specify the change of coordinates

$$(x,\ y) \quad \longleftrightarrow \quad (\xi^1,\ \xi^2)\,, \tag{5.68}$$

an issue which was barely mentioned in the previous sections.

Thus, we take a slightly curved basal surface, $\mathcal{K} = O(\epsilon^{\gamma})$, given by

$$x_1 = x\,, \quad x_2 = y\,, \quad x_3 = b(x,t)\,, \tag{5.69}$$

see Fig. 5.3. We assume that the velocity vector $\boldsymbol{v}$ and the stress tensor $\boldsymbol{\sigma}$ are independent of the variable x_2, and that $\boldsymbol{v}$ has a negligible component in the x_2 direction. One says that the flow is two-dimensional and takes place in the plane Ox_1x_3. In the depth-averaging approach the problem will then become one-dimensional.

We consider the material as being described by the Mohr-Coulomb type Model 2 or Model 3 presented in Sect. 5.2. Since in these models the shear stresses $\overline{\mathbf{p}}$ are negligibly small, the depth-averaged modelling equations (4.97) and (4.98), derived in the conventional route, coincide with (4.113) and (4.114), which are deduced following the non-conventional route.

We choose two changes of variables (5.68), and for each case we explicitly write the system of modelling equations corresponding to (5.69) and to the constitutive laws designated as Model 2 and Model 3.

Option 1—Parameterizing the topographic surface by arc lengths Generally, the coordinates $(\xi^1,\ \xi^2)$ of a point Q on S_b can be taken as the arc lengths measured on the curves obtained by intersecting S_b with the planes $x_1 =$ constant and $x_2 =$ constant passing through Q. For a rigid topographic bed these parameters have been used by De Toni and Scotton [26], and for erodible beds of the form (5.69) by Bouchut et al. [27].

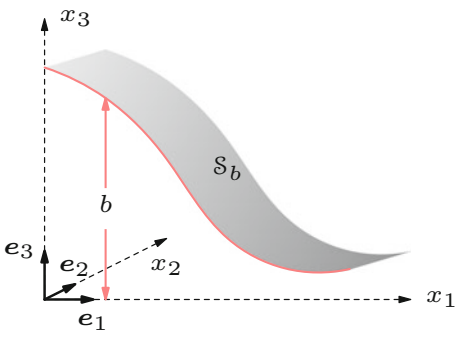

Fig. 5.3 The topographic surface $x_1 = x,\ x_2 = y,$ $x_3 = b(x,t)$

We follow this idea for the case (5.69) which is treated here and define the arc length

$$s(x,t) \equiv \int_{x_0}^{x} \sqrt{1+(\partial b/\partial x)^2}\, dx' \tag{5.70}$$

along the curve

$$x_1 = x\,, \quad x_2 = \text{constant}\,, \quad x_3 = b(x,t)\,,$$

where $x_0 =$ constant is such that the plane $x_1 = x_0$ does not intersect the avalanche body at any moment t. This choice of x_0 allows to assume that $\mathcal{U} = 0$ at those points on $\mathcal{S}_b$ where $x_1 = x_0$ (see (5.85) below how this condition is applied). We consider the time dependent transformation

$$\xi^1 = s(x,t)\,, \quad \xi^2 = y \quad \Longleftrightarrow \quad x = x(\xi^1,t)\,, \quad y = \xi^2\,, \tag{5.71}$$

which induces the parameterization

$$x_1 = x(\xi^1,t)\,, \quad x_2 = \xi^2\,, \quad x_3 = b\,(x(\xi^1,t),\ t) = \tilde{b}(\xi^1,t)$$

of $\mathcal{S}_b$, see (5.69). For the non-negligible component of the depth-averaged velocity we introduce the notation V, that is,

$$\overline{\mathbf{v}} \equiv (V,\ 0)^T\,, \quad V = V(\xi^1,t)\,.$$

Corresponding to the transformation (5.71) we must determine the quantities c, $\mathbf{s}$, $\mathbf{F}$, J_0, $\mathbf{M}_0$, a, $\mathbf{u}_{\mathcal{S}}$ and the stresses $\overline{\mathbf{P}}$, $\mathbf{p}\big|_{\zeta=0}$ as functions of ξ^1 and t. First, we have

$$c = \frac{1}{\sqrt{1+(\partial b/\partial x)^2}}\,, \quad \mathbf{s} = \begin{pmatrix} c\,\dfrac{\partial b}{\partial x},\ 0 \end{pmatrix}^T\,, \quad \mathbf{F} = \begin{pmatrix} c & 0 \\ 0 & 1 \end{pmatrix}\,, \tag{5.72}$$

see (2.33) and (2.45). We can express $\partial b/\partial x$ as a function of the coordinate ξ^1 and time t as follows: It is clear that

$$\frac{\partial b}{\partial x} = \frac{\partial \tilde{b}}{\partial \xi^1}\frac{\partial \xi^1}{\partial x} = \sqrt{1+\left(\frac{\partial b}{\partial x}\right)^2}\,\frac{\partial \tilde{b}}{\partial \xi^1}\,, \tag{5.73}$$

and hence, solving for $\partial b/\partial x$,

$$\frac{\partial b}{\partial x} = \frac{\partial \tilde{b}/\partial \xi^1}{\sqrt{1-(\partial \tilde{b}/\partial \xi^1)^2}}\,. \tag{5.74}$$

Therefore, we have c (as well as $\mathbf{F}$, see $(5.72)_3$) and $\mathbf{s}$ as functions of (ξ^1, t),

$$c = \sqrt{1 - (\partial\tilde{b}/\partial\xi^1)^2}\,, \quad \mathbf{s} = \left(\frac{\partial\tilde{b}}{\partial\xi^1}\,,\ 0\right)^T. \tag{5.75}$$

In particular, note that $\partial b/\partial x$ appears as

$$\frac{\partial b}{\partial x} = \frac{1}{c}\frac{\partial\tilde{b}}{\partial\xi^1}\,, \tag{5.76}$$

see (5.73) or (5.74). Then, from $(2.84)_2$, (2.50) and (5.72) we deduce

$$J_0 = \frac{1}{c}\det\mathbf{F} = 1\,, \quad \mathbf{M}_0 = \mathbf{F}^{-1}(\mathbf{I} - \mathbf{s}\otimes\mathbf{s})\mathbf{F}^{-T} = \mathbf{I}\,. \tag{5.77}$$

Next,

$$\mathbf{W} = \operatorname{grad}\mathbf{s}\,,$$

see $(2.41)_2$, so that elementary computations yield

$$\Omega \equiv \frac{1}{2}\operatorname{tr}\mathbf{W} = \frac{1}{2}\,c^3\,\frac{\partial^2 b}{\partial x^2}\,. \tag{5.78}$$

With (5.76) and $(5.74)_1$,

$$\frac{\partial^2 b}{\partial x^2} = \frac{\partial}{\partial x}\left(\frac{\partial b}{\partial x}\right) = \frac{\partial}{\partial\xi^1}\left(\frac{\partial b}{\partial x}\right)\frac{\partial\xi^1}{\partial x} = \frac{1}{c^4}\,\frac{\partial^2\tilde{b}}{\partial\xi^{1\,2}}\,,$$

implying

$$\Omega = \frac{1}{2c}\,\frac{\partial^2\tilde{b}}{\partial\xi^{1\,2}}\,. \tag{5.79}$$

Furthermore, by definition $(2.38)_2$ of $\mathbf{H}$ we have

$$\mathbf{H} \equiv \operatorname{grad}(\operatorname{grad} b) = \begin{pmatrix} \partial^2 b/\partial x^2 & 0 \\ 0 & 0 \end{pmatrix},$$

so that, see $(2.49)_2$,

$$\tilde{\mathbf{H}} = c\mathbf{F}^T\mathbf{H}\mathbf{F} = \begin{pmatrix} 2\Omega & 0 \\ 0 & 0 \end{pmatrix}, \tag{5.80}$$

and hence the scalar $a \equiv \widetilde{\mathbf{H}}\overline{\mathbf{v}}\cdot\overline{\mathbf{v}}$ is given by

$$a = 2\Omega V^2\,,$$

with Ω shown in (5.79).

Now we prove that, under small curvature assumption, $\mathcal{H} = O(\epsilon^{\gamma'})$, for the quantity $\mathbf{u}_{\mathcal{S}}$ defined in $(2.66)_2$ we have

$$\mathbf{u}_{\mathcal{S}} = O(\epsilon^{1+\gamma'}) . \tag{5.81}$$

From $(2.66)_1$ and (5.71) it follows that

$$\mathbf{v}_{\mathcal{S}} = \left(\frac{\partial x}{\partial t} , 0 \right)^T ,$$

and so formula (2.69) for $\mathbf{u}_{\mathcal{S}}$ yields

$$\mathbf{u}_{\mathcal{S}} = \left(\frac{1}{c} \left(\frac{\partial x}{\partial t} + c\,\mathcal{U} \frac{\partial b}{\partial x} \right) , 0 \right)^T . \tag{5.82}$$

In this expression $\partial x/\partial t$ will be approximated as follows. By differentiating the identity $x = x(\xi^1(x,t),t)$ with respect to t we obtain

$$0 = \frac{\partial x}{\partial t} + \frac{\partial x}{\partial \xi^1} \frac{\partial \xi^1}{\partial t} ,$$

which implies, see (5.70) and $(5.72)_1$,

$$\frac{\partial x}{\partial t} = -\frac{\partial x}{\partial \xi^1} \frac{\partial \xi^1}{\partial t} = -c \frac{\partial \xi^1}{\partial t} = -c \frac{\partial}{\partial t} \int_{x_0}^{x} \frac{1}{c}\, dx' = c \int_{x_0}^{x} \frac{1}{c^2} \frac{\partial c}{\partial t}\, dx' . \tag{5.83}$$

Recalling that $\mathcal{U} = c\ \partial b/\partial t$, see (2.63), from $(5.72)_1$ we have

$$\frac{\partial c}{\partial t} = -c^3 \frac{\partial b}{\partial x} \frac{\partial^2 b}{\partial t \partial x} = -c^3 \frac{\partial b}{\partial x} \frac{\partial}{\partial x} \left(\frac{1}{c} \mathcal{U} \right) = c^4 \mathcal{U} \frac{\partial^2 b}{\partial^2 x} - c^2 \frac{\partial}{\partial x} \left(\mathcal{U} \frac{\partial b}{\partial x} \right) .$$

Since $\Omega = O(\epsilon^{\gamma'})$ and $\mathcal{U} = O(\epsilon)$, the first term on the right-hand side of the above expression of $\partial c/\partial t$ is negligibly small, so that

$$\frac{\partial c}{\partial t} = -c^2 \frac{\partial}{\partial x} \left(\mathcal{U} \frac{\partial b}{\partial x} \right) + O(\epsilon^{1+\gamma'}) . \tag{5.84}$$

Introduction of $\partial c/\partial t$ as given by (5.84) into (5.83) yields

$$\frac{\partial x}{\partial t} = -c\,\mathcal{U} \frac{\partial b}{\partial x} + c \left\{ \mathcal{U} \frac{\partial b}{\partial x} \right\}_{x=x_0} + O(\epsilon^{1+\gamma'}) = -c\,\mathcal{U} \frac{\partial b}{\partial x} + O(\epsilon^{1+\gamma'}) . \tag{5.85}$$

Finally, substitution of $\partial x/\partial t$ as previously deduced into (5.82) shows (5.81).

Next, let us analyse the closure relations for the stresses arising in the depth-averaged modelling equations. We adopt the Mohr-Coulomb type Models 2 and 3 from Sect. 5.2. We will see that for the one-dimensional case discussed here there is no distinction between the emerging modelling equations in each of these models. First we deduce the eigenvalues and eigenvectors of the mean surface stretching tensor, see Sect. 5.2. The tangential velocity vector $\boldsymbol{v}_\tau$ is given by

$$\boldsymbol{v}_\tau = v^\alpha \boldsymbol{g}_\alpha = \left(v^\alpha - \zeta\, \widetilde{W}^\alpha{}_\beta v^\beta\right) \boldsymbol{\tau}_\alpha \,,$$

so that, when $\mathcal{H} = O(\epsilon^\gamma)$, we have

$$\overline{\boldsymbol{v}}_\tau = \overline{v^\alpha}\boldsymbol{\tau}_\alpha + O(\epsilon^{1+\gamma}) = V\boldsymbol{\tau}_1 + O(\epsilon^{1+\gamma}) \,.$$

Consequently, the components $\mathcal{D}^\alpha{}_\beta$ of the mean surface strain-rate are computed with formula (3.53) in which

$$\mathbf{u} = \overline{\mathbf{v}} = (V, 0)^T .$$

Straightforward calculations give

$$(\mathcal{D}^\alpha{}_\beta) = \begin{pmatrix} \dfrac{\partial V}{\partial \xi^1} & 0 \\ 0 & 0 \end{pmatrix},$$

from which we deduce the eigenvalues

$$\lambda_1 = \partial V / \partial \xi^1 \,, \quad \lambda_2 = 0 \,,$$

and the eigenvectors

$$\boldsymbol{f}_1 = \boldsymbol{\tau}_1 \,, \quad \boldsymbol{f}_2 = \boldsymbol{\tau}_2 \,,$$

of the mean surface stretching $\boldsymbol{D}_{\mathcal{S}}$. The two eigenvectors $\boldsymbol{f}_1$ and $\boldsymbol{f}_2$ are ordered as required by Model 3, and the change of basis matrix $\mathbf{C}$ from $\{\boldsymbol{\tau}_1, \boldsymbol{\tau}_2\}$ to $\{\boldsymbol{f}_1, \boldsymbol{f}_2\}$ is $\mathbf{C} = \mathbf{I}$.

Therefore, with $(5.77)_2$ the averaged stresses $\overline{\mathbf{P}}$ in Model 2 turn into

$$\overline{\mathbf{P}} = (1 - \tilde{k})\, \overline{p}\, \mathbf{I} \,, \tag{5.86}$$

where $\tilde{k}$ stands for $\tilde{k}_1$ which simplifies to

$$\tilde{k} \equiv \tilde{k}_1 = \begin{cases} \tilde{k}^1_{act}, & \text{if} \quad \lambda_1 \geq 0 \,, \\ \tilde{k}^1_{pass}, & \text{if} \quad \lambda_1 < 0 \,, \end{cases} \tag{5.87}$$

with $\tilde{k}^1_{act/pass}$ as shown in (5.52)$_2$. Then, recalling that $\mathbf{C} = \mathbf{I}$, Model 3 is described by the averaged stresses

$$\overline{\mathbf{P}} = \overline{p}\,\mathbf{I} - \overline{p}\begin{pmatrix} \tilde{k} & 0 \\ 0 & \tilde{k}_2 \end{pmatrix}, \tag{5.88}$$

where $\tilde{k}_2$ defined in (5.57) takes the form

$$\tilde{k}_2 = \begin{cases} \tilde{k}^1_{act}, & \text{if} \quad \lambda_1 \geq 0\,, \\ 1, & \text{if} \quad \lambda_1 < 0\,. \end{cases} \tag{5.89}$$

Although $\overline{\mathbf{P}}$ has different expressions in the two models, when inserting $\overline{\mathbf{P}}$ as given by (5.86) and (5.88) into the depth-averaged tangential linear momentum balance equation (4.114) the emerging equations are the same. Indeed, in each case we obtain

$$\begin{aligned} \frac{\partial}{\partial t}\{chV\} + \frac{\partial}{\partial \xi^1}\left\{ch\left(m_2V^2 + \tfrac{1}{2}ch\tilde{k}\right)\right\} = -h\left(c + 2m_2\Omega V^2 + V\frac{\partial \mathcal{U}}{\partial \xi^1}\right)\frac{\partial \tilde{b}}{\partial \xi^1} \\ -\frac{\rho_b}{\rho_0}\chi_b c\,\mathcal{U}V - ch(\tan\delta)\left\{c + 2m_2\Omega V^2\right\}_+ \operatorname{sgn} V\,. \end{aligned} \tag{5.90}$$

We may therefore say that Model 2 and Model 3 are indistinguishable in the one-dimensional case discussed here. Equation (5.90) can be simplified by performing the time differentiation on the left-hand side as[4]

$$\frac{\partial}{\partial t}\{chV\} = \frac{\partial c}{\partial t}hV + c\frac{\partial hV}{\partial t}\,,$$

and using

$$\frac{\partial c}{\partial t} = -\frac{\partial \tilde{b}}{\partial \xi^1}\frac{\partial \mathcal{U}}{\partial \xi^1}\,,$$

see Exercise 2.8. We record the result below, together with the depth-averaged mass balance equation (4.97) adapted to the one-dimensional thin flow, and with the equation satisfied by the bed elevation b,

$$\frac{\partial \tilde{b}}{\partial t} = c\,\mathcal{U} + O(\epsilon^{1+\gamma'})\,,$$

which can be deduced by using (2.71).

[4] To avoid this step one could have worked on the form (A.3) of the depth-averaged linear momentum balance equation, written for the case $\mathcal{H} = O(\epsilon^{\gamma'})$.

One-dimensional thin flow of Mohr-Coulomb type—using the arc lengths to parameterize the topographic surface

Consider

- the basal surface (5.69) with curvature $\Omega = O(\epsilon^{\gamma'}),\ 0 < \gamma' < 1$,
- the change of coordinates (5.71),
- the Mohr-Coulomb type Model 2 or Model 3.

Apart from negligible terms the depth-averaged mass and linear momentum balance equations (4.97) and (4.98) emerge as

$$\begin{aligned} \frac{\partial h}{\partial t} + \frac{\partial hV}{\partial \xi^1} &= -\frac{\rho_b}{\rho_0}\mathcal{U}\,, \\ \frac{\partial}{\partial t}\{hV\} + \frac{\partial}{\partial \xi^1}\left\{h\left(m_2 V^2 + \tfrac{1}{2}ch\tilde{k}\right)\right\} &= -h\frac{\partial \tilde{b}}{\partial \xi^1} - \frac{\rho_b}{\rho_0}\chi_b \mathcal{U}V \\ &\quad -h(\tan\delta)\left\{c + 2m_2\Omega V^2\right\}_+ \operatorname{sgn} V\,. \end{aligned} \tag{5.91}$$

The Boussinesq type parameter m_2, the sliding coefficient χ_b, the bed friction angle δ with $\tan\delta = O(\epsilon^{\gamma})$, and the erosion/deposition rate $\mathcal{U}$ must be prescribed. The earth pressure coefficient $\tilde{k}$ is shown in (5.87) and the bed elevation b satisfies the equation

$$\frac{\partial \tilde{b}}{\partial t} = c\,\mathcal{U}\,. \tag{5.92}$$

Complemented by initial and boundary conditions, Eqs. (5.91) and (5.92) stand for the determination of the depth-averaged tangential velocity V, free surface height h and bed elevation b.

Option 2—Parameterizing the topographic surface by the condition $\mathbf{u}_{\mathcal{S}} = \mathbf{0}$
Another possibility of choosing the transformation (5.68) was proposed by Tai and Kuo [23], see Sect. 2.4. Namely, the transformation (5.68) is so chosen that the condition

$$\boldsymbol{w}|_{\zeta=0} = \mathcal{U}\boldsymbol{n}_b \quad \Longleftrightarrow \quad \mathbf{u}_{\mathcal{S}} = \mathbf{0} \tag{5.93}$$

is fulfilled. When applied to the change of parameters on $\mathcal{S}_b$

$$x = x(\xi^1, t)\,, \quad y = \xi^2\,, \tag{5.94}$$

which we take for the surface (5.69), condition (5.93) reads as, see (2.119),

$$\frac{\partial x}{\partial t} = -c\,\mathcal{U}\frac{\partial b}{\partial x}\,, \quad \frac{\partial y}{\partial t} = 0\,. \tag{5.95}$$

Relation $(5.95)_1$, supplemented by the initial condition

$$x(\xi^1, 0) = \tilde{x}(\xi^1)\,, \tag{5.96}$$

stands for the determination of the transformation $(5.94)_1$. If the function $\tilde{x}$ above is taken such that ξ^1 represents the arc length on the curve

$$x_1 = x\,, \quad x_2 = \text{constant}\,, \quad x_3 = b(x, 0)\,, \tag{5.97}$$

condition $(5.95)_1$ and the property (5.85) in Option 1 show that the change of parameters (5.68) in Options 1 and 2 is, practically, the same. So, for the choice (5.93) and $\tilde{x}$ in (5.96) as explained, the system of modelling equations describing the flow of the Mohr-Coulomb type material down the surface (5.69) is the same as that deduced in Option 1, see (5.91) and (5.92).

Yet the central idea when assuming (5.93) was to generate the computational (ξ^1, ξ^2)-grid when advancing in time the numerical algorithm, by simultaneously solving the depth-averaged model equations (4.113), (4.114) and Eq. (2.119) to which (5.93) is equivalent. We outline this idea for the special surface (5.69) and the assumptions on the velocity and stress tensor stated at the beginning of this section. For a 2D case when condition (5.93) is used to specify the transformation (2.58) see Tai et al. [25].

We will write the depth-averaged mass balance equation (4.113) and the form (4.102) of the depth-averaged linear momentum balance equation (4.114) by using the special surface (5.69) and condition (5.93). The property $(5.95)_1$ of (5.94) is not required by any of the subsequent computations which aim to express the fields entering the depth-averaged equations according to our assumptions on the geometry of the topography and the kinematic/constitutive properties of the flow. Relation $(5.95)_1$, defining the computational grid, will be part of the final system of modelling equations, see (5.99) below.

Numerically it is useful to keep the geometric quantities c, $\mathbf{s}$, Ω as functions of (x, t), i.e.,

$$c = \left\{1 + (\partial b/\partial x)^2\right\}^{-1/2}, \quad \mathbf{s} = (c\,\partial b/\partial x,\ 0)^T, \quad \Omega = \frac{1}{2} c^3 \frac{\partial^2 b}{\partial x^2}\,,$$

see $(5.72)_{1,2}$ and (5.79). Then,

$$\mathbf{F} = \begin{pmatrix} \dfrac{\partial x}{\partial \xi^1} & 0 \\ 0 & 1 \end{pmatrix}, \quad J_0 = \frac{1}{c}\frac{\partial x}{\partial \xi^1}\,, \quad \mathbf{M}_0 = \begin{pmatrix} c^2 \left(\dfrac{\partial x}{\partial \xi^1}\right)^{-2} & 0 \\ 0 & 1 \end{pmatrix},$$

and

$$\overline{\mathbb{v}}_\tau = \mathbf{F}\overline{\mathbf{v}} \iff \overline{\mathbb{v}}_\tau = \begin{pmatrix} U \\ 0 \end{pmatrix}, \quad \text{with} \quad U \equiv V \frac{\partial x}{\partial \xi^1}\,,$$
$$\mathbb{v}_\tau\big|_{\zeta=0} = \mathbf{F}\mathbf{v}\big|_{\zeta=0} = \chi_b \mathbf{F}\overline{\mathbf{v}} = \chi_b \overline{\mathbb{v}}_\tau\,.$$

Moreover, see $(2.49)_2$ and $(2.38)_2$,

$$a \equiv \widetilde{\mathbf{H}}\overline{\mathbf{v}} \cdot \overline{\mathbf{v}} = c\mathbf{F}^T\mathbf{H}\mathbf{F}\overline{\mathbf{v}} \cdot \overline{\mathbf{v}} = c\mathbf{H}\overline{\mathbb{v}}_\tau \cdot \overline{\mathbb{v}}_\tau = cU^2\frac{\partial^2 b}{\partial x^2} = \frac{2}{c^2}\Omega U^2\,.$$

Next we refer to the closure relations indicated in Models 2 and Model 3. We need the eigenvalues and an orthonormal basis of eigenvectors corresponding to the mean surface stretching. Straightforward computations using (3.53) yield

$$(\mathcal{D}^\alpha{}_\beta) = \begin{pmatrix} \dfrac{\partial V}{\partial \xi^1} + V\left\{\dfrac{\partial^2 x}{\partial {\xi^1}^2}\left(\dfrac{\partial x}{\partial \xi^1}\right)^{-1} + 2\Omega\dfrac{\partial \tilde{b}}{\partial \xi^1}\right\} & 0 \\ 0 & 0 \end{pmatrix},$$

implying the eigenvalues

$$\lambda_1 = \frac{\partial V}{\partial \xi^1} + V\left\{\frac{\partial^2 x}{\partial {\xi^1}^2}\left(\frac{\partial x}{\partial \xi^1}\right)^{-1} + 2\Omega\frac{\partial \tilde{b}}{\partial \xi^1}\right\}, \quad \lambda_2 = 0\,, \tag{5.98}$$

and the eigenvectors, ordered as required in Model 3,

$$\boldsymbol{f}_1 = \frac{1}{\|\boldsymbol{\tau}_1\|}\boldsymbol{\tau}_1\,, \quad \boldsymbol{f}_2 = \boldsymbol{\tau}_2\,,$$

of the mean surface stretching $\boldsymbol{D}_\mathcal{S}$. Here, see (2.47),

$$\boldsymbol{\tau}_1 = \frac{\partial x}{\partial \xi^1}\boldsymbol{e}_1 + \frac{\partial b}{\partial x}\frac{\partial x}{\partial \xi^1}\boldsymbol{e}_3\,, \quad \boldsymbol{\tau}_2 = \boldsymbol{e}_2\,.$$

The change of basis matrix $\mathbf{C}$, see (5.46), is therefore given by

$$\mathbf{C} = \begin{pmatrix} 1/\|\boldsymbol{\tau}_1\| & 0 \\ 0 & 1 \end{pmatrix} = \begin{pmatrix} c/|\partial x/\partial \xi^1| & 0 \\ 0 & 1 \end{pmatrix}.$$

We can now deduce that,

$$\text{in Model 2,} \quad \mathbf{F}(\,\overline{p}\,\mathbf{M}_0 - \overline{\mathbf{P}}\,) = \tilde{k}\,\overline{p}\begin{pmatrix} c^2/(\partial x/\partial \xi^1) & 0 \\ 0 & 1 \end{pmatrix}, \quad \text{and}$$

$$\text{in Model 3,} \quad \mathbf{F}(\,\overline{p}\,\mathbf{M}_0 - \overline{\mathbf{P}}\,) = \overline{p}\begin{pmatrix} \tilde{k}c^2/(\partial x/\partial \xi^1) & 0 \\ 0 & \tilde{k}_2 \end{pmatrix},$$

where $\tilde{k}$ and $\tilde{k}_2$ are given by (5.87) and (5.89), respectively, with λ_1 having the expression (5.98). With these results at hand the next statements follow at once.

One-dimensional thin flow of Mohr-Coulomb type—using the condition $\mathbf{u}_{\mathcal{S}} = \mathbf{0}$ to parameterize the topographic surface
Consider

- the basal surface (5.69) with curvature $\Omega = O(\epsilon^{\gamma'})$, $0 < \gamma' < 1$,
- the change of parameters (5.94) satisfying

$$\mathbf{u}_{\mathcal{S}} = \mathbf{0} \iff \frac{\partial x}{\partial t} = -c\,\mathcal{U}\frac{\partial b}{\partial x}, \quad \frac{\partial y}{\partial t} = 0, \tag{5.99}$$

- the Mohr-Coulomb type Model 2 or Model 3.

Apart from negligible terms the depth-averaged mass and tangential linear momentum balance equations (4.97) and (4.102) emerge as

$$\begin{aligned}
&\frac{\partial}{\partial t}\{J_0 h\} + \frac{\partial}{\partial \xi^1}\{J_0 h V\} = -J_0\frac{\rho_b}{\rho_0}\mathcal{U}, \\
&\frac{\partial}{\partial t}\{J_0 h U\} + \frac{\partial}{\partial \xi^1}\left\{J_0 h\left(m_2 U^2 + \tfrac{1}{2}c^3 h\tilde{k}\right)\left(\frac{\partial x}{\partial \xi^1}\right)^{-1}\right\} \\
&\quad = -J_0 h\frac{1}{c}\left(c^3 + 2m_2\Omega U^2 + c^2 U\frac{\partial \mathcal{U}}{\partial x}\right)\frac{\partial b}{\partial x} - J_0\frac{\rho_b}{\rho_0}\chi_b U\,\mathcal{U} \\
&\qquad - J_0 h(\tan\delta)\frac{1}{c^2}\frac{\partial x}{\partial \xi^1}\left\{c^3 + 2m_2\Omega U^2\right\}_+ \operatorname{sgn} V .
\end{aligned} \tag{5.100}$$

The Boussinesq type parameter m_2, the sliding coefficient χ_b, the bed friction angle δ with $\tan\delta = O(\epsilon^{\gamma})$, and the erosion/deposition rate $\mathcal{U}$ must be prescribed. The earth pressure coefficient $\tilde{k}$ is shown in (5.87), with λ_1 given by (5.98), and the bed elevation b satisfies the equation

$$\frac{\partial b}{\partial t} = \frac{1}{c}\mathcal{U}. \tag{5.101}$$

Complemented by initial and boundary conditions, Eqs. $(5.99)_2$, (5.100) and (5.101) stand for the determination of the change of parameters (5.94), depth-averaged tangential velocity V, free surface height h and bed elevation b.

Remark If the erosion/deposition rate law shown in Sect. 5.3 is adopted, formula (5.67) for the inclination angle θ emerges as

$$\theta = \begin{cases} \arcsin\left(-\dfrac{\partial \tilde{b}}{\partial \xi^1}\operatorname{sgn} V\right), & \text{in Option 1,} \\ \arcsin\left(-c\,\dfrac{\partial \tilde{b}}{\partial \xi^1}\left|\dfrac{\partial x}{\partial \xi^1}\right|^{-1}\operatorname{sgn} V\right), & \text{in Option 2.} \end{cases}$$

If in Option 2 we have $\det \mathbf{F} > 0$ (see (2.46)), which gives $\partial x/\partial \xi^1 > 0$, we can further compute

$$\frac{\partial \tilde{b}}{\partial \xi^1}\left|\frac{\partial x}{\partial \xi^1}\right|^{-1} = \frac{\partial \tilde{b}}{\partial \xi^1}\left(\frac{\partial x}{\partial \xi^1}\right)^{-1} = \frac{\partial \tilde{b}}{\partial \xi^1}\frac{\partial \xi^1}{\partial x} = \frac{\partial b}{\partial x},$$

so that the inclination angle θ emerges as

$$\theta = \arcsin\left(-c\,\frac{\partial b}{\partial x}\,\operatorname{sgn} V\right).$$

In the numerical computations as explained in Part III, the function $\tilde{x}$ in the initial condition (5.96) for Eq. $(5.95)_1$ is taken such that ξ^1 is the arc length on the curve (5.97). With this choice condition $\det \mathbf{F} > 0$ is fulfilled at time $t = 0$, and $\det \mathbf{F}$ was computed at each time step and found to preserve the initial positive sign.

References

1. I. Luca, K. Hutter, Y.C. Tai, C.Y. Kuo, A hierarchy of avalanche models on arbitrary topography. Acta Mech. **205**, 121–149 (2009)
2. A. Voellmy, Über die Zerstörungskraft von Lawinen. Schweiz. Bauzeitung, Jahrg. 73, s. 159–165, 212–217, 246–249, 280–285. English as: On the destructive force of avalanches. 63p. Alta Avalanche Study Center, Transl **2**, 1964 (1955)
3. J.M.N.T. Gray, Y.C. Tai, On the inclusion of a velocity-dependent basal drag in avalanche models. Ann. Glaciol. **26**, 277–280 (1998)
4. S.P. Pudasaini, K. Hutter, Avalanche Dynamics: Dynamics of Rapid Flows of Dense Granular Avalanches (Springer, 2007)
5. I. Luca, Y.C. Tai, C.Y. Kuo, Modelling shallow gravity-driven solid-fluid mixtures over arbitrary topography. Comm. Math. Sci. **7**(1), 1–36 (2009)
6. C.A. Perazzo, J. Gratton, Thin film of non-Newtonian fluid on an incline. Phys. Rev. **67**, 016307 (2003)
7. C.O. Ng, C.C. Mei, Roll waves on a shallow layer of mud modelled as a power law fluid. J. Fluid. Mech. **263**, 151–183 (1994)
8. X. Huang, M.H. Garcia, A Herschel-Bulkley model for mud flow down a slope. J. Fluid. Mech. **374**, 305–333 (1998)
9. I.R. Ionescu, Viscoplastic shallow flow equations with topography. J. Non-Newtonian Fluid Mech. **193**, 116–128 (2013)
10. I.R. Ionescu, Augmented Lagrangian for shallow viscoplastic flow with topography. J. Comput. Phys. **242**, 544–560 (2013)
11. E. Bovet, B. Chiaia, L. Preziosi, A new model for snow avalanche dynamics based on non-Newtonian fluids. Meccanica **45**, 753–765 (2010)
12. J.M.N.T. Gray, A.N. Edwards, A depth-averaged $\mu(I)$ rheology for shallow granular free surface flows. J. Fluid Mech. **755**, 503–534 (2014)
13. Y.A. Berezin, L.A. Spodareva, Slow motion of a granular layer on an inclined plane. J. Appl. Mech. Tech. Phys. **39**(2), 261–264 (1998)
14. R.M. Iverson, R.P. Denlinger, Flow of variably fluidised granular masses across three-dimensional terrain. I: Coulomb mixture theory. J. Geophys. Res. **106**, 537–552 (2001)

15. S.B. Savage, K. Hutter, The motion of a finite mass of granular material down a rough incline. J. Fluid. Mech. **199**, 177–215 (1989)
16. F. Bouchut, M. Westdickenberg, Gravity driven shallow water models for arbitrary topography. Comm. Math. Sci. **2**(3), 359–389 (2004)
17. K. Hutter, S.B. Savage, Avalanche dynamics: the motion of a finite mass of gravel down a mountain side, in 5th International Symposium on Landslides, Lausanne (1988), pp. 691–697
18. S.B. Savage, K. Hutter, The dynamics of avalanches of granular materials from initiation to runout. part I: analysis. Acta Mech. **86**, 201–223 (1991)
19. E.B. Pitman, C.C. Nichita, A.K. Patra, A.C. Bauer, M. Bursik, A. Weber, A model of granular flows over an erodible surface. Discret. Contin. Dynam. Syst., Series B(3), 589 (2003)
20. M. Naaim, T. Faug, F. Naaim-Bouvet, Dry granular flow modeling including erosion and deposition. Surv. Geophys. **24**, 569 (2003)
21. M.E. Eglit, K.S. Demidov, Mathematical modeling of snow entrainment in avalanche motion. Cold Reg. Sci. Technol. **43**, 10–23 (2005)
22. B. Sovilla, S. Margreth, P. Bartelt, On snow entrainment in avalanche dynamics calculations. Cold Reg. Sci. Technol. **47**, 69–79 (2007)
23. Y.C. Tai, C.Y. Kuo, A new model of granular flows over general topography with erosion and deposition. Acta Mech. **199**, 71–96 (2008)
24. Y.C. Tai, Y.C. Lin, A focused view of the behavior of granular flows down a confined inclined chute into horizontal run-out zone. Phys. Fluids **20**, 123302 (2008)
25. Y.C. Tai, C.Y. Kuo, W.H. Hui, An alternative depth-integrated formulation for granular avalanches over temporally varying topography with small curvature. Geophys. Astrophys. Fluid Dyn. **106**(6), 596–629 (2012)
26. S. De Toni, P. Scotton, Two-dimensional mathematical and numerical model for the dynamics of granular avalanches. Cold Reg. Sci. Technol. **43**, 36–48 (2005)
27. F. Bouchut, E.D. Fernández-Nieto, A. Mangeney, P.-Y. Lagrée, On new erosion models of Savage-Hutter type for avalanches. Acta Mech. **199**, 181–208 (2008)

Chapter 6
Conclusions and Discussions

The aim in Part III of the book was to present a way to deduce depth-averaged model equations for shallow geophysical mass flows down arbitrary topographies, be they active or not. To make the presentation accessible we considered thin one-layer films of a one-component (or single-phase) material.

We followed two approaches, which we called conventional (as in papers by Luca et al. [1, 2]) and non-conventional (as in papers by Tai and Kuo [3] and Tai et al. [4]). What differentiates these approaches is the depth-averaging process related to the linear momentum balance equation. More specifically, in the conventional route the tangential linear momentum balance equation is averaged along the avalanche depth, while in the non-conventional approach, a combination of the horizontal and vertical hybrid linear momentum balance equations is averaged along the avalanche depth.

In both these approaches we started from the same set of intrinsic modelling equations, which we presented in Sect. 4.1. These consist of the mass and linear momentum balance equations, complemented by kinematic and dynamic boundary conditions. The constitutive behavior of the flowing material, the friction law and the erosion/deposition rates are left unspecified, so that the final modelling equations describing the shallow mass flow can be applied for a wide range of constitutive laws, friction laws and erosion/deposition rates.

The mass and linear momentum balance equations were already expressed (see Sect. 3.3) in terms of the topography adjusted coordinates, in both conventional and non-conventional methods. It remained to write the corresponding kinematic and dynamic boundary conditions in these coordinates. Section 4.2 was devoted to this task.

In Sect. 4.3 we collected the balance equations and the boundary conditions as written in the topography-fitted coordinates, now in non-dimensional form. In the non-dimensionalization process we used a single characteristic length, L, "parallel" to the topography. Doing so we gained more flexibility in assuming various orders of magnitude for the curvature of the basal surface and the stresses characterizing the thin flow.

I. Luca et al., *Shallow Geophysical Mass Flows down Arbitrary Topography*,
Advances in Geophysical and Environmental Mechanics and Mathematics,
DOI 10.1007/978-3-319-02627-5_6

The basic idea of the depth-averaging procedure was presented in Sect. 4.4. It was emphasized that different systems of equations, even if equivalent, may lead to different results when applying this procedure. We have thus prepared the reader for the discussion of the results obtained by the two methods, conventional and non-conventional, which are based on different, but equivalent, systems of equations.

In Sect. 4.5 we followed the conventional approach to deduce depth-averaged model equations for a thin flow. In Sect. 4.5.1 the depth-integrated mass and tangential momentum balance equations are deduced. Section 4.5.2 introduced geometric, kinematic and rheological scalings in terms of the aspect ratio ϵ of a typical thickness H, "perpendicular" to the topography, and the typical length L used in the non-dimensionalization procedure. The velocity profile was assumed to satisfy relations of Boussinesq type. For a plug flow and for a power law profile of the velocity, with a power parameter and a slip parameter as measures for the shearing and sliding, explicit expressions for the "Boussinesq coefficients" have been obtained. Rheological scalings concern also the components in the curvilinear coordinate system of the stress tensor. These are separately scaled for the normal and shear stresses on planes tangential to the basal surface and those on planes perpendicular to them. In case of erosion/deposition the velocity of this process was scaled as being of the order of the normal velocity component of the flowing material. Based on these assumptions, from the depth-integrated mass and tangential momentum balance equations the final depth-averaged modelling equations were deduced in Sect. 4.5.3, see (4.92) and (4.93). They are sufficiently general, in the sense that

- the rheology of the flowing material is not accounted for, except for the fact that ordering approximations of the stress components are assumed, and Boussinesq coefficients related to the velocity profile (which is dependent on the material properties) are introduced;
- active topographies are envisaged;
- the parameterization (2.59) of the basal surface is arbitrary.

The thin-layer modelling equations (4.92) and (4.93) have been presented for the first time in this book. When the erosion/deposition rate is set to zero one obtains the equations which correspond to a rigid topographic bed, and which have already been deduced by Luca et al. [2].

Section 4.5.4 classifies the system of depth-averaged modelling equations in terms of the relative weights of the basal shear stress, the depth-average of the shear stresses on planes parallel to the basal surface, and the normal and shear stresses on surfaces normal to the base. The analysis is roughly the same as that done by Luca et al. [2], except that now it refers to model equations accounting for erosion and sedimentation.

When the basal surface is slightly curved, the model equations (4.92) and (4.93) simplify considerably. This is shown in Sect. 4.5.5. Moreover, for negligible shear stresses in the normal direction and parameterization of the basal surface by condition $\mathbf{u}_{\mathcal{S}} = \mathbf{0}$, these equations have been identified as coinciding with those obtained by Tai et al. [4] by using another route, which in this book was called non-conventional. This remark motivated the research done in the next section, aiming to disclose

the relation between the model equations (4.92) and (4.93) and those which can be obtained by using the approach from [4], but in the same general case as that for (4.92) and (4.93).

Thus, Sect. 4.6 follows the non-conventional way, that is, as in the papers by Tai et al. [3, 4], however, this time for arbitrarily large curvature of the basal surface (of course, subject to the condition $J \neq 0$), for arbitrary rheology of the flowing mass (except from that expressed in the thin-layer approximations), and for arbitrary parameterization of the basal surface. The same thin-layer assumptions as in the conventional route are used, but the horizontal component, instead of the tangential component, of the linear momentum balance equation is depth-integrated. In order to be able to use the thin-layer approximations, the depth-integrated vertical linear momentum balance equation was needed. As a matter of fact, a combination of the horizontal and vertical linear momentum balance equations, see (4.108), delivered the final model equation (4.111). It was hoped in [3, 4] that, starting from the more appealing formula (4.50) (to be compared with its analogous (4.44), used to deduce (4.93)), the emerging equation will have a simple form, maybe even a conservative one. For the case treated in [3, 4] this was indeed the case (nevertheless, the modelling equations could be also obtained by the conventional approach). However, for the general case it did not happen to be so. Inspection of equation (4.111) reveals that it differs from its similar counterpart (4.93), and that generally neither (4.93) nor (4.111) is in conservative form. As for the efforts in deducing (4.111)—even if the hybrid form (4.50) of the horizontal linear momentum balance equation is much simpler than (4.44), in the non-conventional route there was at least as much work as there was in the conventional route in order to arrive at the final model equations. In the case of small curvature of the topographic surface, Eq. (4.111) takes the form (4.114). Even for this case the model equations derived by means of the two approaches are not identical. They coincide e.g. on an inclined plane, or when the shear stresses in the normal direction can be neglected. This last assumption is made in the paper by Tai et al. [4], which explains the comment in the Remark ending Sect. 4.5.5. In the general case, the thin-layer equations (4.111) and (4.93) do not coincide, and it is not clear which of them is best suited to describe rapid shallow flows down arbitrary topographies. Performing numerical simulations of experiments/realistic events using both these modelling equations may guide the scales in favour of one of them. Recalling that the only difference in deducing (4.111) and (4.93) consists in the expressions, which are depth-averaged, of the 3D linear momentum balance equation, one may equally ask which is the best suited expression (not necessarily used in this book) of the 3D linear momentum balance equation, to deliver thin-layer modelling equations.

In Chap. 4 the rheological properties of the flowing material were accounted for by the scalings of the stress components and, indirectly, by the Boussinesq type coefficients. However, there are quantities in the final modelling equations which have to be prescribed in terms of the basic unknown fields. Chapter 5 was mainly devoted to the formulation of so-called closure relations for these quantities. For the basal shear stress a Coulomb/viscous law is assumed in Sect. 5.1. The stress components must also be given. In Sect. 5.2.1 it is shown that Newtonian and non-

Newtonian fluids fit the scaling assumptions on the stress components. Then, Mohr-Coulomb type closure relations for the averaged stress components are postulated in Sect. 5.2.2. The proposals in Sects. 5.1 and 5.2 have been discussed by Luca et al. [2, 5]. The last quantity for which a law must be given is the erosion/deposition rate. For it the law suggested by Tai et al. [4] was presented in Sect. 5.3.

So far the change of parameters (2.58) was not specified. Section 5.4 aimed to show how (2.58) can be chosen and implemented in the system of depth-averaged modelling equations. For simplicity and better understanding of the 2D case (i.e., involving quantities depending on both ξ^1 and ξ^2), we confined to the 1D case (i.e., with quantities depending on only one variable, say ξ^1). We considered the model equations deduced for slightly curved basal surface, and chosen a Mohr-Coulomb type material. Since $\overline{\mathbf{p}}$ is negligibly small in the Mohr-Coulomb rheology, the system consisting of (4.97) and (4.98) is the same as that consisting of (4.113) and (4.114), so that either (4.97) and (4.98) or (4.113) and (4.114) were used to treat the 1D case. We indicated two ways of parameterizing the topographic surface. The first one, presented as Option 1, uses the arc lengths on the curves $x_2 =$ constant, $x_1 =$ constant as parameters ξ^1, ξ^2. The model equations were explicitly written for this case, see (5.91). The choice of ξ^1, ξ^2 as indicated above has been used by several authors, e.g. Dressler [6], Dewals et al. [7], De Toni and Scotton [8], Bouchut et al. [9]. The second way, designated as Option 2, has been suggested by Tai and Kuo [3] and Tai et al. [4] in the spirit of the unified coordinate system by Hui and Xu [10]. Now, the computational grid is obtained while advancing in time the numerical algorithm, and is determined by the condition $\mathbf{u}_{\mathcal{S}} = \mathbf{0}$. We pointed out that, for the 1D case treated here the surface coordinate ξ^1 is, practically, the same in both Options, if initially it is the same. However, we illustrated the pattern of ideas behind Option 2. Thus, in (4.97) and (4.98) we only used the assumption $\mathbf{u}_{\mathcal{S}} = \mathbf{0}$, the independence of the field variables of the coordinate ξ^2 and the Mohr-Coulomb rheology. These equations turned out to be (5.100). Condition $\mathbf{u}_{\mathcal{S}} = \mathbf{0}$ is equivalent to a system of differential equations, see (5.99), which must be solved simultaneously with the system of modelling equations, (5.100) and (5.101). The determination of the computational grid as in Option 2 seems to be numerically efficient even when applied to a more elaborate case than the 1D plus small curvature case rendered here (see Tai et al. [4]). The modelling equations, be they (4.92), (4.93) or (4.110), (4.111), simplify under the assumption $\mathbf{u}_{\mathcal{S}} = \mathbf{0}$, and first order differential equations (see (2.119)), for which numerous numerical schemes can be applied, yield the computational grid without numerical effort.

When complex geophysical mass flows are addressed, the mathematical models developed in Chaps. 4 and 5 can be made more realistic, for instance by letting the material to be a mixture of two or more constituents (see Luca et al. [5], Hutter and Luca [11]), and/or by considering two or more material layers (see Luca et al. [12, 13], Hutter and Luca [11]).

The next part of the book is centered on the presentation of a numerical algorithm to solve the system of depth-averaged model equations as in Option 2 discussed above. It will be used to assess the validity of the model equations in experiments and back calculations of realistic events.

References

1. I. Luca, Y.C. Tai, C.Y. Kuo, Non-Cartesian topography-based avalanche equations and approximations of gravity driven flows of ideal and viscous fluids. Math. Mod. Meth. Appl. Sci. **19**, 127–171 (2009)
2. I. Luca, K. Hutter, Y.C. Tai, C.Y. Kuo, A hierarchy of avalanche models on arbitrary topography. Acta Mech. **205**, 121–149 (2009)
3. Y.C. Tai, C.Y. Kuo, A new model of granular flows over general topography with erosion and deposition. Acta Mech. **199**, 71–96 (2008)
4. Y.C. Tai, C.Y. Kuo, W.H. Hui, An alternative depth-integrated formulation for granular avalanches over temporally varying topography with small curvature. Geophys. Astrophys. Fluid Dyn. **106**(6), 596–629 (2012)
5. I. Luca, Y.C. Tai, C.Y. Kuo, Modelling shallow gravity-driven solid-fluid mixtures over arbitrary topography. Comm. Math. Sci. **7**(1), 1–36 (2009)
6. R.F. Dressler, New nonlinear shallow flow equations with curvature. J. Hydraul. Res. **16**, 205–222 (1978)
7. B.J. Dewals, S. Erpicum, P. Archambau, S. Detrembleur, M. Pirotton, Depth-integrated flow modeling taking into account bottom curvature. J. Hydraul. Res. **44**, 785–795 (2006)
8. S. De Toni, P. Scotton, Two-dimensional mathematical and numerical model for the dynamics of granular avalanches. Cold Reg. Sci. Technol. **43**, 36–48 (2005)
9. F. Bouchut, E.D. Fernández-Nieto, A. Mangeney, P.-Y. Lagrée, On new erosion models of Savage-Hutter type for avalanches. Acta Mech. **199**, 181–208 (2008)
10. W.H. Hui, K. Xu, *Computational Fluid Dynamics Based on the Unified Coordinates* (Springer, Berlin, 2012)
11. K. Hutter, I. Luca, Two-layer debris mixture flows on arbitrary terrain with mass exchange at the base and the interface. Continuum Mech. Thermodyn. **24**(4–6), 525–558 (2012)
12. I. Luca, K. Hutter, C.Y. Kuo, Y.C. Tai, Two-layer models for shallow avalanche flows over arbitrary variable topography. Int. J. Adv. Eng. Sci. Appl. Math. **1**, 99–121 (2009)
13. I. Luca, C.Y. Kuo, K. Hutter, Y.C. Tai, Modeling shallow over-saturated mixtures on arbitrary rigid topography. J. Mech. **28**(3), 523–541 (2012)

Part IV
Numerical Implementation, Simulations and Applications

Chapter 7
Numerical Implementation of the Model Equations

In this chapter we present a numerical implementation of the model equations. In general, the numerical schemes for shallow-water-like equation systems are suitable for applications to the proposed equation systems. However, the topography-fitted coordinate system increases the complexity of solving the fluxes by using the Riemann solvers. We focus on the NOC schemes, first proposed by Nessyahu and Tadmor [1], which has been extended for multidimensional computation, see e.g. [2], or for non-staggered grids. see e.g. [3]. The NOC scheme avoids the resolution of Riemann fans as well as the use of Riemann solvers. Hence, it simplifies the computation of the complex fluxes in the equation systems. The emerging numerical scheme is explicite in time.

7.1 Brief Overview of the NOC Scheme

7.1.1 One-Dimensional NOC Scheme

Consider a one-dimensional conservation law with source term,

$$\frac{\partial}{\partial t}u(x,t) + \frac{\partial}{\partial x}f(u(x,t)) = s(u(x,t)), \tag{7.1}$$

where $u(x,t)$ is the conserved physical quantity, $f(u)$ is the nonlinear convection flux and $s(u)$ is the source. Letting $\{x_j\}$ be a uniform partition with $\triangle x = x_{j+1} - x_j$ and $x_{j+1/2} = \frac{1}{2}(x_{j+1} + x_j)$ in a computational domain, we have

$$U_j^n(t) = \frac{1}{\triangle x}\int_{x_{j-1/2}}^{x_{j+1/2}} u(x,t^n)\,\mathrm{d}x, \quad U_{j+1/2}^n(t) = \frac{1}{\triangle x}\int_{x_j}^{x_{j+1}} u(x,t^n)\,\mathrm{d}x \tag{7.2}$$

I. Luca et al., *Shallow Geophysical Mass Flows down Arbitrary Topography*,
Advances in Geophysical and Environmental Mechanics and Mathematics,
DOI 10.1007/978-3-319-02627-5_7

for the cell averages of the solution u at time level t^n. The central scheme on overlapping cells can be written in the from,

$$\begin{aligned} U_j^{n+1} &= \frac{1}{\triangle x}\int_{x_{j-1/2}}^{x_{j+1/2}} u(x,t^n)\,\mathrm{d}x \\ &\quad - \frac{1}{\triangle x}\int_{t^n}^{t^{n+1}}\Big\{f\big(u(x_{j+1/2},t)\big) - f\big(u(x_{j-1/2},t)\big)\Big\}\,\mathrm{d}t \\ &\quad + \frac{1}{\triangle x}\int_{t^n}^{t^{n+1}}\int_{x_{j-1/2}}^{x_{j+1/2}} s\big(u(x,t)\big)\,\mathrm{d}x\,\mathrm{d}t, \\ U_{j+1/2}^{n+1} &= \frac{1}{\triangle x}\int_{x_{j+1}}^{x_j} u(x,t^n)\,\mathrm{d}x \\ &\quad - \frac{1}{\triangle x}\int_{t^n}^{t^{n+1}}\Big\{f\big(u(x_{j+1},t)\big) - f\big(u(x_j,t)\big)\Big\}\,\mathrm{d}t \\ &\quad + \frac{1}{\triangle x}\int_{t^n}^{t^{n+1}}\int_{x_j}^{x_{j+1}} s\big(u(x,t)\big)\,\mathrm{d}x\,\mathrm{d}t, \end{aligned} \tag{7.3}$$

which are obtained by the time and space integration of (7.1) in an obvious way. By applying a TVD, ENO, WENO or any other non-oscillatory reconstruction procedure (see e.g. [4–7]) one obtains a polynomial for cell $I_{j+1/2} := \{x : |x - x_{j+1/2}| \le \frac{\triangle x}{2}\}$ or $I_j := \{x : |x - x_j| \le \frac{\triangle x}{2}\}$, yielding a piecewise linear approximation of the solution at time level t^n,

$$\begin{aligned} &u(x,t^n) \approx \\ &\tilde{u}(x,t^n) = \begin{cases} U_j^n + (u_x)_j^n(x - x_j), & \text{for } \ x \in I_j, \\ U_{j+1/2}^n + (u_x)_{j+1/2}^n(x - x_{j+1/2}), & \text{for } \ x \in I_{j+1/2}, \end{cases} \end{aligned} \tag{7.4}$$

where $(u_x)_j^n$ and $(u_x)_{j+1/2}^n$ approximate the exact derivatives at x_j and $x_{j+1/2}$, respectively. Denoting $\triangle t = t^{n+1} - t^n$ the time step size, with (7.4), as sketched in Fig. 7.1, Eq. (7.3) are approximated by

$$\begin{aligned} U_j^{n+1} &= \frac{1}{2}\left[U_{j-1/2}^n + U_{j+1/2}^n\right] + \frac{\triangle x}{8}\left[(u_x)_{j-1/2}^n - (u_x)_{j+1/2}^n\right] \\ &\quad - \frac{\triangle t}{\triangle x}\left[f\left(u_{j+1/2}^{n+1/2}\right) - f\left(u_{j-1/2}^{n+1/2}\right)\right] + \frac{\triangle t}{2}\left[s(u_{j-1/4}^{n+1/2}) + s\left(u_{j+1/4}^{n+1/2}\right)\right], \\ U_{j+1/2}^{n+1} &= \frac{1}{2}\left[U_j^n + U_{j+1}^n\right] + \frac{\triangle x}{8}\left[(u_x)_j^n - (u_x)_{j+1}^n\right] \\ &\quad - \frac{\triangle t}{\triangle x}\left[f\left(u_{j+1}^{n+1/2}\right) - f\left(u_j^{n+1/2}\right)\right] + \frac{\triangle t}{2}\left[s\left(u_{j+1/4}^{n+1/2}\right) + s\left(u_{j+3/4}^{n+1/2}\right)\right]. \end{aligned} \tag{7.5}$$

In (7.5), the midpoint values, $u_j^{n+1/2}$, $u_{j+1}^{n+1/2}$, $u_{j\pm1/2}^{n+1/2}$, $u_{j\pm1/4}^{n+1/2}$ and $u_{j+3/4}^{n+1/2}$, are predicted by the Taylor expansions,

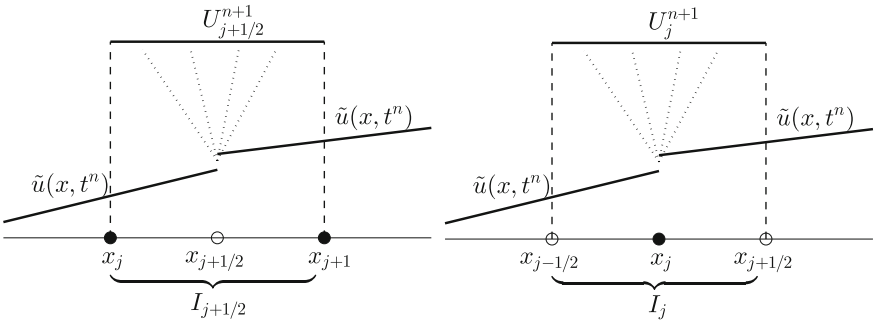

Fig. 7.1 The staggered integration over the local Riemann fan with $\tilde{u}(x,t^n)$ given in (7.4)

$$\begin{aligned} u^{n+1/2}_{j\pm1/2} &= U^n_{j\pm1/2} - \frac{\triangle t}{2}(f_x)^n_{j\pm1/2} + \frac{\triangle t}{2}s^n_{j\pm1/2}, \\ u^{n+1/2}_{j\pm1/4} &= U^n_{j\pm1/2} \mp \frac{\triangle x}{4}(u_x)^n_{j\pm1/2} - \frac{\triangle t}{2}(f_x)^n_{j\pm1/2} + \frac{\triangle t}{2}s^n_{j\pm1/2}, \end{aligned} \tag{7.6}$$

for $(7.5)_1$, and

$$\begin{aligned} u^{n+1/2}_{j} &= U^n_{j} - \frac{\triangle t}{2}(f_x)^n_{j} + \frac{\triangle t}{2}s^n_{j}, \\ u^{n+1/2}_{j+1/4} &= U^n_{j} + \frac{\triangle x}{4}(u_x)^n_{j} - \frac{\triangle t}{2}(f_x)^n_{j} + \frac{\triangle t}{2}s^n_{j}, \\ u^{n+1/2}_{j+3/4} &= U^n_{j+1} - \frac{\triangle x}{4}(u_x)^n_{j+1} - \frac{\triangle t}{2}(f_x)^n_{j+1} + \frac{\triangle t}{2}s^n_{j+1}, \end{aligned} \tag{7.7}$$

for $(7.5)_2$. In (7.6) and (7.7) we have used the notations $(f_x)^n_{j\pm1/2} \equiv f'\left(U^n_{j\pm1/2}\right)(u_x)^n_{j\pm1/2}$ and $(f_x)^n_j \equiv f'\left(U^n_j\right)(u_x)^n_j$ for approximating the derivatives in $I_{j\pm1/2}$ and I_j, respectively. For smooth solutions, at the space-time quadrature points the Courant-Friedrichs-Lewy (CFL) condition

$$\frac{\triangle t}{\triangle x}\left|a^{max}\right| < \frac{1}{2}, \quad a^{max} \equiv \max_j \left|f'(U^n_j)\right| \tag{7.8}$$

at each time level t^n is required in (7.5).

7.1.2 Two-Dimensional NOC Scheme

The one-dimensional NOC scheme, introduced in the previous subsection, can be easily extended to a two-dimensional scheme for the conservation law see, e.g. [2] and [8]

$$\frac{\partial}{\partial t}u(x,y,t)+\frac{\partial}{\partial x}f\big(u(x,y,t)\big)+\frac{\partial}{\partial y}g\big(u(x,y,t)\big)=s\big(u(x,y,t)\big). \tag{7.9}$$

Thus, by analogy, the staggered averages at $(x_{j\pm1/2}, y_{k\pm1/2}, t^{n+1})$ are computed by the cell averages at (x_j, y_k, t^n) and vice versa, see Fig. 7.2.

For a uniform spatial grid system $(x_j, y_k) = (j\triangle x, k\triangle y)$, we define the staggered spatial grids $I_{j+1/2,k+1/2} := \{(x,y) : |x - x_{j+1/2}| \le \frac{\triangle x}{2},\ |y - y_{k+1/2}| \le \frac{\triangle y}{2}\}$ and $I_{j,k} := \{(x,y) : |x - x_j| \le \frac{\triangle x}{2},\ |y - y_k| \le \frac{\triangle y}{2}\}$. In each cell, a two-dimensional, non-oscillatory piecewise-linear polynomial approximation is introduced,

$$\begin{aligned} u(x,\ y,\ t^n) &\approx \tilde{u}_{j,k}(x,\ y,\ t^n) \\ &= U^n_{j,k} + (u_x)^n_{j,k}(x - x_j) + (u_y)^n_{j,k}(y - y_k) \end{aligned} \tag{7.10}$$

for (x, y) in the cell $I_{j,k}$ centered at (x_j, y_k), and

$$\begin{aligned} u(x,\ y,\ t^n) &\approx \tilde{u}_{j+1/2,k+1/2}(x,\ y,\ t^n) \\ &= U^n_{j+1/2,k+1/2} + (u_x)^n_{j+1/2,k+1/2}(x - x_{j+1/2}) \\ &\quad +(u_y)^n_{j+1/2,k+1/2}(y - y_{k+1/2}) \end{aligned} \tag{7.11}$$

in case $(x, y) \in I_{j+1/2,k+1/2}$. Here,

$$\begin{aligned} U^n_{j,k} &= \frac{1}{\triangle x\triangle y}\int_{I_{j,k}} u(x,y,t^n)\,\mathrm{d}x\,\mathrm{d}y, \\ U^n_{j+1/2,k+1/2} &= \frac{1}{\triangle x\triangle y}\int_{I_{j+1/2,k+1/2}} u(x,y,t^n)\,\mathrm{d}x\,\mathrm{d}y\,, \end{aligned} \tag{7.12}$$

stand for the cell averages of the exact solution u at time level t^n, and e.g. $(u_x)^n_{j,k}$ and $(u_y)^n_{j,k}$ approximate the discrete slopes of u at (x_j, y_k) in the x- and y-direction, respectively.

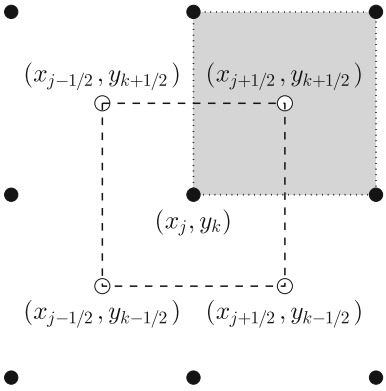

Fig. 7.2 The staggered grid structure in the two dimensional NOC scheme, where the averaged values at $(x_{j\pm1/2}, y_{k\pm1/2}, t^{n+1})$, denoted by "○", are computed by the averages at (x_j, y_k, t^n), represented by "●", and vice versa

Integration of (7.9) over $I_{j+1/2,k+1/2} \times [t^n,\ t^{n+1}]$ yields

$$\begin{aligned} U^{n+1}_{j+1/2,k+1/2} &= \frac{1}{\triangle x \triangle y} \int_{x_j}^{x_{j+1}} \int_{y_k}^{y_{k+1}} u(x,\ y,\ t^n)\, \mathrm{d}x\, \mathrm{d}y \\ &- \frac{1}{\triangle x \triangle y} \int_{t^n}^{t^{n+1}} \int_{y_k}^{y_{k+1}} \Big\{ f\big(u(x_{j+1},\ y,\ t)\big) - f\big(u(x_j,\ y,\ t)\big) \Big\} \mathrm{d}y\, \mathrm{d}t \\ &- \frac{1}{\triangle x \triangle y} \int_{t^n}^{t^{n+1}} \int_{x_j}^{x_{j+1}} \Big\{ g\big(u(x,\ y_{k+1},\ t)\big) - g\big(u(x,\ y_k,\ t)\big) \Big\} \mathrm{d}x\, \mathrm{d}t \\ &+ \frac{1}{\triangle x \triangle y} \int_{t^n}^{t^{n+1}} \int_{x_j}^{x_{j+1}} \int_{y_k}^{y_{k+1}} s\big(u(x,\ y,\ t)\big)\, \mathrm{d}x\, \mathrm{d}y\, \mathrm{d}t\,, \end{aligned} \tag{7.13}$$

see also Fig. 7.2. One may divide each cell into four subcells, the NW-, NE-, SW- and SE-subcell, so that we have e.g.

$$I_{j,k} = I^{\mathrm{SW}}_{j,k} \cup I^{\mathrm{NW}}_{j,k} \cup I^{\mathrm{NE}}_{j,k} \cup I^{\mathrm{SE}}_{j,k}$$

with

$$\begin{aligned} I^{\mathrm{SW}}_{j,k} &= I^{\mathrm{NE}}_{j-1/2,k-1/2}, & I^{\mathrm{NW}}_{j,k} &= I^{\mathrm{SE}}_{j-1/2,k+1/2}, \\ I^{\mathrm{NE}}_{j,k} &= I^{\mathrm{SW}}_{j+1/2,k+1/2}, & I^{\mathrm{SE}}_{j,k} &= I^{\mathrm{NW}}_{j+1/2,k-1/2}, \end{aligned}$$

see the left panel of Fig. 7.3 for $I_{j,k}$ and the right panel for cell $I_{j+1/2,k+1/2}$. In (7.13), the first term on the right-hand side can be rewritten as

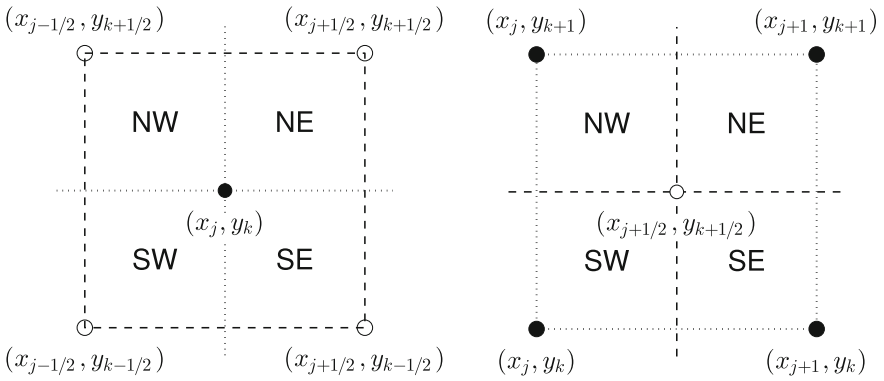

Fig. 7.3 Each cell is divided into four subcells, where the cell $I_{j,k}$ consists of four intersecting subcells of $I_{j-1/2,k-1/2}$, $I_{j-1/2,k+1/2}$, $I_{j+1/2,k+1/2}$ and $I_{j+1/2,k-1/2}$ (*left panel*), and the cell $I_{j+1/2,k+1/2}$ consists of four intersecting subcells with $I_{j,k}$, $I_{j,k+1}$, $I_{j+1,k+1}$ and $I_{j+1,k}$ (*right panel*)

$$\begin{aligned}\int_{x_j}^{x_{j+1}}\int_{y_k}^{y_{k+1}} u(x,\ y,\ t^n)\,\mathrm{d}x\,\mathrm{d}y &= \iint\limits_{I_{j+1/2,k+1/2}} u(x,\ y,\ t^n)\,\mathrm{d}x\,\mathrm{d}y \\ &= \iint\limits_{I^{\mathrm{NE}}_{j,k}} u(x,\ y,\ t^n)\,\mathrm{d}x\,\mathrm{d}y + \iint\limits_{I^{\mathrm{SE}}_{j,k+1}} u(x,\ y,\ t^n)\,\mathrm{d}x\,\mathrm{d}y \\ &+ \iint\limits_{I^{\mathrm{SW}}_{j+1,k+1}} u(x,\ y,\ t^n)\,\mathrm{d}x\,\mathrm{d}y + \iint\limits_{I^{\mathrm{NW}}_{j+1,k}} u(x,\ y,\ t^n)\,\mathrm{d}x\,\mathrm{d}y,\end{aligned} \tag{7.14}$$

where we note the four intersecting cells, $I^{\mathrm{SW}}_{j+1/2,k+1/2} = I^{\mathrm{NE}}_{j,k}$, $I^{\mathrm{NW}}_{j+1/2,k+1/2} = I^{\mathrm{SE}}_{j,k+1}$, $I^{\mathrm{NE}}_{j+1/2,k+1/2} = I^{\mathrm{SW}}_{j+1,k+1}$ and $I^{\mathrm{SE}}_{j+1/2,k+1/2} = I^{\mathrm{NW}}_{j+1,k}$, see the right panel of Fig. 7.3.

There are four fluxes in (7.13), whose values can be approximated by the midpoint quadrature rule for second-order accuracy of the temporal integral and second-order rectangular rule for the spatial integration across the corresponding face. For example, the flux along the face at $x = x_{j+1}$ is approximated by

$$\int_{t^n}^{t^{n+1}}\int_{y_k}^{y_{k+1}} f\big(u(x_{j+1},\ y,\ t)\big)\,\mathrm{d}y\,\mathrm{d}t = \frac{\triangle t \triangle y}{2}\left\{f^{n+1/2}_{j+1,k} + f^{n+1/2}_{j+1,k+1}\right\}. \tag{7.15}$$

Similarly, the flux along the face at $y = y_{k+1}$ then reads

$$\int_{t^n}^{t^{n+1}}\int_{x_j}^{x_{j+1}} g\big(u(x,\ y_{k+1},\ t)\big)\,\mathrm{d}x\,\mathrm{d}t = \frac{\triangle t \triangle x}{2}\left\{g^{n+1/2}_{j,k+1} + g^{n+1/2}_{j+1,k+1}\right\}. \tag{7.16}$$

The values of $f^{n+1/2}_{j+1,k(+1)}$ and $g^{n+1/2}_{j(+1),k+1}$ in (7.15) and (7.16) are determined by $f\left(u^{n+1/2}_{j+1,k(+1)}\right)$ and $g\left(u^{n+1/2}_{j(+1),k+1}\right)$. The midpoint approximated values of the exact solution are evaluated by virtue of the conservation law (7.9), e.g.,

$$\begin{aligned}u^{n+1/2}_{j,k} &= U^n_{j,k} + \frac{\triangle t}{2}\left(\frac{\partial u}{\partial t}\right)^n_{j,k} \\ &= U^n_{j,k} - \frac{\triangle t}{2}\left(\frac{\partial f}{\partial x}\right)^n_{j,k} - \frac{\triangle t}{2}\left(\frac{\partial g}{\partial y}\right)^n_{j,k} + \frac{\triangle t}{2}s\left(U^n_{j,k}\right) \\ &= U^n_{j,k} - \frac{\triangle t}{2}\left(\sigma^f\right)^n_{j,k} - \frac{\triangle t}{2}\left(\sigma^g\right)^n_{j,k} + \frac{\triangle t}{2}s\left(U^n_{j,k}\right).\end{aligned} \tag{7.17}$$

Here $(\sigma^f)^n_{j,k}$ and $(\sigma^g)^n_{j,k}$ are one-dimensional discrete slopes of the fluxes f and g in the x- and y-directions, respectively, which are determined by the non-oscillatory TVD limiters or WENO interpolations. They can be represented by the corresponding Jacobians

$$\left(\sigma^f\right)_{j,k}^n = \left(\frac{\partial f}{\partial u}\right)_{j,k}^n (u_x)_{j,k}^n, \qquad \left(\sigma^g\right)_{j,k}^n = \left(\frac{\partial g}{\partial u}\right)_{j,k}^n (u_y)_{j,k}^n, \tag{7.18}$$

where we recall $(u_x)_{j,k}^n$ and $(u_y)_{j,k}^n$ as the discrete slopes of $\tilde{u}$ in the x- and y-direction, respectively.

The integral of the source term in (7.13) is approximated by the values at the centres of the four intersected subcells, (i.e. $I_{j+1/2,k+1/2}^{SW}$, etc.), see the right panel of Fig. 7.3. That is,

$$\begin{aligned}&\frac{1}{\triangle x \triangle y}\int_{t^n}^{t^{n+1}}\int_{x_j}^{x_{j+1}}\int_{y_k}^{y_{k+1}} s(x,\ y,\ t)\mathrm{d}x\,\mathrm{d}y\,\mathrm{d}t \\ &\quad = \frac{\triangle t}{4}\left\{s_{j+1/4,k+1/4}^{n+1/2} + s_{j+3/4,k+1/4}^{n+1/2} + s_{j+3/4,k+3/4}^{n+1/2} + s_{j+1/4,k+3/4}^{n+1/2}\right\},\end{aligned} \tag{7.19}$$

where, for example, $s_{j+1/4,k+1/4}^{n+1/2} = s\left(u_{j+1/4,k+1/4}^{n+1/2}\right)$. The value of $u_{j+1/4,k+1/4}^{n+1/2}$ is evaluated by the Taylor series expansion,

$$u_{j+1/4,k+1/4}^{n+1/2} = u_{j,k}^{n+1/2} + \frac{\triangle x}{4}(u_x)_{j,k}^n + \frac{\triangle y}{4}\left(u_y\right)_{j,k}^n \tag{7.20}$$

with $u_{j,k}^{n+1/2}$ being computed in (7.17).

Hence, with the help of (7.14)–(7.16) and (7.19), expression (7.13) of the cell-mean value $U_{j+1/2,k+1/2}^{n+1}$ emerges as

$$\begin{aligned}U_{j+1/2,k+1/2}^{n+1} &= \frac{1}{4}\left\{U_{j,k}^n + U_{j+1,k}^n + U_{j+1,k+1}^n + U_{j,k+1}^n\right\} \\ &+ \frac{\triangle x}{16}\left\{(u_x)_{j,k} - (u_x)_{j+1,k} - (u_x)_{j+1,k+1} + (u_x)_{j,k+1}\right\} \\ &+ \frac{\triangle y}{16}\left\{(u_y)_{j,k} + (u_y)_{j+1,k} - (u_y)_{j+1,k+1} - (u_y)_{j,k+1}\right\} \\ &- \frac{\triangle t}{2\triangle x}\left\{f_{j+1,k}^{n+1/2} + f_{j+1,k+1}^{n+1/2} - f_{j,k}^{n+1/2} - f_{j,k+1}^{n+1/2}\right\} \\ &- \frac{\triangle t}{2\triangle y}\left\{g_{j,k+1}^{n+1/2} + g_{j+1,k+1}^{n+1/2} - g_{j,k}^{n+1/2} - g_{j+1,k}^{n+1/2}\right\} \\ &+ \frac{\triangle t}{4}\left\{s_{j+1/4,k+1/4}^{n+1/2} + s_{j+3/4,k+1/4}^{n+1/2} + s_{j+3/4,k+3/4}^{n+1/2} + s_{j+1/4,k+3/4}^{n+1/2}\right\}.\end{aligned} \tag{7.21}$$

Analogously, one has

$$
\begin{aligned}
U_{j,k}^{n+1} = & \\
& \frac{1}{4}\left\{U_{j-1/2,k-1/2}^{n}+U_{j+1/2,k-1/2}^{n}+U_{j+1/2,k+1/2}^{n}+U_{j-1/2,k+1/2}^{n}\right\} \\
& +\frac{\triangle x}{16}\left\{(u_x)_{j-1/2,k-1/2}-(u_x)_{j+1/2,k-1/2}\right. \\
& \qquad \left.-(u_x)_{j+1/2,k+1/2}+(u_x)_{j-1/2,k+1/2}\right\} \\
& +\frac{\triangle y}{16}\left\{(u_y)_{j-1/2,k-1/2}+(u_y)_{j+1/2,k-1/2}\right. \\
& \qquad \left.-(u_y)_{j+1/2,k+1/2}-(u_y)_{j-1/2,k+1/2}\right\} \\
& -\frac{\triangle t}{2\triangle x}\left\{f_{j+1/2,k-1/2}^{n+1/2}+f_{j+1/2,k+1/2}^{n+1/2}-f_{j-1/2,k-1/2}^{n+1/2}-f_{j-1/2,k+1/2}^{n+1/2}\right\} \\
& -\frac{\triangle t}{2\triangle y}\left\{g_{j-1/2,k+1/2}^{n+1/2}+g_{j+1/2,k+1/2}^{n+1/2}-g_{j-1/2,k-1/2}^{n+1/2}-g_{j+1/2,k-1/2}^{n+1/2}\right\} \\
& +\frac{\triangle t}{4}\left\{s_{j-1/4,k-1/4}^{n+1/2}+s_{j+1/4,k-1/4}^{n+1/2}+s_{j+1/4,k+1/4}^{n+1/2}+s_{j-1/4,k+1/4}^{n+1/2}\right\}
\end{aligned}
\tag{7.22}
$$

for the cell-mean value corresponding to the grid cell centered at $(x_j,\ y_k)$ and to the time level t^{n+1}.

Equation (7.21), as well as (7.22), constitutes a heigh-order accurate non-oscillatory scheme, whose non-oscillatory behavior hinges on the reconstructed discrete slopes, u_x, u_y, σ^f and σ^g. As mentioned in [2], through numerical tests with simple linear oblique advection equation $w_t + w_x + w_y = 0$, the time step $\triangle t$ should be restricted by the realistic geometric CFL condition

$$
\max\left(\frac{\triangle t}{\triangle x}\frac{\partial f}{\partial u},\ \frac{\triangle t}{\triangle y}\frac{\partial g}{\partial u}\right) < 1/2. \tag{7.23}
$$

7.2 Numerical Implementation of Thin Flow Models on a Slightly Curved Surface

In this section we illustrate the implementation of the NOC schemes for the models over slightly curved topography introduced in Sect. 4.5.5. According to the DTM, the topographic surface is represented by a set of altitudes of terrain locations over a regular horizontal grid, in which the x_1-axis is perpendicular to the x_2-axis, see Fig. 4.1. The NOC scheme is applicable with the variable x, y as the surface parameters ξ^1, ξ^2.

For ease of expression, we shall consider the thin flow model (4.99) and (4.102), where small extra-stresses $\overline{\mathbf{P}} = O(\epsilon^{1+\gamma})$ and $\overline{\mathbf{p}} = O(\epsilon^{1+\gamma})$ are presumed. That is, the flowing material behaves as an ideal fluid experiencing bottom friction. The

governing equations are written in the general vector form,

$$\frac{\partial \mathfrak{u}}{\partial t} + \frac{\partial \mathbb{f}}{\partial \xi^1} + \frac{\partial \mathfrak{g}}{\partial \xi^2} = \mathfrak{s}, \tag{7.24}$$

in which $\mathfrak{u}$ denotes the vector of conservative variables, $\mathbb{f}$ and $\mathfrak{g}$ represent the transport fluxes in the ξ^1- and ξ^2-directions, respectively, and $\mathfrak{s}$ means the source term. They are

$$\begin{aligned}
\mathfrak{u} &= \begin{pmatrix} J_0 h \\ J_0 h \overline{v_1^\tau} \\ J_0 h \overline{v_2^\tau} \end{pmatrix}, \qquad
\mathbb{f} = \begin{pmatrix} J_0 h \overline{v^1} \\ J_0 h m_2 \overline{v_1^\tau}\,\overline{v^1} + J_0 \beta_{11} h \\ J_0 h m_2 \overline{v_2^\tau}\,\overline{v^1} + J_0 \beta_{21} h \end{pmatrix}, \\
\mathfrak{g} &= \begin{pmatrix} J_0 h \overline{v}^2 \\ J_0 h m_2 \overline{v_1^\tau}\,\overline{v^2} + J_0 \beta_{12} h \\ J_0 h m_2 \overline{v_2^\tau}\,\overline{v^2} + J_0 \beta_{22} h \end{pmatrix}, \quad
\mathfrak{s} = \begin{pmatrix} 0 \\ J_0 s_{\xi^1} \\ J_0 s_{\xi^2} \end{pmatrix}
\end{aligned} \tag{7.25}$$

with

$$\begin{pmatrix} \overline{v_1^\tau} \\ \overline{v_2^\tau} \end{pmatrix} = \overline{\mathbb{v}}_\tau\,, \qquad \begin{pmatrix} \overline{v^1} \\ \overline{v^2} \end{pmatrix} = \overline{\mathbf{v}}, \qquad \begin{pmatrix} \beta_{11} & \beta_{12} \\ \beta_{21} & \beta_{22} \end{pmatrix} = \overline{p}\,\mathbf{F}\,\mathbf{M}_0\,, \tag{7.26}$$

and

$$\begin{pmatrix} s_{\xi^1} \\ s_{\xi^2} \end{pmatrix} = -h\,(c + a m_2 + \mathrm{Grad}\,\mathcal{U}\cdot\overline{\mathbf{v}})\,\mathbf{s} - \frac{\rho_b}{\rho_0}\,\mathcal{U}\,\mathbb{v}_\tau\big|_{\zeta=0} - \mathbf{F}\,\mathbf{p}\big|_{\zeta=0}\,. \tag{7.27}$$

By applying formula (7.21), the cell average $\overline{\mathfrak{u}}^{n+1}_{j+1/2,k+1/2}$, approximating the exact solution $\mathfrak{u}$ on $I_{j+1/2,k+1/2}$ at time level t^{n+1}, is given by

$$\begin{aligned}
\overline{\mathfrak{u}}^{n+1}_{j+1/2,k+1/2} &= \frac{1}{4}\left\{\overline{\mathfrak{u}}^n_{j,k} + \overline{\mathfrak{u}}^n_{j+1,k} + \overline{\mathfrak{u}}^n_{j+1,k+1} + \overline{\mathfrak{u}}^n_{j,k+1}\right\} \\
&+ \frac{1}{16}\left\{\mathfrak{u}'_{j,k} - \mathfrak{u}'_{j+1,k} - \mathfrak{u}'_{j+1,k+1} + \mathfrak{u}'_{j,k+1}\right\} \\
&+ \frac{1}{16}\left\{\mathfrak{u}`_{j,k} + \mathfrak{u}`_{j+1,k} - \mathfrak{u}`_{j+1,k+1} - \mathfrak{u}`_{j,k+1}\right\} \\
&- \frac{\triangle t}{2\triangle \xi^1}\left\{\mathbb{f}\left(\mathfrak{u}^{n+1/2}_{j+1,k}\right) + \mathbb{f}\left(\mathfrak{u}^{n+1/2}_{j+1,k+1}\right) - \mathbb{f}\left(\mathfrak{u}^{n+1/2}_{j,k}\right) - \mathbb{f}\left(\mathfrak{u}^{n+1/2}_{j,k+1}\right)\right\} \\
&- \frac{\triangle t}{2\triangle \xi^2}\left\{\mathfrak{g}\left(\mathfrak{u}^{n+1/2}_{j,k+1}\right) + \mathfrak{g}\left(\mathfrak{u}^{n+1/2}_{j+1,k+1}\right) - \mathfrak{g}\left(\mathfrak{u}^{n+1/2}_{j,k}\right) - \mathfrak{g}\left(\mathfrak{u}^{n+1/2}_{j+1,k}\right)\right\} \\
&+ \frac{\triangle t}{4}\left\{\mathfrak{s}\left(\mathfrak{u}^{n+1/2}_{j+1/4,k+1/4}\right) + \mathfrak{s}\left(\mathfrak{u}^{n+1/2}_{j+3/4,k+1/4}\right) + \mathfrak{s}\left(\mathfrak{u}^{n+1/2}_{j+3/4,k+3/4}\right)\right. \\
&\left. + \mathfrak{s}\left(\mathfrak{u}^{n+1/2}_{j+1/4,k+3/4}\right)\right\}.
\end{aligned} \tag{7.28}$$

In (7.28), $\mathfrak{u}'_{j,k}$ and $\mathfrak{u}'_{j,k}$ denote the mean discrete deviators over the cell,

$$\mathfrak{u}'_{j,k} = \triangle\xi^1 \overline{\left(\frac{\partial \mathfrak{u}}{\partial \xi^1}\right)}_{j,k}, \qquad \mathfrak{u}'_{j,k} = \triangle\xi^2 \overline{\left(\frac{\partial \mathfrak{u}}{\partial \xi^2}\right)}_{j,k}, \tag{7.29}$$

in the ξ^1- and ξ^2-direction, respectively. Their values can be determined by the non-oscillatory TVD limiters or WENO interpolations. Applying the conservative law (7.9), the physical quantities at $t = t^{n+1/2}$ in (7.28) is given by

$$\mathfrak{u}^{n+1/2}_{j,k} = \overline{\mathfrak{u}}^n_{j,k} + \frac{\triangle t}{2}\left(\frac{\partial \mathfrak{u}}{\partial t}\right)^n_{j,k}, \tag{7.30}$$

where the temporal derivative is approximated by

$$\left(\frac{\partial \mathfrak{u}}{\partial t}\right)^n_{j,k} = -\left(\frac{\partial \mathbb{f}}{\partial \xi^1}\right)^n_{j,k} - \left(\frac{\partial \mathfrak{g}}{\partial \xi^2}\right)^n_{j,k} + \mathfrak{s}\left(\overline{\mathfrak{u}}^n_{j,k}\right). \tag{7.31}$$

With the cell reconstructions and the predicted values (7.30) the variables for the source term can be obained by

$$\begin{aligned}
\mathfrak{u}^{n+1/2}_{j+1/4,k+1/4} &= \mathfrak{u}^{n+1/2}_{j,k} + \frac{1}{4}\left\{\mathfrak{u}'_{j,k} + \mathfrak{u}'_{j,k}\right\},\\
\mathfrak{u}^{n+1/2}_{j+3/4,k+1/4} &= \mathfrak{u}^{n+1/2}_{j+1,k} - \frac{1}{4}\left\{\mathfrak{u}'_{j+1,k} - \mathfrak{u}'_{j+1,k}\right\},\\
\mathfrak{u}^{n+1/2}_{j+3/4,k+3/4} &= \mathfrak{u}^{n+1/2}_{j+1,k+1} - \frac{1}{4}\left\{\mathfrak{u}'_{j,k} + \mathfrak{u}'_{j+1,k+1}\right\},\\
\mathfrak{u}^{n+1/2}_{j+1/4,k+3/4} &= \mathfrak{u}^{n+1/2}_{j,k+1} + \frac{1}{4}\left\{\mathfrak{u}'_{j,k+1} - \mathfrak{u}'_{j,k+1}\right\}.
\end{aligned} \tag{7.32}$$

This NOC scheme is assigned to obey the CFL condition

$$\max\left(\frac{\triangle t}{\triangle \xi^1}\left|c^{max}_{\xi^1}\right|, \frac{\triangle t}{\triangle \xi^2}\left|c^{max}_{\xi^2}\right|\right) < \frac{1}{2}, \tag{7.33}$$

where the global maximum wave speeds are

$$\begin{aligned}
c^{max}_{\xi^1} &= \max_{\text{all } j,k}\left(|v^1_{j,k}| + \sqrt{(P^*_{\xi^1})_{j,k}}\right),\\
c^{max}_{\xi^2} &= \max_{\text{all } j,k}\left(|v^2_{j,k}| + \sqrt{(P^*_{\xi^2})_{j,k}}\right).
\end{aligned} \tag{7.34}$$

In (7.34),

$$
\begin{aligned}
P^*_{\xi^1} &= \frac{\partial \overline{p}}{\partial h}\left(F^{-1}_{11}M^0_{11} + F^{-1}_{12}M^0_{21}\right),\\
P^*_{\xi^2} &= \frac{\partial \overline{p}}{\partial h}\left(F^{-1}_{21}M^0_{12} + F^{-1}_{22}M^0_{22}\right),\\
\mathbf{F}^{-1} &= \begin{pmatrix} F^{-1}_{11} & F^{-1}_{12}\\ F^{-1}_{21} & F^{-1}_{22}\end{pmatrix}, \quad \mathbf{M}_0 = \begin{pmatrix} M^0_{11} & M^0_{12}\\ M^0_{21} & M^0_{22}\end{pmatrix},
\end{aligned}
$$

where $\mathbf{F}^{-1}$ is the inverse of $\mathbf{F}$ defined in (2.45), $\mathbf{M}_0$ is defined in (2.50), and $\overline{p}$ is the depth-averaged pressure in (4.91).

In case the basal surface is erodible, i.e. $\mathcal{U} \neq 0$, the meshes evolve with time. As the grid locations are defined in the Cartesian coordinates, the local mesh velocity has to be given in the Cartesian coordinates for describing its evolution. With the definition (2.104) of $\mathbf{w}$ we calculate the local mesh velocity

$$
\begin{pmatrix} w_x\\ w_y\\ w_z\end{pmatrix} = \boldsymbol{A}^{-1}\begin{pmatrix}\mathbf{w}\\ \mathcal{U}\end{pmatrix} \tag{7.35}
$$

in the Cartesian coordinates. With the assumptions $\mathbf{u}_{\mathcal{S}} = \mathbf{0}$ and small curvature of the topographic surface, we have $\mathbf{w} = O(\epsilon^2)$ and $\mathcal{H} = O(\epsilon^{\gamma'})$, see (2.110) and (4.95), so that (7.35) terns into

$$
\begin{pmatrix} w_x\\ w_y\\ w_z\end{pmatrix} = \boldsymbol{P}^{-1}\begin{pmatrix}0\\ 0\\ \mathcal{U}\end{pmatrix} + O(\epsilon^{1+\gamma'}), \tag{7.36}
$$

where $\boldsymbol{P}^{-1} = \boldsymbol{A}\big|_{\zeta=0}$ is defined in (2.54). Letting $(x^n_{j,k},\ y^n_{j,k},\ z^n_{j,k})^T$ denote the position of the j-k-cell in the Cartesian coordinates at time level t^n, the marching of the coordinates is carried out by a trapezoidal integration,

$$
\begin{cases}
x^{n+1}_{j,k} = x^n_{j,k} + 0.5\,\triangle t\left\{(w_x)^n_{j,k} + (w_x)^*_{j,k}\right\},\\
y^{n+1}_{j,k} = y^n_{j,k} + 0.5\,\triangle t\left\{(w_y)^n_{j,k} + (w_y)^*_{j,k}\right\},\\
z^{n+1}_{j,k} = z^n_{j,k} + 0.5\,\triangle t\left\{(w_z)^n_{j,k} + (w_z)^*_{j,k}\right\}.
\end{cases} \tag{7.37}
$$

In (7.37), the time interval $\triangle t = t^{n+1} - t^n$, $\left((w_x)^n_{j,k},\ (w_y)^n_{j,k},\ (w_z)^n_{j,k}\right)^T$ stands for the local mesh velocity of the $j-$cell at time level t^n, and $\left((w_x)^*_{j,k},\ (w_y)^*_{j,k},\ (w_z)^*_{j,k}\right)^T$ is the temporary one computed with physical quantities $\mathfrak{v}^{n+1}_{j,k}$ before the mesh movement. It is noticed that this step is optional and may introduce some errors during the mapping process of (7.37).

References

1. H. Nessyahu, E. Tadmor, Non-oscillatory central differencing for hyperbolic conservation laws. J. Comput. Phys. **87**(2), 408–463 (1990)
2. G.S. Jiang, E. Tadmor, Non-oscillatory central schemes for multidimensional hyperbolic conservation laws. SIAM J. Sci. Comput. **19**(6), 1892–1917 (1998)
3. G.S. Jiang, D. Levy, C. T. Lin, S. Osher, E. Tadmor, High-resolution nonoscillatory central schemes with nonstaggered grids for hyperbolic conservation laws. SIAM J. Sci. Comput. **35**(6), 2147–2168 (1998)
4. H. C. Yee, A class of high-resolution explicit and implicit shock-capturing methods. National Aeronautics and Space Administration, Ames Research Center, (1989)
5. X. D. Liu, S. Osher, T. Chan, Weighted essentially non-oscillatory schemes. Elsevier J. Comput. Phys. **115**(1), 200–212 (1994)
6. D. Levy, G. Puppo, G. Russor, Central WENO schemes for hyperbolic systems of conservation laws. Cambridge Univ Press ESAIM: Math. Model. Numer. Anal. **33**(3), 547–571 (1999)
7. A. Harten, S. Osher, E. Tadmor, B. Engquist, S. R. Chakravarthy, Some results on uniformly high-order accurate essentially nonoscillatory schemes, Elsevier Appl. Numer. Math. **2**(3), 347–377 (1986)
8. Y. C. Tai, Dynamics of granular avalanches and their simulations with shock-capturing and front-tracking numerical schemes, PhD thesis, Darmstadt University of Technology. Shaker Verlag: Aachen, (2000)

Chapter 8
Numerical Tests and Simulations of Granular Avalanches

In this chapter we apply the numerical implementation introduced in Chap. 7 to investigate and illustrate the key features of the models in the topography-fitted coordinate system. The equations, which are numerically solved, consist of

- the depth-averaged mass balance equation (4.99) and
- the depth-averaged linear momentum balance equation (4.102),

where

- a weak rheology ($\overline{\mathbf{p}} = O(\epsilon^{1+\gamma})$, so that $\overline{\mathbf{p}}$ is already neglected when writing (4.102)), and
- the Coulomb bed friction law, (5.17) with $\phi = 1$, at the sliding surface

are adopted. If not explicitly specified, the extra-stress $\overline{\mathbf{P}}$ is assumed to be of order $O(\epsilon^{1+\gamma})$, so that the term $\overline{\mathbf{P}}$ in (4.102) is neglected. This assumption is equivalent to setting $\tilde{k} = 1$ in (5.53).

In case that the erosion/deposition is taken into account, the proposal (5.64) for the erosion/deposition rate is employed,

$$\mathcal{U} = \mathcal{F}_e\,(\theta_n - \theta)\,\tilde{h} \quad \text{with} \quad \mathcal{F}_e = \alpha_e\Big\{\mathcal{F}_{\text{reg}}\,\mathcal{H}(\theta_n - \theta) + \mathcal{H}(\theta - \theta_n)\Big\}, \tag{8.1}$$

where $\mathcal{H}$ is the Heaviside step function and $\mathcal{F}_{\text{reg}}$ is defined in (5.66). For erosion, no momentum is gained from the entrained mass in the computation, because the parcel beneath the non-material basal surface is immobile. For deposition, the momentum loss is approximated according to the local velocity profile along the flow thickness, see (4.80). Letting h_d denote the thickness deposited from the flowing layer during the time interval $[t^n,\ t^{n+1}]$, its value is determined by $h_d = \mathcal{U}\,\triangle t$ with $\triangle t = t^{n+1} - t^n$. Hence, the momentum loss, the integration of the last second term on the right-hand side of (4.102) over the time interval, is given by

I. Luca et al., *Shallow Geophysical Mass Flows down Arbitrary Topography*,
Advances in Geophysical and Environmental Mechanics and Mathematics,
DOI 10.1007/978-3-319-02627-5_8

$$\begin{aligned}\int_{t^n}^{t^{n+1}}\left\{J_0\frac{\rho_b}{\rho_0}\mathcal{U}\mathbb{v}_\tau\big|_{\zeta=0}\right\}\mathrm{d}t &\approx J_0\frac{\rho_b}{\rho_0}\int_0^{h_d}\mathbb{v}_\tau(\zeta)\mathrm{d}\zeta\\ &= J_0\frac{\rho_b}{\rho_0}\mathbb{v}_\tau\big|_{\zeta=h}\left\{h_d+\frac{h(1-\tilde{\chi}_b)}{n+2}\left[\left(1-\frac{h_d}{h}\right)^{n+2}-1\right]\right\}\end{aligned} \tag{8.2}$$

in the computation, where $\mathbb{v}_\tau \approx \mathbf{Fv}$ with the velocity profile given in (4.81), see also [1].

This chapter consists of three parts. In the first two parts we illustrate the key features of the model regarding two numerical benchmark problems: one is the one-dimensional case and the other one is the two-dimensional case. The third part exhibits an experimental validation. In all of the above examples, we simulate the motion of a granular material sliding down an inclined plane and merging onto a horizontal plane.

8.1 One-Dimensional Benchmark Problem—Finite Granular Mass Flowing down an Inclined Plane Chute onto The Horizontal Plane

In the one-dimensional benchmark problem, the chute consists of an inclined part, a horizontal part and a transition region which lies between the inclined slope and the run-out zone, see Fig. 8.1. Since this is a one-dimension problem, we shall take $\xi \equiv \xi^1$ as the down-slope coordinate.

The computational domain is $0 \le \xi \le 60$ (in dimensionless unit), where the inclined slope ranges over $0 \le \xi \le 30$, the transition section lies in the interval $30 \le \xi \le 40$, and the horizontal region is located where $\xi > 40$. The inclination angle of the inclined plane is prescribed as 35°. A smooth change in the topography, from the inclined section to the horizontal zone, is considered, where the inclination angle reads

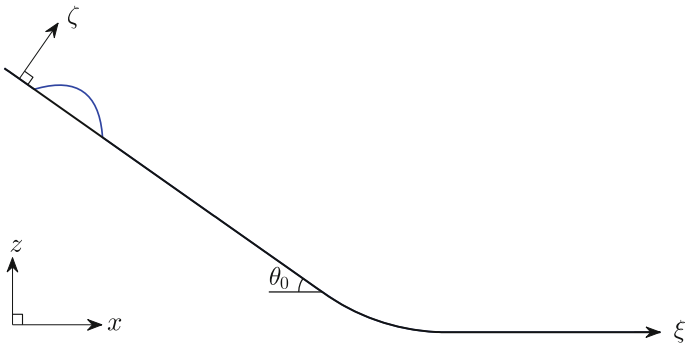

Fig. 8.1 Configuration of the one-dimensional benchmark problem, where x-axis lies in the horizontal plane and the ξ-axis points the down-slope direction

Table 8.1 Parameters employed in the computation

$\theta_0 = \theta_n$	δ_b	θ_d	m_2	α_e	α_v	α_h	e_α	$\alpha_\rho = \rho_b/\rho_0$	ϕ
35°	24°	33°	1.0	2.0	1.0	0.1	20	1.0	1.0

$$\theta(\xi)|_{t=0} = \begin{cases} \theta_0 & 0 \le \xi \le 30 \\ \theta_0(1 - (\xi - 30)/10)\,, & 30 < \xi < 40\,, \\ 0^\circ & 40 \le \xi \end{cases} \quad \text{with} \quad \theta_0 = 35^\circ\,. \tag{8.3}$$

In the computation the "plug flow" motion is considered, i.e. $\tilde{\chi}_b = 1$ in (4.81),

$$\mathbf{v} = \mathbf{v}(\xi, t) = \left(v^\xi(\xi, t),\ 0\right)^T\,,$$

implying $m_2 = 1.0$ and $\overline{\mathbf{v}} = \mathbf{v}\big|_{\zeta=0} = \mathbf{v}$, see (4.81) and (4.82) for details. The angle of the basal friction δ takes two values, δ_b and θ_d, as follows: $\delta = \delta_b$ for the friction between the chute and the flowing material, and $\delta = \theta_d$ for the friction between the flowing and the deposited material. As θ_d we consider the dynamical angle of internal friction of the material and take $\delta_b = 24^\circ$, $\theta_d = 33^\circ$.

At $t = 0$ the finite mass is on the top of the inclined plane and has a parabolic shape, ranging from $\xi = 2.8$ to 9.2, with the center at $\xi = 6.0$. The distributions of the initial depth and initial depth-averaged tangential velocity are given by

$$\begin{cases} h(\xi,\ 0) = 1 - ((\xi - 6.0)/3.2)^2 \\ \overline{v}_\xi(\xi,\ 0) = 1.2 + (\xi - 6.0)/3.2 \end{cases} \quad \text{for} \quad \xi \in [2.8,\ 9.2]\,, \tag{8.4}$$

respectively.

The mesh size is $\Delta\xi = 0.2$, Minmod slope limiter is used for the cell reconstruction of physical quantities, and the CFL number is selected to be 0.4. Taking into account the erosion/deposition, see (8.1), the neutral angle θ_n (angle of repose, angle of internal friction) is chosen to be equal to the inclination angle of the chute $\theta_n = \theta_0 = 35^\circ$. Table 8.1 lists the values of the relevant parameters $(\alpha_e, \alpha_v, \alpha_h, e_\alpha, \alpha_\rho)$ applied in the computation, where $\alpha_\rho = \rho_b/\rho_0$ stands for the density ratio of the flowing layer to the stagnant bottom.

Three scenarios are considered in the computation:

scenario I Erosion and deposition processes are carried out by the proposal (5.64) in which the threshold speed v_{th} is determined by (5.63) with $\alpha_v = 0.4$;

scenario II Neither erosion nor deposition takes place (i.e., $\mathcal{U} = 0$);

scenario III Erosion and deposition processes are implemented without considering the threshold criterion for deposition, i.e. deposition takes place once the inclination angle is less than the neutral angle ($\mathcal{U} > 0$ for $\theta > \theta_n$), see also (5.62) by setting $v_{\text{th}} = \infty$.

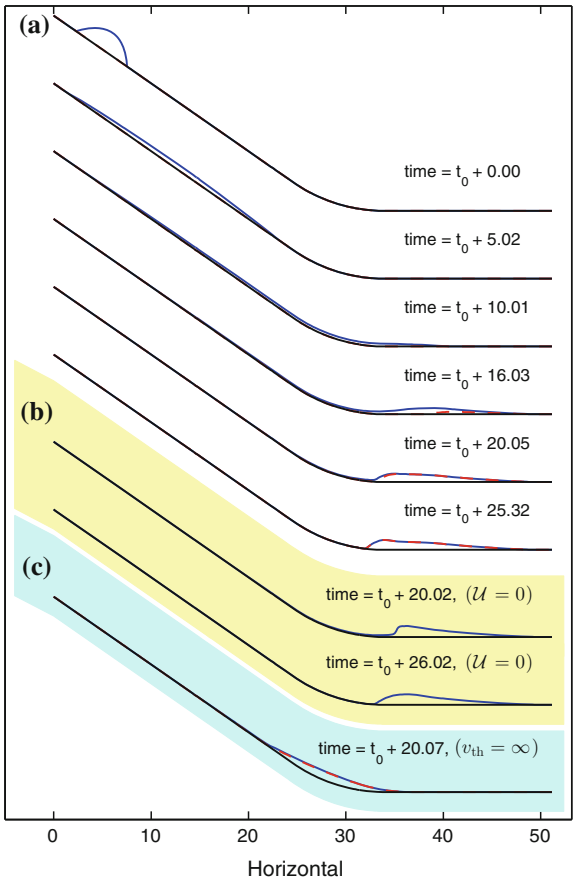

Fig. 8.2 a Process of the simulated granular avalanche in scenario I at different processes dimensionless time levels. b Results of scenario II where neither erosion nor deposition processe are considered ($\mathcal{U} = 0$). c Results of scenario III in which the threshold criterion for deposition does not exit

Figure 8.2 shows the simulated processes as the finite granular mass slides on the inclined plane into the horizontal run-out zone. The blue lines indicate the flow surface at various time levels, the surface of the deposition heap (the actual basal surface in computation) is depicted by the red dashed lines, and the black lines mark the initial chute basal surfaces. Before deposition takes place, the flow behaviors in the three scenarios are identical. Hence, the whole process of scenario I is illustrated in panel a of Fig. 8.2, and only the results of the last two time levels are given for scenario II and the last time level for scenario III (panels b and c). In scenario I, the avalanche body extends on the inclined plane, e.g., see the figure at $t = 5.02$. Once the front reaches the horizontal run-out zone the basal friction brings the front part of the granular material to rest and deposition takes place (see the figure at $t = 16.03$), where the red dashed line represents the surface of the deposition heap, which is the actual basal surface in the computation. At this stage, the rear part accelerates further. The deposition heap develops upwards and upstream (from $t = 16.03$ to 25.32). At $t = 25.32$ the total volume of the flowing body is less than 10^{-2} (ca. 0.12 % of the initial volume 8.52), so we regard the whole avalanche body to be at the state of rest.

In scenario II it is assigned that neither erosion nor deposition takes place in the computation. Without the resistance of the deposition heap, the mass center of the avalanche body moves forward as that in scenario I, see panel b of Fig. 8.2 for the computed depth profiles at $t = 20.02$ and 26.02 (denoted by $\mathcal{U} = 0$). We also found that the whole body never reaches the state of rest if no additional treatment is applied (for the balance between the basal Coulomb friction and the depth gradient corresponding to the angle of repose θ_n). As time increases, the surface slope decreases and becomes much less than the angle of repose, where spurious oscillation could also be observed due to the discontinuity of $\mathrm{sgn}(\boldsymbol{v}_\tau)$ at $\boldsymbol{v}_\tau = \boldsymbol{0}$ in implementing the Coulomb friction law, see also [2]. Now consider the case that the threshold criterion for deposition does not exit (scenario III), which is equivalent to the assumption of an excessively large threshold velocity, $v_{\mathrm{th}} = \infty$. Deposition takes place once the inclination angle is less than the angle of repose (i.e., $\theta < \theta_n$). Consequently, in the computation deposition takes place when the avalanche body passes through the transition zone, see panel c of Fig. 8.2 marked by ($v_{\mathrm{th}} = \infty$). The mass accumulates fast within the transition section, so that both of the duration of movement and the run-out distance have been reduced significantly. As shown in panel c of Fig. 8.2, almost the whole avalanche body is deposited in the transition zone at $t = 20.07$, which is ca. 80 % of the duration in scenario I. This unexpected accumulation within the transition zone is in conflict with the experimental observation, see e.g. [3], which confirms that the introduction of the threshold velocity v_{th} in the proposal (5.64) is a reasonable assumption.

The development of the deposition heap can be mimicked in scenario I. Figure 8.3 illustrates the local view of panel a of Fig. 8.2 for highlighting the evolution of the moving basal surface together with the flow surface. At $t = 15.00$, the front part has reached the horizontal plane, where the local velocity is nearly less than the threshold velocity v_{th} and deposition is about to take place. The basal surface rises beneath the front part first, and the deposition heap develops fast upwards and upstream (from $t = 16.03$ to 19.01). Because the rear part of the moving mass accelerates further, a surface flow is established climbing above the newly generated bed ($t = 19.01$ to 21.03). The depth of this surface flow decreases. At $t = 25.32$, the total volume of the flowing layer is less than 10^{-2} and recognized to be at rest. One may imagine that the whole avalanche body is frozen through this deposition process. The final depth profile is kept at $t = 25.32$ in stationary state.

8.1.1 Effects of the Deposition Heap

It is of no doubt that the existence of the deposition heap will change the flow behavior. Once the deposition heap exists, it will obstruct the sequential flows. That is, the material of the rear part either merges from the back into the deposition heap or climbs over the newly generated heap. In case that the deposit process is ignored, the motion of the material is mainly retarded by the basal friction. Although the whole body never comes to the state of absolute rest, the computed results yield a

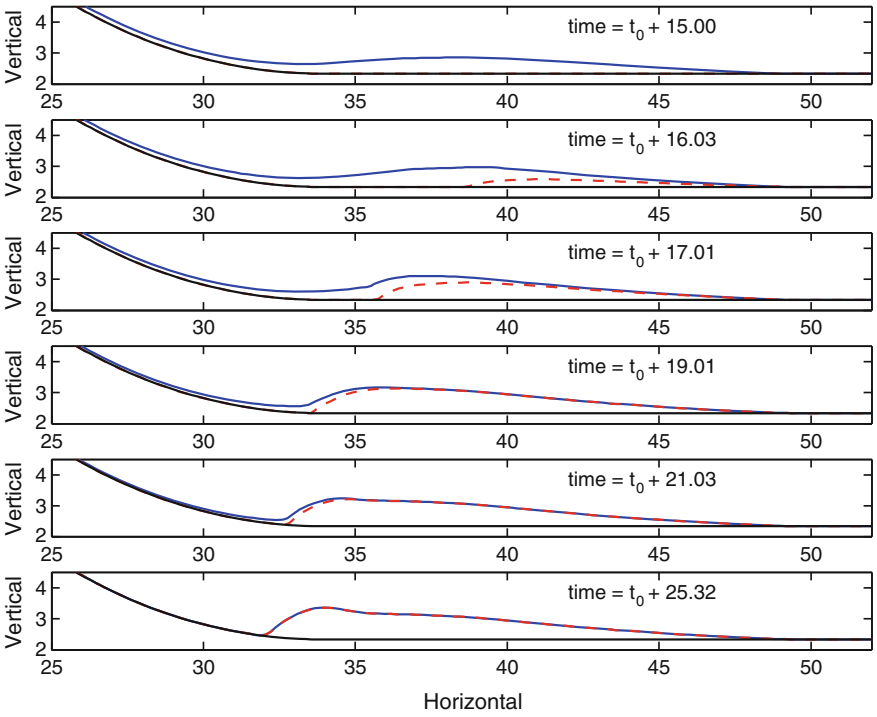

Fig. 8.3 Evolution of the moving basal surface and corresponding flow surface in scenario I. The surface of the deposition heap (the actual basal surface in the computation) is indicated by the *red dashed lines*, the flow surface is marked by *blue lines*, and the *black lines* stand for the initial chute basal surfaces

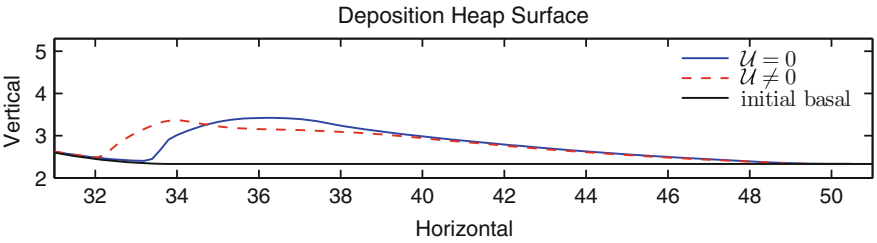

Fig. 8.4 The distributions of the depth profiles when the flow body comes to rest ($\tilde{k} = 1$)

more concentrated deposit shape, see Fig. 8.4. The red dashed line marks the depth profile computed with the deposition process ($\mathcal{U} \neq 0$) at $t = 25.32$, and the blue line represents the depth distribution at $t = 26.02$ when the deposition process is ignored ($\mathcal{U} = 0$). The stretching distribution of the deposition heap computed with deposition processes is evident. It is also noticed that, without the deposition processes, the flowing body can never reach the state of rest, unless additional treatment, such

as the well-balanced technique, is applied to overcome the singularity caused by Coulomb friction, namely $\mathrm{sgn}(\boldsymbol{v}_\tau)$ at $\boldsymbol{v}_\tau = \boldsymbol{0}$, e.g., [4, 5]. With the introduction of the deposition process, the flowing material is frozen into the stagnant heap through this deposition process, so that the flow depth vanishes as its velocity reduces to zero. Once the deposition process is applied, there is no need to apply the well-balanced technique, and it provides the possibility to have a more detailed insight into the mysterious deposition process.

8.1.2 *Effects of the Earth Pressure Coefficient*

In case that the avalanching mass is treated as a fluid of Mohr-Coulomb type, the term $\overline{\mathbf{P}}$ in (4.102) then reads

$$\overline{\mathbf{P}} = (1 - \tilde{k})\, \overline{p}\, \mathbf{M}_0 \,, \tag{8.5}$$

where the value of $\tilde{k}$ is a function of the mean surface stretching $\boldsymbol{D}_{\mathcal{S}}$. In the current one-dimensional problem, $\tilde{k}$ is determined by

$$\tilde{k} = \begin{cases} \tilde{k}_{act} \,, & \text{for} \quad \dfrac{\partial v^\xi}{\partial \xi} \geq 0 \,, \\[2ex] \tilde{k}_{pass} \,, & \text{for} \quad \dfrac{\partial v^\xi}{\partial \xi} < 0 \end{cases} \tag{8.6}$$

with

$$\tilde{k}_{act/pass} = 2 \sec^2 \theta_d \left\{ 1 \mp (1 - \cos^2 \theta_d \sec^2 \delta)^{1/2} \right\} - 1 \,, \tag{8.7}$$

where δ stands for the angle of local basal friction. In (8.7), $\theta_d = 33^\circ$ and $\delta = \delta_b = 24^\circ$ before the development of the deposition but $\delta = \theta_d = 33^\circ$ when the deposition heap exists. The applied values of $\tilde{k}_{act/pass}$ are listed in Table 8.2. Figure 8.5 shows the deposition heaps, where the blue solid line depicts the depth distribution at $t = 26.04$ computed without deposition process (marked by $\mathcal{U} = 0$), the red dashed and the black dotted lines denote the deposition heaps (marked by $\mathcal{U} \neq 0$) computed with $\tilde{k} = 1$ ($t_{\text{end}} = 25.32$) and $\tilde{k} = \tilde{k}_{act/pass}$ ($t_{\text{end}} = 23.78$), respectively. Remarkably, there is no significant difference in the deposited avalanche body among the three cases.

Table 8.2 Values of $\tilde{k}_{act}$ and $\tilde{k}_{pass}$ with respect to the used θ_d and δ

	$\tilde{k}_{act}$	$\tilde{k}_{pass}$
$\theta_d = 33^\circ,\ \delta = 24^\circ$	0.4392	2.3302
$\theta_d = 33^\circ,\ \delta = 33^\circ$	1.3847	1.3847

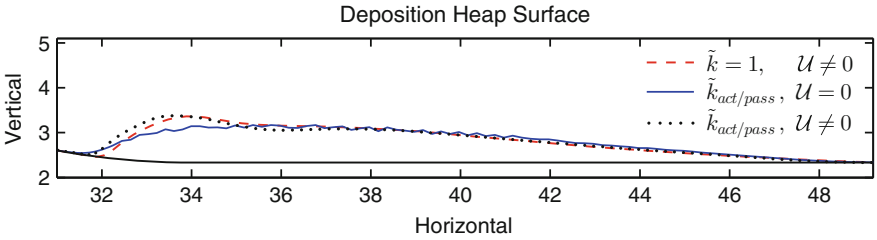

Fig. 8.5 The shapes of the deposition heap, where $\tilde{k}=1$ and $\tilde{k}=\tilde{k}_{act/pass}$ for $\mathcal{U}=0$ and $\mathcal{U}\neq 0$ are taken into account

When the material slides on the horizontal plane, the basal friction decelerates the motion, so that the flowing mass converges (i.e. $\partial v^{\xi}/\partial\xi<0$) yielding $\tilde{k}=\tilde{k}_{pass}$. Before the deposition takes place, the small basal friction $\delta=24^{\circ}$ yields a large value of the earth pressure coefficient ($\tilde{k}_{pass}=2.3302$). With a larger value of $\tilde{k}_{pass}$ the moving body spreads more. Once the deposition heap develops, the surface flow climbs above the newly developed heap and quickly deposits on the heap. At this stage, the local value of $\tilde{k}_{pass}$ reduces from 2.3302 to 1.3847. Since the lifetime of the surface flow on the heap is rather short, the value of $\tilde{k}$ (= 1.3847) can hardly influence the final shape of the deposition heap. The large values of $\tilde{k}$ (2.3302 and 1.3847) also enhance the deposition process and hence shorten the duration of motion (from 25.33 to 23.78). In addition, spurious oscillations are observed by the results computed without deposition process ($\tilde{k}_{act/pass}$, $\mathcal{U}=0$). The spurious oscillation is caused by the discontinuities of $\tilde{k}_{act/pass}$ in (8.6) at $\partial v^{\xi}/\partial\xi=0$ and $v^{\xi}/|v^{\xi}|$ at $v^{\xi}=0$. The employment of the deposition process generally allows to better determine the duration of the moving process; moreover, with it the spurious oscillation is diminished.

8.2 Two-Dimensional Benchmark Problem—Finite Granular Mass Glowing down an Inclined Plane Chute onto The Horizontal Plane

In this two-dimensional benchmark problem the granular material is released from a parabolic cap and slides down a rigid chute, whose configuration is shown in Fig. 8.6. The x-y-plane is the horizontal plane and the z-axis points upwards. The coordinate $\xi=\xi^1$ indicates the down-slope direction whose projection on the horizontal plane coincides with the x-direction; $\eta=\xi^2$ denotes the cross-slope coordinate and its projection on the x-y-plane points in the y-direction. The inclined chute lies in the range of $0<\xi<21.5$ with inclination angle $\theta_0=40^{\circ}$, and the horizontal flat plane ranges from $\xi>27.5$ (in dimensionless units). Transition zone lies between the inclined chute and the horizontal plane. The inclination angle is given by

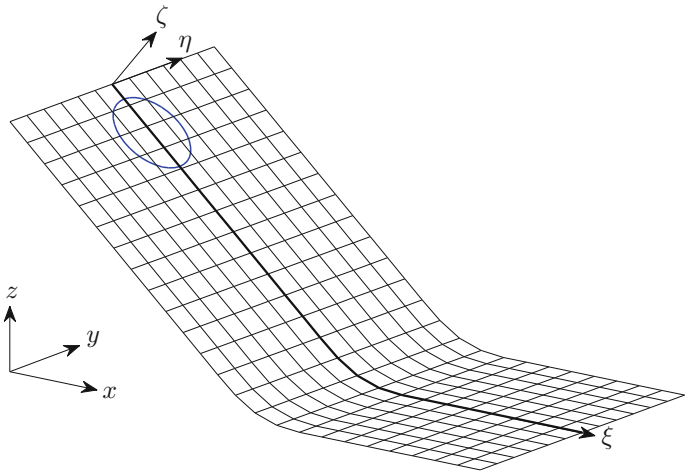

Fig. 8.6 Configuration of the two-dimensional benchmark problem, where the x-y-plane lies on the horizontal plane, the ξ-axis points down-slope and the η-axis indicates the cross-slope direction

$$\theta(\xi,\ \eta)\big|_{t=0} = \begin{cases} \theta_0 & 0 \le \xi \le 21.5\,, \\ \theta_0\,(1-(\xi-21.5)/6)\,, & 21.5 < \xi < 27.5\,, \\ 0^\circ & 27.5 \le \xi\,. \end{cases} \tag{8.8}$$

The initial shape of the mass is a parabolic cap, whose maximum height is 0.5 above the topography with a radius of $r_0 = 2.4$ at the base. That is, the initial depth distribution reads

$$h(\xi,\ \eta)\big|_{t=0} = \begin{cases} 0.5\left(1 - r^2/r_0^2\right) & \text{for} \quad r < r_0\,, \\ 0.0 & \text{for} \quad r \ge r_0\,, \end{cases} \tag{8.9}$$

where r is the distance of $(\xi,\ \eta)$ to the cap center $(4.6,\ 0.0)$ on the ξ-η-surface. The tangential components of the initial velocity are given by

$$\begin{aligned} \overline{v}^{\xi}(\xi,\ \eta)\big|_{t=0} &= \begin{cases} 1.2 + (\xi - 4.6)/r_0 & \text{for} \quad h \ne 0\,, \\ 0.0 & \text{for} \quad h = 0\,, \end{cases} \\ \overline{v}^{\eta}(\xi,\ \eta)\big|_{t=0} &= \quad 0.0 \qquad\qquad\quad \text{overall}\,, \end{aligned} \tag{8.10}$$

with which the horizontal components of the tangential velocity, $\overline{\mathrm{v}}_\tau = (\overline{v}_x^\tau,\ \overline{v}_y^\tau)^T$, can be determined by the relation (4.101).

The chute was assumed to be rigid, so that no material is entrained across the chute surface, but deposition may take place in the horizontal run-out zone. In the computation, the angle of basal friction δ_b against the chute surface is set equal to 23°; the angle of internal friction of the material θ_d is assumed to be of the same value as the angle of repose (neutral angle) θ_n, both being 34°. Once the deposition heap rises at the bottom, the local basal friction is changed to the angle of internal friction of the

Table 8.3 Parameters employed in computation

θ_0	θ_n	δ_b	θ_d	α_e	α_v	α_h	e_α	$\alpha_\rho = \rho_b/\rho_0$	ϕ
40°	34°	23°	34°	2.0	1.0	0.1	20	1.0/0.9	1.0

material, i.e. the angle of friction is changed from 23° to 34°. For ease of comparison with the one-dimensional case, if not explicitly specified, the "plug flow" assumption (i.e., $m_2 = 1.0$) is applied in the computation, although it may not match the reality. The material parameters and the relevant parameters for erosion/deposition processes in (5.64) are summarized and listed in Table 8.3. The mesh size is $\Delta\xi = \Delta\eta = 0.2$; the superbee slope limiter is used for the cell reconstruction of relevant physical quantities; and the CFL number is selected to be 0.4.

The computed results are illustrated in Fig. 8.7, where the thickness contours of the flowing body together with the outlines of the deposition heap are given in a sequence of non-dimensional times. The contour lines are defined at levels 0.001, 0.01, and from 0.04 to 0.1, at increments of 0.03. The red thick lines depict the outlines of the developing deposition heap. The transition zone is indicated by the two dash-dotted lines. In the inclined section, the flowing mass extends in both the down- and transverse-slope directions and accelerates in the down-slope direction. In the horizontal run-out zone, the flowing mass decelerates due to basal friction, and

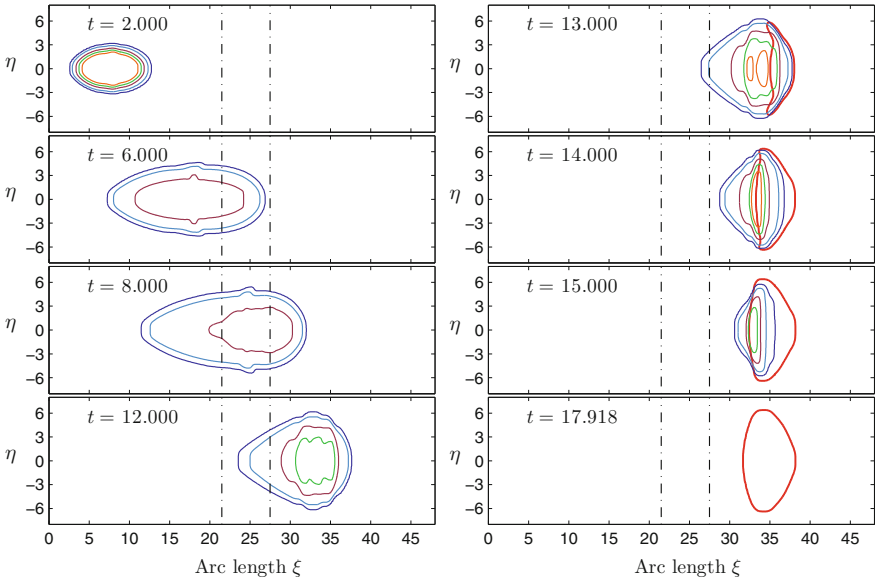

Fig. 8.7 Time sequence of the thickness distribution of a finite granular mass sliding down an inclined chute onto a horizontal run-out plane. The smooth transition zone lies between the pair of *vertical dash-dotted lines*. The *red* ***thick*** *lines* outline the deposition heap at each time slice. The flow (whole body) stops at $t = 17.918$ (Reproduced from [1] with permission.)

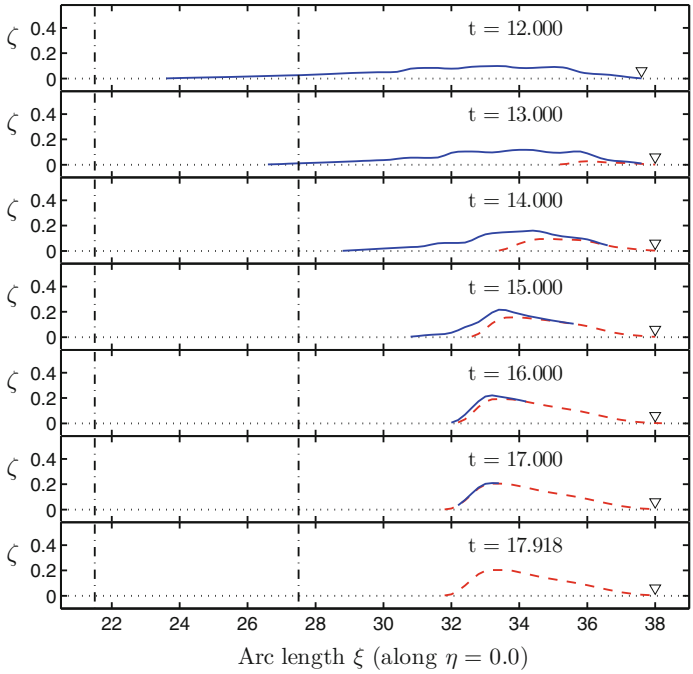

Fig. 8.8 Longitudinal section of the avalanche mass along ξ at $\eta = 0$. The *black dotted lines* at $\zeta = 0$ represent the basal surface of the chute, the *red dashed lines* indicate the interface of the deforming deposition heap and the *blue solid lines* mark the free surface of the flowing layer. The marker "$\triangledown$" indicates the position of the maximum run-out distance, at which the deposition depth is 10^{-3} (Reproduced from [1] with permission.)

the deposition heap begins to form at the front part ($t = 12.0$–14.0). The deposition heap obstructs the movement of the mobile rear part yielding high thickness gradients ($t = 13.0$ to 15.0). At $t = 17.918$ the total volume of the flowing layer reduces to be less than $10^{-6} V_{\text{init}}$ (initial volume $V_{\text{init}} = 4.520$), so we regard the whole avalanche body to be at rest.

The sequential cross-sections along ξ at $\eta = 0.0$ are shown in Fig. 8.8. The black dotted lines represent the surface of the chute, the red dashed lines indicate the evolving surface of the deposition heap and the blue solid lines mark the free surfaces of the flowing layers. It is found that deposition takes place between $t = 12.0$ and 13.0, and the deposit heap rapidly accumulates at its rear side. As also observed in the experiments by [2, 6], the flowing layer becomes thin and flows over the heap when impinging on the deposition heap. It quickly comes to rest when it reaches the top of the frontal zone. Once the material comes to rest, one can imagine it as frozen into the static heap. The development of the deposition heap has simplified the process of determining the maximum run-out distance, because the additional treatment of the well-balanced technique is no longer needed. In Figs. 8.8 and 8.9, we use the marker "$\triangledown$" to indicate the position of the maximum run-out distance, which

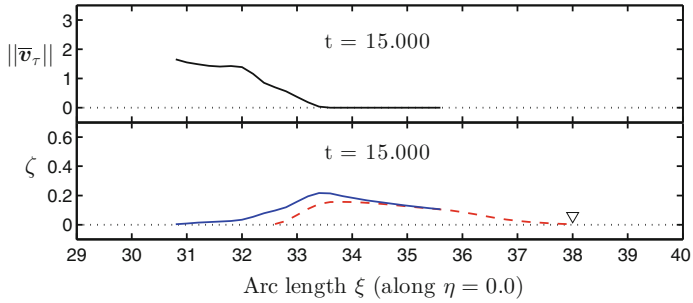

Fig. 8.9 Longitudinal section of the avalanche mass (*bottom*) and the distribution of the corresponding speed (*top*) along ξ at $\eta = 0$ and time $t = 15.0$ (Reproduced from [1] with permission.)

is determined by the deposition thickness of 10^{-3}. It can be seen in Fig. 8.8 that the maximum run-out distance $\xi = 38.0$ was reached at $t = 13.0$, yet, the deposition heap continued developing as the mass approaching the deposition rear continued to flow into/over the heap. Figure 8.9 shows the longitudinal section of the avalanche mass (bottom panel) and the corresponding tangential speed $||\overline{\boldsymbol{v}}_\tau||$ (top panel) along ξ at $\eta = 0$, at time $t = 15.0$. While the flowing material is climbing the deposition heap upslope, it can be seen in the top panel that the material quickly decelerates to rest once the top of the frontal zone is reached.

Along the ξ-direction the deposition heap develops toward upstream, whilst it extends sidewards in the transverse direction. Figure 8.10 depicts the evolution of the growing deposition heap in the transverse direction at $\xi = 33.0$. Prior to $t = 14.0$, the moving mass flows through this cross-section without sedimenting at this position. However, as shown in Fig. 8.8, the mass-flux decreases as it passes through this cross-section (t =12.0–15.0). At time $t = 15.0$ the deposited pile is just about forming at the cross-section. The thickness of the flowing layer decreases rapidly in the time interval from 15.0 to 17.0. The flowing mass vanishes with the whole material frozen in the deposition heap at $t = 17.918$, after that the deposition profile remains in a stagnant state.

8.2.1 Effects of the Velocity Ratio $\tilde{\chi}_b$ and the Velocity Profile

In the momentum equation (4.100), the correction factor m_2 defined in (4.82) is a function of the exponent n and the ratio $\tilde{\chi}_b$ of the basal sliding velocity to the one at the flow surface, see (4.80) for the definitions of n and $\tilde{\chi}_b$. The limiting case $\tilde{\chi}_b = 0$ indicates the no-slip condition at the basal surface; the case $\tilde{\chi}_b = 1$ implies the "plug flow" regime, where $m_2 = 1.0$. By fixing $n = 1$, Fig. 8.11 illustrates the normalized velocity profiles $v/\overline{v}$ (we consider the 1D case) versus various velocity ratios $\tilde{\chi}_b$. It is clear that the choice of the velocity ratio $\tilde{\chi}_b$ has significant impacts on the shape

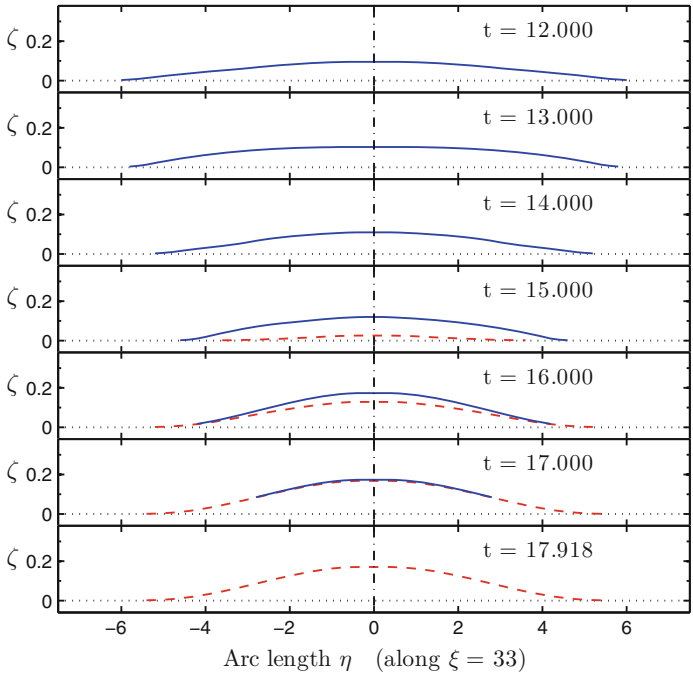

Fig. 8.10 Cross-sectional view of the avalanche mass along η at $\xi = 33.0$. The *black dotted lines* at $\zeta = 0$ represent the basal surface of the chute, the *red dashed lines* indicate the interface of the deforming deposition heap and the *blue solid lines* mark the free surface of the flowing layer (Reproduced from [1] with permission.)

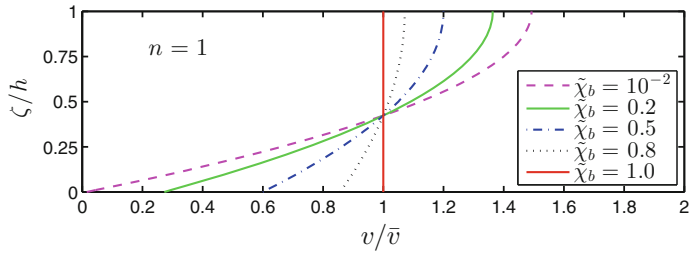

Fig. 8.11 Normalized profiles of the velocity with respect to different values of $\tilde{\chi}_b$, where the mean velocity is equal to one, i.e., $\bar{v} = 1$ (Reproduced from [1] with permission.)

of the velocity profile. With the help of (4.81) one computes the value of χ_b for given $\tilde{\chi}_b$, so that m_2 can be determined by (4.82) once the value of the exponent n is available. Figure 8.12 illustrates the values of m_2 versus the velocity ratio $\tilde{\chi}_b$, in which the exponents $n = 0$, 1, 10 and 10^3 are used. With $n = 10^3$, the velocity distribution is nearly uniform along the flow thickness for any $\tilde{\chi}_b \in [0, 1]$, so that $m_2 \approx 1$. For $n = 1$, the velocity profile exhibits a parabolic shape and the value

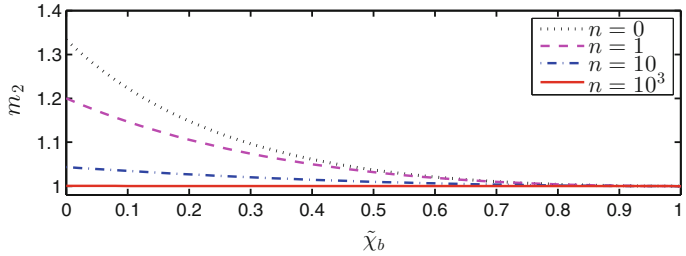

Fig. 8.12 Values of the momentum correction factor m_2 versus $\tilde{\chi}_b$ with respect to different velocity profiles (different values of n) (Reproduced from [1] with permission.)

Table 8.4 Values of m_2 and the corresponding $\tilde{\chi}_b$ (in bracket) with respect to various flow rule approximations

	$\tilde{\chi}_b = 10^{-2}$	$\tilde{\chi}_b = 10^{-1}$	$\tilde{\chi}_b = 0.5$	$\tilde{\chi}_b = 1.0$
$n = 10^3$	1.0005 (0.0100)	1.0004 (0.1001)	1.0001 (0.5002)	1.0 (1.0)
$n = 10^2$	1.0048 (0.0101)	1.0040 (0.1009)	1.0012 (0.5025)	1.0 (1.0)
$n = 1$	1.1941 (0.0149)	1.1469 (0.1429)	1.0320 (0.6000)	1.0 (1.0)
$n = 0$	1.3203 (0.0198)	1.2231 (0.1818)	1.0970 (0.6667)	1.0 (1.0)

of m_2 tends to be 1.2 when the basal velocity tends to vanish, i.e. $m_2 \to 1.2$ for $\mathbf{v}_{\zeta=0} \to 0$ or $\tilde{\chi}_b \to 0$. When $n = 0$, it yields the maximum value of m_2 for $n \geq 0$ at fixed $\tilde{\chi}_b \in [0,\ 1]$, where the velocity increases linearly from the bottom to the flow surface. The values of m_2 with respect to specific velocity ratio $\tilde{\chi}_b$ and exponent n are listed in Table 8.4.

Effects of the Velocity Ratio $\tilde{\chi}_b$

To investigate the impacts of the velocity ratio $\tilde{\chi}_b$ on the flow behavior and the deposition development under a unique condition, although it may not correspond to reality, two regimes are assigned in the following computation: a sliding regime with $n = n^I$; and a deposition regime with $n = n^{II}$. That is, the value of n is changed from n^I (sliding regime) to n^{II} (deposition regime) when deposition takes place. With the exponents $(n^I,\ n^{II}) = (10^3,\ 10^0)$ for the two regimes, the impacts of the velocity ratio $\tilde{\chi}_b$ on the deposition heap are examined with respect to three velocity ratios, $\tilde{\chi}_b = 10^{-2}, 0.5$ and 1.0. Figure 8.13 depicts the outlines of the final deposit in the computation. Remarkably, no significant difference is found among these outlines. Although there is considerable difference among the velocity profiles and m_2-values when $n = 1$ with respect to different values of $\tilde{\chi}_b$ (see Fig. 8.11), the differences among the final deposition heaps are rather minor. A likely reason for the minor differences might be the fact that the run-out distance is mainly determined during the period of sliding regime, under which the value of the exponent n is set to be 10^3, so that the value of m_2 is nearly equal to 1 for any value of $\tilde{\chi}_b \in [0, 1]$.

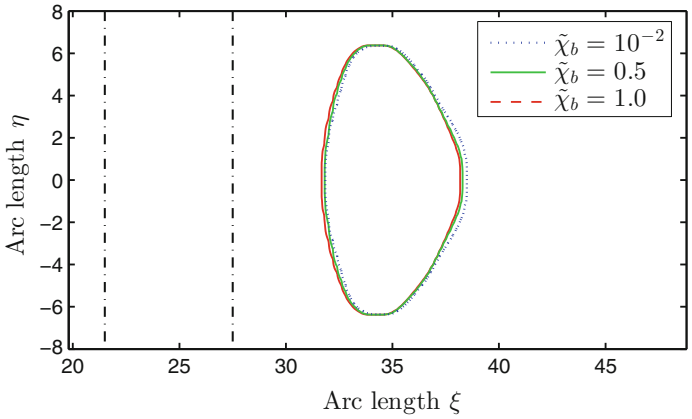

Fig. 8.13 Outlines of the deposition heaps with respect to different velocity ratios $\tilde{\chi}_b$, where the exponents $(n^I,\ n^{II}) = (10^3,\ 10^0)$ are used (Reproduced from [1] with permission.)

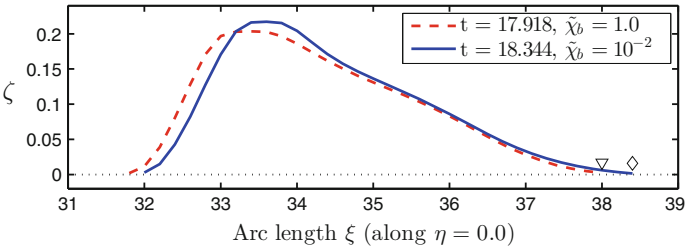

Fig. 8.14 Section views of the final deposition heaps, where the *red dashed line* is obtained with $\tilde{\chi}_b = 1.0$ and the *blue solid line* indicates the result when $\tilde{\chi}_b = 10^{-2}$ (Reproduced from [1] with permission.)

According to the momentum equation (4.100), there would be no substantial difference in the evolution of the momentum when $m_2 \approx 1$. Thus, the deposition heap develops approximately at the same location. Once the kinetic energy (speed) falls below the threshold value and the material begins to be deposited, the flow changes into the deposition regime ($n = 1$). However, because of the small velocity, the whole flowing body comes rapidly to rest and only slight differences are observed thereafter. Figure 8.14 illustrates the section views of the final deposition heaps in Fig. 8.13, where the red dashed line shows the result obtained with $\tilde{\chi}_b = 1.0$ and the blue solid line represents the result computed with $\tilde{\chi}_b = 10^{-2}$. The maximum run-out distances are indicated by the markers "$\triangledown$" and "$\Diamond$" for $\tilde{\chi}_b = 1.0$ and $\tilde{\chi}_b = 10^{-2}$, respectively, where $\triangledown$ points at 38.0 and $\Diamond$ locates at 38.4. The durations of flowing matter are 17.918 and 18.344, respectively. In the deposition regime, $m_2(n = 1,\ \tilde{\chi}_b = 10^{-2}) = 1.1941$ and $m_2\ (n = 1,\ \tilde{\chi}_b = 1.0) = 1.0$. The larger value of m_2 results in a frontward mass distribution of the deposition heap. The larger maximum run-out distance and longer duration are also due to the larger value of m_2.

Table 8.5 Values of n^I, n^{II} with the corresponding m_2 (in bracket) and the relevant parameters in cases A, B and C

	n^I	n^{II}	$\tilde{\chi}_b$	t_{end}
Case A	10^3 (1.0004)	10^0 (1.1469)	0.1	17.9753
Case B	10^3 (1.0004)	0 (1.2231)	0.1	17.8101
Case C	10^2 (1.0040)	0 (1.2231)	0.1	18.4701

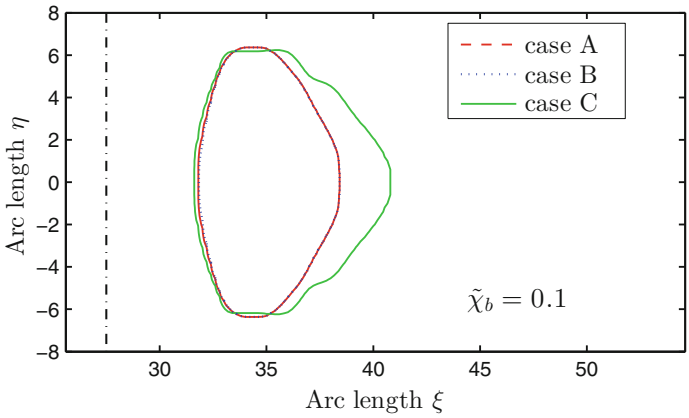

Fig. 8.15 Outlines of the deposition heap in the three cases, where fixed velocity ratio $\tilde{\chi}_b = 0.1$ is used

Effects of the Velocity Profile

The results in the previous example reveal that the values of the velocity ratio are not sensitive to the shape of final deposit once the values of n^I and n^{II} are fixed for the sliding and deposition regimes, respectively. We now examine the impacts of n^I in the sliding regime, where three cases are considered: case A with $(n^I, n^{II}) = (10^3, 10^0)$; case B with $(n^I, n^{II}) = (10^3, 0)$; and case C with $(n^I, n^{II}) = (10^2, 0)$. The parameters are summarized in Table 8.5. The results are shown in Fig. 8.15, where a fixed value for the velocity ratio $\tilde{\chi}_b = 10^{-1}$ is used in the three cases. With the same value $n^I = 10^3$ but different n^{II} (1 and 0, respectively), the shapes of the final deposit are nearly identical, see cases A and B in Fig. 8.15. However, with the same value $n^{II} = 0$, different velocity profiles in the sliding regime (i.e. different values of n^I) yield a significant discrepancy in the shapes of the final deposit, see the notable discrepancy between the results of cases B and C in Fig. 8.15. Figure 8.16 shows the section views along the ξ-axis of the deposition heap in Fig. 8.15. Although the main part locates approximately at the same position, discrepancy appears at small flow thickness (i.e. when $h \to 0$). This discrepancy indicates the fact that the velocity profile in the sliding regime has crucial impacts on the shape of the final deposit as well as the maximum traveling distance. The likely reason for this significant discrepancy might be the long durations and large traveling distances in

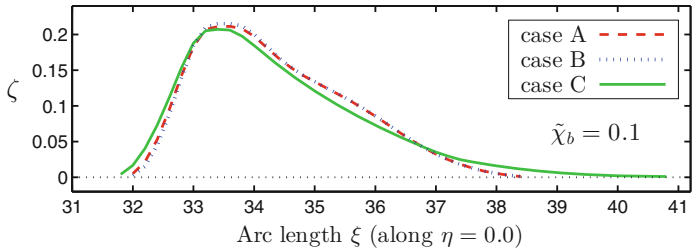

Fig. 8.16 Section views of the final deposition heap for cases A, B and C

the sliding regime, although the change of the value of m_2 is rather tiny (1.0004 to 1.0040 among cases B and C). These results indicate that the computational results are highly sensitive to the value of m_2 in the sliding regime. This would be one of the main challenges in simulating the mass motion, where the velocity is varying with non-uniform distribution.

8.3 Comparison between Theoretical Prediction and Experiments

In this section we are going to demonstrate an experimental validation, which is about the motions of granular avalanches down an inclined plane chute into the horizontal run-out zone. During the experiments, a high-speed digital camera was used to record the sequential motion of the granular flows. Through the techniques of image processing, the sequential outlines of the deposition heap are available for comparing the experimental findings with the computed results. Sound agreements between theoretical predictions and experimental results in (a) the run-out distance, (b) position of the traveling shock wave, and (c) evolution of the shape and position of the growing deposition heap, support the applicability of the proposed model. To have an apposite comparison, we depict the numerical results on the corresponding photographs, so that one can easily compare the run-out distances and the thicknesses of the flowing mass as well as the shapes of deposition heap.

8.3.1 Experimental Setup and Material Preparation

The experiments were carried out in a chute made of plexiglass, where the internal width is 40 mm. Figure 8.17 depicts the sketch of the chute (top panel) and the inclination angle of the chute bed as a function of the arc length (lower panel), where a reservoir locates at the top, and a transition zone lies between the inclined slope and the horizontal zone. The reservoir is equipped with an adjustable vertical gate,

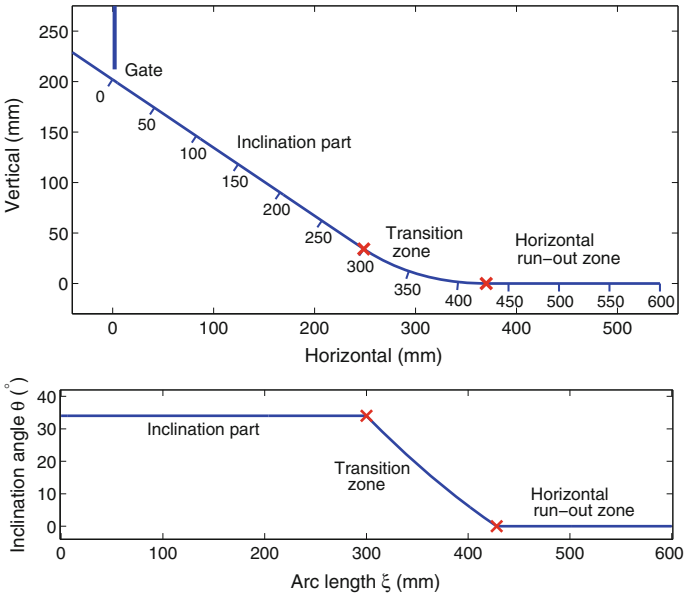

Fig. 8.17 *Upper panel* Sketch of the bed of the chute which consists of three parts: *inclined part*, *transition zone* and *horizontal run-out part*. The arc length is given in mm. *Lower panel* Inclination angle of the chute bed as a function of the arc length ξ, where the upper part is inclined at 34° from the horizon, and the *transition zone* is denoted between the two marks "×"(From [2] with permission.)

Table 8.6 Material coefficients for both types of chute

Chute	ϕ (°)	δ_1 (°)	δ_2 (°)	δ_3 (°)
Type I	34.1 ± 1.4	23.0 ± 1.1	23.0 ± 1.1	23.0 ± 1.1
Type II	34.1 ± 1.4	24.9 ± 1.5	34.1 ± 1.4	34.1 ± 1.4

(From [2] with permission)

and a shutter is mounted to hold the initial granular mass. The shutter is manually lifted to let the mass of the granules slide down through the gate. Counted from the gate, the total arc length of the chute is 600 mm, the upper part is 300 mm long, inclined at 34° from the horizon, and the transition part ranges from 300 to 428 mm. In experiments, we used 300 g (about 0.1701) Ottawa sand (compliant to ASTM C778 20/30, diameter: 0.60–0.85 mm), where about 20 % of the total volume of the sand is colored for visibility purposes.

Two types of basal surfaces were used. In the first Type I, the bed surface of the three parts are made of plexiglass; in the second Type II the bed surface of the upper straight part is covered by writing paper and the remaining bed surface, the transition and horizontal parts, is made rough by gluing Ottawa sand on it. We denote the angle of internal friction of the Ottawa sand by ϕ, and δ_1, δ_2, δ_3 for the angles of basal friction of the upper straight part, the transition zone and the horizontal part, respectively. Table 8.6 lists the separately measured material coefficients (of Ottawa

sand) and angles of basal friction for both chutes. In experiments, it is found that the outflow rates from the reservoir remained constant from the opening of the gate to the complete evacuation of the reservoir [2, 7]. Hence, a constant material supply from the reservoir is kept in the numerical simulation in what follows.

8.3.2 *Development of the Deposition Heap*

The typical flow behavior in the experiments is given in Fig. 8.18, which is performed in chute Type I when a gate opening of 10 mm is employed. The light yellow (solid) lines indicate the plexiglass bottom of the chute. The time slice at the top panel(s)

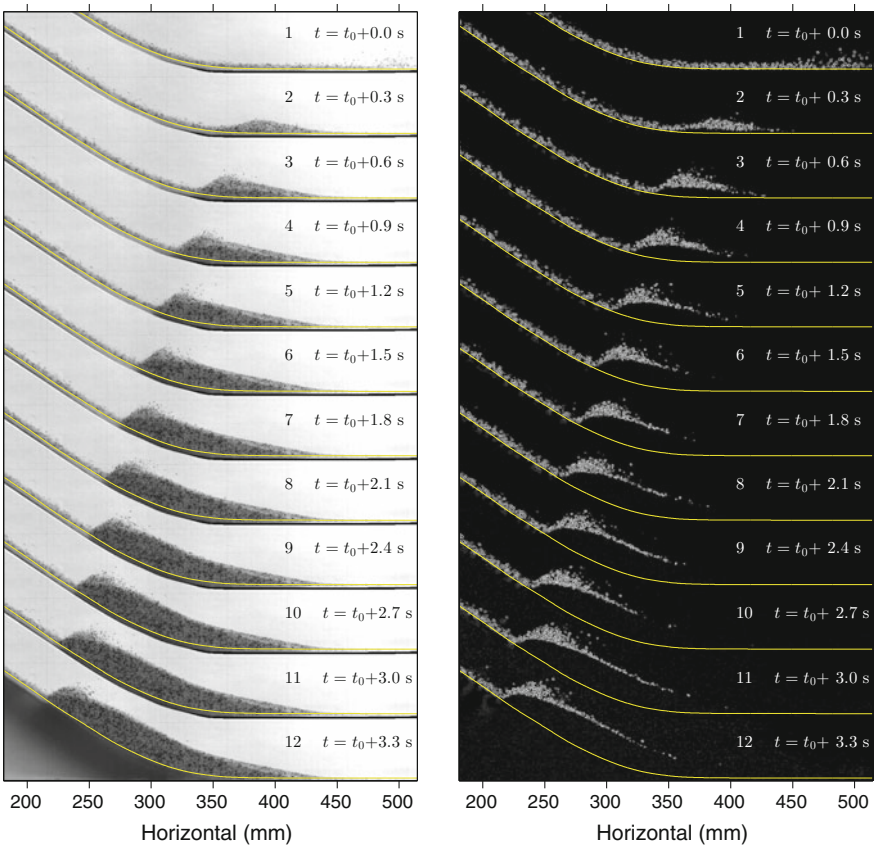

Fig. 8.18 *Left* Consecutive shots that are approximately 0.3 s apart of the down-flowing granular material, where the *light yellow lines* indicate the surface of the plexiglass. *Right* The corresponding outlines of the deposition heap, where the stagnant parts are shown in *dark grey* and the flowing layers are expressed in *light color* (Reproduced from [2] with permission.)

of Fig. 8.18 is defined as t_0, and the sequential photographs are 0.3 s apart. The corresponding sequential outlines of the growing deposition heap can be seen in the right panels of Fig. 8.18, which are obtained by subtracting two consecutive photographs of 1/200 s apart. The stagnant parts are shown in dark grey and the light areas indicate the flowing layers.

When the particles first arrive at the horizontal run-out zone, they are violently jumping over the basal surface; the basal drag reduces the pulsation and the deposition heap begins to develop (panels 1 and 2 in Fig. 8.18). The deposited pile grows and accumulates as the granular flux continues from above. The consecutive photographs show that the deposition heap rises approximately from $t = t_0 + 0.3$ s (panel 2). Once the deposit takes place, the deposited heap grows rapidly and extends upslope. The thickness of the deposition heap remains approximately constant over the straight inclined part (panels 3 to 12). The deposition heap propagates upslope with a "claw-type" shape. This "claw-shape" was kept as final shape, when the reservoir was empty and all the material was at rest. The claw-shape of the growing deposition heap has been recognized as a "granular jump" or "normal shock", which propagates upslope at approximately constant speed (e.g., [8, 9] or [6]). It is noticed that, in the right panels of Fig. 8.18, a thin layer of rapidly flowing material is climbing onto the deposition heap and quickly comes to rest. This thin and short-lived surface flow provides us with a validation example of thin surface flow over a growing deposited pile where the claw-shape front propagates upslope.

8.3.3 Comparison of Theoretical Results with Experiments

Following the experimental setup, the initial inclination angle of the chute in the numerical computation is given by a function of the arc length (in mm) as

$$\theta(0,\,\xi) = \begin{cases} \theta_0 & \text{for} \quad \xi \le 300\,, \\ \theta_0\left(1 - \frac{\xi - 300}{128}\right) & \text{for} \quad 300 \le \xi \le 428\,, \\ 0 & \text{for} \quad 428 \le \xi \le 600\,, \end{cases} \tag{8.11}$$

in which the inclination angle of the slope section is chosen to be equal to the neutral angle (angle of repose, internal friction angle), i.e. $\theta_n = \theta_0 = \theta_i = 34^\circ$. The roughness of the basal surface may induce the density variation of the flowing layer, yielding changes of the density ratio $\alpha_\rho = \rho_b/\rho_0$ and the local basal fricition. On the other hand, the thickness of the flowing layer may limit the bounce of particles near the sliding surface and thus locally increase the volume fraction. In the computation for chute Type I, the density ratio $\rho_0/\rho_b = \alpha_\rho^{-1}$ is then taken to be 0.9 for gate opening 10 mm, and 0.94 for 15 and 20 mm gate openings. For chute Type II, the ratio is selected to be 0.73, where the small value is due to the fact that the basal surface is made rough by covering the surface with writing paper and gluing sand where the particles bounce dramatically yield a small volume fraction (low density).

Table 8.7 Phenomenological coefficients in the computation

Chute	ϕ (°)	δ_1 (°)	δ_2 (°)	δ_3 (°)	k_w (°)
Type I	34.0	23.0	23.0	23.0	9.0
Type II	34.0	25.0	34.0	34.0	9.0

(From [2] with permission)

Table 8.8 Relevant parameters involved in the numerical simulation for erosion/deposition rate

	Type I (10 mm)	Type I (15 mm)	Type I (20 mm)	Type II (10 mm)
α_e	2.0	2.0	2.0	2.0
α_v	1.0	1.0	1.0	1.0
e_α	20.0	20.0	20.0	20.0
α_h	0.05	0.05	0.05	0.05
α_ρ^{-1}	0.90	0.94	0.94	0.73
$(\tan\delta_1)^*$	0.4245	0.4434	0.4434	0.3782
$(\tan\delta_2)^*$	0.4245	0.4434	0.4434	0.5471
$(\tan\delta_3)^*$	0.4245	0.4434	0.4434	0.5471
$(\tan\phi)^*$	0.6745	0.7045	0.7045	0.5471
V_{accu} (l)	0.1659	0.1694	0.1763	0.1644

(From [2] with permission)

Borrowing the concepts from two-fluid/mixture models (e.g. [10] or [11]), the local effective basal friction coefficient is proposed to be proportional to the local volume fraction. The drag induced by the confining side walls of the chute is taken into account by modifying the bed friction angle, the effective one $\delta_{\text{eff}} = \delta + \epsilon k_w h$, where k_w is the correction factor and selected to be 9.0° as in [12] or [13]. Nevertheless, the wall effect is minor and within the measurement uncertainty of the basal friction angle in our computation, because the surface flows are always very thin. The phenomenological coefficients are collected in Table 8.7 and the resultant effective friction coefficients (marked with "$*$"), in which the density ratio is taken into account for different simulation scenarios, are listed in Table 8.8. In all of the numerical simulations, the parameters, the density ratio α_ρ, erosion parameter α_e, threshold speed parameter α_v, regularization parameter e_α and depth parameter α_h, are identical and listed in Table 8.8. As there is finite mass in the reservoir in experiments, the final accumulated volumes V_{accu}, expressed in density of the deposition heap, are given in Table 8.8, in which the maximum deviation (by Type I gate opening 20 mm) to the mean value 0.1690 is 4.3 %.

In all computations, the initial mesh size $\triangle\xi$ is 2 mm, the Minmod TVD slope limiter is used for the cell reconstruction of the physical quantities, and the CFL number is selected to be 0.4. The initial inflow velocities are given in accordance with the experimental data and the material supply is double checked by the final accumulated volume V_{accu} listed in Table 8.8. In Figs. 8.19, 8.20 and 8.21, if not

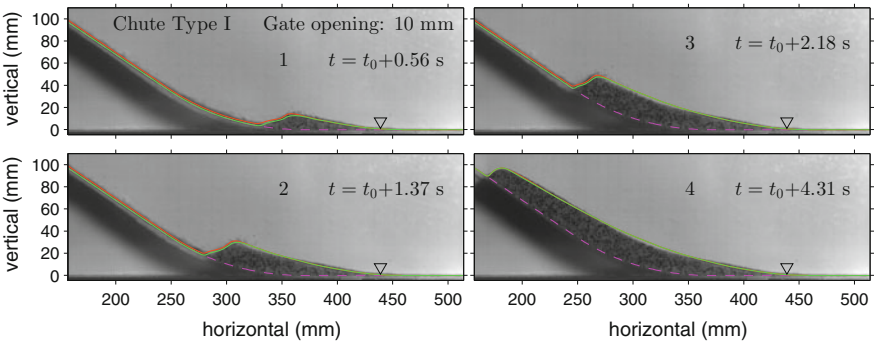

Fig. 8.19 Sequence of comparison between experimental photographs and theoretical prediction for chute Type I with gate opening 10 mm (Reproduced from [2] with permission.)

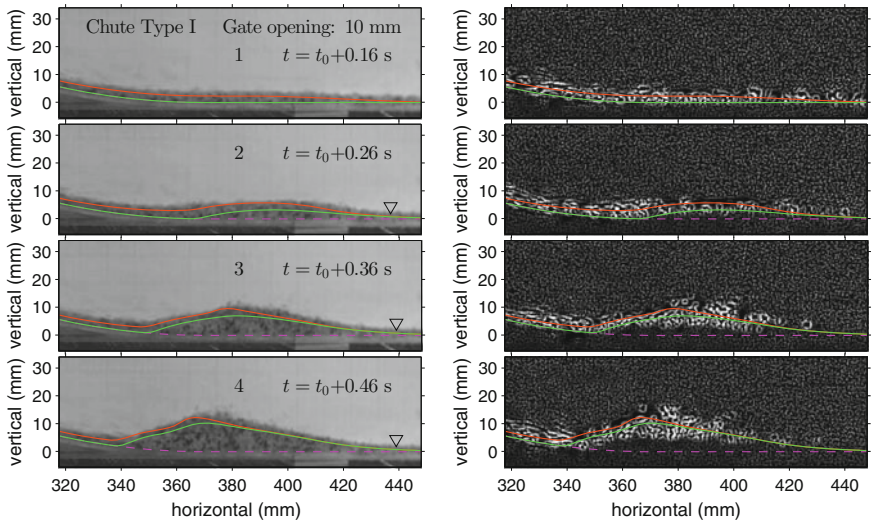

Fig. 8.20 Shots of experiment (*left panels*) and outlines of growing deposition heap (*right panels*) together with the theoretical prediction at the initial stage of deposit (Reproduced from [2] with permission.)

explicitly specified, the red lines at the top of the flowing layer indicate its free surface, the green lines represent the upper surface of the deposition heap (variable basal surface for the flowing layer), and the chute bottom is denoted by dashed magenta lines for a unique expression. For maximum run-out distance, we use the marker "▽" to indicate the position of the deposition depth of 0.725 mm, the mean diameter of the particles, which is recognized as the maximum reachable distance of the moving body in this section.

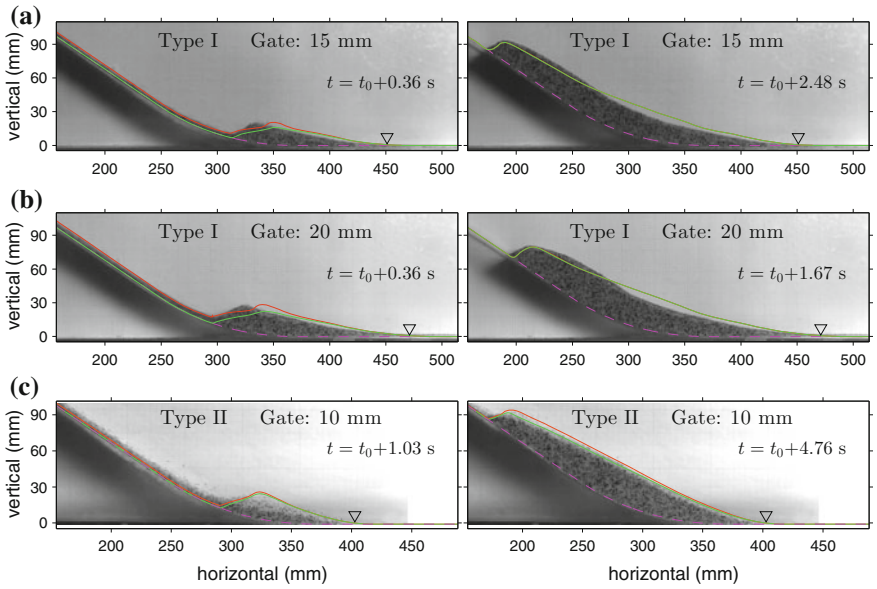

Fig. 8.21 Comparison between experimental photographs and theoretical prediction for chute Type I with gate openings 15 (*panels* a) and 20 mm (*panels* b) at $t = t_0 + 0.36$, respectively. *Panels* c show the experimental photographs by chute Type II (gate open of 10 mm) in comparison with the theoretical predictions (Reproduced from [2] with permission.)

Gate of 10 mm Opening

Figure 8.19 shows a sequence of photographs of the upslope traveling normal shock with the simulated results, when the gate opening is 10 mm. The deposition heap arises shortly before $t = t_0 + 0.56$ s (panel 1) and develops as the granular flux continues from above (panel 2 to 4). The numerical results capture the shape and location of the shock front, the thickness of the deposited pile and the decreasing inclination angle of the free surface of the heap along the arc length. As shown in Fig. 8.19, the numerical results depict a thin flowing layer climbing over the frontal surface and quickly coming to rest after having climbed the frontal top. Although there are several particles bouncing in the vicinity of the rear end, the theoretical prediction coincides with rather good agreement with the experimental data. At $t = t_0 + 4.31$ s the whole body is at the state of rest. This deposit shape then keeps invariant as time advances. The maximum run-out distance can therefore be well determined. Despite of the fact that the material accumulates as the rear part merges, the run-out distance remains unaltered after $t = t_0 + 0.56$ s, see the location of the the marker "▽".

Figure 8.20 illustrates the shots (left panels) and the corresponding outlines of the deposition heap (right panels) together with the theoretical predictions at the initial stage, when the depositing pile is just forming. At time $t = t_0 + 0.16$ s (panel 1) the pile is beginning to form. At $t = t_0 + 0.26$ s (panel 2) it becomes visible and

the maximum run-out distance has not been reached yet (see the different locations of the markers "▽"). The existence of the developing deposition heap provides an additional drag to the subsequent flowing particles and results in dramatic bouncing and dilutely moving particles (panels 2 to 4). As a consequence, it reduces the final run-out distance. Although the evolving shape and position of the deposition heap can roughly be captured by the theoretical prediction, the vivid jumping flowing layer above the stagnant pile is still a challenging task for both modelling work and numerical simulation.

Gate Openings 15 and 20 mm (Type I) and with Different Basal Surface (Type II)

With identical values of parameters in determining the erosion-rate, such as (α_e, α_v, e_α, α_h) listed in Table 8.8, simulations are performed with respect to the experiments in chute Type I (gate open by 15 and 20 mm) and in chute Type II (gate open by 10 mm). The panels a and b in Fig. 8.21 show the comparison by chute Type I at $t_0 + 0.36$ s when the deposit is just taking place, and at the final stage where all the material is at the state of rest. Panel c shows the results for chute Type II (gate open by 10 mm). For the two simulations in chute Type I, the deposit shapes and the locations of the traveling wave front can be roughly captured. However, moderate deviation in the thickness of the deposition heap are observed over the transition zone and over the inclined straight part. The deposition heaps have thicker depth (overestimated) within the transition zone but thinner (underestimated) in the upper straight part.

Since the basal surface in chute Type II is roughened by gluing Ottawa sand over the transition and horizontal run-out zones, it induces a higher basal drag and the maximum run-out distance should be shorter in comparison with the results for chute Type I (panels a and b). The right panel of c in Fig. 8.21 depicts the earlier deposition that the major part of the deposition heap locates over the transition zone the inclined straight part. In comparison with the results by chute Type I, it is notable that the free surface of the deposition heap tends to become a straight line with a slope approximately equal to the angle of repose of the material. The straight line slope and early deposition are mainly due to the high basal drag. In Fig. 8.21 the evolving shapes and locations of the deposition heap are fairly captured by the theoretical prediction. Although the applied erosion/deposition rate is a most simplistic proposal, the sound agreements between experimental data and theoretical predictions indicate the potential of application.

Results without Deposition Process

By shutting off the deposition/erosion in the numerical code, i.e., $\mathcal{U} = 0$ in (8.1), one obtains dramatically different results even if all the applied parameters and conditions are identical. The computed results together with the corresponding photographs of the experiment are given in Fig. 8.22. We list the essential differences following the time sequence. In panel 1, the traveling distance of the whole body is considerably longer in comparison with panel 1 of Fig. 8.19. This is suspected to be caused by the lack of additional drag force induced by the deposition heap to decelerate the

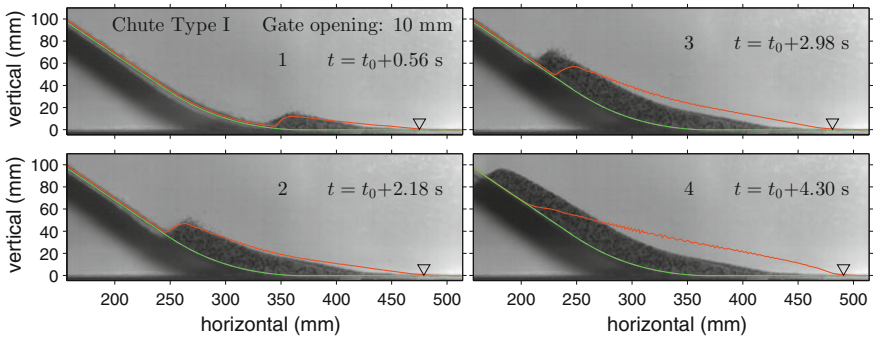

Fig. 8.22 A sequence of photographs as shown in Fig. 8.19 with the simulated results, in which no deposition/erosion process is adopted, $\mathcal{U} = 0$ (Reproduced from [2] with permission.)

subsequent flow. In panel 2 the simulated travelling wave front travels upslope with a convex shape at the flow surface, but the front position lags significantly while climbing over the upper inclined straight part (panels 3) although the material is accumulated. It is observed that the flow thickness over the transition and horizontal run-out zones is increasing as time advances, and its free surface tends to be a straight line (panels 3 and 4). One also notices that the run-out distance increases with time, i.e. the position of the marker "▽" travels toward the righ hand direction. It is due to the fact of inappropriate balance between the depth gradient and the basal friction. Hence, if neglecting the deposition process, an additional treatment for balancing the depth gradient with the basal friction is highly requested (e.g. see a proposal in [14] or the condition of rest lake, suggested in [4]).

8.4 Concluding Remarks

In this chapter we reported the numerical results for highlighting the key features of the models in the topography-fitted coordinate system. The deposition and erosion were taken into account, so that the basal surface deformed with time.

In the one-dimensional benchmark problem, we investigated the characteristics of the model through three scenarios. The results reflected

- the need of introducing the threshold speed for the deposition and its value should be finite, if the proposal (5.64) is employed;
- the fact that the deposition heap reduces the run-out distance;
- the achievements of determining the travelling duration and the run-out distance;
- the capability of mimicking the development of the deposition heap.

We studied the evolution and the final shape of the deposition heap in the two-dimensional benchmark problem. In addition to the above characteristics, we investigated the impacts of the non-uniform velocity profile and the corresponding velocity

ratio. For the sake of isolating the complex process, we decomposed the whole process into sliding regime and deposition regime. In each regime a fixed velocity profile was assigned. It is found that the shape of final deposit is not sensitive to the velocity ratio, if the velocity profiles in the regimes ($n^I = 10^3$ and $n^{II} = 10^0$) are fixed. On the contrary, the computational results are highly sensitive to the value of the correction factor m_2 in the sliding regime, pointing out the challenging task by numerical simulation.

We also reported the validation against a series of laboratory experiments of granular flow along an inclined plane chute into the horizontal run-out zone. In the experiments the Ottawa sand (compliant to ASTM C778 20/30) was used. We focused on the observed traveling shock waves, the distance traveled by the granular mass and the evolution of the growing deposition heap. The sound agreement between the numerical predictions and the experimental data proves the adequacy of the model equations, and the results indicate the capability of the simplistic proposal to mimick the complicated process of mass exchange at the basal surface.

References

1. Y.C. Tai, C.Y. Kuo, W.H. Hui, An alternative depth-integrated formulation for granular avalanches over temporally varying topography with small curvature. Geophys. Astrophys. Fluid Dyn. **106**(6), 596–629 (2012)
2. Y.C. Tai, Y.C. Lin, A focused view of the behavior of granular flows down a confined inclined chute into horizontal run-out zone. Phys. Fluids **20**, 123302 (2008)
3. Y.C. Tai, C.Y. Kuo, A new model of granular flows over general topography with erosion and deposition. Acta Mech. **199**, 71–96 (2008)
4. F. Bouchut, *Nonlinear Stability of Finite Volume Methods for Hyperbolic Conservation Laws and Well-Balanced Schemes for Sources* (Birkhäuser Verlag, Basal Boston Berlin, 2004)
5. S. Noelle, N. Pankratz, G. Puppo, J. Natvig, Well-balanced finite volume schemes of arbitrary order of accuracy for shallow water flows. J. Comput. Phys. **213**(2), 474–499 (2006)
6. S.P. Pudasaini, K. Hutter, S.S. Tai, Y. Wang, R. Katzenbach, Rapid flow of dry granular materials down inclined chutes inpinging on rigid walls. Phys. Fluids **19**, 053302 (2007)
7. J. Smid, S.S. Hsiau, W.D. Tu, C.H. Lin, S.M. Ma, Shear device for measurement of wall friction in designing granular moving bed filters. Adv. Powder Technol. **17**, 49 (2006)
8. S.B. Savage, Gravity flow of cohesionless granular materials in chutes and channels. J. Fluid Mech. **92**(01), 53–96 (1979)
9. J.M.N.T. Gray, Y.C. Tai, S. Noelle, Shock waves, dead-zones and particle-free regions in rapid granular free surface flows. J. Fluid Mech. **491**, 161–181 (2003)
10. R.M. Iverson, R.P. Denlinger, Flow of variably fluidised granular massesacross three-dimensional terrain. I: Coulomb mixture theory. J. Geophys. Res. **106**, 537–552 (2001)
11. E.B. Pitman, L. Le, A two-fluid model for avalanche and debris flows. Phil. Trans. R. Soc. Lond. A **363**, 1573–1601 (2005)
12. K. Hutter, T. Koch, Motion of a granular avalanche in an exponentially curved chute: experiments and theoretical predictions. Phil. Trans. R. Soc. A **334**, 93–138 (1991)
13. R. Greve, K. Hutter, Motion of a granular avalanche in a convex and concave curved chute: experiments and theoretical predictions. Phil. Trans. R. Soc. A **342**, 573–600 (1993)
14. O. Pouliquen, Y. Forterre, Friction law for dense granular flows: appication to the motion of a mass down a rough inclined plane. J. Fluid Mech. **453**, 133–151 (2002)

Chapter 9
Applications to Avalanching Landslides in Taiwan

9.1 Introduction

The continuum, shallow-water type landslide models, derived in the previous chapters are applied to two devastating landslides in Taiwan for back-analysis of the landslide motion. The two landslides are the Tsaoling and Hsiaoling landslides, which were large-scale rapid avalanche landslides triggered by the Chi-Chi earthquake, 1999, and the excessive rainfall brought by the Morakot typhoon, 2009. In addition to the two example landslides, small scale landslides and debris flows have been repeatedly occurring in Taiwan because of the natural geological settings of the island.

The island is located in the northern hemispherical subtropical region such that there are a regular annual monsoon season and frequent typhoon events in summers and falls. The monsoon season occurs at the alternative period when the cold north eastern winter wind system shifts to the warm south east summer wind. During the shift, the two wind systems generate stationary weather fronts spreading over the south east China and Taiwan areas from the mid of Mays to Junes, for example, a strong monsoon front occurred on the 20th, May, 2015, Fig. 9.1. The interaction between the cold and warm air yields long-lasting precipitation for weeks and contributes to an average annual amount about 500–600 mm in Taiwan.

Typhoons (hurricanes) on the other hand are initially tropical cyclones which form on the tropical sea surface. They typically move north west towards the subtropical zone then change courses north east towards the temperate zone. The historical typhoon trajectories around Taiwan are shown in Fig. 9.2. Typhoons themselves often carry extreme rainfalls. In addition, they often bring in southwest airflows from the South China Sea and form stationary fronts when passing over Taiwan. Like monsoons, these stationary fronts can cause days of severe rainfalls after typhoon strikes. Roughly speaking, this type of weather system annually contributes from 800 to 2000 mm of rainfall. Together with the local convective weather system, the

I. Luca et al., *Shallow Geophysical Mass Flows down Arbitrary Topography*,
Advances in Geophysical and Environmental Mechanics and Mathematics,
DOI 10.1007/978-3-319-02627-5_9

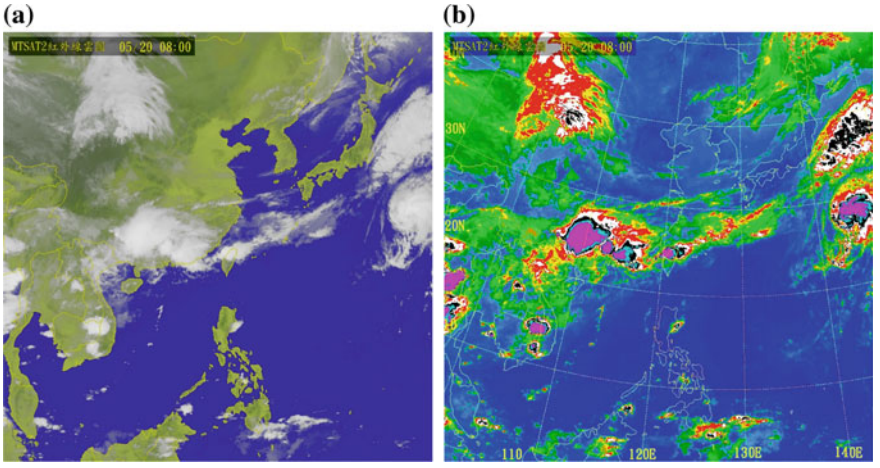

Fig. 9.1 Monsoon weather front at AM 8:00, 20, May, 2015 (local time). **a** Infra-red image of the cloud system and **b** pseudo-color enhanced for deep convective clouds. *Purple* and *white colors* indicate strong convective cells. *Data source* MTSAT-2 satellite, Central Weather Bureau, Taiwan, http://www.cwb.gov.tw/eng/

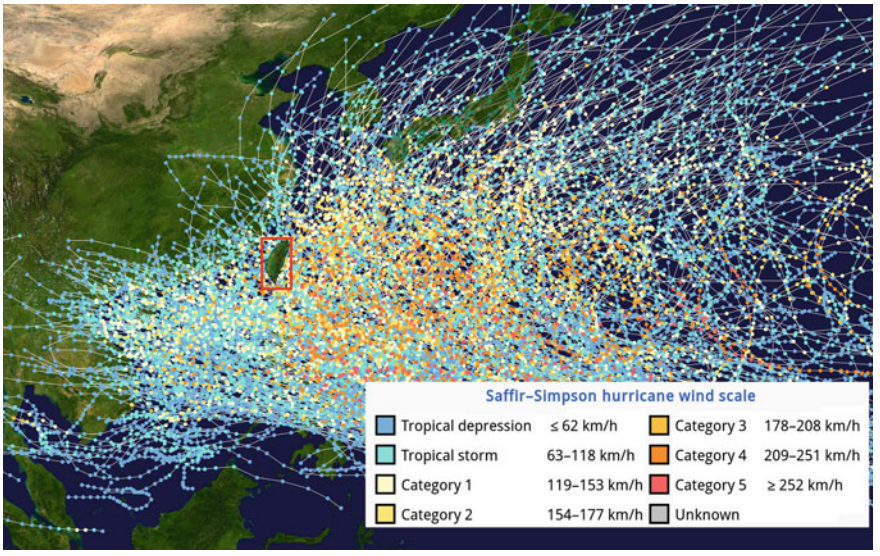

Fig. 9.2 Typhoon trajectories from 1980 to 2005. Modified from the image released at https://commons.wikimedia.org/wiki/File:Pacific_typhoon_tracks_1980-2005.jpg, created by Wikipedia Tropical cyclones/Tracks WikiProject. The background image is from the land and ocean image published by NASA and typhoon trajectories are based on the typhoon database of the Joint Typhoon Warning Center. The warmer *color dots* indicate the stronger wind scales of the passing typhoons

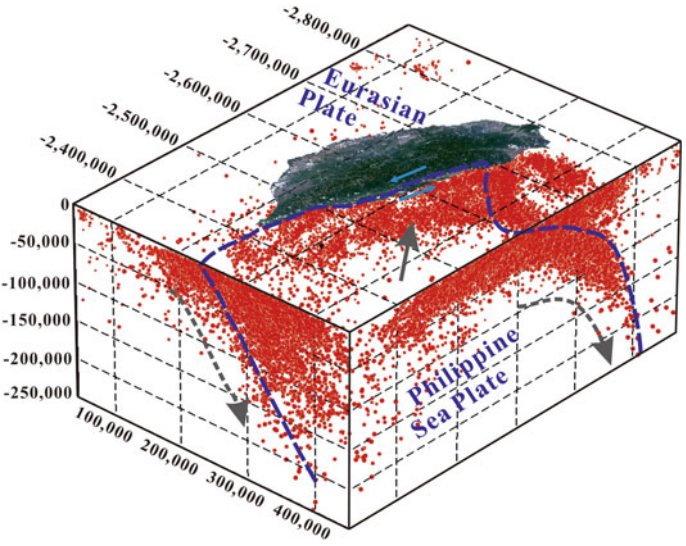

Fig. 9.3 Three-dimensional distribution of earthquake focii in Taiwan. The inventory contains more than 30,000 earthquakes recorded in 2012 with magnitudes higher than 0.08 (Ritchter scale, local magnitude scale). *Data source* Central Weather Bureau, Taiwan. The configuration and movement direction of Philippine Sea Plate and Eurasian Plate [2], are superposed for the correlation of the tectonic motion and earthquakes

island-wise annual precipitation, between 1949 and 2009, is about 2,500 mm (Source: Water Resource Agency, Ministry of Economic Affairs, Taiwan).

Geologically, Taiwan island is located between the Philippine Sea plate and the Eurasian plate, with the two opposite-verging subduction systems of the Ryukyu arctrench and Luzon arcs. Therefore, Taiwan is one of the regions on Earth with the highest seismic activity. The distribution epicenter diagram for earthquakes and the tectonic plate configuration are shown in Fig. 9.3. The tectonic plate motion leads to active crustal deformation and forms the central mountain belt in the island. The average annual lift rate in the central mountain range of the island is estimated about 0.2–18.5 mm/year [1].

Because of the active deformation, the central mountain belt is young and composed of a series of high elevation peaks with steep slopes. It is like other typical orogens which have metamorphic rock cores in the mountain belt central range, surrounded and overlayed by slate formations. Outside the metamorphic cores and slate formations, fold-and-thrust belts commonly appear and they mainly consist of sedimentary rocks. As a result, dip slopes are common in the mountain slopes. Both dip slopes and sedimentary rocks are geostructurally and mechanically weak and they are prone to failure subjected to weathering and seismic motion. The slope failures often lead to landslides and pose serious hazard threats to human lives and society. In hazard mitigation warning system, to be able to predict the influencing zones of slope

failures is therefore one of the top important tasks. For this purpose, the continuum model developed in the previous chapters can be a valuable tool.

To illustrate the model capabilities and validations, two representative large-scale avalanche landslides, Tsaoling and Hsiaoling, are presented in detail. The implication of the long run-outs on rheological parameters is also addressed.

9.2 Tsaoling Landslide

On the 21st of September, 1999, Chi-Chi earthquake ($M_L = 7.3$) struck central Taiwan at 01:47 local time. This earthquake was the most destructive one in the last century in Taiwan and caused more than 2,450 fatalities and wide spread damage. The earthquake caused a surface rupture, more than 90 km from Miaoli to Chiayi County, along the Chelungpu fault. Vertical offsets on average from 2 to 4 m from the south to the north of the fault and the widest horizontal offsets up to 10 m is observed, Fig. 9.6 [4]. It also triggered more than 9,000 landslides over 128 km^2 in the central mountain area of the island [5]. Among the landslides, Tsaoling landslide is one of the most catastrophic landslides [6]. More than 0.126 km^3 of material ran over a distance of 1.6 km with 500 m descent in elevation [7]. The deposit volume increased to about 0.150 km^3 due to rupture of the sliding mass at motion. The deposit caused the fourth formation of the block dam of Chinsui River at the foothill of the slope in the recorded history of the local area [7]. Thirty-nine people were killed and seven survived in a van after gliding with the landslide.

The Tsaoling area is located in the northeast of Yunlin County, the foothill of the central mountain region, Fig. 9.4, near the southern end of the Chelunpu fault.

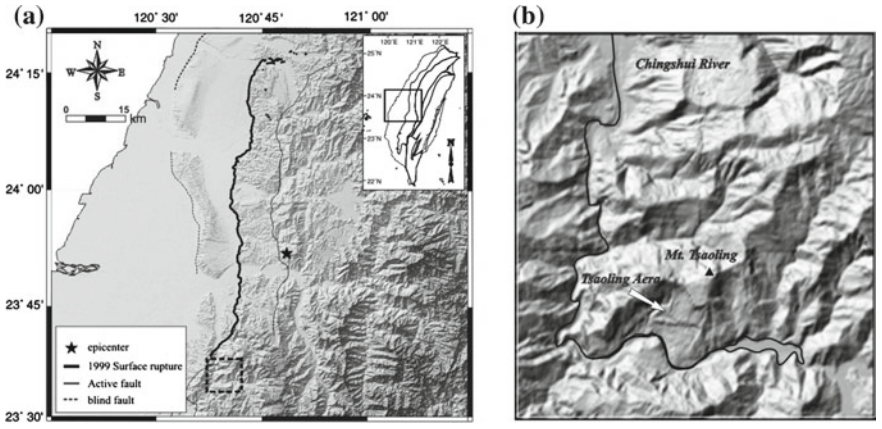

Fig. 9.4 **a** Central-west of Taiwan and the surface rupture of the Chelungpu Fault and the 1999 Chi-Chi earthquake epicenter. **b** Shaded topographic map of the Tsaoling region before the earthquake, on 1989 40 × 40 m DTM (Reproduced from [3] with permission)

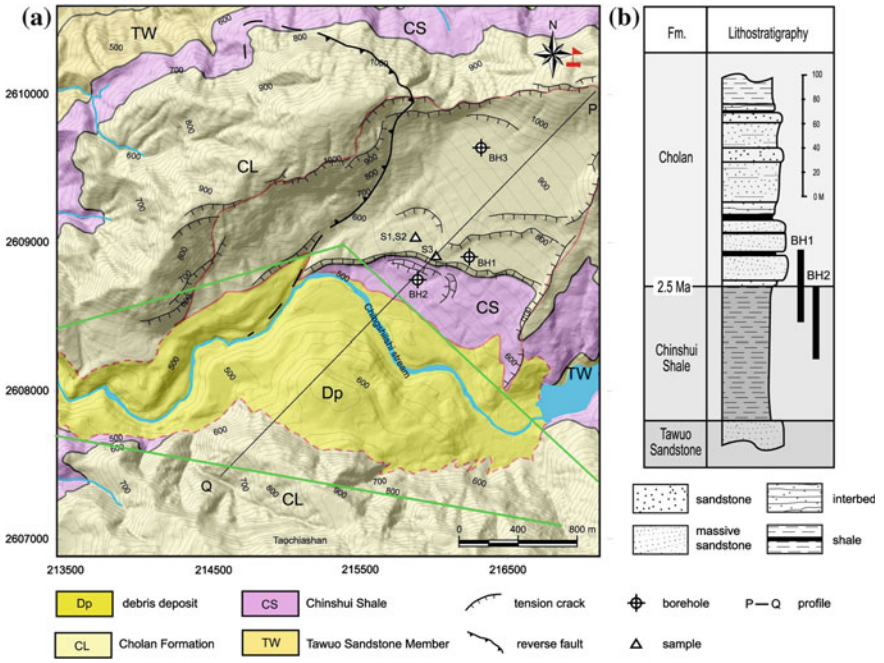

Fig. 9.5 **a** Geological map and **b** representative stratigraphic section of the study area. Shaded relief map of the Tsaoling region, with 25 m contour interval by the airborne-photo derived DTM, 2000. S1, S2, S3 and BH1, BH2, BH3 are the sampling locations and bore-holes reported by [8], prior to the earthquake. The tension crack through BH1 and BH2 forms a cliff of 30 m, called Chunqiu Cliff. The *triangular area* bounded by the *thick green lines* is the deposit area used for numerical calibration for rheological parameters, cf. Sect. 9.2.2. The *red* flag at the *top-right corner* of panel (**a**) indicates the location of seismograph station CHY080, cf. Sect. 9.2.4 (Reproduced from [3] with permission)

The study area is shown in Fig. 9.5. Chinshui River flows along the base of the dip slope from the east to west through the deposit zone, and then turns to the north. The river cuts into the toe of the slope and causes the bedding of the foothill of the slope exposed to the surface. The elevation of the slope ranges from 500 to 1200 m above the sea level. The usual representative profile for the landslides is along the line $\overline{PQ}$, sketched in the figure. Near the profile, there are material sampling positions, S1, S2, S3 and the investigated bore-holes, BH1, BH2, BH3, of [8, 9], which are also marked for references. Photographs, Fig. 9.6, present the visual overview of the area and the result of the landslide.

The geological condition of Tsaoling is one of the typical weak slopes that makes it susceptible to earthquakes and heavy rainfalls. There were landslide events recorded since 1862 and details of each event have been documented, Table 9.1, see [7, 8, 10, 11] and the references therein. This is because the morphology of the area is dominated by sedimentary rocks that dip in the same direction as the slope, 14° on

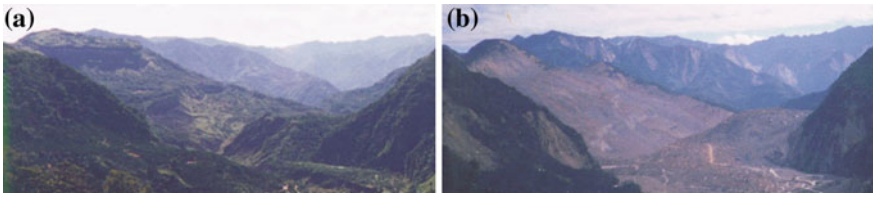

Fig. 9.6 Overview of the Tsaoling landslide, looking from west to east. **a** Photograph taken before 1999 Chi-Chi earthquake. **b** Photograph taken from the same view point after the earthquake (Reproduced from [3] with permission)

Table 9.1 Historical events in the Tsaoling area, excerpted from [7]

Time	Cause	Slide volume (km^3)
1862	Earthquake ($M_L = 6$–7)	–
1898	Rainfall	–
1941	Earthquake ($M_L = 7.1$)	0.10–0.15
1942	Rainfall (776 mm)	0.15–0.20
1951	Rainfall (770 mm)	0.120
1979	Rainfall (327 and 624 mm)	0.026 and 0.040
1999	Earthquake ($M_L = 7.3$)	0.126

average. The profiles, Fig. 9.7, along $\overline{PQ}$ depict the change of topography by the 1941, 1979 and the 1999 landslides. They also present the two major geological surface layers: the Cholan formation and the Chinshui shale below. A typical geological stratigraphic profile is shown in Fig. 9.5b.

The Cholan formation consists mainly of fine-grained sandstones and intercalated shales. This layer constitutes most of the landslide mass. It has a loose structure with high permeability. On the other hand, the Chinshui shale, on average over 110 m thick, consists of massive mudstone and shale, which has low permeability and loses strength significantly when the water content is high. Extensive material tests have been performed [8, 11] and references therein, but variations among the tests have been found due to the highly irregular natural materials. One of the representative reports is exerted in Table 9.2. Underneath these layers is the bedrock Tawuo Sandstone formation, which is over 1100 m thick.

There are several weak interfaces in the two layers. They are first the interface between the Cholan formation and the Chinshui shale and the second is the intercalated shales within the Cholan formation. Landslides before 1979 (incl.) all happened due to slip at the interface between the two layers because of the low strength of Chinshui shale. The shale layer is hence exposed to the surface and forms the tension crack through BH1 and BH2, Fig. 9.5a. The crack is referred as the 1979 scarp, or now called the Chunqiu Cliff. The cliff has an average 50 m difference in elevation.

On the contrary, the landslide in 1999 is the first one for which the rock ruptures in the Cholan layer. Field investigation reveals that the failure takes place in the weak

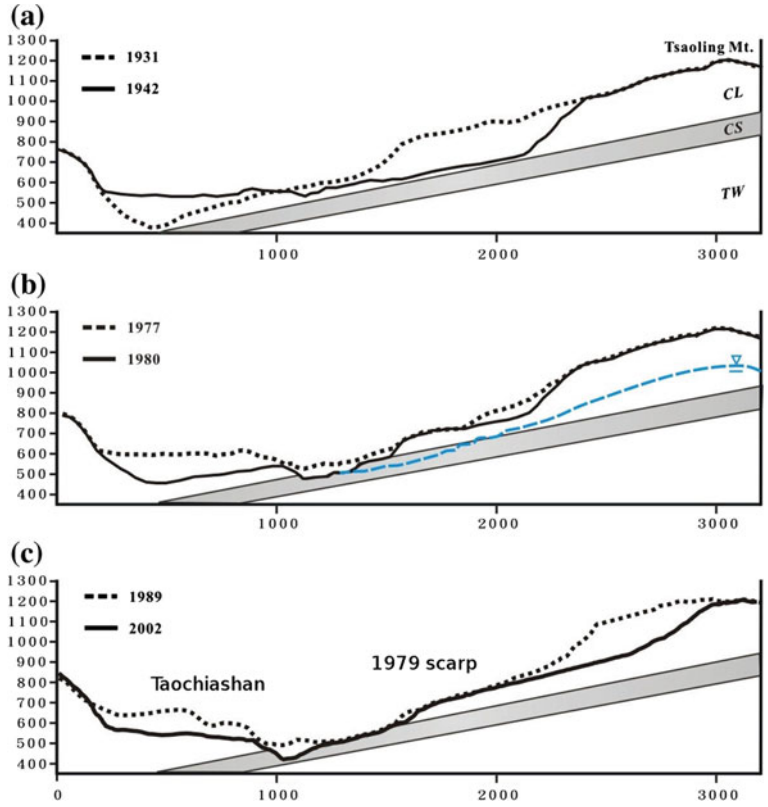

Fig. 9.7 Reconstructed cross-section of the Tsaoling landslide. **a** Topography change after the 1941 event. **b** After 1979 event and **c** the 1999 landslide (by the Chi-Chi earthquake). Also in **b** the estimated ground-water table [9] and **c** the Chunqiu Cliff and the deposit, now called Taochiashan (Reproduced from [3] with permission)

thin shale layer in Cholan formation [13]. This echoes the weak material strength of the intercalated shale Table 9.2. At the detachment surface, numerous brittle features were found. Most fractures, especially open fissures, are approximately perpendicular to bedding planes and reflect the tensile failure. There are localized pseudotachylyte spots found on the sliding surfaces and this indicates that the rock melting processes take place due to friction of the materials [14].

The high saturation indicates the existence of ground-water in the formation. [9] estimated the ground-water level, sketched in Fig. 9.7b. This is based on the findings that constant water outflow is observed from the Chunqiu Cliff interface and rock joints and the water content from samples of the three site bore-holes. The close incidence of the water level and the landslide basal interface strongly indicates the correlation between the strength yield of submerged shale and the earthquake movement. The remaining section of the Cholan layer after the Chi-Chi earthquake

Table 9.2 Material properties at the sampling positions [8]

	CL shale (S1)	CL sandstone (S2)	CS (S3)
Specific weight	2.66	2.68	2.66
Water content	4.0 %	2.5 %	2.2 %
Void ratio	12.79 %	12.38 %	5.64 %
Saturation	72.03 %	47.47 %	96.84 %
Peak friction angle ϕ_p	20.5	75.3	34.1
Residue friction angle ϕ_r	21.5	38.8	34.1
Peak cohesion C_p (kPa)	152	272	524
Residue cohesion C_r (kPa)	75	109	71
Slake durability index Id_2	4.8 %	67.5 %	69.8 %
Durability classification†	Very low	Medium	Medium
Plastic limit %	17 %	NP	NP

CL Cholan formation, *CS* Chinshui shale, *NP* Non-plastic. †According to [12] (Reproduced from [3] with permission)

along the main profile is still estimated about 100 m and its volume is about 0.27 km^3. This mass is still vulnerable to future hazard events according to the risk analysis by [10].

After the landslide, field investigations and reported data revealed that the landslide is a typical rock avalanche in many aspects [8]. The evidence of its rapid motion includes chaotic distribution of large rock blocks, flow morphology and internal structure and relative thinness in comparison to large aerial extent, high porosity, angularity of fragments, and the lobate forms etc. Although many field investigation reports extensively documented the geomorphological evolution, rock material properties, and risk analysis [8, 11, 15]. It has become increasingly popular to analyze the landslide motion and dynamics of the landslide using DEM simulations. For example, based on the commercial PFC 3D code, the Tsaoling landslide was simulated by [16, 17]. After calibration of many micro-scopic contact parameters, they found that the friction coefficient was small (about 0.15) and argue that the pore water pressure played a key role. Whether this conclusion holds for alternative methods is also one topic of interest.

The continuum models described in the previous chapters are applied for this purpose. As seen in the theories, one of the important factors controlling the landslide flow motion is the material constitutive law. For avalanche flows with solid particles, the materials in the flows have been increasingly in common to be modeled using the Mohr-Coulomb constitutive law [18–22], and its variations, for example the Coulomb mixture models [23–25]. These works demonstrated the capability of the continuum models to reproduce the rapid motion of landslide mass densely packed with discrete granules/particles.

The Mohr-Coulomb constitutive relation is rooted in classical soil mechanics. When applied in avalanche flows, it states that the materials at motion are everywhere subjected to the yield stress and the shear stress is equal to the Coulomb

friction that the basal surface exerts on the flowing material, in reacting to the flow pressure. The soil (granular) solid property, e.g. active or passive stress state according to compression or stretch in the flow, is modeled through the effect of earth pressure coefficients, previous Sects. 5.2.2 or 8.1.2. However, there remain heuristic hypotheses in this approach: for example, the principal axes of the stress are commonly assumed parallel to the flow direction and the determination of the passive/active earth pressure coefficient of the flow varies according to different model proposals, e.g. [20, 23, 25–27].

While these variations among models are shown appropriate for debris flows in well-defined chute channels in laboratory experiments, they may lead to undesired complications in the present Tsaoling slide, not only by introducing a few extra degrees of freedom of the choices of earth pressure coefficients, but also lacking of a robust numerical scheme with account of these earth pressure effects for general topography. The main reason is because of the river valley at the foothill of the sliding slope, which provides an impingement zone and splits the avalanche flow into two separate directions, cf. Sect. 9.2.3. Change of the flow direction causes sophisticated flow interactions in the impingement area, which significantly affect the strain (compression or stretching), and hence, stress states of the materials. To avoid these undesired complications, we set the earth pressure coefficient to one in this and next chapters. This simplification effectively reduces the Mohr-Coulomb continuum model to a hydraulic model.

Further in the hydraulic model, detail composition of the geological materials is neglected and the avalanching mass is assumed incompressible, thin and with a uniform velocity profile across the depth. Because the viscosity in the flow layer does not play a role in the model, the material constituent of the flow is sometime referred to as an Eulerian fluid. This approach has been widely applied in snow avalanches in the early Russian literature, see p. 121, [22]. [28] shows that, even under these aggressive simplifications, the model can accurately predict the outstanding physical phenomena, e.g. granular shock waves, dead zones etc., observed in debris avalanches. Using a plane chute flow [27] addressed the differences between the hydraulic model and two variants of Mohr-Coulomb constitutive models, and they pointed out that the main effects of the earth pressure are on the spreading of the flow, while flow velocities and depths remain moderately influenced. These observations justify the applicability of the present simplifications.

Despite the simplification made to the flow materials, the Coulomb friction on the basal surface is retained as the resisting force. With the simple Coulomb friction law, there is one parameter to determine, the friction coefficient. In addition, it is also common to surplus the Coulomb friction with a fluid-like drag force, called Voellmy law [29], of which the magnitude is proportional to the kinetic energy of the flow. When using the simple Coulomb or Voellmy basal friction law, there are at most two parameters: the friction coefficient and the drag coefficient. These parameters are referred as rheological parameters in the following texts. They are assumed constant everywhere on the landslide course and are to be determined by an iterative process that minimizes the differences between the simulation deposit and field measurement.

To refrain ourselves in the model derived in the scope of the book, we re-performed a similar analysis as described in [3] using the model, (4.99) and (4.102), derived in Sect. 4.5.5. The valuable niche of the present model is that it is derived in a way to convenience many practical applications, such as incorporating GIS data without the need of performing a coordinate transformation. The initiation mechanisms are also neglected. These include the failure of the interface under the earthquake motion, rock rupture, and volume dilation of the mass. We assume the process takes place in a relatively short time (compared to the total duration) after the landslide is triggered.

In Taiwan, aerial photograph interpretation and mapping are routinely performed by the Agricultural and Forestry Aerial Survey Institute of Taiwan. To close monitor the geomorphological changes after the Tsaoling landslide, frequent surveys were taken and, as a result, there are digital elevation models for 1999, 2000, 2001, 2004, 2007 and 2009 available. The 1989 and 2000 DTMs were used in [3] because the 1999 DTM was not released at the time of the study. In the present chapter, we update the landslide simulation by taking the 1989 and 1999 DTMs. They are based on the aerial photos with ground measurement corrections and have mesh resolutions 40×40 m and 10×10 m respectively. Comparing the different sets of data, we estimate the landslide-related mass transfer and basal topography in the numerical model.

Because small amount of outflow was found in [3], we enlarge the present computational domain to minimize the outflow mass. The computation domain of $5{,}085 \times 4{,}335$ m, as shown in Fig. 9.5, is setup and discretized into 339×289 rectangular cells. The non-oscillatory numerical scheme of [30] was adopted for numerical calculations. Each grid cell has a size 15×15 m. A small cut-off depth is set to 1 mm. The maximum time for the simulation is set to 180 s and, in all the calculation cases, mass movements come to rest within about two minutes. Outgoing conditions are used on the four borders. The model cannot cope with volume dilation at initiation, therefore, we increase the initial scar depth by a linear factor. The reasonable range of the factor is from 1.0 to 1.3 and we use 1.06. This leads to the fact that the volume of the simulation deposit, after numerical calibration, Sect. 9.2.2, has only about ± 2 % error compared to the real measurement.

9.2.1 Statistical Empirical Scaling Laws of Friction

Apparent friction coefficients of landslides have long been studied by performing statistical regression analyses using real landslide data. Based on the balance of the total energy and frictional dissipation of a rigid sliding body, a simple guideline expression for the apparent friction coefficient can be immediately obtained, which reads $\mu_e = H/L$, with H the descending level and L the traveling distance [31, 32]. Besides the transportation characteristic quantities H and L, landslide volumes V are often used as a primary controlling variable in various statistical analyses [33, 34]. These regression analyses led to the well known phenomenological conclusion that the friction coefficient is inversely correlated to the landslide volume.

Because of the complexity of the natural geological contents, physical variables are subjected to uncertainties. For this landslide, the gravity centers of the measured scar and deposit volumes are used to estimate the associated parameters: the horizontal displacement (center to center) is about 2000 m (L) and the descent in elevation is 500 m (H) on the main slide profile $\overline{PQ}$; see also Fig. 9.5 (figures later) and [35]. The apparent friction coefficient is therefore approximately 0.25 ($\approx H/L$). The standard deviation, as given in [33], is 0.14. This value may have been overestimated because the traveling distance L could have been significantly underestimated. The main reason is that the slide mass impact on the south bank slope of the Chinsui river, changed the flow direction and caused a wide spread, more than 3 km, of mass deposit along the river channel. It is therefore likely that the friction coefficient value is substantially lower than the quoted value, as in [3]. Based on the previous discussion and study, the initial guess of the apparent angle of the basal friction in the present updated analysis is set to 7.5°. Geotechnicians associate such low values with high pore pressure [22, 25] and recently with the high pressure shearing, Sect. 9.4 and [36, 37].

These statistical-based analyses were referred as empirical scaling laws of friction. The reverse dependence of the friction on the landslide volume was the one of the most intriguing characteristics of landslides and it was called the volume-induced lubrication [32]. In this mechanism, debris spreading plays an important role in the volume-dependent phenomena [38]. The spreading length L_* and the total volume have a regression relation $L_* = 9.98V^{0.32}$. With the volume of the present landslide, the spreading length was estimated 4.1 km, which agrees with the spreading length in the Chinsui river. The landslide run-out can be decomposed into two major contributors: sliding and spreading. The indicator for determining the dominant contributor in the run-out is the ratio between the vertical projection of the characteristic length of the landslide mass and the descending level. This ratio is explicitly $V^{1/3}/(H \sin\theta)$ for a three-dimensional terrain, where θ is the inclination angle of the slope. Taking the average inclination angle, 14°, of the Tsaoling Slope for θ, the ratio was 4.4, which was greater than one and therefore the run-out was dominated by the spreading of debris according to [32]. This spreading dominant motion also justifies the application of the present continuum hydrodynamic type of landslide model in the analysis.

9.2.2 Calibration of Rheological Parameters

The best fit of the basal friction and drag is evaluated by minimizing the depth difference between the simulation and the real data over the Chinshui deposit valley. Both Coulomb friction and Voellmy laws are simulated for the landslide. For the two rheological rules, there are at most two controlling parameters and the minimization process is performed in the parameter domain. For the Coulomb friction, the parameter domain consists of only one parameter: the friction coefficient μ. The object minimization function is defined as the average of the square of the difference

between the simulation and the measurement over the main deposit area. Therefore, the optimization scheme reads

$$h_{std}^2(\mu) = \min_{\mu} \frac{1}{A} \int_A (h(\mathbf{x};\mu) - h_{meas}(\mathbf{x}))^2 \, dA \tag{9.1}$$

where $h_{std}(\mu)$ is the standard deviation between the two compared deposit depths, $h_{meas}(\mathbf{x})$ and $h(\mathbf{x};\mu)$. The $h_{meas}(\mathbf{x})$ is the measured deposition depth and the $h(\mathbf{x};\mu)$ is the simulated depth with the friction coefficient μ. The A is the area of the main deposit zone. The main deposit zone, which is the area of interest, was made slightly larger than the area between the simulated and measured deposits, i.e., A is the triangular outlined area in Fig. 9.5. The simulation time is set sufficiently long, here 180 s, to ensure that the flow speed in the main deposit area is less than the average 2 m/s, 3.3 % of the maximum flow speed, at the end of the simulation. For simplicity and robustness in the minimization procedures, the simplex method is used [39]. By using the present optimization process, the subjective visual inspection of the simulation results, which was commonly seen in practice, is eliminated.

It is often argued that the water content and debris collision in avalanche materials introduce a flow drag to the landslide motion. Thus, we assume the fluid-like drag force, proportional to the square of the flow speed, as an additional term to the Coulomb friction force. That is, we consider the bed friction law (4.101) of the Voellmy rheology, with $\boldsymbol{\tau}_{viscous}$ quadratic in $\boldsymbol{v}_\tau$, see also [26, 40, 41].

Summarizing, to describe the Tsaoling landslide, the equations which are numerically solved consist of (4.99) and (4.102), with

- $\mathcal{U} = 0$ (no erosion/deposition),
- $\bar{\mathbb{v}}_\tau = \mathbb{v}_\tau$ (plug-flow was assumed, so $\bar{\mathbf{v}} = \mathbf{v}$, and equality $\mathbb{v}_\tau = \mathbf{F}\mathbf{v}$ holds, see (5.7)),
- $m_2 = 1$ (plug-flow was assumed),
- $\overline{\mathbf{P}} = \mathbf{0}$ (weak rheology), and
- the momentum source term, either incorporating solely the basal Coulomb friction,

$$\varsigma_\xi = -J_0 N_b \mathbf{s} - J_0 \mu \, N_b \frac{\mathbb{v}_\tau}{\|\boldsymbol{v}_\tau\|}, \tag{9.2}$$

or incorporating both Coulomb and viscous drag as a Voellmy rheology,

$$\varsigma_\xi = -J_0 N_b \mathbf{s} - J_0 \left[\mu \, N_b + \frac{1}{\alpha} \|\boldsymbol{v}_\tau\|^2 \right] \frac{\mathbb{v}_\tau}{\|\boldsymbol{v}_\tau\|}. \tag{9.3}$$

In (9.2) and (9.3),

$$N_b \equiv p\Big|_{\zeta=0} = h(c+a), \quad \|\boldsymbol{v}_\tau\| = \sqrt{\mathbf{M}_0^{-1}\mathbf{v}\cdot\mathbf{v}},$$

see (4.90) and (5.10), $\mu \equiv \tan\delta$ (δ—the angle of the basal friction), and α is a dimensionless constant rheological parameter arising in the viscous drag law, expressed with the classical Voellmy rheology symbol. The apparent drag coefficient α^{-1}, denoted as $\tilde{c}$ in (5.37), is also calibrated for the Tsaoling landslide for comparison.

For the reader convenience we reproduce the Eqs. (4.99) and (4.102) under the above listed assumptions:

$$\frac{\partial}{\partial t}\Big\{J_0 h\Big\} + \mathrm{Div}\Big\{J_0 h\,\mathbf{v}\Big\} = 0\,, \tag{9.4}$$

$$\frac{\partial}{\partial t}\Big\{J_0 h \mathbb{v}_\tau\Big\} + \mathrm{Div}\Big\{J_0 h\Big[\mathbb{v}_\tau \otimes \mathbf{v} + \tfrac{1}{2}\,c\,h\,\mathbf{FM_0}\Big]\Big\} = \varsigma_\xi\,. \tag{9.5}$$

The result of application of the Coulomb friction law is first presented. The best-fit angle of the basal friction corresponding to the minimum error is 7.813°. An example of the progress of the minimization is tabulated in Table 9.3. The value is independent of the initial guess of the angle of the basal friction and it is in a reasonable range of the estimation presented in Fig. 5 of [34]. The new result is about 30 % higher than the previous study. The reason is attributed to the use of the new 1999 landslide DTM. Because of the loosely-packed deposit, it was found that sediment transportation mechanism was highly active in the first few years after the landslide. The deposit depth changed as much as 60 m in the Chinshui river channel and the post-landslide erosion-deposition process caused the deposit spread wider along the river valley within a single year [7, 42, 43]. These geomorphological changes lead to the adjustment of the calibration result.

Table 9.3 Iteration of simplex minimization

Iteration no.	Friction angle (°)	Standard dev. (m)
1	7.5000	24.4904
2	7.7000	24.4028
3	7.9000	24.3918
4	8.1000	24.4901
5	8.1000	24.4901
6	7.8000	24.3877
7	7.7000	24.4028
8	7.8500	24.3905
9	7.7500	24.3908
10	7.8250	24.3868
11	7.8500	24.3905
12	7.8125	24.3868

Initial guess of the angle of the basal friction is 7.5°. Initial offset step size is 0.2° and optimization error is set 0.01 m

The calibrated angle of the basal friction is considerably lower, 63 %, than the angle of the internal peak friction of the Cholan formation shale, see Table 9.2. It agrees excellently with the discrete element simulation which is $0.15 \approx \tan 8.53°$. The average standard deviation of the deposit height in the calibrated region is 24.4 m. The striking phenomenon: the lowering of the angle of the basal friction from the material internal friction angle is confirmed from the simulation point of view.

This material strength weakening phenomenon can be partly explained by the collective behavior of granular flows [44]. Based on the DEM simulation [45] show a negative correlation between the apparent basal friction and the flow volume by fixing the discrete particle size uniformly at 1 m in diameter. Another important factor is the water pore-pressure effect, i.e., fluidization of the debris flow by pore water pressure [34, 46]. In the field, the existence of the water content is backed by the fact that fresh water seepages from the interfaces between the geological formations and joints [11]. These microscopic effects are not modeled by the current shallow flow theory however, with advances of laboratory measuring techniques, the lowering of the angle of the basal friction can be experimentally measured in high pressure and high speed rotary shearing tests. Together with the next Hsiaoling landslide example, we abbreviated the experiments in Sect. 9.4.

The parameters of the Voellmy rheology law were also calculated using the same procedure and they are calibrated to 7.05° for the angle of the basal friction and 5.75×10^{-5} for the drag coefficient α^{-1}. The introduction of the fluid-like drag causes a reduction of the angle of the basal friction from the pure Coulomb friction law. The loss of resistant force required to stop the landslide flow was then compensated by the drag force. The relative order of magnitudes between the two types of resistant force components was inspected by normalizing (9.3) with respect to N_b. In the assessment, the characteristic flow depth and velocity were set to 40 m and 60 m/s, taken near the Chunqiu Cliff at $t = 32$ s, when the flow had the maximum kinetic energy. Under this condition, the drag force was estimated only about 4.0 % compared to the Coulomb friction. Because of the relative insignificance of the drag force, the motion of the landslide with the Voellmy rheology was virtually indistinguishable from that with the Coulomb friction. In the following section, only the case of Coulomb friction is presented.

9.2.3 Landslide Motion

With the calibrated angle of the basal friction, we recapitulate the landslide motion in this section. Although the present model is different from that used in [3] for the scope of the book, the flow characteristic is similar. In what follows in this section, we describe the flow with the updated result in parallel to [3].

The transient total kinetic energy, normalized with respect to the unit weight, of the landslide flow is shown in Fig. 9.8a. The maximum kinetic energy is reached at 32 s after the landslide initiation. At this moment, the distribution of the flow velocity is shown in Fig. 9.8b. The threshold speed of the top 10 % of flow elements is as high

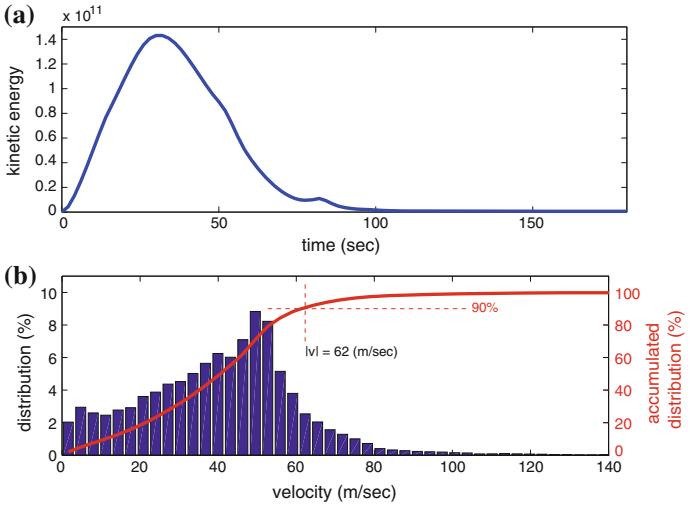

Fig. 9.8 **a** Total kinetic energy of the landslide flow, normalized with respect to the unit weight. **b** Distribution of the flow velocity at $t = 32$ s. The maximum velocity is defined 62 m/s, 90 % coverage of the velocity distribution

as 62 m/s; the maximum distributed speed is 50 m/s, and the average speed is 41 m/s. These statistics agree with related studies on this landslide [3, 17, 47].

Figure 9.9a, b shows the sequence of transient flow depths and speeds of the debris flow motion. For clarity, the outline of the flow is set to 10 m deep (about a tenth of the mean flow depth). At about $t = 22.0$, the first wave of landslide flow reaches the north bank of the Chinshui River. Between $t = 22.0$ and 36.0, the flow enters the Chinshui River valley, exhibits strong interactions, and expands along the river valley, particularly noticeably into the upstream. The velocity snapshots show that the maximum flow velocity, reaching as high as 70 m/s, occurs around the Chunqiu Cliff where the terrain in this area has a steep descent, Fig. 9.9b. At such a speed, the simulation confirms the field observation that the landslide is of rock avalanche type, according to the classification by [48, 49]. By this momentum, the flow further crosses Chinshui river at about half a minute after the initiation and deposits at the opposite of the river band. The flow is also diverted and spread into the river channel.

Dramatic flow interactions can be seen from the transient sequence of the main $\overline{PQ}$ profile, Fig. 9.10. The two major flow fronts are seen in the profile at $t = 18$ s. Around $t = 36$ s, the main flow reaches the river valley. The second front quickly catches up with the first when it is decelerated by the river bed. An upstream traveling shock, with a magnitude over 100 m, is finally formed upon the flow impinging on the opposite bank of the river channel. While the shock propagates slowly upstream (from $t = 36$–90 s), the flow is continuously fed into the deposit region and forms a secondary surge front. Both surges are then dissipated by the friction force and settle into a profile with a smooth surface.

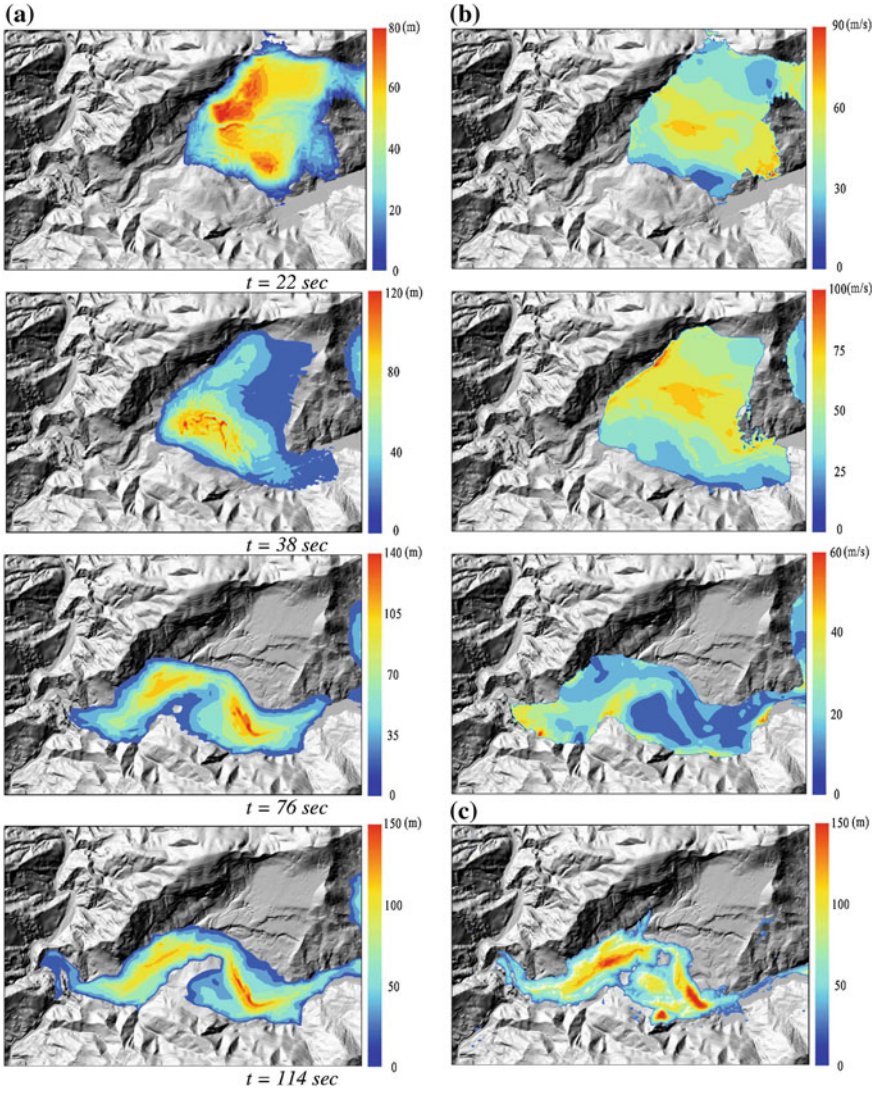

Fig. 9.9 Simulation snapshots. **a** Flow depths normal to the basal topography, **b** velocity and **c** measurement in the year 2000

At $t = 114$ s, the flow is almost at rest. The simulated deposit, say Fig. 9.9a$_4$, is compared with the measurements. The thickest deposit occurs at the middle section of the Chinshui river. The depth of the deposit opposite to the river, however, is underestimated by the simulation nor the deposit hill, Taochiashan, is seen. This is because the Eulerian constituent does not have the angle of the internal friction at which the flow reposes. Simulation beyond $t = 114$ s shows indistinguishable surface

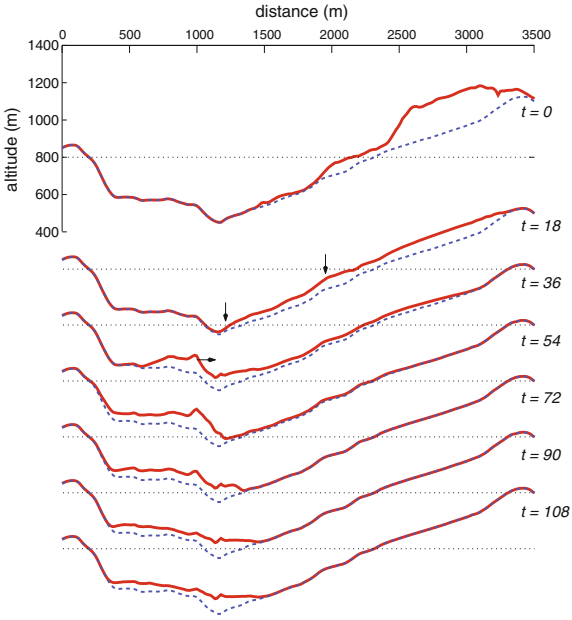

Fig. 9.10 'Waterfall' plot of the landslide sequence on the $\overline{PQ}$ profile

change. Along the river bank, a similar effect of the fluid can be seen and shows that the simulation deposit is more wide-spread than in reality. These discrepancies call for investigations with different material constitutive laws.

9.2.4 Landslide Induced Co-seismic Ground Motion

It is also of interest whether such a landslide induces additional ground motion which is ever recorded in the nearby strong-earthquake station. Because of the high seismicity and high population density of Taiwan island [50], government agencies and research institutes built one of the densest earth-quake monitoring networks in the world, serving a variety of purposes, e.g. early warning and earthquake identification. A strong motion seismo-station, code-named CHY080 (120.67770 E, 23.59720 N, El. 840 m, TWD97 standard) was installed on top of the Tsaoling slope in the 1990s. The station is located less than 1 km north-west of the depleted mass center, approximately 200 m from the landslide boundary, as indicated in Fig. 9.5, thus was safe from the violent seismic shaking, the landslide flow, and remained fully functional throughout the earthquake event.

The total duration of the earthquake signals recorded by CHY080 is 159 s at a standard sampling rate of 200 Hz. The recorded peak ground acceleration (PGA) values are 792.4, 841.5, and 715.9 gal for the EW, NS, and vertical components, respectively [51]. The P-wave arrived at 20.0 s, and the S-wave arrived at 25.2 s.

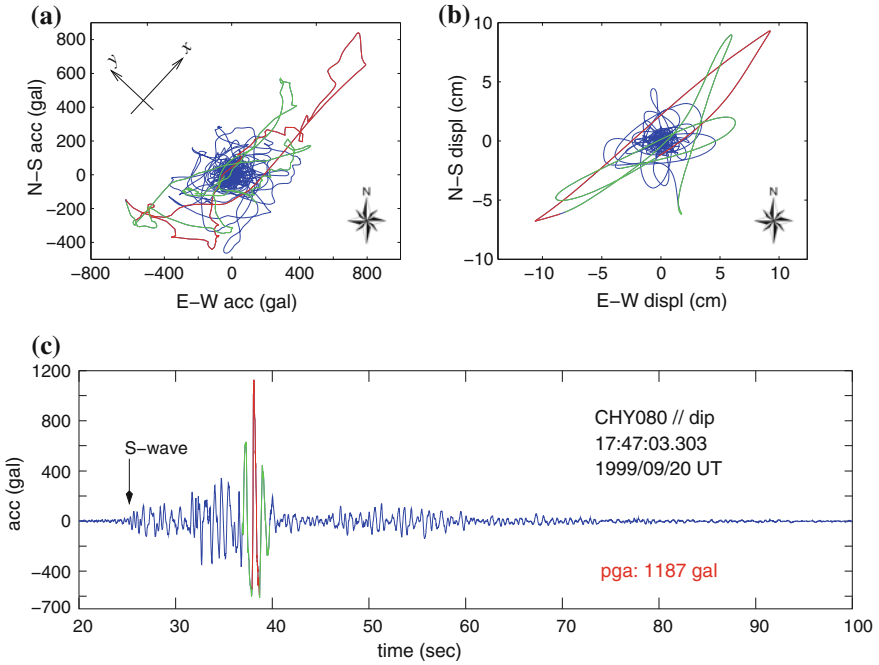

Fig. 9.11 Seismic records from the CHY080 strong motion station. Horizontal trajectories of **a** acceleration, **b** displacement, and **c** the transient acceleration component in the dip direction. The *colored line* segments (*red*/*green*/*magenta*) highlight the wave polarization among the *figure panels* at instances surrounding the peak ground motion (Reproduced from [35] with permission)

The horizontal trajectories of the acceleration and displacement are shown in Fig. 9.11a, b. The signals and trajectories show a sharp instance of activity at approximately 38.1 s. The signals around this time, highlighted by the red/green line segments for clarity, show ground motion with well-defined principal orientations. Both the acceleration and displacement are in the NE–SW direction, with principal directions 47° and 37° to the east, respectively, from the principal component analysis. Despite minor discrepancies, these directions are nearly parallel to the direction of the slide and the strata dip. The acceleration signals, rotated into the principal direction, are shown in Fig. 9.11c.

Applying a modified ensemble empirical mode decomposition (EEMD, [52]), [53] decomposed the acceleration of the earthquake between 30 and 45 s and found that there is a burst of sharp signals at 38.1 s. The decomposed signal components of interest are shown in Fig. 9.12. The acceleration components are defined in the principal coordinates (x in the landslide direction) and the three components have two distinctive characteristics. The y component, in the transverse direction of the landslide slide path, has a longer continuous motion at a much lower frequency range than the others. The x and z components, on the other hand, have localized and correlated high frequency wave packets which form a two-dimensional xz plane

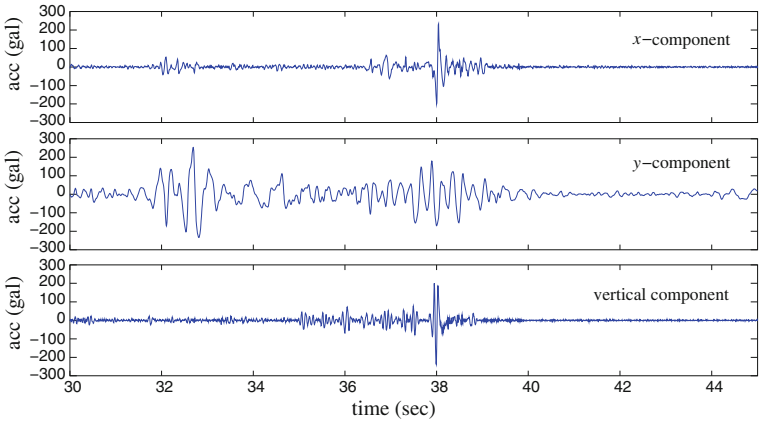

Fig. 9.12 The fracturing seismic signals. From the *top panel*: the x (landslide direction), y (transverse), and vertical components of the fracturing induced acceleration

motion. The motion was further analyzed in the cited paper by using an idealized homogeneous and isotropic two-dimensional elastic wave model and it is confirmed that a sudden release of the landslide mass generates ground acceleration at similar order of magnitudes and time scale. The initiation time was optimally fitted to 37.9 s which agrees excellently with the Newmark analysis with consideration of friction weakening of the rock material [37].

The impact of the landslide flow to the slope of the south Chinshui River bank was also observed. The main profile, as defined in Fig. 9.5, is oriented in the direction of the steepest descent of the slope, with the shortest distance to the river valley at the slope foothill. As a consequence, the landslide flow impinges normally onto the opposite slope and effectively generates a backward shock wave and impact seismic waves.

The recorded impact signals were found at about $t = 75.8$ s and lasted for about 2 s. The vertical acceleration and the decomposed component of interest is shown in Fig. 9.13. These wave packets are almost at the end of a series of intermittent signals, further intermittent signals becoming much less frequent and smaller in amplitude. They were neither associated with aftershocks nor appeared in records of other seismo-stations nearby. Comparing the EEMD decomposed acceleration component, the peak acceleration of the burst is about 815 gal, implying that if there were no background main earthquake, the ground motion would be equivalent to a small earthquake of $M_L = 4$. This magnitude is in agreement with the energy release of the landslide impact, estimated based on the rigid body sliding model; see also [36, 37, 54, 55]. Assuming that the impact wave directly propagates to CHY080 from the impact region (3 km apart), the traveling time of the wave is about 1 s and, hence, the impact of the landslide is estimated to occur at about 74.8 s. The interested readers are referred to [35] for the other EW (east-west) and NS acceleration components and the full verification.

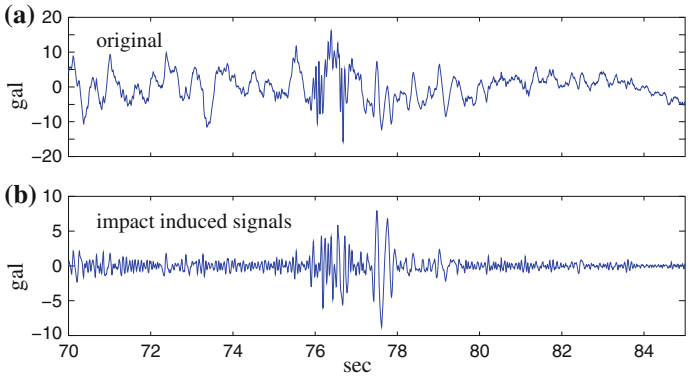

Fig. 9.13 **a** The vertical acceleration component of the seismic motion between 70 and 85 s; **b** the impact induced seismic motion

Based on the observation of the seismic motion, the fracturing of the landslide was identified at 37.9 s and the impingement was at 74.8 s. The fracturing and impact time could be cross-examined with the landslide simulation by making a time shift of 37.9 s to align with the seismic data. As observed in the third panel in Fig. 9.10, the impingement of the landslide flow to the river bank occurred at about 73.9 s and this impact time was in excellent agreement with the seismic analysis. Secondary diversionary landslide flows began spreading in the river valley when the landslide mass came to the river, with the entire motion lasting for a further minute or so. However, this late motion did not generate any further seismic motions that were distinguishable from the background earthquake.

9.2.5 Summary

From the simulation results, we conclude that the landslide roughly takes 2 min, which grossly agrees with the estimation of local survivors. The best fit of the angle of the basal friction is 7.813°. This value is slightly different from what was concluded (6°) in [3]. It is because the new released 1999 post landslide digital terrain model was used instead of the former study and the change of the model may have also some minor contribution. The essential friction weakening phenomenon nevertheless remains the same. Part of the reasons for the strength weakening of the material may be attributed to the weak slake durability index and it is subjected to a loss of strength when it is weathered in the ground-water table and ruptured during the earthquake. The angle of the basal friction further reduces when the mass movement is initiated.

Using the Voellmy rheology law, the angle of the basal friction is calibrated to 7.05° and the drag coefficient (α^{-1}) is 5.75×10^{-5}. The initial volume dilation factors are about 1.06 and 1.02 for the two rheology laws, respectively. The introduction of

the fluid-like drag causes the reduction of the angle of the basal friction to compensate the basal surface shear stresses. Comparing the magnitudes of the friction and drag forces, the former type of resistant force dominates the Tsaoling landslide. Because both rheology rules lead to virtually indistinguishable flow motions, only the flow with Coulomb friction was addressed in detail.

The maximum landslide velocity reaches about 62 m/s, which occurs in the region near the Chunqiu Cliff, where the deepest descent on the slope occurs. Generally, good agreements are found in both the height and spread area of the deposit comparing the simulation and field measurements, at an average standard deviation of 24 m, based on the calibration domain, compared to the maximum deposit depth about 140 m. The major discrepancies are that the simulation deposit is more wide-spread in the river channel and the thinner deposit on the south opposite river bank, which, in reality, was formed as a small deposit hill, called Taochiashan.

The rapid motion of the Tsaoling landslide has been previously identified by field observations and the landslide simulation. The initiation time of the event cannot be deduced from these methods. Nevertheless, the simulation provided evidence for inspecting landslide-induced signals in seismic records. The entire seismic motion was recorded by a near-by seismo-station. In the records, the precise landslide fracturing and impact time were identified.

9.3 Hsiaoling Landslide

Typhoon Morakot was an example of precipitation extremes, which released more than 2,000 mm of rain on southern Taiwan within three days beginning 7 August 2009 [56]. This rainfall almost equals the annual precipitation average in Taiwan. According to the National Disaster Prevention and Protection Commission in Taiwan, the resultant flooding caused 724 deaths. Of these, 474 were in a landslide and debris-flow event in Hsiaolin Village, Kaohsiung. This catastrophe had a severe socio-cultural impact on three Taiwanese aboriginal tribes of the Pingpu group. The content of this section is mainly based on the study presented in [57], enriched with the associated seismic verification of the landslide motion [58].

From the routine aerial photographs and immediate response of the Agricultural and Forestry Aerial Survey Institute of Taiwan, DTMs were generated at a 5-m resolution for the Hsiaolin landslide. The geological settings were summarized in Fig. 9.14 and Refs. [56, 59]. According to the DTMs and the field survey, the major landslide body had an extent of 57×10^4 m^2 (cool colors in Fig. 9.14a) and was estimated to have a volume[1] about 24 ± 2 million m^3, distributed at an average depth of 42 ± 3 m. The landslide moved in the westward direction as indicated by the thick hollow arrows in Fig. 9.14a. The landslide flow was divided into two streams at about the middle of the run-out. This was so because there had been a small ridge at 590 m above sea level (marked by the solid black triangle in Fig. 9.14b) and two

[1] The precision is justified based on the precision of the pre/post-event DTMs, see Sect. 9.3.2.

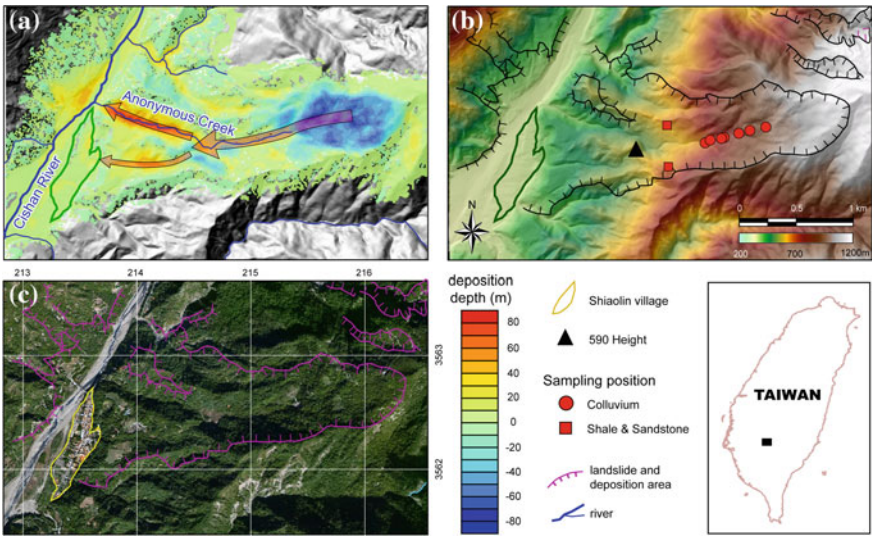

Fig. 9.14 The Hsiaolin area and the geological settings. **a** Aerial photo before the catastrophic landslide superimposed with the elevation differences between the two versions of the digital terrain models (before and after Typhoon Morakot and the block dam breach. Both were taken in 2009). Negative deposit depth (*cold colors*) represents the scar area. The main deposit is in the Anonymous Creek Valley and the Cishan River channel. The *arrows* indicate the main run-out paths. **b** The elevation of the landslide area. The *solid red circles* and *squares* are the sampling locations for colluvium and shale. The *large solid black triangle* marks the 590 Height, a ridge at an elevation 590 m above the sea level. **c** The birds-eye view of the landscape before the landslide and Hsiaolin village. The Cishan River flows from NE to SW. The horizontal coordinates follow the TWD97 (Taiwan Datum 97) standard system (Reproduced by courtesy of AGU Pub)

valleys extended from the west side of the ridge. This ridge is referred as the 590 Height hereafter. The 590 Height had a volume about 1.5 ± 0.2 million m^3 which was removed by the landslide.

The two debris streams, after interacting with the 590 Height, flowed along the two valleys and about a third of the sliding mass further flowed into Cishan River, running from NE to SW. The debris in the Cishan river formed a short-lived block dam and a dam breach occurred about 20 min after the landslide, which removed most of the deposit in the river channel except a minor portion of 5 ± 1 million m^3. The remaining deposit, mainly in the two valleys to the river, formed the main deposit area (warm colors in Fig. 9.14a). The deposit materials mainly composed of fine particles and fragmented shale blocks with sizes up to a few meters [56]. No substantial erosion was found in the exposed run-out (mainly between the scar area and the 590 Height), and, therefore, the erosion mechanism was not considered. The total combined volume in the main deposit area was 13 ± 2 million m^3 and the average basal inclination angle was about 15° (±12°, averaging over the slopes by the valleys). The northern valley of the two valleys is now referred as the Anonymous Creek Valley in the present paper and the deposit was in the SWW-NEE direction. The

southern valley is referred as the Hsiaolin Slope which was much smoother than the Anonymous Creek Valley. It was this Hsiaolin Slope that directed the landslide flow into the Hsiaolin Village. If a loose-measure volume of the sliding body is assumed to have expanded 10 %, the flushed materials by the dam breach were estimated about 11 ± 2 million m^3. After the landslide and the dam breach, the village (blocked by the thick green line in Fig. 9.14a) was completely buried.

Reconstruction of the run-out path due to the debris avalanche event is fundamental to understand the complex mass movement process. For this purpose, we adopt a continuum model, similar to the shallow water equations, to simulate the landslide. One of the important issues in the model is to include the topographic effect which interacted significantly with the landslide mass in this Hsiaolin event. For example, the topographic effect can be seen from the diversion of the landslide flow into the Anonymous Creek Valley and Hsiaolin Village after the slip mass interacted with the 590 Height and the surrounding ridges. Taking the topographic effects into the shallow water system is not trivial, mainly because of the complexity of the terrain geometry. [60] derived the (1D) model equations in the terrain-fitted curvilinear coordinates. [20, 61] extended the Savage-Hutter theory to multi-dimensions in which the curvature effect is included only in the down-slope direction. Alternatively, [21] formulated their theory with a curved and twisted coordinate system for a smooth, curved run-out path. In the further pursuit of the continuum model for real topography, several distinctive theoretical techniques have been proposed in the past decade: (1) the Lagrangian models [25, 40, 60, 62, 63], (2) the coordinate-based approaches [64, 65] and (3) the dynamic-based approaches [66, 67].

For this landslide, the same model as in the last section was applied for simulation analysis. The avalanche flow in the model is assumed to be single constituent, incompressible, thin and with a uniform velocity profile across the depth, flowing on a fixed topographic surface described by a Coulomb or Voellmy friction law. The topographic effect is manifested as the source of the kinetic momentum as shown in the derivation in the previous theoretical chapters. For the interested readers, extensive efforts have also been made to incorporate material constitutive laws, yield criteria or multi-phase constituent into the dynamic models for both two-dimensional [24, 68–70] and three-dimensional flows [71].

When the Coulomb friction or Voellmy law is applied, the friction and drag coefficients are the only two rheological parameters to determine. The iteration procedure used in Sect. 9.2.2 is applied to optimize for the model parameters. It was found in large scale landslides, e.g. the Tsaoling and current Hsiaolin landslides, the dominant rheology parameter in controlling the landslide motion is the Coulomb friction coefficient. The simple parameter further enables us to directly verify it by using high pressure rotary shearing tests on field debris samples. Together with the tests of the Tsaoling landslide, the experiments are briefly described in Sect. 9.4.

Although the landslide was triggered by excessive rainfall, we did not consider a mixture model in the present simulation. Instead, the focus was on the kinematics of the fast moving mass and its interaction with the run-out topography. The constant friction coefficient was determined with the help of laboratory experiments, in which the Coulomb friction coefficient is calculated by the total reacting torque and

the applied normal stress. Hence, the effect of pore water pressure was implicitly lumped into the friction coefficient and the single constituent frictional model was adequate for the present purpose. The key validation of the landslide simulation of the continuum model was performed by the corroboration with near-surface magnetic surveys over the buried village area, as presented in Sect. 9.3.4.

Nevertheless, we need to mention that the pore pressure plays an important role in regulating landslide motion [72], or lowering the friction force through the frictional heating mechanism when landslides are in motion [73–75]. For a landslide with a saturated water content, one may need to apply mixture models [23, 24, 76], but currently the application is beyond the scope of the chapter.

9.3.1 Simulation Setup and Parameter Calibration

In 2009, the Agricultural and Forestry Aerial Survey Institute of Taiwan released the DTM of the Hsiaolin area (photographed on 7, Jan.). It was acquired by aerial photography technology. After the landslide, an updated DTM was derived using aerial photos taken on 13 August 2009 by the same institute with the same method and analysis settings. The flight routes and the aerial photography cameras were arranged to ensure that the resolutions of ground images were higher than 30 cm/pixel. The DTMs acquired from the photograph interpretation have a horizontal resolution of 5×5 m with a total image unit weight RMSE[2] of less than 1 m. The precision of the pre/post-event DTMs was evaluated by inspecting the elevation deviation for regions without visible slope failures. Five such regions (see the supplement) were identified. The average elevation difference was about 0.4 m and the elevation standard deviation was 2.9 m. Subtracting the two DTMs, the scar and the deposit areas were identified, cf. Fig. 9.14. The deposit has been re-sketched in Fig. 9.15a, in which the small scale and thin deposits outside the main deposit area have been filtered for clarity.

The computational domain was $3,710 \times 2,220\ \mathrm{m}^2$. The topography was coarsened by selecting every alternative grid in the DTMs to a $10 \times 10\ \mathrm{m}^2$ mesh and processed with a spatial Gaussian filter to eliminate high wave-number irregularities for better numerical performance and convergence. The standard deviation caused by these artificial adjustments are smaller than 0.9 m, which is in the range of the precision error of the DTMs. The initial volume was set directly from the DTMs without a presumed volume dilation. In the simulation, there were two scar areas: the main scar and the 590 Height scar. The sliding volume of the former was $(24 \pm 2) \times 10^6\ \mathrm{m}^3$ and that of the latter was $(1.5 \pm 0.2) \times 10^6\ \mathrm{m}^3$. The sliding mass was released at $t = 0$. Along with the main sliding mass, the secondary landslide mass, the 590 Height scar, was released simultaneously for simplicity; i.e., the impact of the main slid mass onto the 590 Height was neglected. Different release conditions were tested but no significant changes to the main flow were found because the volume of the 590 Height was only about 6 % of the total.

[2]Root mean square error.

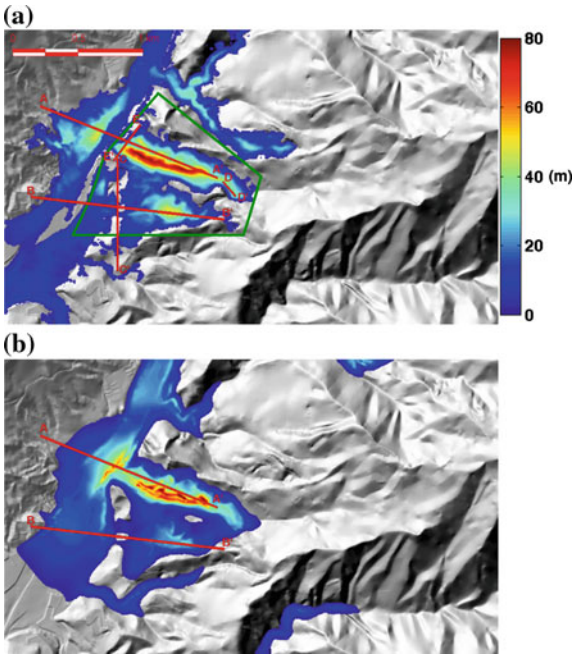

Fig. 9.15 **a** Actual deposit (after the dam breach) and **b** simulated deposit (without dam breach). The deposit depths are coded with the same color axis. The area boxed by the *bold dark green* polygon is the region for the minimization scheme, (9.1). Five profiles are defined for detailed inspection. Profiles $\overline{AA'}$ and $\overline{BB'}$ are for comparison of the deposits in Anonymous Creek and the Hsiaolin Slope. Profiles $\overline{CC'}$, $\overline{DD'}$, and $\overline{EE'}$ are for volume flux calculations (Reproduced from [57] with courtesy of AGU Pub)

When applying continuum models to landslides, the assumption that the fracture mechanisms of the sliding mass had been simplified to instant initiation was automatically made. These fracture mechanisms include the rock buckling failure, crack propagation etc. The fracture procedures of the landslide mass were therefore assumed to be completed shortly after initiation such that the fluid model could work. This may be an acceptable assumption because the propagation of internal cracks are of the order of sound speed in rocks which is much faster than the flow speed. This assumption was also made for the previous Tsaoling landslide.

The same Coulomb friction and Voellmy rheology law are used to model the landslide flow. The friction coefficient μ in both rheology laws are associated with the angle of the basal friction δ by $\mu = \tan\delta$, while the fluid-like drag coefficient, α^{-1}, is defined the same as in the last section. For numerical calibration of the parameters, the same optimization process was used.

Before using the minimization scheme, described in Sect. 9.2.2, to determine the accurate friction coefficient, two prerequisites are to be used: the deposit area for the parameter calibration and the initial estimation of the friction coefficient. Because there was a dam breach after the landslide in the Hsiaolin catastrophe, most of the deposit in the Cishan River channel was flushed away, and a new river channel was quickly formed by the stream flow before the aerial measurements were performed. To eliminate the errors caused by the dam breach, the Cishan River valley was excluded from the minimization process. The remaining deposit areas were the Anonymous Creek Valley and the Hsiaolin Slope, the slope towards the

Hsiaolin township. The resultant area for the calibration was defined as the region surrounded by the bold red outlines in Fig. 9.15a.

The initial estimation of the friction coefficient was obtained by referring to the empirical scaling laws of friction and the rotary shearing tests, Sects. 9.2.1 and 9.4. The determination of the friction coefficient by the empirical laws was as follows: In the landslide, the gravity centers of the measured scar and deposit volumes were used to estimate the associated parameters in the statistical empirical laws which yielded an end-to-end displacement $L = 2000$ m and $H = 460$ m. Based on the precision of the DTMs, a couple of tens of meters error bounds in the estimation were expected (assuming a few folds of the standard deviation of the DTMs, cf. Sect. 9.3.2). With these parameters, the apparent friction coefficient was approximately 0.23 ($\approx H/L$), or 0.29 (Scheidegger's regression formula). The standard deviation, as given in [33], was 0.14. Using a similar method, [59] quoted the apparent friction coefficient to be 0.25. These values, however, may have been somewhat overestimated because the traveling distance L was underestimated because: (1) the travel-ling distance was constrained by the slope on the west bank of Cishan river such that the landslide flow was redirected into the river valley, and (2) the flush-away debris by the follow-up dam breach was neither included in the calculation of the gravity center which led to the underestimation of the traveling distance. With the above consideration in mind, it was conjectured that the friction coefficient value was on the negative side of the quoted values.

The initial guess of the apparent friction coefficient was therefore set to 0.2 (the angle of the basal friction 11.31°). For convenience, the minimization scheme was started at the angle of the basal friction 11°. In the calibration iterations, the simulation time is set sufficiently long, here 180 s, to ensure that the flow speed in the main deposit area is less than the average 2 m/s, 4 % of the maximum flow speed, at the end of each simulation. The outflow condition was applied on the domain boundaries. The progress of the minimization for the Coulomb friction law is tabulated in Table 9.4. The optimized friction coefficient was calibrated to $\mu = \tan(11.47°) = 0.203$, which had only a minute difference from the empirical law.

The minimization scheme was also performed for the Voellmy friction law, (9.3), and the parameters converged to $(\mu, \alpha^{-1}) = (0.194, 8.75 \times 10^{-4})$ with a standard depth deviation of 7.75 m. These parameters formed an adjacent local minimum of

Table 9.4 Minimization iterations

Iteration number	Friction angle δ (°)	Depth deviation (m)
1	11.40	7.651
2	11.50	7.612
3	11.45	7.611
4	11.47	7.610
5	11.47	7.610

The friction coefficient μ is related to the angle of the basal friction δ by $\mu = \tan\delta$. The convergence condition of the minimization is set to 0.01 (Reproduced by courtesy of AGU Pub)

the object function that was slightly worse than the case with Coulomb friction alone. Nevertheless, the flow details were almost identical to the flow with the Coulomb friction because the contribution of the turbulent drag to the landslide flow was found to be much smaller than that of the Coulomb friction. This also agrees with that found in the Tsaoling landslide. In addition, assuming a constant volume dilation of 20 %, the minimization schemes were repeated for both rheological laws (Coulomb and Voellmy). It was found that the best-fit rheological parameters were $\mu = 0.200$ for the Coulomb friction and $(\mu, \alpha^{-1}) = (0.193, 4.21 \times 10^{-4})$ for the Voellmy law. These parameters with the dilated sliding volume deviated only slightly from those without the volume dilation, indicating that the effect of the volume dilation factor on the rheological parameters was also negligible.

9.3.2 Landslide Motion

Because the results of both the Coulomb and Voellmy friction laws were quantitatively similar, only the case of the Coulomb friction is the focus in the following discussion. The simulated deposit is depicted in Fig. 9.15b. Except for the minor valleys north and south, good agreements were achieved in the calibration region. The deposit in the Cishan river channel was, however, more confined in the downstream section (the lower-left corner) compared to what was observed in the field. The total simulated deposit in the calibration region was about 11.5 million m^3, less than the 13 ± 3 million m^3 from the measurement, and the depth deviation was 7.6 m. The simulated deposit in the river channel was roughly 14.1 million m^3 (before being washed away by the dam breach). The deposit volume was probably slightly underestimated because no volume dilation was presumed in the simulation. For granular flows or landslides, the volume dilation ratio is customarily between 10 and 20 %, and at this ratio, the discrepancy between the simulated and measured deposit volumes can be largely explained.

To further inspect the deposits in detail, two profiles were defined, $\overline{AA'}$ and $\overline{BB'}$. They cut through the deposit along the center-lines of the Anonymous Creek Valley and the Hsiaolin Slope and were extended across the Cishan River to the opposite river bank. The deposits on the profiles are drawn in Fig. 9.16. An excellent agreement between the simulation and the measurements in the Anonymous Creek Valley was obtained. A maximum discrepancy of about 50 % in depth, however, was found in the Hsiaolin slope. This was because the west end of the $\overline{BB'}$ profile was near the 590 Height where the impact between the landslide flow and the height was not correctly simulated (simplified). This implies that the momentum reduction due to the impact as the flow entering the Hsiaolin Slope was somewhat underestimated in the simulation and thus deferred its deposition on the slope. In addition, the solid properties, such as the angle of internal friction, angle of repose, and earth pressure properties, of the landslide materials, which are largely omitted in the present model, may also have contributed in part to the discrepancy. From a comparison of the left halves of the profiles in the Cishan River channel, the effects of the second stage

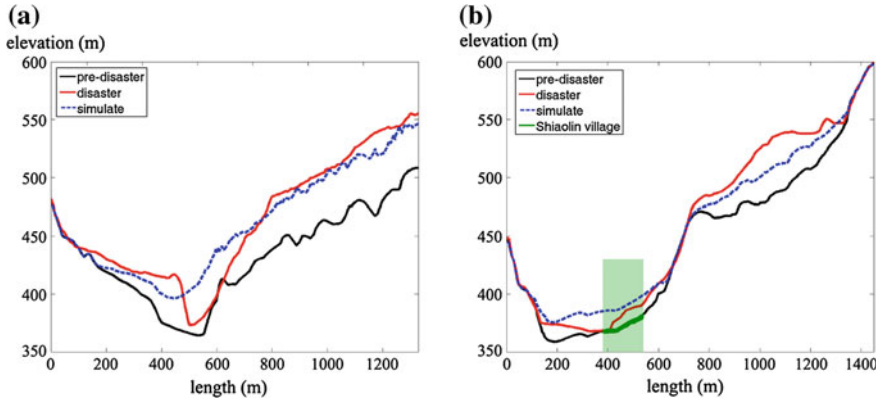

Fig. 9.16 Comparison of the actual and the simulated deposits on **a** the $\overline{AA'}$ profile, Anonymous Creek, and **b** the $\overline{BB'}$ profile, the Hsiaolin Slope. Points A and B are the origins of the $x-$axes in the sub-figures. The *black lines* are the original basal topography, the *red lines* are the post-event topography, and the *blue dashed lines* are the simulated deposits. The *green shaded* regions indicate the location of the village (Reproduced from [57] with courtesy of AGU Pub)

dam breach were identified and the excavation mechanism reshaped the river. The simulated deposit volume in the river has been applied in a hydrological study of the dam breach stage of the event [77].

The shape of the simulated deposit has the typical feature that is commonly seen in simulations using the continuum model. This feature is that the deposit surface is usually smoother than the real deposit of landslides; see [3]. The reason is that the resting surface slope in the model, with the present simplifications, is constrained only by the basal friction. This theoretical property can be seen by substituting $\mathbf{u} = \mathbf{0}$ into the model equations, which leads to the equation for the surface slope in terms of the friction and the gravity force. Incorporating the angle of internal friction, the solid constitutives, such as the Mohr-Coulomb constitutive law [26, 66, 71], or the erosion/deposition mechanism [44, 64, 78], may further improve the accuracy of the simulation. However, applying these additional constitutive relations and erosion/deposition mechanisms would involve solving the internal stress states of the flow in detail which challenges the numerical convergence, stability, and the justification of the extra rheological parameters. It is therefore beyond the scope of the present chapter. In the literature, both [24, 26] performed simulations with considerations of earth pressure coefficients which brought certain solid properties of the landslide materials into the landslide flow.

Having confirmed the deposits, the landslide motion is examined. Two snapshots at t = 42 and t = 62 s are shown in Fig. 9.17a, b. These time-steps correspond to the peak landslide flow at the 590 Height and the west bank of the Cishan River. Upon hitting the 590 Height, the flow split into two run-out paths (Fig. 9.17a). The main stream was diverted to flow along the Anonymous Creek Valley, and the second flow moved through the southern part of the 590 Height into the Hsiaolin Slope and the

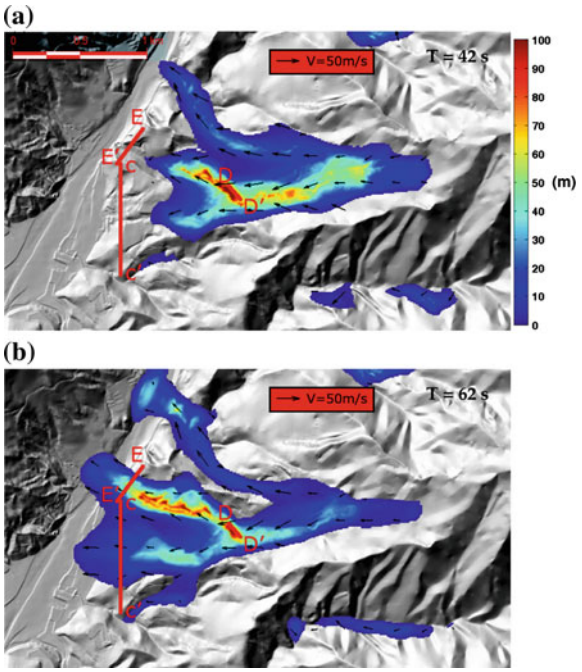

Fig. 9.17 Landslide snapshots at **a** $t = 42$ s, **b** $t = 62$ s. The profiles were defined for volume flux calculations. Profile $\overline{CC'}$ was defined to capture the volume flux flowing into the village, profile $\overline{DD'}$ was for resolving the 590 Height impingement, and profile $\overline{EE'}$ was for estimating the arrival of the landslide at the Cishan River bank. The *arrows* represent the flow velocity, and the maximum speed was about 50 m/s along Anonymous Creek (Reproduced from [57] with courtesy of AGU Pub)

Hsiaolin village. The maximum speed was as fast as 50 m/s along the main run-out path.

Three key features of the Hsiaolin landslide remain to be further addressed: (1) The first impression on the impact of the flow upon the 590 Height; (2) The approach of the mass flow to the Cishan River valley; and (3) The flow towards the village. For these purposes, three profiles, $\overline{DD'}$, $\overline{EE'}$, and $\overline{CC'}$ were defined and the landslide volume fluxes crossing these profiles were calculated by integrating over the length of the profiles. They are plotted in Fig. 9.18a.

A few marking time-stamps were first identified. The front of the landslide flux reached the 590 Height at 20 s. There was a small negative preceding flux which was the result from the simplified instantaneous release of the materials of the 590 Height. Then the flux quickly peaked at 42 s. Diverted by the 590 Height, the landslide flow splits into two parts as previously discussed. The split fluxes arrived at the Cishan River bank, $\overline{EE'}$, and flowed toward the village, $\overline{CC'}$, at almost the same time, about 50 s, and both reached the maximum at about 62 and 64 s. The landslide motion came to rest within about 110 s, and in the model the fluxes became less than 10 % of the maximum.

The profile $\overline{CC'}$ was defined adjacent to the Hsiaolin village, which was used to capture the volume flux flowing through the village. Integrating the volume flux with respect to time, it was found that the total debris volume through the village was about 1.58×10^6 m^3, only roughly 7 % of the sliding volume. This volume, however,

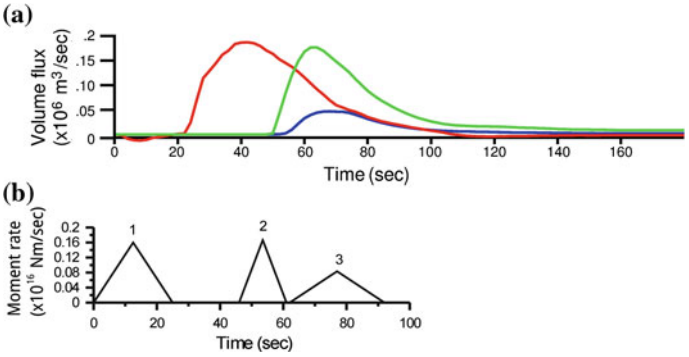

Fig. 9.18 **a** Transient volume fluxes across the profiles defined in Fig. 9.17. The *red line* is for $\overline{DD'}$, the *green line* is for $\overline{EE'}$, and the *blue line* is for $\overline{CC'}$. **b** The inverted seismic moment source, cf. Sect. 9.3.3. The origins in both panels are shift for visual comparison of the temporal association between landslide impacts and inverted seismic moment rate sources (Reproduced from [57], **a** with courtesy of AGU Pub. and [58], **b** with courtesy of InTech Pub)

was the most devastating branch of the landslide stream, and it will be examined in detail in Sect. 9.3.4.

9.3.3 Associated Seismic Motion

Similar to the previous Tsaoling case, the landslide signals had been captured by the seismographic network. The ground motions, especially Rayleigh waves, generated by the landslide were recorded by broadband seismographs [58, 79–81]. The arrival time of 25 s (period) Rayleigh waves recorded at 8 stations was used to locate the position of the landslide. In the landslide position determination process, a simple half-space model with a 3.75 km/s S-wave speed and the inversion algorithm [82] were adopted. The occurrence time (local) was at 6:16 am and the estimated position was at (23.2637° N, 120.6267° E). Compared to the Hsiaolin Village (23.1625° N, 120.6444° E), the error was about 11.4 km which may arise due to errors in the arrival time measurements or the simplified model. Another estimation for the landslide location can be seen in [80].

Take two records for example, Fig. 9.19. The data were recorded at the seismogram station YHNB and SCZB. It was clearly identified that the waveforms composed of three sub-events (marked by the arrows in the panels of the seismic signals in Fig. 9.19). In the waveforms, the frequency contents between 0.033 and 0.05 Hz were taken for seismic source inversion calculation. For the landslide motion, an equivalent single-force representation was used [83]. The velocity structure was again the simple half-space model at a uniform density 2,800 kg/m^3 with a P-wave speed 6.5 km/s and an S-wave speed 3.75 km/s. The surface wave synthetic program [84] was used. To

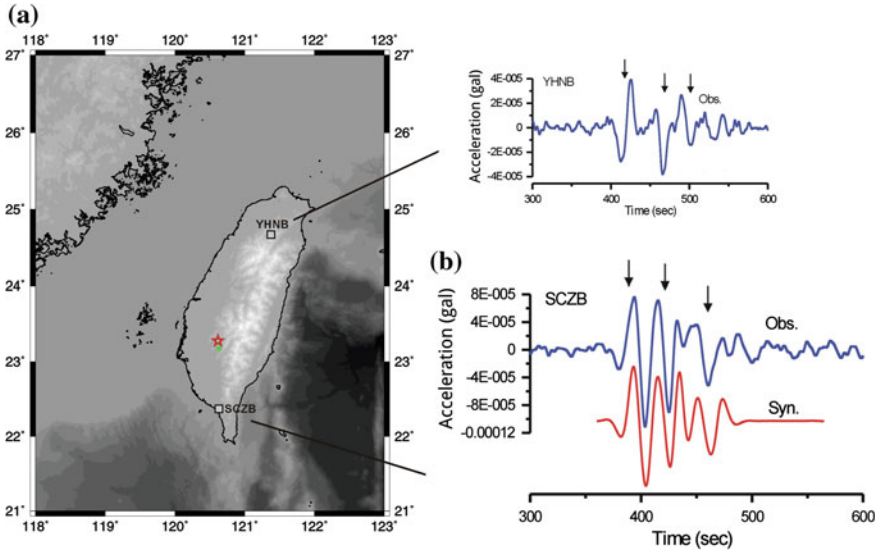

Fig. 9.19 **a** Identified location of the landslide (23.2637° N, 120.6267° E), marked by the *red* hollow start and located by means of seismic recordings. The Hsiaolin Village (23.1625° N, 120.6444° E), marked by the *green solid dot*. Also shown are two example seismograms recorded by seismogram station SCZB and YHNB (*squares*). **b** The seismogram, *thick blue line*, recorded by SCZB station and the synthesized seismic motion, *thick red line* (vertically offset for clarity), with the three triangular distributed seismic moment rates. The best-fit seismic moment rates have been plotted in Fig. 9.18b (Reproduced from [58] with courtesy of InTech Pub)

minimize the interferences from the geo-structure inhomogeneities, the waveform at the closer station (SCZB) was used.

We assumed that there are three sources, expressed in terms of the moment rates, and they all had simple isosceles-triangular-shaped temporal distributions. For each sub-event, we adjusted the occurrence time, duration and the total moment to fit the forward synthetic waveform at SCZB against the observed one. The best fit of the synthesized waveform was shown by the red thick line in Fig. 9.19b and the three distributed moment rate was plotted in Fig. 9.18b. The total seismic moments of these three sub-events were, respectively, 6.0, 1.4 and 3.0 $\times 10^{16}$ Nm, and the ground motion corresponded to a moment magnitude scale $M_w = 5.0 - 5.2$. The converted single force magnitude was about the order of 10^{11} N. The inversion calculation showed that the second and third sub-events occurred at 34 and 55 s after the occurrence of the first sub-event.

If we assume that the first sub-event represents the landslide initiation, these two moments were quite coincident to the landslide flow which reached the 590 Height and the channel of the Cishan River. Recall the landslide simulation result, the volume flux impacting on the 590 Height was approximately the flux through the $\overline{DD'}$ profile and that reaching the Cishan River was the flux through $\overline{CC'}$ and $\overline{EE'}$. For better visual comparison between the landslide impacts and the inverted seismic sources,

the origins in Fig. 9.18 are deliberately shifted. The amount of the time shift may also be associated with simulation errors in the seismic inversion calculation.

Despite the coincidences of the three inverted sub-event sources with the landslide initiation and impacts, we noted that there were somewhat unnatural vanishing seismic sources while the landslide was in motion. It was because the seismic sources were assumed to be composed only of three triangular shaped moment rates such that the real continuous seismic sources, the landslide motion induced stresses, were lumped into the three discrete effective sources. The artifact of this simplified approach was that the resolution of the seismic sources to the landslide motion was partially lost. Inspecting the seismic data for different perspectives, Lin et al. [80] estimated the landslide volume to 5×10^6 m^3 and Stark et al. [81] reported the estimated landslide speed as about 50 m/s. These estimations agreed well with both the field investigations and landslide simulations.

There have been growing interests and research achievements on the studies of seismic response due to landslides. For other worldwide examples, one may refer to [41, 85] and references therein. In Taiwan, a nation-wide research project has been initiated in 2014 for feasibility study to extend the capability of the seismic monitoring network for future landslide identification.

9.3.4 Near-Surface Magnetic Survey and Flow in the Village

The near-surface magnetic survey was performed by using high sensitivity magnetic sensors (Geometrics model G-856, with a sensitivity of 0.1 nT) to measure the total magnetic field strength on the ground surface. Because the magnetic field reacted strongly to magnetizable materials such as iron and steel, anomalies caused by the buried artifact structures/objects, e.g. reinforced concrete structures and cars, can be detected by the magneto-meters and analyzed. With this technology, a set of high-resolution (20×5 m) near-surface magnetic data covering the main township of Hsiaolin Village was obtained. The survey was performed in October 2009, the month after the landslide occurred. The instruments and technical details can be found in [86].

The magnetic anomaly map (colors in Fig. 9.20a) presents the anomalous patterns of the magnetic dipole fields, and it can be used to derive the amplitude distribution (contours in Fig. 9.20a) of the zeroth-order analytic signals of the magnetic sources [87–89]. Superimposing the distributions of the magnetic sources onto the aerial photograph taken before Typhoon Morakot, it was clearly identified that all of the magnetic sources corresponded closely with the buildings located in the southern part of the township, Fig. 9.20b. The sharp boundary of the destruction front of the landslide, the thick dashed lines in Fig. 9.20b, could be defined by a comparison between the magnetic anomalies and the aerial photograph. The results suggested

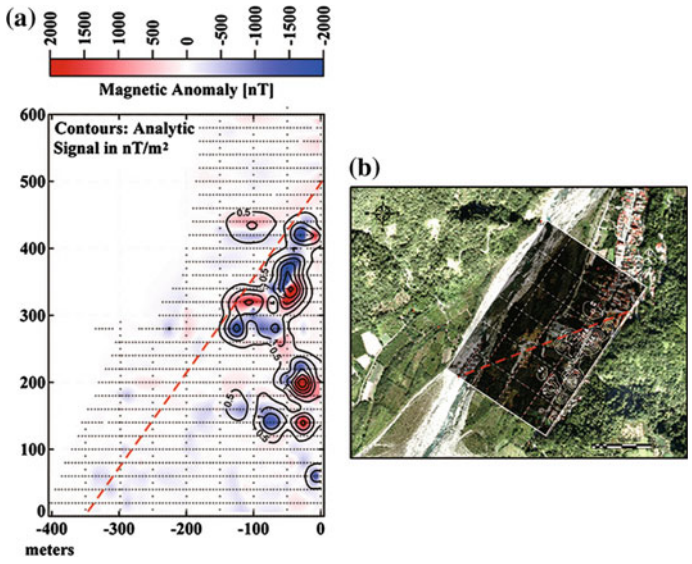

Fig. 9.20 **a** Magnetic anomaly (*colors*) and amplitude of the magnetic zeroth-order analytic signal (contours) over the main area of Hsiaolin Village. *Crosses* denote the survey locations. **b** Aerial photograph taken before Typhoon Morakot, superimposed with the magnetic analytic signal (*white* contours). The *thick red dashed line* in each *panel* depicts the sharp destruction boundary of the debris suggested by the results of the magnetic survey (Reproduced from [57] with courtesy of AGU Pub)

that the buildings located to the north of the boundary were removed from their original locations by the impact of the landslide.

The simulation showed that there was a very destructive front. In Fig. 9.21, snapshots of the landslide flow in the village during the peak flux period were presented. The first three snapshots indicated the propagation of the landslide front and the flow velocity field. The flow entered the village from the north-west side of the village boundary. More specifically, it was near the exit of the Hsiaolin Slope, which was around the midpoint of the $\overline{CC'}$ profile. The flow direction was toward the west. The measured boundary of the magnetic anomalies, the bold red dashed line, were found to be well coincident with the flow boundary, defined by the contour line of 1 m deep. Further south at the boundary, the flow was thinner than 1 m. The simulation hence provided strong evidence that the buildings and the artifact objects in the north of the village were dislocated into the Cishan river by the landslide while in the south, the flow did not have enough momentum to shear off the buildings. After the passing of the flow front, the debris then buried the north side of the village and flowed into the river channel, cf. the snapshot at $t = 100$ s.

The kinematic properties of the landslide were examined along the $\overline{BB'}$ profile. The momentum and the velocity are sketched in Fig. 9.22. The time when the flow front swept through the village was specifically analyzed and it was between 54 and

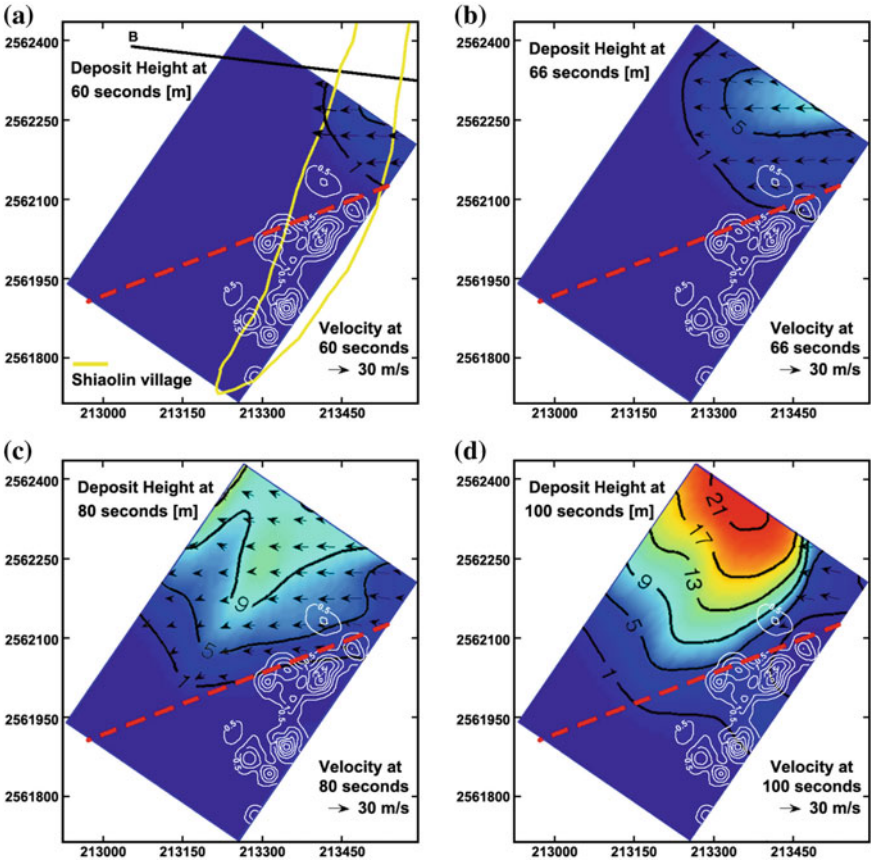

Fig. 9.21 The flow snapshots in the region of the near-surface magnetic surveys. The time-steps were chosen in the peak flux period, cf. the $\overline{CC'}$ flux in Fig. 9.18a. The village area is enclosed by the *yellow line*. The *thick bold black line* is the east part of Profile $\overline{BB'}$. The profile cuts almost perpendicularly to the landslide flow front. The *thick dashed line* indicates the boundary of the landslide flow defined by the magnetic surveys. The magnetic anomalies are superimposed for comparison. The color axis, from *dark blue* to *red*, represents flow thickness from 0 to 25 m. The *arrows* represent the flow velocity (Reproduced from [57] with courtesy of AGU Pub)

60 s in the simulation. During these moments, the flow speed reached 35–50 m/s and the momentum (per unit density) was about 250 m^2/s. The flow height at the impact was 6–7 m. A much thicker debris then flooded the village at a much later time, 100 s, in the form of a reflected surge wave, Fig. 9.23. The surge was reflected by the slope on the opposite side of the Cishan River. The final debris deposit was roughly 17 m deep. A similar behavior was also found in the Tsaoling landslide when its debris mass interacted with the foothill river valley [3].

The agreements between simulation and the magnetic surveys on the flow that entered the Hsiaolin village are a critical justification of the simulation model. The

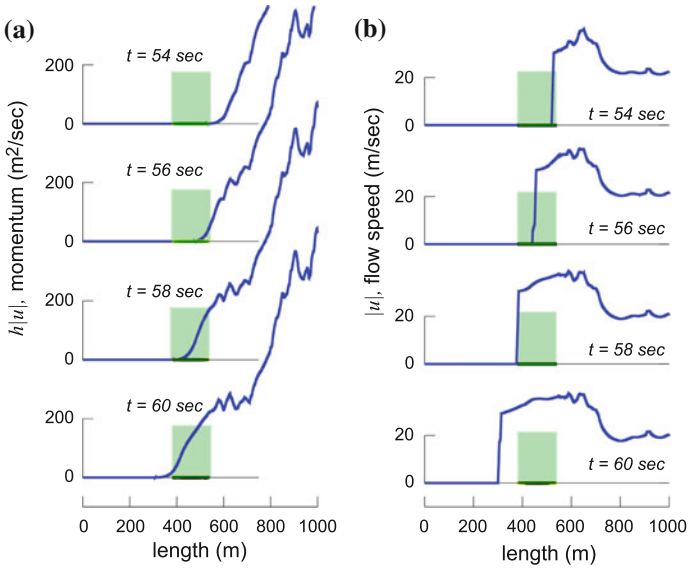

Fig. 9.22 **a** Momentum and **b** velocity on profile $\overline{BB'}$. The *green shaded* regions indicate the location of the village. Point B is the origin of the x-axis. The figures show the progress of the landslide front. The flow speed was about 35–40 m/s when it swept over the village which may be somewhat overestimated because interactions with the village buildings were neglected in the model (Reproduced from [57] with courtesy of AGU Pub)

achieved good agreements may be attributed to the fact that the landslide was a spreading dominant flow. In addition to the same conclusion from the empirical scaling laws of friction, it could be also confirmed by the field observations that the deposit was composed of grains from fine particles (sub-millimeters in size) to shale blocks with sizes up to a few meters [56]. Comparing to the characteristic lengths of the landslide, say $V^{1/3}$ approximately 290 m, or the flow thickness, approximately 40 m, the grain sizes were small. Hence, the collective behavior of the landslide mass showed the characteristics of fluid flows and can be modeled accurately by the continuum model.

9.3.5 Summary

The rainfall brought by Morakot typhoon triggered the Hsiaolin landslide and devastated the township of Hsiaolin Village. The event was composed of two sub-events: the landslide and the dam breach. With the present hydrodynamic model, the landslide was accurately reconstructed. Both the empirical scaling laws of friction and rotary shearing tests of the rock properties indicated that the friction coefficient was about 0.2. This estimated friction coefficient value was confirmed by the numerical

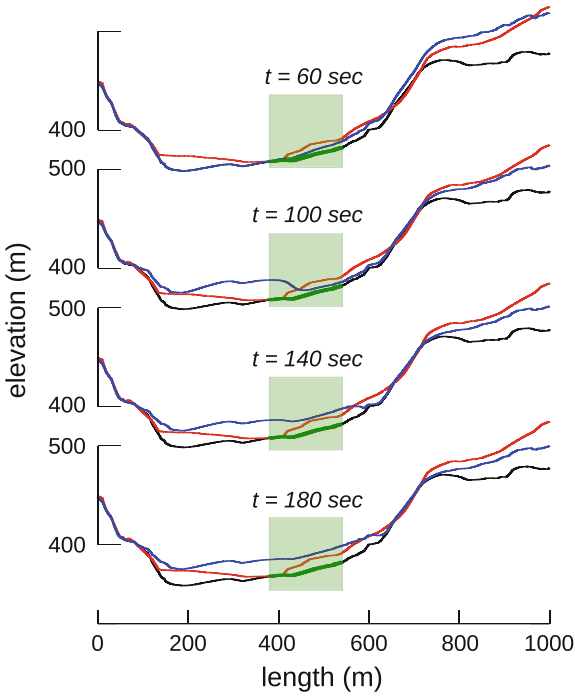

Fig. 9.23 Flow depth on profile $\overline{BB'}$. Point B is the origin of the x–axis. The *black line* is the original basal topography, the *red line* is the post-event topography, and the *blue line* is the simulated deposit. The *green shaded* regions indicate the location of the village. The figure shows that the thick deposit was formed by the debris surge being reflected by the slope on the opposite side of the Cishan River. The thickness over the village was about 17 m. The regress, or discrepancy between the simulation and the field survey, in the river channel was caused by the dam breach after the landslide (Reproduced from [57] with courtesy of AGU Pub)

calibration based on the minimization of the difference between the simulation and the measurements. The Voellmy friction law was also tested which yielded a virtually identical landslide flow. The volume dilation, assumed up to 20 %, also showed an insignificant effect on the rheological parameters.

The main deposit of the landslide was in the Anonymous Creek and on the Hsiaolin Slope. Its maximum speed reached about 50 m/s, and the overall landslide duration was about 110 s. The simulation also showed that there was one branch stream of the landslide debris created as the result of the landslide impact on the 590 Height, and it was this stream that overflowed the Hsiaolin Slope into the village. Even though it was only a minute portion of the landslide mass, this branch stream was the most devastating flow, sweeping over the northern part of the village at a speed of 40 m/s. Its destruction of the village was confirmed by corroboration of the near-surface magnetic measurements and the flow details of the simulation. This good corroboration is also the key validation of the landslide model for its applicability in landslide assessments. The simulation deposit in the river channel has been further integrated with hydrology calculations to resolve the second stage dam breach sub-event [77].

The Hsiaolin landslide was a large-scale geological failure, and the topography of the run-out path significantly influenced the flow direction. This large-scale geological failure has urged Taiwan government authorities to initiate detailed surveys to identify potential hazardous sites further beyond shallow slope failures. The surveys

included predictions of the landslide pathways and deposits with topographies properly taken into consideration. The present benchmark landslide demonstrated that the hydrodynamic model can be a valuable analytic tool for this purpose.

9.4 Rotary Shearing Test

A common intriguing phenomenon in avalanche landslides is the high mobility of the moving mass and it is associated to the low surface drag force. In the spirit of Coulomb friction law, the friction coefficient is low. According to the statistic empirical laws, Sect. 9.2.1, the apparent friction coefficient is in general inversely proportional to the volume of landslides. The volumetric dependency may arise from two major causes: the loading pressure and shear rate on the basal surface. With advances of laboratory measurement techniques, the friction weakening phenomena can be partially explained by experiments. One of the major techniques is the high-pressure high-speed rotary shearing test. In this section, the laboratory measurement technique and typical results are briefly presented. The physical understanding of the peculiar property, which may involve plasticity of pressure-dependent yield properties of soils and rocks, is currently undergoing and shall not be mentioned.

The high-pressure high-speed rotary-shearing speed tests originated from experimental studies on the frictional material behavior in faults during earthquake motions in the 1990s, e.g. [90–92]. Since then, researchers have been increasingly performing tests under an in-situ stress condition to measure the apparent friction coefficient for landslides [93, 94]. The experimental apparatus is shown in Fig. 9.24a. In the tests, the sample powders are sandwiched between a pair of solid-cylindrical rock specimens (Belfast dolerite, or recently Titanium alloy) as shown in Fig. 9.24b. The contact surfaces of the holding rock cylinders were deliberately roughened to ensure that the shearing deformation would take place within the sample, and a Teflon sleeve was mounted to hold the sample powder and its water content while shearing was applied. The sample diameter is 2.5 cm with a thickness about from 1 to 2 mm.

The in-situ pressure exerted on the slide surface is modeled by the normal stress, $\sigma = F/(\pi R^2)$, where R is the radius of the sample and F is the axial force. The normal pressure is adjustable between 0 and 10 MPa, which corresponds approximately to a landslide depth between 0 and 400 m, having assumed that the mass density is about 2.5 kg/m^3. After the normal stress is applied, a displacement-controlled rotary mechanism applies a constant rotational angular speed to the sample. The torque T and angular displacement are then recorded for calculation of the apparent friction coefficient of the sample and related physical quantities. During the tests, the sample is assumed at yield condition such that the shear stress, τ, is uniformly distributed on the yield surface. The torque is therefore $T = \frac{2}{3}\pi\tau R^3$. The apparent friction coefficient is calculated straightforwardly by $\mu = \tau/\sigma = 3T/(2RF)$.

Although rigorously speaking, the friction in the rotary tests was caused by the yielding within the sample material and the inferred friction coefficient represented the capability of providing the resisting force versus the normal pressure by the thin

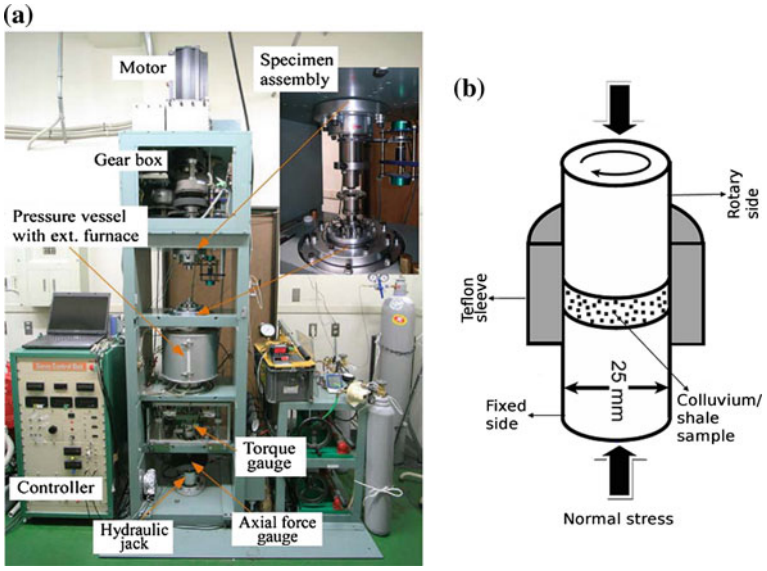

Fig. 9.24 **a** The high speed rotary shearing apparatus in National Central University, Taiwan, **b** the rotary shear cell. The samples were sandwiched between two dolerites as host rocks and tested under room temperature and humidity (Reproduced from [57] with courtesy of AGU Pub)

shearing layer between the moving part against the stationary part. On natural terrains, the shearing layers of landslides are formed adjacent to the basal surface with similar material composites to both sides of the test samples. It is, hence, conjectured that the surface friction force can be inferred by using the apparent friction coefficient measured in the experiments.

A slightly indirect physical quantity but often referred in the rotary test is called the shear speed v_{eq}, which is defined as the ratio between the total rate of shear work W done to the sample material and the shear force $\pi\tau R^2$, i.e. $v_{eq} = W/(\pi\tau R^2)$. The total rate of work applied to the sample is $W = \int_0^R dW = 2\pi \int_0^R \dot{\theta}\tau r^2\, dr$, where $\dot{\theta}$ is the angular velocity in radian. Because of technological limits, the present maximum achievable shear speed is about 1.3 m/s. Although this is still at orders of magnitude far below the maximum speed of avalanche flows, the measured friction coefficient is by-far the most direct evidence for the friction coefficient. Furthermore, a shear displacement, d_{eq}, is defined as the product of the shear speed and the elapsed time when the shearing is applied [90]. The experimental procedures can be found in [95–97]. Recently, it has become increasingly popular to summarize the result of the rotary shearing tests into a functional form of the apparent friction coefficient in terms of shear speed or displacement. The friction law is called the 'velocity-dependent friction law' in the related literature.

There are two additional minor concerns about the rotary shearing tests. The Teflon sleeve could not fully prevent water or heated steam escaping from the sample

compartment because of the shear-induced and thermal pressurization. Hence there existed pore-pressure effects during tests. However, these effects were implicitly lumped into the calculation of the friction coefficient because the total stress approach was applied. Because fluids probably could escape more easily from our small specimen assembly than in the natural landslide, the measured friction was probably an upper bound for friction that occurred in the real scenario. The other concern is that Teflon may be decomposed due to Teflon-rock friction. Fluorine from decomposed Teflon may enter into the gouge sample because fluorine-containing crystals were recognized occasionally near the Teflon contact. It is doubted however that Teflon pieces intrude deep into the gouge sample under pressure. Even if they did, the Teflon pieces did not affect the observed behavior because the tests with gouge containing Teflon pieces up to a few tens of percents (by weight) did not show significant changes in the frictional behavior, Sect. 4.4 in [97]).

In the following two subsections, the results for both landslides are briefly presented. A complete velocity-dependent friction law has only been completed recently for the Tsaoling landslide [36, 37], but is still ongoing research for the other landslide. Therefore, we present the test results in a reversed order to sketch the progression of the related experimental research.

9.4.1 Rotary Shearing Tests for Hsiaolin Landslide

The mass of the Hsiaolin landslide consisted mainly of Pliocene shale and colluvium [56]. Both types of materials were collected for the test. The thin, black colluvium, disturbed by the landslide just above the bed rocks, was sampled using a shovel near the source scar area (solid red circles in Fig. 9.14b. The shale, on the other hand, was prepared by crushing and grinding from 25 mm intact cores of the shale rock, sampled using a portable drilling machine on the slip surface (solid red squares in Fig. 9.14b). The initial particle size of both types of the samples was finer than 1 mm. It is speculated that these sample materials were similar to those on the basal surface.

The natural water contents of total 31 colluvium samples were distributed between 9 and 25 %, Fig. 9.25a. Accordingly, the following samples were selected in the test: one colluvium sample with a natural water content of 23 % by weight, one colluvium sample with 10 % (wt) added pure water, and one shale sample with 20 % (wt) added pure water. These samples were assumed to provide good coverage of the water content of the landslide material during the landslide. In the tests, the sample powders were sandwiched in the rotary shearing cell, Fig. 9.24b. The filling gap was 1 mm and the total sample weight in each test was about 1 gw. The samples were sustained under a normal stress 1.0 MPa during the tests to mimic a 40 m thick avalanche layer.

Figure 9.25b shows the experimental results of the high-speed frictional tests. The vertical axis is the friction coefficient, and the horizontal axis is the shear displacement. These samples had similar properties: The maximum friction coefficients occurred near the initial moment, and their values rapidly dropped to constants as the shearing progressed. The friction coefficients can be expressed as a function of

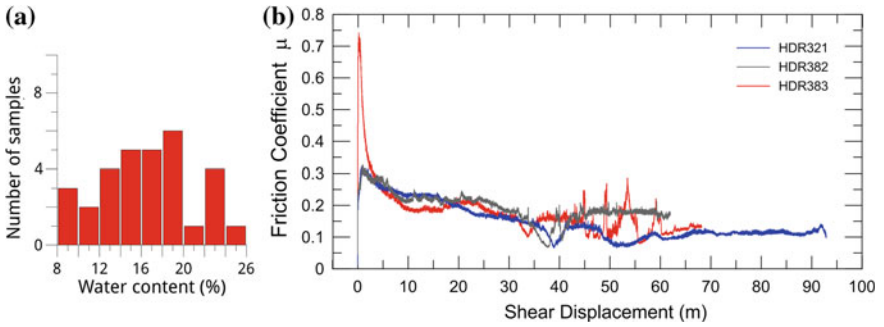

Fig. 9.25 Measurement of friction coefficients for the Hsiaolin landslide. **a** Water content distribution of the samples. **b** The friction coefficients versus the accumulative shearing displacement. The normal stress was 1.0 MPa and the shearing speed was 1.3 m/s. The shearing distance is defined as the product of the shearing speed and the elapsed time when the shearing is applied [90]. The colluvium and shale samples were collected from the landslide field. Sample HDR 382 (shale powders) was prepared with crushed, dried shale core with added pure water at 10 % by weight. Sample HDR 383 was colluvium with the water content at 10 % by weight. Sample HDR 321 was colluvium with (preserved) saturated natural water content (23 % wt) (Reproduced from [57] with courtesy of AGU Pub)

the shear displacement, the shear speed and the normal pressure, which is referred to as the velocity-dependent friction law in the literature [98].

For the present samples, the peak friction coefficients were about 0.3 except that of the sharp initial peak of the colluvium of 10 % water. The constant steady-state friction coefficients were between 0.1 and 0.2, which correspond to the angles of the basal friction 5.7° and 11.3°, and the colluvium samples had the lower values. The data indicated that the friction coefficient rapidly reduced to the steady-state values within a few meters of slip. These values agree excellently with that calibrated by the numerical simulation. It is then assumed that these constant terminal values of the friction coefficient remain for the rest of landslide motion. Further tests with a wider range of shear speeds reveal that the asymptotic behavior and the terminal value of the friction coefficient are dependent on the shear speed. In the literature, the terminal value is called steady-state friction coefficient. The extrapolation of using the constant value relies on the asymptotic behavior of the friction coefficient with respect to the shear speed and it is experimentally verified with the Tsaoling landslide case in the next section.

9.4.2 Rotary Shearing Tests for Tsaoling Landslide

Similar close correlation between the measured friction coefficient and the back-analysis simulation was also found by comparing the results from separated experimental and theoretical studies on the Tsaoling landslide. The landslide was triggered

by the Chi-Chi earthquake and had a sliding mass about five times of the Hsiaolin landslide. The initial scar depths was estimated between 120 and 200 m at an average depth about 140 m [6, 8]. The test samples prepared for the tests were mainly consisted of crushed shale and fault gouge. Shale is the weaker material in the alternated sandstone and shale beds in the landslide site. The materials were collected from the Cholan formation immediately below the sliding surface. The powdered gouge is thought to control the frictional sliding behavior rather than other stronger materials such as sandstones. The normal stress was set to 3.0 MPa, which corresponds to an overburden pressure of the landslide mass of about 140 m thickness (assumed density about 2,430 kg/m^3 [37]). Both wet (25 % wt) and dry conditions were tested.

The yield properties of the samples exhibit two types of characteristics: friction (slip) strengthening and weakening as the material is sheared. They are classified according to a critical shear speed v_{cr}. For the Tsaoling landslide, the critical shear speed is around 0.1 and 0.15 m/s, below which friction strengthening occurs. Because only fast avalanche landslides are presented, we do not pursue the friction strengthening regime further. When being sheared with high speeds, the apparent friction coefficient in general exhibits a typical behavior: it rapidly reaches a peak value; then decays exponentially and settles to a steady-state value. For the Tsaoling shale powder, Fig. 9.26a presents four sets of test results at three shear speeds. It can be seen that the steady-state values of the friction coefficient decreases as increasing of the shear speed. An idealized sketch of the apparent friction coefficient versus the shear displacement is shown in Fig. 9.26b. Parameters controlling the behavior are also defined therein. Note that our parameter symbols are slightly different from those defined in [37].

In the velocity-dependent friction law, the apparent angle of the basal friction was proposed to be a function of the shear velocity (displacement). We focus on the friction weakening regime of the friction law which can be fitted with the following expression

$$\mu(d_{eq}) = \mu_{ss} + (\mu_p - \mu_{ss}) \exp(\ln(0.05)\, d_{eq}/D_c), \tag{9.6}$$

where μ_{ss}, μ_p and D_c are the steady-state, peak friction coefficient and the shear displacement at 95 % reduction of the friction coefficient from the peak to steady-state value, as defined in Fig. 9.26b. For the friction weakening tests, including those presented in Fig. 9.26a, the best-fitted values for parameters in (9.6) are tabulated in Table 9.5.

Repeating the test procedure for various shear speeds, the steady-state friction coefficients are collected and, in the friction weakening regime, they can be fitted against the shear speed by

$$\mu_{ss} = \mu_{ss}^{\infty} + (\mu_p - \mu_{ss}^{\infty}) \exp(-v_{eq}/v_{cr}), \tag{9.7}$$

where μ_{ss}^{∞} is the steady-state friction coefficient at infinite shear speed and v_{cr} is a material-associated critical shear speed that distinguishes the friction strengthening and weakening regimes. Using the Tsaoling landslide materials, the data and fitted

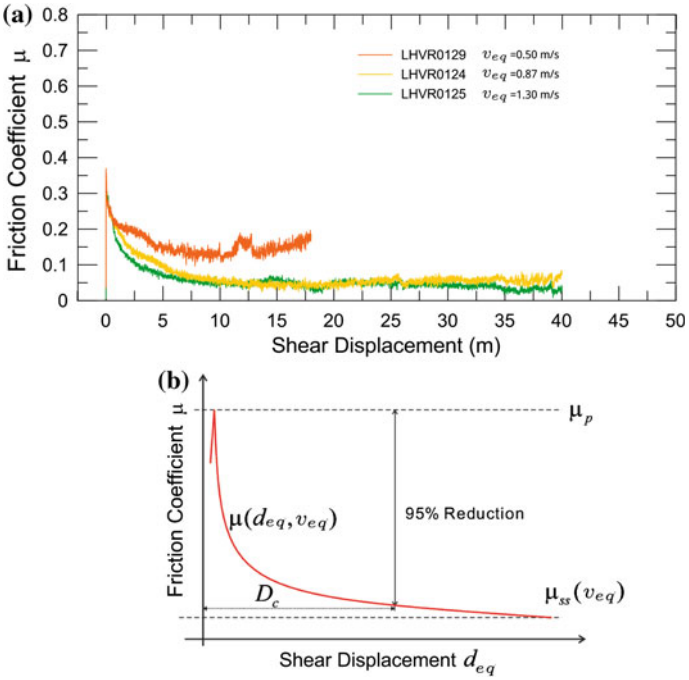

Fig. 9.26 Measurement of friction coefficients for the Tsaoling landslide. **a** Friction coefficients versus accumulative shearing displacement. The normal stress was 3.0 MPa. The shearing speed varies from 0.5 to 1.3 m/s, as indicated by the data legends. The samples were fault gouge collected from the landslide field. The water contents of the samples were all 25 % (wt). **b** A typical friction coefficient in the friction weakening regime, as a function versus the shear displacement, (9.6)

Table 9.5 Friction weakening parameters in (9.6)

Test number	v_{eq} (m/s)	μ_p	μ_{ss}	D_c (m)
LHVR0123	0.43	0.40	0.18	8.55
LHVR0258	0.43	0.36	0.13	8.55
LHVR0129	0.50	0.37	0.15	2.94
LHVR0124	0.87	0.36	0.05	5.60
LHVR0125	1.30	0.36	0.05	3.97
LHVR0291	1.30	0.40	0.08	3.42

The normal pressure for all tests is 3.0 MPa

values are shown in Fig. 9.27. For clarity, only the wet sample data points are plotted while both fitted expressions for both wet and dry samples are presented.

For the avalanche landslide, the apparent friction coefficient is expected to approach μ_{ss}^{∞} in virtue of the velocity-dependent friction law because of the rapid landslide motion. With the present available data [36, 37], μ_{ss}^{∞} is 0.162 (9.20°) for the dry samples and 0.076 (4.35°) for the wet samples. In the wet samples,

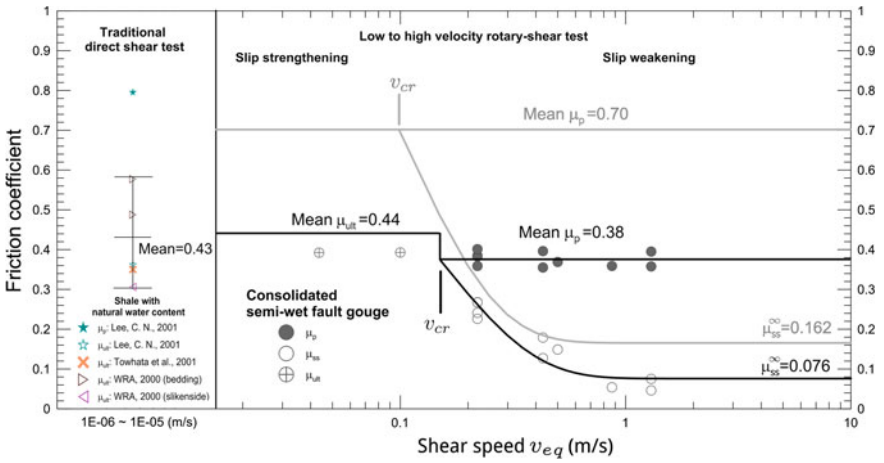

Fig. 9.27 Apparent friction coefficient as function of shear velocity. The measurement data are from the wet fault gouge samples taken from [37] and the normal pressure is 3.0 MPa. The *dark thick solid lines* are the fitted expressions for the wet samples: the constant ultimate friction coefficient (μ_{ult}) in the friction strengthening regime, the constant peak friction coefficient (μ_p) and the friction weakening curve (9.7). The friction strengthening and weakening regime are divided by the critical shear speed (v_{cr}), which is about 0.15 m/s. The fitted expressions, as *light grayed lines*, of the dry samples [36], are superimposed for comparison. The asymptotic friction coefficients, μ_{ss}^{∞}, of the dry and wet samples form a bound of the friction coefficient for the fast landslide motion. The direct shear tests, equivalent to low shear speed tests, are also plotted. The direct shear tests correspond to the friction strengthening regime and the friction coefficient is at the level of μ_{ult}

the pore pressure of the liquid reduces the effective stress, therefore, the material strength, and leads to a lower value of the friction coefficient than the dry samples. Finally, for the Tsaoling landslide, the samples were tested under 3.0 MPa normal stress to mimic the overburden pressure at 140 m deep. Under such confinement constraint, the bound of the steady-state friction coefficient based on the samples, $\mu_{ss}^{\infty} \in (0.076, 0.162)$, is found on the lower side compared to that measured for the Hsiaolin landslide. This bound also perfectly brackets the result of the numerical calibration ($\mu = \tan 7.813^{\circ} = 0.137$).

For the two landslides, the tests were performed under the normal stresses according to the overburden pressure the landslide mass exerted on the slip surfaces. The experimental results show that the Tsaoling landslide has a lower apparent friction coefficient than the Hsiaolin landslide. Because the overburden pressure scales proportionally to the landslide mass in usual situations, the experiments indicate that the well-known inverse proportionality of the apparent friction coefficient with respect to the landslide volume is likely to be associated with the dependence of the friction weakening phenomena on the confinement stresses. The physical mechanisms may involve the plasticity or microscopic fracturing of the landslide materials. Concentrating on the kinematics of landslide motion, we do not pursue the physical understandings of the friction weakening phenomena further and the interested readers are referred to the work of credited research groups.

References

1. K.E. Ching, M.L. Hsieh, K.M. Johnson, K.H. Chen, R.J. Rau, M. Yang, Modern vertical deformation rates and mountain building in Taiwan from precise leveling and continuous GPS observations, 2000–2008. J. Geophys. Res. **116**, B08406 (2011)
2. J. Angelier, J.C. Lee, H.T. Chu, J.C. Hu, C.Y. Lu, Y.C. Chan, T.J. Lin, Y. Font, B. Deffontaines, Y.B. Tsai, The Chichi earthquake, 1999, and its role in the Taiwan orogen. C.R. Acad. Sci. Paris Ser. IIa Earth Planet. Sci. **333**, 5–21 (2001)
3. C.Y. Kuo, Y.C. Tai, F. Bouchut, A. Mangeney, M. Pelanti, R.F. Chen, K.J. Chang, Simulation of Tsaoling landslide, Taiwan, based on Saint Venant equations over general topography. Eng. Geo. **104**(3–4), 181–189 (2009)
4. A. Lin, T. Ouchi, A. Chen, T. Maruvama, Co-seismic displacements, folding and shortening structures along Chelungpu surface rupture zone occurred during the 1999 Chi-Chi (Taiwan) earthquake. Tectonophysics **330**, 225–244 (2001)
5. H.W. Liao, Landslides triggered by Chi-Chi earthquake. Master's thesis, National Central Univ. Chungli in Chines (2000)
6. J.J. Hung, Chi-Chi earthquake induced landslides in Taiwan. Earthq. Eng. Eng. Seismol. **2**, 25–33 (2000)
7. R.F. Chen, K.J. Chang, J. Angelier, Y.C. Chan, B. Deffontaines, C.T. Lee, M.L. Lin, Topographical changes revealed by high-resolution airborne LiDAR data:the 1999 Tsaoling landslide induced by the Chi-Chi earthquake. Eng. Geo. **88**, 160 (2006)
8. J.J. Hung, C.T. Lee, M.L. Lin, Tsao-Ling rockslides, Taiwan, in *Catastrophic landslides: effects*, occurrence, and mechanisms, vol. 15, ed. by S.G. Evans, J.V. DeGraff (Geo. Soc. Am. Rev. Eng. Geo, Boulder, Colorado, 2002), pp. 91–115
9. J.J. Hung, M.L. Lin, C.T. Lee, A stability analysis of the Tsaoling landslide area. Rock Engineering Symposium in Taiwan. Chung-Li, pp. 459–467 (1994)
10. C.S. Huang, H.C. Ho, H.C. Liu, The geology and landslide of Tsaoling area, Yun-Lin Taiwan. Bull. Central Geol. Surv. **2**, 95–112 (1983)
11. T.C. Chen, M.L. Lin, J.J. Hung, Pseudostaic analysis of Tsaoling rockslide caused by Chi-Chi earthquake. Eng. Geol. **71**, 31–47 (2003)
12. E.T. Brown (ed.), Rock Characterization, Testing and Monitoring: International Society of Rock Mechanics Suggested Method (Pergamon Pressm, Oxford, 1981)
13. M. Chigira, W.N. Wang, T. Furuya, T. Kamai, Geological causes and geomorphological precursors of the Tsaoling landslide triggered by the 1999 Chi-Chi earthquake, Taiwan. Eng. Geol. **68**, 259–273 (2003)
14. A. Lin, A. Chen, C.F. Liau, C.T. Lee, C.C. Lin, P.S. Lin, S.C. Wen, T. Ouchi, Frictional fusion due to coseismic landsliding during the 1999 Chi-Chi (Taiwan) 7.3 earthquake. Geo. Res. Lett. **28**, 4011–4014 (2001)
15. R.F. Chen, Y.C. Chan, J. Angelier, Y.C. Chan, B. Deffontaines, C.T. Lee, M.L. Lin, Large earthquake-triggered landslides and mountain belt erosion: the Tsaoling case Taiwan. C.R. Geosci. **337**, 1164–1172 (2005)
16. C.L. Tang, J.C. Hu, 3-D numerical investigation of the Tsaoling landslide induced by Chi-Chi earthquake, Taiwan. Eos Trans. AGU Fall Meet. Suppl. **85**, 11A–1008 (2004)
17. C.L. Tang, J.C. Hu, M.L. Lin, J. Angelier, C.Y. Lu, Y.C. Chan, H.T. Chu, The Tsaoling landslide triggered by the Chi-Chi earthquake, Taiwan: insights from a discrete element simulation. Eng. Geo. **106**(1), 1–19 (2009)
18. S.B. Savage, K. Hutter, The motion of a finite mass of granular material down a rough incline. J. Fluid. Mech. **199**, 177–215 (1989)
19. S.B. Savage, K. Hutter, The dynamics of avalanches of granular materials from initiation to runout. Part I: Analysis. Acta Mech. **86**, 201–223 (1991)
20. J.M.N.T. Gray, M. Wieland, K. Hutter, Gravity-driven free surface flow of granular avalanches over complex basal topography. Proc. R. Soc. A **455**, 1841–1874 (1999)
21. S.P. Pudasaini, K. Hutter, Rapid shear flows of dry granular masses down curved and twisted channels. J. Fluid Mech. **495**, 193–208 (2003)

22. S.P. Pudasaini, K. Hutter, Avalanche dynamics: dynamics of rapid flows of dense granular avalanches (Springer, 2007)
23. R.M. Iverson, R.P. Denlinger, Flow of variably fluidised granular masses across three-dimensional terrain. I: Coulomb mixture theory. J. Geophys. Res. **106**, 537–552 (2001)
24. R.P. Denlinger, R.M. Iverson, Flow of variably fluidised granular masses across three-dimensional terrain. II: numerical predictions and experimental tests. J. Geophys. Res. **106**, 552–566 (2001)
25. S. McDougall, O. Hungr, A model for the analysis of the rapid landslide motion across three dimensional terrain. Canad. Geotech. J. **41**(6), 1084–1097 (2004)
26. K. Kelfoun, T.H. Druitt. Numerical modeling of the emplacement of Socompa rock avalanche. J. Geophys. Res. **110**, B12, 202 (2005)
27. W.C. Chen, C.Y. Kuo, K.M. Shyue, Y.C. Tai, Gas kinetic scheme for anisotropic Savage-Hutter model. Comm. Comp. Phys. **13**, 1432–1454 (2013)
28. J.M.N.T. Gray, Y.C. Tai, S. Noelle, Shock waves, dead-zones and particle-free regions in rapid granular free surface flows. J. Fluid Mech. **491**, 161–181 (2003)
29. A. Voellmy, über die Zerstörungskraft von Lawinen. Schweiz. Bauzeitung, Jahrg. 73, s. 159–165, 212–217, 246–249, 280–285. English as: On the destructive force of avalanches. 63p. Alta Avalanche Study Center, Transl, 2:1964 (1955)
30. G.S. Jiang, E. Tadmor, Nonoscillatory central schemes for multidimensional hyperbolic conservation laws. SIAM J. Sci. Comput. **19**(6), 1892–1917 (1998)
31. A. Heim, Bergsturz und menchenleben. Zurich Vierteljahrsschrift **77**, 218 (1932)
32. L. Staron, E. Lajeunesse. Understanding how volume affects the mobility of dry debris flows. Geophys. Res. Lett. **36**, L12, 402 (2009)
33. A.E. Scheidegger, On the prediction of the reach and velocity of catastrophic landslides. Rock Mech. **5**, 231–236 (1973)
34. F. Legros, The mobility of long-runout landslides. Eng. Geo. **63**, 301–331 (2002)
35. K.J. Chang, S.K. Wei, R.F. Chen, Y.C. Chan, P.W. Tsai, C.Y. Kuo, Empirical modal decomposition of near field seismic signals of Tsaoling landslide, in *Earthquake-Induced Landslides*, ed. by K. Ugai, H. Yagi, A. Wakai (Springer, Kiryu, 2012), pp. 421–430
36. T. Togo, T. Shimamoto, J.J. Dong, C.T. Lee, C.M. Yang, Triggering and runaway processes of catastrophic Tsaoling landslide induced by the 1999 Taiwan Chi-Chi earthquake, as revealed by high-velocity friction experiments. Geophys. Res. Lett. **41**, 1907–1915 (2014)
37. C.M. Yang, W.L. Yu, J.J. Dong, C.Y. Kuo, T. Shimamoto, C.T. Lee, T. Togo, Y. Miyamoto, Initiation, movement, and run-out of the giant Tsaoling landslide what can we learn from a simple rigid block model and a velocity displacement dependent friction law? Eng. Geo. **182**, Part B, 158–181 (2014) Special Issue on the Long-Term Geologic Hazards in Areas Struck by Large-Magnitude Earthquakes
38. T.R.H. Davies, Spreading of rack avalanche debris by mechanical fluidization. Rock Mech. **15**, 9–24 (1982)
39. J.A. Nelder, R. Mead, A simplex method for function minimization. Comp. J. **7**, 308–315 (1965)
40. O. Hungr, S. McDougall, Two numerical models for landslide dynamic analysis. Comp. Geosci. **35**, 978–992 (2009)
41. D. Schneider, P. Bartelt, J. Caplan-Auerbach, M. Christen, C. Huggel, B.W. McArdell, Insights into rock-ice avalanche dynamics by combined analysis of seismic recordings and a numerical avalanche model. J. Geophys. Res. **115**, F04, 026 (2010)
42. R.Y. Wu, R.F. Chen, C.Y. Kuo, K.J. Chang, Application of 1979–2009 digital orthophotos and digital terrain models to investigate surface changes in Tsaoling landslide area. J. Geograph. Sci. (in Chinese) **75**, 1–27 (2014). in Chinese
43. C.Y. Kuo, R.F. Chen, R.Y. Wu, K.J. Chang, Use of multiple digital terrain models and aerial orthphotos for landscape evolution in Tsaoling landslide area, in Engineering Geology for Society and Territory, vol. 2, pp. 455–460, Torino, Italy (2014). IAEG XII Congress, Springer
44. Y.C. Tai, Y.C. Lin, A focused view of the behavior of granular flows down a confined inclined chute into horizontal run-out zone. Phys. Fluids **20**, 123302 (2008)

45. C.S. Campbell, P.W. Cleary, M. Hopkins, Large-scale landslide simulations: global deformation, velocities and basal friction. J. Geo. Res. **100**, 8267–8273 (1995)
46. J. Goguel, Scale-dependent rockslide mechanisms, with emphasis on the role of pore fluid vaporization, in *Rockslides and Avalanchs, 1. Natural Phenomena*, ed. by B. Voight (Elsevier, Amsterdam, 1978), pp. 693–705
47. J.H. Wu, C.H. Chen, Application of DDA to simulate characteristics of Tsaolin landslide. Comp. Geotech. **38**, 741–750 (2011)
48. D.M. Cruden, D.J. Varnes, Landslide type and processes, in *Landslide Investigetion and Mitigation*, ed. by A.K. Turner, R.L. Schuster. Transp. Res. Board, vol. spacial Rep. 247 (US National Res. Council, Washington, DC, 1996), pp. 36–75
49. O. Hungr, S.G. Evans, M. Bovis, J.N. Hutchinson, Review of the classification of landslide of the flow type. Environ. Eng. Geosci. **7**, 221–238 (2001)
50. Y.B. Tsai, C.P. Lee, Strong motion instrumentation programs in Taiwan. Volume 58 of NATO Science Series (Springer, Netherlands, 2005), pp. 255–278
51. W.H.K. Lee, T.C. Shin, K.W. Kuo, K.C. Chen, C.F. Wu, Data files from CWB free-field strong-motion data from the 921 Chi-Chi (Taiwan) earthquake. Bull. Seismol. Soc. Am. **91**, 1370–1376 (2001)
52. C.Y. Kuo, S.K. Wei, P.W. Tsai, Ensemble empirical mode decomposition with supervised cluster analysis. Adv. Adap. Data Anal. **5**, 1350005 (2013)
53. C.Y. Kuo, K.J. Chang, P.W. Tsai, S.K. Wei, R.F. Chen, J.J. Dong, C.M. Yang, Y.C. Chan, Y.C. Tai, Identification of co-seismic ground motion due to fracturing and impact of the Tsaoling landslide, Taiwan. Eng. Geo. **196**, 268–279 (2015)
54. J.J. Dong, C.M. Yang, W.L. Yu, C.T. Lee, Y. Miyamoto, T. Shimamoto, Velocity-displacement dependent friction coefficient and the kinematics of giant landslide, in *Earthquake-induced landslides*, ed. by K. Ugai, H. Yagi, A. Wakai, pp. 397–403, Kiryu (2012). International Symposium on Earthquake-induced Landslides. Springer
55. T.C. Chen, M.L. Lin, K.L. Wang, Landslide seismic signal recognition and mobility for an earthquake-induced rockslide in Tsaoling, Taiwan. Eng. Geo. **171**, 31–44 (2014)
56. J.J. Dong, Y.S. Li, C.Y. Kuo, R.T. Sung, M.H. Li, C.T. Lee, C.C. Chen, W.R. Lee, The formation and breach of a short-lived landslide dam at Hsiaolin Village, Taiwan-part I: post-event reconstruction of dam geometry. Eng. Geo. (2011)
57. C.Y. Kuo, Y.C. Tai, C.C. Chen, K.J. Chang, A.Y. Siau, J.J. Dong, R.H. Han, T. Shimamoto, C.T. Lee, The landslide stage of the Hsiaolin catastrophe: simulation and validation. J. Geophys. Res. **116**, F04007 (2011)
58. C.C. Chen, J.J. Dong, C.Y. Kuo, R.D. Hwang, M.H. Li, C.T. Lee, Reconstruction of the kinematics of landslide and debris flow through numerical modeling supported by multidisciplinary data: the 2009 Siaolin, Taiwan landslide, in *Sediment Transport- Flow and Morphological Processes, chapter 12*, ed. by F. Bhuiyan, pp. 249–260 (2011) (InTech.)
59. C.Y. Tsou, Z.Y. Feng, M. Chigira, Catastrophic landslide induced by Typhoon Morakot, Shiaolin, Taiwan. Geomorphology **127**, 166–178 (2011)
60. R. Greve, K. Hutter, Motion of a granular avalanche in a convex and concave curved chute: experiments and theoretical predictions. Phil. Trans. R. Soc. A **342**, 573–600 (1993)
61. M. Wieland, J.M.N.T. Gray, K. Hutter, Channelized free surface flow of cohessionless granular avalanches in a chute with shallow lateral curvature. J. Fluid Mech. **392**, 73–100 (1999)
62. R. Greve, T. Koch, K. Hutter, Unconfined flow of granular avalanches along a partly curved surface. I: theory. Proc. R. Soc. A **445**, 399–413 (1994)
63. H. Chen, C.F. Lee, Numerical simulation of debris flows. Can. Geotech. J. **37**, 146–160 (2000)
64. Y.C. Tai, C.Y. Kuo, A new model of granular flows over general topography with erosion and deposition. Acta Mech. **199**, 71–96 (2008)
65. I. Luca, Y.C. Tai, C.Y. Kuo, Non-Cartesian topography-based avalanche equations and approximations of gravity driven flows of ideal and viscous fluids. Math. Mod. Meth. Appl. Sci. **19**, 127–171 (2009)
66. R.P. Denlinger, R.M. Iverson, Granular avalanches across irregular three-dimensional terrain. I: theory and computation. J. Geophys. Res. **109**(F1) (2004)

67. R.M. Iverson, M. Logan, R.P. Denlinger, Granular avalanches across irregular three-dimensional terrain. II: Experimental tests. J. Geophys. Res. **109**(No. F1), F01015 (2004). doi:10.1029/2003JF000084
68. S. De Toni, P. Scotton, Two-dimensional mathematical and numerical model for the dynamics of granular avalanches. Cold Regions Sci. Technol. **43**, 36–48 (2005)
69. I. Luca, K. Hutter, Y.C. Tai, C.Y. Kuo, A hierarchy of avalanche models on arbitrary topography. Acta Mech. **205**, 121–149 (2009)
70. Y.S. Kuo, Y.J. Tsai, Y.S. Chen, C.L. Shieh, K. Miyamoto, T. Ito, Movement of deep-seated rainfall-induced landslide at Hsiaolin Village during Typhoon Morakot. Landslides **10**, 191–202 (2013)
71. G.B. Crosta, S. Imposimato, D. Roddeman, Numerical modeling of 2-d granular step collapse on erodible and nonerodible surface. J. Geophys. Res. **114**, F03, 020 (2009)
72. R.M. Iverson, Regulation of landslide motion by dilatancy and pore pressure feedback. J. Geophys. Res. **110**, F02015 (2005)
73. I. Vardoulakis, Dynamic thermo-poro-mechanical analysis of catastrophic landslides. Géotech. **52**, 157–171 (2002)
74. I. Vardoulaski, Steady shear and thermal run-away in clayey gouges. Int. J. Solids Struct. **39**, 3831–3844 (2002)
75. K.J. Chang, A. Taboada, M.L. Lin, R.F. Chen, Analysis of landslide by earthquake shaking using a block-on-slope thermo-mechanical model: example of Jiufengershan landslide, central Taiwan. Eng. Geo. **80**, 151–163 (2005)
76. E.B. Pitman, L. Le, A two-fluid model for avalanche and debris flows. Phil. Trans. R. Soc. Lond. A **363**, 1573–1601 (2005)
77. M.H. Li, R.T. Sung, J.J. Dong, C.T. Lee, C.C. Chen, The formation and breaching of a short-lived landslide dam at Hsiaolin Village, Taiwan–part II: simulation of debris flow with landslide dam breach. Eng. Geo. **123**(1), 60–71 (2011)
78. Y.C. Tai, C.Y. Kuo, W.H. Hui, An alternative depth-integrated formulation for granular avalanches over temporally varying topography with small curvature. Geophys. Astrophys. Fluid Dyn. **106**(6), 596–629 (2012)
79. C.C. Chen, Tragic moment of Shiaolin debris avalanche, Taiwan, reconstructed by near surface geophysical/geological and simulation evidence, in *Proceedings from the 2010 AGU Western Pacific Geophysics Meeting*. American Geophysical Union, 2000 Florida Ave., N. W. Washington DC 20009 USA (2010)
80. C.H. Lin, H. Kumagai, M. Ando, T.C. Shin, Detection of landslides and submarine slumps using broadband seismic networks. Geophys. Res. Lett. **37**, L22, 309 (2010)
81. C.P. Stark, G. Ekstrom, C. Lin, R. Rau, W.L.R. Chen, Triggering and frictional sliding of large landslides during typhoon Morakot constrained by seismic wave inversion and modeling. Eos Trans. AGU, vol. 91 (2010)
82. S. Stein, M. Wysession, *An Introduction to Seismology, Earthquake, and Earth Structure* (Blackwell Publishing, UK, 2003)
83. F.A. Dahlen, Single-force representation of shallow landslide sources. Bull. Seism. Soc. Am. **83**, 130–143 (1993)
84. C.Y. Wang, Wave theory for seismogram synthesis. PhD thesis, Saint Louis University, USA (1981)
85. G. Ekström, M. Nettles, G.A. Abers, Glacial earthquakes. Science **302**, (2003)
86. W.B. Doo, S.K. Hsu, C.C. Chen, H.H. Hsieh, H.Y. Yen, Y.G. Chen, W.Y. Chang, Magnetic signature of Siaolin village, southern Taiwan, after burial by a catastrophic landslide due to Typhoon Morakot. Nat. Hazards Earth Syst. Sci. **11**, 759–764 (2011)
87. S.K. Hsu, D. Coppens, C.T. Shyu, Depth to magnetic source using the generalized analytic signal technique. Geophys. **63**, 1947–1957 (1998)
88. S.K. Hsu, Imaging magnetic sources using Euler's equation. Geophys. Prospect. **50**, 15–25 (2002)
89. W.B. Doo, S.K. Hsu, C.H. Tsai, Y.S. Huang, Using analytic signal to determine magnetization/density ratios of geological structures. Geophys. J. Int. **179**, 112–124 (2009)

90. T. Hirose, T. Shimamoto, Growth of molten zone as a mechanism of slip weakening of simulated faults in gabbro during frictional melting. J. Geo. Res. **110**, B05, 202 (2005)
91. G.T. Hirose, S. Nielsen, G. Pennacchioni, T. Shimamoto, Natural and experimental evidence of melt lubrication of faults during earthquakes. Science **311**, 647–649 (2006)
92. R. Han, T. Shimamoto, T. Hirose, J.H. Ree, J. Ando, Ultra-low friction of carbonate faults caused by thermal decomposition. Science **316**, 878–881 (2007)
93. Y. Miyamoto, T. Shimamoto, T. Togo, J.J. Dong, C.T. Lee, Dynamic weakening of shale and bedding-parallel fault gouge as a possible mechanism for Tsaoling landslide induced by 1999 Chi-Chi earthquake, in *Proceedings of the Next Generation of Research on Earthquake-induced Landslides: An International Conference in Commemoration of 10th Anniversary of the Chi-Chi Earthquake*, p. 398 (2009)
94. K. Yano, T. Shimamoto, K. Oohashi, J.J. Dong, C.T. Lee, Ultra-low friction of shale and clayey fault gouge at high velocities: implication for Jiufengershan landslide induced by 1999 Chi-Chi earthquake, in *Proceedings of the Next Generation of Research on Earthquake-induced Landslides: An International Conference in Commemoration of 10th Anniversary of the Chi-Chi Earthquake*, p. 401 (2009)
95. T. Togo, T. Shimamoto, S. Ma, T. Hirose, High-velocity friction experiments on the Longmenshan fault gouge towards the understanding of dynamic rupture propagation of the 2008 Wenchuan earthquake, in *Proceedings of the Next Generation of Research on Earthquake-induced Landslides: An International Conference in Commemoration of 10th Anniversary of the Chi-Chi Earthquake*, p. 401 (2009)
96. K. Mizoguchi, T. Hirose, T. Shimamoto, E. Fukuyama, Reconstruction of seismic faulting by high-velocity friction experiments: An example of the 1995 Kobe earthquake. Geophys. Res. Lett. **34**, L01, 308 (2007)
97. H. Kitajima, J.S. Chester, F.M. Chester, T. Shimamoto, High-speed friction of disaggregated ultracataclasite in rotary shear: characterization of frictional heating, mechanical behavior, and microstructure evolution. J. Geophys. Res. **115**, B08, 408 (2010)
98. R. Han, T. Hirose, T. Shimamoto, Strong velocity weakening and powder lubrication of simulated carbonate faults at seismic slip rates. J. Geophys. Res. **115**, B03, 412 (2010)

Appendix A
Some Proofs

A.1 Proof of the Asymptotic Expansions (4.86)

Here we prove approximations (4.86) by using the thin-layer assumptions $\zeta = O(\epsilon)$, $\mathbf{v} = O(1)$, $\mathcal{U} = O(\epsilon)$ and (4.84). The functions on the left-hand sides in (4.86), except $\Gamma(\mathbf{v})$, are expanded up to terms of order $O(\epsilon^{1+\gamma})$.

- Relation (4.86a) was already deduced in (4.73).
- Estimations (4.86b), (4.86c) are direct consequences of (4.86a) and $\mathbf{v} = O(1)$.
- For (4.86d) we use (2.88) as follows:

$$\begin{aligned}\mathbf{M} &\equiv (\mathbf{I} - \zeta\widetilde{\mathbf{W}})^{-1}\,\mathbf{M}_0\,(\mathbf{I} - \zeta\widetilde{\mathbf{W}})^{-T}\\ &= (\mathbf{I} + \zeta\widetilde{\mathbf{W}} + O(\epsilon^2))\,\mathbf{M}_0\,(\mathbf{I} + \zeta\widetilde{\mathbf{W}} + O(\epsilon^2))^T = \mathbf{M}_0 + O(\epsilon).\end{aligned}$$

  Then, assumptions $p = O(\epsilon)$, $\mathbf{P} = O(\epsilon)$ and $J = J_0 + O(\epsilon)$ immediately yield (4.86d).
- In order to deduce (4.86e) we use definition (4.32) of $\mathbf{\Gamma}(-p\,\mathbf{M}, \mathbf{0})$, assumption $p = O(\epsilon)$, definition $2\Omega \equiv \operatorname{tr}\widetilde{\mathbf{W}}$ of the mean curvature Ω, and approximations

$$J = J_0 + O(\epsilon), \quad \mathbf{B} \equiv \mathbf{F}(\mathbf{I} - \zeta\widetilde{\mathbf{W}}) = \mathbf{F} + O(\epsilon), \quad \mathbf{M} = \mathbf{M}_0 + O(\epsilon).$$

- With $\mathbf{B} = \mathbf{F} + O(\epsilon)$ and $\mathbf{P} = O(\epsilon)$, the term $\Gamma(\mathbf{P})$ defined in (4.35) and arising in expression (4.33) of $\mathbf{\Gamma}(\mathbf{P}, \mathbf{p})$ is estimated as

$$\Gamma(\mathbf{P}) \equiv -\mathbf{B}^T\mathbf{F}^{-T}\widetilde{\mathbf{H}}\cdot\mathbf{P} = -\widetilde{\mathbf{H}}\cdot\mathbf{P} + O(\epsilon^2) = O(\epsilon).$$

  Then, $J = J_0 + O(\epsilon)$ and $\mathbf{p} = O(\epsilon^{\gamma})$ turn $J\mathbf{\Gamma}(\mathbf{P}, \mathbf{p})$ into (4.86f).
- Now, inserting $\mathbf{B} = \mathbf{F}(\mathbf{I} - \zeta\mathbf{W})$ into expression $(4.35)_2$ of $\Gamma(\mathbf{v})$ we obtain

I. Luca et al., *Shallow Geophysical Mass Flows down Arbitrary Topography*,
Advances in Geophysical and Environmental Mechanics and Mathematics,
DOI 10.1007/978-3-319-02627-5

$$\begin{aligned}\Gamma(\mathbf{v}) &\equiv -\mathbf{B}^T\mathbf{F}^{-T}\widetilde{\mathbf{H}}\cdot(\mathbf{v}\otimes\mathbf{v}) = -(\mathbf{I}-\zeta\widetilde{\mathbf{W}})^T\widetilde{\mathbf{H}}\cdot(\mathbf{v}\otimes\mathbf{v})\\ &= -\widetilde{\mathbf{H}}\cdot(\mathbf{v}\otimes\mathbf{v}) + \zeta\widetilde{\mathbf{W}}^T\widetilde{\mathbf{H}}\cdot(\mathbf{v}\otimes\mathbf{v}) = -\widetilde{\mathbf{H}}\cdot(\mathbf{v}\otimes\mathbf{v}) + O(\epsilon),\end{aligned}$$

which shows (4.86g).

- Combining the above exact expression of $\Gamma(\mathbf{v})$ with approximation (4.86a) of J yields (4.86h).
- The equality asserted by (4.86i) follows from definition (4.34) of $\mathbf{\Gamma}(\mathbf{v}, \mathrm{v})$ by using estimations (4.86a) and (4.86h) of J and $J\Gamma(\mathbf{v})$, respectively, the remark that $\mathrm{v} = O(\epsilon)$ and the relations

$$\begin{aligned}\mathbf{B}^{-1} &= (\mathbf{I}-\zeta\widetilde{\mathbf{W}})^{-1}\mathbf{F}^{-1} = (\mathbf{I}+\zeta\widetilde{\mathbf{W}})\mathbf{F}^{-1} + O(\epsilon^2),\\ \mathbf{B}^{-1}\frac{\partial\mathbf{B}}{\partial\xi^\alpha} &= (\mathbf{I}+\zeta\widetilde{\mathbf{W}})\mathbf{F}^{-1}\frac{\partial}{\partial\xi^\alpha}(\mathbf{F}-\zeta\mathbf{F}\widetilde{\mathbf{W}}) + O(\epsilon^2)\\ &= \mathbf{F}^{-1}\frac{\partial\mathbf{F}}{\partial\xi^\alpha} + \zeta\underbrace{\left(\widetilde{\mathbf{W}}\mathbf{F}^{-1}\frac{\partial\mathbf{F}}{\partial\xi^\alpha} - \mathbf{F}^{-1}\frac{\partial\mathbf{F}\widetilde{\mathbf{W}}}{\partial\xi^\alpha}\right)}_{-\mathbf{F}^{-1}\frac{\partial}{\partial\xi^\alpha}(\mathbf{F}\widetilde{\mathbf{W}}\mathbf{F}^{-1})\,\mathbf{F}} + O(\epsilon^2).\end{aligned}$$

- Approximation of $J\mathbf{b}$ given in (4.86j) is obtained by straightforward calculations using the expansions of J and $\mathbf{B}^{-1}$, and expression $(4.36)_1$ of the gravity components $\mathbf{b}$.
- The non-dimensional components of the surface velocity $\boldsymbol{u}_{\mathcal{S}}$ and mesh velocity $\boldsymbol{w}$ are formally the same as those from (2.69) and (2.110), respectively. Therefore, with $\mathcal{U} = O(\epsilon)$ we have

$$\mathbf{w} = \mathbf{u}_{\mathcal{S}} - \zeta(\mathbf{I}-\zeta\widetilde{\mathbf{W}})^{-1}\mathbf{M}_0\,\mathrm{Grad}\,\mathcal{U} = \mathbf{u}_{\mathcal{S}} + O(\epsilon^2) = \mathbf{F}^{-1}(\mathbf{v}_{\mathcal{S}} + \mathcal{U}\mathbf{s}) + O(\epsilon^2),$$

which, combined with (4.86a), immediately gives (4.86k).

- All we need to do to obtain (4.86l) is to take the dyadic product of $\mathbf{v} = O(1)$ with (4.86k).
- The last relation in (4.86) is deduced by noticing that

$$\mathrm{v}\frac{\partial\mathbf{w}}{\partial\zeta} = O(\epsilon^2),$$

$$\begin{aligned}J(\mathrm{Grad}\,\mathbf{w})\mathbf{v} &= J_0(1-2\Omega\zeta)\Big(\mathrm{Grad}\,(\mathbf{F}^{-1}\mathbf{v}_{\mathcal{S}} + \mathcal{U}\mathbf{F}^{-1}\mathbf{s})\Big)\mathbf{v} + O(\epsilon^2)\\ &= J_0(1-2\Omega\zeta)\Big(\mathrm{Grad}\,(\mathbf{F}^{-1}\mathbf{v}_{\mathcal{S}})\Big)\mathbf{v} + J_0\Big(\mathrm{Grad}\,(\mathcal{U}\mathbf{F}^{-1}\mathbf{s})\Big)\mathbf{v}\\ &\quad + O(\epsilon^2).\end{aligned}$$

With this the proof of (4.86) is complete.

A.2 Proof of the Thin-Layer Modelling Equations (4.92) and (4.93)

In this section we show that, under the asymptotic expansions (4.86) and the Boussinesq approximations (4.70), (4.72), the depth-integrated mass and tangential linear momentum balance equations (4.65), (4.66) take the forms (4.92) and (4.93). We start with the depth-integrated mass balance equations (4.65), which we rewrite here by numbering the terms which we next will refer to:

$$\underbrace{\frac{\partial}{\partial t}\int_0^h J\,d\zeta}_{①} + \underbrace{\mathrm{Div}\int_0^h J(\mathbf{v}-\mathbf{w})\,d\zeta}_{②} = -J_0\frac{\rho_b}{\rho_0}\mathcal{U}. \tag{A.1}$$

Using approximation (4.86a) of J, for the first underbraced term in the above Eq. (A.1) we obtain

$$① = \int_0^h J_0(1-2\Omega\zeta)\,\mathrm{d}\zeta + O(\epsilon^3) = J_0 h(1-\Omega h) + O(\epsilon^3).$$

For the second term we use (4.86b), (4.86k) and $(4.70)_1$ to get

$$\begin{aligned} ② &= \int_0^h J\mathbf{v}\,d\zeta - \int_0^h J\mathbf{w}\,d\zeta = \int_0^h J_0\Big\{\mathbf{v}-2\Omega(\zeta\mathbf{v})\Big\}\,\mathrm{d}\zeta \\ &\quad - \int_0^h J_0\Big\{\mathbf{u}_{\mathcal{S}} - 2\Omega\zeta\mathbf{F}^{-1}\mathbf{v}_{\mathcal{S}}\Big\} + O(\epsilon^3) \\ &= J_0 h\Big\{(1-m_1\Omega h)\,\overline{\mathbf{v}} - \mathbf{u}_{\mathcal{S}} + \Omega h\mathbf{F}^{-1}\mathbf{v}_{\mathcal{S}}\Big\} + O(\epsilon^{2+\gamma}). \end{aligned}$$

Insertion of ① and ② as derived above into (A.1) proves Eq. (4.92).

Now we examine the tangential linear momentum balance equations (4.65), for which most of the terms are identified by numbers as follows:

$$\begin{aligned} &\underbrace{\frac{\partial}{\partial t}\int_0^h J\,\mathbf{v}\,d\zeta}_{①} + \underbrace{\mathrm{Div}\int_0^h J\,\{\mathbf{v}\otimes(\mathbf{v}-\mathbf{w}) + p\mathbf{M}-\mathbf{P}\}\,d\zeta}_{②} \\ &\qquad + \underbrace{\int_0^h J\,\boldsymbol{\Gamma}(-p\,\mathbf{M},\mathbf{0})\,d\zeta}_{③} + \underbrace{\int_0^h J\,\boldsymbol{\Gamma}(\mathbf{P},\mathbf{p})\,d\zeta}_{④} \end{aligned} \tag{A.2}$$

$$= -J_0 \left\{ \frac{\rho_b}{\rho_0} \mathcal{U}\, \mathbf{v} + \mathbf{p} \right\}_{\zeta=0} + \underbrace{\int_0^h J\, \mathbf{b}\, d\zeta}_{⑤} + \underbrace{\int_0^h J\, \mathbf{\Gamma}(\mathbf{v}, \mathrm{v})\, d\zeta}_{⑥}$$
$$\underbrace{- \int_0^h J \left\{ (\mathrm{Grad}\, \mathbf{w})\mathbf{v} + \mathrm{v} \frac{\partial \mathbf{w}}{\partial \zeta} \right\} d\zeta}_{⑦}.$$

By computations as above, for the underbraced terms in (A.2) we obtain

$$\begin{aligned}
① &= J_0 h (1 - m_1 \Omega h)\, \overline{\mathbf{v}} + O(\epsilon^{2+\gamma}),\\
② &= J_0 h \Big[(m_2 - m_3 \Omega h)\, \overline{\mathbf{v}} \otimes \overline{\mathbf{v}} + \overline{p}\, \mathbf{M}_0 - \overline{\mathbf{P}} - \overline{\mathbf{v}} \otimes \mathbf{u}_{\mathcal{S}} + m_1 \Omega h\, \overline{\mathbf{v}} \otimes \mathbf{F}^{-1} \mathbf{v}_{\mathcal{S}} \Big]\\
&\quad + O(\epsilon^{2+\gamma}),\\
③ &= J_0 h\, \overline{p} \left[\mathbf{F}^{-1} \frac{\partial \mathbf{F}}{\partial \xi^\alpha} \mathbf{M}_0 \mathbf{e}_\alpha + 2\Omega \mathbf{F}^{-1} \mathbf{s} \right] + O(\epsilon^{2+\gamma}),\\
④ &= -J_0 h \left[\mathbf{F}^{-1} \frac{\partial \mathbf{F}}{\partial \xi^\alpha} \overline{\mathbf{P}}\, \mathbf{e}_\alpha - 2 \widetilde{\mathbf{W}} \overline{\mathbf{p}} + (\widetilde{\mathbf{H}} \cdot \overline{\mathbf{P}}) \mathbf{F}^{-1} \mathbf{s} \right] + O(\epsilon^{2+\gamma}),\\
⑤ &= -J_0 h c \Big[(1 - \Omega h)\, \mathbf{F}^{-1} \mathbf{s} + \tfrac{1}{2} h\, \widetilde{\mathbf{W}} \mathbf{F}^{-1} \mathbf{s} \Big] + O(\epsilon^3),\\
⑥ &= -J_0 h (m_2 - m_3 \Omega h) \mathbf{F}^{-1} \frac{\partial \mathbf{F}}{\partial \xi^\alpha} (\overline{\mathbf{v}} \otimes \overline{\mathbf{v}}) \mathbf{e}_\alpha\\
&\quad + \tfrac{1}{2} J_0 m_3 h^2 \mathbf{F}^{-1} \frac{\partial}{\partial \xi^\alpha} (\mathbf{F} \widetilde{\mathbf{W}} \mathbf{F}^{-1}) \mathbf{F} (\overline{\mathbf{v}} \otimes \overline{\mathbf{v}}) \mathbf{e}_\alpha\\
&\quad + 2 J_0 h \left[\left(1 - \frac{\rho_b}{\rho_0} \right) \mathcal{U} + \tfrac{1}{2} \beta h \right] \widetilde{\mathbf{W}} \overline{\mathbf{v}}\\
&\quad - J_0 h \Big[a (m_2 - m_3 \Omega h) - \tfrac{1}{2} m_3 \tilde{a} h \Big] \mathbf{F}^{-1} \mathbf{s} - \tfrac{1}{2} J_0 m_3 a h^2 \widetilde{\mathbf{W}} \mathbf{F}^{-1} \mathbf{s} + O(\epsilon^{2+\gamma}),\\
⑦ &= J_0 h \left[\mathrm{Grad}\, \mathbf{u}_{\mathcal{S}} - m_1 \Omega h\, \mathrm{Grad}\, (\mathbf{F}^{-1} \mathbf{v}_{\mathcal{S}}) \right] \overline{\mathbf{v}} + O(\epsilon^2),
\end{aligned}$$

where

$$\tilde{a} \equiv \widetilde{\mathbf{W}}^T \widetilde{\mathbf{H}} \cdot (\overline{\mathbf{v}} \otimes \overline{\mathbf{v}}) = \widetilde{\mathbf{H}}\, \overline{\mathbf{v}} \cdot \widetilde{\mathbf{W}}\, \overline{\mathbf{v}}.$$

Inserting the preceding expressions of the terms ①–⑦ into (A.2) and making use of formula (4.91) for the mean pressure, we find

$$
\begin{aligned}
&\frac{\partial}{\partial t}\Big\{J_0h(1-m_1\Omega h)\,\overline{\mathbf{v}}\Big\}\\
&\qquad+\mathrm{Div}\Big\{J_0h\Big[(m_2-m_3\Omega h)\,\overline{\mathbf{v}}\otimes\overline{\mathbf{v}}+\overline{p}\,\mathbf{M}_0-\overline{\mathbf{P}}-\overline{\mathbf{v}}\otimes\mathbf{u}_{\mathcal{S}}\\
&\qquad\qquad+m_1\Omega h\,\overline{\mathbf{v}}\otimes\mathbf{F}^{-1}\mathbf{v}_{\mathcal{S}}\Big]\Big\}\\
&=-J_0\left\{\frac{\rho_b}{\rho_0}\,\mathcal{U}\,\mathbf{v}+\mathbf{p}\right\}_{\zeta=0}-2J_0h\,\widetilde{\mathbf{W}}\left[\overline{\mathbf{p}}-\left(1-\frac{\rho_b}{\rho_0}\right)\mathcal{U}\,\overline{\mathbf{v}}-\tfrac{1}{2}\beta h\overline{\mathbf{v}}\right]\\
&\qquad-J_0h\mathbf{F}^{-1}\frac{\partial\mathbf{F}}{\partial\xi^\alpha}\left[\overline{p}\,\mathbf{M}_0-\overline{\mathbf{P}}+(m_2-m_3\Omega h)\,\overline{\mathbf{v}}\otimes\overline{\mathbf{v}}\right]\mathbf{e}_\alpha\\
&\qquad-J_0h\left[\left(c+am_2-\tfrac{1}{2}m_3\tilde{a}h-\widetilde{\mathbf{H}}\cdot\overline{\mathbf{P}}\right)\mathbf{I}+\overline{p}\,\widetilde{\mathbf{W}}\right]\mathbf{F}^{-1}\mathbf{s}\\
&\qquad+\tfrac{1}{2}J_0m_3h^2\mathbf{F}^{-1}\frac{\partial}{\partial\xi^\alpha}\,(\mathbf{F}\widetilde{\mathbf{W}}\mathbf{F}^{-1})\mathbf{F}(\overline{\mathbf{v}}\otimes\overline{\mathbf{v}})\mathbf{e}_\alpha\\
&\qquad-J_0h\left[\mathrm{Grad}\,\mathbf{u}_{\mathcal{S}}-m_1\Omega h\mathrm{Grad}\,(\mathbf{F}^{-1}\mathbf{v}_{\mathcal{S}})\right]\overline{\mathbf{v}}+O(\epsilon^{2+\gamma}).
\end{aligned}
\tag{A.3}
$$

Equation (A.3) can be further written in the more compact form (4.93) if we multiply it from the left by $\mathbf{F}$. So, appeal to (1.17) and

$$
\frac{\partial\mathbf{F}}{\partial t}=\mathrm{Grad}\,\mathbf{v}_{\mathcal{S}}
$$

yields

$$
\begin{aligned}
&\frac{\partial}{\partial t}\Big\{J_0h(1-m_1\Omega h)\,\mathbf{F}\overline{\mathbf{v}}\Big\}\\
&\qquad+\mathrm{Div}\Big\{J_0h\mathbf{F}\Big[(m_2-m_3\Omega h)\,\overline{\mathbf{v}}\otimes\overline{\mathbf{v}}+\overline{p}\,\mathbf{M}_0-\overline{\mathbf{P}}-\overline{\mathbf{v}}\otimes\mathbf{u}_{\mathcal{S}}\\
&\qquad\qquad+m_1\Omega h\,\overline{\mathbf{v}}\otimes\mathbf{F}^{-1}\mathbf{v}_{\mathcal{S}}\Big]\Big\}\\
&\qquad=-2J_0h\,\mathbf{F}\widetilde{\mathbf{W}}\left[\overline{\mathbf{p}}-\left(1-\frac{\rho_b}{\rho_0}\right)\mathcal{U}\,\overline{\mathbf{v}}-\tfrac{1}{2}\beta h\overline{\mathbf{v}}\right]\\
&\qquad-J_0h\left(c+am_2-\tfrac{1}{2}m_3\tilde{a}h-\widetilde{\mathbf{H}}\cdot\overline{\mathbf{P}}\right)\mathbf{s}-J_0h\overline{p}\,\mathbf{F}\widetilde{\mathbf{W}}\mathbf{F}^{-1}\mathbf{s}\\
&+\tfrac{1}{2}J_0m_3h^2\frac{\partial}{\partial\xi^\alpha}\,(\mathbf{F}\widetilde{\mathbf{W}}\mathbf{F}^{-1})\mathbf{F}(\overline{\mathbf{v}}\otimes\overline{\mathbf{v}})\mathbf{e}_\alpha-J_0\frac{\rho_b}{\rho_0}\,\mathcal{U}\,\mathbf{F}\,\mathbf{v}\Big|_{\zeta=0}+J_0\mathbf{F}\mathbf{f}_b\\
&\qquad+J_0h(1-m_1\Omega h)\,\underbrace{(\mathrm{Grad}\,\mathbf{v}_{\mathcal{S}})\,\overline{\mathbf{v}}}-J_0h\mathbf{F}(\mathrm{Grad}\,\mathbf{u}_{\mathcal{S}})\overline{\mathbf{v}}\\
&\qquad\qquad+J_0m_1\Omega h^2\,\underbrace{\mathbf{F}\left(\mathrm{Grad}\,(\mathbf{F}^{-1}\mathbf{v}_{\mathcal{S}})\right)\overline{\mathbf{v}}}\\
&\qquad+J_0h\frac{\partial\mathbf{F}}{\partial\xi^\alpha}\left(-\overline{\mathbf{v}}\otimes\mathbf{u}_{\mathcal{S}}+m_1\Omega h\overline{\mathbf{v}}\otimes\mathbf{F}^{-1}\mathbf{v}_{\mathcal{S}}\right)\mathbf{e}_\alpha+O(\epsilon^{2+\gamma}).
\end{aligned}
\tag{A.4}
$$

We derive useful expressions for the underbraced terms. Recall that

$$
\mathbf{u}_{\mathcal{S}}=\mathbf{F}^{-1}(\mathbf{v}_{\mathcal{S}}+\mathcal{U}\mathbf{s}),
$$

see (2.69), so that

$$\begin{aligned}\operatorname{Grad}\mathbf{v}_{\mathcal{S}} &= \operatorname{Grad}\left(\mathbf{F}\mathbf{u}_{\mathcal{S}} - \mathcal{U}\mathbf{s}\right)\\ &= \mathbf{F}\operatorname{Grad}\mathbf{u}_{\mathcal{S}} + \frac{\partial \mathbf{F}}{\partial \xi^{\alpha}}\mathbf{u}_{\mathcal{S}} \otimes \mathbf{e}_{\alpha} - \mathcal{U}\operatorname{Grad}\mathbf{s} - \mathbf{s} \otimes \operatorname{Grad}\mathcal{U}\\ &= \mathbf{F}\operatorname{Grad}\mathbf{u}_{\mathcal{S}} + \frac{\partial \mathbf{F}}{\partial \xi^{\alpha}}\mathbf{u}_{\mathcal{S}} \otimes \mathbf{e}_{\alpha} - \mathcal{U}\mathbf{F}\widetilde{\mathbf{W}} - \mathbf{s} \otimes \operatorname{Grad}\mathcal{U},\end{aligned}$$

and hence

$$\begin{aligned}(\operatorname{Grad}\mathbf{v}_{\mathcal{S}})\,\overline{\mathbf{v}} = \mathbf{F}(\operatorname{Grad}\mathbf{u}_{\mathcal{S}})\overline{\mathbf{v}} + \frac{\partial \mathbf{F}}{\partial \xi^{\alpha}}(\mathbf{u}_{\mathcal{S}} \otimes \overline{\mathbf{v}})\mathbf{e}_{\alpha} - \mathcal{U}\mathbf{F}\widetilde{\mathbf{W}}\overline{\mathbf{v}}\\ -(\overline{\mathbf{v}} \cdot \operatorname{Grad}\mathcal{U})\mathbf{s}.\end{aligned} \tag{A.5}$$

Then, using (1.15), we have

$$\begin{aligned}\mathbf{F}\left(\operatorname{Grad}\left(\mathbf{F}^{-1}\mathbf{v}_{\mathcal{S}}\right)\right)\overline{\mathbf{v}} &= \left(\operatorname{Grad}\mathbf{v}_{\mathcal{S}} - \frac{\partial \mathbf{F}}{\partial \xi^{\alpha}}\left(\mathbf{F}^{-1}\mathbf{v}_{\mathcal{S}} \otimes \mathbf{e}_{\alpha}\right)\right)\overline{\mathbf{v}}\\ &= (\operatorname{Grad}\mathbf{v}_{\mathcal{S}})\overline{\mathbf{v}} - \frac{\partial \mathbf{F}}{\partial \xi^{\alpha}}(\mathbf{F}^{-1}\mathbf{v}_{\mathcal{S}} \otimes \overline{\mathbf{v}})\mathbf{e}_{\alpha}.\end{aligned} \tag{A.6}$$

With (A.5) and (A.6), we can now compute the sum of the last four significant terms in Eq. (A.4). We also use formula (1.19) with $\mathbf{A} \equiv \mathbf{F}$.[1] We obtain

$$\begin{aligned}&J_0 h(1 - m_1\Omega h)(\operatorname{Grad}\mathbf{v}_{\mathcal{S}})\,\overline{\mathbf{v}} - J_0 h\mathbf{F}(\operatorname{Grad}\mathbf{u}_{\mathcal{S}})\overline{\mathbf{v}}\\ &\qquad + J_0 m_1\Omega h^2\mathbf{F}\left(\operatorname{Grad}\left(\mathbf{F}^{-1}\mathbf{v}_{\mathcal{S}}\right)\right)\overline{\mathbf{v}}\\ &\qquad + J_0 h\frac{\partial \mathbf{F}}{\partial \xi^{\alpha}}\left(-\overline{\mathbf{v}} \otimes \mathbf{u}_{\mathcal{S}} + m_1\Omega h\overline{\mathbf{v}} \otimes \mathbf{F}^{-1}\mathbf{v}_{\mathcal{S}}\right)\mathbf{e}_{\alpha}\\ &= J_0 h\left\{(\operatorname{Grad}\mathbf{v}_{\mathcal{S}})\,\overline{\mathbf{v}} - \mathbf{F}(\operatorname{Grad}\mathbf{u}_{\mathcal{S}})\overline{\mathbf{v}} - \frac{\partial \mathbf{F}}{\partial \xi^{\alpha}}\left(\overline{\mathbf{v}} \otimes \mathbf{u}_{\mathcal{S}}\right)\mathbf{e}_{\alpha}\right\}\\ &\qquad - J_0 m_1\Omega h^2\left\{(\operatorname{Grad}\mathbf{v}_{\mathcal{S}})\,\overline{\mathbf{v}} - \mathbf{F}\left(\operatorname{Grad}\left(\mathbf{F}^{-1}\mathbf{v}_{\mathcal{S}}\right)\right)\overline{\mathbf{v}}\right.\\ &\left.\qquad - \frac{\partial \mathbf{F}}{\partial \xi^{\alpha}}\left(\overline{\mathbf{v}} \otimes \mathbf{F}^{-1}\mathbf{v}_{\mathcal{S}}\right)\mathbf{e}_{\alpha}\right\} = -J_0 h\mathcal{U}\mathbf{F}\widetilde{\mathbf{W}}\overline{\mathbf{v}} - J_0 h(\overline{\mathbf{v}} \cdot \operatorname{Grad}\mathcal{U})\mathbf{s}\\ &\qquad + J_0 h\frac{\partial \mathbf{F}}{\partial \xi^{\alpha}}\left\{\mathbf{u}_{\mathcal{S}} \otimes \overline{\mathbf{v}} - \overline{\mathbf{v}} \otimes \mathbf{u}_{\mathcal{S}}\right\}\mathbf{e}_{\alpha}\\ &\qquad + J_0 m_1\Omega h^2\frac{\partial \mathbf{F}}{\partial \xi^{\alpha}}\left\{\overline{\mathbf{v}} \otimes \mathbf{F}^{-1}\mathbf{v}_{\mathcal{S}} - \mathbf{F}^{-1}\mathbf{v}_{\mathcal{S}} \otimes \overline{\mathbf{v}}\right\}\mathbf{e}_{\alpha}\\ &\qquad = -J_0 h\mathcal{U}\mathbf{F}\widetilde{\mathbf{W}}\overline{\mathbf{v}} - J_0 h(\overline{\mathbf{v}} \cdot \operatorname{Grad}\mathcal{U})\mathbf{s}.\end{aligned}$$

[1] In earlier papers by Luca et al. [1, 2] we did not notice formula (1.19). As a consequence, the corresponding depth-averaged tangential linear momentum balance equations contain terms which are actually zero. These terms are of the form $\frac{\partial \mathbf{F}}{\partial \xi^{\alpha}}(\mathbf{u} \otimes \mathbf{v} - \mathbf{v} \otimes \mathbf{u})\mathbf{e}_{\alpha}$.

Insertion of this result into (A.4) yields the tangential linear momentum balance equation (4.93).

A.3 Proof of the Depth-Integrated Hybrid Linear Momentum Balance Equation (4.109)

Here we prove that the combination (4.108), that is,

$$\begin{aligned} c\,\frac{\partial}{\partial t}\int_0^h J\,\mathbb{v}\,d\zeta + c\,\mathrm{Div}\int_0^h J\,\{\mathbb{v}\otimes(\mathbf{v}-\mathbf{w})-\mathbb{S}\}\,d\zeta \\ + \left(\frac{\partial}{\partial t}\int_0^h J\,v\,d\zeta\right)\mathbf{s} + \left(\mathrm{Div}\int_0^h J\,\{v(\mathbf{v}-\mathbf{w})-\mathbb{t}\}\,d\zeta\right)\mathbf{s} \\ = -J_0 c\,\frac{\rho_b}{\rho_0}\,\mathcal{U}\mathbb{v}\Big|_{\zeta=0} - J_0 c\,\mathbb{s}\Big|_{\zeta=0} - J_0\frac{\rho_b}{\rho_0}\,\mathcal{U}v\Big|_{\zeta=0}\mathbf{s} \\ - J_0\,\sigma\Big|_{\zeta=0}\mathbf{s} - \left(\int_0^h J\,d\zeta\right)\mathbf{s}, \end{aligned} \tag{A.7}$$

can be stated as (4.109).

First, we compute the sum of the terms involving the time derivative on the left-hand side of (A.7). Clearly, since c and $\mathbf{s}$ are independent of the variable ζ, we have

$$\begin{aligned} c\,\frac{\partial}{\partial t}\int_0^h J\,\mathbb{v}\,d\zeta + \left(\frac{\partial}{\partial t}\int_0^h J\,v\,d\zeta\right)\mathbf{s} \\ = \frac{\partial}{\partial t}\int_0^h J\,(c\,\mathbb{v}+v\,\mathbb{s})\,d\zeta - \int_0^h J\left(\frac{\partial c}{\partial t}\mathbb{v} + v\,\frac{\partial \mathbb{s}}{\partial t}\right)d\zeta. \end{aligned} \tag{A.8}$$

We rely on the relations

$$\mathbb{v} = \mathbf{B}\mathbf{v} - \mathrm{v}\mathbb{s}, \qquad v = \frac{1}{c}\mathbf{B}\mathbf{v}\cdot\mathbf{s} + c\mathrm{v},$$

see (2.96), to compute $c\,\mathbb{v} + v\,\mathbb{s}$ in the first integral on the right-hand side of (A.8) as follows:

$$c\,\mathbb{v} + v\,\mathbb{s} = c(\mathbf{B}\mathbf{v} - \mathrm{v}\mathbb{s}) + \left(\frac{1}{c}\mathbf{B}\mathbf{v}\cdot\mathbf{s} + c\mathrm{v}\right)\mathbf{s} = c\,\mathbb{B}\mathbf{v} + \frac{1}{c}(\mathbf{s}\otimes\mathbf{s})\mathbf{B}\mathbf{v}.$$

Therefore, we have

$$c\,\mathbb{v} + v\,\mathbb{s} = c\left(\mathbf{I} + \frac{1}{c^2}\mathbf{s}\otimes\mathbf{s}\right)\mathbf{B}\mathbf{v}. \tag{A.9}$$

Then, for the second integral on the right-hand side of (A.8) we invoke the formulae

$$\frac{\partial c}{\partial t} = -c\mathbf{s}\cdot\mathbf{F}^{-T}(\widetilde{\mathbf{H}}\mathbf{u}_{\mathcal{S}} + \mathrm{Grad}\,\mathcal{U}), \quad \frac{\partial \mathbf{s}}{\partial t} = \mathbf{F}\widetilde{\mathbf{W}}\mathbf{u}_{\mathcal{S}} + \mathbf{F}\mathbf{M}_0\mathrm{Grad}\,\mathcal{U},$$

see Exercise 2.8. For simplicity, we use these relations in the form

$$\frac{\partial c}{\partial t} = -c\,\mathbf{a}\cdot\mathbf{s}, \quad \frac{\partial \mathbf{s}}{\partial t} = \frac{1}{c}\frac{\partial c}{\partial t}\,\mathbf{s} + \mathbf{a}, \quad \mathbf{a} \equiv \mathbf{F}^{-T}(\widetilde{\mathbf{H}}\mathbf{u}_S + \mathrm{Grad}\,\mathcal{U}), \tag{A.10}$$

which can be deduced by recalling $\widetilde{\mathbf{W}} = \mathbf{M}_0\widetilde{\mathbf{H}}$ and expression (2.50) of $\mathbf{M}_0$. Thus, we have

$$\begin{aligned}
\frac{\partial c}{\partial t}\mathbb{v} + v\,\frac{\partial \mathbf{s}}{\partial t} &= \frac{\partial c}{\partial t}(\mathbf{B}\mathbf{v} - \mathrm{v}\mathbf{s}) + \left(\frac{1}{c}\mathbf{B}\mathbf{v}\cdot\mathbf{s} + c\mathrm{v}\right)\frac{\partial \mathbf{s}}{\partial t} \\
&= \frac{\partial c}{\partial t}\mathbf{B}\mathbf{v} + \frac{1}{c}(\mathbf{B}\mathbf{v}\cdot\mathbf{s})\frac{\partial \mathbf{s}}{\partial t} + \mathrm{v}\left(-\frac{\partial c}{\partial t}\mathbf{s} + c\,\frac{\partial \mathbf{s}}{\partial t}\right) \\
&= \frac{\partial c}{\partial t}\mathbf{B}\mathbf{v} + \frac{1}{c^2}(\mathbf{B}\mathbf{v}\cdot\mathbf{s})\frac{\partial c}{\partial t}\mathbf{s} + \frac{1}{c}(\mathbf{B}\mathbf{v}\cdot\mathbf{s})\,\mathbf{a} + c\mathrm{v}\mathbf{a} \\
&= \frac{\partial c}{\partial t}\left(\mathbf{I} + \frac{1}{c^2}\,\mathbf{s}\otimes\mathbf{s}\right)\mathbf{B}\mathbf{v} + \frac{1}{c}(\mathbf{B}\mathbf{v}\cdot\mathbf{s})\,\mathbf{a} + c\mathrm{v}\mathbf{a} \\
&= -c\,(\mathbf{a}\cdot\mathbf{s})\left(\mathbf{I} + \frac{1}{c^2}\,\mathbf{s}\otimes\mathbf{s}\right)\mathbf{B}\mathbf{v} + \frac{1}{c}(\mathbf{B}\mathbf{v}\cdot\mathbf{s})\,\mathbf{a} + c\mathrm{v}\mathbf{a}.
\end{aligned}$$

Using the result above and formula (A.9), relation (A.8) can be further written as

$$\begin{aligned}
c\,\frac{\partial}{\partial t}\int_0^h J\mathbb{v}\,d\zeta + \left(\frac{\partial}{\partial t}\int_0^h J v\,d\zeta\right)\mathbf{s} = \frac{\partial}{\partial t}\left\{c\left(\mathbf{I} + \frac{1}{c^2}\mathbf{s}\otimes\mathbf{s}\right)\int_0^h J\mathbf{B}\mathbf{v}\,d\zeta\right\} \\
+ c\,(\mathbf{a}\cdot\mathbf{s})\left(\mathbf{I} + \frac{1}{c^2}\,\mathbf{s}\otimes\mathbf{s}\right)\int_0^h J\mathbf{B}\mathbf{v}\,d\zeta \\
-\frac{1}{c}\left\{\left(\int_0^h J\mathbf{B}\mathbf{v}\,d\zeta\right)\cdot\mathbf{s}\right\}\mathbf{a} - c\left(\int_0^h J\mathrm{v}\,d\zeta\right)\mathbf{a}.
\end{aligned} \tag{A.11}$$

Finally, we want to take the matrix

$$c\left(\mathbf{I} + \frac{1}{c^2}\mathbf{s}\otimes\mathbf{s}\right) \tag{A.12}$$

out of the time differentiation operator arising on the right-hand side of (A.11). Using (A.10) we deduce

$$\begin{aligned}
&\frac{\partial}{\partial t}\left\{c\left(\mathbf{I} + \frac{1}{c^2}\,\mathbf{s}\otimes\mathbf{s}\right)\right\} \\
&\qquad = \frac{\partial c}{\partial t}\left(\mathbf{I} + \frac{1}{c^2}\mathbf{s}\otimes\mathbf{s}\right) - \frac{2}{c^2}\,\frac{\partial c}{\partial t}\,\mathbf{s}\otimes\mathbf{s} + \frac{1}{c}\left(\frac{\partial \mathbf{s}}{\partial t}\otimes\mathbf{s} + \mathbf{s}\otimes\frac{\partial \mathbf{s}}{\partial t}\right) \\
&\qquad = \frac{\partial c}{\partial t}\left(\mathbf{I} + \frac{1}{c^2}\mathbf{s}\otimes\mathbf{s}\right) + \frac{1}{c}\,(\mathbf{a}\otimes\mathbf{s} + \mathbf{s}\otimes\mathbf{a})\,,
\end{aligned}$$

so that relation (A.11) turns into

$$c\,\frac{\partial}{\partial t}\int_0^h J\mathbb{v}\,d\zeta+\left(\frac{\partial}{\partial t}\int_0^h J\,v\,d\zeta\right)\mathbf{s}=c\,\left(\mathbf{I}+\frac{1}{c^2}\mathbf{s}\otimes\mathbf{s}\right)\frac{\partial}{\partial t}\int_0^h J\mathbf{B}\mathbf{v}\,d\zeta \\ +\frac{1}{c}\left\{\left(\int_0^h J\mathbf{B}\mathbf{v}\,d\zeta\right)\cdot\mathbf{a}\right\}\mathbf{s}-c\left(\int_0^h J\mathbb{v}\,d\zeta\right)\mathbf{a}. \tag{A.13}$$

The next step in the proof of (4.109) is the computation of the sum of the two terms in (A.7) involving the divergence operator. We use the formulae

$$f\,\mathrm{Div}\,\mathbf{T}=\mathrm{Div}\,(f\mathbf{T})-\mathbf{T}\mathrm{Grad}\,f,$$
$$(\mathrm{Div}\,\mathbf{v})\,\mathbf{u}=\mathrm{Div}\,(\mathbf{u}\otimes\mathbf{v})-(\mathrm{Grad}\,\mathbf{u})\,\mathbf{v},$$

to obtain

$$c\,\mathrm{Div}\int_0^h J\,\{\mathbb{v}\otimes(\mathbf{v}-\mathbf{w})-\mathbb{S}\}\,d\zeta+\left(\mathrm{Div}\int_0^h J\,\{v(\mathbf{v}-\mathbf{w})-\mathbb{t}\}\,d\zeta\right)\mathbf{s} \\ =\mathrm{Div}\int_0^h J\,\underbrace{\left\{c\left(\mathbb{v}\otimes(\mathbf{v}-\mathbf{w})-\mathbb{S}\right)+\mathbf{s}\otimes\left(v(\mathbf{v}-\mathbf{w})-\mathbb{t}\right)\right\}}_{①}d\zeta \\ -\int_0^h J\,\underbrace{\left\{\left(\mathbb{v}\otimes(\mathbf{v}-\mathbf{w})-\mathbb{S}\right)\mathrm{Grad}\,c\;+(\mathrm{Grad}\,\mathbf{s})\left(v(\mathbf{v}-\mathbf{w})-\mathbb{t}\right)\right\}}_{②}d\zeta. \tag{A.14}$$

By virtue of (A.9) and

$$\mathbb{S}=\mathbf{B}\mathbf{T}-\mathbf{s}\otimes\mathbf{t},\quad \mathbb{t}=\frac{1}{c}\,\mathbf{T}\mathbf{B}^T\mathbf{s}+c\,\mathbf{t},$$

see (2.98), for the term above denoted by ① we deduce

$$①=(c\,\mathbb{v}+v\,\mathbf{s})\otimes(\mathbf{v}-\mathbf{w})-c(\mathbf{B}\mathbf{T}-\mathbf{s}\otimes\mathbf{t})-\mathbf{s}\otimes\left(\frac{1}{c}\,\mathbf{T}\mathbf{B}^T\mathbf{s}+c\,\mathbf{t}\right) \\ =(c\,\mathbb{v}+v\,\mathbf{s})\otimes(\mathbf{v}-\mathbf{w})-c\,\mathbf{B}\mathbf{T}-\frac{1}{c}\,(\mathbf{s}\otimes\mathbf{s})\,\mathbf{B}\mathbf{T} \\ =(c\,\mathbb{v}+v\,\mathbf{s})\otimes(\mathbf{v}-\mathbf{w})-c\left(\mathbf{I}+\frac{1}{c^2}\mathbf{s}\otimes\mathbf{s}\right)\mathbf{B}\mathbf{T} \\ =c\left(\mathbf{I}+\frac{1}{c^2}\mathbf{s}\otimes\mathbf{s}\right)\mathbf{B}\left(\mathbf{v}\otimes(\mathbf{v}-\mathbf{w})-\mathbf{T}\right). \tag{A.15}$$

To compute ② we first invoke

$$(\mathbb{v}\otimes(\mathbf{v}-\mathbf{w}))\,\mathrm{Grad}\,c=(\mathbb{v}\otimes\mathrm{Grad}\,c)\,(\mathbf{v}-\mathbf{w})$$

to rewrite ② as

$$② = \underbrace{\Big(\mathbb{v} \otimes \operatorname{Grad} c \; + v \operatorname{Grad} \mathbf{s}\Big)\,(\mathbf{v}-\mathbf{w})}_{\text{(}\lambda\text{)}} - \underbrace{\Big(\mathbb{S}\operatorname{Grad} c + (\operatorname{Grad} \mathbf{s})\mathbb{t}\Big)}_{\text{(}\mu\text{)}}\,. \tag{A.16}$$

Then, recall the relations

$$\operatorname{Grad} c = -c\,\widetilde{\mathbf{H}}\mathbf{F}^{-1}\mathbf{s}, \quad \operatorname{Grad} \mathbf{s} = \mathbf{F}\widetilde{\mathbf{W}} = (\mathbf{I}-\mathbf{s}\otimes\mathbf{s})\mathbf{F}^{-T}\widetilde{\mathbf{H}}, \tag{A.17}$$

see (2.51), and obtain

$$\begin{aligned}
\text{(}\lambda\text{)} &= \Big(-(c\mathbb{v}+v\,\mathbf{s})\otimes\widetilde{\mathbf{H}}\mathbf{F}^{-1}\mathbf{s} + v\mathbf{F}^{-T}\widetilde{\mathbf{H}}\Big)\,(\mathbf{v}-\mathbf{w}) \\
&= -\Big((c\mathbb{v}+v\,\mathbf{s})\otimes(\mathbf{v}-\mathbf{w})\Big)\,\widetilde{\mathbf{H}}\mathbf{F}^{-1}\mathbf{s} + v\mathbf{F}^{-T}\widetilde{\mathbf{H}}(\mathbf{v}-\mathbf{w}) \\
&= -c\left(\mathbf{I}+\frac{1}{c^2}\mathbf{s}\otimes\mathbf{s}\right)\mathbf{B}\Big(\mathbf{v}\otimes(\mathbf{v}-\mathbf{w})\Big)\,\widetilde{\mathbf{H}}\mathbf{F}^{-1}\mathbf{s} + v\mathbf{F}^{-T}\widetilde{\mathbf{H}}(\mathbf{v}-\mathbf{w}).
\end{aligned}$$

The above mentioned expressions of $\mathbb{S}$, $\mathbb{t}$, $\operatorname{Grad} c$ and $\operatorname{Grad}\mathbf{s}$ are accounted for to deduce

$$\begin{aligned}
\text{(}\mu\text{)} &= (\mathbf{B}\mathbf{T}-\mathbf{s}\otimes\mathbf{t})\operatorname{Grad} c + \operatorname{Grad}\mathbf{s}\left(\frac{1}{c}\,\mathbf{T}\mathbf{B}^T\mathbf{s} + c\,\mathbf{t}\right) \\
&= \mathbf{B}\mathbf{T}\operatorname{Grad} c + \frac{1}{c}\,(\operatorname{Grad}\mathbf{s})\mathbf{T}\mathbf{B}^T\mathbf{s} + (c\operatorname{Grad}\mathbf{s} - \mathbf{s}\otimes\operatorname{Grad} c\,)\mathbf{t} \\
&= \mathbf{B}\mathbf{T}\operatorname{Grad} c + \frac{1}{c}\,(\operatorname{Grad}\mathbf{s})\mathbf{T}\mathbf{B}^T\mathbf{s} + c\mathbf{F}^{-T}\widetilde{\mathbf{H}}\mathbf{t} \\
&= \mathbf{B}\mathbf{T}\operatorname{Grad} c + \frac{1}{c}\left(\mathbf{F}^{-T}\widetilde{\mathbf{H}} + \frac{1}{c}\mathbf{s}\otimes\operatorname{Grad} c\right)\mathbf{T}\mathbf{B}^T\mathbf{s} + c\mathbf{F}^{-T}\widetilde{\mathbf{H}}\mathbf{t} \\
&= \mathbf{B}\mathbf{T}\operatorname{Grad} c + \frac{1}{c^2}\,(\mathbf{s}\otimes\mathbf{B}\mathbf{T}\operatorname{Grad} c)\,\mathbf{s} + \frac{1}{c}\,\mathbf{F}^{-T}\widetilde{\mathbf{H}}\mathbf{T}\mathbf{B}^T\mathbf{s} + c\mathbf{F}^{-T}\widetilde{\mathbf{H}}\mathbf{t} \\
&= \mathbf{B}\mathbf{T}\operatorname{Grad} c + \frac{1}{c^2}\,(\mathbf{s}\otimes\mathbf{s})\,\mathbf{B}\mathbf{T}\operatorname{Grad} c + \frac{1}{c}\,\mathbf{F}^{-T}\widetilde{\mathbf{H}}\mathbf{T}\mathbf{B}^T\mathbf{s} + c\mathbf{F}^{-T}\widetilde{\mathbf{H}}\mathbf{t} \\
&= -c\left(\mathbf{I}+\frac{1}{c^2}\mathbf{s}\otimes\mathbf{s}\right)\mathbf{B}\mathbf{T}\widetilde{\mathbf{H}}\mathbf{F}^{-1}\mathbf{s} + \frac{1}{c}\,\mathbf{F}^{-T}\widetilde{\mathbf{H}}\mathbf{T}\mathbf{B}^T\mathbf{s} + c\mathbf{F}^{-T}\widetilde{\mathbf{H}}\mathbf{t}.
\end{aligned}$$

Inserting ⓛ and ⓜ as given above into (A.16) it follows that

$$\begin{aligned}
② = &-c\left(\mathbf{I}+\frac{1}{c^2}\mathbf{s}\otimes\mathbf{s}\right)\mathbf{B}\Big(\mathbf{v}\otimes(\mathbf{v}-\mathbf{w}) - \mathbf{T}\Big)\,\widetilde{\mathbf{H}}\mathbf{F}^{-1}\mathbf{s} \\
&- \frac{1}{c}\,\mathbf{F}^{-T}\widetilde{\mathbf{H}}\mathbf{T}\mathbf{B}^T\mathbf{s} + \mathbf{F}^{-T}\widetilde{\mathbf{H}}\Big(v(\mathbf{v}-\mathbf{w}) - c\mathbf{t}\Big)\,.
\end{aligned}$$

Furthermore, by means of

$$\begin{aligned} v(\mathbf{v}-\mathbf{w}) &= \frac{1}{c}(\mathbf{B}\mathbf{v}\cdot\mathbf{s})(\mathbf{v}-\mathbf{w}) + c\mathrm{v}(\mathbf{v}-\mathbf{w}) \\ &= \frac{1}{c}(\mathbf{v}\cdot\mathbf{B}^T\mathbf{s})(\mathbf{v}-\mathbf{w}) + c\mathrm{v}(\mathbf{v}-\mathbf{w}) \\ &= \frac{1}{c}\ ((\mathbf{v}-\mathbf{w})\otimes\mathbf{v})\,\mathbf{B}^T\mathbf{s} + c\mathrm{v}(\mathbf{v}-\mathbf{w}), \end{aligned}$$

we arrive at

$$\begin{aligned} ② = &-c\left(\mathbf{I}+\frac{1}{c^2}\mathbf{s}\otimes\mathbf{s}\right)\mathbf{B}\left(\mathbf{v}\otimes(\mathbf{v}-\mathbf{w})-\mathbf{T}\right)\widetilde{\mathbf{H}}\mathbf{F}^{-1}\mathbf{s} \\ &+\frac{1}{c}\,\mathbf{F}^{-T}\widetilde{\mathbf{H}}\left\{\mathbf{B}\left(\mathbf{v}\otimes(\mathbf{v}-\mathbf{w})-\mathbf{T}\right)\right\}^T\mathbf{s} + c\,\mathbf{F}^{-T}\widetilde{\mathbf{H}}\left(\mathrm{v}(\mathbf{v}-\mathbf{w})-\mathbf{t}\right). \end{aligned} \tag{A.18}$$

Now, substitution of ① and ② in (A.14) with their expressions given by (A.15) and (A.18), respectively, yields

$$\begin{aligned} c\,\mathrm{Div}\int_0^h J\,\{\mathbb{v}\otimes(\mathbf{v}-\mathbf{w})-\mathbb{S}\}\,d\zeta + \left(\mathrm{Div}\int_0^h J\,\{v(\mathbf{v}-\mathbf{w})-\mathbb{t}\}\,d\zeta\right)\mathbf{s} \\ = \mathrm{Div}\left\{c\left(\mathbf{I}+\frac{1}{c^2}\mathbf{s}\otimes\mathbf{s}\right)\int_0^h J\mathbf{B}\left(\mathbf{v}\otimes(\mathbf{v}-\mathbf{w})-\mathbf{T}\right)d\zeta\right\} \\ +c\left(\mathbf{I}+\frac{1}{c^2}\mathbf{s}\otimes\mathbf{s}\right)\left\{\int_0^h J\mathbf{B}\left(\mathbf{v}\otimes(\mathbf{v}-\mathbf{w})-\mathbf{T}\right)d\zeta\right\}\widetilde{\mathbf{H}}\mathbf{F}^{-1}\mathbf{s} \\ -\frac{1}{c}\,\mathbf{F}^{-T}\widetilde{\mathbf{H}}\left\{\int_0^h J\mathbf{B}\left(\mathbf{v}\otimes(\mathbf{v}-\mathbf{w})-\mathbf{T}\right)d\zeta\right\}^T\mathbf{s} \\ -c\,\mathbf{F}^{-T}\widetilde{\mathbf{H}}\int_0^h J\left(\mathrm{v}(\mathbf{v}-\mathbf{w})-\mathbf{t}\right)d\zeta. \end{aligned} \tag{A.19}$$

As in the case of (A.11), we want to take the matrix (A.12) out of the divergence operator arising on the right-hand side of (A.19). To this end we use the formula

$$\mathrm{Div}\,(\mathbf{A}\mathbf{B}) = \mathbf{A}\,(\mathrm{Div}\,\mathbf{B}) + (\mathrm{Grad}\,\mathbf{A})\,\mathbf{B}^T, \tag{A.20}$$

valid for the second order matrix functions $\mathbf{A}$ and $\mathbf{B}$, where

$$\mathrm{Grad}\,\mathbf{A} \equiv \frac{\partial\mathbf{A}}{\partial\xi^\alpha}\otimes\mathbf{e}_\alpha. \tag{A.21}$$

We explain the dyadic product on the right-hand side of (A.21). For the two-column matrix $\mathbf{v}$ and the second order matrix $\mathbf{A}$, by $\mathbf{A}\otimes\mathbf{v}$ and $\mathbf{v}\otimes\mathbf{A}$ we understand

$$(\mathbf{A}\otimes\mathbf{v})\mathbf{B}\equiv\mathbf{A}\mathbf{B}^T\mathbf{v},\quad (\mathbf{v}\otimes\mathbf{A})\mathbf{B}\equiv(\mathbf{B}\cdot\mathbf{A}^T)\mathbf{v}, \tag{A.22}$$

for any second order matrix $\mathbf{B}$. Note that, if $\mathbf{a}$, $\mathbf{b}$ and $\mathbf{c}$ are two-column matrices, then

$$(\mathbf{a}\otimes\mathbf{b})\otimes\mathbf{c}=\mathbf{a}\otimes(\mathbf{b}\otimes\mathbf{c}). \tag{A.23}$$

Definition $(A.22)_1$ clarifies the meaning of (A.21), and $(A.22)_2$, (A.23) will be subsequently used. Thus, we have

$$\begin{aligned}
&\mathrm{Grad}\left\{c\left(\mathbf{I}+\frac{1}{c^2}\mathbf{s}\otimes\mathbf{s}\right)\right\}=\frac{\partial}{\partial\xi^\alpha}\left\{c\left(\mathbf{I}+\frac{1}{c^2}\mathbf{s}\otimes\mathbf{s}\right)\right\}\otimes\mathbf{e}_\alpha\\
&=\frac{\partial c}{\partial\xi^\alpha}\left(\mathbf{I}+\frac{1}{c^2}\mathbf{s}\otimes\mathbf{s}\right)\otimes\mathbf{e}_\alpha+c\,\frac{\partial}{\partial\xi^\alpha}\left(\frac{1}{c^2}\mathbf{s}\otimes\mathbf{s}\right)\otimes\mathbf{e}_\alpha\\
&=\left(\mathbf{I}+\frac{1}{c^2}\mathbf{s}\otimes\mathbf{s}\right)\otimes\mathrm{Grad}\,c-\frac{2}{c^2}\,(\mathbf{s}\otimes\mathbf{s})\otimes\mathrm{Grad}\,c\\
&\quad+\frac{1}{c}\left(\frac{\partial\mathbf{s}}{\partial\xi^\alpha}\otimes\mathbf{s}+\mathbf{s}\otimes\frac{\partial\mathbf{s}}{\partial\xi^\alpha}\right)\otimes\mathbf{e}_\alpha\\
&=\left(\mathbf{I}+\frac{1}{c^2}\mathbf{s}\otimes\mathbf{s}\right)\otimes\mathrm{Grad}\,c-\frac{2}{c^2}\,(\mathbf{s}\otimes\mathbf{s})\otimes\mathrm{Grad}\,c\\
&\quad+\frac{1}{c}\left(\frac{\partial\mathbf{s}}{\partial\xi^\alpha}\otimes\mathbf{s}\right)\otimes\mathbf{e}_\alpha+\frac{1}{c}\,\mathbf{s}\otimes\mathrm{Grad}\,\mathbf{s}\\
&=\left(\mathbf{I}-\frac{1}{c^2}\mathbf{s}\otimes\mathbf{s}\right)\otimes\mathrm{Grad}\,c+\frac{1}{c}\left(\frac{\partial\mathbf{s}}{\partial\xi^\alpha}\otimes\mathbf{s}\right)\otimes\mathbf{e}_\alpha+\frac{1}{c}\,\mathbf{s}\otimes\mathrm{Grad}\,\mathbf{s}.
\end{aligned} \tag{A.24}$$

To make transparent the computations in the right-hand side of (A.19) we introduce the notation

$$\mathbf{X}\equiv\int_0^h J\mathbf{B}\left(\mathbf{v}\otimes(\mathbf{v}-\mathbf{w})-\mathbf{T}\right)d\zeta, \tag{A.25}$$

so that, using (A.20), the divergence term on the right-hand side of (A.19) reads

$$\begin{aligned}
&\mathrm{Div}\left\{c\left(\mathbf{I}+\frac{1}{c^2}\mathbf{s}\otimes\mathbf{s}\right)\mathbf{X}\right\}\\
&\quad=c\left(\mathbf{I}+\frac{1}{c^2}\mathbf{s}\otimes\mathbf{s}\right)\mathrm{Div}\,\mathbf{X}+\mathrm{Grad}\left\{c\left(\mathbf{I}+\frac{1}{c^2}\mathbf{s}\otimes\mathbf{s}\right)\right\}\mathbf{X}^T.
\end{aligned} \tag{A.26}$$

With the result stated in (A.24) and definitions given by (A.22) we have

$$
\begin{aligned}
&\text{Grad}\left\{c\left(\mathbf{I}+\frac{1}{c^2}\mathbf{s}\otimes\mathbf{s}\right)\right\}\mathbf{X}^T\\
&=\left(\mathbf{I}-\frac{1}{c^2}\mathbf{s}\otimes\mathbf{s}\right)\mathbf{X}\text{Grad}\,c+\frac{1}{c}\left(\frac{\partial\mathbf{s}}{\partial\xi^\alpha}\otimes\mathbf{s}\right)\mathbf{X}\mathbf{e}_\alpha+\frac{1}{c}\left(\mathbf{X}\cdot\text{Grad}\,\mathbf{s}\right)\mathbf{s}\\
&=\mathbf{X}\text{Grad}\,c\;-\frac{1}{c^2}\left(\mathbf{X}\text{Grad}\,c\cdot\mathbf{s}\right)\mathbf{s}\;+\frac{1}{c}\left(\frac{\partial\mathbf{s}}{\partial\xi^\alpha}\otimes\mathbf{X}^T\mathbf{s}\right)\mathbf{e}_\alpha\\
&\quad+\frac{1}{c}\left(\mathbf{X}\cdot\text{Grad}\,\mathbf{s}\right)\mathbf{s}\;=\mathbf{X}\text{Grad}\,c\;-\frac{1}{c^2}\left(\mathbf{X}\text{Grad}\,c\cdot\mathbf{s}\right)\mathbf{s}\\
&\quad+\frac{1}{c}\left(\text{Grad}\,\mathbf{s}\right)\mathbf{X}^T\mathbf{s}+\frac{1}{c}\left(\mathbf{X}\cdot\text{Grad}\,\mathbf{s}\right)\mathbf{s}.
\end{aligned}
$$

Substituting Grad c and Grad $\mathbf{s}$ with their expressions (A.17) we further obtain

$$
\begin{aligned}
&\text{Grad}\left\{c\left(\mathbf{I}+\frac{1}{c^2}\mathbf{s}\otimes\mathbf{s}\right)\right\}\mathbf{X}^T\\
&\quad=-c\left(\mathbf{I}+\frac{1}{c^2}\,\mathbf{s}\otimes\mathbf{s}\right)\mathbf{X}\widetilde{\mathbf{H}}\mathbf{F}^{-1}\mathbf{s}+\frac{1}{c}\,\mathbf{F}^{-T}\widetilde{\mathbf{H}}\mathbf{X}^T\mathbf{s}+\frac{1}{c}(\mathbf{X}\cdot\mathbf{F}^{-T}\widetilde{\mathbf{H}})\,\mathbf{s},
\end{aligned}
$$

and hence, see (A.26),

$$
\begin{aligned}
\text{Div}\left\{c\left(\mathbf{I}+\frac{1}{c^2}\mathbf{s}\otimes\mathbf{s}\right)\mathbf{X}\right\}&=c\left(\mathbf{I}+\frac{1}{c^2}\mathbf{s}\otimes\mathbf{s}\right)\text{Div}\,\mathbf{X}\\
-c\left(\mathbf{I}+\frac{1}{c^2}\,\mathbf{s}\otimes\mathbf{s}\right)\mathbf{X}\widetilde{\mathbf{H}}\mathbf{F}^{-1}\mathbf{s}&+\frac{1}{c}\,\mathbf{F}^{-T}\widetilde{\mathbf{H}}\mathbf{X}^T\mathbf{s}+\frac{1}{c}(\mathbf{X}\cdot\mathbf{F}^{-T}\widetilde{\mathbf{H}})\,\mathbf{s}.
\end{aligned}
\tag{A.27}
$$

It only remains to use (A.27) in (A.19) to deduce

$$
\begin{aligned}
c\,\text{Div}\int_0^h J\left\{\mathbb{v}\otimes(\mathbf{v}-\mathbf{w})-\mathbb{S}\right\}d\zeta+\left(\text{Div}\int_0^h J\left\{v(\mathbf{v}-\mathbf{w})-\mathbb{t}\right\}d\zeta\right)\mathbf{s}&\\
=c\left(\mathbf{I}+\frac{1}{c^2}\mathbf{s}\otimes\mathbf{s}\right)\text{Div}\,\mathbf{X}+\frac{1}{c}(\mathbf{X}\cdot\mathbf{F}^{-T}\widetilde{\mathbf{H}})\,\mathbf{s}&\\
-c\,\mathbf{F}^{-T}\widetilde{\mathbf{H}}\int_0^h J\left(\mathrm{v}(\mathbf{v}-\mathbf{w})-\mathbf{t}\right)d\zeta.&
\end{aligned}
\tag{A.28}
$$

Next, we need to express the terms which are evaluated at $\zeta=0$ in (A.7) in terms of the boundary conditions (4.52), (4.53) and (4.38). First note that

$$
\begin{aligned}
J_0c\,\frac{\rho_b}{\rho_0}\,\mathcal{U}\mathbb{v}\Big|_{\zeta=0}+J_0c\,\mathbb{s}\Big|_{\zeta=0}+J_0\frac{\rho_b}{\rho_0}\,\mathcal{U}v\Big|_{\zeta=0}\mathbf{s}+J_0\,\sigma\Big|_{\zeta=0}\mathbf{s}&\\
=J_0\frac{\rho_b}{\rho_0}\,\mathcal{U}\left(c\,\mathbb{v}+v\mathbf{s}\right)\Big|_{\zeta=0}+J_0\left(c\,\mathbb{s}+\sigma\mathbf{s}\right)\Big|_{\zeta=0}.&
\end{aligned}
\tag{A.29}
$$

Then, recall relation (A.9) and use

$$c\,\mathbb{s}+\sigma\mathbf{s}=c\left(\mathbf{I}+\frac{1}{c^2}\,\mathbf{s}\otimes\mathbf{s}\right)\mathbf{Bt},$$

together with $\mathbf{B}\Big|_{\zeta=0}=\mathbf{F}$ and boundary condition (4.38), to turn (A.29) into

$$\begin{aligned}J_0c\,\frac{\rho_b}{\rho_0}\,\mathcal{U}\mathbb{v}\Big|_{\zeta=0}+J_0c\,\mathbb{s}\Big|_{\zeta=0}+J_0\frac{\rho_b}{\rho_0}\,\mathcal{U}v\,\Big|_{\zeta=0}\mathbf{s}+J_0\,\sigma\Big|_{\zeta=0}\mathbf{s}\\ =c\left(\mathbf{I}+\frac{1}{c^2}\,\mathbf{s}\otimes\mathbf{s}\right)\left(J_0\,\frac{\rho_b}{\rho_0}\,\mathcal{U}\mathbf{F}\mathbf{v}\Big|_{\zeta=0}-J_0\mathbf{F}\mathbf{f}_b\right).\end{aligned}\tag{A.30}$$

Now, with (A.13), (A.28) and (A.30), Eq. (A.7) reads

$$\begin{aligned}c\left(\mathbf{I}+\frac{1}{c^2}\mathbf{s}\otimes\mathbf{s}\right)\left\{\frac{\partial}{\partial t}\int_0^h J\mathbf{B}\mathbf{v}\,d\zeta+\operatorname{Div}\mathbf{X}\right\}+\underbrace{\frac{1}{c}(\mathbf{X}\cdot\mathbf{F}^{-T}\widetilde{\mathbf{H}})\,\mathbf{s}}_{①}\\ \underbrace{-c\,\mathbf{F}^{-T}\widetilde{\mathbf{H}}\int_0^h J\left(\mathrm{v}(\mathbf{v}-\mathbf{w})-\mathbf{t}\right)d\zeta}_{②}\\ \underbrace{+\frac{1}{c}\left\{\left(\int_0^h J\mathbf{B}\mathbf{v}\,d\zeta\right)\cdot\mathbf{a}\right\}\mathbf{s}}_{③}\underbrace{-c\left(\int_0^h J\,\mathrm{v}\,d\zeta\right)\mathbf{a}}_{④}\\ =c\left(\mathbf{I}+\frac{1}{c^2}\mathbf{s}\otimes\mathbf{s}\right)\left\{-J_0\frac{\rho_b}{\rho_0}\,\mathcal{U}\mathbf{F}\mathbf{v}\Big|_{\zeta=0}+J_0\mathbf{F}\mathbf{f}_b\right\}-\left(\int_0^h J\,d\zeta\right)\mathbf{s}.\end{aligned}\tag{A.31}$$

In (A.31) the sums ① + ③ and ② + ④ can be further simplified. Indeed, recalling definition (A.10) of $\mathbf{a}$ we have

$$\begin{aligned}\mathbf{B}\mathbf{v}\cdot\mathbf{a}&=\mathbf{B}\mathbf{v}\cdot(\mathbf{F}^{-T}\widetilde{\mathbf{H}}\mathbf{u}_{\mathcal{S}}+\mathbf{F}^{-T}\operatorname{Grad}\mathcal{U})\\&=\mathbf{B}\mathbf{v}\cdot\mathbf{F}^{-T}\widetilde{\mathbf{H}}\mathbf{u}_{\mathcal{S}}+\mathbf{v}\cdot\mathbf{B}^T\mathbf{F}^{-T}\operatorname{Grad}\mathcal{U}\\&=\mathbf{B}\mathbf{v}\cdot\mathbf{F}^{-T}\widetilde{\mathbf{H}}\mathbf{u}_{\mathcal{S}}-\zeta\widetilde{\mathbf{W}}\mathbf{v}\cdot\operatorname{Grad}\mathcal{U}+\mathbf{v}\cdot\operatorname{Grad}\mathcal{U},\end{aligned}$$

and based on the relation

$$(\mathbf{I}-\zeta\widetilde{\mathbf{W}})^T\widetilde{\mathbf{H}}=\widetilde{\mathbf{H}}-\zeta\widetilde{\mathbf{W}}^T\widetilde{\mathbf{H}}=\widetilde{\mathbf{H}}-\zeta\widetilde{\mathbf{H}}\mathbf{M}_0\widetilde{\mathbf{H}}=\widetilde{\mathbf{H}}(\mathbf{I}-\zeta\widetilde{\mathbf{W}})$$

and expression $(2.110)_1$ of $\mathbf{w}$ we compute

$$\begin{aligned}\mathbf{B}(\mathbf{v}\otimes\mathbf{w})\cdot\mathbf{F}^{-T}\widetilde{\mathbf{H}} &= \mathbf{B}\mathbf{v}\cdot\mathbf{F}^{-T}\widetilde{\mathbf{H}}\mathbf{w}\\ &= \mathbf{B}\mathbf{v}\cdot\mathbf{F}^{-T}\widetilde{\mathbf{H}}\left(\mathbf{u}_{\mathcal{S}}-\zeta(\mathbf{I}-\zeta\widetilde{\mathbf{W}})^{-1}\mathbf{M}_0\mathrm{Grad}\,\mathcal{U}\right)\\ &= \mathbf{B}\mathbf{v}\cdot\mathbf{F}^{-T}\widetilde{\mathbf{H}}\mathbf{u}_{\mathcal{S}}-\zeta\mathbf{v}\cdot\mathbf{B}^{T}\mathbf{F}^{-T}\widetilde{\mathbf{H}}(\mathbf{I}-\zeta\widetilde{\mathbf{W}})^{-1}\mathbf{M}_0\mathrm{Grad}\,\mathcal{U}\\ &= \mathbf{B}\mathbf{v}\cdot\mathbf{F}^{-T}\widetilde{\mathbf{H}}\mathbf{u}_{\mathcal{S}}-\zeta\mathbf{v}\cdot\widetilde{\mathbf{H}}\mathbf{M}_0\mathrm{Grad}\,\mathcal{U}\\ &= \mathbf{B}\mathbf{v}\cdot\mathbf{F}^{-T}\widetilde{\mathbf{H}}\mathbf{u}_{\mathcal{S}}-\zeta\widetilde{\mathbf{W}}\mathbf{v}\cdot\mathrm{Grad}\,\mathcal{U}=\mathbf{B}\mathbf{v}\cdot\mathbf{a}-\mathbf{v}\cdot\mathrm{Grad}\,\mathcal{U}.\end{aligned}$$

Consequently, by means of definition (A.25) of $\mathbf{X}$, we arrive at

$$\begin{aligned}①+③ &= \frac{1}{c}\left\{\left(\int_0^h J\mathbf{B}(\mathbf{v}\otimes\mathbf{v}-\mathbf{T})d\zeta\right)\cdot\mathbf{F}^{-T}\widetilde{\mathbf{H}}\right\}\mathbf{s}\\ &\quad+\frac{1}{c}\left\{\int_0^h J\left(-\mathbf{B}(\mathbf{v}\otimes\mathbf{w})\cdot\mathbf{F}^{-T}\widetilde{\mathbf{H}}+\mathbf{B}\mathbf{v}\cdot\mathbf{a}\right)d\zeta\right\}\mathbf{s}\\ &= \frac{1}{c}\left\{\left(\int_0^h J\mathbf{B}(\mathbf{v}\otimes\mathbf{v}-\mathbf{T})\,d\zeta\right)\cdot\mathbf{F}^{-T}\widetilde{\mathbf{H}}\right\}\mathbf{s}\\ &\quad+\frac{1}{c}\left\{\left(\int_0^h J\mathbf{v}d\zeta\right)\cdot\mathrm{Grad}\,\mathcal{U}\right\}\mathbf{s}.\end{aligned}$$

Then,

$$②+④ = c\,\mathbf{F}^{-T}\widetilde{\mathbf{H}}\int_0^h J\,(\mathrm{v}\mathbf{v}-\mathbf{t})\,d\zeta+c\int_0^h J\mathrm{v}\left(\mathbf{a}-\mathbf{F}^{-T}\widetilde{\mathbf{H}}\mathbf{w}\right)d\zeta.$$

With $\widetilde{\mathbf{H}}=\mathbf{M}_0^{-1}\widetilde{\mathbf{W}}$ and using again the expressions of $\mathbf{a}$ and $\mathbf{w}$, we obtain

$$\begin{aligned}\mathbf{a}-\mathbf{F}^{-T}\widetilde{\mathbf{H}}\mathbf{w} &= \mathbf{F}^{-T}(\widetilde{\mathbf{H}}\mathbf{u}_{\mathcal{S}}+\mathrm{Grad}\,\mathcal{U}-\widetilde{\mathbf{H}}\mathbf{w})\\ &= \mathbf{F}^{-T}\left(\zeta\widetilde{\mathbf{H}}(\mathbf{I}-\zeta\widetilde{\mathbf{W}})^{-1}\mathbf{M}_0+\mathbf{I}\right)\mathrm{Grad}\,\mathcal{U}\\ &= \mathbf{F}^{-T}\left(\zeta\mathbf{M}_0^{-1}\widetilde{\mathbf{W}}(\mathbf{I}-\zeta\widetilde{\mathbf{W}})^{-1}\mathbf{M}_0+\mathbf{I}\right)\mathrm{Grad}\,\mathcal{U}\\ &= \mathbf{F}^{-T}\mathbf{M}_0^{-1}\left(\zeta\widetilde{\mathbf{W}}(\mathbf{I}-\zeta\widetilde{\mathbf{W}})^{-1}+\mathbf{I}\right)\mathbf{M}_0\mathrm{Grad}\,\mathcal{U}\\ &= \mathbf{F}^{-T}\mathbf{M}_0^{-1}\left(\zeta\widetilde{\mathbf{W}}(\mathbf{I}-\zeta\widetilde{\mathbf{W}})^{-1}+(\mathbf{I}-\zeta\widetilde{\mathbf{W}})(\mathbf{I}-\zeta\widetilde{\mathbf{W}})^{-1}\right)\mathbf{M}_0\mathrm{Grad}\,\mathcal{U}\\ &= \mathbf{F}^{-T}\mathbf{M}_0^{-1}(\mathbf{I}-\zeta\widetilde{\mathbf{W}})^{-1}\mathbf{M}_0\mathrm{Grad}\,\mathcal{U}\\ &= \left(\mathbf{I}+\frac{1}{c^2}\mathbf{s}\otimes\mathbf{s}\right)\mathbf{F}(\mathbf{I}-\zeta\widetilde{\mathbf{W}})^{-1}\mathbf{M}_0\mathrm{Grad}\,\mathcal{U},\end{aligned}$$

so that

$$②+④ = c\left(\mathbf{I}+\frac{1}{c^2}\mathbf{s}\otimes\mathbf{s}\right)\mathbf{F}\left\{\int_0^h J\mathrm{v}\,(\mathbf{I}-\zeta\widetilde{\mathbf{W}})^{-1}\,d\zeta\right\}\mathbf{M}_0\mathrm{Grad}\,\mathcal{U}.$$

Equation (A.31) therefore becomes

$$
\begin{aligned}
c\left(\mathbf{I}+\frac{1}{c^2}\mathbf{s}\otimes\mathbf{s}\right)\left\{\frac{\partial}{\partial t}\int_0^h J\mathbf{B}\mathbf{v}\,d\zeta+\operatorname{Div}\mathbf{X}\right\}&\\
=-\frac{1}{c}\left\{\left(\int_0^h J\mathbf{B}(\mathbf{v}\otimes\mathbf{v}-\mathbf{T})\,d\zeta\right)\cdot\mathbf{F}^{-T}\widetilde{\mathbf{H}}\right\}\mathbf{s}&\\
+c\,\mathbf{F}^{-T}\widetilde{\mathbf{H}}\int_0^h J\,(\mathrm{v}\mathbf{v}-\mathbf{t})\,d\zeta-\frac{1}{c}\left\{\left(\int_0^h J\mathbf{v}\,d\zeta\right)\cdot\operatorname{Grad}\mathcal{U}\right\}\mathbf{s}&\\
+c\left(\mathbf{I}+\frac{1}{c^2}\mathbf{s}\otimes\mathbf{s}\right)\mathbf{F}\left\{\int_0^h J\mathrm{v}\,(\mathbf{I}-\zeta\widetilde{\mathbf{W}})^{-1}\,d\zeta\right\}\mathbf{M}_0\operatorname{Grad}\mathcal{U}&\\
+c\left(\mathbf{I}+\frac{1}{c^2}\mathbf{s}\otimes\mathbf{s}\right)\left\{-J_0\frac{\rho_b}{\rho_0}\mathcal{U}\mathbf{F}\mathbf{v}\Big|_{\zeta=0}+J_0\mathbf{F}\mathbf{f}_b\right\}-\left(\int_0^h J\,d\zeta\right)\mathbf{s}.&
\end{aligned}
\tag{A.32}
$$

The last step in proving Eq. (4.109) consists in multiplying (A.31) by $(1/c)(\mathbf{I}-\mathbf{s}\otimes\mathbf{s})$, $\mathbf{I}-\mathbf{s}\otimes\mathbf{s}$ being the inverse matrix of (A.12). We obtain

$$
\begin{aligned}
\frac{\partial}{\partial t}\int_0^h J\mathbf{B}\mathbf{v}\,d\zeta+\operatorname{Div}\int_0^h J\mathbf{B}\left(\mathbf{v}\otimes(\mathbf{v}-\mathbf{w})-\mathbf{T}\right)\,d\zeta&\\
=-\left\{\left(\int_0^h J\mathbf{B}(\mathbf{v}\otimes\mathbf{v}-\mathbf{T})\,d\zeta\right)\cdot\mathbf{F}^{-T}\widetilde{\mathbf{H}}\right\}\mathbf{s}&\\
+\mathbf{F}\widetilde{\mathbf{W}}\int_0^h J\,(\mathrm{v}\mathbf{v}-\mathbf{t})\,d\zeta-\left\{\left(\int_0^h J\mathbf{v}\,d\zeta\right)\cdot\operatorname{Grad}\mathcal{U}\right\}\mathbf{s}&\\
-c\left(\int_0^h J\,d\zeta\right)\mathbf{s}+\mathbf{F}\left\{\int_0^h J\mathrm{v}(\mathbf{I}-\zeta\widetilde{\mathbf{W}})^{-1}\,d\zeta\right\}\mathbf{M}_0\operatorname{Grad}\mathcal{U}&\\
-J_0\frac{\rho_b}{\rho_0}\mathcal{U}\mathbf{F}\mathbf{v}\Big|_{\zeta=0}+J_0\mathbf{F}\mathbf{f}_b.&
\end{aligned}
\tag{A.33}
$$

Expressing the stress components $\mathbf{T}$, $\mathbf{t}$ as $\mathbf{T}=-p\mathbf{M}+\mathbf{P}$ and $\mathbf{t}=\mathbf{p}$, see (3.59), we can conclude that (A.33) is exactly relation (4.109) which we wanted to show.

A.4 Another Proof of the Depth-Integrated Hybrid Linear Momentum Balance Equation (4.109)

There is another way to prove (4.109). The idea is to multiply the tangential linear momentum balance equation (4.44) from the left by $\mathbf{B}$ and then integrate the emerging relation from 0 to h. Thus, the multiplication of (4.44) by $\mathbf{B}$ and the use of (A.20) yield

$$\begin{aligned}
&\frac{\partial}{\partial t}\{J\mathbf{B}\mathrm{v}\}+\mathrm{Div}\left\{J\,\mathbf{B}\left(\mathrm{v}\otimes(\mathrm{v}-\mathbf{w})-\mathbf{T}\right)\right\}+\frac{\partial}{\partial\zeta}\left\{J\,\mathbf{B}\left((\mathrm{v}-\mathcal{U})\mathrm{v}-\mathbf{p}\right)\right\}\\
&=J\underbrace{\frac{\partial\mathbf{B}}{\partial t}\mathrm{v}}_{①}+J\underbrace{\frac{\partial\mathbf{B}}{\partial\xi^\alpha}\left(\mathrm{v}\otimes(\mathrm{v}-\mathbf{w})-\mathbf{T}\right)\mathbf{e}_\alpha}_{②}\\
&\quad+J\underbrace{\frac{\partial\mathbf{B}}{\partial\zeta}\left((\mathrm{v}-\mathcal{U})\mathrm{v}-\mathbf{p}\right)}_{③}-J\underbrace{\left(\mathbf{B}\boldsymbol{\Gamma}(-p\,\mathbf{M},\mathbf{0})+\mathbf{B}\boldsymbol{\Gamma}(\mathbf{P},\mathbf{p})\right)}_{④}\\
&\quad+J\underbrace{\mathbf{B}\mathbf{b}}_{⑤}+J\underbrace{\mathbf{B}\boldsymbol{\Gamma}(\mathrm{v},\mathrm{v})}_{⑥}-J\underbrace{\mathbf{B}(\mathrm{Grad}\,\mathbf{w})\mathrm{v}}_{⑦}-J\mathrm{v}\underbrace{\mathbf{B}\frac{\partial\mathbf{w}}{\partial\zeta}}_{⑧}.
\end{aligned}\tag{A.34}$$

We compute the circled terms. First, we recall that

$$\mathbf{B}=\mathbf{F}(\mathbf{I}-\zeta\widetilde{\mathbf{W}})=\mathbf{F}-\zeta\mathbf{F}\widetilde{\mathbf{W}}=\mathbf{F}-\zeta\mathrm{Grad}\,\mathbf{s},$$

see (2.51), and

$$\begin{aligned}
&\frac{\partial\mathbf{F}}{\partial t}=\mathrm{Grad}\,\mathbf{v}_{\mathcal{S}}=\mathrm{Grad}\,(\mathbf{F}\mathbf{u}_{\mathcal{S}}-\mathcal{U}\mathbf{s}),\\
&\frac{\partial\mathbf{s}}{\partial t}=\mathbf{F}\widetilde{\mathbf{W}}\mathbf{u}_{\mathcal{S}}+\mathbf{F}\mathbf{M}_0\mathrm{Grad}\,\mathcal{U},\\
&\mathbf{w}=\mathbf{u}_{\mathcal{S}}-\zeta(\mathbf{I}-\zeta\widetilde{\mathbf{W}})^{-1}\mathbf{M}_0\mathrm{Grad}\,\mathcal{U},
\end{aligned}$$

see $(2.66)_1$, (2.69), Exercise 2.8 and (2.110). Now, using formulae (1.14) and (1.16), we have

$$\begin{aligned}
\frac{\partial\mathbf{B}}{\partial t}&=\frac{\partial\mathbf{F}}{\partial t}-\zeta\mathrm{Grad}\,\frac{\partial\mathbf{s}}{\partial t}=\mathrm{Grad}\,(\mathbf{F}\mathbf{u}_{\mathcal{S}}-\mathcal{U}\mathbf{s})-\zeta\mathrm{Grad}\,\frac{\partial\mathbf{s}}{\partial t}\\
&=\mathrm{Grad}\,\left(\mathbf{F}\mathbf{u}_{\mathcal{S}}-\mathcal{U}\mathbf{s}-\zeta(\mathbf{F}\widetilde{\mathbf{W}}\mathbf{u}_{\mathcal{S}}+\mathbf{F}\mathbf{M}_0\mathrm{Grad}\,\mathcal{U})\right)\\
&=\mathrm{Grad}\,\left(\mathbf{B}\mathbf{u}_{\mathcal{S}}-\mathcal{U}\mathbf{s}-\zeta\mathbf{F}\mathbf{M}_0\mathrm{Grad}\,\mathcal{U}\right)=\mathrm{Grad}\,\left(\mathbf{B}\mathbf{w}-\mathcal{U}\mathbf{s}\right)\\
&=\mathbf{B}\mathrm{Grad}\,\mathbf{w}+\frac{\partial\mathbf{B}}{\partial\xi^\alpha}\mathbf{w}\otimes\mathbf{e}_\alpha-\mathcal{U}\mathrm{Grad}\,\mathbf{s}-\mathbf{s}\otimes\mathrm{Grad}\,\mathcal{U}\\
&=\mathbf{B}\mathrm{Grad}\,\mathbf{w}+\frac{\partial\mathbf{B}}{\partial\xi^\alpha}\mathbf{w}\otimes\mathbf{e}_\alpha-\mathcal{U}\mathbf{F}\widetilde{\mathbf{W}}-\mathbf{s}\otimes\mathrm{Grad}\,\mathcal{U},
\end{aligned}$$

so that

$$\begin{aligned}
①-⑦&=\frac{\partial\mathbf{B}}{\partial\xi^\alpha}(\mathbf{w}\otimes\mathbf{e}_\alpha)\,\mathbf{v}-\mathcal{U}\mathbf{F}\widetilde{\mathbf{W}}\mathbf{v}-(\mathbf{v}\cdot\mathrm{Grad}\,\mathcal{U})\,\mathbf{s}\\
&=\frac{\partial\mathbf{B}}{\partial\xi^\alpha}(\mathbf{w}\otimes\mathbf{v})\,\mathbf{e}_\alpha-\mathcal{U}\mathbf{F}\widetilde{\mathbf{W}}\mathbf{v}-(\mathbf{v}\cdot\mathrm{Grad}\,\mathcal{U})\,\mathbf{s}.
\end{aligned}$$

Next,

$$②=\frac{\partial\mathbf{B}}{\partial\xi^\alpha}(\mathbf{v}\otimes\mathbf{v})\mathbf{e}_\alpha-\frac{\partial\mathbf{B}}{\partial\xi^\alpha}(\mathbf{v}\otimes\mathbf{w})\mathbf{e}_\alpha-\frac{\partial\mathbf{B}}{\partial\xi^\alpha}\mathbf{T}\,\mathbf{e}_\alpha,$$

and

$$③ = -\mathbf{F}\widetilde{\mathbf{W}}\left((\mathrm{v}-\mathcal{U})\mathbf{v}-\mathbf{p}\right) = -\mathbf{F}\widetilde{\mathbf{W}}\,(\mathrm{v}\mathbf{v}-\mathbf{p}\,)+\mathcal{U}\mathbf{F}\widetilde{\mathbf{W}}\mathbf{v}.$$

Then, relying on definitions (4.32) and (4.33) of $\boldsymbol{\Gamma}(-p\,\mathbf{M},\mathbf{0})$ and $\boldsymbol{\Gamma}(\mathbf{P},\mathbf{p})$, respectively, we deduce

$$\begin{aligned} ④ &= p\left\{\frac{\partial \mathbf{B}}{\partial \xi^\alpha}\,\mathbf{M}\mathbf{e}_\alpha + \mathrm{tr}\,(\widetilde{\mathbf{W}}(\mathbf{I}-\zeta\widetilde{\mathbf{W}})^{-1})\,\mathbf{s}\right\} - \frac{\partial \mathbf{B}}{\partial \xi^\alpha}\,\mathbf{P}\mathbf{e}_\alpha + 2\mathbf{F}\widetilde{\mathbf{W}}\mathbf{p} + \Gamma(\mathbf{P})\mathbf{s} \\ &= -\frac{\partial \mathbf{B}}{\partial \xi^\alpha}\,\mathbf{T}\mathbf{e}_\alpha + \left\{p\left(\widetilde{\mathbf{W}}\cdot(\mathbf{I}-\zeta\widetilde{\mathbf{W}})^{-T}\right) + \Gamma(\mathbf{P})\right\}\mathbf{s} + 2\mathbf{F}\widetilde{\mathbf{W}}\mathbf{p}. \end{aligned}$$

Furthermore, we use

$$\Gamma(\mathbf{P}) \equiv -\mathbf{B}^T\mathbf{F}^{-T}\widetilde{\mathbf{H}}\cdot\mathbf{P} = -\mathbf{B}\mathbf{P}\cdot\mathbf{F}^{-T}\widetilde{\mathbf{H}},$$

see (4.35), and, with definition (2.86) of $\mathbf{M}$,

$$\begin{aligned} \widetilde{\mathbf{W}}\cdot(\mathbf{I}-\zeta\widetilde{\mathbf{W}})^{-T} &= \mathbf{M}_0\widetilde{\mathbf{H}}\cdot(\mathbf{I}-\zeta\widetilde{\mathbf{W}})^{-T} = \widetilde{\mathbf{H}}\cdot\mathbf{M}_0(\mathbf{I}-\zeta\widetilde{\mathbf{W}})^{-T} \\ &= \widetilde{\mathbf{H}}\cdot(\mathbf{I}-\zeta\widetilde{\mathbf{W}})\mathbf{M} = \widetilde{\mathbf{H}}\cdot\mathbf{F}^{-1}\mathbf{B}\mathbf{M} = \mathbf{B}\mathbf{M}\cdot\mathbf{F}^{-T}\widetilde{\mathbf{H}}, \end{aligned}$$

to obtain

$$④ = -\frac{\partial \mathbf{B}}{\partial \xi^\alpha}\,\mathbf{T}\mathbf{e}_\alpha - (\mathbf{B}\mathbf{T}\cdot\mathbf{F}^{-T}\widetilde{\mathbf{H}})\,\mathbf{s} + 2\mathbf{F}\widetilde{\mathbf{W}}\mathbf{p}.$$

Now, accounting for (4.36), we easily get

$$⑤ = \mathbf{B}(-c\mathbf{B}^{-1}\mathbf{s}\,) = -c\,\mathbf{s}.$$

Then, definitions (4.34) and (4.35) of $\boldsymbol{\Gamma}(\mathbf{v},\mathrm{v})$ and $\Gamma(\mathbf{v})$, respectively, yield

$$\begin{aligned} ⑥ &= -\frac{\partial \mathbf{B}}{\partial \xi^\alpha}\,(\mathbf{v}\otimes\mathbf{v})\mathbf{e}_\alpha + 2\mathrm{v}\mathbf{F}\widetilde{\mathbf{W}}\mathbf{v} + \Gamma(\mathbf{v})\,\mathbf{s} \\ &= -\frac{\partial \mathbf{B}}{\partial \xi^\alpha}\,(\mathbf{v}\otimes\mathbf{v})\mathbf{e}_\alpha + 2\mathrm{v}\mathbf{F}\widetilde{\mathbf{W}}\mathbf{v} - \left(\mathbf{B}(\mathbf{v}\otimes\mathbf{v})\cdot\mathbf{F}^{-T}\widetilde{\mathbf{H}}\right)\,\mathbf{s}. \end{aligned}$$

Finally, we compute ⑧ as follows:

$$\begin{aligned} ⑧ &= \mathbf{B}\frac{\partial \mathbf{w}}{\partial \zeta} = \frac{\partial \mathbf{B}\mathbf{w}}{\partial \zeta} - \frac{\partial \mathbf{B}}{\partial \zeta}\mathbf{w} = \frac{\partial}{\partial \zeta}\,(\mathbf{B}\mathbf{u}_{\mathcal{S}} - \zeta\mathbf{F}\mathbf{M}_0\mathrm{Grad}\,\mathcal{U}) + \mathbf{F}\widetilde{\mathbf{W}}\mathbf{w} \\ &= -\mathbf{F}\widetilde{\mathbf{W}}\mathbf{u}_{\mathcal{S}} - \mathbf{F}\mathbf{M}_0\mathrm{Grad}\,\mathcal{U} + \mathbf{F}\widetilde{\mathbf{W}}\mathbf{w} = -\mathbf{F}\mathbf{M}_0\mathrm{Grad}\,\mathcal{U} + \mathbf{F}\widetilde{\mathbf{W}}(\mathbf{w}-\mathbf{u}_{\mathcal{S}}) \\ &= -\mathbf{F}\mathbf{M}_0\mathrm{Grad}\,\mathcal{U} - \zeta\mathbf{F}\widetilde{\mathbf{W}}(\mathbf{I}-\zeta\widetilde{\mathbf{W}})^{-1}\mathbf{M}_0\mathrm{Grad}\,\mathcal{U} \\ &= -\mathbf{F}\left\{\mathbf{I}+\zeta\widetilde{\mathbf{W}}(\mathbf{I}-\zeta\widetilde{\mathbf{W}})^{-1}\right\}\mathbf{M}_0\mathrm{Grad}\,\mathcal{U} \\ &= -\mathbf{F}\left\{(\mathbf{I}-\zeta\widetilde{\mathbf{W}})(\mathbf{I}-\zeta\widetilde{\mathbf{W}})^{-1} + \zeta\widetilde{\mathbf{W}}(\mathbf{I}-\zeta\widetilde{\mathbf{W}})^{-1}\right\}\mathbf{M}_0\mathrm{Grad}\,\mathcal{U} \\ &= -\mathbf{F}(\mathbf{I}-\zeta\widetilde{\mathbf{W}})^{-1}\mathbf{M}_0\mathrm{Grad}\,\mathcal{U}. \end{aligned}$$

Now, we substitute the circled quantities in (A.34) with the results above and obtain the intermediate result

$$\begin{aligned}\frac{\partial}{\partial t}\{J\mathbf{B}\mathrm{v}\}+\mathrm{Div}\left\{J\mathbf{B}\left(\mathbf{v}\otimes(\mathbf{v}-\mathbf{w})-\mathbf{T}\right)\right\}+\frac{\partial}{\partial\zeta}\left\{J\mathbf{B}\left((\mathrm{v}-\mathcal{U})\mathbf{v}-\mathbf{p}\right)\right\}\\ =-J\left\{\mathbf{B}(\mathbf{v}\otimes\mathbf{v}-\mathbf{T})\cdot\mathbf{F}^{-T}\widetilde{\mathbf{H}}\right\}\mathbf{s}+J\mathbf{F}\widetilde{\mathbf{W}}(\mathrm{v}\mathbf{v}-\mathbf{p})\\ -J(\mathbf{v}\cdot\mathrm{Grad}\,\mathcal{U})\,\mathbf{s}-Jc\,\mathbf{s}+J\mathrm{v}\mathbf{F}(\mathbf{I}-\zeta\widetilde{\mathbf{W}})^{-1}\mathbf{M}_0\mathrm{Grad}\,\mathcal{U}\\ +\underbrace{J\frac{\partial\mathbf{B}}{\partial\xi^\alpha}(\mathbf{w}\otimes\mathbf{v}-\mathbf{v}\otimes\mathbf{w})\mathbf{e}_\alpha}.\end{aligned}\tag{A.35}$$

We prove that the underbraced term above vanishes. Indeed,

$$\frac{\partial\mathbf{B}}{\partial\xi^\alpha}=\frac{\partial\mathbf{F}}{\partial\xi^\alpha}-\zeta\frac{\partial\mathbf{F}\widetilde{\mathbf{W}}}{\partial\xi^\alpha}=\frac{\partial\mathbf{F}}{\partial\xi^\alpha}-\zeta\frac{\partial\mathrm{Grad}\,\mathbf{s}}{\partial\xi^\alpha},$$

and both $\mathbf{F}$ and $\mathrm{Grad}\,\mathbf{s}$ enjoy the property (1.18). Therefore, it follows from (1.19) that

$$\frac{\partial\mathbf{B}}{\partial\xi^\alpha}(\mathbf{w}\otimes\mathbf{v}-\mathbf{v}\otimes\mathbf{w})\mathbf{e}_\alpha=\mathbf{0},$$

and with this Eq. (A.35) becomes

$$\begin{aligned}&\frac{\partial}{\partial t}\{J\mathbf{B}\mathrm{v}\}+\mathrm{Div}\left\{J\mathbf{B}\left(\mathbf{v}\otimes(\mathbf{v}-\mathbf{w})-\mathbf{T}\right)\right\}+\frac{\partial}{\partial\zeta}\left\{J\mathbf{B}\left((\mathrm{v}-\mathcal{U})\mathbf{v}-\mathbf{p}\right)\right\}\\ &=-J\left\{\mathbf{B}(\mathbf{v}\otimes\mathbf{v}-\mathbf{T})\cdot\mathbf{F}^{-T}\widetilde{\mathbf{H}}\right\}\mathbf{s}+J\mathbf{F}\widetilde{\mathbf{W}}(\mathrm{v}\mathbf{v}-\mathbf{p})\\ &\quad-J(\mathbf{v}\cdot\mathrm{Grad}\,\mathcal{U})\mathbf{s}-Jc\,\mathbf{s}+J\mathrm{v}\mathbf{F}(\mathbf{I}-\zeta\widetilde{\mathbf{W}})^{-1}\mathbf{M}_0\mathrm{Grad}\,\mathcal{U}.\end{aligned}\tag{A.36}$$

Now, one integrates (A.36) from 0 to h. Using the Leibniz rules (4.56) and boundary conditions (4.46), (4.38), (4.47) and (4.40), one proves Eq. (4.109).

A.5 Proof of the Modelling Equation (4.111)

Derivation of the following asymptotic expansions is similar to the derivation of the asymptotic expansions from Appendix A.1:

$$J\mathbf{B}\mathbf{v}=J_0\mathbf{F}\left\{\mathbf{v}-(2\Omega\mathbf{I}+\widetilde{\mathbf{W}})(\zeta\mathbf{v})\right\}+O(\epsilon^2),\tag{A.37a}$$

$$\begin{aligned}&J\mathbf{B}\left(\mathbf{v}\otimes(\mathbf{v}-\mathbf{w})+p\mathbf{M}-\mathbf{P}\right)\\ &=J_0\mathbf{F}\Big\{(\mathbf{v}\otimes\mathbf{v})-\mathbf{v}\otimes\mathbf{u}_{\mathcal{S}}-(2\Omega\mathbf{I}+\widetilde{\mathbf{W}})\left((\zeta\mathbf{v}\otimes\mathbf{v})-(\zeta\mathbf{v})\otimes\mathbf{u}_{\mathcal{S}}\right)\\ &\qquad+p\,\mathbf{M}_0-\mathbf{P}\Big\}+O(\epsilon^2),\end{aligned}\tag{A.37b}$$

$$J\mathbf{B}\left(\mathbf{v}\otimes\mathbf{v}+p\mathbf{M}-\mathbf{P}\right) = J_0\mathbf{F}\left\{(\mathbf{v}\otimes\mathbf{v})-(2\Omega\mathbf{I}+\widetilde{\mathbf{W}})(\zeta\mathbf{v}\otimes\mathbf{v})+p\mathbf{M}_0-\mathbf{P}\right\}+O(\epsilon^2), \tag{A.37c}$$

$$J\,(\mathrm{v}\mathbf{v}-\mathbf{p}) = J_0\,(\mathrm{v}\mathbf{v}-\mathbf{p})+O(\epsilon^{1+\gamma}), \tag{A.37d}$$

$$J\mathbf{v}\cdot\mathrm{Grad}\,\mathcal{U} = J_0\mathbf{v}\cdot\mathrm{Grad}\,\mathcal{U}+O(\epsilon^2), \tag{A.37e}$$

$$J = J_0(1-2\Omega\zeta)+O(\epsilon^2), \tag{A.37f}$$

$$J\mathrm{v}\mathbf{F}(\mathbf{I}-\zeta\widetilde{\mathbf{W}})^{-1}\mathbf{M}_0\mathrm{Grad}\,\mathcal{U} = O(\epsilon^2). \tag{A.37g}$$

We depth-integrate the preceding relations and obtain

$$\begin{aligned}\int_0^h J\mathbf{B}\mathbf{v}\,d\zeta &= J_0\mathbf{F}\left[h\overline{\mathbf{v}}-(2\Omega\mathbf{I}+\widetilde{\mathbf{W}})\tfrac{1}{2}m_1h^2\overline{\mathbf{v}}\right]+O(\epsilon^{2+\gamma})\\ &= J_0h\mathbf{F}\left[(1-m_1\Omega h)\overline{\mathbf{v}}-\tfrac{1}{2}m_1h\widetilde{\mathbf{W}}\overline{\mathbf{v}}\right]+O(\epsilon^{2+\gamma}),\end{aligned} \tag{A.38a}$$

$$\begin{aligned}&\int_0^h J\mathbf{B}\left(\mathbf{v}\otimes(\mathbf{v}-\mathbf{w})+p\mathbf{M}-\mathbf{P}\right)d\zeta\\ &= J_0\mathbf{F}\Big\{m_2h(\overline{\mathbf{v}}\otimes\overline{\mathbf{v}})-h(\overline{\mathbf{v}}\otimes\mathbf{u}_{\mathcal{S}})+h\,\overline{p}\,\mathbf{M}_0-h\overline{\mathbf{P}}\\ &\quad-(2\Omega\mathbf{I}+\widetilde{\mathbf{W}})\left[\tfrac{1}{2}m_3h^2(\overline{\mathbf{v}}\otimes\overline{\mathbf{v}})-\tfrac{1}{2}m_1h^2(\overline{\mathbf{v}}\otimes\mathbf{u}_{\mathcal{S}})\right]\Big\}+O(\epsilon^{2+\gamma})\\ &= J_0h\mathbf{F}\Big[(m_2-m_3\Omega h)(\overline{\mathbf{v}}\otimes\overline{\mathbf{v}})-(1-m_1\Omega h)(\overline{\mathbf{v}}\otimes\mathbf{u}_{\mathcal{S}})\\ &\quad+\overline{p}\,\mathbf{M}_0-\overline{\mathbf{P}}-\tfrac{1}{2}h\widetilde{\mathbf{W}}\overline{\mathbf{v}}\otimes(m_3\overline{\mathbf{v}}-m_1\mathbf{u}_{\mathcal{S}})\Big]+O(\epsilon^{2+\gamma}),\end{aligned} \tag{A.38b}$$

$$\begin{aligned}&\int_0^h J\mathbf{B}\left(\mathbf{v}\otimes\mathbf{v}+p\mathbf{M}-\mathbf{P}\right)d\zeta\\ &\quad= J_0h\mathbf{F}\left\{(m_2-m_3\Omega h)(\overline{\mathbf{v}}\otimes\overline{\mathbf{v}})+\overline{p}\,\mathbf{M}_0-\overline{\mathbf{P}}-\tfrac{1}{2}m_3h\widetilde{\mathbf{W}}\overline{\mathbf{v}}\otimes\overline{\mathbf{v}}\right\}\\ &\qquad\qquad+O(\epsilon^{2+\gamma}),\end{aligned} \tag{A.38c}$$

$$\begin{aligned}&\int_0^h J\,(\mathrm{v}\mathbf{v}-\mathbf{p})\,d\zeta\\ &\quad= J_0h\left\{\left(1-\frac{\rho_b}{\rho_0}\right)\mathcal{U}\overline{\mathbf{v}}+\tfrac{1}{2}\beta h\overline{\mathbf{v}}-\overline{\mathbf{p}}\right\}+O(\epsilon^{2+\gamma}),\end{aligned} \tag{A.38d}$$

$$\int_0^h J\mathbf{v}\cdot\mathrm{Grad}\,\mathcal{U}\,d\zeta = J_0h\overline{\mathbf{v}}\cdot\mathrm{Grad}\,\mathcal{U}+O(\epsilon^3), \tag{A.38e}$$

$$\int_0^h J\,d\zeta = J_0h(1-\Omega h)+O(\epsilon^3). \tag{A.38f}$$

Inserting (A.38) into (4.109) and using the flow rule approximations to cancel the last integral in (4.109) we deduce

$$\begin{aligned}
&\frac{\partial}{\partial t}\left\{J_0 h\mathbf{F}\left[(1-m_1\Omega h)\overline{\mathbf{v}}-\tfrac{1}{2}m_1 h\widetilde{\mathbf{W}}\,\overline{\mathbf{v}}\right]\right\}\\
&\quad+\mathrm{Div}\left\{J_0 h\mathbf{F}\Big[(m_2-m_3\Omega h)\overline{\mathbf{v}}\otimes\overline{\mathbf{v}}+\overline{p}\,\mathbf{M}_0-\overline{\mathbf{P}}\right.\\
&\qquad\left.-(1-m_1\Omega h)\overline{\mathbf{v}}\otimes\mathbf{u}_{\mathcal{S}}-\tfrac{1}{2}h\widetilde{\mathbf{W}}\,\overline{\mathbf{v}}\otimes(m_3\overline{\mathbf{v}}-m_1\mathbf{u}_{\mathcal{S}})\Big]\right\}\\
&=-J_0 h\left\{\Big[(m_2-m_3\Omega h)\overline{\mathbf{v}}\otimes\overline{\mathbf{v}}+\overline{p}\,\mathbf{M}_0-\overline{\mathbf{P}}\right.\\
&\qquad\left.-\tfrac{1}{2}m_3 h\widetilde{\mathbf{W}}\,\overline{\mathbf{v}}\otimes\overline{\mathbf{v}}\Big]\cdot\widetilde{\mathbf{H}}\right\}\mathbf{s}\\
&\quad+J_0 h\mathbf{F}\widetilde{\mathbf{W}}\left(\tfrac{1}{2}\beta h\overline{\mathbf{v}}-\overline{\mathbf{p}}\right)-J_0 h(\overline{\mathbf{v}}\cdot\mathrm{Grad}\,\mathcal{U})\,\mathbf{s}-J_0 hc(1-\Omega h)\,\mathbf{s}\\
&\quad-J_0\frac{\rho_b}{\rho_0}\mathcal{U}\mathbf{F}\mathbf{v}\Big|_{\zeta=0}-J_0\mathbf{F}\mathbf{v}\Big|_{\zeta=0}.
\end{aligned}\tag{A.39}$$

Furthermore, expression (4.91) of $\overline{p}$ and

$$\begin{aligned}
&\mathbf{M}_0\cdot\widetilde{\mathbf{H}}=\mathrm{tr}\,(\mathbf{M}_0\widetilde{\mathbf{H}})=\mathrm{tr}\,\widetilde{\mathbf{W}}=2\Omega,\\
&(\overline{\mathbf{v}}\otimes\overline{\mathbf{v}})\cdot\widetilde{\mathbf{H}}=\widetilde{\mathbf{H}}\overline{\mathbf{v}}\cdot\overline{\mathbf{v}}\equiv a,\qquad\left(\widetilde{\mathbf{W}}\,\overline{\mathbf{v}}\otimes\overline{\mathbf{v}}\right)\cdot\widetilde{\mathbf{H}}=\widetilde{\mathbf{W}}\,\overline{\mathbf{v}}\cdot\widetilde{\mathbf{H}}\overline{\mathbf{v}}\equiv\tilde{a},
\end{aligned}$$

turn Eq. (A.39) into (4.111), which we wanted to show.

References

1. I. Luca, K. Hutter, C.Y. Kuo, Y.C. Tai, Two-layer models for shallow avalanche flows over arbitrary variable topography. Int. J. Adv. Eng. Sci. Appl. Math. **1**, 99–121 (2009)
2. K. Hutter, I. Luca, Two-layer debris mixture flows on arbitrary terrain with mass exchange at the base and the interface. Continuum Mech. Thermodyn. **24**(4–6), 525–558 (2012)

Solutions

Solutions to Exercises in Chap. (2)

2.1 From the definitions of $\boldsymbol{\tau}_\alpha$, $\tilde{\boldsymbol{\tau}}_\alpha$, $\mathbf{F}$ we have

$$\tilde{\boldsymbol{\tau}}_\alpha = \frac{\partial \tilde{\boldsymbol{r}}}{\partial \xi^\alpha} = \frac{\partial \boldsymbol{r}}{\partial \Delta^\gamma}\,\frac{\partial \Delta^\gamma}{\partial \xi^\alpha} = F_{\gamma\alpha}\boldsymbol{\tau}_\gamma, \tag{\$-1}$$

so that

$$\begin{aligned}\tilde{\phi}_{\alpha\beta} = \tilde{\boldsymbol{\tau}}_\alpha \cdot \tilde{\boldsymbol{\tau}}_\beta = (F_{\gamma\alpha}\boldsymbol{\tau}_\gamma)\cdot(F_{\delta\beta}\boldsymbol{\tau}_\delta) = F_{\gamma\alpha}F_{\delta\beta}(\boldsymbol{\tau}_\gamma\cdot\boldsymbol{\tau}_\delta) = F_{\gamma\alpha}F_{\delta\beta}\,\phi_{\gamma\delta}\\ = F^T_{\alpha\gamma}\,\phi_{\gamma\delta}F_{\delta\beta} = (\mathbf{F}^T(\phi_{\gamma\delta})\mathbf{F})_{\alpha\beta},\end{aligned}$$

showing $(2.17)_1$. Next,

$$\begin{aligned}\tilde{b}_{\alpha\beta} = -\tilde{\boldsymbol{\tau}}_\alpha\cdot\frac{\partial \boldsymbol{n}}{\partial \xi^\beta} = -(F_{\gamma\alpha}\boldsymbol{\tau}_\gamma)\cdot\left(\frac{\partial \boldsymbol{n}}{\partial \Delta^\delta}\frac{\partial \Delta^\delta}{\partial \xi^\beta}\right) = -F_{\gamma\alpha}F_{\delta\beta}\left(\boldsymbol{\tau}_\gamma\cdot\frac{\partial \boldsymbol{n}}{\partial \Delta^\delta}\right)\\ = F_{\gamma\alpha}F_{\delta\beta}b_{\gamma\delta} = F^T_{\alpha\gamma}b_{\gamma\delta}F_{\delta\beta} = (\mathbf{F}^T(b_{\gamma\delta})\mathbf{F})_{\alpha\beta},\end{aligned}$$

that is, $(2.17)_2$. Formula $(2.17)_3$ can be easily deduced by using $(2.17)_{1,2}$ as follows:

$$\begin{aligned}\widetilde{\mathbf{W}} = (\tilde{\phi}^{\alpha\gamma})(\tilde{b}_{\gamma\beta}) = (\tilde{\phi}_{\alpha\gamma})^{-1}(\tilde{b}_{\gamma\beta}) = (\mathbf{F}^T(\phi_{\alpha\gamma})\mathbf{F})^{-1}\mathbf{F}^T(b_{\gamma\beta})\mathbf{F}\\ = \mathbf{F}^{-1}(\phi_{\alpha\gamma})^{-1}(b_{\gamma\beta})\mathbf{F} = \mathbf{F}^{-1}(\phi^{\alpha\gamma})(b_{\gamma\beta})\mathbf{F} = \mathbf{F}^{-1}\mathbf{W}\mathbf{F}.\end{aligned}$$

2.2 Here we use (\$-1):

$$\begin{aligned}\tilde{\boldsymbol{\tau}}_1\times\tilde{\boldsymbol{\tau}}_2 = (F_{\alpha1}\boldsymbol{\tau}_\alpha)\times(F_{\beta2}\boldsymbol{\tau}_\beta) = (F_{11}\boldsymbol{\tau}_1 + F_{21}\boldsymbol{\tau}_2)\times(F_{12}\boldsymbol{\tau}_1 + F_{22}\boldsymbol{\tau}_2)\\ = F_{11}F_{22}\,(\boldsymbol{\tau}_1\times\boldsymbol{\tau}_2) + F_{21}F_{12}\,(\boldsymbol{\tau}_2\times\boldsymbol{\tau}_1)\\ = (F_{11}F_{22} - F_{21}F_{12})\,\boldsymbol{\tau}_1\times\boldsymbol{\tau}_2 = (\det\mathbf{F})\,\boldsymbol{\tau}_1\times\boldsymbol{\tau}_2.\end{aligned}$$

I. Luca et al., *Shallow Geophysical Mass Flows down Arbitrary Topography*,
Advances in Geophysical and Environmental Mechanics and Mathematics,
DOI 10.1007/978-3-319-02627-5

2.6 First we deduce the relation between the components σ_{ij} and Σ^{ik} of $\boldsymbol{\sigma}$ in the representations $\boldsymbol{\sigma} = \sigma_{ij}\boldsymbol{e}_i \otimes \boldsymbol{e}_j = \Sigma^{ik}\boldsymbol{e}_i \otimes \boldsymbol{g}_k$. To this end we substitute $\boldsymbol{g}_k = A^{-1}_{jk}\boldsymbol{e}_j$ into the mixed representation, so that we obtain

$$\sigma_{ij}\boldsymbol{e}_i \otimes \boldsymbol{e}_j = \Sigma^{ik}A^{-1}_{jk}\boldsymbol{e}_i \otimes \boldsymbol{e}_j \quad \Longleftrightarrow \quad \sigma_{ij} = \Sigma^{ik}A^{-1}_{jk}. \tag{\$-2}$$

We use this relation in the definition of div $\boldsymbol{\sigma}$ and recall formula (3.10) to deduce that

$$\begin{aligned}\operatorname{div}\boldsymbol{\sigma} &\equiv \frac{\partial \sigma_{ij}}{\partial x_j}\boldsymbol{e}_i = \frac{\partial \sigma_{ij}}{\partial \xi^m}\frac{\partial \xi^m}{\partial x_j}\boldsymbol{e}_i = \frac{\partial}{\partial \xi^m}\left(\Sigma^{ik}A^{-1}_{jk}\right)A_{mj}\boldsymbol{e}_i \\ &= \left\{\frac{\partial \Sigma^{ik}}{\partial \xi^m}A^{-1}_{jk}A_{mj} + \Sigma^{ik}\frac{\partial A^{-1}_{jk}}{\partial \xi^m}A_{mj}\right\}\boldsymbol{e}_i = \left\{\frac{\partial \Sigma^{ik}}{\partial \xi^k} + \Sigma^{ik}A_{mj}\frac{\partial A^{-1}_{jm}}{\partial \xi^k}\right\}\boldsymbol{e}_i \\ &= \left\{\frac{\partial \Sigma^{ik}}{\partial \xi^k} + \Sigma^{ik}\frac{1}{J}\frac{\partial J}{\partial \xi^k}\right\}\boldsymbol{e}_i = \frac{1}{J}\frac{\partial}{\partial \xi^k}\left(J\,\Sigma^{ik}\right)\boldsymbol{e}_i,\end{aligned}$$

which shows (3.11).

2.7 By definition $(2.75)_2$ of $\boldsymbol{A}^{-1}$ and relation $(3.38)_1$ we have

$$\frac{\tilde{\partial}A^{-1}_{jk}}{\partial t} = \frac{\tilde{\partial}}{\partial t}\left(\frac{\partial x_j}{\partial \xi^k}\right) = \frac{\partial}{\partial \xi^k}\left(\frac{\partial x_j}{\partial t}\right) = \frac{\partial w_j}{\partial \xi^k} = \frac{\partial A^{-1}_{jl}w^l}{\partial \xi^k},$$

and consequently, from (3.39) we get

$$\frac{\partial A^{-1}_{jk}}{\partial t} = \frac{\tilde{\partial}A^{-1}_{jk}}{\partial t} - \frac{\partial A^{-1}_{jk}}{\partial \xi^l}w^l = \frac{\partial A^{-1}_{jl}w^l}{\partial \xi^k} - \frac{\partial A^{-1}_{jl}}{\partial \xi^k}w^l = A^{-1}_{jl}\frac{\partial w^l}{\partial \xi^k},$$

which justifies relation (3.70).

2.8 Expressed in the Cartesian basis $\{\boldsymbol{e}_1, \boldsymbol{e}_2, \boldsymbol{e}_3\}$, the unit normal vector $\boldsymbol{n}_b$ to the basal surface is, see (2.36),

$$\boldsymbol{n}_b = -s_1\boldsymbol{e}_1 - s_2\boldsymbol{e}_2 + c\boldsymbol{e}_3,$$

so that

$$\frac{\partial \tilde{\boldsymbol{n}}_b}{\partial t} = -\frac{\partial s_1}{\partial t}\boldsymbol{e}_1 - \frac{\partial s_2}{\partial t}\boldsymbol{e}_2 + \frac{\partial c}{\partial t}\boldsymbol{e}_3. \tag{\$-3}$$

On the other hand, we have

$$\frac{\partial \tilde{\boldsymbol{n}}_b}{\partial t} = a^1\boldsymbol{g}_1 + a^2\boldsymbol{g}_2, \tag{\$-4}$$

see (2.108). The components a^1 and a^2 are shown in formula (2.109), that is,

$$a^\alpha = -g^{\beta\alpha}(\delta^\gamma_{\ \beta} - \zeta\widetilde{W}^\gamma_{\ \beta})\left(\tilde{b}_{\omega\gamma}\mathcal{U}^\omega + \frac{\partial\mathcal{U}}{\partial\xi^\gamma}\right), \quad \alpha = 1,\ 2,$$

or in matrix form,

$$\mathbf{a} \equiv \begin{pmatrix} a^1 \\ a^2 \end{pmatrix} = -\mathbf{M}(\mathbf{I} - \zeta\widetilde{\mathbf{W}})^T(\widetilde{\mathbf{H}}\mathbf{u}_\mathcal{S} + \mathrm{Grad}\,\mathcal{U}). \tag{\$-5}$$

In the above formula we have used

$$\widetilde{\mathbf{H}} \equiv (\tilde{b}_{\alpha\beta}), \quad \mathbf{u}_\mathcal{S} \equiv (\mathcal{U}^1, \mathcal{U}^2)^T, \quad (g^{\alpha\beta}) = \mathbf{M},$$

see $(2.48)_2$, $(2.66)_2$ and $(2.85)_1$, respectively. Now, since the change of basis matrix from $\{\boldsymbol{e}_1, \boldsymbol{e}_2, \boldsymbol{e}_3\}$ to $\{\boldsymbol{g}_1, \boldsymbol{g}_2, \boldsymbol{g}_3\}$ is $\mathbf{A}^{-1}$, the relation between the Cartesian components and the contravariant components of the vector $\partial\tilde{\boldsymbol{n}}_b/\partial t$ is given by

$$\begin{pmatrix} -\dfrac{\partial s_1}{\partial t} \\ -\dfrac{\partial s_2}{\partial t} \\ \dfrac{\partial c}{\partial t} \end{pmatrix} = \mathbf{A}^{-1}\begin{pmatrix} a^1 \\ a^2 \\ 0 \end{pmatrix} \quad \Longleftrightarrow \quad \begin{pmatrix} -\dfrac{\partial \mathbf{s}}{\partial t} \\ \dfrac{\partial c}{\partial t} \end{pmatrix} = \mathbf{A}^{-1}\begin{pmatrix} \mathbf{a} \\ 0 \end{pmatrix}.$$

Using expression (2.80) of $\mathbf{A}^{-1}$, the preceding relation emerges as

$$\frac{\partial \mathbf{s}}{\partial t} = -\mathbf{B}\mathbf{a}, \quad \frac{\partial c}{\partial t} = \frac{1}{c}\mathbf{B}^T\mathbf{s}\cdot\mathbf{a},$$

which, with the aid of (\$-5), can be further written to give the relations stated in Exercise 2.8.

Glossary

ASTM	American Society for Testing and Materials.
CFL	Courant-Friedrichs-Lewy.
DEM	Discrete element method.
DTM	Digital terrain model.
ENO	Essentially non-oscillatory.
GIS	Geographic information systems.
InSAR	Interferometric synthetic aperture radar.
LIDAR	Light detection and ranging.
NOC	Non-oscillatory central.
TVD	Total variation diminishing.
UC	Unified coordinates.
WENO	Weighted essentially non-oscillatory.

I. Luca et al., *Shallow Geophysical Mass Flows down Arbitrary Topography*,
Advances in Geophysical and Environmental Mechanics and Mathematics,
DOI 10.1007/978-3-319-02627-5

Index

I. Luca et al., *Shallow Geophysical Mass Flows down Arbitrary Topography*,
Advances in Geophysical and Environmental Mechanics and Mathematics,
DOI 10.1007/978-3-319-02627-5